UNIVERSITY OF SOUTHAMPTON
Faculty of Physical Sciences and Engineering
School of Electronics and Computer Science
Southampton SO17 1BJ
United Kingdom

Radio Over Fiber Architectures for Optical/Wireless Integration

by

Varghese Antony Thomas
B.E(Honours), M.Sc (Distinction)

A doctoral thesis submitted in partial fulfilment of the
requirements of the award of Doctor of Philosophy
at the University of Southampton

November 2015

SUPERVISORS: 1. Professor Lajos Hanzo
FREng, FIEEE, FIEE, Dsc, EIC IEEE Press
Chair of CSPC
2. Dr Mohammed El-Hajjar
School of Electronics and Computer Science
Faculty of Physical And Applied Sciences
University of Southampton
Southampton SO17 1BJ
United Kingdom

Radio Over Fiber Architectures for Optical/Wireless Integration

by

Varghese Antony Thomas

Abstract

Optical fiber based communication has revolutionized the world of wired communication by providing low-attenuation, high-bandwidth communication channels. The field of Radio Over Fiber (ROF) aims at integrating the world of wireless and optical communication to achieve the common aim of faster and more reliable communication for the end user. It involves transmitting RF signals to and from a BS, which carries out centralised signal processing. These RF signals arrive from and are transmitted to a number of remote antennas, where little or no signal processing is done. The ROF technique employs the high-bandwidth, low-attenuation optical fibers for transmitting signals between the BS and the remote antennas. This technique helps in improving the coverage, cellular capacity, data rates and power efficiency.

This treatise takes the reader from the basics to the state-of-the art techniques in a step-by-step manner. In Chapter 2, the basics of the classical Analog ROF (AROF) link are introduced along with its simulation-based analysis. The discussion of the AROF basics also provides an introduction to the various optical components that are employed both in the basic AROF link of Chapter 2 as well as in the more advanced links discussed in the subsequent chapters. After discussing the basic AROF links found in the current literature, Chapter 2 presents and mathematically characterizes a novel AROF architecture along with a discussion of the results obtained through its simulation. Then, we introduce the concepts behind designing advanced ROF links in Chapter 3. We commence with an extensive study of diverse ROF links that were designed using each of the three approaches discussed in Section 1.5, namely the ROF links employing a) performance improvement techniques, b) cost reduction techniques and c) optical RF-generation techniques. In the the rest of the thesis, we present novel architectures that were designed employing these three approaches. In Chapter 4, we present three novel architectures that employed both cost-reduction as well as optical RF-generation techniques, while Chapter 5 focuses on the benefits of the performance-improvement technique of Digitized ROF (DROF). A simulation based study of the DROF technique and a novel DROF-based architecture are presented in Chapter 5. The DROF technique improves the attainable performance at the cost of an increased link cost. We conclude in Chapter 6 and propose a range of future research ideas. Amongst others, we propose the employment of Plastic Optical Fiber (POF) in a ROF link as a potential direction of future research. Explicitly, as a first step in this direction, we propose to combine the employment of the cost-saving state-of-the-art Plastic Optical Fiber (POF) with the employment of the improved-performance DROF technique in a single ROF link in order to strike an appealing cost-performance tradeoff. Hence, in Chapter 6, we first discuss the basics of POF-based optical communication and then present the novel proposal of a DROF-based ROF link that employs POF. Additionally, we present our conclusions in Chapter 6, where we provide design guidelines for ROF links and also discuss avenues for future research.

Acknowledgments

I would like to take this opportunity to thank my supervisor Prof Lajos Hanzo for introducing me to the interesting research field of radio over fiber communications. Without his continuous support and guidance, I would not have been able to accomplish this formidable task. I would also take this opportunity to thank my second supervisor Dr Mohammed El-Hajjar for his continuous support and guidance.

My sincere thanks are also due to my colleagues Prof. Ana Gracia Armada, Dr Salman Ghafoor, Dr. Dandan Liang, Ateeq Ur Rehman and Suman Kumar for helping and collaborating with me at various stages of my research. I would also like to thank my family and friends, whose constant support was crucial for me, especially during times when the going was tough.

I also extend my heartfelt gratitude to University of Southampton for supporting my studies here. Last but not the least I would like to acknowledge my gratitude to God, without whose grace I would not have been able to complete this task.

Academic Thesis: Declaration Of Authorship

I, **Varghese Antony Thomas**

declare that this thesis and the work presented in it are my own and has been generated by me as the result of my own original research.

Radio Over Fiver Architectures for Optical/Wireless Integration

I confirm that:

1. This work was done wholly or mainly while in candidature for a research degree at this University;
2. Where any part of this thesis has previously been submitted for a degree or any other qualification at this University or any other institution, this has been clearly stated;
3. Where I have consulted the published work of others, this is always clearly attributed;
4. Where I have quoted from the work of others, the source is always given. With the exception of such quotations, this thesis is entirely my own work;
5. I have acknowledged all main sources of help;
6. Where the thesis is based on work done by myself jointly with others, I have made clear exactly what was done by others and what I have contributed myself;
7. Either none of this work has been published before submission, or parts of this work have been published as seen in the list of publications.

Signed: Varghese Antony Thomas

Date:

List of publications

Peer Reviewed Journal Publications

- [1] S. Ghafoor, **V.A. Thomas** and L. Hanzo, "Duplex Digitized Transmission of 64-QAM Signals over a Single Fiber Using a Single Pulsed Laser Source," IEEE Communications Letters, vol.16, no.8, pp.1312-1315, August 2012.

- [2] **V. A. Thomas**, S. Ghafoor, M. El-Hajjar and L. Hanzo, "A Full-Duplex Diversity-Assisted Hybrid Analogue/Digitized Radio Over Fibre for Optical/Wireless Integration," IEEE Communications Letters, vol.17, no.2, pp.409-412, February 2013.

- [3] **V. A. Thomas**, S. Ghafoor, M. El-Hajjar and L. Hanzo, "Baseband Radio over Fiber Aided Millimeter-Wave Distributed Antenna for Optical/Wireless Integration," IEEE Communications Letters, vol.17, no.5, pp.1012-1015, May 2013.

- [4] **V. A. Thomas**, M. El-Hajjar and L. Hanzo, "Performance Improvement and Cost Reduction Techniques For Radio Over Fiber Communications," IEEE Communications Surveys and Tutorials, vol.17, no.2, pp.627-670, January 2015.

- [5] **V. A. Thomas**, M. El-Hajjar and L. Hanzo, "Millimeter-Wave Radio Over Fiber Optical Upconversion Techniques relying on Link Non-Linearity," IEEE Communications Surveys and Tutorials, Early Access, March 2015.

- [6] **V. A. Thomas**, M. El-Hajjar and L. Hanzo, "Simultaneous Optical Phase and Intensity Modulation Transmits Independent Signals in Radio Over Fiber Communication," IEEE Communications Letters, vol.19, no.4, pp.557-560, April 2015.

- [7] **V. A. Thomas**, M. El-Hajjar and L. Hanzo, "Single ODSB Radio-over-fiber signal supports STBC at each RAP," IEEE Communications Letters, vol.19, no.8, pp.1331-1334, May 2015.

- [8] **V. A. Thomas**, M. El-Hajjar and L. Hanzo, "Radio Over Fiber for High Data-Rate Wireless Personal Area Networks," IEEE Microwave Magazine, vol.16, no.9, pp.64-78, October 2015.

- [9] **V. A. Thomas**, M. El-Hajjar and L. Hanzo, "Optical single sideband signal generation relying on a single-drive MZM for radio over fiber communications," (Accepted for publication with minor corrections by IET Communications).

- [10] **V. A. Thomas*** , Dantong Liu* , M. El-Hajjar and L. Hanzo, "Experimental demonstration of plastic optical fibre-based digitised radio over fibre downlink" IET Electronics Letters, vol.51, no.21, pp.1679-1681, August 2015. ($*$- both are co-first authors).

- [11] **V. A. Thomas*** , S. Kumar* , S. Kalyani, M. El-Hajjar, K. Giridhar and L. Hanzo, "Error Vector Magnitude Analysis of Fading SIMO Channels Relying on MRC Reception," (Accepted for publication with major corrections by IEEE Transactions on Communications) ($*$- both are co-first authors).

- [12] S. Kumar*, **V. A. Thomas*** , A.U. Rehman, S. Kalyani, M. El-Hajjar, K. Giridhar and L. Hanzo, "Error Vector Magnitude Analysis of Fading SIMO Channels Relying on Selection Combining," (to be submitted to IEEE Transactions on Vehicular Technology) (∗- both are co-first authors).

- [13] A.U. Rehman, C. Dong, **V. A. Thomas**, L. Liang and L. Hanzo, "Performance of Cognitive Go-back-N Hybrid ARQ Scheme," (Under preparation).

- [14] A.U. Rehman, **V. A. Thomas** , L. Liang and L. Hanzo, "Performance of Cognitive Selective Repeat Hybrid ARQ Scheme," (Under preparation).

Peer Reviewed Conference Publications

- D. Liang, **V.A. Thomas**, X.Xu, S.X. Ng, M. El-Hajjar and L. Hanzo, "Adaptive Soft-Decision Aided Differential Modulation for Cooperative Uplink Transmission Relying on Radio-Over-Fiber Backhaul,"IEEE Vehicular Technology Conference, pp.1-5, September 2014.

- A. G. Armada, **V.A. Thomas**, M. El-Hajjar and L. Hanzo, "Radio-over-fiber Aided Base Station Coordination for OFDM," on Radio-Over-Fiber Backhaul,"IEEE Vehicular Technology Conference, pp.1-6, September 2014.

Contents

List of Symbols

f_{RF}: Center Frequency of RF signal
$E_{laser}(t)$: Optical field of laser's output
P_{in}: Laser's output power
I_{bias}: Bias current for direct modulation of laser
$I_{RF}(t)$: RF current for direct modulation of laser
I_{drive}: Total drive current for direct modulation of laser
V_{bias}: Bias voltage for external optical modulation
$V(t)$: RF signal for external optical modulation
V_{π}: Switching voltage of MZM
V_{drv}:Total drive voltage applied to a single drive MZM
V_{dc1}, V_{dc2}: Differential bias voltage for the two arms of a DD-MZM
$V_1(t), V_2(t)$: Differential RF voltage for the two arms of a DD-MZM
$E_{single}(t)$: Output optical field of single drive MZM
P_{single}; Output optical power of single drive MZM
$E_{dual}(t)$: Output optical field of dual drive MZM
P_{dual}; Output optical power of dual drive MZM
f_r: Laser's relaxation resonance frequency
f_{3dB}: laser's modulation bandwidth
$V_{RF}cos(\omega_{RF}t)$: Electronic RF tone
$J_n()$: Bessel function of n^{th} order
$\omega_c(\lambda_c)$: Angular frequency (wavelength) of the optical carrier
γ: Extinction ratio parameter of MZM
ϵ: Extinction ratio of MZM
$V_{RF1}\sin(\omega_{RF1}t)$,$V_{RF2}\sin(\omega_{RF2}t)$: Sinusoidal signals applied to the arms of a DD-MZM
α_{chirp}: Chirp factor of the DD-MZM
$V_{drv1}(t), V_{drv2}(t)$: Total drive voltages (differential DC bias and differential RF voltages) appled to the two arms of the MZM
$T(V)$: Amplitude transmittance of EAM at applied voltage V
$E_{EAM}(t)$: Output optical field of a EAM
$E_{PM}(t)$: Output optical field of a optical phase modulator
z: Distance of optical propagation
T: Time measured in a frame of reference moving with the optical signal
$A(z,T)$: Envelope of the optical carrier
α: Fiber attenuation constant
γ_{nl}: Fiver non-linearity parameter
β_2: Second derivative of fiber propagation constant
v_g: Group velocity of fiber propagation
P_{trans}: Optical power entering the fiber
P_{rec}: Optical power output from the fiber
$n_r(\omega)$: Fiber's refractive index at an optical angular frequency of ω
D: Dispersion parameter of the fiber c: Speed of light in vacuum
$P_{fib}(t)$: Instantaneous optical pwower in the fiber

L: Total length of fiber
$\phi_{SPM}(t)(\delta\omega_{SPM})(t)$: Instantaneous phase shift (and frequency chirping) due to SPM
$\phi_{XPM}(t)(\delta\omega_{XPM})(t)$: Instantaneous phase shift (and frequency chirping) due to XPM
f_{FWM}: Frequencies generated by FWM
R: Responsivity of photodiode
η_{sp}: Quantum efficiency of the photodiode
e: Charge on an electron
h: Plank's constant
I_p: Photodetected DC current for constant received power P_{rec}
B_{RF}: Bandwidth of RF signal f_u: Highest frequency of RF signal
$\tau_{transit}, \tau_{RC}, tau_{rise}$: Transit time, RC time constant and rise time of photodiode, respectively
$E_{rec}(t)$: Optical field of signal received at photodiode
ω_c^{LO}: Local oscillator laser's frequency Δf_{noise}: Noise bandwidth of the optical receiver
I_{dc}: Average photocurrent
σ^2_{RIN}: RIN noise power
G_{amp}: Gain of optical amplifier
n_{sp}: Spontaneous emission factor of optical amplifer
σ^2_{shot}: Shot noise power
$\sigma^2_{thermal}$: Thermal noise power
k_B: boltzmann's constant
T_{ab}: Absolute Temperature
R_L: Load Resistor
F_n: Noise figure of receiver amplifier
I_{noisy}: Noisy photodetected signal
$n_{tot}(t)$: Total noise in photodetected signal
σ^2_{total}: Total noise power in photodetected signal
$f_{lower}(f_{upper})$: Lower (upper) sideband frequency of an ODSB signal
f_{side}: Frequency of sideband of an OSSB signal
P_{RF}: Photodetected RF power
$E_{FM}(t)$: Optical field of frequency modulated optical signal
E_{MZI}: Optical field at the output of the MZI
P_{MZI}: Optical power at the output of the MZI
ϕ_{PM}: Phase of a phase modulated optical carrier
R_{DL}: Downlink bit rate for each RAP in a DAS. R_{TDM}: Time division multiplexed downlink bit rate in a DAS
E_{TDM}: Optical field of TDM optical signal
E_{clock}: Optical field of optical cloack signal
f_{inst}: Instantaneous optical frequency
$\Delta f_{chirp}(t)$: Dispersion induced frequency chirping
$I_{PD}(t)$: Photo-detected current
T_{FWHM}: FWHM of pulse
x_{clk}: Envelope of optical clock signal
$x_k(t)$: Envelope of the pulsed optical for the k^{th} RAP in a DAS

$\Delta\omega_c$: Angular frequency spacing between optical carriers
$omega_i$: i^{th} optical carrier
s_i: Sideband of i^{th} optical carrier
$P_{MZM,1}, P_{MZM,2}$: First and second output of dual output MZM
f_{LO}: Electron RF tone
f_{IF}: Intermediate frequency
η_{c1}, η_{c2}: Power splitting (combining) ratio of an optical splitter (coupler)
I_{RF}: Photo-detected RF signal
γ_r: Ratio of RF modulating voltages of a linearized MZM
r_π: Ratio of the switching voltages at two different wavelengths
$r_{\pi,p}$: Ratio of the switching voltages at two different polarizations
A_{amp}: Ratio of electronic amplification
D_{comp}: Dispersion parameter of dispersion compensation fiber
L_{comp}: Length of dispersion compensation fiber
$\omega_{baseband}$: Optical carrier transmitting baseband modulating signal
ω_{ROF}: Optical carrier transmitting RF modulating signal
P_{BB}: Power of optical carrier modulated by a baseband signal
$E_{BB}(t)$: Optical field of optical carrier modulated by a baseband signal
P_{total}: Power of optical carrier modulated by both baseband and RF signal
$E_{total}(t)$: Power of optical carrier modulated by both baseband and RF signal
$V_{LO}\cos(\omega_{LO}(t))$: Local oscillator electronic tone
$b(t)$: Baseband electronic signal
V_b: Amplitude of baseband signal $b(t)$
$V_{tot}(t)$: Combined baseband/IF and RF signal
ω_{LOOS}: Optical center frequency of LOOS
$E_{LOOS}(t)$: Optical field of LOOS
$P_{LOOS}(t)$: Optical power of LOOS
$P_c(t)$: Power of the signal at an optical frequency of ω_c
$V_g(t)$: Baseband signal employing gaussian pulses
$H_{fiber}(f)$: Frequency response of a fiber at an electronic modulating frequency of f
f_{null}: Electronic frequency at which $H_{fiber}(f) = 0$
f_{max}: Electronic frequency at which $H_{fiber}(f)$ peaks
$g(t), m(t), d(t)$: Gaussian, monocyle and doublet pulses, respectively
t_{attn} Insertion loss of MZM
P_{LO} : Power of local oscillator lasr signal
ϕ_{rec}: Phase of the optical signal exiting the fiber
ϕ_{LO}: Phase of the local oscillator laser's output
I_{dc}: DC current
$I_{squarer}$: Output signal of a squarer
$I_x(t)(I_y(t))$: Photo-detected currents carrying signals $V_x(t)(V_y(t))$
$u(t)$: Sawtooth signal
ϕ_{disp}: Dispersion induced phase rotation
h_{wl}: Complex wireless channel coefficient

t_{sp}: Insertion loss of optical coupler/splitter
$E_{c,1}(t), E_{c,2}(t)$: The optical field outputs of an optical splitter
$V_{samp}[n]$: Bandpass sampled RF signal
$V_{quant}[n]$: Quantized bandpass sampled signal
f_{samp}: Bandpass sampling rate $f_u(f_l)$: Highest (lowest) frequency in the RF signal
$V^{max}(V_{min})$: Maximum (Minimum) value of $V(t)$
V^i: The quantized values after bandpass sampling
ΔV: Quantization step
$I_0(I_1)$: Direct modulation drive current for bit '0' (bit '1')
$P_0(P_1)$: Output optical power for bit '0' (bit '1')
τ: Time normalized w.r.t to bit duration
T_{half}: Half width of electronic pulse
V_{DAC}: Output signal of DAC
N_o: In-band noise spectral density
SNR_{RF}: SNR of RF signal $V(t)$
f_{max}^{DAC}: Maximum frequency handled by the ADC
N_{out}: Out-of-band noise spectral density
SNR_{samp}: SNR of bandpass sampled RF signal
Δt_{jit}: Sampling jitter
$e_{quant}[n]$: Quantization error
$p_e(e)$: Probability of quantization error
SNR_{quant}: Quantization SNR
$\Delta B_{low}(\Delta B_{high})$: Lower (higher) RF guardband
$f_u^{min}(f_u^{max})$: Lowest (highest) permissible value of f_u
$\Delta f_{samp}, \Delta f_{samp}^{low}, \Delta f_{samp}^{high}$): Total, lower and higher tolerance margin on f_{samp} that ensures no aliasing, respectively
D_{SNR}: SNR degradation due to bandpass sampling R_{DROF}: DROF bit rate
R_{RF}: RF bit rate
n_i: Noise added by the i^{th} receive antenna when using MRC reception or noise added in the i^{th} time slot when using STBC transmission
$\overrightarrow{N}$: Noise vector
y_i: Symbol received by the i^{th} receive antenna when using MRC detection or symbol received by the i^{th} time slot whne using STBC transmission
$\overrightarrow{Y}$: Received symbol vector
x: Wireless symbol
$\overrightarrow{H}$: Wireless channel matrix
W: Filter weights implementing MRC
$\overrightarrow{W}$: Filter vector implementing MRC
E_s: Power of each wireless symbol
γ_{inst}: Instantaneous SNR after MRC detection
$\gamma_{i,inst}$:Instantaneous SNR of the signal received at the i^{th} receive antenna
M: The total number of receive antennas in MRC detection or transmit antennas in STBC transmission

K: The total number of constellation points in the wireless signal
L_{slot}: Number of time slots for transmitting M symbols using STBC
f_{dwn1}, f_{dwn2}: Downlink RF frequencies
$k_{dwn}(k_{up})$: Depth of downlink (uplink) intensity modulation
$n_r(r, \omega)$: The refractive index at a radial distance r from core axis at an optical angular frequency of ω
α_{GI}: The core index exponent of a graded index POF
Δ_n: Refractive index contrast between core and cladding
$\vec{E}_{POF}(\vec{r}, \omega)$: Electric field in a SI-POF
$\vec{H}_{POF}(\vec{r}, \omega)$: Magnetic field in a SI-POF
$K_u(\cdot)$: Modified bessel function of order u. a: Core radius of POF
m: Pinciple mode number
m_{max}:Maximum principle mode number
θ_i: Angle of incidence of light into the POF
θ: The propagation angle with respect to the core axis
N_{mode}: Total number of potentially excitable modes in a POF
k_0: Wavenumber
β: propagation constant

Note that Symbols f and ω with the same subscripts are the frequency and angular frequency of the same signal, respectively.

Frequently Used Abbreviations

ADC: Analog to Digital Converter
AROF: Analog Radio Over Fiber
ASE: Amplified Stimulated Emission
AWG: Arrayed Waveguide Grating
BB: Baseband
BER: Bit Error Rate
BPF: Band Pass Filter
BS: Base Station
CU: Central Unit
CDM: Code Division Multiplexing
CDD: Code Division De-multiplexing
DAC: Digital to Analog Converter
DAS: Distributed Antenna System
DCF: Dispersion Compensation Fiber
DEMUX: Demultiplexer
DIPP: Dispersion Induced Power Penalty
DL: Downlink
DROF: Digitized Radio Over Fiber
DSP: Digital Signal Processing
DWDM: Dense Wavelength Division Multiplexing
EAM: Electro Absorption Modulator
E-O: Electronic to Optical
FBG: Fiber Bragg Grating
FCC: Federal Communication Commission
FP: Fabry Perot
FTTH: fiber To The Home
FWHM: Full Width at Half Maximum
GI-POF: Graded Index Plastic Optical Fiber
GVD: Group Velocity Dispersion
HNL-DSF: Highly Nonlinear Dispersion Shifted Fiber
IF: Intermediate Frequency
IL: Interleaver
IR-UWB- Impulse Radio Ultra Wide Band
LD: Laser Diode
LOOS: Local Oscillator Optical Signal
LPF: Low Pass Filter
MATP: Maximum Transmission Point
MB-OFDM- Multi Band Orthogonal Frequency Division Multiplexing
MIMO: Multiple Input Multiple Output
MITP: Minimum Transmission Point
MUX: Multiplexer
MZI: Mach Zehnder Interferometer

MZM: Mach Zehnder Modulator
MRC: Maximal Ratio Combining
NF: Noise Figure
NLS: Non-Linear Schrödinger
NRZ: Non Return to Zero
O-E: Optical to Electronic
OADM: Optical Add Drop Multiplexer
OC: Optical Circulator
OCG: Optical Carrier Generator
OCRR: Optical Carrier Recovery and Re-use
OCS: Optical Carrier Suppression
ODSB: Optical Double Side Band
OFM: Optical Frequency Multiplication
OIL: Optical Injection Locking
OIPLL: Optical Injection Phase Lock Loop
ONU: Optical Network Unit
OOK: On Off Keying
OPC:Optical Phase Conjugation
OPLL: Optical Phase Loacked Loop
OSIL: Optical Sideband Injection Locking
OSSB: Optical Single Side Band
P-I: Power vs Current
PD: Photodiode
PMF: Polarization Maintaining Fiber
PMMA: Polymethyl Methacrylate
POF: Plastic Optical Fiber
QP: Quadrature Point
RAP: Radio Access Point
RF: Radio Frequency
RIN: Relative Intensity Noise
ROF: Radio Over Fiber
RSOA: Reflective Semiconductor Optical Amplifier
SBS: Stimulated Brilloin Scattering
SCM: Sub Carrier Multiplexing
SFDR: Spurious Free Dynamic Range
SI-POF: Step Index Plastic Optical Fiber
SNR: Signal to Noise Ratio
SOA: Semiconductor Optical Amplifier
SPM: Self Phase Modulation
SRS: Stimulated Raman Scattering
SSFM: Split Step Fourier Method
STBC: Space Time Block Coding
TLCG: Tapered Linearly Chirped Grating

UL: uplink
UWB: Ultra Wide Band
WDM: Wavelength Division Multiplexing
WI-WDM: Wavelength Interleaved Wavelength Division Multiplexing
WI-DWDM: Wavelength Division Multiplexing
WPAN: Wireless Personal Area Network
XAM: Cross Absorption Modulation
XGM: Cross Gain Modulation
XPM: Cross Phase Modulation

Chapter 1

Introduction to radio over fiber

Radio Over Fiber (ROF) techniques facilitate high-bandwidth wireless communication by exploiting the advantages of an optical back-haul network, which may be employed both for in-building as well as for outdoor cellular networks. Both the coverage quality as well as their throughput may be enhanced. Additionally, they potentially reduce the cost of establishing the network. Some of the proposed applications for this technique are as follows:

1. High speed downlink video transport to mobile terminals [15];
2. Setting up wireless hotspots inside homes (femto cells) by exploiting the expanding Fiber To The Home (FTTH) technique [16];
3. Setting up Wireless Personal Area Networks (WPAN) in office buildings by exploiting the distributed antenna concept to implement MIMO techniques [17];
4. Antenna remoting applications [18];
5. Intra-vehicular communication, such as broadband wireless connections in ships, planes and trains [19].

In this chapter, we first discuss the need for ROF solutions in Section 1.1 and then provide the background in Section 1.2. We then discuss the advantages of ROF and compare it to other backhaul techniques in Sections 1.3 and 1.4, respectively. In Section 1.5, we discuss the various approaches that may be adopted for designing advanced ROF links. We then present the organization of this thesis in Section 1.6 and finally offer our conclusions in Section 1.7.

1.1 Need for radio over fiber solutions

The wireless data rates provided by the cellular operators and the number of users with access to wireless connectivity escalated during the last two decades. While in 1991, the proportion of the world's population owning a mobile handset was less than 1% [20], the same figure was about 78% as of 2010 [20]. Figure 1.1 below illustrates the trends in the market penetration of wireless services.

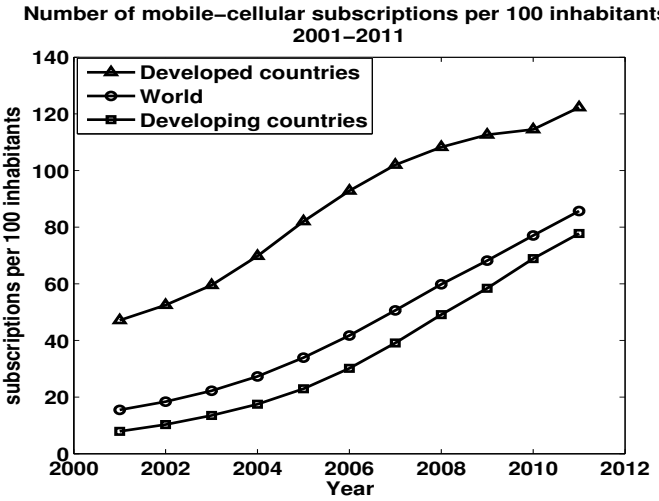

Figure 1.1: Number of mobile-cellular subscriptions per 100 inhabitants (2001-2011) [20].

Although the size of the subscriber base in the developed countries is saturating gradually, there is still a substantial increase in the number of subscribers in the developing countries, where the majority of the world's population lives. Cellular telephony is increasingly stepping out of the traditional notion of primarily providing voice connectivity owing to the recent paradigm shift to providing high speed data connectivity. This trend has been reflected in the formulation of the second generation (2G), third generation (3G) and the latest fourth generation (4G) mobile standards. Fig. 1.2 below illustrates, how the extent of Internet usage through mobile handsets has increased over the years [20].

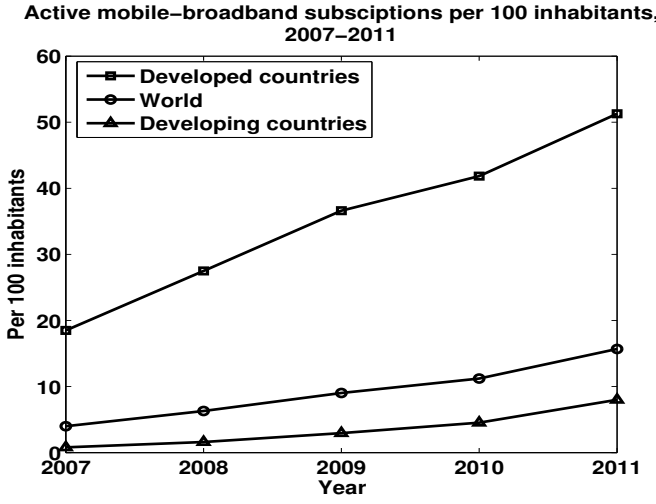

Figure 1.2: Active mobile broadband subscriptions per 100 inhabitants (2007-2011) [20].

A steady increase in the number of mobile broadband subscriptions can be observed from Fig. 1.2 right across the world. The extent of wireless Internet usage is predicted to follow the same trend as that obeyed by the number of subscriptions, except for a time lag. This time lag accounts for the delay in the affordability of sophisticated handsets, that can support high data rates. The intense competition among the wireless service providers coupled with the decreasing manufacturing costs of integrated chips would increase the affordability of these handsets in the near future.

Since its standardization in 1997, Wireless Local Area Networks (WLANs) have also experienced

tremendous growth. Apart from the increased number of WLANs in public spaces, like airports and railway stations, there has been an increasing desire to provide high wireless data rates in a wide variety of other wireless hot spots. Table 1.1 illustrates the evolution of the IEEE 802.11 WLAN standard, where it can be seen that over the years, the attempt has been to achieve higher data rates coupled with increased mobility.

Table 1.1: Basic features of the IEEE 802.11 wireless communication systems family [21]

Standard	**Release Date**	**Maximum data rate(Mbps)**	**Indoor range(m)**	**Outdoor range(m)**
802.11	June 1997	2	20	100
802.11 a	September 1999	54	35	120
802.11 b	September 1999	11	38	140
802.11 g	June 2003	54	38	140
802.11 n (20 MHz bandwidth)	October 2009	72.2	70	250
802.11 n (20 MHz bandwidth)	October 2009	150	70	250

Table 1.2: Carrier frequencies used in diverse wireless communication systems

Wireless Systems	**Carrier Frequency (GHz)**
UMTS/3G systems	2.0
LTE/LTE-A	2.6
IEEE 802.11 b/g	2.4
IEEE 802.11 a/n	5.0
IEEE 802.16 WiMaX	2-11
Indoor Wireless LANs	17/19
Fixed Wireless Access: point to multipoint	28
Fixed Wireless Access: Picocellular	38
IEEE 802.15 WPAN	57-64
IEEE 802.16	10-66

Over the years, the service providers have been exploring newer avenues to meet the ever-increasing customer demand for high-speed ubiquitous connectivity. Table 1.2 below documents the carrier frequencies that are used by diverse wireless systems. It can be observed from Table 1.2, that over the years there has been a steady increase in the carrier frequency employed by the family of wireless communication systems. This is because of the higher bandwidths that are available at the higher frequencies. However, the higher wireless attenuation experienced at higher frequencies requires a cellular architecture relying on small cells. The employment of small cells has the added advantage of the cellular system being able to support a larger number of users in a unit area, because of a higher degree of frequency re-use. This has been illustrated in Fig. 1.3, where the frequency bands of f_1, f_2andf_3 employed in the architecture of Fig. 1.3(a) have been re-used in the non-adjacent smaller

cells in the architecture of Fig. 1.3(b).

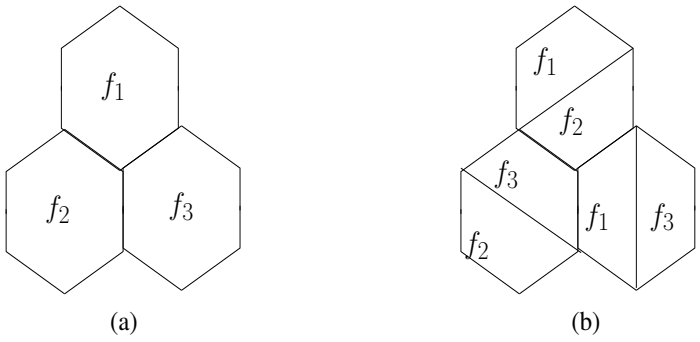

Figure 1.3: Increasing cellular capacity through use of smaller cells.

Fig. 1.4 shows a cellular system, where the Base Station (BS) of the cells is connected to the wireless network's backhaul, which usually employs digital optical communication. A fully-fledged BS has several components having a high installation cost, especially when migrating to higher frequencies. Hence, the economics of setting up a cellular system in which each small cell is served by a BS , as shown in Fig. 1.4, is challenging, due to the large number of BSs required. The challenges to the deployment of small cells with high RF carriers are as follows:

1. An increase in the infrastructural costs because of the need to employ a large number of BSs.
2. The use of an expensive high-frequency radio front-end increases the cost of each BS.
3. A drop in the transistor efficiency results in a higher power consumption by the RF devices at higher carrier frequencies. The power efficiency of the active RF devices is approximately 30% at millimetre-wave frequencies [22]. Any increase in the BS power consumption increases the operational cost of the cellular network.

Radio over fiber techniques [23],[24], [25], [26] constitute a promising solution to the challenge of having a large number of small cells with high RF-frequencies [27]. Fig. 1.5 shows a cellular architecture relying on ROF solutions, where multiple cells are served by a single BS by using Radio Access Points (RAPs) that are connected to the BS using optical fiber, which is often referred to as a Distributed Antenna System (DAS) [2]. The RAP performs low-complexity signal processing and hence it is inexpensive, while most of the signal processing hardware is accommodated by the BS and it is shared by multiple cells.

In the next section we provide the background information on a basic ROF link. We also compare a cellular architecture relying on macrocells, as shown in Fig. 1.4, with a ROF aided cellular architecture relying on smaller cells, as shown in Fig. 1.5.

1.2 Radio over fiber- preliminaries

ROF solutions aim for integrating both wireless and optical communication for achieving the common design objective of faster and more reliable communication for the end user. They involve transmitting

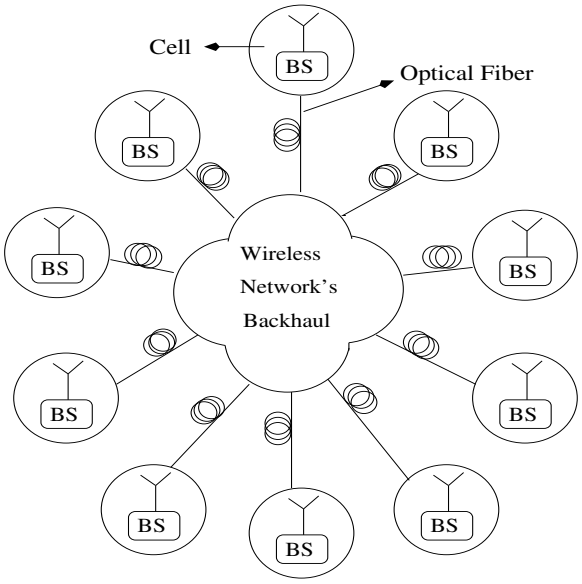

Figure 1.4: Current cellular system.

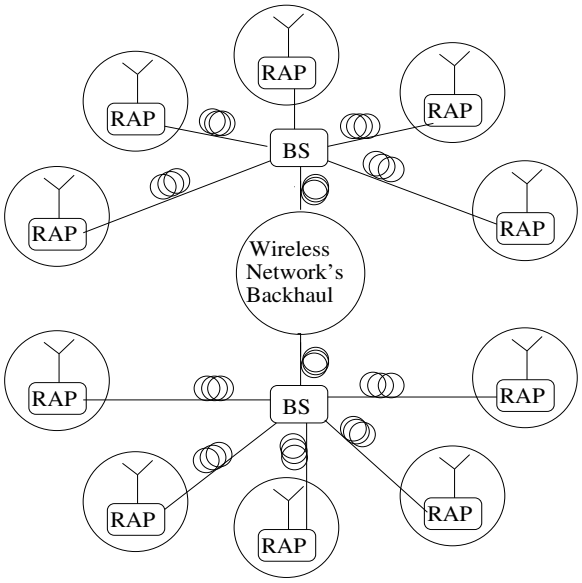

Figure 1.5: Structure of a Cellular system employing ROF.

RF signals to and from a BS. The BS centrally processes the signals received from and transmitted to a number of remote Radio Access Points (RAPs), where little or no signal processing is required. The associated signals are conveyed by high-bandwidth, low-attenuation optical fibers, in an effort to improve the attainable cellular coverage, capacity, data rate and power efficiency.

One of the major access network solutions for future high-bandwidth wireless communication systems is based on optical fibers for the transmission of radio signals between the BS and RAPs, which is generally referred to as a ROF solution [1], [2], [3], [28], [29]. Fig. 1.6 shows the simplified architecture of a ROF downlink, where the wireless Radio Frequency (RF) signal is converted into an optical signal in an electronic-to-optical (E-O) converter at the BS [30]. The optical signal is transmitted through the fiber and detected at the RAP, where an optical-to-electronic (O-E) converter recovers the original RF signal, which is amplified and transmitted from the RAP antenna to the Mobile Station (MS), as shown in Fig. 1.6.

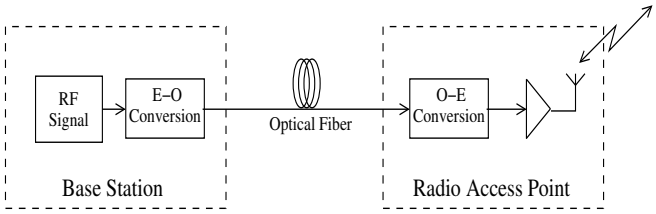

Figure 1.6: Simple ROF link

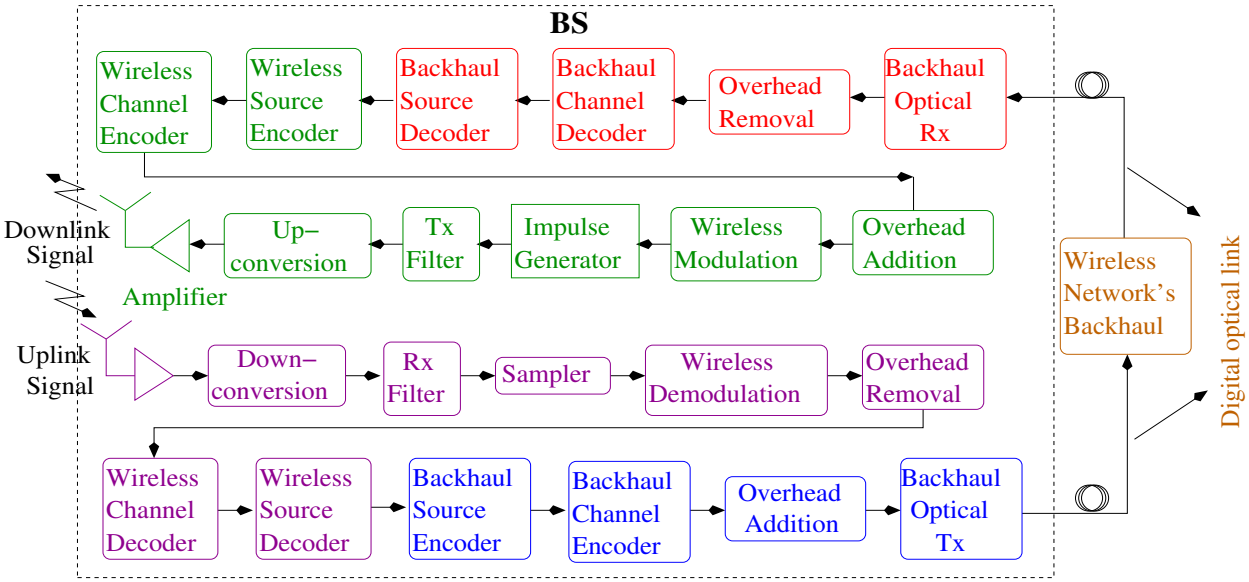

Figure 1.7: Block diagram of a BS used in operational networks (Red - backhaul receiver; Green - wireless transmitter; Magenta - wireless receiver; Blue - backhaul transmitter; Brown - wireless network's backhaul)

Fig. 1.7 shows the components of a BS in the typical mobile system architecture of Fig. 1.4, where the RF signal received at the BS is firstly amplified and then down-converted, followed by receive filtering. As shown in Fig. 1.7, the filtered signal is sampled and then fed to the wireless demodulator, where the symbols are converted into bit frames based on the uplink wireless modulation scheme used by the MS. Subsequently, these bit frames are stripped of the control as well as signalling bits and

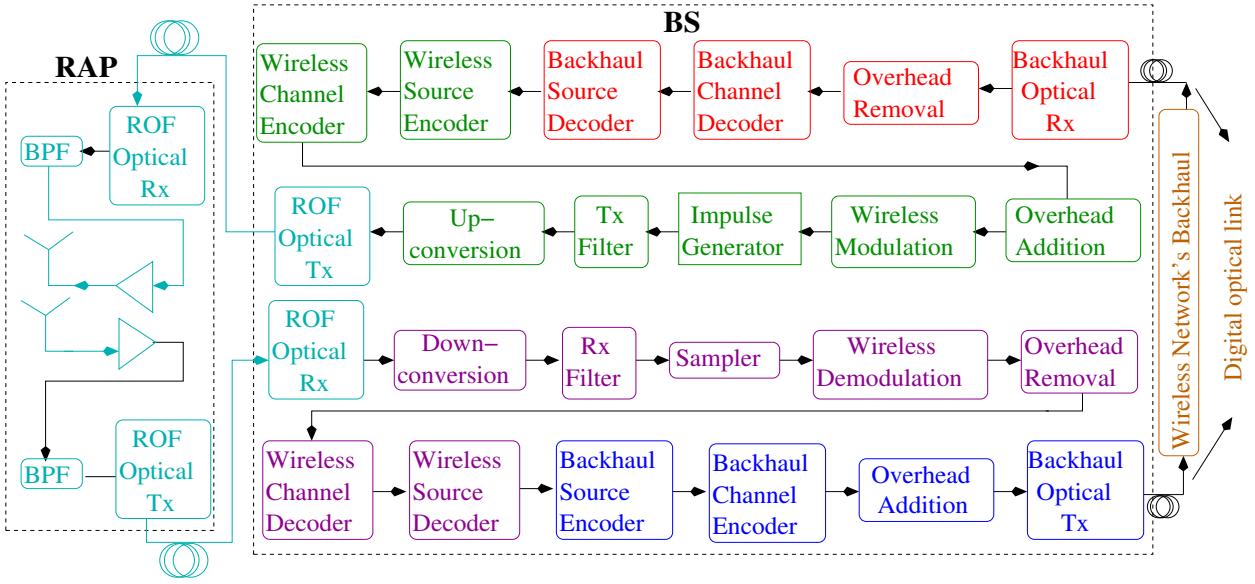

Figure 1.8: Block diagram of a ROF link

they are then fed to the wireless channel decoder, whose output is forwarded to the wireless source decoder to recover the bits transmitted by the MS. As shown in Fig. 1.7, these bits are then fed to the backhaul source encoder whose output is fed to the backhaul channel encoder. Finally, the relevant control and signalling bits are incorporated in order to generate bit frames, which are employed by a laser-fed optical modulator of the optical transmitter for transmission into the backhaul.

On the other hand, as shown in Fig. 1.7, the bit frames that are received from the optical backhaul are photo-detected by the optical receiver. The detected frames are stripped off control and signalling bits. Subsequently, the bits enter the backhaul channel decoder, whose output enters the backhaul source decoder to finally recover the payload of the transmitted backhaul frames. As shown in Fig. 1.7, the detected payload bits are then fed to the wireless source encoder whose output is fed to the wireless channel encoder. Afterwards, the control and signalling bits are incorporated for generating the wireless bit frames. These wireless bit frames are then converted into symbols, based on the downlink wireless modulation scheme that is employed at the BS. As shown in Fig. 1.7, these symbols are thereafter converted into an impulse stream, which is fed to the RF front end, where the signal is transmit-filtered, up-converted, amplified and finally transmitted to the MS.

As mentioned previously, a ROF architecture concentrates most of the signal processing in a BS that is shared by multiple cells, while each cell is served by a RAP that has minimum signal processing. While Fig. 1.6 showed only the simplified ROF downlink of Fig. 1.5, Fig. 1.8 shows both the ROF downlink and uplink of Fig. 1.5, in greater detail. Comparing Fig. 1.8 to Fig. 1.7, it can seen that during the downlink communication phase of Fig. 1.8, the generation of the RF signal is carried out at the BS, where this RF signal is then converted to an optical signal. This specific optical signal is typically referred to as a microwave optical signal. Subsequently, this microwave optical signal is transmitted to the RAP through the optical fiber, where it is photo-detected and filtered in order to recover the downlink RF signal. As shown in Fig. 1.8, this RF signal is then amplified and wirelessly transmitted to the MS. On the other hand, the uplink signal received at the RAP is filtered, amplified and then employed in optical modulation in order to generate the uplink microwave optical signal.

Afterwards, this optical signal is transmitted to the BS, where it is photo-detected and filtered in order to recover the RF signal, which is thereafter down-converted and detected, as shown in Fig. 1.8. It should be noted that the microwave optical signal is different from the digital optical signals used in the fiber links connecting the BSs of Fig. 1.7 and Fig. 1.8 with the backhaul. These digital optical signals transmit digital electronic signals, i.e. bits streams, unlike the microwave optical signals of the ROF link seen in Fig. 1.8, which transmit RF signals.

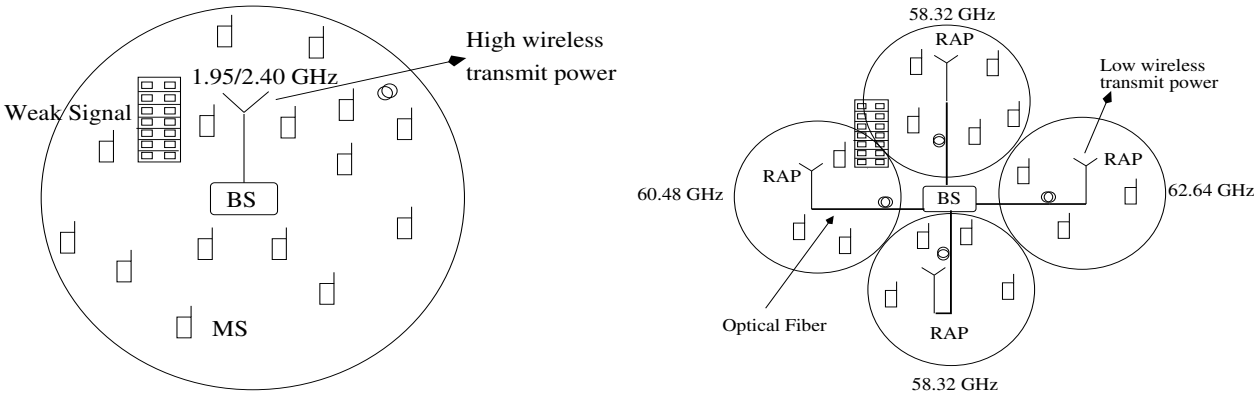

(a) Without using ROF (b) Using ROF

Figure 1.9: Cellular Architecture (BS- Base Station; RAP- Radio Access Point; MS- Mobile Station)

Having discussed the basic components of a ROF link, in the next section we will discuss the advantages of the ROF link.

1.3 Advantages of radio over fiber links

Fig. 1.9 shows two cellular architectures, namely one with and one without using ROF assistance, where Fig. 1.9(a) represents the existing cellular systems that are based on macrocells, while Fig. 1.9(b) is a futuristic cellular architecture that relies on a ROF backhaul designed for supporting smaller cells. The architecture seen in Fig. 1.9(a) has a lower-quality wireless coverage, a lower power efficiency and a limited ability to exploit all the other benefits of small cells. The low quality of the wireless coverage is due to the presence of areas having a weak received signal, especially behind large man-made and geographical structures, in tunnels etc. This phenomenon is referred to as shadowing. The low power efficiency of the current cellular systems arises from having to employ a high transmit power for overcoming the wireless pathloss of the macrocells. Finally, directly employing the architecture of Fig. 1.9(a) in a small-cell-based network is not economically feasible because of the large number of base stations that would be needed. These challenges are overcome in the architecture of Fig. 1.9(b) at the added cost of laying more fiber, as discussed below.

As seen from the previous discussions, ROF solutions belong to the family of hybrid techniques, since they rely on both optical and wireless communication. The strength of a ROF system is its ability to amalgamate the benefits of these two diverse communication techniques. Explicitely, the advantages of an ROF system can be summarised as follows:

1. *Low fiber attenuation*: The low attenuation of glass optical fiber[1] (0.2 dB/km) facilitates the deployment of a geographically distributed large system of antennas that are connected to the BS, as shown in Fig. 1.9(b), where the BS is connected to four RAPs via optical fiber. This architecture is referred to as a DAS [29], where each BS illuminates a large geographical area by using optical fibers as long as 30 km without amplification.

2. *High fiber bandwidth*: The optical fiber is characterised by a high bandwidth. For example, the Third Telecommunication Window (TTW), which is also known as the Erbium band, spans the optical wavelengths of 1530 nm to 1565 nm, which corresponds to a frequency range of 191.56 THz to 195.94 THz [31] and it is characterised by a bandwidth of a few tens of TeraHertz. Hence, the deployment of high-frequency carriers in small cells, as shown in Fig. 1.9(b), would assist us in achieving the high data (audio+video+Internet) rates that are envisioned for future wireless systems [31]. Techniques that utilise this large bandwidth will be discussed in Section 2.1.3 of this treatise.

3. *Economically viable small cells*: Each BS is capable of serving a number of RAPs, as shown in Fig. 1.9(b), where employing centralised signal processing at the BS and utilising RAPs associated with simple architecture ensures that the cost of setting up a cellular system that employs small cells is significantly reduced [32]. This is one of the major aims of the architectures and techniques discussed in this treatise.

4. *Ease of system upgrade*: The ROF link is mostly perfectly transparent to the RF signal employed. Thus, upgrading the wireless technology can be achieved without any alteration to the existing ROF physical layer. Moreover, the concentration of most of the signal processing in the BS ensures that upgrades in technology and hardware can be made easily.

5. *Improved wireless coverage*: As shown in Fig. 1.9(b), the presence of regions that do not receive the wireless signal at a sufficient strength - known as shadow regions - is minimized in a ROF assisted cellular architecture [28]. Tunnels, valleys and regions behind large buildings are some typical examples of shadow regions, that are present in the current cellular architecture. Various network topologies can be employed for providing an improved ROF coverage to all geographical regions, and these are discussed in detail in Section 2.1.3.3 of this treatise.

6. *Ability to implement Multiple Input Multiple Output (MIMO) schemes*: The wireless communication schemes that employ multiple transmit and receive antennas for achieving communication with a single mobile user, are referred to as MIMO schemes [33]. These schemes are capable of increasing the attainable throughput by beneficially exploiting the signal fading characteristics of the wireless channel. As it will be detailed in Section 3.1.12, the DAS architecture permits the design of networks in which each MS of Fig. 1.9(b) is served by multiple RAPs. Thus, MIMO schemes can be readily implemented in the context of a ROF network [2].

7. *Efficient resource allocation*: The centralised nature of the signal processing at the BS can be exploited for statistical multiplexing using dynamic resource allocation algorithms [34] in the ROF networks, which are detailed in Section 2.1.3.3 of this treatise.

[1]Glass optical fiber refers to optical fibers made from silica.

8. *Power Efficiency*: The employement of smaller cells, as is seen from Fig. 1.9(b), typically provides a stronger line of sight link and ensures a lower wireless path loss [28]. Hence, a lower wireless transmit power is needed at the RAPs, which has the added advantage of reduced inter-cell interference [35].

Naturally, the discussion of ROF techniques would not be complete without the critical appraisal of its design alternatives. Hence, in the next section, we compare the ROF backhaul to other possible backhaul techniques.

1.4 Comparison to other backhaul techniques

The microwave-based wireless backhaul constitutes a competing backhaul counterpart of the fiber-based wired backhaul. The advantage of the wireless backhaul is that the installation cost does not scale significantly with the distance between the transmitter and receiver. Moreover, a wireless backhaul can be readily installed as well as disassembled and set up elsewhere [36]. However, a wireless backhaul also suffers from several disadvantages. Firstly, it requires wireless spectrum, which could otherwise have been employed for wireless communication with mobile devices. Moreover, in the case of a microwave backhaul, line of sight communication is a necessity [36]. Finally, the quality of the wireless backhaul is influenced by the climatic conditions [36].

On the other hand, a fiber-based backhaul does not require wireless spectrum and has a significantly higher usable bandwidth than the wireless backhaul. Additionally, a fiber-based backhaul does not require line of sight communication and it is not influenced by the climatic conditions [36]. However, the installation cost of a fiber-based backhaul is higher than that of a wireless backhaul, especially when the terrain is rough and this cost increases, as the distance between the transmitter and receiver increases. Finally, in contrast to the wireless backhaul, a fiber-based backhaul cannot be readily set-up or moved [36]. At this point it is worth noting that a copper wire based backhaul has severe bandwidth restrictions and it might become obsolete, unless substantial further bandwidth expansions become possible by invoking sophisticated signal processing.

When employing the fiber-based backhaul, the designer has two options, namely the standard digital fiber-based backhaul shown in Fig. 1.4 or the ROF backhaul of Fig. 1.5 proposed in this treatise. In case of the digital PCM-over-fiber backhaul, each small cell of Fig. 1.9(b) would need a full fledged BS for detecting/transmitting the wireless signal as well as for transmitting/detecting the bits to/from the backhaul, which typically relies on the Ethernet protocol. However, as discussed earlier, a ROF backhaul will ensure that multiple cells are served by a single BS, as shown in Fig. 1.9(b), thereby reducing the network's installation cost. Moreover, the ROF technique involves the transmission of the analog RF signal to the BS and hence it will reduce the latency, because the signal processing carried out in the RAP is minimized. ROF is a potential backhaul technique for the Long Term Evolution Advanced (LTE-A) [37] [38] standard as well as for future millimeter wave standards [39]. At this point, it is worth mentioning that the Open Base Station Architecture Initiative (OBSAI) standard ensures compatibility between the different BS modules manufactured by different companies, thereby resulting in cost savings.

Having established the argument in favour of ROF solutions, in the next section we will discuss

the various approaches that have been employed by the research community for designing advanced ROF links.

1.5 Designing advanced ROF links

Designing advanced ROF links may rely on the following three approaches:

1. ROF links employing techniques aimed at improving its performance;
2. ROF links employing techniques aimed at reducing the cost of employment;
3. ROF links aimed at supporting high-RF signals;

We introduce the above three concepts in Sections 1.5.1, 1.5.2 and 1.5.3, respectively.

1.5.1 ROF links employing techniques aimed at improving its performance

The target BER of a ROF link is 10^{-9} or even lower, where the received optical power required for achieving this is referred to as the optical sensitivity. The BER of a ROF link is limited by the depth of optical modulation, by the presence of optical noise and by fiber impairments, like dispersion and non-linearity. Advanced techniques can be designed for overcoming each of these limitations, such as low biasing of the optical modulator, optical carrier suppression, balanced photodetection and others [40], [41], [42], [43], as we will detail in Section 3.1. Additionally, a range of techniques have been designed for increasing the number of RAPs that may be supported by a ROF backhaul [44].

Moreover, wireless standards impose stringent limits on the adjacent channel interference, thereby requiring the ROF backhaul to be very linear. Hence, advanced schemes have been designed for improving the linearity of optical modulation [45]. Finally, state-of-the-art techniques have also been proposed for amalgamating the advantages of ROF and that of a digital optical link [46]. These techniques will be discussed in more detail in Chapter 3.

In the next section, we discuss the second approach that may be employed for designing advanced ROF links, namely the cost-reduction based system design.

1.5.2 ROF links employing techniques aimed at reducing the cost of employment

It is clear from the discussions in Section 1.2 that, the cardinal rule of a ROF link is to achieve the best possible performance at the lowest possible cost. Several advanced ROF techniques have been designed for meeting this goal. Some examples include techniques designed for using the existing fiber infrastructure [47], for reducing the number of components in the RAP [48] and for reducing the number of lasers in the BS [49]. These techniques will be discussed in greater detail in Chapter 3.

Future RF networks are expected to rely on high-RF carriers, where the generation of these high-RF signals poses a challenge. The next section discusses how the optical generation of these RF signals is capable of tackling this challenge and how this can be amalgamated with the ROF technique.

1.5.3 ROF links aimed at supporting high-RF signals

Networks employing a high RF carrier would have a small cell size due to the higher wireless attenuation [39], as exemplified by a Wireless Personal Area Network (WPAN). A WPAN allows the wireless devices in a user's personal workspace to be connected to the network. High data rate WPANs may be implemented based on the Federal Communications Commission (FCC) compliant Ultra Wide Band (UWB) standard [50] or on the IEEE 802.15.3c standard [51]. The UWB signal was defined by the FCC as a signal having a bandwidth larger than 20% of the carrier frequency or a bandwidth of at least 500 MHz in the 3.1 GHz to 10.6 GHz band. On the other hand, IEEE 802.15.3c relies on a carrier frequency in the 60 GHz license-free Industrial, Scientific and Medical (ISM) band. The WPAN standards are discussed in Sections 1.5.3.1 and 1.5.3.2, while the challenges to their implementation are discussed in Section 1.5.3.3.

1.5.3.1 FCC compliant ultra wide band standard

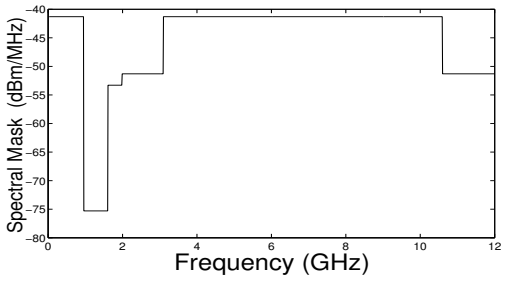

Figure 1.10: UWB spectral mask

The UWB signal spectrum should be within the mask shown in Fig. 1.10, as defined by the FCC, where it is shown that the UWB systems may operate in the spectral range of 3.1 GHz to 10.6 GHz [50]. In the downlink of a UWB ROF system, we typically transmit high data rate UWB signals to the personal devices, while in the UL we often transmit lower-rate signals [52]. UWB systems tend to employ two different wireless technologies [53], namely Impulse Radio-UWB (IR-UWB) and Multi Band Orthogonal Frequency Division Multiplexing (MB-OFDM) [53].

The IR-UWB technique transmits short duration pulses, whose bandwidth is within the 3.1 GHz to 10.6 GHz spectral range. The bits are transmitted with the aid of these short pulses using modulation schemes such as OOK, Pulse Position Modulation, Pulse Polarity Modulation (PPM) and Pulse Shape Modulation (PSM).

On the other hand, MB-OFDM signals may also be employed for generating UWB signals, where the FCC allowed the UWB spectrum to be divided into 14 bands of 528 MHz width each. The MB-OFDM signals consist of a 528 MHz wide OFDM signal, which hops across these 14 bands based on a Time Frequency Code (TFC) [53].

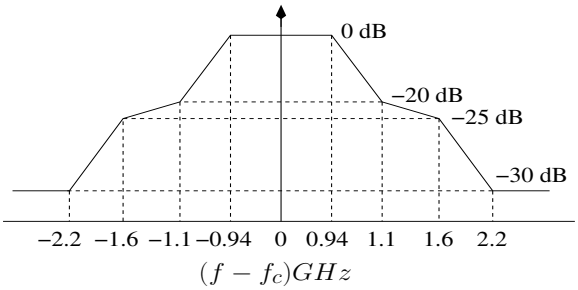

Figure 1.11: IEEE 802.15.3c spectral mask

1.5.3.2 IEEE 802.15.3c standard

The IEEE 802.15.3c standard was developed for the 60 GHz spectrum band. It divides the available spectrum in the 60 GHz license-free ISM band into 4 subbands of 2.16 GHz each, where the corresponding spectrum mask of each band is shown in Fig. 1.11. The spectrum of the transmitted signal must be contained within the spectral mask shown in Fig. 1.11. This standard supports both conventional single carrier communication as well as OFDM based multicarrier communication and it can send Gigabit data streams over short distances. The size of the cells is small because of the high wireless pathloss suffered by the 60 GHz signals owing to the attenuation imposed by absorption by oxygen molecules. Unlike the FCC compliant HR-WPAN, the wireless signals at 60 GHz cannot pass through thick walls and hence this technique is eminently suitable for line-of-sight indoor coverage [54], because there is no interference between adjacent rooms.

Having discussed the various high-RF WPAN standards, in the next section, we discuss the challenges to their implementation.

1.5.3.3 Implementation challenges

There are two main challenges in the design of these high-rate WPANs, which includes the following:

1. *The distribution of the RF signals*: As seen in Fig. 1.10, the tolerable UWB wireless transmission power is very low in order to avoid intentional interference. Hence, the wireless transmission range of UWB signals is limited to a few dozens of meters [55]. Similarly, the high-frequency millimeter-wave carriers that provide large bandwidths also suffer from a low wireless transmission range owing to the high atmospheric attenuation. Thus, WPAN networks would require a large number of BSs. Moreover, network operators often have to resort to splitting large cells into smaller cells to meet the increasing demand of bandwidth per user. However, the increase in infrastructure costs makes increasing the number of BSs an expensive option [28].

2. *The generation of the high frequency RF signals*: While the electronic technology of generating baseband OFDM/MB-OFDM signals is quite mature, the overall BER performance achieved by a high-RF link is severely affected by the quality of the inexpensive broadband electronic mixers [56], especially in the case of millimeter-wave links. On the other hand, IR-UWB techniques are carrier-free, hence they do not require upconversion and mixing. However, the pulses must have a duration of around 200 ps in order to cover the entire UWB spectral range spanning from 3.1 to 10.6 GHz [53],

where the generation of such broadband signals in the electronic domain is challenging. Thus, the imperfections of electronics impose a major limitation on the generation of WPAN signals.

The solution to the first challenge is to employ ROF communication, while the solution to the second challenge is to rely on the optical generation of the RF signals in a ROF link. Optical generation of the RF signals allows us to avoid the use of high-RF broadband mixers, when employing OFDM or MB-OFDM, whilst allowing the generation of pulses which are less than 200 ps wide, when employing IR-UWB. The optical generation of the RF signals exploits the broadband low-loss nature of optical signal processing [52].

1.6 Organization of the thesis

The organization of this thesis is shown in Fig. 1.12. The thesis takes the reader from the basics to the state-of-the art techniques in a step-by-step manner. In Chapter 2, the basics of the classical ROF link, namely the Analog ROF (AROF) link, are introduced along with a simulation-based analysis of the AROF link. The discussion of the AROF basics also provides an introduction to the various optical components that are employed both in the basic AROF link of Chapter 2 as well as in the more advanced links discussed in the subsequent chapters. After discussing the basic AROF links found in the current literature, Chapter 2 presents and mathematically characterizes a novel AROF architecture along with a discussion of the results obtained through its simulation. Then, we introduce the concepts behind designing advanced ROF links in Chapter 3. We commence with an extensive study of diverse ROF links that were designed using each of the three approaches discussed in Section 1.5, namely the ROF links employing a) performance improvement techniques, b) cost reduction techniques and c) optical RF-generation techniques. In the the rest of the thesis, we present novel architectures that were designed employing these three approaches. In Chapter 4, we present three novel architectures that employed both cost-reduction as well as optical RF-generation techniques, while Chapter 5 focuses on the benefits of the performance-improvement technique of Digitized ROF (DROF). A simulation based study of the DROF technique and a novel DROF-based architecture are presented in Chapter 5. The DROF technique constitutes a performance improvement technique, which however results in an increased link cost. Chapter 6 is the culmination of this thesis, where we propose the employment of Plastic Optical Fiber (POF) in a ROF link as a potential direction of future research. Explicitly, as a first step in this direction, we propose to combine the employment of the cost-saving state-of-the-art Plastic Optical Fiber (POF) with the employment of the improved-performance DROF technique in a single ROF link in order to strike an optimal cost-performance tradeoff. Hence, in Chapter 6, we first discuss the basics of POF-based optical communication and then present the novel proposal of a DROF-based ROF link that employs POF. Finally, we present our conclusions in Chapter 6, where we provide design guidelines for ROF links and also discuss avenues for future research.

Having outlined the organization of this thesis, in the next section , we highlight its novel contributions.

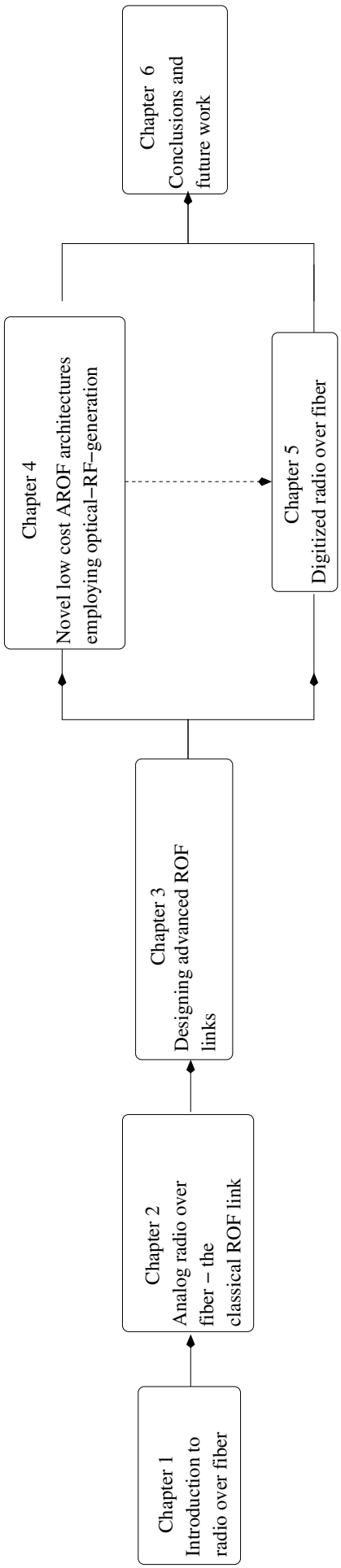

Figure 1.12: Organization of the thesis

1.7 Novel contributions of this thesis

This dissertation is based on references [2, 3, 4, 5, 6, 7, 8, 9, 10]. A comprehensive literature survey and tutorial on designing advanced ROF links was presented in [4], [5] and [8], while novel architectures were proposed in [2, 3, 6, 7, 9, 10]. The novel contributions of this thesis are as follows:

1. An AROF architecture is proposed, where up to four Radio Frequency (RF) carriers can be generated, while using the heterodyne photo-detection of only two optical signals. This proposed AROF architecture has a star-like structure and it is composed of six RAPs, where data is transmitted from the Central Unit (CU) to the BS and from the BS to the RAP over a distance of 20 km and 0.3 km, respectively, at a rate of 768 Mbps. The performance of the system supporting four carrier frequencies drops by at most 1dB, at a BER of 10^{-9}, compared to conventional heterodyne photo-detection. These novel contributions were published in [3].

2. We propose and mathematically characterize a novel optical modulation technique conceived for personal area networks, which uses a single optical modulator to modulate the intensity and phase of an optical carrier with two independent signals. This is achieved by the careful selection of the drive voltages applied to a dual-drive MZM. The detection of these two independent signals is also described in this section along with four possible applications of the proposed architecture. These applications allowed for the simultaneous transmission of baseband and RF signals through the optical fiber. The viability of the proposed architecture was verified by our simulation-based study. These novel contributions were published in [6].

3. Optical Single Sideband (OSSB) signals are conventionally generated using a dual-drive Mach-Zehnder Modulator (MZM) or by using a single-drive MZM in conjunction with a Fiber Bragg Grating (FBG) filter. In this thesis, we propose and mathematically characterize a novel ROF downlink in which an OSSB signal is generated using a single-drive, rather than dual-drive, MZM without any additional filtering. Additionally, our proposed scheme supports the optical upconversion of the electronic signal. Furthermore, in addition to its cost advantages, the proposed scheme's BER performance is better than that of the classical OSSB signal generation scheme. These novel contributions were disseminated in [9].

4. We propose and mathematically characterize a novel ROF downlink, where the RAP benefits from the transmit diversity gain of space time block coding (STBC). Significantly, this transmit diversity is achieved using a single optical modulator in the BS. In the proposed architecture, each RAP is fed with a single optical double side band (ODSB) signal, where each sideband transmits one of the two STBC encoded signals. This optical signal is generated in the BS by performing simultaneous optical upconversion of the baseband STBC signals using a single MZM. The proposed optical backhaul is designed to impose a negligible degradation in addition to that imposed by the dominant wireless link, thereby enabling the designer to exploit the advantages offered by a wireless link having a diversity gain. These novel contributions were published in [7].

5. Fiber links that are a few hundreds of meters long are required for constructing a fiber-based in-building network. However, the transmission of RF signals through the low-cost, easily installable Plastic Optical Fiber (POF) is severely limited by the typical bandwidth-length products of

POFs. DROF converts the RF signal into a baseband signal through bandpass sampling prior to fiber transmission, thereby reducing the fiber bandwidth required for transmitting the RF signal. In this thesis, we propose for the first time a POF-based DROF link as well as present our initial experimental results for a link that employs a 143 m long SI-POF and uncoded RF modulation. The results of this study were published in [10].

The family of ROF techniques facilitates the creation of small cells relying on high RF carriers that can support high-speed wireless communication. Its strength lies in its ability to amalgamate the advantages of optical and wireless communication techniques, while ensuring a low cost for the overall system. In the next chapter, we study the basics of a classical ROF link, which is also referred to as the Analog ROF link. The discussion of the AROF preliminaries also provides an introduction to the various optical components that are employed both in the basic AROF link of Chapter 2 as well as in the more advanced links discussed in the subsequent chapters.

Chapter 2

Analog radio over fiber - the classical ROF link

The block diagram of a typical ROF link is shown in Fig. 2.1 [30], where this classical ROF link is also referred to as Analog Radio Over Fiber (AROF). In the BS, the downlink baseband signal is generated and multiplied with the oscillator output to generate the RF signal. The RF signal is essentially the baseband spectrum that has been shifted to the RF carrier. This translation is referred to as up-conversion, while the reverse is called down-conversion, as shown in Fig. 2.1. After the up-conversion of Fig. 2.1, Electronic-to-Optical (E-O) conversion is achieved by modulating the optical carrier by the analogue RF signal [57] [58], using the techniques discussed in Section 2.1.1.2. Afterwards, the signal propagates through the fiber to the RAP, where the various fiber impairments that effect the propagating optical signal are discussed in Section 2.1.1.3. At the RAP of Fig. 2.1, O-E conversion is achieved using the techniques that will be discussed in Section 2.1.1.4, where the electronic signal generated by the O-E conversion is filtered using a Band Pass Filter (BPF), to obtain the RF signal. As shown in Fig. 2.1, this RF signal is then amplified and transmitted wirelessly by the antenna to the MS.

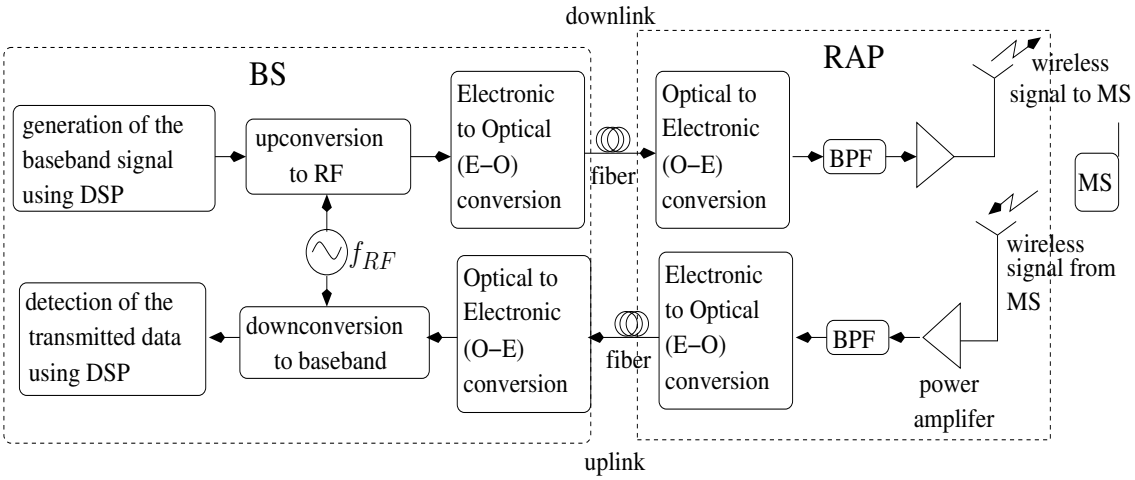

Figure 2.1: Block diagram of a ROF link

The uplink RF signal, that is the received at the RAP from the MS, is bandpass filtered and E-O

converted to generate the uplink optical signal. The uplink optical signal is transmitted over the fiber and subsequently O-E converted at the BS, followed by bit detection. Besides fiber-imposed impairments, the optical signal suffers degradations due to non-linearities in the O-E and E-O processes.

2.1 ROF communication basics

In this section, we first discuss the transmitter, fiber propagation and receiver of a AROF link. Subsequently, we discuss optical modulation schemes that are commonly employed in a AROF link. We then discuss the multiplexing techniques and network topologies employed in a typical AROF network. Finally, we present the results of our simulation-based parametric study of a typical AROF link.

2.1.1 Typical analog radio over fiber link

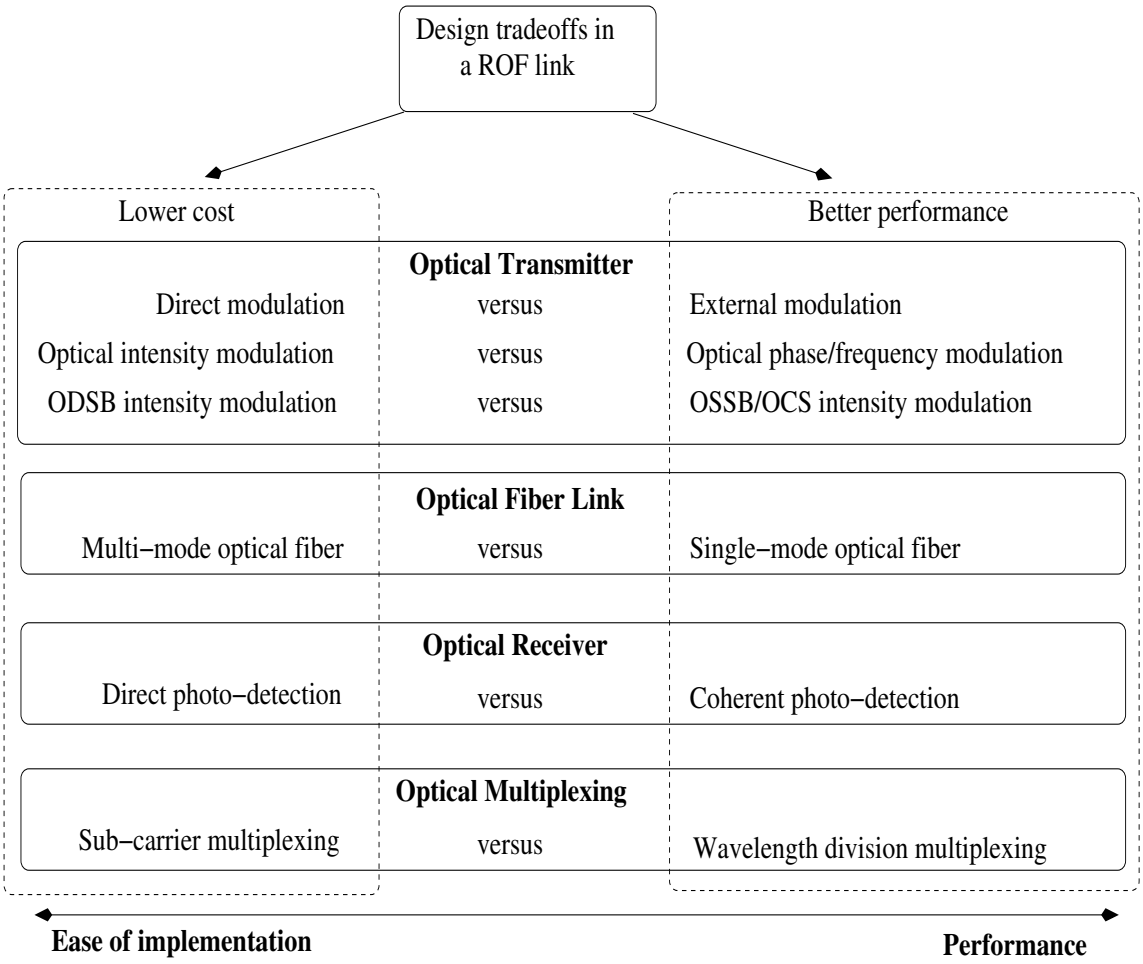

Figure 2.2: Trade-offs in the design of a conventional ROF link

Fig. 2.2 shows the trade-offs in the design of a conventional ROF link, including the various design options in the optical transmitter, optical fiber link, optical receiver and in optical multiplexing. These design options present the designer with a cost versus performance trade-off. The techniques shown

in Fig. 2.2 are discussed in this section (Section 2.1.1) as well as in Sections 2.1.2 and 2.1.3.

In this section (Section 2.1.1) we discuss the various parts of a typical ROF link. The working of a laser and the optical modulation techniques are discussed in Sections 2.1.1.1 and 2.1.1.2, respectively. Subsequently, the fiber channel and the photodetector are discussed in Sections 2.1.1.3 and 2.1.1.4, respectively.

2.1.1.1 Continuous wave semiconductor laser

A laser is an optical transmitter which generates a highly coherent radiation at a single frequency. This optical frequency is used as a carrier to transmit various modulating signals [31].

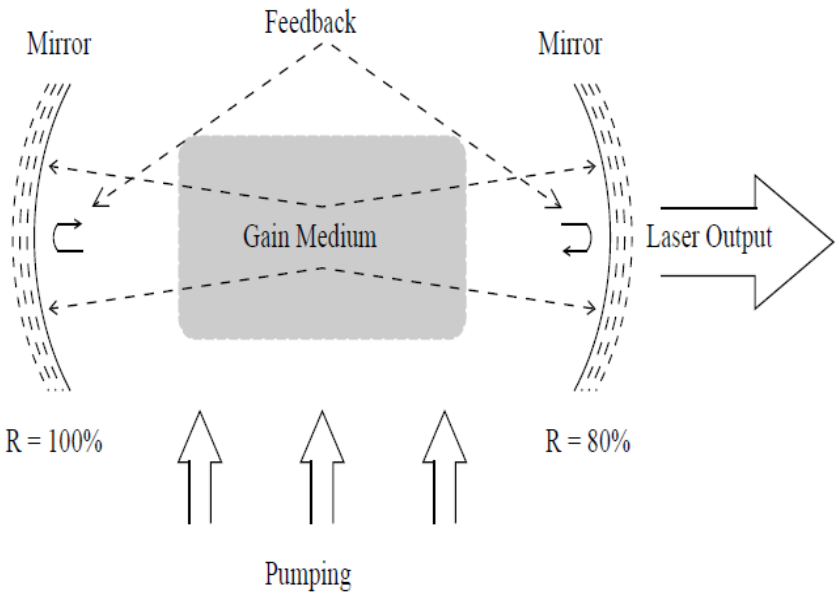

Figure 2.3: Principle of laser operation [59].

Operational principle of a continous wave Laser: A laser emits coherent infrared [60], visible or ultraviolet [61] electromagnetic radiations. The generation of these coherent radiations is based on the principle of stimulated emission [31]. The process of stimulated emission involves electrons that are in an excited state (i.e. high energy state) being impinged by photons, resulting in the electron falling to a lower energy state. This process is accompanied by the emission of a photon whose frequency and phase are exactly the same as that of the stimulating photon. The major components of a lasing source, illustrated in Figure 2.3, are as follows [31]:

1. The gain medium: The gain medium consists of atoms or ions that have electrons which can be stimulated to higher energy states.

2. The pumping mechanism: The constant pumping of energy to the atoms of the gain medium results in population inversion, i.e. a situation where there are higher number of electrons in the excited higher energy state than in the lower energy state.

3. The optical feedback mechanism: Stimulated emission results in photons being released into the laser cavity here they oscillate because of the provided feedback mechanism. The feedback mechanism ensures that most of the photons are reflected back into the cavity where they result in further stimulated emissions. However, some walls in the laser cavity are designed to have a low reflectivity resulting in the escape of some of the photons. The process of stimulated emission ensures that all the escaping photons are coherent. Their frequency depends upon the band-gap of the gain medium used.

There is a competing process of spontaneous emission, that occurs inside a laser, in which electrons in the higher energy state spontaneously drop down to a lower energy state. This process too is accompanied by the emission of a photon. Continuous emission of light from a laser source can occur only if the rate of stimulated emission (R_{stim}) is higher than the rate of spontaneous emission (R_{spon}) i.e. [31]:

$$R_{stim}/R_{spon} = \{exp(hf/k_BT) - 1\}^{-1} \gg 1, \tag{2.1}$$

where h denotes the Plank's constant, f is the frequency of the laser output, k_B represents the Boltzmann constant and T denotes the absolute temperature. The above condition is met when the electrons in the high energy state are higher in number than those in the ground state.

Design of a semiconductor laser: Semiconductor lasers are those lasers in which the gain medium consists of semiconductor materials [61]. Impurities (dopants) are added to these intrinsic (undoped) semiconductor materials to form n and p type semiconductors that have a higher concentration of electrons and holes respectively. When n and p type semiconductor materials are brought in contact with each other, it results in the diffusion of electrons and holes because of the concentration gradient across the junction. The diffusion stops when an equilibrium state is achieved. Such a junction is referred to as a P-N junction [31]. Figure 2.4 provides the illustration of a P-N junction. The presence of a high concentration of opposite charges on either side of the junction results in a strong electric field across the junction. The application of an external voltage across the junction results in the reduction of the electric field and enables the diffusion of electrons and holes across the junction. The diffusion of an electron across the junction and into a hole is accompanied by the emission of a photon. The strength of the electric field that is established across the P-N junction decides the wavelength of the emitted photon. The electric field strength can in turn be controlled by the extent of doping in the n and p type semiconductor materials that are used to form the P-N junction. The change in the refractive index between the laser and the outer material at the cleaved ends of the semiconductor material provide high reflectivity surfaces. This enables optical feedback by reflecting approximately 30% of the emitted photons back into the semiconductor material.

Distributed Feedback Lasers are one of the most frequently employed laser source for achieving optical communication [62]. Optical Feedback in these lasers occurs not only at the facets but throughout the length of the cavity. This is achieved by using a grating that contains alternate portions of high and low refractive indices as can be seen from Figure 2.5. The junctions between these portions serve as reflecting surfaces. Coupling of light travelling in the forward and backward direction can occur only at certain wavelengths. The value of these permitted wavelengths depend upon the periodicity

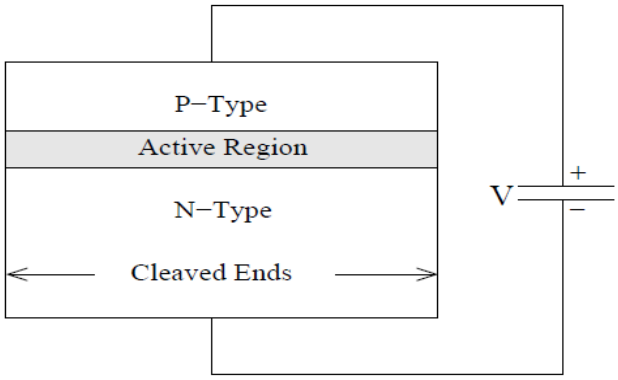

Figure 2.4: Semiconductor laser structure (©S.Ghafoor 2011) [59].

of the low and high refractive index portions within the grating. Hence lasers operating at various optical frequencies can be designed by changing this periodicity.

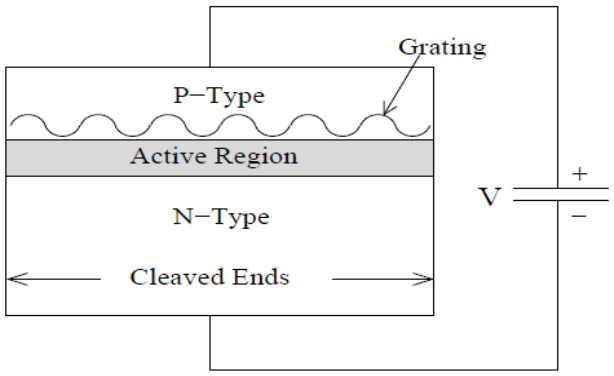

Figure 2.5: DFB semiconductor laser (©S.Ghafoor 2011) [59].

For an ideal laser, i.e for a laser whose output is perfectly coherent and is at a single frequency, the output signal may be modelled by the following equation

$$E_{laser}(t) = \sqrt{2P_{in}}e^{j\omega_c t} \tag{2.2}$$

where P_{in} and ω_c are the operating power and angular frequency of the laser output, respectively.

2.1.1.2 Modulation techniques

As shown in Fig. 2.1, E-O conversion is performed by optical modulation. Modulation of the optical carrier can be achieved by either directly modulating the optical source or by using a separate optical modulator. These two techniques are typically referred to as direct modulation and external modulation, respectively.

Direct modulation: In **direct modulation**, a Laser Diode (LD) is driven by a current I_{drive} in order to generate an optical output [31]. As shown in Fig. 2.6(a), modulation of the optical

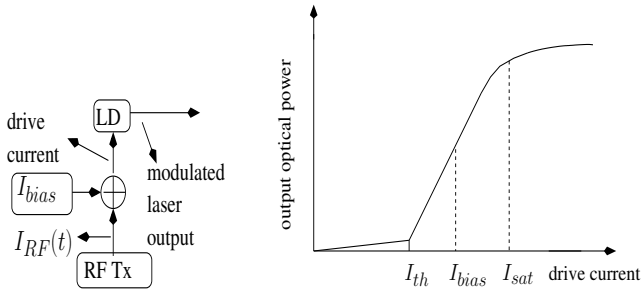

(a) Direct modulation setup

(b) Power vs. drive current curve of a laser

Figure 2.6: Direct modulation

output power[1] of a laser can be inexpensively accomplished by varying the drive current level using an electronic RF Transmitter, referred to as RF Tx in Fig. 2.6(a). This is normally referred to as direct modulation of lasers. Fig. 2.6(b) illustrates the Power vs. Current (P-I) characteristic of a laser, showing in a stylized manner the output optical power level for different values of the drive current. Within the linear region of the P-I characteristic in Fig. 2.6(b), the output power is related to the drive current as follows: $P(t) = k(I_{drive} - I_{th}) = k(I_{bias} + I_{RF}(t) - I_{th})$, where I_{th} is the threshold current of the laser, I_{bias} is the bias current, $I_{RF}(t)$ is the modulating RF signal, while k is the proportionality constant that depends on the laser source employed.

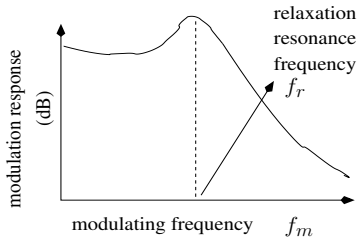

Figure 2.7: Direct modulation bandwidth of the laser

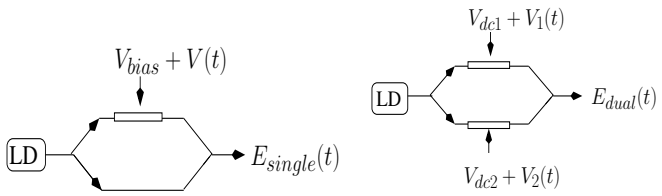

(a) Single Drive MZM

(b) Dual Drive MZM

Figure 2.8: Single and Dual-drive MZM external modulators

When direct modulation of lasers is employed, the following considerations are important:

1. As shown in Fig. 2.6(b), there is a linear region of operation beyond which (i.e. $I_{drive} > I_{sat}$) the laser output saturates and before which (i.e. $I_{drive} < I_{th}$) the output is negligible [31]. The drive current of a laser should be biased at a point that ensures the laser operates within the linear region of the P-I curve in Fig. 2.6(b).

[1]Optical power can also be measured in terms of optical intensity, which is defined as the optical power per unit area

2. Fig. 2.7 plots the modulation response versus the modulation frequency, where the modulation response at f_m Hz is the strength of the modulated signal when a sinusoidal modulating signal having a frequency of $f_m = \frac{\omega_m}{2\pi}$ Hz is employed. The transfer function and 3-dB bandwidth is mathematically given by the following low pass filter expressions [31],

$$H(\omega_m) = \frac{\omega_r^2 + \Gamma_r^2}{(\omega_r + \omega_m - i\Gamma_r)(\omega_r - \omega_m + i\Gamma_r)}$$
$$f_{3dB} = \frac{1}{2\pi}[\omega_r^2 + \Gamma_r^2 + 2(\omega_r^4 + \Gamma_r^4 + \omega_r^2\Gamma_r^2)^{1/2}]^{1/2}.$$

As seen from Fig. 2.7, the modulation response peaks at $f_m = f_r = \frac{\omega_r}{2\pi}$, beyond which the modulation response decreases dramatically. Here, f_r is called the relaxation resonance frequency. When a laser is turned on, the output optical power oscillates with a decay rate of Γ_r before settling down to the steady state value. For typical lasers $\omega_r \gg \Gamma_r$. Hence the expression for the 3 dB cutoff frequency simplifies to $\sqrt{3}f_r = (\sqrt{3}\omega_r)/(2\pi)$ [31]. The designer should ensure that the modulating current has frequencies which are well below f_r.

External modulation: Furthermore, the optical carrier is a sinusoidal signal, also often referred to as a tone, that has an amplitude, phase and frequency. The Frobenius norm of the tone is referred to as the intensity. Both the intensity [63] and the angle [64] of the optical carrier can be modulated using **external modulators**. External intensity modulation can be implemented using a Mach-Zehnder Modulator (MZM) or an Electro-Absorption Modulator (EAM).

A MZM [65] is one of the popular optical external modulators, where the incoming signal is split into two arms, as shown in Fig. 5.11. The MZMs, which apply a drive voltage to either one or to both of the arms are referred to as single-drive and dual-drive MZMs, respectively. The output optical field $E_{single}(t)$ and the intensity $P_{single}(t)$ of a single-drive MZM that is biased at a voltage of V_{bias} and driven by an electronic signal $V(t)$ (i.e. a total drive voltage of $V_{drv} = V_{bias} + V(t)$) can be represented as follows:

$$\begin{aligned} E_{single}(t) &= \frac{1}{2}[e^{j(\frac{\pi V_{drv}}{V_\pi})} + 1]\sqrt{2P_{in}}e^{j\omega_c t} \\ &= \frac{1}{2}[e^{j(\frac{\pi V_{bias}}{V_\pi} + \frac{\pi V(t)}{V_\pi})} + 1]\sqrt{2P_{in}}e^{j\omega_c t} \\ &= \cos(\frac{\pi V_{bias}}{2V_\pi} + \frac{\pi V(t)}{2V_\pi})e^{j(\frac{\pi V_{bias}}{2V_\pi} + \frac{\pi V(t)}{2V_\pi})}\sqrt{2P_{in}}e^{j\omega_c t}, \end{aligned} \tag{2.3a}$$

$$\begin{aligned} P_{single}(t) &= |E_{single}(t)|^2 \\ &= P_{in}[1 + \cos(\frac{\pi V_{bias}}{V_\pi} + \frac{\pi V(t)}{V_\pi})], \end{aligned} \tag{2.3b}$$

where $f_c = \frac{\omega_c}{2\pi}$ is the optical carrier frequency, V_π is the switching voltage of the MZM and P_{in} is the output optical power of the laser feeding the MZM. The switching voltage of a MZM is the voltage that changes the phase of the propagating signal by π radians, when applied to the arm of a MZM. In the case of the dual-drive MZM of Fig. 5.11, the bias voltage V_{bias} is applied differentially via voltages V_{dc1} and V_{dc2}, while the modulating voltage $V(t)$ is applied differentially via the voltages $V_1(t)$ and $V_2(t)$. Mathematically, the drive voltages applied to the two arms are

$$V_{drv1} = V_{dc1} + V_1(t), \tag{2.4}$$
$$V_{drv2} = V_{dc2} + V_2(t), \tag{2.5}$$

where $V_{bias} = V_{dc1} - V_{dc2}$ and $V(t) = V_1(t) - V_2(t)$. The output optical field and the intensity of the dual-drive MZM are given by the following equations:

$$
\begin{aligned}
&E_{dual}(t) \\
&= \frac{1}{2}[e^{j\frac{\pi V_{drv1}}{V_\pi}} + e^{j\frac{\pi V_{drv2}}{V_\pi}}]\sqrt{2P_{in}}e^{j\omega_c t} \\
&= \frac{1}{2}[e^{j(\frac{\pi V_{dc1}}{V_\pi}+\frac{\pi V_1(t)}{V_\pi})} + e^{j(\frac{\pi V_{dc2}}{V_\pi}+\frac{\pi V_2(t)}{V_\pi})}]\sqrt{2P_{in}}e^{j\omega_c t} \\
&= \cos(\frac{\pi(V_{dc1}-V_{dc2})}{2V_\pi} + \frac{\pi(V_1(t)-V_2(t))}{2V_\pi}) \\
&\quad e^{j[\frac{\pi(V_{dc1}+V_{dc2})}{2V_\pi}+\frac{\pi(V_1(t)+V_2(t))}{2V_\pi}]}\sqrt{2P_{in}}e^{j\omega_c t} \qquad (2.6a) \\
&= \cos(\frac{\pi V_{bias}}{2V_\pi} + \frac{\pi V(t)}{2V_\pi})e^{j[\frac{\pi(V_{dc1}+V_{dc2})}{2V_\pi}+\frac{\pi(V_1(t)+V_2(t))}{2V_\pi}]}\sqrt{2P_{in}}e^{j\omega_c t} \qquad (2.6b) \\
&= \cos(\frac{\pi V_{bias}}{2V_\pi} + \frac{\pi V(t)}{2V_\pi})e^{j\phi_{chirp}(t)}\sqrt{2P_{in}}e^{j\omega_c t} \qquad (2.6c) \\
&P_{dual}(t) = |E_{dual}(t)|^2 \\
&= P_{in}[1 + \cos(\frac{\pi V_{bias}}{V_\pi} + \frac{\pi V(t)}{V_\pi})], \qquad (2.6d)
\end{aligned}
$$

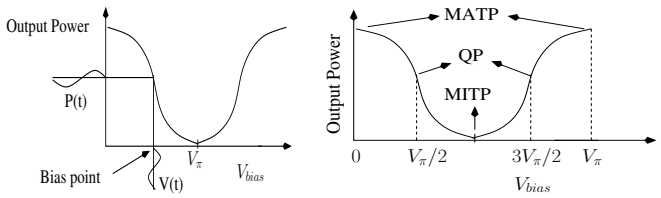

(a) MZM transmittance (b) MZM bias points

Figure 2.9: Biasing for MZM

Fig. 2.9(a) shows the transmittance plot of a MZM, where the output optical power $P(t)$ of the MZM is plotted for various values of the bias voltage V_{bias}. Modulation can be interpreted as a voltage variation around the bias point. It can be seen from Equations (2.3a) and (2.6b) that the output optical field has exponential terms of the form $e^{j\phi(t)}$. Thus, there is residual phase modulation, which is referred to as chirp. This residual phase modulation is potentially converted to intensity modulation during its transmission over the fiber, thereby corrupting the signal that was transmitted using intensity modulation. The chirp in a dual-drive scenario is adjustable, where the dual-drive MZM modulation scheme of Fig. 5.11 would be chirp free if we have: $V_1(t) = -V_2(t) = \frac{V(t)}{2}$. This is referred to as the push-pull mode of operation, because the voltages $V_1(t)$ and $V_2(t)$ are equal in magnitude and opposite in sign.

Fig. 2.9(b) shows the various MZM biasing techniques that can be employed, which include Quadrature Point (QP) biasing, Minimum Transmission Point (MITP) biasing and Maximum Transmission Point (MATP) biasing. QP biasing corresponds to $V_{bias} = V_\pi/2 + m2V_\pi$ or $V_{bias} = -V_\pi/2 + m2V_\pi$, while MITP biasing corresponds to $V_{bias} = V_\pi + m2V_\pi$, where m is an integer. Furthermore, MATP biasing corresponds to $V_{bias} = 0 + m2V_\pi$. When a sinusoidal modulating signal of $V(t) = V_{RF}\cos(\omega_{RF}t)$ is employed, the mathematical expression for the photo-detected signals in

each of these biasing scenarios can be obtained from Equation (2.6d) as follows:

$$\begin{aligned} & I_{QP}(t) \propto P_{QP}(t) \\ & = P_{in}\left[1 \mp \sin(\frac{\pi V_{RF}\cos(\omega_{RF}t)}{V_\pi})\right] \\ & = P_{in}\left[\frac{1}{2} \pm \sum_{n=1}^{\infty}(-1)^n J_{2n-1}(\frac{\pi V_{RF}}{V_\pi})\cos((2n-1)\omega_{RF}t)\right] \end{aligned} \tag{2.7}$$

$$\begin{aligned} & I_{MITP}(t) \propto P_{MITP}(t) \\ & = P_{in}\left[1 - \cos(\frac{\pi V_{RF}\cos(\omega_{RF}t)}{V_\pi})\right] \\ & = P_{in}\Bigg[1 - J_0(\frac{\pi V_{RF}}{V_\pi}) \\ & - 2\sum_{n=1}^{\infty}(-1)^n J_{2n}(\frac{\pi V_{RF}}{V_\pi})\cos(2n\omega_{RF}t)\Bigg] \end{aligned} \tag{2.8}$$

$$\begin{aligned} & I_{MATP}(t) \propto P_{MATP}(t) \\ & = P_{in}\left[1 + \cos(\frac{\pi V_{RF}\cos(\omega_{RF}t)}{V_\pi})\right] \\ & = P_{in}\Bigg[1 + J_0(\frac{\pi V_{RF}}{V_\pi}) \\ & + 2\sum_{n=1}^{\infty}(-1)^n J_{2n}(\frac{\pi V_{RF}}{V_\pi})\cos(2n\omega_{RF}t)\Bigg] \end{aligned} \tag{2.9}$$

The minimum value of $P(t)$ deviates from the ideal value of zero in realistic MZMs, where the extent of deviation is represented by the extinction ratio, $\epsilon = P_{max}/P_{min}$, where P_{max} and P_{min} are the maximum and minimum values of $P(t)$. From Equations (2.3b) and (2.6d), the minimum value of $P(t) = 0$ occurs when $V_{bias} = V_\pi$ and $V(t) = 0$. Thus, the ideal value of extinction ratio is ∞. However, non-ideal MZMs have a finite extinction ratio, where the optical field at the output of a non-ideal MZM is:

$$E_{single}(t) = \frac{1}{2}[e^{j(\frac{\pi V_{bias}}{2V_\pi} + \frac{\pi V(t)}{2V_\pi})} + \gamma \cdot 1]\sqrt{2P_{in}}e^{j\omega_c t} \tag{2.10a}$$

$$\begin{aligned} & E_{dual}(t) \\ & = \frac{1}{2}[e^{j(\frac{\pi V_{dc1}}{V_\pi} + \frac{\pi V_1(t)}{V_\pi})} + \gamma e^{j(\frac{\pi V_{dc2}}{V_\pi} + \frac{\pi V_2(t)}{V_\pi})}]\sqrt{2P_{in}}e^{j\omega_c t}, \end{aligned} \tag{2.10b}$$

where, $\gamma = (\sqrt{\epsilon} - 1)/(\sqrt{\epsilon} + 1)$.

The performance of an intensity modulator w.r.t to the inflicted chirp is quantified by the chirp parameter α which is the ratio of the rate of phase modulation (i.e. frequency deviation) to the rate of intensity modulation i.e. [66], [67]

$$\alpha = \frac{\frac{d\phi_{chirp}}{dt}}{\frac{1}{2P_{dual}}\frac{dP_{dual}}{dt}}, \tag{2.11}$$

where $P_{dual}(t)$ and $\phi_{chirp}(t)$ is instantaneous intensity and undesired phase modulation at the output of the intensity modulator, respectively. Using Equations (2.6d) and (2.6c), the chirp factor of a

DD-MZM is given by the following expression [67]:

$$\alpha_{chirp} = \frac{V'_{drv1}(t) + \gamma^2 V'_{drv2}(t) + \gamma(V'_{drv1}(t) + V'_{drv2}(t))\cos\{(\pi/v_\pi)[V_{drv1}(t) - V_{drv2}(t)]\}}{-\gamma(V'_{drv1}(t) - V'_{drv2}(t))\sin\{(\pi/v_\pi)[V_{drv1}(t) - V_{drv2}(t)]\}}. \quad (2.12)$$

where

$$V'_{drv1}(t) = \frac{dV_{drv1}(t)}{dt},$$
$$V'_{drv2}(t) = \frac{dV_{drv2}(t)}{dt}.$$

If the drive signals are of Equations (2.4) and (2.4) are

$$V_{drv1}(t) = V_{dc1} + V_{RF1}\sin(\omega_{RF}t), \quad (2.13a)$$
$$V_{drv2}(t) = V_{dc2} + V_{RF2}\sin(\omega_{RF}t), \quad (2.13b)$$

and assuming quadrature point biasing of the DD-MZM (i.e. $V_{bias} = [V_{dc1} - V_{dc2}] = V_\pi/2$) and small signal optical modulation (i.e. the RF signal voltages are much smaller than V_{bias}) the equation 2.12 simplifies to [67]:

$$\alpha = \frac{V_{RF1} + \gamma^2 V_{RF2}}{\gamma(V_{RF1} - V_{RF2})} \quad (2.14)$$

It can be seen from Equation (2.14) that a more practical finite value of extinction ratio ($\gamma \approx 1$ but less than 1) results in some residual chirp being present, even when the DD-MZM is operated in the push-pull mode.

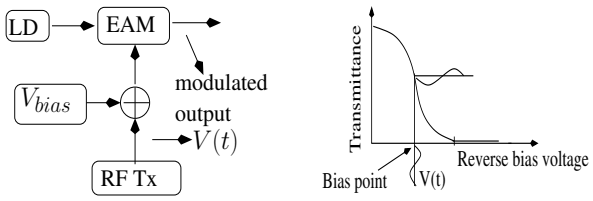

(a) optical modulation using an EAM

(b) EAM Transmittance vs. applied voltage

Figure 2.10: External modulation using an EAM (LD- Laser diode; RF Tx- RF Transmitter; EAM- Electro-Absorption Modulator

On the other hand, as shown in Fig. 2.10(a), an EAM modulates the intensity of the optical signal by using an electric voltage that controls the absorption[1] of the modulator, which is referred to as the Franz-Keldysh effect [68]. As the reverse bias voltage V_{bias} of the EAM increases, the amplitude of the output optical field is reduced by a factor of $T(V)$, where $T(V)$ is the amplitude transmittance.

Fig. 2.10(b) shows the variation of $T(V)$ as a function of the reverse bias voltage applied[69], where $T(V) = 0$ corresponds to complete extinction of the MZM output, while $T(V) = 1$ corresponds to the extinction-free scenario. The output optical field $E(t)$ of the EAM modulator seen in Fig. 2.10(a), that is biased at a voltage of V_{bias} and driven by an electronic signal $V(t)$ is given by the following expression : $E_{EAM}(t) \propto T(V_{bias} + V(t))$.

[1]The absorption of an optical device refers to the phenomenon of a portion of the propagating optical power being absorbed by the device material.

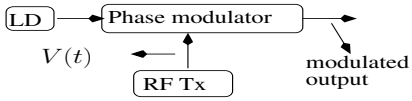

Figure 2.11: Optical phase modulator

Additionally, external optical phase modulation is implemented in ROF links using an optical phase modulator. This is implemented by using the same concept as in the MZMs of Fig. 5.11 with the difference that a phase modulator, unlike the MZM, has a single arm. If an electronic signal $V(t)$ is used for driving a phase modulator as shown in Fig. 2.11, then the output optical field may be written as:

$$E_{PM}(t) = e^{j\frac{\pi V(t)}{V_\pi}}\sqrt{2P_{in}}e^{j\omega_c t}, \tag{2.15}$$

where f_c is the optical carrier frequency, V_π is the switching voltage of the phase modulator and P_{in} is the operating laser power.

Comparison of external modulators:

The most common material used in the manufacture of MZMs is $LibNO_3$. The advantages of using a $LibNO_3$ MZM over an EAM include low optical loss, high power handling capacity, broader optical bandwidth, zero or tunable chirp and insensitivity to temperature [68]. In the push-pull mode, the dual drive MZM would inflict zero chirp on the optical signal [67], while the cost of a dual-drive MZM is higher than that of a single-drive MZM. On the other hand, unlike the EAM, the $LibNO_3$ MZM is much larger in size, has issues of drifting bias voltage, is sensitive to optical polarization and requires higher drive voltages [68]. The MZM is polarization sensitive because the voltage-induced refractive index change in the arms is not the same along the two axes of the arm's cross-section. The smaller size of EAMs enable their integration with the optical source, while the performance of $LibNO_3$ MZM is usually better [68]. However, one of the major advantages of using an EAM is its ability to simultaneously perform the functions of photo-detection and modulation [70], [71].

External versus direct modulation: External modulation is more expensive than direct modulation due to the need for additional equipment, while the direct modulation of lasers suffers from several drawbacks, thereby giving rise to the cost versus performance trade-off alluded to in Fig. 2.2. Not withstanding the cost advantages, direct modulation of lasers has the following disadvantages:

1. Limited modulation bandwidth [31]: The modulation bandwidth of the laser restricts the spectrum of usable modulating signals to a few Gigahertz. Hence, ROF transmissions employing high frequency carriers and high bit-rates cannot be easily achieved using direct modulation.

2. Limited laser output power[72]: Direct modulation of lasers operating at high powers is not easily accomplished due to the fact that the linear relation between the drive current and output optical power is not valid near or within the saturation region of the P-I characteristic curve of Fig. 2.6(b). Operating near or within the saturation region results in clipping and in the generation of harmonics.

3. Laser Chirping [31]: Direct modulation of the output power of the laser is accompaned by chirping, where chirping refers to an instantaneous change in the laser output frequency with changes in the output optical power. This chirp is converted to intensity variations after fiber propagation, thereby corrupting the signal employed in intensity modulation.

4. Increase in intensity noise [68]: If a laser is directly modulated using signals which have frequencies close to its relaxation resonance frequency f_r in Fig. 2.7, then it results in an increase of the optical intensity in the laser output. The relaxation resonance frequency was shown in Fig. 2.7.

It must be noted at this point, employing high-RF signals does not constraint the designer to employ external modulation. The designer may employ direct modulation and a pair of optical carriers instead. The wireless baseband signal may be directly modulated onto one of the optical carriers at the transmitter, while at the receiver it is heterodyne photodetected along with the second optical carrier. Heterodyne photodetection will be discussed in Section 2.1.1.4.

Let us now discuss the various aspects of the fiber channel employed in a ROF link.

2.1.1.3 Fiber impairments

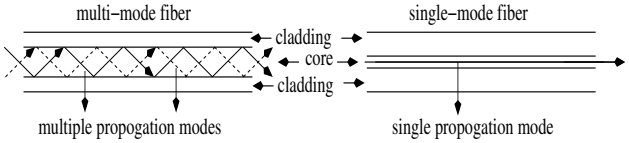

Figure 2.12: Multi-mode and single-mode fiber

An optical fiber consists of an inner core through which the light propagates and an outer cladding. Optical fibers may operate either in a single-mode or in multi-mode fashion, depending on whether single or multiple propagation modes exist in the fiber. Fig. 2.12 shows the propagation modes of the single-mode and multi-mode fiber, where the cross-section of the core in the multi-mode fiber is larger than that of the single-mode fiber [73]. All the architectures considered in this report employ a Single Mode Fiber (SMF), because it provides a larger optical bandwidth and hence it is capable of supporting longer transmission distances without a repeater [73]. However, we hasten to add that the cost of multi-mode fibers is lower than that of a single-mode fiber, thereby giving rise to the cost versus performance trade-off alluded to in Fig. 2.2.

Optical signal propagation in a SMF is governed by a Non-Linear Schrödinger (NLS) equation [74] that is mathematically formulated as follows [74]:

$$\frac{\partial A}{\partial z} = -\frac{\alpha}{2} - j\frac{\beta_2}{2}\frac{\partial^2 A}{\partial T^2} + j\gamma_{nl}\{|A|^2 A\}. \tag{2.16}$$

Here $A(z,T)$ is the envelope (or amplitude) of the optical carrier after it has propagated through z km of SMF. Recall that the optical intensity (i.e. square of the optical carrier's amplitude) has been modulated using a MZM. Continuing, α is the fiber attenuation constant, β_2 is the second derivative

of the fiber propagation constant, γ_{nl} is the parameter which accounts for fiber non-linearity, while T is the time measured in a frame of reference moving with the optical signal (as it propagates along the fiber) at group velocity v_g i.e.

$$T = t - \frac{z}{v_g}.$$

Here t denotes the real-time value and v_g is the velocity with which the envelope of the optical carrier propagates along the fiber. Each of the above mentioned fiber parameters have been dealt with in the following sections.

Fiber attenuation: The optical power attenuates as the signal propagates through the SMF. This attenuation can largely be attributed to the following factors [74]:

1. Material absorption: Two physical processes which contribute towards material absorption are as follows:
   (a) Intrinsic Absorption: This is largely due the electronic resonances in silica which is a major constituent of the SMF.
   (b) Extrinsic Absorption: Imperfections in the the manufacturing process of SMF results in the presence of impurities within the optical fiber. The vibrational resonances of these impurities contribute to the overall material absorption. A major impurity that is present in an optical fiber is water vapour. The extrinsic absorption due to the OH^- ion within the water molecule results in a peak at an optical wavelength of 1.4 μm in the attenuation $vs.$ optical wavelength trend.
2. Rayleigh Scattering: During fiber manufacturing fluctuations in the material density, which get frozen into the fused silica that is used to make the SMF, leads to sudden variations in the refractive index. Sudden variations of the refractive index lead to a scattering of the light in all directions within the fiber through multiple refractions. The scattering of light leads to a loss of the wave guiding nature of the SMF and its fallout is a reduction in the power of the signal that is being guided through the optical fiber. Attenuation due to Rayleigh scattering is inversely proportional to the fourth power of the optical wavelength employed.

Mathematically, the net signal power attenuation occurring within an optical fiber can be expressed as follows [74]:

$$P_{rec} = P_{trans}\ e^{-\alpha z}, \tag{2.17}$$

where $P_{transmitted}$ is the optical power that is coupled into the optical fiber, $P_{received}$ is the optical signal power after propagation through z km of SMF and α is the fiber attenuation constant having the units of km^{-1}. In literature, the attenuation constant is commonly reported in the units of dB/km. A conversion to these units is done through the following expression:

$$\alpha_{db/km} = -10\log_{10}(\frac{P_{rec}}{P_{trans}}) = 4.343\ \alpha.$$

A typical value of $\alpha_{db/km}$ is 0.2 dB/km [31].

Fiber dispersion: As an optical wave propagates, it interacts with the bound electrons of the medium of propagation, which in our case is the SMF. The exact nature of this interaction is dependent on the frequency of the optical wave. Also, the waveguide design contributes to the frequency dependence of the refractive index. This leads to a dependence of the refractive index ($n_r(\omega)$) of the SMF on the frequency ($f = \frac{\omega}{2\pi}$) of the optical signal passing through it [31]. Mathematically, the refractive index of the optical fiber can be defined as [75]:

$$n_r(\omega) = \frac{\text{velocity of the optical wave in vacuum}}{\text{phase velocity of the optical wave in the optical fiber}},$$

or

$$v_p(\omega) = \frac{c}{n_r(\omega)}.$$

Here v_p is the phase velocity of the optical wave as it propagates through the fiber i.e. the velocity with which the phase of an optical wave changes and c is the velocity of the optical wave in vacuum. From the above discussion it is evident that the phase velocity depends upon the frequency of the optical wave because of the dependence of refractive index on the optical frequency. A modulated optical carrier is no longer a single frequency signal and each frequency propagates at slightly different phase velocities leading to changes (broadening) in the shape of the envelope (i.e. the modulated signal that is being transmitted). Higher is the range of frequencies present in the optical signal (i.e. higher optical bandwidth) higher is the extent of the broadening. Note that the group velocity is the "average" velocity with which the envelope is propagating and it remains constant. The extent of pulse broadening is quantified by the parameter β_2. Mathematically,

$$\beta_2 = [\frac{1}{c}(2\frac{dn}{d\omega} + \omega\frac{d^2n}{d\omega^2})]_{\omega=\omega_c}. \tag{2.18}$$

Here ω_c is the angular frequency around which the optical spectrum is centred i.e. the frequency of the optical carrier. In the literature dispersion parameter, D is frequently used in place of β_2. This parameter is related to β_2 through the following relation:

$$D = -\frac{2\pi c}{\lambda_c^2}\beta_2 = -\frac{\omega_c^2}{2\pi c}\beta_2. \tag{2.19}$$

Here λ_c is the wavelength of the optical carrier. The variation of dispersion parameter with the optical carrier frequency can be seen from Figure [31]. The above explained fiber dispersion is also referred to as Group Velocity Dispersion (GVD) or chromatic dispersion. There are other types of fiber dispersions, whose effect is much less pronounced at the optical frequencies typically used in ROF communication [31] using SMF. Hence the term fiber dispersion has been used to refer to GVD in this chapter.

Fiber nonlinearity: A dielectric medium (e.g. a fiber) is an electrical insulator that can be polarized by an applied electric field. Fiber non-linearity arises from the fact that the total polarization responds non-linearly to the electric field E of the light, especially when the optical intensity is high [31]. This results in effects like non-linear refractive index and four wave mixing, which are described in the following paragraphs.

Non-linear refractive index:

The previous section dealt with fiber dispersion arising from the optical frequency dependence of the refractive index. Similarly, fiber non-linearity arises from the dependence of the refractive index, of the optical fiber, on the total optical power of the propagating signals. The refractive index of the optical fiber is given by the following expression [74]:

$$n_r(\omega, P(t)) = n_r(\omega) + n_2 \frac{P_{fib}(t)}{A_{eff}}. \tag{2.20}$$

Here $n_r(\omega)$ is the linear part of the refractive index (i.e. the value of the refractive index if the optical fiber was linear), $P(t)$ is the instantaneous optical power of the propagating signals, A_{eff} is the effective area of the fiber core, c is the speed of light in vacuum and n_2 is the non-linearity index of the fiber. The second term in equation 2.20 represents the deviation from linear behaviour. The extent fiber non-linearity is quantified through its non-linearity parameter γ which is defined as follows [31]:

$$\gamma_{nl} = \frac{n_2 \omega_c}{c A_{eff}}, \tag{2.21}$$

where c is the speed of light and ω_c is the optical carrier's angular frequency. The varying nature of $P(t)$ results in a time varying refractive index, which in turn modulates the phase of the optical signal. Time varing phase shifts result in the instantaneous optical angular frequency deviating from its nominal value of ω_c. This is referred to as frequency chirping. Phase modulation arising from fiber non-linearity is of two types, which are as follow:

1. Self-Phase Modulation (SPM): This occurs because of the time varying nature of the propagating signal's own instantaneous power. The mathematical expression for the time varying phase shift ($\phi_{SPM}(t)$) and frequency chirping ($\delta\omega_{SPM}(t)$) are as follows [74], [31]:

$$\begin{aligned} \phi_{SPM}(t) &= \gamma_{nl} Ł_{eff} P_{fib}(t), \\ \delta\omega_{SPM} &= \frac{d\phi_{SPM}(t)}{dt} = \gamma_{nl} Ł_{eff} \frac{dP_{fib}(t)}{dt}. \end{aligned} \tag{2.22}$$

   For a fiber of length L and attenuation α, $Ł_{eff}$ is defined as follows:

$$Ł_{eff} = \frac{1 - e^{-\alpha L}}{\alpha}.$$

2. Cross-Phase Modulation (XPM): In a Wavelength Division Multiplexed (WDM) system two or more optical carriers are simultaneously employed for transmitting multiple signals. The optical power in each optical channel contributes to the total optical power in the fiber. In such a case the extent of non-linear distortion suffered by each channel depends not only on its own optical power, but also on the optical power in the co-propagating channels. The mathematical expression for the time varying phase shift ($\phi_{XPM,j}(t)$) and frequency chirping ($\delta\omega_{XPM,j}(t)$) experienced by the signal in j^{th} channel are as follows [74], [31]:

$$\begin{aligned} \phi_{XPM}(t) &= \gamma_{nl,j} Ł_{eff} [P_j(t) + 2 \sum_{i=1, i\neq j}^{J} P_i(t)], \\ \delta\omega_{XPM} &= \frac{d\phi_{XPM}(t)}{dt} = \gamma_{nl,j} Ł_{eff} \frac{d[P_j(t) + 2\sum_{i=1,i\neq j}^{J} P_i(t)]}{dt}, \end{aligned} \tag{2.23}$$

where $\gamma_{nl,j}$ is the fiber non-linearity parameter for the signal in the j^{th} channel, P_j is power of the optical signal in the j^{th} channel and L_{eff} is as defined previously. The factor 2 in the equation 2.23 indicates that XPM is twice as effective as SPM for the same amount of optical power.

In addition to the non linearities arising from the optical frequency dependence of the refractive index there are other types of non-linear effects which are present in a fiber. However these are not significant for the power levels, fiber lengths and the optical frequencies utilised in ROF communication [31].

Four-Wave Mixing (FWM):

The non-linear interaction of multiple optical signals that are propagating in a single optical fiber leads to the generation of optical signals at new frequencies. This phenomenon is typically called FWM. For example, when signals at optical frequencies of $f_{c,1}$, $f_{c,2}$ and $f_{c,3}$ Hz are propagating in the fiber, FWM results in the generation of an optical signal at $f_{FWM} = f_{c,1} \pm f_{c,2} \pm f_{c,3}$ Hz, where the most significant are those at [31]:

$$f_{FWM} = f_{c,i} + f_{c,j} - f_{,ck}, \tag{2.24}$$

where $i, j, k \in 1, 2, 3$. The above expression includes frequencies of the form

$$f_{FWM} = 2f_{c,i} - f_{c,j} \tag{2.25}$$

$$\tag{2.26}$$

FWM is most significant at low absolute values of the dispersion parameter D [31].

Other non-linear effects

Other major non-linear effects include Stimulated Brillouin Scattering (SBS) and Stimulated Raman Scattering (SRS) [31], where in both cases photons of the incident field get annihilated. In other words, optical energy is transferred from a signal propagating at a particular optical frequency to a signal at a lower frequency. SBS occurs in the backward direction, where the lower frequency optical signal propagates in a direction that is opposite to that of the incident higher frequency signal. On the other hand, SRS can occur in both directions [31].

Now that we have discussed both optical modulation and fiber transmission, let us now continue our discourse by considering optical photo-detection.

2.1.1.4 Photodetector

Photo-detection is the process of detecting an optical signal using a photo-diode, where a photo-diode generates an electronic current that is proportional to the incident optical power. This process is referred to as square-law photo-detection, where the responsivity R of a photo-diode is the ratio of the output photo-current to the incident optical power.

Design of a photodetector: When illuminated, the electrons in the valence shell of the semiconductor absorb the impinging photons, thereby gaining their energy [76]. This propels them into the

conduction band. This transition is possible only if the energy of the impinging photon is equal to the energy difference between an electron in the valence band and an electron in the conduction band. Such a phenomenon is referred to as photoelectric effect and is illustrated in Figure 2.13. The electronic transition results in the generation of an electron-hole pair, with the free electron being in the conduction band and the hole being in the valence band [76]. When an external potential difference is applied, these electron-hole pairs give rise to a current, which is referred to as photocurrent. A basic photodetector (PD) consists of a reverse biased p-n junction, which is referred to as a photodiode, that generates a photocurrent on being illuminated. A p-n junction has three regions namely, a p-type region, a depletion region and a n-type region. Two parameters that characterize the performance of a photodiode are as follows:

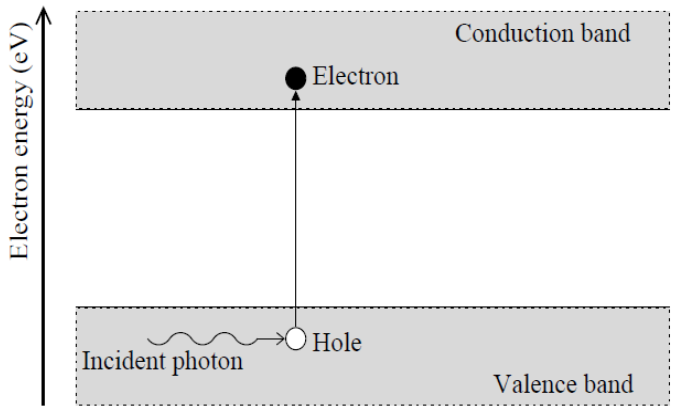

Figure 2.13: Photoelectric Effect (©S.Ghafoor 2011) [59]

1. Responsivity: If a constant illumination of power $P_{received}$ is incident on the photo-diode and it results in a constant current I_p, then the responsivity, R, of the photodiode is defined as:

$$R = \frac{I_p}{P_{rec}}. \tag{2.27}$$

The responsivity of a photodiode depends upon its quantum efficiency. The quantum efficiency, η_{pd}, of a photodiode is defined as the efficiency with which the diode utilises the incident photons to generate electron-hole pairs [31]. Mathematically, it is equal to the ratio of the rate of generation of the free electrons to the rate of the photon impingement. As the photocurrent, I_p, is the rate of flow of the electronic charge, I_p/q is equal to the rate of flow (and hence generation) of the free electrons, where e is the charge on a single electron. Similarly, the rate of incidence of photons is equal to the ratio of the total optical energy incident per unit time (i.e. the optical power P_{rec}) to the optical energy carried by each impinging photon. The optical energy carried by a photon propagating at a frequency f_c is hf_c, where h is the Plank's constant. Thus, the quantum efficiency of a photodiode is formulated as follows:

$$\begin{aligned}\eta_{pd} &= \frac{Rate\ of\ generation\ of\ the\ electrons\ through\ photoelectric\ effect}{Rate\ of\ incidence\ of\ photons} \\ &= \frac{I_p/e}{P_{received}/hf_c}.\end{aligned} \tag{2.28}$$

Using equation 2.29 in equation 2.28, we get:

$$R = \frac{e}{hf_c}\eta_{pd}$$

The quantum efficiency and hence the responsivity of a photodiode can be increased by increasing the surface area on which the light is incident. An increase in the surface area can be achieved by increasing the dimensions (length or width) of the photodiode.

2. Bandwidth: The bandwidth of a photodiode limits the bandwidth of the optical signal that can be detected using that photodiode. Note here that the bandwidth of the optical signal is defined as the difference between the highest and lowest significant frequency that is present in the optical signal. Hence the bandwidth of a optical double side band signal, that has been generated by modulating an optical carrier using an RF electronic signal, would have a bandwidth of $2f_u = 2(f_{RF} + (B/2))$, where f_u, f_{RF} and B_{RF} are the highest frequency, carrier frequency and bandwidth of the RF signal. The effect of the photodiode's 3-dB bandwidth can be neglected, provided it is greater than the highest significant frequency present in the modulating electronic signal [77]. Mathematically, the 3 dB bandwidth of the photodiode, B_{PD}, is formulated as follows [31]:

$$B_{PD} = 1/[2\pi(\tau_{transit} + \tau_{RC})], \tag{2.29}$$

where $\tau_{transit}$ is the transit time and τ_{RC} is the RC time constant of the photodiode. The transit time of a photodiode is the time required for an electron to travel a length l_{PD} from one end of the photodiode to the other end at velocity $v_{electron}$ i.e:

$$t_{transit} = l_{PD}/v_{electron}. \tag{2.30}$$

The photodiode has a lumped model (i.e neglecting the effect of the physical dimensions), which is that of a low pass RC circuit with a time constant τ_{RC}. The capacitance, and hence the RC time constant increases as the length of the depletion region increases [31]. The rise time, τ_{rise}, of a photodiode is defined as the time taken time taken by the photocurrent to rise from 10% to 90% of the final steady state value when there is a step increase in the incident optical power. Mathematically, τ_{rise} is formulated as follows:

$$\tau_{rise} = ln(9)(\tau_{transit} + \tau_{RC}), \tag{2.31}$$

Hence,

$$\tau_{rise} = 0.35/B_{PD}, \tag{2.32}$$

Thus, the bandwidth of the photodiode decides how promptly the photodiode responds to changes in the incident optical power. Higher is the bandwidth, the faster is the response. From equation 2.29 it can be observed that the bandwidth of the photodiode can be increased by decreasing the transit time. This can be achieved by decreasing the length of the photodiode.

PIN photodetector: From the above discussion it is evident that there is a bandwidth-responsivity trade-off in the design of a photodiode. The responsivity and bandwidth are directly and inversely

proportional to the length of the photodiode respectively [31]. An alternative approach is to design a PIN photodiode.

The generated photocurrent has two parts which are [31]:

1. Diffusion current: This is generated due to the impinging of photons on the p-type and n-type regions. For a reverse biased photodiode, the flow of diffusion current is a slow process. Hence its response to a sudden change in the intensity of the incident light is slow. In other words, if the photocurrent is dominated by the diffusion current, then the detection bandwidth would be severely restricted.

2. Drift current: This is generated by the impinging of photons on the depletion region and constitutes the desired part of the generated photocurrent. The width of the depletion decides the number of electron-hole pairs that are created, and hence controls the strength of the generated drift current.

For a fixed length of the photodiode, inserting an intrinsic (undoped) semiconductor material in between the p-type and n-type materials would increase the length of the depletion region and decrease the length of the n-type and p-type regions [78]. This would ensure that the drift current is dominant over the diffusion current and hence increase the bandwidth of the photodiode without compromising with its responsivity. Such a photodiode is referred to as a PIN photodiode and has been shown in Figure 2.14.

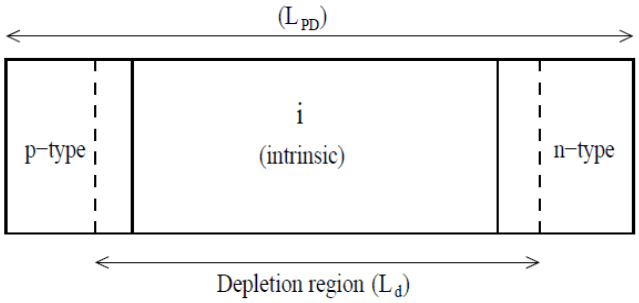

Figure 2.14: PIN photodiode (©S.Ghafoor 2011) [59].

Photodetection techniques: The two kinds of photo-detection are direct photo-detection [57] and coherent photo-detection. In direct photo-detection, if $E_{rec}(t)$ is the optical field of the received signal, then the generated photo-current $I(t)$ is $I(t) = R|E_{rec}(t)|^2$ [57]. On the other hand, in coherent photo-detection, the received optical signal is mixed with a local oscillator optical signal, followed by their joint photo-detection. Mathematically, this can be represented as:

$$I(t) = R|E_{rec}(t) + E_{LO}(t)|^2, \tag{2.33}$$

where $E_{rec}(t)$ and $E_{LO}(t)$ are the optical fields of the received optical signal and the local oscillator signal, respectively. Expanding the expression in equation (2.33) would result in one of the terms being a product of the two fields, which is referred to as the beat signal. The two types of coherent

photo-detection are homodyne photo-detection and heterodyne photo-detection. In homodyne photo-detection the optical frequency $f_{LO} = \frac{\omega_c^{LO}}{2\pi}$ of the local oscillator signal is equal to the carrier frequency $f_{rec} = \frac{\omega_c}{2\pi}$ of the received optical signal. In such a scenario, the photo-detected signal $I(t)$ is:

$$\begin{aligned} I(t) &= R|A_{rec}e^{j\omega_c t+\phi_{rec}} + A_{LO}e^{j\omega_c t+\phi_{LO}}|^2 \\ &= R[A_{rec}^2 + A_{LO}^2 + 2|A_{rec}||A_{LO}|\cos(\phi_{rec} - \phi_{LO})], \end{aligned} \tag{2.34}$$

where A_{rec} and A_{LO} are the amplitudes of the received optical signal and the local oscillator signal, respectively, while ϕ_{rec} and ϕ_{LO} are the phases of the two optical fields. On the other hand, in heterodyne photo-detection the optical frequency f_{LO} of the local oscillator signal is not equal to the carrier frequency f_{rec} of incident optical signal. In such a scenario, the photo-detected signal $I(t)$ is:

$$\begin{aligned} I(t) &= R|A_{rec}e^{j\omega_c t+\phi_{rec}} + A_{LO}e^{j\omega_c^{LO} t+\phi_{LO}}|^2 \\ &= R[A_{rec}^2 + A_{LO}^2 + 2|A_{rec}||A_{LO}|\cos(\omega_{diff}t + \phi_{rec} - \phi_{LO})], \end{aligned} \tag{2.35}$$

where $\omega_{diff} = \omega_c - \omega_c^{LO}$. As shown in Fig. 2.15(b), heterodyne photo-detection can be used to achieve the up-conversion of the baseband/IF signal to an RF frequency of f_{RF} Hz, which can be done by ensuring that $\omega_{diff} = 2\pi f_{RF}$ and then filtering the beat signal.

This complexity of coherent photo-detection may be reduced by locating the local oscillator laser in the BS and transmitting the signal remotely from the BS to RAP through the optical fiber. When two laser sources are employed, the phase noise of the local oscillator laser would be uncorrelated with that of the of optical signal's laser. This would result in the photo-detected signal having significant phase noise [79]. The data carrying optical signal and the local oscillator signals may also be derived from the same source.

Thus, direct photo-detection is simpler and hence more cost-effective than coherent photo-detection, while coherent photo-detection provides a better performance, thereby giving rise to the cost versus performance trade-off seen in Fig. 2.2.

The discussions so far assumed a noise-free optical link, while the next section details the various sources of noise in a ROF link.

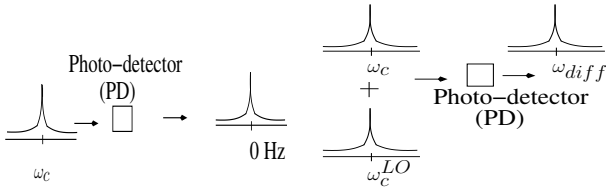

(a) Direct photo-detection (b) Heterodyne photo-detection

Figure 2.15: Basic types of photo-detection

2.1.1.5 Noise in a ROF link

Assuming Δf_{chirp} is the bandwidth over which the noise power is measured at the receiver [31], the major sources of noise in an optical link are as follows:

1. Relative Intensity Noise (RIN): The output of a laser that is driven using a constant current exhibits certain fluctuations in the output phase, frequency and intensity[31], which constitutes the above-mentioned **RIN**. The primary source of this is the spontaneous emission of photons, where the intensity noise results in a Signal To Noise Ratio (SNR) degradation, while the phase/frequency noise leads to a non-zero spectral linewidth (splillage) around the output frequency [31]. Mathematically, the RIN noise power is formulated as follows [31]:

$$\sigma_{RIN}^2 = K_{RIN} I_{dc}^2 \Delta f_{chirp}, \tag{2.36}$$

where K_{RIN} is a device dependent value, which is usually expressed in dB/Hz and I_{dc} is the average photo-current value. Typically K_{RIN} has values around -150 dB/Hz.

2. Amplified Spontaneous Emission (ASE) noise is produced by spontaneous emission in an optical amplifier and then amplified by the amplifier's gain mechanism [31]. The power spectral density of ASE noise is expressed as $S_{ASE}(f) = (G_{amp} - 1) n_{sp} hf$ [31], where G_{amp} is the amplifier gain, n_{sp} is the device dependent spontaneous emission factor, h is the planck constant, while f is the optical frequency.

3. Shot Noise: Shot noise occurs due to the fact that the photodetected current consists of a stream of electrons that are *generated* at random times [80],[81]. In the true sense it is a stationary random process with Poisson statistics. However it is well approximated by Gaussian statistics. Also it has a constant Power Spectral Density (PSD). In other word, it is white. noise variance is formulated as follows [31],[82]: Mathematically, the shot noise power is given by[31]:

$$\sigma_{shot}^2 = 2eI_{dc}\Delta f_{chirp}, \tag{2.37}$$

where e is the charge carried by an electron.

4. Thermal Noise: The random *thermalmotion* of the electrons manifests itself as a fluctuating current even when there is no applied voltage. It is also referred to as Nyquist noise or Johnson noise. It is modelled as a stationary Gaussian random process with a white (constant) PSD. Thermal noise is added by both, the photodiode and the receiver amplifier. Mathematically, the variance of the thermal noise is formulated as follows [31]:

$$\sigma_{thermal}^2 = \frac{4k_B T_{ab}}{R_L} F_n \Delta f_{chirp}, \tag{2.38}$$

where k_B is the Boltzmann constant, T_{ab} is the absolute temperature, R_L is the load resistor, F_n is the noise figure of the receiver's electronic amplifier.

The noisy photodetected current at the output of the photo-detector is:

$$I_{noisy}(t) = I_{PD}(t) + I_{dark} + n_{tot}(t), \tag{2.39}$$

where $I_{PD}(t), I_{dark}, n_{tot}(t)$ is the photocurrent, dark current and total noise current respectively. The dark current I_{dark} is the current that is generated in a photodiode even when it is not illuminated with any required optical signal. It is produced due to the background illumination, stray radiations etc. Since the various types of receiver noise operate independently, the variance of the zero mean noise current for a link that does not employ optical amplification is as follows:

$$\sigma_{total}^2 = \sigma_{shot}^2 + \sigma_{thermal}^2 + \sigma_{RIN}^2. \tag{2.40}$$

Our discourse on modulation techniques in Section 2.1.1.2 introduced the various optical modulators, while the discussion in Section 2.1.2 will cover the commonly employed modulation schemes.

2.1.2 Common ROF optical modulations schemes

ROF systems may rely on modulating either the intensity or the angle, i.e. phase/frequency, of the optical carrier. In the following sections we will describe the optical intensity modulation and the optical angle modulation.

2.1.2.1 Optical intensity modulation

By definition, Intensity Modulation (IM) involves the modulation of the intensity[1] of the optical signal by the modulating electronic signal, where detection can be carried out by using both the direct or coherent photo-detection schemes discussed in Section 2.1.1.4. Intensity modulation may be of single-sideband or double-sideband nature or may result in a carrier suppressed output. The corresponding Optical Double Side Band (ODSB), Optical Single Side Band (OSSB) and Optical Carrier Suppression (OCS) intensity modulation schemes are described in the following sections.

Optical double side band intensity modulation: Fig. 2.16(a) shows the stylized spectrum of an ODSB signal, which consists of the optical carrier frequency f_c as well as of the lower and upper optical sidebands. If the centre frequencies of the lower and upper optical sidebands are f_{lower} and f_{upper} respectively, then in Fig. 2.16(a) we have $f_c - f_{lower} = f_{upper} - f_c = f_{RF}$[83], where f_{RF} is the center frequency of the modulating RF signal. Direct modulation of lasers and external modulation using an EAM can be invoked for generating an ODSB signal [58]. Additionally, an ODSB signal may be generated by the single-drive MZM of Fig. 2.8(a), by setting $V_{bias} = V_\pi/2 + m2V_\pi$ or $V_{bias} = -V_\pi/2 + m2V_\pi$ in Equations (2.3b), where m is an integer [63], [84] and $V(t)$ is the RF signal to be transmitted. The specific bias condition employed for generating ODSB signals is referred to as quadrature biasing. The same condition is true for the dual-drive MZM of Fig. 2.8(b), along with the additional condition that there should be a phase difference of π between the RF signals $V_1(t)$ and $V_2(t)$ in Equation (2.6d).

While the ODSB signal of Fig. 2.16(a) has two modulation sidebands, the OSSB signal to be discussed in the next section has a single modulation sideband.

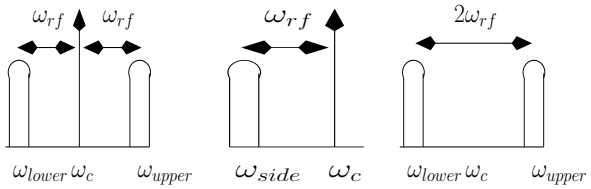

(a) ODSB signal (b) OSSB signal (c) OCS signal

Figure 2.16: Optical modulation formats

[1]The intensity of an optical signal is the square of its amplitude.

Optical single side band intensity modulation: Fig. 2.16(b) shows the stylized spectrum of an OSSB signal, which consists of the optical carrier frequency f_c and only one of the two possible sidebands at f_{side} Hz. As seen from Fig. 2.16(b), we have $f_c - f_{side} = f_{RF}$, where f_{RF} is the frequency of the modulating RF signal. There are several techniques that can be employed for generating OSSB signals, including the employment of the Fiber Bragg Gratings (FBGs) [85] and the Dual-Drive MZM of Fig. 2.8(b).

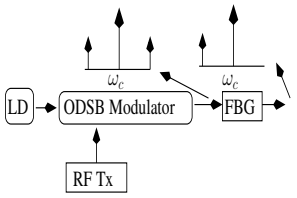

Figure 2.17: OSSB generation using a FBG

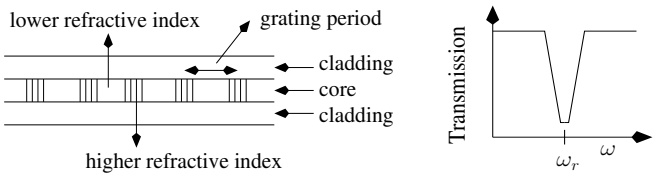

(a) A FBG filter

(b) FBG transmission

Figure 2.18: Structure and transmission spectrum of a Fiber Bragg Grating

A FBG can be used for filtering out one of the sidebands of an ODSB signal, as shown in Fig. 2.17 [85]. A FBG filter consist of a periodic perturbation of the effective refractive index along the length of the fiber core, as shown in Fig. 2.18(a) [86]. The length of one period of this perturbation is referred to as the grating period [86]. A FBG filter has a transmission profile as shown in Fig. 2.18(b), where the signal at frequency f_r is reflected. The value of f_r depends on both the periodicity of the perturbation and on the effective refractive index of the fiber core. This technique conceived for OSSB signal generation needs high-selectivity filters for retaining only the desired sideband, especially when the RF carrier involved is not high. Moreover, the temperature-dependent variations of the refractive index results in the reflected wavelength value being temperature-sensitive [87]. Furthermore, an OSSB signal can also be generated by the **Dual-Drive MZM** of Fig. 2.8(b), when it is quadrature biased by setting $V_{bias} = V_\pi/2 + m2V_\pi$ or $V_{bias} = -V_\pi/2 + m2V_\pi$ in Equation (2.6d), where m is an integer, whilst simultaneously ensuring that a phase shift of 90^o is maintained between the RF signals applied to its two arms seen in Fig. 2.8(b) [84],[65], [43]. Recall that the ODSB and OSSB signals of Figures 2.16(a) and 2.16(b), respectively, include the optical carrier, but this is not the case for the OCS signal discussed in the next section.

Optical carrier suppression modulation: As seen from Fig. 2.16(c), an OCS based signal consists of a suppressed optical carrier frequency at f_c Hz and two sidebands at $f_c \pm f_{RF}$ Hz, where the frequency of the RF signal employed is f_{RF} Hz. An OCS signal can be generated by the MZM of Fig. 5.11, when it is MITP biased, as illustrated in Fig. 2.9. This is achieved by setting $V_{bias} = V_\pi + m2V_\pi$ in Equations (2.3b) or (2.6d), where m is an integer [48]. The photo-detection of the OCS signal

generates a signal at $2f_{RF}$ Hz, which is a result of the above-mentioned beating between the two optical sidebands during photo-detection [88].

Choice of the intensity modulation format: A designer is required to make an informed-choice between ODSB and OSSB, especially in the case of direct detection links. The advantage of employing ODSB modulation, especially through direct modulation, is that it requires a simple [83] and inexpensive [58] set-up. Even when employing external modulation, ODSB signal generation require a less sophisticated architecture than OSSB signal generation. However, the disadvantage of employing ODSB modulation is the chromatic dispersion induced power penalty, where the chromatic dispersion modifies the phase of the optical signal propagating through the fiber. The frequency-dependent phase change inflicted by chromatic dispersion results in a phase difference between the upper and lower sidebands, where the photo-detected signal is proportional to the optical power $P(t) = |E(t)|^2$ with $E(t)$ being the optical field. The optical power is attenuated because of the destructive interference between the beat signals, where this optical power attenuation is referred to as Dispersion Induced Power Penalty (DIPP). The attenuation of the optical power results in the attenuation of the power P_{RF} of the photo-detected signal at f_{RF} Hz, where the extent of attenuation is given by the following expression [83]:

$$P_{RF} \propto \cos^2 \left[\frac{\pi \cdot L \cdot D \cdot \lambda_c^2 \cdot f_{RF}^2}{c \cdot [1 - \frac{2}{\pi} \cdot \arctan(\alpha_{chirp})]} \right] \tag{2.41}$$

where $D = -\frac{2\pi c}{\lambda_c^2}\beta_2$ is the chromatic dispersion parameter, β_2 is the second derivative of the optical propagation constant, L is the length of the fiber, λ_c is the wavelength of the optical carrier and α_{Chirp} is the chirp parameter of the signal. Thus, chromatic dispersion limits the usable fiber lengths and the usable modulating-signal frequencies when ODSB modulation is employed [89]. The effects of chromatic dispersion can be mitigated either by using other optical modulation schemes or by optical signal processing.

Optical modulation schemes that are tolerant to power attenuation due to chromatic dispersion include OSSB modulation and OCS. Thus, employing OSSB modulation would be more power efficient than ODSB when the chromatic dispersion induced power penalty in ODSB is greater than the loss in power due to the use of a single sideband in OSSB. Moreover, OSSB modulation has a higher level of spectral efficiency because of the lower bandwidth it occupies [84]. In the links where the optical noise added by the optical amplifier is the most dominant noise, filtering out the noise added to the suppressed sideband prior to photo-detection will improve the receiver sensitivity when OSSB modulation is employed [90]. The comparison between the ODSB and OSSB has been summarised in Table 3.7.

Thus, there is a cost vs. performance trade-off, which was alluded to in Fig. 2.2

Now that we have become familiar with the basic intensity modulation techniques, we move on to discussing optical angle modulation in the next section.

2.1.2.2 Optical angle modulation

Optical angle modulation involves the modulation of the phase or frequency of the optical signal, which are typically referred to as the use of optical Frequency Modulation (FM) and Phase Modulation

Table 2.1: Comparison of ODSB and OSSB

comparison parameter	ODSB	OSSB
generation complexity and cost	simpler	complex
Chromatic dispersion induced power penalty	higher	lower
Spectral efficiency	lower	higher
generation technique	Direct and external modulation	Only external modulation

(PM), respectively. The mathematical expression for phase modulation was provided in Equation (2.15), while frequency modulation is expressed as follows:

$$\begin{aligned} E_{FM}(t) &= \sqrt{2P_{in}}e^{\int_0^t \omega(\tau)d\tau} = \sqrt{2P_{in}}e^{\int_0^t [\omega_c+\omega_\Delta V(\tau)]d\tau} \\ &= \sqrt{2P_{in}}e^{\omega_c t+\omega_\Delta \int_0^t V(\tau)d\tau}, \end{aligned} \tag{2.42}$$

where ω_Δ decides the depth of frequency modulation, $V(t)$ is the modulating voltage, P_{in} is the input optical power and ω_c is the optical carrier. From Equation (2.42) we can say that frequency modulation is essentially phase modulation in which the modulating signal is first integrated and then applied to the phase modulator[64]. Hence, the techniques designed for phase modulation are also applicable to frequency modulation and vice-versa.Optical angle modulated signals can be detected coherently or directly, where coherent detection is straight-forward, while direct detection requires a prior conversion of the angle modulated signal to a intensity modulated signal using a discriminator, which is located in the RAP. A discriminator is an optical equipment which has a frequency dependent output intensity. Some of the major discriminator implementations employ mach-zehnder delay interferometers, chromatic dispersion or optical filtering.

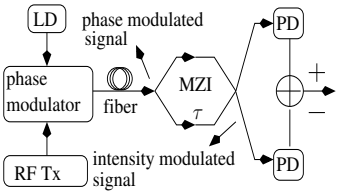

Figure 2.19: phase modulation using MZI

The **Mach-Zehnder delay Interferometer (MZI)** is shown in Fig. 2.19, where the output of a laser operating at a frequency of $f_c = \frac{\omega_c}{2\pi}$ Hz and at a optical power of P_{in} is phase modulated and transmitted over the fiber. Assuming a non-dispersive, linear optical fiber, the angle modulated signal entering the MZI is:

$$E_{rec}(t) = \sqrt{2P_{rec}}e^{j\omega_c t+\phi(t)} \tag{2.43}$$

where $\phi_{PM}(t)$ depends on the modulating electronic signal and the intensity of the angle modulated signal $|E_{rec}(t)|^2$ is constant. The incoming angle modulated signal is divided into the two arms of

the MZI, where the signal in one of the arms experiences a delay of τ with respect to the other. The outputs of the two arms are combined to generate an optical field E_{MZI}, whose intensity P_{MZI} is as follows [91]:

$$\begin{aligned} P_{MZI} &= |E_{MZI}|^2 \\ &= \frac{1}{4}\left|\sqrt{2P_{rec}}e^{j\omega_c t+\phi_{PM}(t)} + \sqrt{2P_{rec}}e^{j\omega_c(t-\tau)+\phi_{PM}(t-\tau)}\right|^2 \\ &= \frac{P_{rec}}{2}[1+1+2\cos(\omega_c\tau+\Delta\phi_{PM}(t))] \end{aligned}$$

where $\Delta\phi_{PM}(t) = \phi_{PM}(t) - \phi_{PM}(t-\tau)$ and the MZI is quadrature biased with $\omega_c\tau = -\pi/2$. Subsequently, using the small signal approximation that $\sin(\Delta\phi_{PM}(t)) \approx \Delta\phi_{PM}(t)$, we get [91], [92]:

$$P_{MZI} = P_{rec}[1+\sin(\Delta\phi_{PM}(t))] = P_{rec}[1+\Delta\phi_{PM}(t)] \tag{2.44}$$

Thus, the optical signal is now intensity modulated and can be detected by a direct photo-detection [91]. Additionally, the MZI generates a complementary output whose intensity is $P_{out,2} = P_{rec}[1 - \Delta\phi_{PM}(t)]$ [91]. Balanced photo-detection can be achieved by subtracting the two photo-detected outputs [91], where the advantages of balanced photo-detection will be discussed in Section 3.1.4.

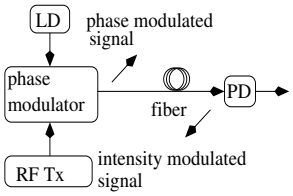

Figure 2.20: Phase Modulaton using dispersion

On the other hand, in the **Chromatic dispersion** based technique, the output of the laser is phase modulated by a RF signal $V(t)$, which for this discussion is assumed to be an electronic tone, i.e. $V(t) = V_{RF}cos(\omega_{RF}(t))$ in Equation (2.15). Using the Jacobi-Anger expansion, the optical field of the modulated signal of Fig. 2.20 is then given by [93]:

$$E_{PM}(t) \propto e^{j(\omega_c t+\frac{\pi V_{RF}}{V_\pi}\cos(\omega_{RF}t))} = \sum_{k=\infty}^{\infty} j^k J_k(\frac{\pi V_{RF}}{V_\pi})e^{j(\omega_c+k\omega_{RF})t}, \tag{2.45}$$

where $f_{RF} = \frac{\omega_{RF}}{2\pi}$ Hz and $f_c = \frac{\omega_c}{2\pi}$ Hz are the frequency of the electronic tone and laser output, respectively. The intensity ($|E_{pm}(t)|^2$) of the signal presented in Equation (2.45) is constant and its photo-detection would result in a DC photo-current . As shown in Fig. 2.20, the phase modulated signal propagates through a dispersive fiber with a dispersion parameter D, negligible non-linearity and having length L, where the optical field after transmission in the fiber is given by [93]:

$$E_{rec}(t) \propto \sum_{k=\infty}^{\infty} j^k J_k(\frac{\pi V_{RF}}{V_\pi})e^{j((\omega_c+k\omega_{RF})t+\frac{1}{2}\beta_2 Lk^2\omega_{RF}^2)}, \tag{2.46}$$

where β_2 is given by Equation (2.19) and the intensity of the optical signal ($|E_{rec}(t)|^2$) is no longer constant. The photo-detected signal now contains the various harmonics of the modulated electronic tone. The strength of the photo-detected signal P_{RF} at $\omega_{RF} = 2\pi f_{RF}$ is given by [93]:

$$P_{RF} \propto \sin^2(\frac{\pi \cdot L \cdot D\lambda_c^2 \cdot f_{RF}^2}{c}). \tag{2.47}$$

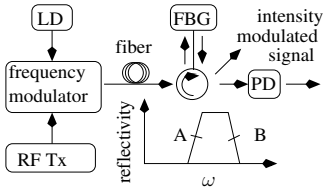

Figure 2.21: Phase modulation using FBG

Finally, a discriminator can be designed by using an **Optical Filter** whose transmittance (or reflectivity) varies linearly with the frequency of the incident frequency-modulated signal. As shown in Fig. 2.21, the output of a laser operating at $f_c = \frac{\omega_c}{2\pi}$ Hz is modulated using an optical phase modulator, which is is driven by the signal $V(t)$ [55]. The output of the phase modulator enters a FBG filter, whose reflectivity profile is shown in Fig. 2.21 [55]. This filter achieves phase to intensity conversion by serving as a frequency discriminator, where points A and B of the reflectivity curve in Fig. 2.21 are located in the linear slope regions of the profile. If the optical carrier is located at frequencies corresponding to points A and B, then the photo-detected signal is proportional to the first derivative of $V(t)$ [55]. As was stated in this section, in the case of frequency modulation, the drive signal is obtained by integrating the modulating electronic signal $V(t)$. Hence, the direct detection of the frequency modulated signal after it has been passed through the FBG filter, generates the original electronic modulating signal $V(t)$.

Besides using FBG technology, a 10^{th} order Finite Impulse Response (FIR) optical filter, whose electric field transmittance varies linearly with frequency, can be implemented by employing the Planar Lightwave Circuits (PLC) technology [94]. An advantage of deploying such a filter includes the absence of distortions that are higher than the second order.

The dynamic range of an angle modulated link that relies on direct photo-detection, largely depends on both the non-linearity of the discriminator and on the residual IM present in the signal that is transmitted from the BS [94].

2.1.2.3 Comparison of optical intensity and angle modulation

Intensity modulated signals can be detected using the simpler direct photodetection without any additional hardware. However, the direct photo-detection of angle modulated links requires an additional discriminator in the RAP, thereby increasing the complexity of the RAP.

The cross-talk level in multi-channel systems is lower when employing phase modulation than when employing intensity modulation [91]. Moreover, optical intensity modulation requires biasing, while the phase modulator is not biased. Thus intensity modulation suffers from the drifting bias voltage and hence needs bias stabilization circuits [93]. When employing direct detection, angle modulated systems can exploit the chromatic dispersion to perform phase to intensity conversion. In contrast, chromatic dispersion results in a power penalty, when employing the easily generated ODSB intensity modulated signal. This can be overcome only by employing more complex intensity modulation schemes or signal-processing techniques [93]. An advantage of implementing an angle modulated direct detection link using a MZI is that balanced detection can be implemented with a single BS-RAP fiber link [91],

where balanced photo-detection results in a higher optical link SNR.

However, optical angle modulated systems either need a sophisticated technique to convert the angle modulation to intensity modulation or they have to employ the more complex coherent detection. Moreover, the optical angle modulation index needs to be kept low [93]. It can be seen from Equations (2.44) and (2.47), that the frequency response of the MZI or chromatic dispersion based discriminator is periodic [91], [93], thereby limiting the modulation bandwidth. Moreover, not all values of the angle-modulation depths and fiber lengths can be used when employing a MZI or chromatic dispersion based discriminator. A MZI also introduces a high level of third order distortion. The major comparison points between intensity and angle modulation have been summarised in table 2.2.

Table 2.2: Comparison of intensity and angle modulation

comparison parameter	intensity modulation	angle modulation
photo-detection complexity	simpler	complex
crosstalk	higher	lower
Chromatic dispersion induced impairment	usually higher	usually lower
bias stabilization circuitry	required	not required
generation technique	Direct and external modulation	mostly external modulation

Thus, there is a cost versus performance trade-off, which was portrayed in the stylized illustration of Fig. 2.2. Having covered the basics of a single ROF link, we now discuss the various ROF multiplexing techniques in Section 2.1.3.

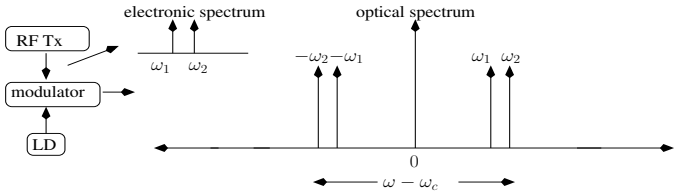

Figure 2.22: A SCM transmitter model

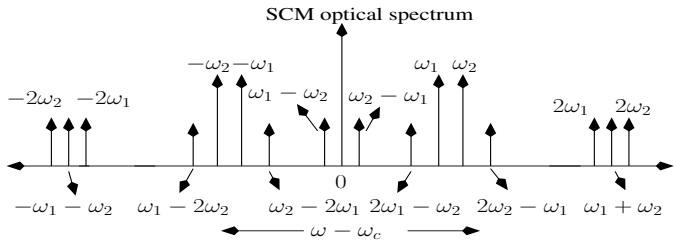

Figure 2.23: SCM optical spectrum

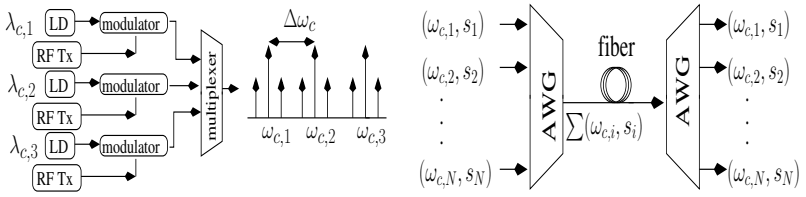

(a) A ODSB-WDM transmitter model

(b) A basic MUX/DEMUX

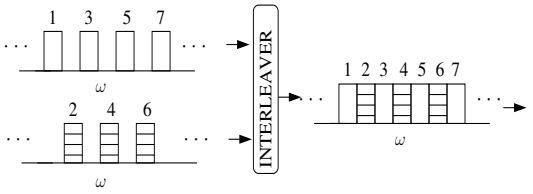

(c) An interleaver

Figure 2.24: Wavelength division multiplexing

2.1.3 Multiplexing

Optical multiplexing employed in multi-user/multi-RAP scenarios allows us to increase the throughput of an optical fiber link. There are two basic types of optical frequency multiplexing schemes, which can be employed in ROF systems, namely sub-carrier multiplexing [95] and wavelength division multiplexing [96].

2.1.3.1 Sub-carrier multiplexing

Sub-Carrier Multiplexing (SCM) refers to frequency multiplexing multiple modulating signals/sub-carriers/channels, for example $f_1 = \frac{\omega_1}{2\pi}$ and $f_2 = \frac{\omega_2}{2\pi}$ Hz, and then employing the combined signal in direct [97] or external modulation [90] of the optical carrier at $f_c = \frac{\omega_c}{2\pi}$ Hz, as shown in Fig. 2.22. The optical spectrum of the modulating electronic signal and the modulated optical signal have been shown in Fig. 2.22. As shown in Fig. 2.22, the desired sidebands (also called optical channels) of the ODSB modulated modulated SCM signal are located at $\omega_c \pm \omega_1$ and $\omega_c \pm \omega_2$. The advantages of employing SCM are as follows:

1. The transmission bandwidth of the optical fiber is large, hence a number of sidebands can be accommodated on either side of the optical carrier in Fig. 2.22 by using SCM [95]. Thus, SCM assists in efficient exploitation of the large optical bandwidth [95].

2. It is possible to utilise a number of network architectures and protocols because each channel is independent and continuously available [98]. For example, each SCM channel could serve a unique user. SCM enables dynamic channel assignment in cellular networks in addition to allowing flexible allocation of bandwidths, which caters to changes in technology or the user needs [99]. For example, multiple SCM channels can be allocated to a user with high data-rate requirement.

3. Chromatic dispersion induces degradations which are dependent on the modulating signal's center-frequency (ω_1, ω_2) and on its bandwidth (BW_{ω_1}, BW_{ω_1}). It was mentioned in Section

2.1.2.1 that the centre-frequency-dependent power penalty can be overcome by employing OSSB signals. An additional advantage of employing SCM-OSSB [90] is that, for a given total bit-rate, the bit-rate per sub-carrier is low. In other words, the bandwidth per channel would be low, and hence SCM signals are more resilient to the bandwidth-dependent degradation than a single-channel baseband optical system having the same total bit rate.

4. For the same total optical power as the single-channel baseband communication system, the optical power per sub-carrier is lower in a SCM based system, which means that the SCM transmission is more resilient to SPM[1] [90].

5. As seen from Fig. 2.22, SCM generates sidebands at $\omega_c \pm \omega_i$, where ω_i is the RF carrier of the i^{th} SCM channel. In contrast, the signal in a baseband optical communication system is situated at the optical carrier ω_c, which implies that SCM systems can co-exist with the baseband optical communication systems [95].

6. The ability to transmit multiple signals using the same optical carrier provides cost benefits by reducing the number of lasers and external modulators that are required [100].

While the optical spectrum in Fig. 2.22 was an idealised spectrum, the one in Fig. 2.23 shows the optical harmonics and intermodulation products that are generated during SCM. If the number of SCM channels $N = 2$, then, the desired sidebands are at $\omega_c \pm \omega_1$ and $\omega_c \pm \omega_2$. The spectrum in Fig. 2.23 also contains other sidebands, where the sidebands at $\omega_c \pm m\omega_1$ and $\omega_c \pm m\omega_2$, with m being an integer, are referred to as optical harmonics. The sidebands located at $\omega_c \pm (2\omega_1 - \omega_2)$, $\omega_c \pm (2\omega_2 - \omega_1)$ and $\omega_c \pm (\omega_1 + \omega_2)$ in Fig. 2.23 are referred to as optical intermodulation products. Similarly, the harmonics in the photo-detected signal are located at $m\omega_1$ and $m\omega_2$, while second and third order intermodulation products are located at $\omega_i \pm \omega_j$ and $\omega_h \pm \omega_i - \omega_j$, respectively, where $h, i, j \in \{1, 2, ..N\}$, and h, i and j are SCM channel numbers [100]. The major sources of inter-modulation and harmonic non-linear distortion in SCM systems vary for direct and external modulation in addition to the fiber-induced distortion.

In **direct modulation**, non-linear productsresults from the non-linear nature of the P-I curve of Fig. 2.6(b) as well as the mixing of the electrons and photons in the laser cavity. The P-I curve of Fig. 2.6(b) has a threshold value below which optical output is negligible and a saturation region. If the modulating drive current value falls below the threshold value or enters the saturation region, then it results in clipping. Additionally, even the linear region of the P-I curve is not perfectly linear. On the other hand, mixing of electrons and photons in the laser cavity is related to the dynamic non-linearity of the laser[99]. Its effect is negligible when the modulating signal does not contain frequencies close to the laser relaxation resonance frequency. However, its significance increases in wideband-SCM systems i.e SCM systems with high RF carriers of several GHz.

Furthermore, in **external modulation**, the intensity is modulated in a non-linear fashion around the bias point, when an EAM and MZM is employed, respectively, as seen from Fig. 2.9(a) and Fig.2.10(b). This creates harmonics and inter-modulation products.

Finally, the **optical fibe**r introduces non-linear distortions including those arising from fiber dispersion [101], [97] and fiber non-linearity [101]. Even when ideal intensity modulation is performed,

[1]Self Phase Modulation (SPM) was discussed in Section 2.1.1.3

the optical spectrum of $E(t)$ has harmonics and intermodulation products, because it is $|E(t)|^2$ and not $E(t)$ that varies linearly with the modulating signal. However, these distortions would not be present in the photo-detected signal, provided that the transmission was dispersion free, because the photo-detector output is proportional to $|E(t)|^2$. Furthermore, chromatic dispersion changes the relative phase delays of the optical harmonics and inter-modulation products, which means that there exists residual non-linear distortion in the photo-detected signal [97]. Besides chromatic dispersion, the non-linear dependence of the fiber refractive index on the propagating optical power leads to the generation of non-linear distortion. These are usually negligible in typical SCM links because of the low optical power levels per channel.

The maximum number of third-order products is bounded by the value $3K^2/8$, where K is the total number of SCM channels [100]. Hence, the number of intermodulation products exponentially with the number of channels. If the K channels are numbered as $1, 23....K$, then the centre channel is the $K/2^{th}$ channel. The center channel suffers from maximum inter-modulation distortion [100]. Finally, the challenges to implementing SCM can be summarised as follows:

1. When employing a large number of SCM channels, the highest frequency component in the modulating signal would be high. Hence, it can be stated that a laser having a large modulation bandwidth is needed to support a large number of SCM channels, when employing direct modulation.

2. Third order inter-modulation products are the most significant non-linear product in the optical signal and in the photo-detected signal, since it lies within the SCM transmission bandwidth. However, second-order distortions also become significant for wideband SCM transmission [99].

3. XPM and FWM, described in Section 2.1.1.3.a, result in non-linear cross-talk among the channels in a SCM system [90]. These non-linear phenomena are more significant when the operating wavelength is near the zero-dispersion wavelength. Decreasing the sub-carrier spacing can help achieve high total data rates, however, it results in higher non-linear cross talk[90].

4. As the number of SCM channels increase, the modulation index per channel has to be reduced [90], thereby resulting in a lower receiver sensitivity of each channel. Employing an optical amplifier can only partially alleviate this problem because the optical amplifier itself adds ASE noise and that an increase in the received optical power level increases the photo-detected signal power but also increases the shot noise level.

2.1.3.2 Wavelength division multiplexing

While SCM employs a single optical carrier to transmit multiple modulating signals, Wavelength Division Multiplexing (WDM) involves the fiber-based transmission of multiple optical carrier frequencies. As shown in Fig. 2.24(a), each carrier frequency is modulated by an electronic signal, thereby generating sidebands around that carrier. Subsequently, the signals are multiplexed to generate the spectrum seen in Fig. 2.24(a), where the spectrum consists of three optical carriers. The corresponding sidebands appear on either side of each carrier. In **Dense Wavelength Division Multiplexing (DWDM)** [96], the channel spacing $\Delta\omega_c$ of Fig. 2.24(a) has standardized values of 12.5, 25, 50, 100 or 200 GHz [102]. The advantages of WDM are as follows:

1. The wavelengths, i.e. the optical carrier frequencies, that are employed in optical communication, belong to transmission windows that have been selected using criteria like low fiber attenuation or low fiber dispersion. The maximum number of wavelengths that can be multiplexed depends on the spectral width of the transmission window being employed. All the fiber transmission windows consists of a large range of wavelengths, which results in WDM supporting higher data rates through better utilization of the optical bandwidth.

2. The flexibility to design complex optical communication networks, where different channels are injected and extracted from the network by using Optical Add Drop Multiplexers (OADMs), Wavelength Multiplexers (MUXs) and Demultiplexers (DEMUXs). These equipments will discussed later in this section.

3. When the user capacity requirement increases, the transmission rate can be increased by employing new wavelengths. Hence, the ability to support multiple users, without having to lay new optical fibers, is a major advantage of WDM.

Various optical components are employed in WDM based ROF networks, including a multiplexer /demultiplexer and Optical Add Drop Multiplexer (OADM), which are detailed below.

A MUX and a DEMUX is used for combining and separating the optical signals appearing at different optical carrier frequencies, respectively. Most DEMUXs are also capable of operating as a MUX, when operated in the reverse direction, i.e. when light enters from the output ports. As seen in Fig. 2.24(b), the most basic MUX/DEMUX consists of a $(1 \times N)$ Arrayed Waveguide Grating (AWG), which relies on the principle of diffracting the light in order to separate/combine the wavelengths [103]. Each channel consists of the optical carrier along with its sidebands, as represented by $(\omega_{c,i}, s_i)$ in Fig. 2.24(b), while the multiplexed signal is indicated as $(\sum \omega_{c,i}, s_i)$.

The different parts in an $1 \times N$ AWG are shown in Fig. 2.25 [104]. The working principle of the AWG is as follows:*A certain wavelength can be separated out, from a multiplexed set of wavelengths, by ensuring that the desired wavelength interferes constructively, while all other wavelengths interfere in a non-constructive manner.* The light enters the first slab of Fig. 2.25, diverges and enters the arrayed waveguides. At the other end of the arrayed waveguides is the second slab, where the light is collected into the N different output waveguides. The arrayed waveguides have that specific length, which would ensure constructive interference of a unique optical wavelength at the input of each of the output waveguides of Fig. 2.25.

The MUX of Fig. 2.24(b) multiplexes individual frequency bands, while the interleaver of Fig. 2.24(c) is employed for bundling sets of even and odd indexed frequency bands. As shown in Fig. 2.26, the interleaver can be operated in the reverse direction to implement de-interleaving. The OADM of Fig. 2.27 is employed at the RAP to "drop", i.e. demultiplex, a downlink WDM channel, while "adding", i.e.multiplexing, an uplink signal at the same or possibly different optical frequency. Fig. 2.27 shows the block diagram of an OADM, where the downlink signal carried by the optical carrier at $f_{c,2} = \frac{\omega_{c,2}}{2\pi}$ Hz is dropped and an uplink signal at the same optical carrier frequency is added.

The challenges to the implementation of WDM in ROF networks are as follows:

1. The added cost of OADMs, MUXs and DEMUXs increases the overall implementation cost. Using a lower inter-wavelength spacing results in better optical spectral utilisation, but the need

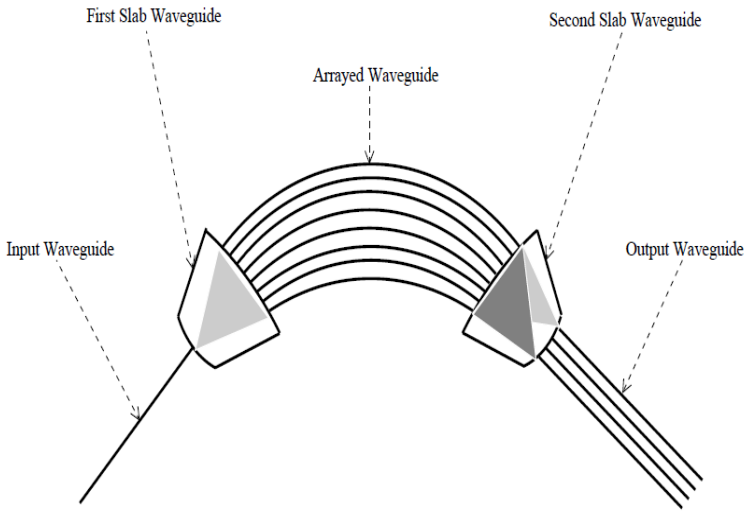

Figure 2.25: Structure of an AWG (©S.Ghafoor 2011)[59].

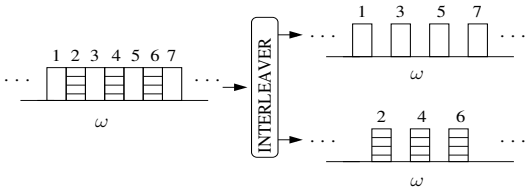

Figure 2.26: An interleaver operated as a de-interleaver

to employ high-selectivity optical filtering in the OADMs and DEMUXs increases their cost.

2. The need to have multiple laser sources increases transmitter cost.

3. WDM transmission suffers from crosstalk due to XPM, FWM, SRS [42]. Lower inter-wavelength spacing increases the achievable transmission rates but also increases the non-linear crosstalk as discussed in Section 2.1.1.3 [42].

4. The imperfect isolation of the ports of the OCs result in crosstalk [105]. Additionally, the performance of the DEMUXs and OADMs is temperature dependent as they are usually built from AWGs and FBG filters. The central wavelength in conventional AWGs depend on the temperature because of the temperature dependent change of the refractive index and of the optical path lengths of the arrayed waveguides [96]. Hence, they need temperature stabilization. Additionally, FBG filters are temperature sensitive [87].

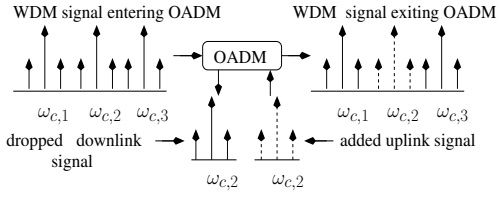

Figure 2.27: Optical add drop multiplexer

Thus, the throughput that can be achieved using WDM is higher than that, which can be achieved using SCM. However, this comes at the cost of having to use multiple laser sources, MUXs, DEMUXs and OADMs, thereby giving rise to the cost versus performance trade-off indicated in Fig. 2.2. In the next section we discuss the results obtained by simulating an AROF link.

2.1.3.3 Network topology

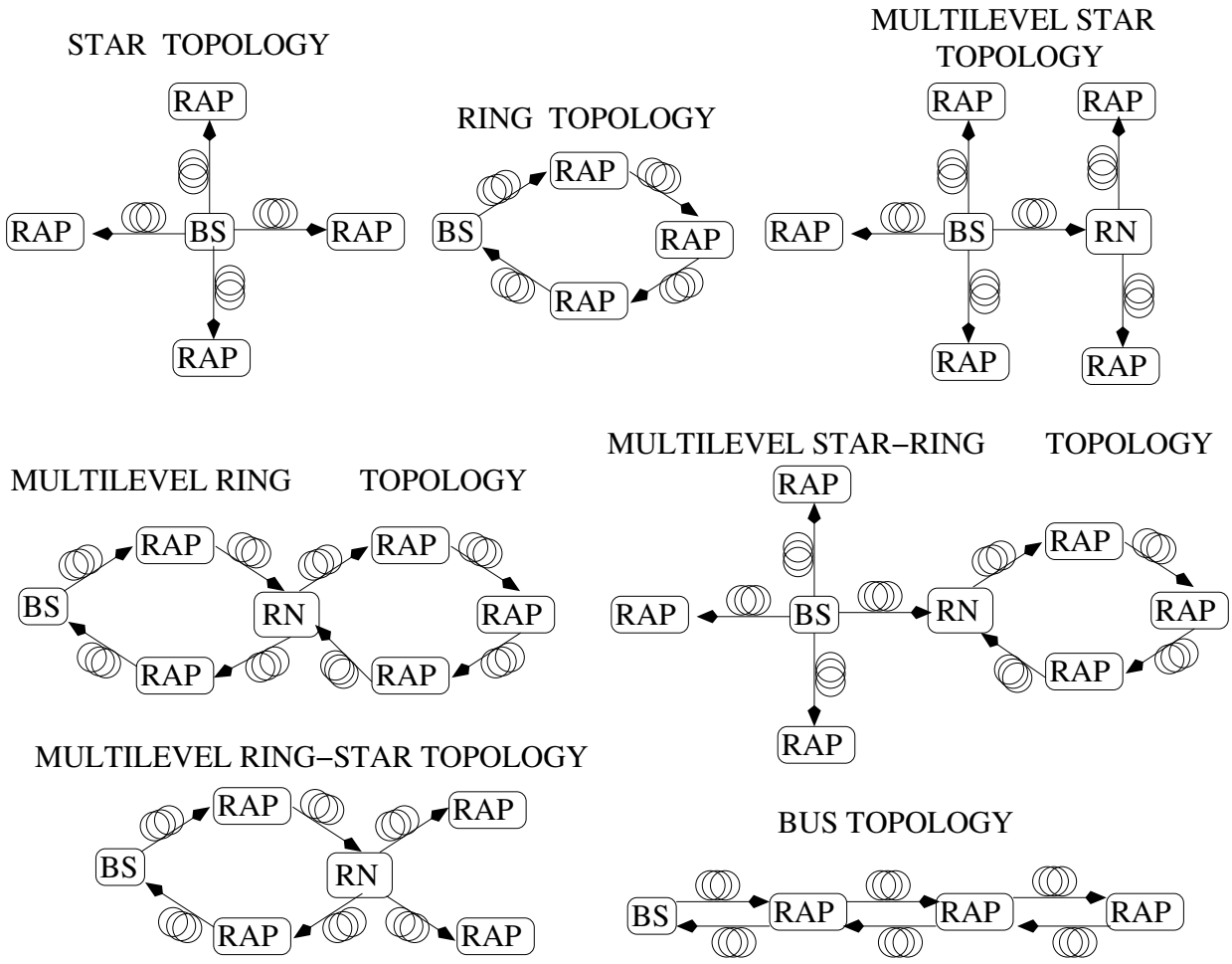

Figure 2.28: ROF network topologies

A multiplexed ROF signal can support a large number of RAPs, where the network can employ a large number of possible topologies, as shown in in Fig. 2.28 [106]. The factors to be decided in choosing a network topology are security, reliability and availability [106]. Reliability is a probability measure and is defined as the probability that there exists an operational path between the communicating devices, which in this case is the BS and the RAP. Reliability depends on the distance between the BS and RAP, probability of failure of the fiber connection and on the number of paths between the BS and RAP. The reliability can be improved by employing $1 + 1 disjoint protection$, which involves the laying of two fibers along each path. The destination chooses the better of the two signals, while in the case of a failure it switches to the alternative path. The multilevel rings topology of Fig. 2.28 has the best reliability both in the unprotected case and in the case of 1+1 disjoint protection, while the star topology has the least reliability[106]. This is because the number of hops and link distance

from the BS to the other RAPs, in all topologies except multilevel ring, increases as the number of RAPs increases. Besides, in the star topology, unlike the multilevel ring topology, there exists a single path between the BS and the RAP and the highest fiber link distance [106].

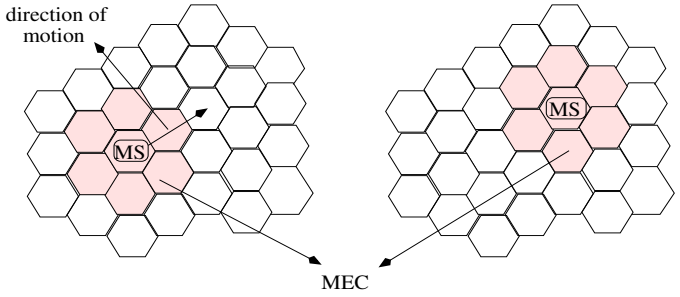

Figure 2.29: ROF network employing the concept of MEC

The performance of a ROF microcellular system is limited by the dynamic range requirement of the uplink [107]. Employing multiple distributed antenna reduces the dynamic range requirements than the case of a single fiber fed antenna [108]. Other techniques to improve the dynamic range include modulating multiple lasers with the same data and combine the outputs or the deployment of an AGC in the uplink path which adjusted the laser drive a current as per the strength of the received uplink signal [109]. Another factor effecting the performance of an ROF network is the large number of hand-offs between the many small cells. One solution to this challenge is to employ the concept of a Moving Extended Cell (MEC) [110]. In this concept, the user is always surrounded by a set of cells (called the the Moving Extended Cell), as shown in Fig. 2.29, that transmit the same user specific data, thereby eliminating the need for handover. These MECs follow the users mobility pattern and thus the challenge to such a technique would be the needed to implement tracking algorithms and reduced network capacity due to redundancy in the transmitted information. One of the performance metrics of a communication network is the steady state call blocking. Dynamic channel assignment, using devices like multimode sources, optical switches [34] and reconfigurable OADMs [111], is found to improve the blocking probability [112].

The maximum capacity of a WDM network that utilises optical amplification is limited by the bandwidth of the optical amplifier like EDFA [105]. Optical amplification can be done immediately after multiplexing in the BS or it can be carried out at the Remote Node (RN). The former is referred to optical pre-amplification, while the latter is referred to as optical post-amplification. When pre-amplification is employed at the BS, the network reach lengths that can be employed when operating at maximum capacity is limited by the amplifier saturation [105]. This constraint can be relaxed by employing post-amplification at the RN. This however increases the cost of the RN and compromises with the goal of performing centralised signal processing.

2.1.4 Split step Fourier transform

As stated previously in Section 2.1.1.3, the propagation of optical signals though a single mode glass optical fiber obeys the following relation [74]:

$$\frac{\partial A}{\partial z} = -\frac{\alpha}{2}A - j\frac{\beta_2}{2}\frac{\partial^2 A}{\partial T^2} + j\gamma_{nl}\{|A|^2 A\}. \tag{2.48}$$

Here $A(z,T)$ is the envelope (or amplitude) of the optical carrier after it has propagated through z km of SMF. Recall that the optical intensity (i.e. square of the optical carrier's amplitude) has been modulated using a MZM. Continuing, α is the fiber attenuation constant, β_2 is the second derivative of the fiber propagation constant, γ is the parameter which accounts for fiber non-linearity, while T is the time measured in a frame of reference moving with the optical signal (as it propagates along the fiber) at group velocity v_g i.e.

$$T = t - \frac{z}{v_g}.$$

Here t denotes the real-time value and v_g is the velocity with which the envelope of the optical carrier propagates along the fiber. Equation (2.48) can be rewritten as follows:

$$\frac{\partial A}{\partial z} = (\hat{D} + \hat{N})A, \tag{2.49}$$

where the non-commuting operators $\hat{D}$ and $\hat{N}$ are defined as follows,

$$\hat{D} = -\frac{\alpha}{2} - j\frac{\beta_2}{2}\frac{\partial^2}{\partial T^2} \tag{2.50}$$

$$\hat{N} = j\gamma_{nl}|A|^2. \tag{2.51}$$

If we divide the total fiber length into segments of length h_δ, then the numerical solution to Equation 2.49 is as follows:

$$A(z + h_\delta, T) = e^{[h_\delta(\hat{D}+\hat{N})]}A(z,T). \tag{2.52}$$

The Baker-Hausdorff relation for two non-commuting operators is formulated as follows:

$$e^{\hat{a}}e^{\hat{b}} = e^{\hat{a}+\hat{b}+0.5(\hat{a}\hat{b}-\hat{b}\hat{a})+ \textit{ higher order terms which can be neglected}} \tag{2.53}$$

$$\approx e^{\hat{a}+\hat{b}+0.5(\hat{a}\hat{b}-\hat{b}\hat{a})}. \tag{2.54}$$

Hence

$$e^{h_\delta\hat{D}}e^{h_\delta\hat{N}} \approx= e^{h_\delta\hat{D}+h_\delta\hat{N}+0.5h_\delta^2(\hat{D}\hat{N}-\hat{N}\hat{D})}. \tag{2.55}$$

If accuracy to the first order in h is sufficient, then Equation (2.55) can be re-written as follows:

$$e^{h_\delta\hat{D}}e^{h_\delta\hat{N}} \approx e^{h_\delta\hat{D}+h_\delta\hat{N}}. \tag{2.56}$$

Using Equation (2.56) in Equation (2.52) we get the following:

$$A(z + h_\delta, T) = e^{h_\delta\hat{D}}e^{h_\delta\hat{N}}A(z,T). \tag{2.57}$$

The accuracy of the solution obtained through Equation (2.57) improves, when the value of the step size h decreases. Hence the total fiber of length L is split into small sections of length h and Equation (2.57) is used recursively. The computational complexity involved in solving Equation (2.57) can be reduced, through a Fourier domain computation. In the Fourier domain, the highly efficient Fast Fourier Transform (FFT) algorithm can be employed. Hence Equation (2.57) can be re-written as follows [74]:

$$A(z + h_\delta, T) = F_T^{-1}[e^{h_\delta\hat{D}(-j\omega)}F_T(e^{h_\delta\hat{N}}A(z,T))], \tag{2.58}$$

where $F_T(.)$ and $F_T^{-1}(.)$ are the Fourier transform and inverse Fourier transform functions respectively, while $\hat{D}(-j\omega)$ is the Fourier transform of $\hat{D}$ operator. Mathematically, it is formulated as follows:

$$\hat{D}(-j\omega) = -\frac{\alpha}{2} - j\frac{\beta_2}{2}\omega^2. \tag{2.59}$$

The above discussed algorithm is referred to as the Split Step Fourier Method (SSFM). Physically, Equation 2.57 is equivalent to assuming that fiber dispersion and fiber non-linearity act independently, within each section of length h. It can be shown through a numerical analysis, that the accuracy of Equation 2.57 improves when re-written as follows:

$$A(z + h_\delta, T) = e^{\frac{h_\delta}{2}\hat{D}} e^{\frac{h_\delta}{2}\hat{N}} e^{\frac{h_\delta}{2}\hat{D}} A(z, T). \tag{2.60}$$

Physically, Equation 2.60 is equivalent to assuming that the optical signal propagates through the first $h_\delta/2$ metres in each section, under the effect of only fiber dispersion and attenuation. Fiber non-linearity is assumed to influence the optical signal at the middle of each section, after which the signal propagates through the remaining $h_\delta/2$ metres in the section, experiencing only fiber dispersion and attenuation. This modified propagation model is also referred to as symmetrized SSFM [74]. The symmetrized SSFM was employed in the simulations that were performed in this thesis.

2.1.5 Simulation based performance analysis of the classical AROF system

In this section we study the effect of various ROF link parameters on the performance of the classical AROF link of Fig. 2.1. The most common type of AROF link employs the ODSB intensity modulation of Section 2.1.2.1 and the direct photo-detection discussed in Section 2.1.1.4, which are also the techniques considered in this section.

Table 2.3: Simulation parameters of the AROF link

Parameter	**Value**	**Parameter**	**Value**
Bit rate RF signal	32 Mbps	MZM insertion loss t_{attn}	4 dB
Laser RIN	-155 dBc/Hz	MZM switching voltage V_π	5.5 V
optical wavelength λ_c	1550 nm	fiber length L	10 km
Laser linewidth	10 MHz	PD trans-impedance	125 Ω
fiber dispersion D	16 ps/km-nm	fiber Non-linearity	1.2 /W/km
Filter roll-off factor	0.5	Dark current	1 nA
fiber attenuation α	0.2 dB/km	photo-receiver NF	6 dB
PD responsivity R	0.8 A/W	f_{rf} (GHz)	2.3, 2.4 and 2.5

2.1.5.1 Link parameters employed in the simulation

Unless otherwise stated, the link parameters used in our simulations are shown in Table 5.2. The most common type of multiplexing scheme employed is the SCM technique discussed in Section 2.1.3.1, while the most commonly employed network topology is the star topology discussed in Section 2.1.3.3. In this section, we simulate a single point-to-point ROF downlink, where a star topology consists of multiple point-to-point links. Furthermore, an important application of ROF is for providing triple play services, i.e. employing ROF for the simultaneous transmission of voice, data and video services

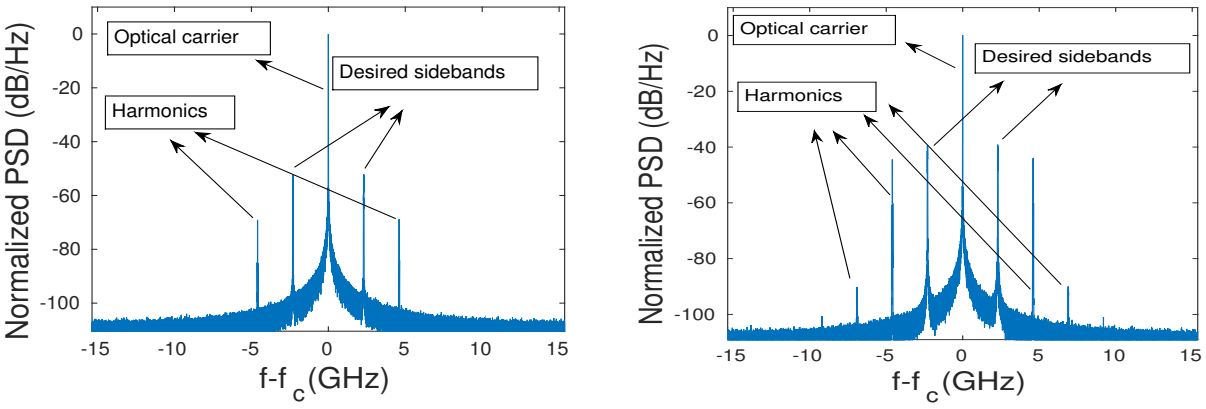

(a) m_{RF}=5% (b) m_{RF}=20%

Figure 2.30: Optical spectra for different depths of optical modulation m_{RF}

[113]. Hence, in this section we employ SCM of three BPSK RF signals at 2.3 GHz, 2.4 GHz and 2.5 GHz, which were generated using Root Raised Cosine (RRC) filters having a roll-off factor of 0.5. These RF signals had a bit rate of 32 Mbps each.

A commercially available laser presented in Section 2.1.1.1, which generates a 1550 nm optical carrier having a linewidth of 10 MHz and imposing a RIN noise of -155 dBc/Hz is employed in the optical transmitter [31]. The dual-drive MZM presented in Section 2.1.1.2 is used to perform the ODSB modulation discussed in Section 2.1.2, where the MZM is assumed to have a switching voltage of $V_\pi = 5.5$ V [114]. Unless otherwise mentioned, an ideal MZM with an extinction ratio of ∞ dB is assumed, where we will discuss the impact of a non ideal extinction ratio in Section 2.1.5.4. Similarly, unless otherwise mentioned, ideal biasing of the MZM at $\frac{V_\pi}{2}$ V is assumed, where the impact of non-ideal biasing will be discussed in Section 2.1.5.5. A 10 km long single mode fiber introduced in Section 2.1.1.3 having standard parameter values, i.e. $\alpha_{dB} = 0.2$ dB/km, $D = 16$ ps/km-nm and $\gamma_{nl} = 1.2$ /km/w is employed [31], where optical propagation is simulated using the split-step technique discussed in Section 2.1.4. Photodetection is performed using the photodiode presented in Section 2.1.1.4 having a responsivity of 0.8 A/W, a dark current of 1 nA and a wide detection bandwidth, i.e. a detection bandwidth significantly greater than 2.5 GHz, where such photodetectors are easily available [115] [116]. A low cost optical receiver having a noise figure of 6 dB and load resistance of 125 Ω is considered [117], where the noise processes operating in the optical receiver are discussed in Section 2.1.1.5. Note that all the spectra presented in the following sections are normalized power spectral density plots, where the power values are normalized with respect to the peak power value. In other words, the peak power in a normalized power spectral density plot is 0 dB/Hz. A second point to note is that all the spectra are one-sided spectra. Typically, an AROF link imposes a BER of less than 10^{-9}. Hence, the overall BER is dominated by the wireless link. The simulations of this section assumed an ideal wireless channel that imposes no noise in order to analyse the impact of the optical link.

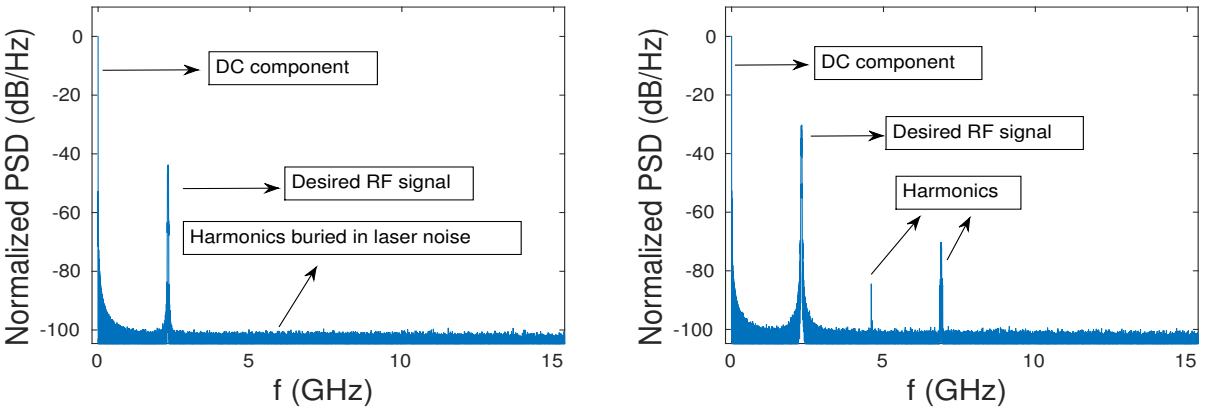

(a) m_{RF}=5% (b) m_{RF}=20%

Figure 2.31: Spectra of photodetected signal for different optical modulation depths m_{RF}

2.1.5.2 Effect of the depth of the optical modulation on the AROF performance

If m_{RF} is the depth of optical modulation of an RF signal $V(t)$, then we have:

$$m_{RF} = \frac{V_{max}(t)}{V_{\pi}} \times 100, \tag{2.61}$$

where $V_{max}(t)$ is the maximum value of $V(t)$. In our simulations, we assume $m_{RF,1} = m_{RF,2} = m_{RF,1} = m_{RF}$ to be the depth of optical modulation of the signals at 2.3 GHz, 2.4 GHz and 2.5 GHz, respectively. As we discussed in Section 2.1.1.2, the non-linear nature of the transfer function shown in Fig. 2.9(a) results in the generation of non-linear products, when carrying out external modulation. The generation of these intermodulation products and harmonics was discussed in Section 2.1.3.1.

In order to illustrate the generation of harmonics, optical modulation is performed using a single RF signal at 2.3 GHz. Fig. 2.30(a) and Fig. 2.30(b) show the spectra of the optical signal after ODSB modulation using a MZM having an ideal extinction ratio of ∞ dB, where the depth of optical modulation is 5% and 20%, respectively. Fig. 2.31(a) and Fig. 2.31(b) show the photodetected signal generated, when the depth of optical modulation is 5% and 20%, respectively. The effects of the noise imposed by the photodetector are also considered. It can be seen from Fig. 2.30 and Fig. 2.31 that increasing the depth of optical modulation increases the strength of the desired optical/electronic sideband but also increases the strength of the harmonics. However, these harmonics can be readily filtered out after photodetection using electronic filters.

Next we carried out optical modulation using two RF signals at 2.4 GHz and 2.5 GHz in order to study the effects of intermodulation. Fig. 2.32(a) and Fig. 2.32(b) show the spectra of the optical signal after ODSB modulation using a MZM having an ideal extinction ratio of ∞ dB, where the depth of optical modulation is 30% and 40%, respectively. Fig. 2.33(a) and Fig. 2.33(b) shows the photodetected signal generated, when the depth of optical modulation is 30% and 40%, respectively. The effects of the noise added by the photodetector are also considered. It can be seen from Fig. 2.32 and Fig. 2.33 that increasing the depth of optical modulation, increases the strength of the desired optical/electronic sideband, but also increases the strength of the intermodulation products. Fig. 2.34(a) shows the desired sideband to third order intermodulation (IM3) product power ratio in the spectrum of the optical signal for various depths of optical modulation. Unlike the harmonics, these

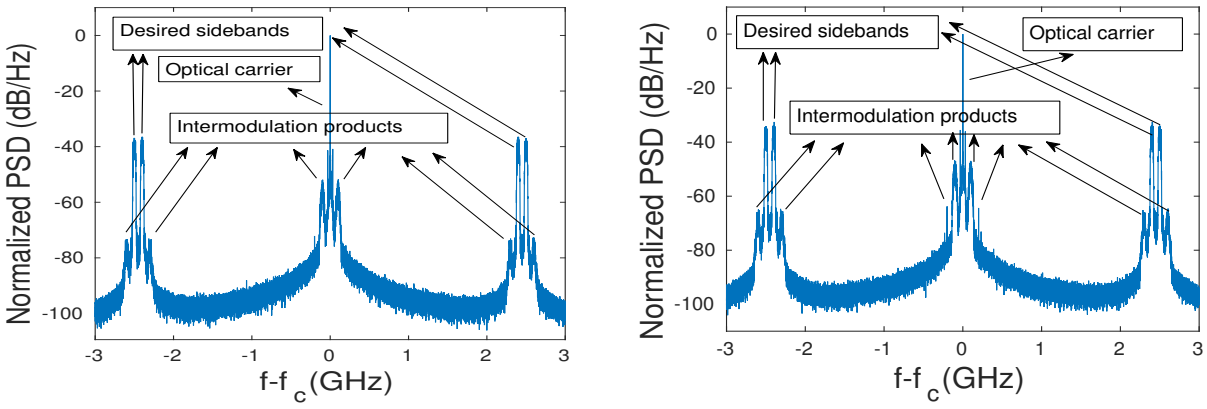

(a) m_{RF}=30% (b) m_{RF}=40%

Figure 2.32: Optical spectra for different optical modulation depths m_{RF}

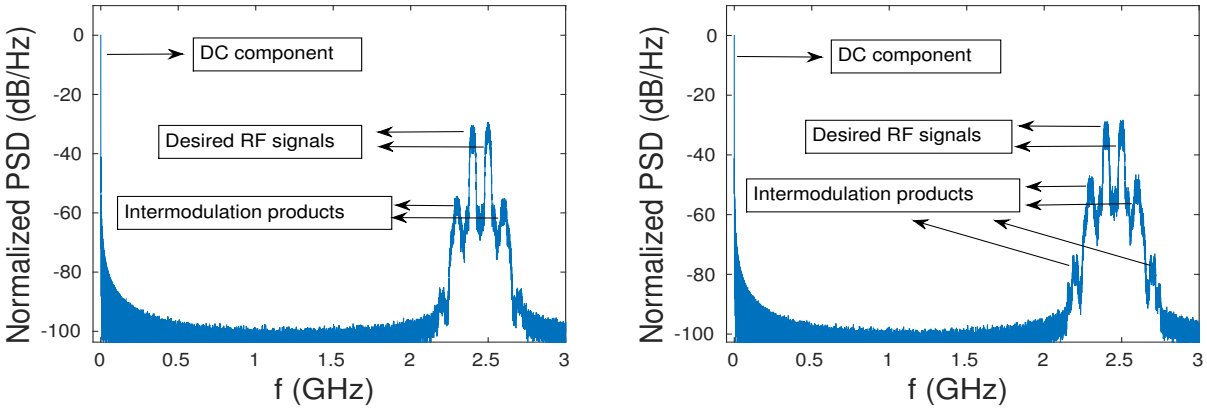

(a) m_{RF}=30% (b) m_{RF}=40%

Figure 2.33: Spectra of the photodetected signal for different optical modulation depths m_{RF}

intermodulation products cannot be readily filtered out after photodetection using electronic filters, because some of them are at frequencies very close to the desired sidebands. In fact, it is the IM3 products that cause maximum performance degradation. Firstly, they lie close to the sidebands that generate them, which hence requires sharp filters. Furthermore, they may also corrupt other desired sidebands in a SCM application. It can be seen from Fig. 2.32(b) that the optical IM3 products generated by the RF signals at 2.4 GHz and 2.5 GHz are located at $f_c \pm 2.3$ GHz and $f_c \pm 2.6$ GHz in the optical spectrum. Similarly, it can be seen from Fig. 2.33(b) that the photodetected IM3 products generated by the RF signals at 2.4 GHz and 2.5 GHz are located at 2.3 GHz and 2.6 GHz in the optical spectrum. Thus, in an SCM application of say three signals at 2.3 GHz, 2.4 GHz and 2.5 GHz, the IM3 products of two channels would corrupt the third.

Hence, the optimal modulation index $m_{RF} = m_{opt}$ corresponds to the specific depth of optical modulation, which minimizes the BER. Operating at $m_{RF} < m_{opt}$ would degrade the BER, because a weaker desired sideband results in a lower SNR, while operating at $m_{RF} > m_{opt}$ would also degrade the BER, because a stronger IM3 product results in a lower Signal-to-Interference Ratio (SIR). The value of m_{opt} depends on the particular number of RF signals being multiplexed, on the noise added by

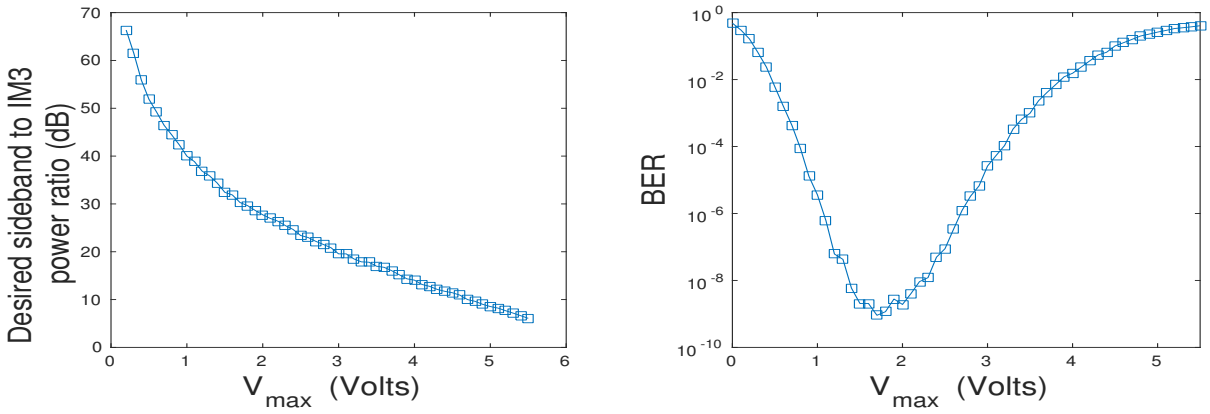

(a) Desired sideband to IM3 power ratio at various optical modulation depths

(b) BER at various optical modulation depths

Figure 2.34: Performance at various optical modulation depths

the ROF link and on the exact frequencies of the RF signals that are being multiplexed. Additionally, the value of m_{opt} is hard limited by the maximum drive voltage that can be applied to an MZM as per its datasheet. Fig. 2.34(b) shows the $BER\ versus\ V_{max}$ plot for the link parameters discussed in Section 2.1.5.1, where the laser is operated at an optical power, which would give a best-case BER of approximately 10^{-9} and optical modulation is carried out using SCM of three RF signal. The results seen in Fig. 2.34(b) are characteristic of the 2.3 GHz RF signal, while the 2.4 GHz and 2.5 GHz RF signals follow a similar trend. The BER is minimized at $V_{max} = 1.7V$, i.e. $m_{opt} = (1.7/5.5) \times 100 = 30.91\%$. Note that some authors define $m_{RF} = V_{rms}/V_{\pi}$ with V_{rms} being the root mean square value of the RF signal, where this would result in $m_{opt} = 15.28$ %. It should also be noted that the value of m_{opt} would decrease, as the number of RF signals that are being multiplexed increases, which leads us to the discussions of the next section, where we analyse the effects of the number of RF signals being multiplexed on the BER performance attained.

2.1.5.3 Effect of the number of subcarriers on the AROF performance

Fig. 2.35(a) shows the BER performance of an AROF link for the link parameters discussed in Section 2.1.5.1, when the number of RF channels N_{SCM} employed in SCM is increased from 2 to 21, where the first RF signal is at 2.3 GHz and the RF carrier separation is 100 MHz. The results seen in Fig. 2.35(a) are characteristic of the 2.3 GHz RF signal. The laser is operated at an optical power that would result in a BER of approximately 10^{-9}, when three RF signals are multiplexed, i.e. when RF carriers at 2.3 GHz, 2.4 GHz and 2.5 GHz are employed. Additionally, we assume $m_{RF} = 30.91$ %. As seen from Fig. 2.35(a), the BER performance drops when the number of RF signals increases. This trend arises due to two reasons. Firstly, the optical power available per RF signal decreases, as the number of RF signals that are multiplexed increases. Secondly, as discussed in Section 2.1.3.1, the strength of the intermodulation products corrupting the RF signals increases, as the number of RF signals being multiplexed increases. Hence, the BER degradation due to an increase in the number of channels being multiplexed can be offset by first decreasing the depth of optical modulation of each channel in order to decrease the strength of the intermodulation products and then accordingly

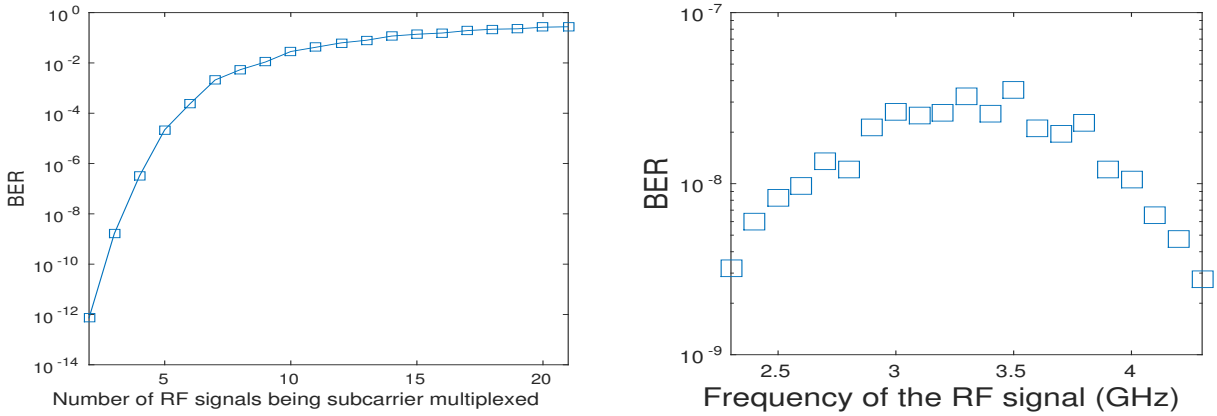

(a) BER for various values of N_{SCM}

(b) BER of the various RF signals when $N_{SCM} = 21$

Figure 2.35: Performance at various depths of optical modulation

increasing the operating power of the laser.

For the scenario, where $N_{SCM} = 21$ RF signals are multiplexed, m_{opt} is found to be 10.91 % by repeating the study in Section 2.1.5.2, which is lower than the m_{opt} for the scenario of $N_{SCM} = 3$ RF signals. Moreover, this satisfies the routinely employed approximate relation that $m_{opt} \propto \sqrt{N_{SCM}}$ [118]. Fig. 2.35(b) shows the BER vs RF carrier frequency trend for a scenario, where 21 RF signals are multiplexed in conjunction with $m_{RF} = m_{opt} = 10.91\%$ and where the laser is operated at a power that would give a BER of approximately 10^{-9} for the RF signal at 2.3 GHz. Note that the laser has to be operated at a power that is higher than the operating power for the three signal SCM scenario of Section 2.1.5.2. It can be seen from Fig. 2.35(b) that when SCM is employed, the BERs of the channels in the middle are higher than those of the outer channels. This is because, as discussed in Section 2.1.3.1, the channels in the middle suffer from a higher level of signal corruption by the intermodulation products. Thus, in order to ensure that all channels have a BER $< 10^{-9}$, we have to further increase the operating power of the laser. In the next section, we consider the effect of employing a MZM having a non-ideal extinction ratio.

2.1.5.4 Effect of the Mach Zehnder Modulator's extinction ratio on the AROF performance

An ideal MZM has an extinction ratio ϵ of ∞ dB, while commercially available MZMs have a finite extinction ratio, where the mathematical expression for the output of a MZM having a finite extinction ratio was provided in Equation 2.10. We have carried out a simulation-based study of the classical AROF link using the parameters discussed in a Section 2.1.5.1, where various values of the extinction ratio are employed. Fig. 2.36(a) shows the penalty in the power of the photodetected RF signal at 2.3 GHz for various values of the extinction ratio, where the RF signals at 2.4 GHz and 2.5 GHz follow a similar trend. In the result shown in Fig. 2.36(a), the power penalty is calculated with respect to the power of the photodetected RF signal for the ideal case of an ∞ extinction ratio. If P_{ideal} and $P_{nonideal}$ are the powers of the ideal and non-ideal cases, respectively, then the penalty is defined as $10 \times \log_{10}(\frac{P_{ideal}}{P_{nonideal}})$. It can be seen from Fig. 2.36(a) that as the extinction ratio decreases from its ideal value of ∞, the strength of the photodetected signal decreases and it suffers a higher power

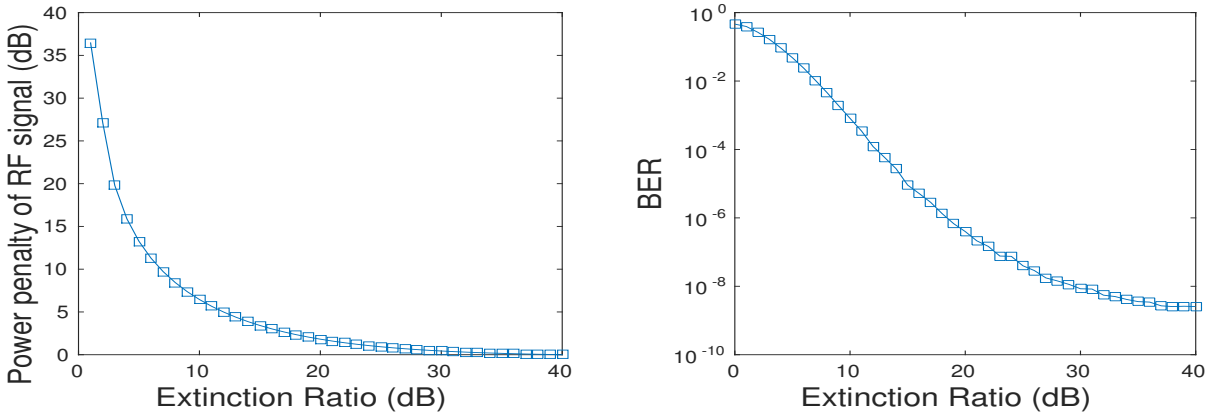

(a) Power penalty

(b) BER performance

Figure 2.36: Performance at various extinction ratios

penalty. In fact, at an extinction ratio of 0 dB there is no photodetected RF signal, as seen from Equation (2.10). The photodetected current of the scenario of 0 dB extinction ratio may be expressed as follows by substituting $\epsilon = 0$ dB, i.e.$\gamma = 0$, in Equation (2.10):

$$I_{PD} \propto |E_{dual}(t)|^2 = \frac{Pin}{2}. \tag{2.62}$$

The photodetected signal only has a DC component and RF components, when the extinction ratio is 0 dB. Fig. 2.37 shows the spectra of the photodetected signal for the case of an extinction ratio of 5 dB and for the case of a near-ideal extinction ratio of 40 dB, where we can observe that the power at the RF frequency of 2.3 GHz, 2.4 GHz and 2.5 GHz is higher, when the extinction ratio is higher. Fig. 2.36(b) shows the BER at various values of the extinction ratio. The BER decreases as the extinction ratio reduces, because the strength of the photodetected RF signal decreases. It can be seen from Fig. 2.36(b) that the BER degradation with respect to an ideal MZM having an extinction ratio of ∞ remains within an order of magnitude, when using commercially available MZMs having an extinction ratio of 20 dB [114] instead. Having considered the impact of a non-ideal extinction ratio, in the next section, we will discuss the effect of another non-ideal phenomenon imposed by the optical modulator, namely that of the bias voltage deviation from its ideal value.

2.1.5.5 Effect of variations in the bias voltage of AROF

Another impairment in the design of AROF transmitters is the bias voltage drift. This may occur because of impairments in the driving circuitry or because of a drift in the transmittance characteristics shown in Fig. 2.9(a) [78], [119]. Hence, in the study presented in this section, we vary the bias voltage from its ideal value of $\frac{V_\pi}{2}$ V for ODSB modulation and employ the link parameters discussed in Section 2.1.5.1. The laser transmit power is kept constant at a value that would result in a BER of approximately 10^{-9} for the case of ideal biasing. Fig. 2.38(a) shows the penalty in the photodetected RF power at 2.3 GHz for various percentages of bias variation, where the penalty is calculated with respect to the photodetected RF power for the case of ideal biasing at $\frac{V_\pi}{2}$ V. If P_{ideal} and $P_{nonideal}$ are the powers for the ideal and non-ideal cases, respectively, then the penalty is defined as $10 \times \log_{10}(\frac{P_{ideal}}{P_{nonideal}})$. The percentage variation of the bias voltage V_{bias} from its ideal value is

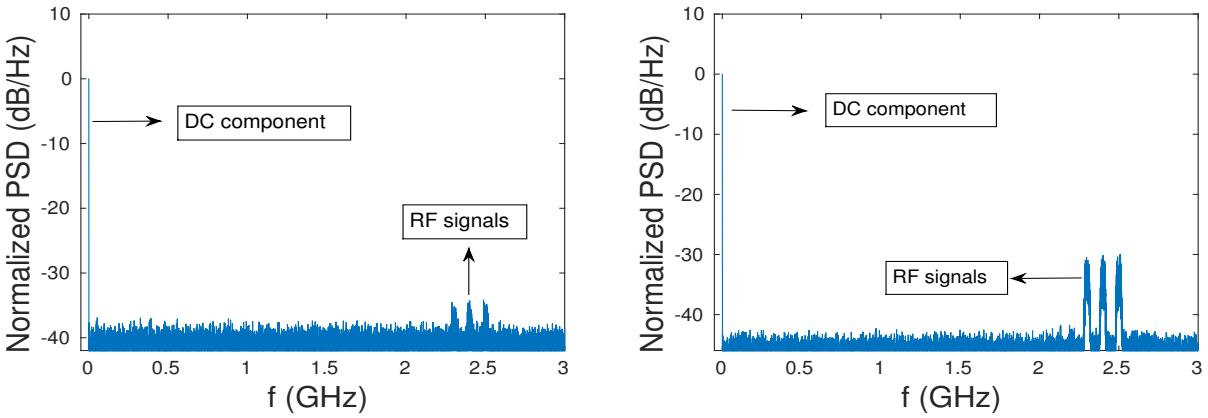

(a) 5 dB extinction ratio

(b) 40 dB extinction ratio

Figure 2.37: Spectrum of the photodetected signal

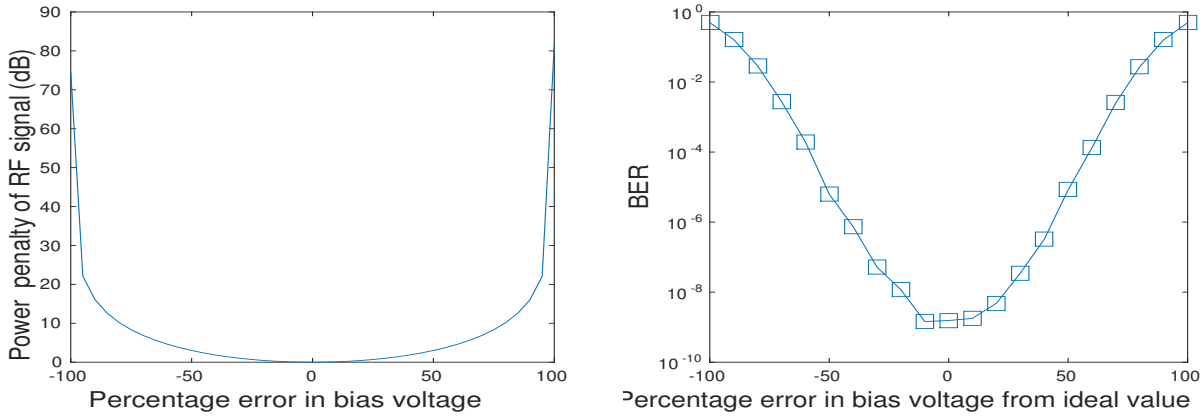

(a) Power penalty of the RF signal versus the bias voltage error

(b) BER for various bias voltage errors

Figure 2.38: Performance at various errors in bias voltage

$\frac{V_{bias}-\frac{V_\pi}{2}}{100} \times 100$. Note that a similar trend is observed for the RF signals at 2.4 GHz and 2.5 GHz. It can be seen from Fig. 2.38(a) that an increase in the deviation of the bias voltage from its ideal value results in a weaker photodetected RF signal. Fig. 2.38(b) shows the BER results of this study, where it can be observed that an increase in the deviation of the bias voltage from its ideal value results in a higher BER. This may be attributed to having a weaker photodetected RF signal. This point is further highlighted through the results shown in Fig. 2.39, where Fig. 2.39 shows the spectra of the photodetected signal for 5 % and 75 % variation of the bias voltage. It can be seen from Fig. 2.39 that a variation of the bias voltage from its ideal value reduces the strength of the desired RF signals. It can be seen from Fig. 2.38(b) that a maximum of 20 % variation in the bias voltage results in a BER degradation within an order of magnitude.

2.1.5.6 Effect of varying the modulating signal's carrier frequency

The chromatic dispersion phenomenon discussed in Section 2.1.1.3 increases the BER of the ROF link, because it results both in a symbol-broadening [31] and in a power-reduction penalty [83]. The

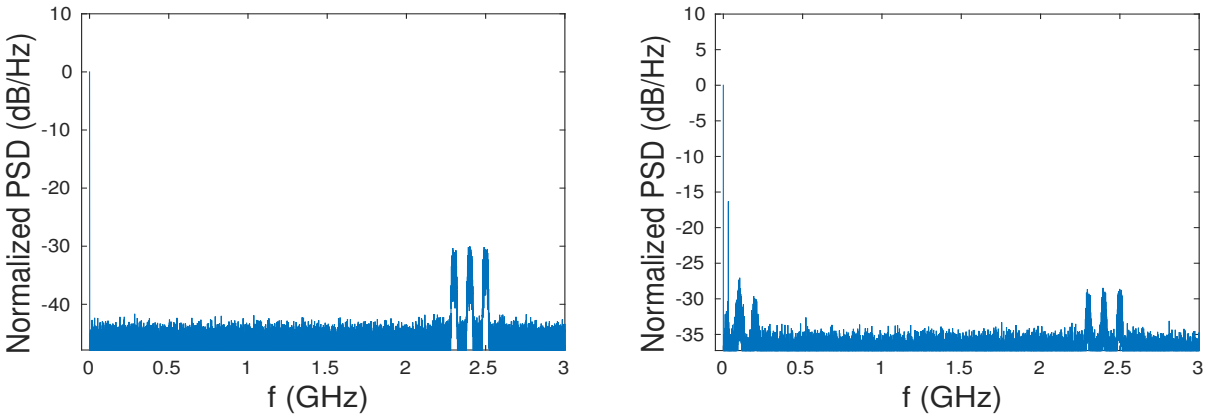

(a) 5% error in bias voltage

(b) 75% error in bias voltage

Figure 2.39: Spectrum at various errors in bias voltage

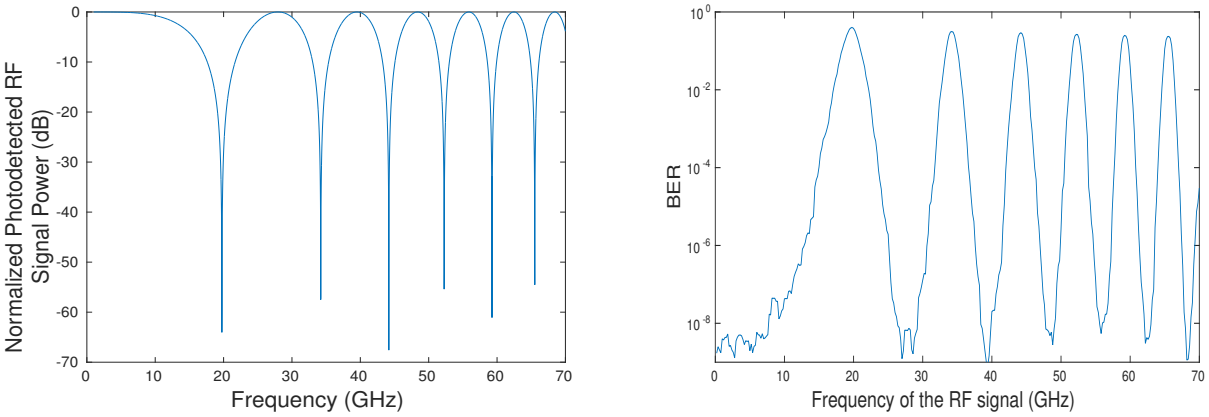

(a) Normalized photoedetected RF power

(b) BER performance

Figure 2.40: Performance for RF signals at various frequencies

most common ROF implementation employs the direct photo-detection technique of Fig. 2.15(a) for photodetecting the ODSB signal shown in Fig. 2.16(a). Its low cost as well as low complexity is the reason for the popularity of this ROF technique. However, these type of ROF links suffers from the above-mentioned chromatic dispersion-induced power penalty. Propagation through the fiber imposes a chromatic dispersion-induced phase-shift on the optical signal, which is frequency-dependent. Hence, chromatic dispersion results in a phase-difference between the two sidebands in the ODSB signal of Fig. 2.16(a), which in turn results in an attenuation of the optical power owing to the destructive interference between the beating sidebands. This optical power-attenuation is referred to as dispersion-induced power-penalty. If the RF signal is at f_{RF} Hz, then the extent of attenuation suffered by the photodetected RF power P_{RF} is given by [83]:

$$P_{RF} \propto \cos^2\left[\frac{\pi \cdot L \cdot D \cdot \lambda_c^2 \cdot f_{RF}^2}{c \cdot [1 - \frac{2}{\pi} \cdot \arctan(\alpha_{chirp})]}\right], \tag{2.63}$$

where λ_c is the wavelength of the optical carrier, c is the speed of light in vacuum, D is the chromatic-dispersion parameter (also called GVD parameter), L is the length of the fiber and α_{Chirp} is the chirp parameter of the signal. Chirping in an intensity-modulated optical signal refers to a time-dependent

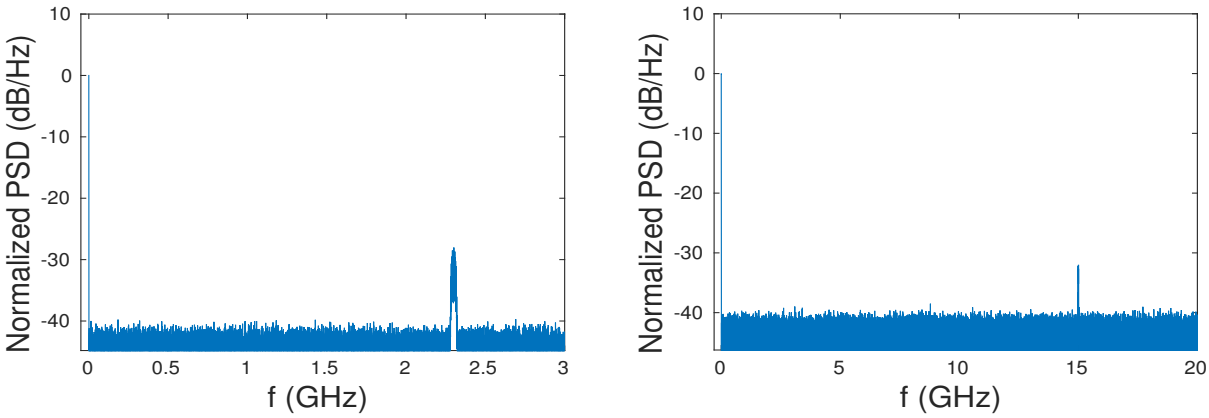

(a) 2.3 GHz RF signal

(b) 15 GHz RF signal

Figure 2.41: PSD of photodetected signals at various frequencies

deviation of the instantaneous optical frequency from its ideal value of $f_c = \frac{c}{\lambda_c}$ Hz. Fig. 2.40(a) shows the photodetected RF power for various RF frequencies, where the power is normalized with respect to the power in the zero-dispersion scenario. Fig. 2.40(b) shows the BER for RF signals at various frequencies, where the other link parameters were as discussed in Section 2.1.5.1. The laser is operated at a transmit power that would result in a BER of 10^{-9} for the zero-dispersion scenario. Upon comparing Fig. 2.40(b) to Fig. 2.40(a), it can be stated that the chromatic dispersion-induced power penalty increases the BER of the ROF link. Fig. 2.41(a) and Fig. 2.41(b) shows the spectrum of the photodetected signal, when RF frequencies of 2.3 GHz and 15 GHz are employed, respectively. It can be seen in Fig. 2.42 that the photodetected RF power at 15 GHz is lower than that at 2.3 GHz. This can also be seen from Fig. 2.40(a). Thus, for the case of ODSB modulation, both the affordable fiber lengths L and the usable RF frequencies f_{RF} are limited by the chromatic dispersion [89].

2.1.5.7 Effect of varying the received optical power

Fig. 2.42(a) shows the BER performance for various received optical powers, when the link parameters of Section 2.1.5.1 are used. A drive voltage of 1.7 volts is employed for each RF signal. It can be seen from Fig. 2.42(a) that a lower received optical power results in a higher BER. This is because a lower received optical power translates to a weaker photodetected optical signal. This in turn results in a lower signal-to-noise ratio of the photodetected signal, which results in a higher BER. Fig. 2.42(b) shows the SNR of the photodetected RF signal. The received optical power would change, if the laser's operating power is changed or if the length of the fiber is changed. Note that the attenuation imposed by the optical fiber on a propagating optical signal is 0.2 dB/km.

2.2 Proposed AROF architecture

In this section we discuss an architecture that we proposed in [3]. It was shown in [3] that this architecture performed better than a conventional AROF link that relies on ODSB modulation and direct photo-detection. The proposed architecture employed pulsed digital optical modulation and heterodyne photo-detection.

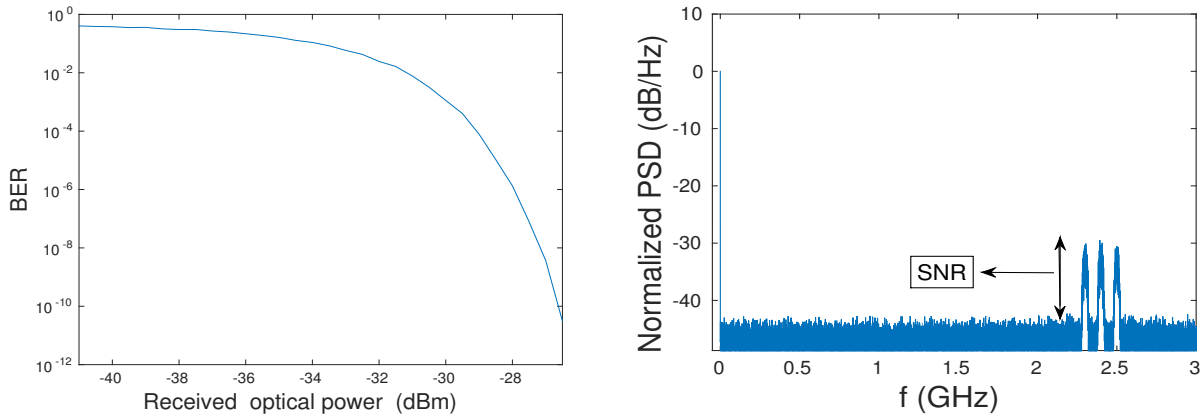

(a) BER performance for different received optical power levels

(b) SNR of the photodetected RF signal

Figure 2.42: AROF link performance

The conventional digital fiber optic links employ TDM of optical pulses, while AROF links employ SCM or WDM discussed in Section 2.1.3. TDM has the advantage of employing fewer laser sources than WDM. Moreover, in typical AROF links employing ODSB modulation, the achievable data-rates and fiber-lengths are severely limited by fiber dispersion and the optical link's non-linearity [89]. In this section we propose an AROF architecture that enables the use of TDM and employs heterodyne photo-detection to overcome the dispersion induced power attenuation. Moreover, conventional heterodyne photo-detection of two optical signals is capable of generating a signal only at a single RF carrier at the difference of the two optical frequencies [89]. In this section, we propose a system to overcome this limitation. We propose a DAS constituted by RAPs that are fed using techniques in the star-like network topology of Fig. 2.43(d). The RAPs of each cell are connected to a Central Unit (CU) via a BS. Our study used VPITransmissionMaker 8.6 (www.vpiphotonics.com) - a commercial optical simulation software.

We propose an optical fiber back-bone that is based on our novel technique that generates wireless signals at multiple RF carriers, while retaining the ability to use a digital optical link and a single optical source. Against this background, the new contributions of this architecture are:

1. The proposed system is capable of transmitting signals at multiple RF carriers, while using heterodyne detection of only two optical signals and without any significant change of hardware components. The extent of overlap between the pulses in the two optical signals was varied, using optical delay lines, for the sake of generating multiple RF carriers.

2. The proposed system is capable of simultaneously performing photo-detection and conversion from optical-TDM to wireless Frequency Division Multiplexing (FDM). The conversion is achieved by varying the optical delay.

3. We propose the heterodyning of two pulsed optical signals that are generated from a single pulsed semiconductor laser.

Experimental proof of a similar concept was provided in [120], where an unbalanced optical modulator was used with no heterodyne detection. The proposed technique draws its motivation from

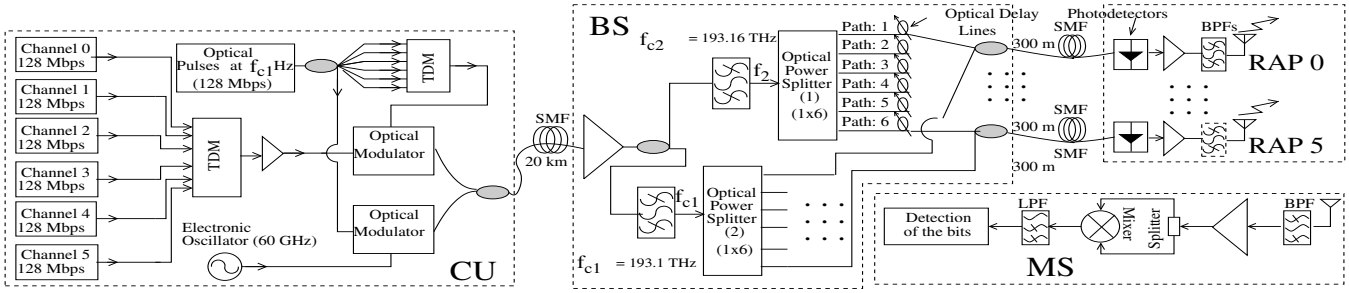

(a) Physical layer architecture of the baseband DAS

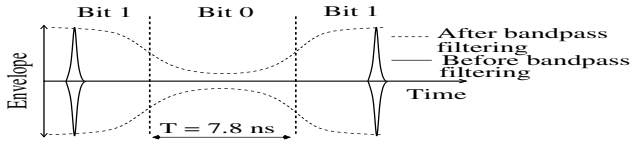

(b) Envelope of photo-detected, amplitude-modulated RF signal at RAP.

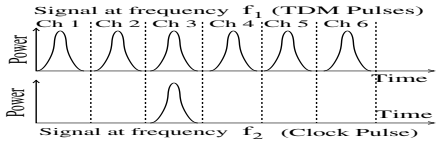

(c) Time domain pulses at 3^{rd} RAP (not to scale).

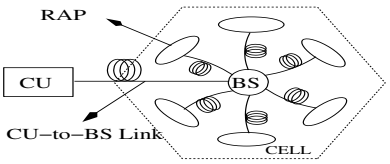

(d) Architecture of the proposed DAS

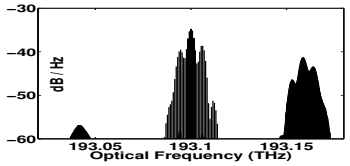

(e) Spectrum of the filtered optical signal

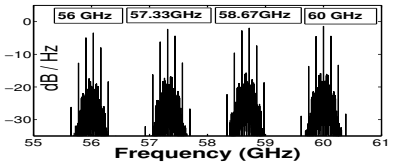

(f) Filtered photo-detected signal at the RF carriers

Figure 2.43: System architecture and functioning

optical serrodyne modulation [121], [122], which uses modulation-induced chirp for optical frequency translation.

2.2.1 Physical layer of the baseband distributed antenna system

2.2.1.1 Control unit of the distributed antenna system

The DL signal transmitted to each of the six RAPs has a bit-rate of $R_{DL} = 128$ Mbps, where the RAPs are represented by the index k ($k = 0, 1, ..5$) in Fig. 2.43(a). They are multiplexed using TDM, resulting in a total bit-rate of $R_{TDM} = (6 \times 128)$ Mbps. The baseband TDM data is On Off Keying (OOK)modulated onto a (6×128) Mbps optical pulse stream. This pulse stream is generated by time-multiplexing the output of a 128 Mbps pulsed semiconductor laser that operates at a frequency of $f_{c1} = 193.1$ THz and has a pulse Full Width at Half Maximum (FWHM) $T_{FWHM} = 40$ ps. In OOK modulation, the optical modulator is driven by the TDM signal, which has a value of 0 for bit '1' and V_π for bit '0'. Hence, as per fig 2.9(a), the transmittance of the MZM is maximum for bit '1' and zero for bit '0 '. In other words, the modulator transmits the incoming pulse for bit '1' and suppresses it for bit '0'. Simultaneously, as shown in Fig. 2.43(a), clock pulses are generated by ODSB modulating a 60 GHz electronic oscillator signal onto one of the 128 Mbps pulsed outputs from the laser. The outputs of the two optical modulators are multiplexed and transmitted to the BS over a 20 km Single Mode Fiber (SMF) link. This multiplexed optical signal consists of a (6×128) Mbps OOK signal at 193.1 THz and of 128 Mbps clock pulse streams at the pair of frequencies of 193.1 $THz \pm 60$ GHz.

The use of a single laser reduces complexity and cost.

2.2.1.2 Base station of the distributed antenna system

At the BS of Fig 2.43(a), the incoming optical signal is amplified by an amplifier having a noise figure of 6 dB and then split into two paths. Optical filters having center frequencies of $f_1 = 193.1\ THz$ and $f_2 = 193.1\ THz + 60\ GHz\ =\ 193.16\ THz$ are used in each path for isolating the pulsed TDM signal and one of the two pulsed clock signals, respectively. These are transmitted to the RAPs through a 0.3 km fiber link. The six paths carrying the pulsed clock signal, as shown in Fig. 2.43(a), include Delay Lines (DLs) to perform demultiplexing and up-conversion. The DLs ensure the selection of a particular TDM channel by ensuring that its pulses overlap with the pulses in the 128 Mbps clock channel. The DL also controls the extent of overlap between the pulses in the clock channel and the selected channel. This in turn decides the up-converted frequency after photo-detection. Optical DLs have been widely used for time-synchronization [123] and optical signal processing [124]. Furthermore, efficient synchronization, coherent heterodyne photo-detection and up-conversion has been made possible by the availability of variable optical DLs with femtosecond sensitivity as well as by the use of a single pulsed optical source at the CU. Polarization control and time-domain overlap has been reported for optical pulses that are significantly shorter than the ones used in this report [125], [126] , with the intention of using XPM.

2.2.1.3 Radio access point of the distributed antenna system

The photo-detected RF signal consists of up-converted impulses whose temporal width equals that of the optical pulses. As shown in Fig 2.43(a), the RF signals are amplified and then band-limited by the transmit-filtering using a BPF with 256 MHz bandwidth and a Gaussian shaped time-domain response. As seen from Fig. 2.43(b), bandpass filtering broadens these impulses. This signal is then transmitted to the MS, where it is filtered, amplified and down-converted to baseband, without an oscillator, through self-mixing [127], as shown in Fig 2.43(a). The signal is then Low Pass Filtered (LPF) and decoded.

2.2.1.4 Uplink communication in the distributed antenna system

The uplink (UL) RF signal is down-converted to baseband by self-mixing [127]. The 193.16 THz clock pulses do not carry OOK data and can be reused at the RAP to carry the UL baseband signal, thereby reducing the RAP complexity just like in [1]. The UL optical signals from the RAPs are sent to the BS, where they are time-multiplexed and then sent to the CU, for direct photo-detection. Heterodyne photo-detection is not needed, since there is no up-conversion at the CU. The narrow photo-detected pulses are low-pass filtered (thereby broadening them), Time Division Demultiplexed and used for bit detection.

2.2.2 Theoretical analysis

2.2.2.1 Time division demultiplexing

Let $x_k(t)$ be the envelope of the pulsed optical signal for the k^{th} RAP. Then, the TDM optical signal, $E_{TDM}(t)$, that is received at the RAPs and is centred at an optical frequency of f_{c1}, can be represented as:

$$E_{TDM}(t) = \sum_{k=0}^{5} x_k(t - kT_{bit}) e^{j2\pi f_{inst1}\{t-kT_{bit}\}(t-kT_{bit})}$$

where $f_{inst1}\{t\}$ is the instantaneous frequency, while $T_{bit} = 1/R_{TDM}$ is the multiplexing delay. The clock signal received at an optical frequency of f_2 is:

$$E_{clock}(t) = x_{clk}(t) e^{j2\pi f_{inst2}\{t\}t}, \tag{2.64}$$

where $x_{clk}(t)$ is the envelope of the pulsed clock signal, while $f_{inst2}\{t\}$ is the instantaneous frequency. As seen from Fig. 2.43(c), channel selection is achieved by delaying the clock pulse by kT_{bit} seconds to ensure that the pulses in the clock signal overlap with the pulses in the desired TDM channel, where $t_{od},\ with\ |t_{od}| \ll T_{bit}$, is the additional delay applied for variable up-conversion. Note that the actual delay applied to the clock would vary slightly from the theoretically calculated value, in order to account for the difference in the optical pulse propagation velocities at frequencies of f_{c1} and f_{c2}.

The electronic signal I_{RF}, that is obtained at the RAP by using a heterodyne photo-detection with responsivity of $R = 0.9$ A/W followed by bandpass filtering is represented as follows:

$$\begin{aligned} I_{RF}(t) &= bpf\{R \cdot |E_{TDM}(t) + E_{clock}(t - kT_{bit} - t_{od})|^2\}, \\ &= bpf\{r \cdot \sum_{k=0}^{5} x_k^2(t - kT_{bit}) + R \cdot x_{clk}^2(t - kT_{bit} - t_{od}) \\ &\quad + 2R \cdot E_{TDM}(t) \cdot E_{clock}(t - kT_{bit} - t_{od})\}, \end{aligned} \tag{2.65}$$

where $bpf\{.\}$ is the bandpass filtering function centred at f_{pd} Hz. The first 2 terms of Eq. (2.65) and one of the terms obtained from the trigonometric expansion represent baseband spectral components that are removed by the bandpass filter. Hence, the filtered signal can be represented as:

$$\begin{aligned} I_{RF}(t) &= 2R \cdot E_{clock}(t - kT_{bit} - t_{od}) \cdot E_{TDM}(t) \\ &= 2x_{clk}(t - kT_{bit} - t_{od}) \cdot x_k(t - kT_{bit}) \\ &\quad \cdot \cos[2\pi f_{inst1}\{t - kT_{bit}\}(t - kT_{bit}) - 2\pi f_{inst2}\{t - kT_{bit} - t_{od}\}(t - kT_{bit} - t_{od})], \\ &= 2R \cdot \tilde{x}_k(t - kT_{bit}) \cdot \cos[\Delta\phi_{het}(t)], \end{aligned} \tag{2.66}$$

where $\tilde{x}_k(t)$ carries the same OOK information as $x_k(t)$ but consists of approximately squared Gaussian pulses. Thus, the filtered signal consists of the envelope of pulsed optical signal for the k^{th} RAP, i.e. time division demultiplexing is achieved. The demultiplexed signal is generated at a frequency f_{pd} that depends on $\Delta\phi_{het}(t)$.

2.2.2.2 Variable up-conversion

The instantaneous frequencies $f_{inst1}\{t\}$ and $f_{inst2}\{t\}$ of the optical TDM signal and the clock signal are as follows:

$$f_{inst1}\{t\} = f_{c1} + \Delta f_{chirp}\{t\}, \tag{2.67}$$

$$f_{inst2}\{t\} = f_{c2} + \Delta f_{chirp}\{t\}. \tag{2.68}$$

where $\Delta f_{chirp}\{t\}$ is the linear frequency chirp. This chirp is introduced by either one or both of the following factors - 1) Linear chirp due to fiber dispersion [74], 2) Additional linear-chirp may be obtained by employing pulsed optical sources that are chirped. If τ is the time normalised by the bit-period in the n^{th} bit duration ($n = 0, 1, 2...$), then $\tau = -\frac{T_{bit}}{2} + t - nT_{bit}$. Hence $-\frac{T_{bit}}{2} \leq \tau < \frac{T_{bit}}{2}, \ \forall \ t$. Now, $\Delta f_{chirp}\{t\} = M\tau$, where $M = [C/(2\pi T_0^2)]$ [74], [31]. Here C is the chirp parameter and $T_0 = T_{FWHM}/1.665$. Additionally, M can be adjusted by employing chirped optical sources and by varying the chirp parameter of the generated pulses. Thus, as seen in Fig. 2.44, the instantaneous frequency changes linearly across each pulse and it is centred around the optical carrier frequency. Hence the spectra of these optical signals are centred around the frequencies f_1 and f_2, which is also seen from Fig. 5.2.1.4. The spectra become wider as the optical pulses become narrower. Time instances, which are separated by integer multiples of the bit period have the same normalised time instant. Hence we have,

$$\Delta f_{chirp}\{t - kT_{bit}\} = \Delta f_{chirp}\{t\} = M\tau. \tag{2.69}$$

In addition to the delay that is applied to perform channel selection, an additional overlap delay, $t_{od} \ll T_{bit}$, is applied to the clock signal. This results in a slight overlap mismatch between the clock pulse and the pulse in the selected channel. The chirp in the delayed clock signal is as follows:

$$\Delta f_{chirp}\{t - kT_{bit} - t_{od}\} = \Delta f_{chirp}\{t - t_{od}\} = M(\tau - t_{od}). \tag{2.70}$$

The signal generated during the heterodyne photo-detection of the TDM and clock signals at the RAP has a centre frequency, f_{pd}, that is equal to the derivative of the instantaneous phase difference $\Delta\phi_{het}(t)$ between the two optical signals. Thus:

$$\begin{aligned} f_{pd} &= \frac{1}{2\pi}\frac{d(\Delta\phi_{het}(t))}{dt} \\ &= \frac{d}{dt}\{\int_0^{t-kT_{bit}-t_{od}} f_{inst2}\{t'\}dt' - \int_0^{t-kT_{bit}} f_{inst1}\{t'\}dt'\}, \end{aligned}$$

where t' is the integration variable. However, it is known from calculus that for a function $u(x)$, $\frac{d}{dx}\{\int_a^x u(x')\ dx'\} = u(x)$ holds. Hence the above expression of f_{pd} becomes:

$$\begin{aligned} f_{pd} &= f_{inst2}\{t - kT_{bit} - t_{od}\} - f_{inst1}\{t - kT_{bit}\} \\ &= f_2 + \Delta f_{chirp}\{t - kT_{bit} - t_{od}\} - (f_1 + \Delta f_{chirp}\{t - kT_{bit}\}) \\ &= (f_2 - f_1) + (\Delta f_{chirp}\{t - kT_{bit} - t_{od}\} - \Delta f_{chirp}\{t - kT_{bit}\}) \\ &= 60 \times 10^9 - Mt_{od} \ [\ using\ equations\ (2.69)\ and\ (2.70)\ ]. \end{aligned} \tag{2.71}$$

Hence, the centre frequency of the photo-detected signal can be varied by varying the extent of mismatch. On the other hand, conventional heterodyne detection generates RF signals at a single frequency for a given pair of optical signals.

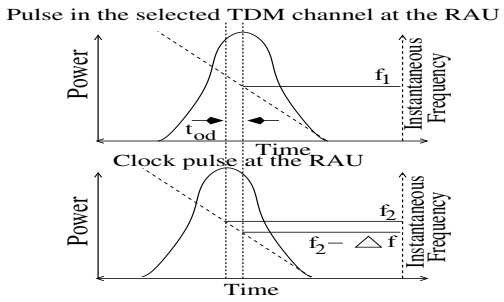

Figure 2.44: Pulses at frequencies f_1 and $f_2 (M < 0, t_{od} < 0)$.

2.2.3 Performance of the proposed distributed antenna system

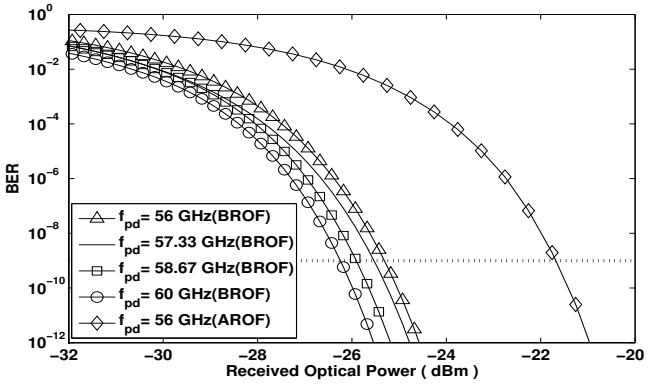

Figure 2.45: BER vs. received optical power for the proposed method and AROF

Simulations were carried out by exploiting the fiber-dispersion induced chirp. The cell was operated using signals at RF carriers of 56 GHz, 57.33 GHz, 58.67 GHz and 60 GHz. These are shown in Fig. 5.34. The dispersion parameter of single mode fibers at a wavelength of 1550 nm is D= 16 ps/km-nm [31]. Using pulses having $T_{FWHM} = 40ps$ results in a value of $C = -0.9516$ [74], which in turn gives a value of $M = -2.6241 \times 10^{20}$. Hence, from Eq. 2.71, $t_{od} = 3.8$ ps produces a frequency variation of 1 GHz. The tolerable deviation in the photo-detected signal's frequency from 60 GHz is dictated by the condition that the overlap mismatch should not cause a significant BER degradation and receiver sensitivity drop at BER = 10^{-9}. The tolerable deviation in the photo-detected signal's frequency from 60 GHz is dictated by the condition that the overlap mismatch should not cause a significant BER degradation and receiver sensitivity drop at BER = 10^{-9}. The BER of conventional heterodyne photo-detection has been dealt with in chapter ten of [31]. The various factors that cause a BER penalty when compared to conventional heterodyne detection are-

1. Pulse mismatch: The detected signal is down-converted and sampled. Sampling occurs at the bit-center. There is a performance penalty, when a 2^{nd} delayed Gaussian pulse is multipled.

2. Bit boundary mismatch: The difference in the instantaneous optical frequency will not be equal to the target value at the bit boundaries. This, however, is negligible for very small t_{od} because the pulse amplitude at the bit boundary is negligible. Its significance, nevertheless, increases as t_{od} increases.

The performance drop of the system supporting the four RF carriers is within 1dB, at a BER of 10^{-9}, compared to conventional heterodyne photo-detection. Furthermore, the advantage of using the proposed architecture that employs a digital optical modulation in preference to the more commonly employed AROF architecture relying on ODSB modulation can also be seen from Fig. 2.45. The severity of fiber-dispersion and the consequent sideband-cancellation, increases with the carrier frequency in analogue optical links. The BER performance of 60 GHz-band AROF links relying on ODSB modulation is limited by chromatic dispersion.

2.3 Chapter conclusion

In this chapter, we introduced the concept of ROF transmissions and then proceeded to discuss the various techniques and design trade-offs of the ROF link of Fig. 2.1 in Sections 2.1.1, 2.1.2 and 2.1.3, including the optical transmitter, the optical fiber, the optical receiver and the optical network. These trade-offs were summarised in the stylized illustration of Fig. 2.2. We then analysed the effect of various parameters on the performance of the link. Finally, a novel technique was proposed for varying the carrier frequency of the signal, that is generated by heterodyne photo-detection of two given optical signals. This technique varies the extent of overlap between the pulses in the two optical channels in order to exploit the pulse chirp. Its performance in a architecture, constituted by a star-like DAS of RAPs, was quantified. Also, the BER performance at the 4 RF carriers used in the proposed system was better than that of a conventional AROF link relying on ODSB modulation. Having introduced the basics of a ROF link, we now introduce a set of performance improving, cost reduction and optical RF-generation enabling techniques for advanced ROF links in the next chapter.

Chapter 3

Designing Advanced ROF links

It was clear from the discussion in Section 1.5, that the cardinal rule of a ROF link is to get the best performance at the lowest possible cost. Moreover, ROF is a potential backhaul technique for future high-RF based networks, where, as discussed in Section 1.5.3, optical generation of these RF signals would be beneficial. Hence, this chapter consists of an extensive study of various advanced ROF links that were designed using three approaches, namely ROF links employing a) performance improving techniques, b) cost reducing techniques and c) optical RF-generation techniques.

Fig. 3.1 illustrates the various design challenges of the ROF network. For example, the deployment of higher RF frequencies results in higher fiber dispersion, which degrades the BER. The BER may be reduced by using dispersion compensation mechanisms, which however increase the implementation al complexity and cost of the system. Alternatively, the BER may be reduced by using lower-order modulation schemes, which would however reduce the overall throughput. On the other hand, the overall throughput may be improved by ensuring better optical spectral efficiency through schemes like Dense Wavelength Division Multiplexing (DWDM), which however would increase the implementation al complexity and cost. Thus, most design questions usually boil down to a cost versus performance trade-off. This chapter presents a range of techniques that are either aimed at cost reduction or at performance improvement.

Subsequently, we discuss techniques that are aimed at optically generating RF signals in a ROF link in order to address the challenge of generating high-RF signals, as was discussed in Section 1.5.3.

3.1 ROF performance improvement techniques

There are numerous challenges associated with efficient millimeter-wave ROF communication, including the generation and reliable transmission of the wireless signal over the optical channel. In this section we describe several techniques that may be employed for improving the ROF link's performance in terms of throughput, Noise Figure (NF) or dynamic range.

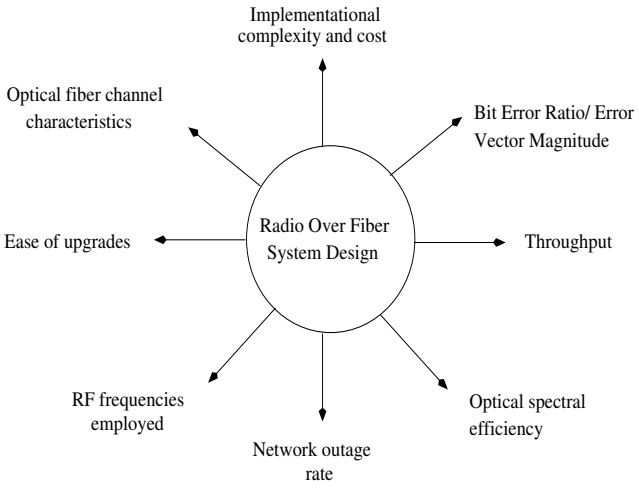

Figure 3.1: Stylized representation of the design challenges involved in the design of the ROF network

Table 3.1: ROF Performance Improvement Techniques (Part 1)

Technique	Year	Authors	Contribution
Wavelength Interleaved Wavelength Division Multiplexing	2001	Lim *et al.* [128]	Designed a WI-WDM system using OADMs.
	2003	Toda *et al.* [96]	Implemented of WI-WDM using a MUX/DEMUX that employed $(2 \times N)$ AWG with a FP filter.
	2006	Bakaul *et al.* [44]	Achieved simultaneous demultiplexing of the N downlink WI-WDM channels and multiplexing of the N uplink channels into a WI-WDM signal using an AWG with loopbacks.
Carrier Suppression	2002	Rongqing *et al.* [90]	A tunable FP filter was used for suppressing the optical carrier of an OSSB signal in order to improve the receiver sensitivity.
	2005	Attygalle *et al.* [40]	A FBG filter was used for suppressing the optical carriers of OSSB and ODSB signals, which improved the receiver sensitivity by upto 7 dB.
Low biasing the optical modulator	1993	Farwell *et al.* [41]	Operated a MZM at an optical bias below the quadrature biasing point to increase the linear dynamic range.
	2007	Ackerman *et al.* [129]	Operated a MZM at an optical bias below the quadrature biasing point to increase the SNR.
Balanced photo-detection	2007	McKinney *et al.* [130]	Designed a ROF link having a NF of less than 10 dB by relying on a dual-output MZM and differential detection.
Optical Injection Locking	1998	Braun *et al.* [131]	A 64 GHz, 140 -155 Mbps signal having a low phase noise <-100 dBc/Hz and a bit rate of was generated using OSIL.
	2003	Johansson *et al.* [132]	A RF signal having a low phase noise and a data rate of 148 Mbps was generated in the 26-40 GHz range using an OIPLL for transmission distances upto 65 km.
	2006	Chrostowski *et al.* [133]	Presented the various advantages of using OIL in a ROF link, including higher laser power, higher bandwidth, lower noise and lower non-linearity.
	2010	Ng'oma *et al.* [134]	Direct modulation of the output of an optically injection locked laser was done to generate a multi-Gbps RF signal at 60 GHz.
Optical feed-forward linearization	2007	Ismail *et al.* [135]	Achieved simultaneous reduction of 3rd-order Intermodulation Distortion (IMD) by 26-dB and laser-noise by 7-dB at 5.2 GHz using feed-forward linearization.

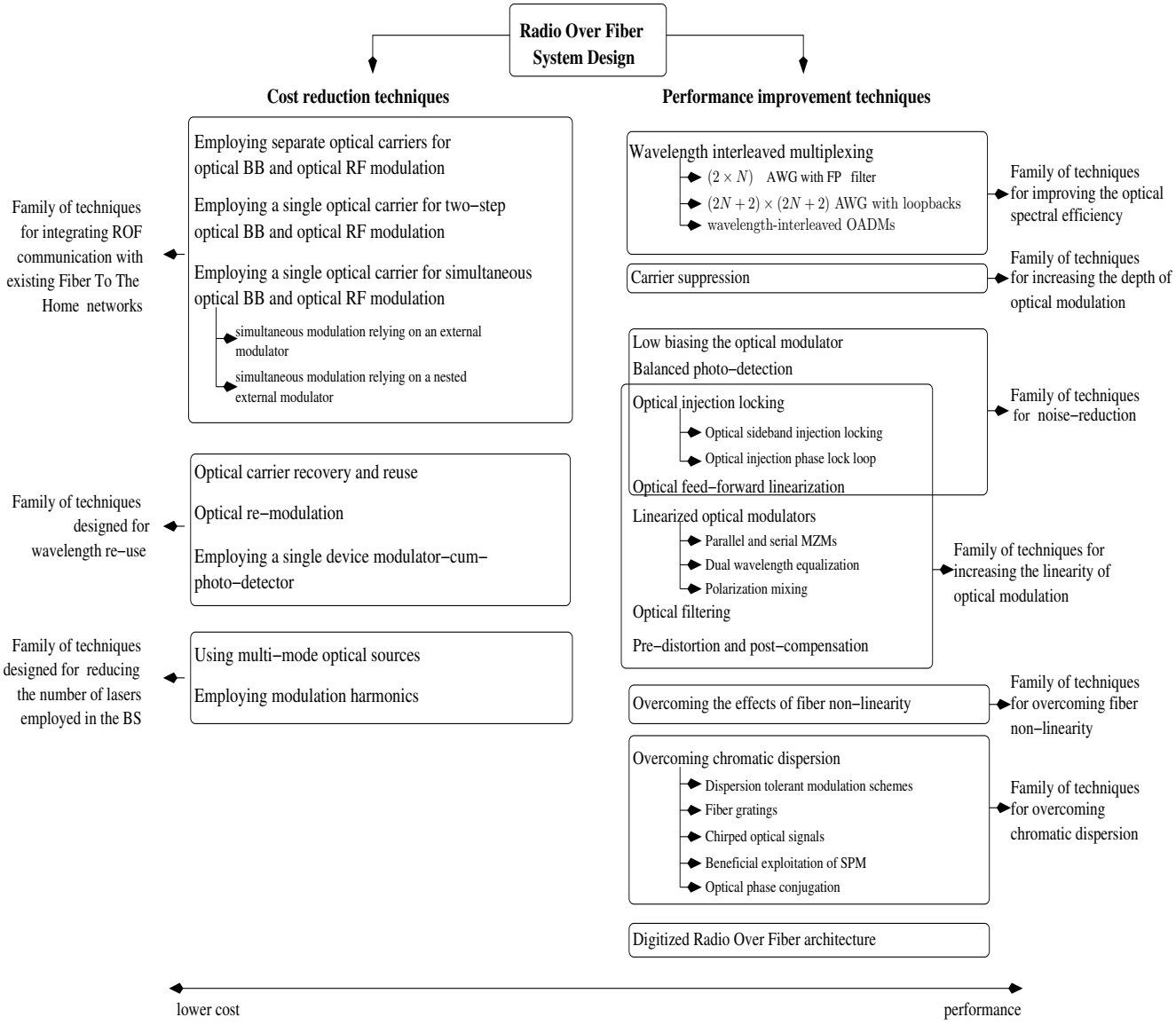

Figure 3.2: The various cost reduction and performance improvement techniques for ROF communications

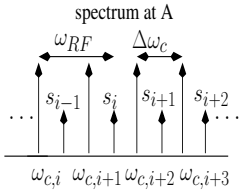

Figure 3.3: WI-DWDM signal

3.1.1 Wavelength interleaved multiplexing

As per definition, in a Wavelength Interleaved Wavelength Division Multiplexing (WI-WDM) system, the frequency spacing between the optical carrier at $f_{c,i} = \frac{\omega_{c,i}}{2\pi}$ Hz and its sideband at $\frac{s_i}{2\pi}$ Hz is higher than the frequency spacing $\Delta f_c = \frac{\Delta\omega_c}{2\pi}$ Hz between the adjacent optical carriers, which results in the interleaved spectrum shown in Fig. 3.3. The spectrum of Fig. 3.3 is generated by multiplexing signals that are generated using the OSSB modulation schemes discussed in Section 2.1.2.1 [96]. In other words, as shown in Fig. 3.3, we have $f_{RF} > \Delta f_c$, where f_{RF} is the frequency of the modulating RF signal. This technique is usually implemented along with the DWDM technique that was discussed in Section 2.1.3.2. WI-WDM results in a higher spectral efficiency than the conventional non-interleaved WDM, but requires more sophisticated techniques for multiplexing and demultiplexing the signals [96] [128]. In the following paragraphs we highlight some of these techniques, assuming OSSB modulation.

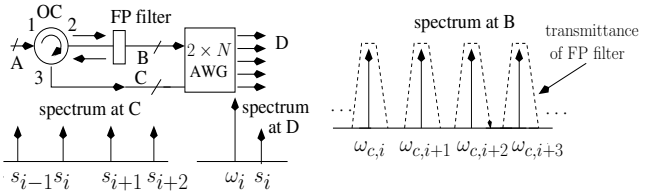

Figure 3.4: WI-WDM demultiplexer using FP filter

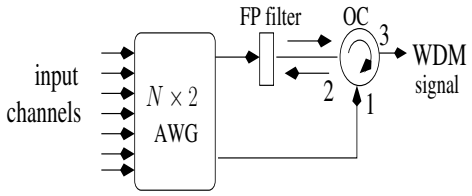

Figure 3.5: WI-DWDM MUX using FP filter

$(2 \times N)$ **arrayed waveguide grating with fabry perot filter** A $(a \times b)$ AWG consists of a input ports and b output ports, while a Fabry Perot (FP) filter is an optical filter having alternating transmission and reflection bands. Hence, effectively it acts as a comb filter. The incident optical wave will be either transmitted through or reflected by the FP filter, depending on the optical frequency. A DEMUX and MUX pair using an AWG and a FP filter is shown in Figures 3.4 and 3.5, respectively [96]. The corresponding spectra at points A, B, C and D of the DEMUX architecture using the FP filter are shown in Figures 3.3 and 3.4. In the DEMUX of Fig. 3.4, the Wavelength Interleaved Dense Wavelength Division Multiplexing (WI-DWDM) signal, whose spectrum is shown in Fig. 3.3, enters port 1 of the Optical Circulator (OC) and leaves from its port 2, where the set of sidebands seen in the WI-WDM signal of Fig. 3.3 are reflected, while the set of carriers are transmitted by the FP filter. The reflected sidebands re-enter port 2 of the OC and leave from port 3. The separated carriers-set and sidebands-set are then fed into the two input ports of the AWG of Fig. 3.4, whose output consists of the demultiplexed signals. As indicated by the spectrum at point D of Fig. 3.4, each separated signal contains the carrier ω_i and its corresponding sideband s_i [96].

The MUX of Fig. 3.5 operates in a similar fashion, except that the direction of signal-flow is

reversed [96]. As shown in Fig. 3.5, the independent channels enter the MUX, while the set of carriers and the set of sidebands appear at the top and bottom output port of the AWG in Fig. 3.5, respectively. The top and bottom outputs of the AWG in Fig. 3.5 have stylized spectra similar to those seen at points B and C of Fig. 3.4, respectively. The set of sidebands then enter port 1 and exit from port 2 of the OC, where, as shown in Fig. 3.5, these sidebands are reflected by the FP filter, re-enter port 2 and finally exit from port 3 of the OC. On the other hand, the set of carriers that exited from the top port of the AWG of Fig. 3.5 are transmitted through the FP filter. Hence, they too exit from port 3 of the OC. Thus, the multiplexed signal becomes available from port 3 of the OC [96] of Fig. 3.5.

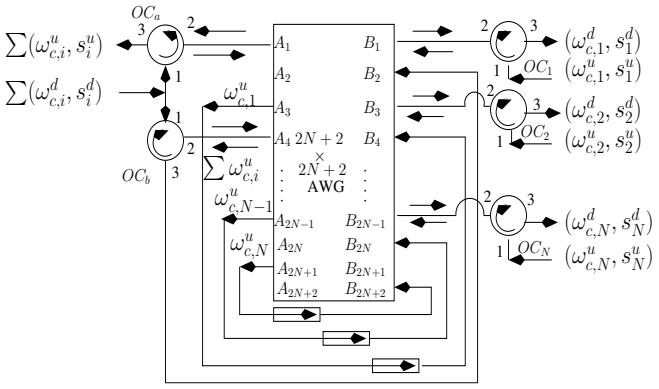

Figure 3.6: MUX/DEMUX employing an AWG in loopback configuration

$(2N + 2) \times (2N + 2)$ **arrayed waveguide grating with loopbacks** A loopback architecture is one in which the output ports are connected to the input ports of the AWG. The architecture shown in Fig. 3.6 implements simultaneous demultiplexing of the N downlink channels and multiplexing of the N uplink channels or vice-versa in a ROF system that employs WI-WDM. While the discussion below assumes a scenario in which the downlink channels are demultiplexed and uplink signals are multiplexed, the process is similar for the case of uplink demultiplexing and downlink multiplexing.

In Demultiplexing [44], the downlink WI-DWDM signal, which consist of the N optical carriers and their corresponding single sidebands, is portrayed in Fig. 3.6 as $\sum(\omega^d_{c,i}, s^d_i)$. The downlink power is split by a coupler and it enters ports A_1 and A_4 of the AWG via the circulators OC_a and OC_b of Fig. 3.6, respectively. The optical carriers along with their respective sidebands exit from ports $B_1,\ B_3\ \cdot\cdot B_{2N-1}$ of Fig. 3.6. These are obtained from port 3 of OC_1 to OC_N and are indicated in Fig. 3.6 as $(\omega^d_{c,i}, s^d_i)$ [44].

In Multiplexing [44], the N uplink optical signals enter ports $B_1,\ B_3\ \cdot\cdot B_{2N-1}$ via the OCs and are represented as $(\omega^u_{c,i}, s^u_i)$ in Fig. 3.6. The optical carriers exit from port A_4 while the sidebands exit from port A_1 in Fig. 3.6. The output of port A_4 is indicated as $\sum \omega^u_{c,i}$ in Fig. 3.6, which are then looped back into port B_2. This results in the N separated optical carriers ω_i output at $A_3,\ A_5\ \cdot\cdot A_{2N+1}$, which are then again looped back to ports $B_4,\ B_6\ \cdot\cdot B_{2N+2}$. This results in the combined optical carriers $\sum \omega^u_{c,i}$ leaving from port A_1 of Fig. 3.6. Thus, both the optical carriers and their sidebands exit from port A_1. This WI-DWDM optical signal then exits from port 3 of OC_a and it is represented as $\sum(\omega^u_{c,i}, s^u_i)$ in Fig. 3.6 .

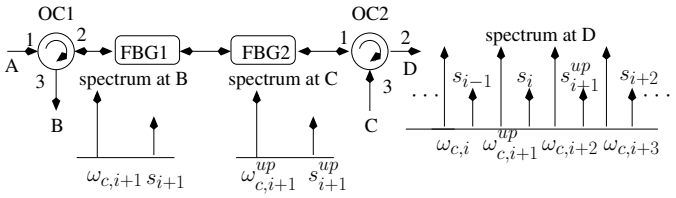

Figure 3.7: Optical add-drop multiplexer

Wavelength-interleaved optical add-drop multiplexers In Fig. 3.7, the optical OSSB-WDM signal of Fig. 3.3 enters into port 1 of OC1 and leaves from port 2 [128]. Subsequently, the optical carrier $\omega_{c,i+1}$, that is to be dropped, is reflected by the FBG filter 1 (FBG1), while the corresponding sideband s_{i+1} is reflected by FBG2 [128], as shown in Fig. 3.7. The rest of the signal enters port 1 of OC2 The reflectivity profile of the FBG1 and FBG2 filters is as shown in Fig. 2.18(b), where the centre frequency $f_r = \frac{\omega_r}{2\pi}$ has values of $f_{c,i+1} = \frac{\omega_{c,i+1}}{2\pi}$ Hz and $\frac{s_{i+1}}{2\pi}$ Hz, respectively. The signals that are reflected by FBG1 & FBG2 back-propagate and re-enter port 2 of OC1 and they are dropped from port 3, where the spectrum of the signal exiting from port 3 is shown at point B of Fig. 3.7. The uplink signal, whose spectrum is shown at point C of Fig. 3.7, enters port 3 of OC2 and exits from port 1. This uplink signal having a carrier $\omega^{up}_{c,i+1}$ and sideband s^{up}_{i+1} gets reflected by the FBG filters, because they are at the same frequencies as the previously dropped signal and they re-enter port 1 of OC2. Hence, the total signal entering port 1 of OC2 includes the channels within the signal at point A, which were not reflected by the FBG filters, along with the added uplink channel. The signal entering port 1 finally exits from port 2 of OC2, where the spectrum exiting from port 2 is shown at point D of Fig. 3.7. Thus, a downlink channel is dropped from the spectrum of Fig. 3.3 and replaced by the uplink channel to obtain the spectrum at point D of Fig. 3.7.

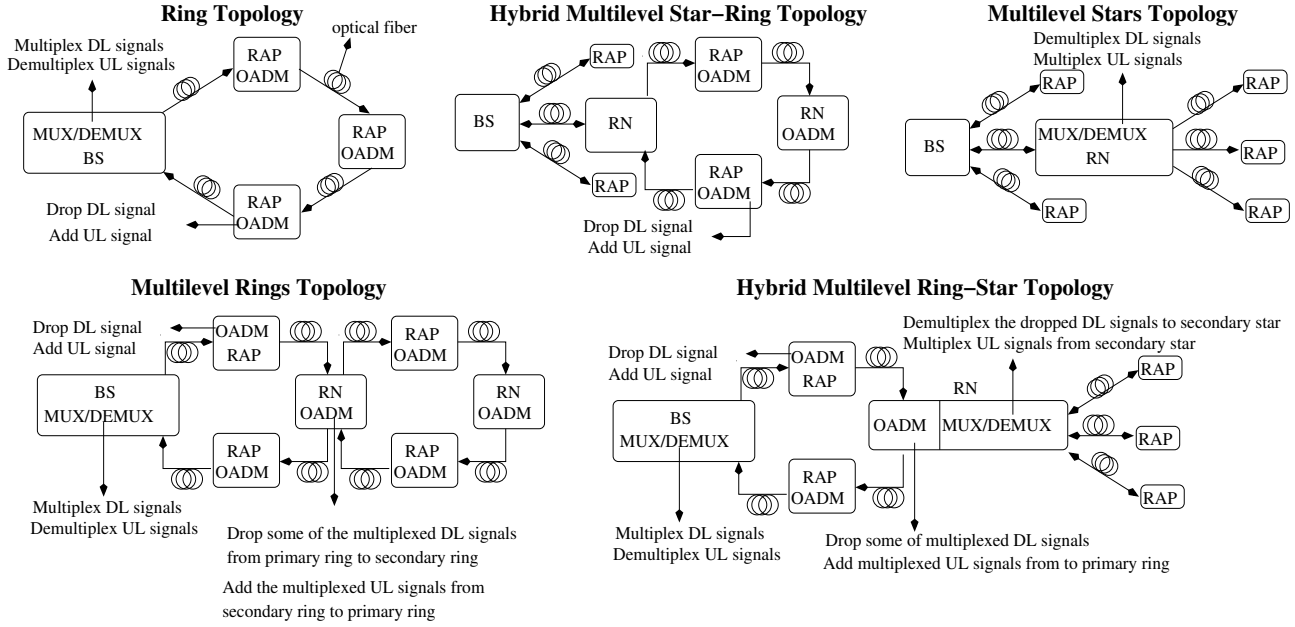

Figure 3.8: Use of MUXs/DEMUXs and OADMs in different ROF topologies

Upon concluding our discussion on WI-WDM, recall that the first MUX/DEMUX architecture

relies on a $(2 \times N)$ AWG, a FP filter as well as on an OC and can either perform multiplexing or demultiplexing. On the other hand, the second MUX/DEMUX architecture employs the more complex $(2N + 2) \times (2N + 2)$ AWG with loopbacks along with several OCs, but can achieve simultaneous multiplexing and demultiplexing of the signals. However, none of these MUX/DEMUX architectures permits access to an individual channel or to a set of channels within the multiplexed signal without having to demultiplex all the channels. This can be implemented using the OADM alluded to in the previous discussion. Fig. 3.8 shows some commonly used ROF network topologies along with the BSs, Remote Nodes (RNs) and RAPs, where the MUX/DEMUX and OADMs are employed assuming that duplex communication with each RAP is achieved using a unique wavelength. Fig. 3.8 also shows the operations that MUX/DEMUXs and OADMs perform on both the DL and UL ROF signals.

Let us now move on from the family of techniques conceived for improving optical spectral efficiency to carrier suppression techniques, which are capable of increasing the depth of optical modulation, thereby improving the receiver sensitivity.

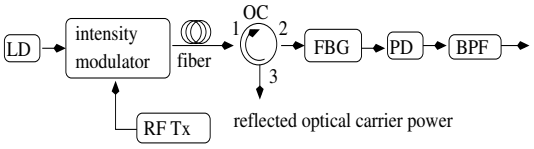

Figure 3.9: Carrier suppression

3.1.2 Carrier suppression

Suppressing the optical carrier with respect to the modulation sidebands increases the depth of optical modulation, thereby beneficially improving the attainable receiver sensitivity [40], [136], [137], [90], where the typical value of the optimum carrier to sideband ratio is 0 dB. Fig. 3.9 portrays an architecture that implements carrier suppression, where the output of the laser is intensity modulated using the RF signal and transmitted over the fiber to the RAP. In the RAP, the modulated optical signal enters port 1 of the OC of Fig. 3.9 and then exits from port 2, where it enters the FBG filter that implements carrier suppression. The FBG filter, originally discussed in Fig. 2.18, reflects a portion of the optical carrier power corresponding to the desired suppression, but ideally allows 100 % transmission of the optical sidebands. The reflected optical carrier power enters port 2 and then exits from port 3 of the OC, where it can be re-used for uplink modulation. The FBG filter of Fig. 3.9 can also be employed before fiber transmission in order to simplify the RAP architecture [40]. However, this latter technique would prevent the implementation of wavelength re-use, since the reflected carrier power would no longer be available at the RAP but only at the BS.

Following this rudimentary introduction to the pertinent issues of carrier suppression, we now consider the family of techniques designed for reducing the noise imposed by the ROF link, which in turn improves both the optical receiver sensitivity as well as the dynamic range. These techniques include low-biasing the optical modulator, balanced photo-detection as well as Optical Injection Locking (OIL) and optical feed-forward linearization.

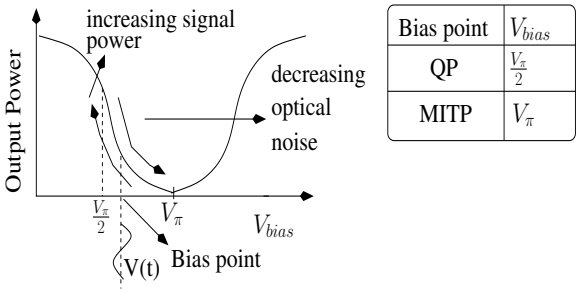

Bias point	V_{bias}
QP	$\frac{V_\pi}{2}$
MITP	V_π

Figure 3.10: Biasing the optical modulator at an optical power below that of QP biasing

3.1.3 Low-biasing the optical modulator

As discussed in Section 2.1.2, if the ODSB/OSSB modulation of Fig. 2.16 was carried out at the transmitter using a RF signal at f_{RF} Hz, then the desired photo-detected signal is also generated at f_{RF} Hz. However, no signal is generated at f_{RF} Hz for the OCS modulation scheme of Fig. 2.16, where a frequency-doubled photo-detected signal is generated at $2f_{RF}$ Hz instead. ODSB/OSSB modulation requires a QP biased MZM that is associated with $V_{bias} = V_\pi/2$, while OCS modulation requires a MITP biased MZM with $V_{bias} = V_\pi$. If no frequency doubling is desired then, the QP biased MZM of Fig. 5.11 is employed. Fig. 3.10 shows the trade-off between the optical noise and optical signal power, when the bias point indicated by an arrow moves from the QP towards the MITP of Fig. 3.10 [41]. It can be seen from Equations (3.30) and (3.34) that unlike in the QP biased scenario of Fig. 3.10, the MITP biased scenario of Fig. 3.10 has a suppressed first harmonic, which implies that the power of the photo-detected f_{RF} Hz RF signal decreases, when the bias point indicated by the arrow moves from the QP towards the MITP. However, it can be seen from Equations (3.30) and (3.34), that the DC value in the photo-detected signal is higher for the case of QP biasing than for MITP biasing. Thus, observe from Equations (2.36) and (2.37) that the shot noise, RIN and signal-ASE beat noise level, which together constitute the optical noise, decrease at a faster rate, when the bias point moves from the QP towards MITP [129] [41], as shown in Fig. 3.10. If the dominant source of noise in an optical link that employs a QP biased MZM is the optical noise, then the output SNR increases as the bias is shifted from the QP towards the MITP, which can be deduced from Fig. 3.10. The SNR increases till the photo-detector's thermal noise becomes the dominant source of noise, beyond which the SNR starts to decrease. Therefore, the optimum bias value corresponding to the maximum SNR lies between the QP and MITP, where its actual value depends on the optical power at the MZM's input. The expression for the NF and its relation to the SFDR of an optical link is as follows on a decibel (dB) scale [129], [138]:

$$NF[dB] = SNR_{in}[dB] - SNR_{out}[dB], \tag{3.1}$$

$$SFDR[dB] = \frac{2}{3}\{IP3[dB] - (-174 + NF[dB])\}, \tag{3.2}$$

where IP3 is the level of the third-order inter-modulation products. Hence, optimising the bias point not only reduces the noise figure, but also results in an increase of the link dynamic range. A similar performance improvement can be achieved by low-biasing the EAM of Fig. 2.10(a) [139][140] to an optical power level below that shown in Fig. 2.10(b).

However, the limitation of this technique is that it assumes that the effect of the stronger second-

order distortion, including harmonics and intermodulation distortion, generated by low-biasing can be neglected. It can be seen from Equation (3.30) and Equation (3.34) that unlike in the QP biased scenario, the MITP biased scenario has a strong second order harmonic. In a SCM system having N channels, the second order harmonics do not lie within the transmission bandwidth if we have $2f_i > f_N \; \forall \; i$, where f_i is the electronic frequency of the i^{th} channel being modulated onto the optical carrier. The non-linearity that generates second-order harmonics also results in the generation of second-order intermodulation products of the form of $f_i \pm f_j$, where $i, j \in \{1, 2, ...N\}$. Second-order intermodulation products can be neglected if they do not lie within the SCM signals bandwidth i.e. $(f_i \pm f_j) < f_1$ *or* $(f_i \pm f_j) > f_N \; \forall \; i, j$. The conditions for neglecting the second-order harmonic and intermodulation distortion are met, if the SCM signals are within an octave, i.e. $f_N < 2f_1$ [41].

Let us now discuss a second technique that assists in reducing the noise imposed by the optical link, namely balanced photo-detection.

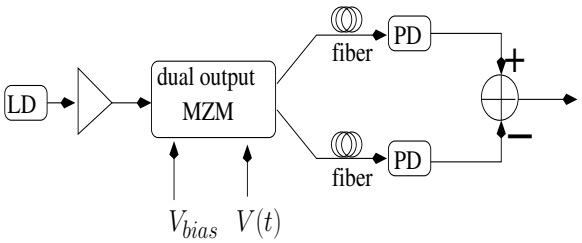

Figure 3.11: Balanced photo-detection

3.1.4 Balanced photodetection

Balanced photo-detection schemes involve the subtraction of two received signals, which results in the desired components in those signals being added, while the noise being mitigated. Fig. 3.11 shows the block diagram of balanced photo-detection, where the laser output is fed to the dual-output MZM that generates a pair of modulated outputs [130]. The first output is the standard output of an MZM with an intensity of $P_{MZM,1}(t) = P_{in}[1 + \cos(\frac{\pi V_{bias}}{V_\pi} + \frac{\pi V(t)}{V_\pi})]$, while the other output has an intensity of [141]:

$$\begin{aligned} P_{MZM,2}(t) = |E(t)|^2 &= \left| \sin(\frac{\pi V_{bias}}{2V_\pi} + \frac{\pi V(t)}{2V_\pi}) \sqrt{2P_{in}} e^{j\omega_c t} \right|^2 \\ &= P_{in}[1 - \cos(\frac{\pi V_{bias}}{V_\pi} + \frac{\pi V(t)}{V_\pi})], \end{aligned} \tag{3.3}$$

Both outputs are photo-detected after transmission through the fiber and as shown in Fig. 3.11, balanced photo-detection involves the subtraction of the two photo-detected signals, where the balanced photo-detector output is given by [130]:

$$\begin{aligned} I_{balanced} &= I_1(t) - I_2(t) \\ &\propto R \cdot P_{MZM,1}(t) - R \cdot P_{MZM,2}(t) \\ &= 2R \cdot P_{in} \cdot \cos(\frac{\pi V_{bias}}{V_\pi} + \frac{\pi V(t)}{V_\pi}), \end{aligned} \tag{3.4}$$

where R is the responsivity of the photo-diode. Again, it can be seen from Equation (3.4) that the desired signals are added, while the intensity noise that is common to the two photo-detected signals is suppressed by the difference operation [130]. A link that has a sub-10 dB NF can be achieved using balanced photo-detection [130].

The next two techniques belonging to the family of optical noise-reduction techniques, namely OIL and optical feed-forward linearization, also belong to the family of techniques designed for increasing the linearity of optical modulation. We now discuss OIL, which assists in generating high-power, low-noise laser outputs.

3.1.5 Optical injection locking

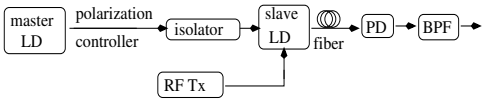

Figure 3.12: Optical injection locking

OIL is a technique conceived for generating a high-power laser output that has both a low intensity noise and a low phase noise. Fig. 3.12 shows the schematic of OIL, where the output of the low-power, low-noise master-laser of Fig. 3.12 is injected into a high-power slave-laser. The slave-laser is constrained to operate at the frequency of the injected laser, provided that this frequency is sufficiently close to its own free-running frequency. The difference between the free-running frequency and the injection-locked frequency of the slave-laser is referred to as the frequency detuning, where using a higher injected power results in a higher allowable frequency detuning. As shown in Fig. 3.12, the output of the slave-laser is directly modulated by the electronic RF transmitter before transmission over the fiber, while the isolator ensures that no reflected signals enter the master-laser.

OIL has several advantages [133]. For example, when using OIL, the laser's relaxation oscillation frequency f_r, as shown in Fig. 2.7, increases. Hence, direct modulation results in weaker dynamic non-linearity induced harmonics and inter-modulation [142]. Additionally, it can be seen from Fig. 2.7 that the increase in f_r is accompanied by an increase in the modulation bandwidth of the laser [134]. Furthermore, it is possible to directly modulate the laser using frequencies that are close to its relaxation oscillation frequency without the usual increase in the RIN noise [134]. When OIL is used, it becomes possible to generate a high-fidelity, high-power optical signal, which enables the designer to achieve a high link-SNR. Finally, OIL can also be employed for generating OSSB signals [143].

Two variations of OIL that employ heterodyne photo-detection are discussed in the following subsections, including Optical Sideband Injection Locking and Optical Injection Phase Locked Loops. These techniques result in performance improvements at the cost of an increased transmitter complexity.

Optical sideband injection locking A so-called dual-mode signal consists of two optical frequencies, where heterodyne detection may be used for generating a RF signal, as discussed in Section 2.1.1.4. The performance of a link that employs this technique can be improved by additionally invoking the concept of OIL. Typically, it is the slave laser's output that is RF modulated during

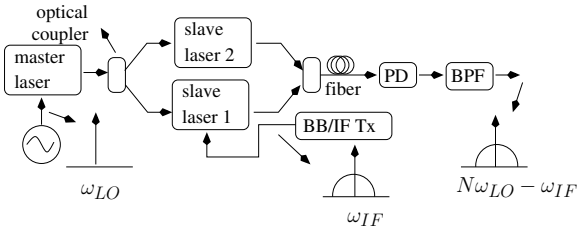

Figure 3.13: Optical sideband injection locking

OIL. However, as shown in Fig. 3.13, it is also possible to injection-lock two -rather than just one- slave lasers to different sidebands of a master-laser [144] that has been modulated using a RF tone at $f_{LO} = \frac{\omega_{LO}}{2\pi}$ Hz. This OIL operation is then followed by the modulation of either one or of both sidebands using the baseband (BB) /IF signal at $f_{IF} = \frac{\omega_{IF}}{2\pi}$ Hz. As shown in Fig. 3.13, the subsequent heterodyne photo-detection of these high-power sidebands generates the high-fidelity up-converted RF signal appearing at $]N \cdot f_{LO} - f_{IF}]$ Hz. More explicitly, Optical Sideband Injection Locking (OSIL) facilitates the injection locking of the slave-lasers to higher-order optical sidebands, i.e to harmonics that are present within the output of the RF-modulated master-laser [131], where the up-converted photodetected signals can be generated at $[N \cdot f_{LO} \pm f_{IF}]$ Hz with N being an integer.

The optical phase noise can be further reduced by amalgamating OIL with Optical Phase Lock Loops (OPLLs), which however results in added transmitter complexity. This hybrid technique is discussed in the next section.

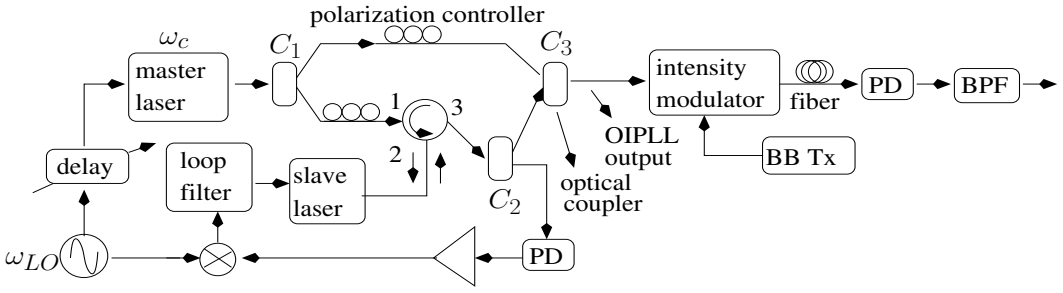

Figure 3.14: Optical injection phase locked loop

Optical injection phase locked loop The OPLL relies on an architecture designed for maintaining phase coherence between the signals that are employed in coherent photo-detection. An OPLL reduces the optical phase noise imposed on the signal transmitted over a ROF link. OIL can be combined with the OPLL technique in order to amalgamate the benefits of both techniques. Such a transmitter is referred to as an Optical Injection Phase Locked Loop (OIPLL) [145], [132], which is shown in Fig. 3.14. The master-laser operating at an optical frequency of $f_c = \frac{\omega_c}{2\pi}$ Hz, is modulated by a RF tone at $f_{LO} = \frac{\omega_{LO}}{2\pi}$ Hz, as shown in Fig. 3.14. The master-laser output is split by the coupler C_1 into two parts, one of which enters port 1 and exits via port 2 of the OC, where this signal is employed in injection locking. The slave-laser in Fig. 3.14 is injection locked to one of the first-order ($N = 1$) or higher-order sidebands ($N > 1$) in the output of the master-laser. The slave-laser in Fig. 3.14 generates the injection locked output at $[f_c + N \cdot f_{LO}]$ Hz and also reflects the output of the master-

laser. As shown in Fig. 3.14, the output of the slave-laser exits from port 3 of the OC, followed by a splitting operation by the coupler C_2 [145]. The upper output of C_2 in Fig. 3.14 is combined with the upper output of C_1 to generate the OIPLL output, while the lower output of C_2 is locally heterodyne photo-detected to generate a RF tone at $N \cdot f_{LO}$ Hz, which is then input to the feedback loop. In the feedback loop, output of the f_{LO} Hz oscillator is frequency-multipled by N and mixed with the photo-detected $N \cdot f_{LO}$ Hz RF tone. The mixer output depends on the phase difference between the two signals. As shown in Fig. 3.14, this mixer output is fed to a loop filter which generates a feedback that modulates the slave-laser. Hence, the loop-filter assists in phase-matching. Meanwhile, the OIPLL output is intensity modulated by the Baseband Transmitter (BB Tx), then transmitted over the fiber and finally photo-detected to generate an up-converted signal at $N \cdot f_{LO}$ Hz [145].

In addition to noise reduction, OIL also resulted in the enhanced linearity of the direct optical modulation scheme of Fig. 2.6(a) [133]. We now move on to another technique, namely optical feed-forward linearization, that helps enhance the linearity of both direct as well as external optical modulation, apart from suppressing the optical noise.

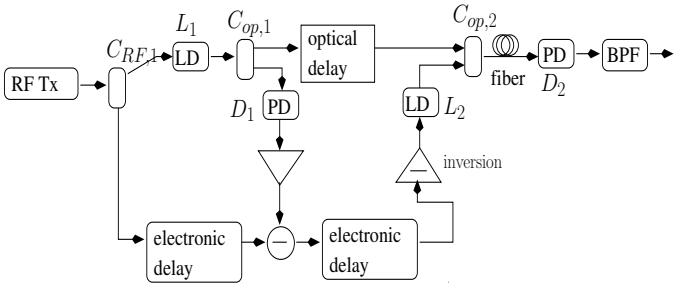

Figure 3.15: Optical feed-forward linearization

3.1.6 Optical feed-forward linearization

Optical feed-forward linearization is a technique that may be employed at the transmitter for pre-compensating the non-linear effects of optical modulation. This technique is implemented using the architecture seen in Fig. 3.15 [135]. As seen in Fig. 3.15, the input RF signal power is split into two branches by the RF coupler $C_{RF,1}$, where the upper branch modulates the optical carrier generated by laser L_1, while the lower branch is used as an uncorrupted reference signal. The modulated optical output of L_1 seen in Fig. 3.15 contains both the RF signal as well as the inter-modulation and harmonic distortion terms, which are additionally corrupted by RIN noise. This optical signal from L_1 is then split using a 50:50 optical coupler $C_{op,1}$, as seen in Fig. 3.15, where the lower-branch output of $C_{op,1}$ is photo-detected by the photo-diode D_1, amplified and then subtracted from the lower branch output of the RF coupler $C_{RF,1}$. The output of the RF coupler $C_{RF,1}$ does not suffer from the degradations and noise imposed by optical modulation, because it is generated by the electronic RF transmitter and not by photo-detecting the modulated optical signal [135]. Hence, the subtraction operation generates a difference signal that ideally contains only the distortion terms imposed by optical modulation and the RIN noise [135]. This electronically delayed difference signal is then inverted in Fig. 3.15 and modulated onto the output of laser the L_2. Note that the laser L_2 operates at an optical frequency $f_{L2} = \frac{\omega_{L2}}{2\pi}$, which is significantly different from the optical frequency $f_{L1} = \frac{\omega_{L1}}{2\pi}$ of L_1. As seen in Fig.

3.15, the modulated output of laser L_2 is then combined with the optically delayed modulated output of laser L_1 using the 90:10 optical coupler $C_{op,2}$ and transmitted over the fiber. If $A_1(t)e^{j\omega_{L1}t}$ and $A_2(t)e^{j\omega_{L2}t}$ are the optical signals received at photo-detector D_2 from lasers L_1 and L_2, respectively, then their coherent photo-detection by photo-detector D_2 results in the signal:

$$\begin{aligned} P_{linear} &= R|A_1(t)e^{j\omega_{L1}t} + A_2(t)e^{j\omega_{L2}t}|^2 \\ &= R|A_1(t)|^2 + R|A_2(t)|^2 \\ &+ 2R|A_1(t)||A_2(t)|\cos[j(\omega_{L1} - \omega_{L2})t], \end{aligned} \tag{3.5}$$

where again, R is the photo-diode's responsivity. Since the operating frequencies of the two lasers are significantly different, i.e. $(\omega_{L1} - \omega_{L2})$ is large, the third term of Equation (3.5) would be located within the electronic spectrum at a frequency that is far higher than that of the first two terms. The first two terms represent the coherent addition of the two signals. Since $R|A_2(t)|^2$ carries an inverted replica of the distortion plus RIN noise in $R|A_1(t)|^2$, this addition results in the cancellation of the distortion plus RIN noise term [135]. Hence, as per Equation (3.2), the SFDR will be significantly improved, because the feed-forward linearization technique of Fig. 3.15 suppresses the both inter-modulation products as well as the laser RIN over a large bandwidth.

We now conclude our discussions on the family of noise-reduction techniques. Low-biasing of the optical modulator is simpler than the subsequently discussed balanced photo-detection, but the former technique constrains the usable SCM signals to be within an octave. While the extent of noise-reduction obtained from the various noise-reduction techniques discussed in this chapter depends on the specifications of the components used, OIL in general provides a much higher performance improvement than the rest. However, this comes at the cost of a higher transmitter complexity.

As mentioned previously, the last two techniques in the family of optical noise-reduction techniques, namely OIL and optical feed-forward linearization, also assist in increasing the linearity of optical modulation. Let us now continue our discourse by moving on to another subset of techniques that help increase the linearity of optical modulation, namely to the family of linearized optical modulators.

Table 3.2: ROF Performance Improvement Techniques (Part 2)

Technique	Year	Authors	Contribution
Linearized optical modulators	1990	Korotky *et al.* [146]	Two parallel modulators increased the linearity of modulation at the cost of a tolerable increase in the optical power and drive voltage used.
	1991	Skeie *et al.* [147]	The cascading of modulators suppressed the 3rd harmonic by 95 dB when using a single tone modulating signal at a modulation depth of 20%.
	1999	Ackerman *et al.* [148]	Simultaneous modulation of optical carriers at two wavelengths achieved a dynamic range of 74 dB in 1 MHz over a bandwidth higher than an octave.
	2009	Masella *et al.* [45]	A linear polarizer was employed both before and after a mixed-polarization MZM to achieve 13 dB increase in the SFDR when employing OSSB modulation.
Optical filtering	2007	Lim *et al.* [149]	The optical sidebands that contribute most to the 3rd-order IMD in the photo-detected RF signal were filtered out using an optical filter to obtain an increase of 9 dB in the IMD suppression.
Pre-distortion and post-compensation	2002	Fernando *et al.* [150]	Pre-distortion in downlink and post-compensation in uplink using high -order adaptive filters linearized the link, while keeping the RAP simple.
	2003	Roselli *et al.* [151]	Low cost pre-distortion circuits were designed for compensating 2nd and 3rd order distortions that arise from direct modulation of lasers.

3.1.7 Linearized optical modulators

There are several architectures that linearize the transfer-characteristics of the MZM of Fig. 2.9(a), which result in the efficient suppression of the even-order and third-order inter-modulation products in the photo-detected signal. As a result of linearization, the SFDR of the links employing these architectures is maximised, since the SFDR of Equation (3.2) now depends on the much weaker fifth-order inter-modulation products, rather than on the third-order inter-modulation products. Some of the architectures within this subset include both the parallel and serial MZMs architectures, as well as the dual wavelength equalization and polarization mixing to be detailed below.

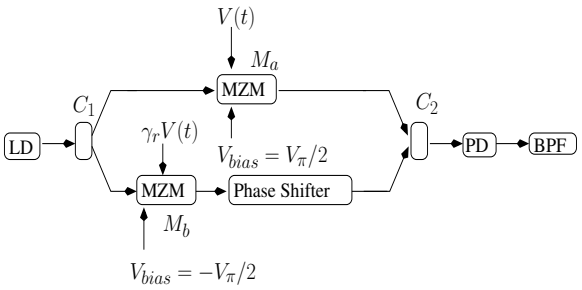

Figure 3.16: Linearization using dual parallel MZMs

Parallel and serial optical modulators It can be observed from Equation (3.30) that the QP biasing of a MZM results in negligible second-order distortions, but significant third-order distortions in the photo-detected signal, where the polarity of the third-order distortion depends on the quadrature bias voltage that is applied in Fig. 5.11. Dual-parallel linearization draws its motivation from the fact that the third-order distortions can be suppressed by superimposing signals in which the polarity of the third-order distortion is opposite [146]. As shown in Fig. 3.16, the output of the LD is fed to the coupler C_1 having a power splitting ratio of η_{c1}, where the pair of outputs gleaned from the coupler C_1 are fed to the MZMs M_a and M_b, which are QP biased at $V_\pi/2$ and $-V_\pi/2$, respectively [146]. As shown in Fig. 3.16, the pair of MZMs are driven by the same RF signal $V(t)$, which have a voltage ratio of γ_r. The outputs of the pair of MZMs are combined by the coupler C_2 of Fig. 3.16 having a power combining ratio of η_{c2}. Using Equation (2.6a), the expression describing the photo-detected signal becomes:

$$I_{PD}(t) = I_0|\sqrt{1-\eta_{c1}}\sqrt{1-\eta_{c2}}\cos(\frac{\pi}{4}+\frac{V(t)}{2V_\pi})e^{j\phi_a} + \sqrt{\eta_{c1}}\sqrt{\eta_{c2}}\cos(-\frac{\pi}{4}+\frac{\gamma_r V(t)}{2V_\pi})e^{j\phi_b}|^2, \quad (3.6)$$

where I_0 is the photo-detected signal, if there was no dual-parallel modulation. The optical phase shifter of Fig. 3.16 ensures that the phase-difference of the optical fields at the output of the pair of

modulators is $\phi_a - \phi_b = \pi/2$. Then, the expression of Equation (3.6) becomes [146]:

$$\begin{aligned} I_{PD}(t) &= I_0[(1-\eta_{c1})(1-\eta_{c2})\cos^2(\frac{\pi}{4}+\frac{V(t)}{2V_\pi}) \\ &+ \eta_{c1}\eta_{c2}\cos^2(-\frac{\pi}{4}+\frac{\gamma_r V(t)}{2V_\pi})] \\ &= I_0[(1-\eta_{c1})(1-\eta_{c2})(1-\sin(\frac{V(t)}{2V_\pi})) \\ &+ \eta_{c1}\eta_{c2}(1+\sin(\frac{\gamma_r V(t)}{2V_\pi}))] \\ &= \sum_{k=0}^{\infty} c_k[V(t)]^k. \end{aligned} \tag{3.7}$$

Using the Taylor series expansion of the $\sin(x)$ in the Equation (3.7), it may be readily shown that there are no even harmonics in the photo-detected signal at all. Hence, naturally there would be no second-order or fourth-order distortions in the photo-detected signal either. The third-order inter-modulation product I_{IM3} and the desired RF signal I_{RF} is proportional to the Taylor series coefficients c_3 and c_1, respectively. Hence [146], we have

$$I_{IM3} \propto c_3 \propto \left[(1-\eta_{c1})(1-\eta_{c2}) - \eta_{c1}\eta_{c2}\gamma_r^3\right] \tag{3.8}$$

$$I_{RF} \propto c_1 \propto \left[(1-\eta_{c1})(1-\eta_{c2}) - \eta_{c1}\eta_{c2}\gamma_r\right]. \tag{3.9}$$

It may be observed from Equation (3.8) that if the condition of $(1-\eta_{c1})(1-\eta_{c2}) = \eta_{c1}\eta_{c2}\gamma_r^3$ is satisfied, then this would ensure having $c_3 = 0$ and hence we suppress the third-order inter-modulation products. However, this would also reduce the value of c_1 in Equation (3.9), which would attenuate the desired signal. Hence, this linearization comes at the cost of a weaker desired signal, which would in turn result in a reduced output SNR and an increased NF.

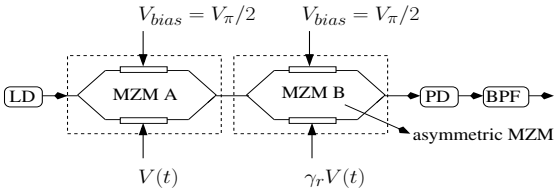

Figure 3.17: Linearization using serial MZMs

This concept of using those values of power-splitting ratio and drive-voltage ratio that suppress the third-order distortion can be extended to the architecture of Fig. 3.17 as well, where two dual-drive MZMs, namely MZM-A and MZM-B, are connected in series and are QP biased with $V_{bias} = V_\pi/2$ [147]. The splitter as well as the coupler of MZM-B has an asymmetric power coupling ratio of η, while the ratio of the RF drive voltages to the MZMs is γ_r. Assuming the MZMs of Fig. 3.17 operate

in the push-pull mode of operation discussed in Section 2.1.1.2, the photo-detected signal is:

$$
\begin{aligned}
I_{PD}(t) &= I_o \left| \frac{1}{2} e^{j(\frac{\pi V_{bias}}{2V_\pi} + \frac{\pi V(t)}{2V_\pi})} + \frac{1}{2} e^{-j(\frac{\pi V_{bias}}{2V_\pi} + \frac{\pi V(t)}{2V_\pi})} \right|^2 \\
&\times \left| \sqrt{\eta}\sqrt{\eta} e^{j(\frac{\pi V_{bias}}{2V_\pi} + \frac{\pi \gamma_r V(t)}{2V_\pi})} + \sqrt{1-\eta}\sqrt{1-\eta} e^{-j(\frac{\pi V_{bias}}{2V_\pi} + \frac{\pi \gamma_r V(t)}{2V_\pi})} \right|^2 \\
&= 0.25 I_o [1 + \cos(\frac{\pi V_{bias}}{V_\pi} + \frac{\pi V(t)}{V_\pi})] \\
&\times [0.5\eta^2 + 0.5(1-\eta)^2 + \eta(1-\eta)\cos(\frac{\pi V_{bias}}{V_\pi} + \frac{\pi \gamma_r V(t)}{V_\pi})] \\
&= 0.25 I_o [1 - \sin(\frac{\pi V(t)}{V_\pi})] \\
&\times [0.5\eta^2 + 0.5(1-\eta)^2 - \eta(1-\eta)\sin(\frac{\pi \gamma_r V(t)}{V_\pi})] \qquad (3.10) \\
&= \sum_{k=0}^{\infty} c_k (V(t))^k. \qquad (3.11)
\end{aligned}
$$

Using the Taylor series expansion of Equation (3.10) we get $c_k = 0$ for all even k in Equation (3.11), while those values of γ_r and η are chosen which would result in $c_3 = 0$, thereby suppressing the third-order distortions.

It is seen from Fig. 3.16 and Fig. 3.17 that linearizing the optical modulation using parallely or serially connected MZMs relies on a single laser and on multiple MZMs. We now discuss an alternate technique designed for linearizing optical modulation, namely dual-wavelength equalization, which relies on multiple lasers and on a single MZM.

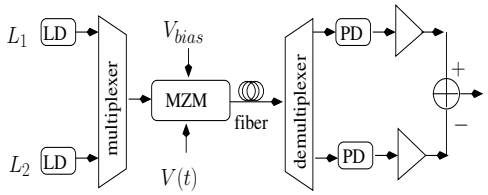

Figure 3.18: Dual-wavelength equalization (LD- Laser Diode; MZM- Mach-Zehnder Modulator; PD- Photodiode)

Dual-wavelength equalization The strength of both the required signal and of the intermodulation products in the photo-detected signal depend on the switching voltage V_π of the MZM in Fig. 5.11. If two optical signals modulated by the same data are photo-detected and subtracted from each other, as seen in Fig. 3.18, then it is possible to suppress the third-order intermodulation products without totally suppressing the required signal, provided that the switching voltages employed in the two modulations schemes are different [148]. To expand a little further, Fig. 3.18 shows the block diagram of an architecture that implements dual-wavelength equalization, where the outputs of two laser diodes L_1 and L_2 are multiplexed using the WDM scheme of Fig. 2.24(b) and fed into a MZM modulator that is driven by the RF signal $V(t)$ and biased at V_{bias} Volts. Each of the two laser diodes operates at different wavelengths, where we set the ratio of the MZM switching voltages V_π of Equations (2.3b) or (2.6d) at these wavelengths to r_π [148]. As shown in Fig. 3.18, after transmission

through the fiber, the signal is demultiplexed using the scheme of Fig. 2.24(b) and the two wavelengths are separately photo-detected, amplified and then subtracted. The ratio of the photo-detected signals after amplification is A_{amp}, when there is no optical modulation. The mathematical expression of the difference signal is as follows:

$$\begin{aligned} I_{PD}(t) &= I_o[1+\cos(\frac{\pi V_{bias}}{V_\pi}+\frac{\pi V(t)}{V_\pi})] \\ &- A_{amp}I_o[1+\cos(\frac{\pi V_{bias}}{V_\pi}+\frac{\pi V(t)}{r_\pi V_\pi})] \\ &= \sum_{k=0}^{\infty} c_k[V(t)]^k. \end{aligned} \tag{3.12}$$

Using the Taylor series expansion of the $\cos(x)$ terms and exploiting the fact that the desired RF component I_{RF} as well as the third-order inter-modulation product I_{IM3} are proportional to the co-efficients c_1 and c_3, respectively, we arrive at [148]:

$$I_{RF} \propto c_1 \propto \left[\sin(\frac{\pi V_{bias}}{V_\pi}) - \frac{A_{amp}}{r_\pi}\sin(\frac{\pi V_{bias}}{r_\pi V_\pi})\right] \tag{3.13}$$

$$I_{IM3} \propto c_3 \propto \left[\sin(\frac{\pi V_{bias}}{V_\pi}) - \frac{A_{amp}}{r_\pi^3}\sin(\frac{\pi V_{bias}}{r_\pi V_\pi})\right]. \tag{3.14}$$

The bias voltage V_{bias} is chosen so that the MZM is QP biased or at least near-QP biased for both wavelengths, where we have $\frac{\pi V_{bias}}{V_\pi} = \frac{2m+1}{2}\pi$ and $\frac{\pi V_{bias}}{r_\pi V_\pi} = \frac{2n+1}{2}\pi$ with m and n being integers. When this specific biasing is used, we have $c_2 = [\cos(\frac{\pi V_{bias}}{V_\pi}) - \frac{A_{amp}}{r_\pi^2}\cos(\frac{\pi V_{bias}}{rV_\pi})] \approx 0$, i.e. the photo-detected signal would only contain highly suppressed second-order inter-modulation products. When the MZM is QP biased, I_{IM3} of Equation(3.14) becomes [148]: $I_{IM3} \propto \left[1 - \frac{A_{amp}}{r_\pi^3}\right]$. Hence, the third-order inter-modulation products can be suppressed, provided that the condition of $A_{amp} = r_\pi^3$ is maintained [148]. However, maintaining this would reduce the strength of I_{RF} in Equation(3.13) and hence would increase the NF.

The techniques conceived for linearizing the MZM transfer curve of Fig. 2.9(a) that have been discussed so far either employed multiple MZMs, as seen from Fig. 3.16 and Fig. 3.17, or employed multiple lasers, as seen from Fig. 3.18. We now continue our discourse about linearized optical modulators by discussing a technique that relies on a single MZM and a single laser to linearize optical modulation, but requires a polarizer.

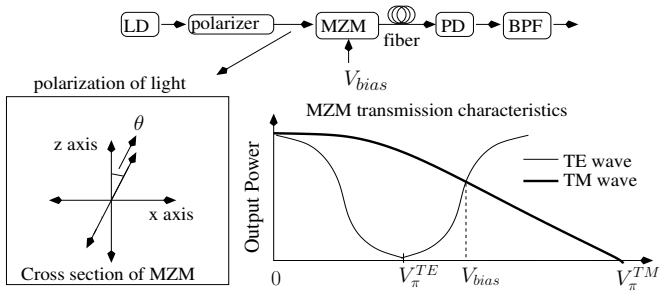

Figure 3.19: Linearization using polarization mixing

Polarization mixing The polarization of light characterizes the direction of its electric field vector. If an optical signal that is propagating along the y-axis and is polarized at an angle θ with respect to the z axis, as seen from Fig. 3.19, enters the modulator, then it results in a super-position of a pair of waves within the MZM that have orthogonal polarizations, which are typically referred to as the Transverse Electric (TE) and the Transverse Magnetic (TM) waves [152]. Since the MZMs are sensitive to the polarization of the optical signal, the switching voltages V_π^{TE} and V_π^{TM} are different for each of these polarizations, as shown in the MZM transfer characteristics of Fig. 3.19. The switching voltages and the bias voltage V_{bias} applied satisfy the following conditions:

$$\frac{\pi V_{bias}}{V_\pi^{TE}} = \frac{\pi(4m+1)}{2} \text{ and } \frac{\pi V_{bias}}{V_\pi^{TM}} = \frac{\pi(4n+3)}{2}, \tag{3.15}$$

where m as well as n are integers and $r_{\pi,p} = \frac{V_\pi^{TE}}{V_\pi^{TM}}$ may be used for denoting the ratio of V_π^{TE} and V_π^{TM}. It can be seen from the MZM transfer characteristics of Fig. 3.19 that for a bias voltage of V_{bias} both waves experience QP biased modulation, and that the transfer characteristics have opposite slopes at this bias voltage. The pair of waves can be mathematically described by the orthogonal components of a vector. Hence, the photo-detected signal becomes:

$$\begin{aligned}
I_{PD}(t) &= I_0|\sin(\theta)\cos(\frac{\pi}{4} + \frac{V(t)}{2V_\pi})\hat{x} \\
&+ \cos(\theta)\cos(-\frac{\pi}{4} + \frac{r_{\pi,p}V(t)}{2V_\pi})\hat{z}|^2 \\
&= I_0[\sin^2(\theta)\cos^2(\frac{\pi}{4} + \frac{V(t)}{2V_\pi}) \\
&+ \cos^2(\theta)\cos^2(-\frac{\pi}{4} + \frac{r_{\pi,p}V(t)}{2V_\pi})] \\
&= I_0[\sin^2(\theta)(1 - \sin(\frac{V(t)}{2V_\pi})) \\
&+ \cos^2(\theta)(1 + \sin(\frac{r_{\pi,p}V(t)}{2V_\pi}))] = \sum_{k=0}^{\infty} c_k(V(t))^k.
\end{aligned} \tag{3.16}$$

Here I_0 is the unmodulated photo-detected signal. Using the Taylor series expansion of the trigonometric terms in Equation (3.16), it may be readily observed that there are no even harmonics (i.e. we have $c_k = 0$ for k being even) in the photo-detected signal. This is because the MZM is QP biased for both modes. The third-order inter-modulation I_{IM3} and the desired RF signal I_{RF} are proportional to the Taylor series coefficients c_3 and c_1, respectively. Hence from Equation (3.16) we have,

$$I_{IM3} \propto c_3 \propto \left[\sin^2(\theta) - \cos^2(\theta)r_{\pi,p}^3\right] \tag{3.17}$$

$$I_{RF} \propto c_1 \propto \left[\sin^2(\theta) - \cos^2(\theta)r_{\pi,p}\right] \tag{3.18}$$

If the condition of $\frac{\cos^2(\theta)}{\sin^2(\theta)} = \frac{1}{r_{\pi,p}^3}$ is satisfied, then this would ensure $c_3 = 0$ in Equation (3.17) and hence we would suppress third-order inter-modulation products in the photo-detected signal $I_{PD}(t)$ of Equation (3.16) [152], where physically $\frac{\cos^2(\theta)}{\sin^2(\theta)}$ is the ratio of the optical power in the TE and TM modes of Fig. 3.19. However, according to Equation (3.18), this would also reduce the value of c_1, i.e. it would reduce the desired signal. On the other hand, unlike the architecture of Fig. 3.19 discussed here, the one in [45] did not rely on the TE and TM modes having opposite slopes at the QP of

the MZM transfer curves in Fig. 3.19. Instead, it relied on two linear polarizers for suppressing the non-linear sidebands within the optical field. Explicitly, the authors of [45] cancelled some of the optical sidebands that contribute to the third-order distortion of the photo-detected signal, namely the sidebands at $f_c + 2f_1 - f_2$ Hz and $f_c + 2f_2 - f_1$ Hz. Here, f_c Hz is the optical frequency of the laser whose output was externally modulated using a dual-tone RF signal at f_1 Hz and f_2 Hz by the linearized modulator. Finally, similar polarization mixing techniques may also be employed for linearizing a phase modulator [153].

Having studied the subset of linearized modulators within the family of techniques designed for increasing the linearity of optical modulation, we now study how optical and electrical filtering can be invoked for increasing the linearity of optical modulation in the next two techniques to be discussed below.

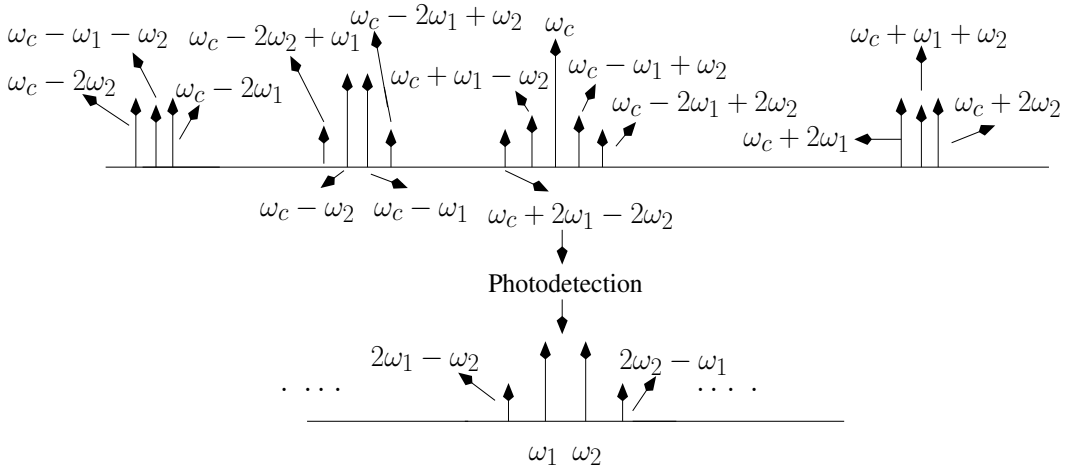

Figure 3.20: Optical spectrum of non-linear OSSB modulation

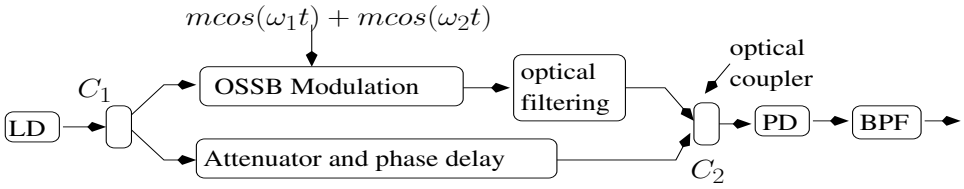

Figure 3.21: Linearization using optical filtering

3.1.8 Optical filtering

:Fig. 3.20 [149] shows the optical spectrum after an optical carrier at $f_c = \frac{\omega_c}{2\pi}$ Hz has been OSSB modulated by two RF tones having frequencies of $f_1 = \frac{\omega_1}{2\pi}$ Hz and $f_2 = \frac{\omega_2}{2\pi}$ Hz. Fig. 3.20 also shows the spectrum of the photo-detected signal. As shown in Fig. 3.20, the most significant inter-modulation products in the photo-detected signal are the third-order inter-modulation products which are located at $(2\omega_1 - \omega_2)$ and $(2\omega_2 - \omega_1)$. The major pairs in the optical spectrum of Fig. 3.20 that beat together during photo-detection and generate the third-order inter-modulation product at $(2\omega_1 - \omega_2)$ are those at $\{\omega_c, \omega_c - 2\omega_1 + \omega_2\}$ and $\{\omega_c - \omega_1, \omega_c + \omega_1 - \omega_2\}$. Similarly, the major pairs in the optical spectrum

of Fig. 3.20, that beat together during photo-detection and generate the inter-modulation product at $(2\omega_2 - \omega_1)$ are those at $\{\omega_c, \omega_c - 2\omega_2 + \omega_1\}$ and $\{\omega_c - \omega_2, \omega_c - \omega_1 + \omega_2\}$. While the sidebands at $(\omega_c - \omega_1)$ and $(\omega_c - \omega_2)$ in Fig. 3.20 are the required modulation sidebands, those at $(\omega_c - 2\omega_1 + \omega_2)$ and $(\omega_c - 2\omega_2 + \omega_1)$ are too close to the required sidebands to be easily filtered out using low-cost optical filters. By contrast, the sidebands at $(\omega_c + \omega_1 - \omega_2)$ and $(\omega_c - \omega_1 + \omega_2)$ may be readily filtered out using inexpensive optical filters. The architecture that implements this filtering technique is shown in Fig. 3.21, where the unmodulated laser output power is split into two halves using the coupler C_1. One of the outputs of C_1, namely the upper branch, is OSSB modulated followed by optical filtering for removing the sidebands at $(\omega_c + \omega_1 - \omega_2)$ and $(\omega_c - \omega_1 + \omega_2)$ in Fig. 3.20. The optical filter also filters out the optical carrier at ω_c. Then, after accurate attenuation and phase-shift, the optical carrier is re-introduced using the other output of coupler C_1, namely the lower branch of Fig. 3.21. This technique can also be extended to three-tone modulation by filtering out the components at $(\omega_c \pm \omega_m \mp \omega_n)$ for $m, n \in \{1, 2, 3\}$.

We now study the final technique designed for increasing the linearity of optical modulation, namely pre-distortion and post-compensation. These techniques, unlike the previous techniques of the family, are implemented in the electronic domain, rather than in the optical domain.

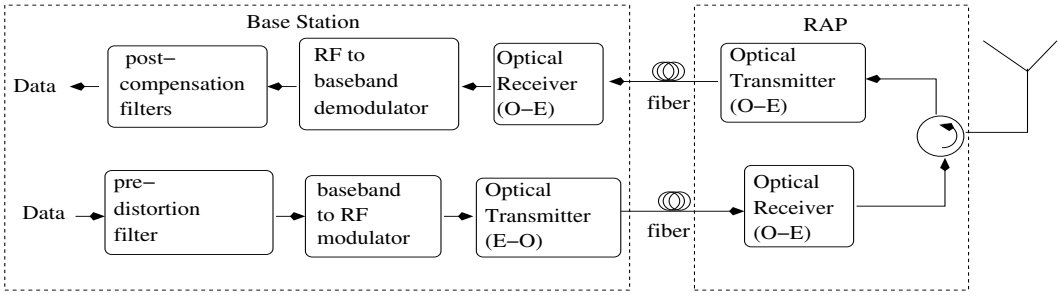

Figure 3.22: Linearization using pre-distortion and post-compensation filters

3.1.9 Pre-distortion and post-compensation

The non-linearities encountered in optical modulation can be compensated for at the optical transmitter and receiver by pre-distortion and post-compensation, respectively, using electronic filters. Fig. 3.22 shows the block diagram of an architecture that employs transmitter pre-distortion and receiver post-compensation filters in the BS, where again, the pre-distortion filter compensates for the non-linear effects of the ROF Downlink (DL) prior to the actual transmission, while the post-compensation filter removes the higher order sidebands generated by the non-linear effects after the ROF UL transmission [150]. Both these filters are located at the BS and hence have the advantage of centralised signal processing. This filter-based compensation technique may be used in ROF links employing both the direct [151] as well as the external modulation schemes of Fig. 2.6(a) and Fig. 5.11, respectively.

During DL transmission, the data signal is firstly pre-distorted using the non-linear characteristic of the filter, then up-converted to RF and finally employed in modulating the DL optical carrier, as seen in Fig. 3.22. This DL optical signal is transmitted to the RAP, where it is photo-detected and then wirelessly transmitted to the MS. The UL wireless signal received at the RAP of Fig. 3.22 is employed for modulating the UL optical carrier followed by transmission to the BS, where the UL ROF

signal is photo-detected and then down-converted. Finally, the signal is fed to the post-compensation filter of Fig. 3.22 and then decoded. These filters can also be made adaptive, since the modulated response varies significantly between various lasers [150]. The sinusoidal transfer function of a MZM shown in Fig. 2.9(a) can be compensated by applying a arcsine filter[1] to the modulating signal prior to optical modulation [154].

We now conclude our discussions on the family of techniques conceived for increasing the linearity of optical modulation. While the OIL techniques of Fig. 3.12, Fig. 3.13 and Fig. 3.14 significantly increase the linearity of direct optical modulation, they cannot be used for increasing the linearity of the external optical modulation of Fig. 5.11. Moreover, they significantly increase the complexity of the optical transmitter. It requires polarization matching between the master- and slave-laser, which are connected using sophisticated polarization maintaining fibers. Unlike OIL, the optical feed-forward linearization technique of Fig. 3.15 may be beneficially applied for eliminating the distortions in the case of both direct as well as external modulation [135]. However, this technique requires both accurate amplitude and phase matching for attaining a beneficial distortion and noise reduction, which may be achieved by using the amplifiers and delay elements of Fig. 3.15. The phase-mismatch introduced by the chromatic dispersion of the fiber may be compensated, provided that the transmitter is designed for a fixed fiber length, which would however relatively limit the employement of such a transmitter. Additionally, it is worth noting that this linearization technique is also associated with a relatively high implementation al cost [151]. Employing the linearized MZMs of Fig. 3.16, Fig. 3.17, Fig. 3.18 and Fig. 3.19 results in the suppression of the distortion, but it is accompanied by the suppression of the desired signal as well. The subsequently discussed optical filter-based linearization of optical modulation. as shown in Fig. 3.21, results in significant performance improvements. However, this scheme relies on the filtered sidebands found at $(\omega_c+\omega_1-\omega_2)$ and $(\omega_c-\omega_1+\omega_2)$ in the optical spectrum of Fig. 3.20 being sufficiently far from the desired sidebands at $(\omega_c-\omega_1)$ and $(\omega_c-\omega_2)$, thereby imposing restrictions on the usable RF frequencies. We finally discussed the electronic filter-based technique of Fig. 3.22, which is effective in the case of external modulation, but cannot easily suppress both the higher harmonics and the inter-modulation products in direct modulation [135]. Moreover, the operational bandwidth of these electronic techniques is limited [135]. Nevertheless, their strength is their relatively low implementation al cost, when compared to other optical techniques [151].

Having focussed our attention on the benefits of increasing the linearity of optical modulation, let us now concentrate our attention on the family of techniques that help in overcoming fiber-non linearity.

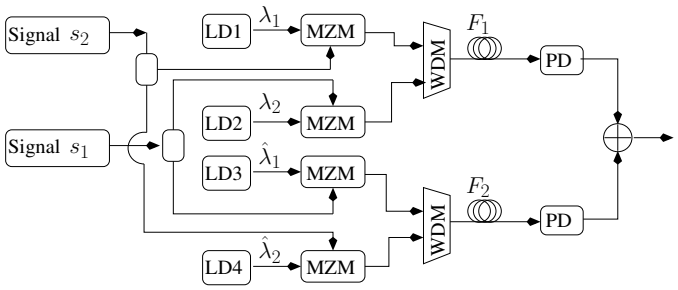

Figure 3.23: Multiple fiber transmission for overcoming the effects of fiber non-linearity

[1] A filter in which the output is related to the input through a inverse sine function.

Table 3.3: ROF Performance Improvement Techniques (Part 3)

Technique	Year	Authors	Contribution
Overcoming fiber non-linearity	2000	Yang *et al.* [42]	Signal transmission using 2 parallel fibers reduced the crosstalk by 15 dB over 200 MHz, while carrier suppression reduced the crosstalk by 20 dB over 2 GHz.
Overcoming Chromatic Dispersion	1997	Marti *et al.* [155]	Chromatic dispersion was overcome by compensating the differential delay between the optical frequencies using a TLCG.
	1997	Smith *et al.* [43]	An OSSB signal was generated using a dual-drive MZM and was shown to suffer from lower dispersion-induced power penalty than ODSB signal.
	1997	Smith *et al.* [65]	It was shown that the deteriorating effects of chromatic dispersion can be reduced by using chirped OSSB signals.
	1998	Ramos *et al.* [156]	Fiber non-linearity induced SPM was gainfully used for generating chirp having polarity that is opposite to the dispersion-induced chirp.
	1999	Sotobayashi *et al.* [157]	The dispersion-induced power penalty inflicted on an ODSB signal carrying a 60 GHz RF signal was reduced by using mid-way OPC.
	2006	Yu *et al.* [158]	It was shown that OCS modulation has a high spectral efficiency and receiver sensitivity and small dispersion-induced power penalty.
Digitized ROF	2009	Nirmalathas *et al.* [46]	It was shown that DROF ensured greater link linearity and exhibited the performance advantages of a digital optical link.
	2014	Yang *et al.* [159]	

3.1.10 Overcoming the effects of fiber non-linearity

As was discussed in Section 2.1.1.3, XPM and SPM are the undesired consequences of the fiber's non-linearity. The detrimental effects of these phenomena can be greatly reduced by using constant-amplitude optical modulation schemes like optical frequency and optical phase modulation, which however requires additional components for photo-detection, as was discussed in Section 2.1.2.2. Additionally, two basic techniques have been proposed in the literature for suppressing the effects of fiber non-linearity, including multiple fiber transmission [42] and carrier suppression [42]. Multiple fiber transmission is similar to the balanced photo-detection technique of Fig. 3.11, since both techniques involve the removal of the undesired components by adding two replicas of the same signal. However, multiple fiber transmission requires the transmission of the signals through a pair of identical fibers at different wavelengths. For example, as seen in Fig. 3.23, a pair two signals s_1 and s_2 may be modulated onto the wavelengths λ_1 generated by laser LD1 and λ_2 generated by laser LD2, respectively and then transmitted through the fiber F_1 for photo-detection. Similarly, these signals are also modulated onto the wavelengths $\hat{\lambda}_2$ generated by laser LD4 and $\hat{\lambda}_1$ generated by laser LD3 and then transmitted through the fiber F_2 for photo-detection, as portrayed in Fig. 3.23. The specific choice of these four wavelengths should meet the following criteria [42]: $\lambda_1 - \lambda_2 = \hat{\lambda}_1 - \hat{\lambda}_2$ and $D_1 = -D_2$, where D_1 and D_2 are the dispersion parameters of the fibers F_1 and F_2, respectively, as defined in Section 2.1.1.3. In such a scenario the XPM crosstalk contamination imposed on the received signals in the pair of optical fibers are 180^0 out of phase and hence they would cancel out each other after their addition[42]. The disadvantage of this technique is the need to transmit the same signal through multiple fibers, thereby reducing the achievable throughput.

On the other hand, as discussed in Section 3.1.2, carrier suppression improves the receiver sensitivity of the link, which implies that the transmitter can operate at a lower transmit power, thereby reducing the effects of fiber non-linearity.

Let us now continue our discourse by considering the family of techniques designed for overcoming chromatic dispersion.

3.1.11 Overcoming chromatic dispersion

Chromatic dispersion, originally discussed in Section 2.1.1.3, results in symbol-broadening [31] and an associated power-reduction penalty [83], and hence increases the BER of the ROF link. A ROF link that employs the ODSB modulation technique of Fig. 2.16(a) along with the direct photo-detection technique of Fig. 2.15(a) constitutes the most common ROF implementation, which is a direct consequence of its low cost as well as low complexity. However, the disadvantage of employing ODSB modulation is the above-mentioned chromatic dispersion-induced power penalty, where the chromatic dispersion imposes a phase-shift of the optical signal propagating through the fiber. The frequency-dependent phase-change imposed by chromatic dispersion results in a phase-difference between the upper and lower sidebands in the ODSB signal of Fig. 2.16(a). The photo-detected signal is proportional to the optical power $P(t) = |E(t)|^2$, with $E(t)$ being the optical field-strength of the ODSB signal, where the optical power is attenuated owing to the destructive interference between the beating sidebands. Hence, this optical power-attenuation is referred to as dispersion-induced power-penalty. The attenuation of the optical power results in the attenuation of the electronic power P_{RF} of the photo-detected signal at f_{RF} Hz, where the extent of attenuation is given by [83]:

$$P_{RF} \propto \cos^2\left[\frac{\pi \cdot L \cdot D \cdot \lambda_c^2 \cdot f_{RF}^2}{c \cdot [1 - \frac{2}{\pi} \cdot \arctan(\alpha_{chirp})]}\right], \tag{3.19}$$

where D is the chromatic-dispersion parameter (also called GVD parameter) of Equation (2.19) discussed in Section 2.1.1.3, L is the length of the fiber, λ_c is the wavelength of the optical carrier, c is the speed of light in vacuum and α_{Chirp} is the chirp parameter of the signal. Chirping in an intensity-modulated optical signal refers to a time-dependent variation of the instantaneous optical frequency from its ideal value of $f_c = \frac{c}{\lambda_c}$ Hz. Thus, chromatic dispersion limits the both the affordable fiber lengths L and the modulating-signal frequencies f_{RF}, when ODSB modulation is employed [89]. Chromatic dispersion can be compensated by using specialised fibers called Dispersion Compensation Fibers (DCF) [31]. If D_{comp} is the dispersion parameter of the DCF, then chromatic dispersion can be overcome by propagating the optical signal through L_{comp} meters of the DCF, after it has propagated through L meters of the standard SMF, provided that the following condition is met [31]:

$$D_{comp} \cdot L_{comp} = -D \cdot L. \tag{3.20}$$

Additionally, other techniques that have been proposed in the literature for overcoming chromatic dispersion include employing dispersion-tolerant schemes like the OSSB and OCS modulation schemes of Fig. 2.16(b) and Fig. 2.16(c), apart from employing the fiber-gratings of Fig. 3.26, chirped optical signals, the optical phase conjugation technique of Fig. 3.30 and the exploitation of SPM [156], which are detailed below.

Dispersion-tolerant modulation schemes Employing the OSSB and OCS optical modulation formats of Fig. 2.16(b) and Fig. 2.16(c), respectively, results in a high degree of immunity to the dispersion-induced power penalty [43], [158]. Additionally, the BS transmitter may modulate a BB signal onto the optical carrier, while, at the RAP, the heterodyne photo-detection technique of Fig.2.15(b) would ensure the generation of an up-converted RF signal that does not suffer from the dispersion-induced power penalty.

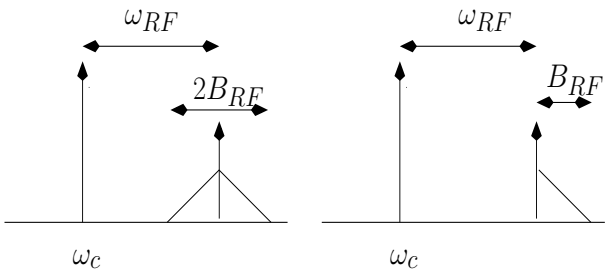

(a) Using Electronic Double Side Band (EDSB) signal

(b) Using Electronic Single Side Band (ESSB) signal

Figure 3.24: Optical single side band signal spectrum

The detrimental effect of chromatic dispersion increases as the optical bandwidth of the signal increases. Hence, the resilience of OSSB modulation to chromatic dispersion can be further improved by employing electronic single-sideband modulating signals during optical modulation, instead of the usual electronic double-sideband signal [83]. Fig. 3.24(a) and Fig. 3.24(b) illustrate the optical spectra of OSSB signals that have been generated using electronic double-sideband and single-sideband signals, respectively [83]. Even when OSSB modulation is employed, some residual chromatic dispersion persists because the modulating signal has a finite bandwidth of $2B_{RF}$ around the RF carrier f_{RF}, as seen in Fig. 3.24(a). As seen from Fig. 3.24(b), the excess-bandwidth can be eliminated by employing an electronic single-sideband signal during optical modulation, instead of the usual electronic DSB signal [83], which leads to a further reduction of the detrimental effects of chromatic dispersion.

However, unlike the ODSB modulation, the OSSB and OCS modulations, primarily rely on the external modulation technique of Fig. 2.8(b) that employs a dual-drive MZM [83]. Thus, if we are constrained to employ ODSB modulation, then we may overcome the limitations imposed by chromatic dispersion by relying on the techniques discussed below, where employing fiber-gratings is discussed first.

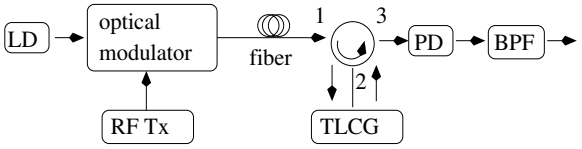

Figure 3.25: Chromatic dispersion compensation using a TLCG

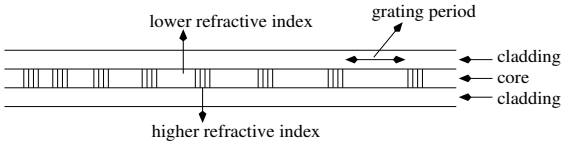

Figure 3.26: Linearly chirped FBG

Fiber gratings As discussed in Section 2.1.1.3, chromatic dispersion occurs because the propagation velocity of the different frequencies contained in the optical signal are different. Thus, chromatic

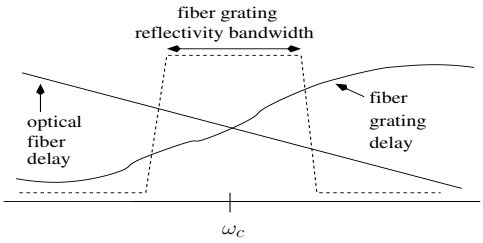

Figure 3.27: Optical delay of TLCG

dispersion manifests itself in the form of the various frequency components having different delays. This delay difference can be equalized by using the technique of Fig. 3.25 that relies on the Tapered Linearly Chirped Grating (TLCG)[1] optical filter [155], where the output of a laser operating at an optical frequency of $f_c = \frac{\omega_c}{2\pi}$ Hz is modulated using a RF signal and then transmitted over the fiber. At the receiver of Fig. 3.25, the optical signal enters port 1 and exits from port 2 of the OC. The signal then enters the TLCG and it is reflected back into port 2 of the OC. Finally, the signal exits from port 3 and then it is photo-detected. As seen from Fig. 3.27, within its reflectivity bandwidth[2] that is centered around the optical carrier of ω_c, the TLCG introduces an optical delay that is a near-linear function of the optical frequency. Thus, as seen from Fig. 3.27, the frequency-dependent dispersion-induced delay introduced by the optical fiber can be compensated by using a TLCG [155].

While this technique is potentially capable of compensating the effects of chromatic dispersion, it also requires an additional optical filter with a carefully designed optical delay profile. In the next section, we discuss a technique, namely the employement of chirped optical signals, that is easier to implement.

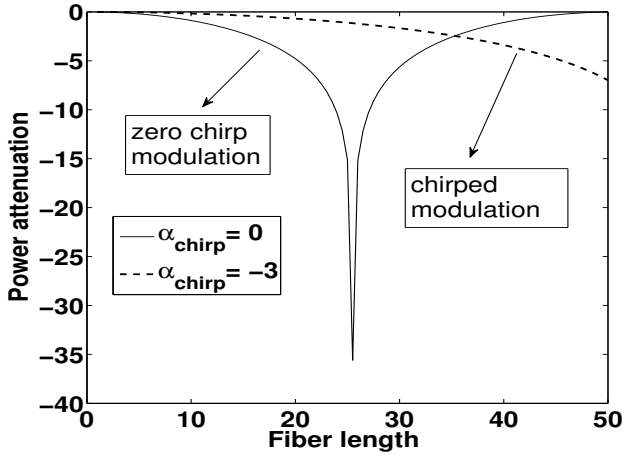

Figure 3.28: Power attenuation induced by chromatic dispersion [65]

[1]The linearly chirped FBG of Fig. 3.26, unlike the conventional FBG of Fig. 2.18(a), has a linear increase/decrease of the otherwise constant grating period. The TLCG consists of a linearly chirped fiber grating that is implemented in a tapered fiber.

[2]Band of frequencies pre-dominantly reflected by the optical filter.

Chirped optical signals The dispersion-induced power-reduction of ODSB signals was formulated in Equation (4.39), where it can be observed that the extent of power-reduction depends on both the magnitude and polarity of the chirp parameter α_{chirp} of the transmitted signals. Fortunately, the power-reduction could be lessened by introducing chirp in the transmitted signal, as shown in Fig. 3.28, while ensuring that this chirp has the reverse polarity with respect to the chirp induced by the chromatic dispersion [65]. It can be seen from Equation (2.6a) that the dual-drive MZM of Fig. 2.8(b) introduces an adjustable chirp, where the value of α_{chirp} depends on the amplitudes of both the drive voltages that are applied to the arms of the dual-drive MZM, i.e. on $V_1(t)$ and $V_2(t)$. As discussed in Section 2.1.1.2, zero-chirp operation is possible, if the dual-drive MZM of Fig. 2.8(b) operates in the push-pull mode. If $V_1(t)$ and $V_2(t)$ are sinusoidal signals associated with amplitudes of V_{RF1} and V_{RF2}, respectively, then we have [65]:

$$\begin{aligned}\alpha_{chirp} &= \frac{V_{RF1}+V_{RF2}}{V_{RF1}-V_{RF2}}\tan\left(\frac{\pi(V_{bias}-V_\pi)}{2V_\pi}\right)\\ &= \pm\frac{V_{RF1}+V_{RF2}}{V_{RF1}-V_{RF2}} \quad \text{(ODSB signal)},\end{aligned} \tag{3.21}$$

where $V_{bias} = \frac{(2n+1)V_\pi}{2}$ for ODSB modulation for $n = 0, 1, ...$ The dual-drive MZM typically has a non-ideal extinction ratio of $\gamma \neq 1$, where for the case of ODSB signal transmission we have $\alpha_{chirp} = \frac{V_{RF1}+\gamma^2 V_{RF2}}{\gamma(V_{RF1}-V_{RF2})}$ [67]. As discussed in Section 2.1.1.2, the ideal value of γ is 1. Fig. 3.28 compares the dispersion-induced power attenuation when using unchirped and chirped optical signals, where the dispersion-induced power attenuation is shown for the case of ODSB transmission, that employs an optical wavelength of 1550 nm, a sinusoidal RF modulating signal of 12 GHz and a fiber having a dispersion parameter of $D = 17ps/nm/km$ [65]. It can be seen from Fig. 3.28, that using negative values of α_{chirp} reduces the dispersion-induced power attenuation [65].

While the above techniques rely on a MZM for generating a chirp that compensates the dispersion-induced chirp, the technique discussed in the next section relies on the otherwise undesired effect of SPM for compensating the the dispersion-induced chirp.

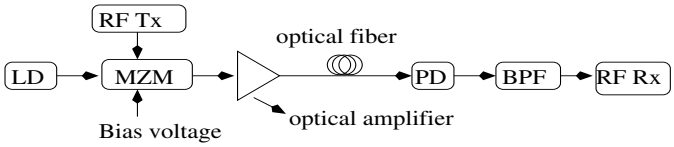

Figure 3.29: Chromatic dispersion compensation using SPM

Beneficial exploitation of self phase modulation As discussed in Section 2.1.1.3, SPM is imposed by the fiber's non-linearity and it becomes significant, when a high optical transmit-power is employed. This is the case in the architecture of Fig. 3.29 owing to inserting an optical amplifier in the transmitter. SPM introduces a chirp that has the opposite polarity to the chirp that is introduced by chromatic dispersion [156]. Thus, SPM can be employed for reducing the effects of chromatic dispersion [156], where the extent of SPM-induced chirp depends both on the optical power levels and on the fiber length. However, the technique of Fig. 3.29 may need the use of an additional optical equipment, namely an optical amplifier, which also adds ASE noise. The main limitation of this technique is the inevitable accompanying non-linear phenomenon of SBS, which was discussed in Section 2.1.1.3. Hence, the resultant SBS must be suppressed using other techniques. Additionally, the

high optical power levels used in this technique may result in fiber's non-linearity inducing significant inter-modulation in SCM systems and XPM in WDM systems.

We now continue our discourse on the family of techniques designed for overcoming chromatic dispersion by considering the optical phase conjugation technique that aims for eliminating the dispersion-induced phase-difference between the upper and lower sidebands in the ODSB signal of Fig. 2.16(a).

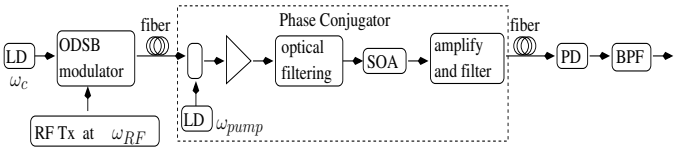

Figure 3.30: Chromatic dispersion compensation using Optical Phase Conjugation

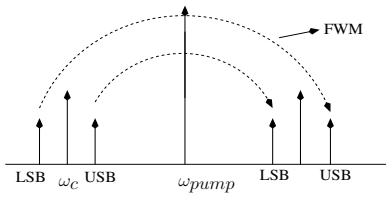

Figure 3.31: Optical phase conjugation using FWM

Optical phase conjugation An ODSB signal suffers from the dispersion-induced power-reduction imposed by the phase-difference between the upper and lower sidebands. This power-penalty can be avoided by swapping the two sidebands midway through the fiber-length [157]. This would ensure a similar dispersion-induced phase-shift in both the upper and the lower sidebands, which eliminates the detrimental phase-difference. This technique is referred to as Optical Phase Conjugation (OPC). Fig. 3.30 shows the block diagram of optical phase conjugation, where an ODSB signal is generated by modulating an optical carrier at ω_c using a RF signal at ω_{RF}. The ODSB signal consists of the optical carrier along with lower and upper sidebands at $\omega_c - \omega_{RF}$ and $\omega_c + \omega_{RF}$, respectively. The signal enters the phase conjugator of Fig. 3.30 after propagating half-way through the fiber length. As shown within the phase conjugator of Fig. 3.30, a high-power optical carrier at ω_{pump}, that is referred to as the pump signal, is coupled with the optical signal being transmitted. This combined signal is optically amplified, followed by optical filtering to remove the optical amplifier's out-of-band ASE noise discussed in Section 2.1.1.5 and it then enters a Semiconductor Optical Amplifier (SOA). The FWM process originally introduced in Section 2.1.1.3, that occurs within the SOA between the pump signal ω_{pump} and the modulated signal, generates an additional signal as per Equations (2.24) and (2.25) [157], where the signal-spectrum at the output of the conjugator is shown in Fig. 3.31. It should be noted that the wavelength-conversion efficiency is polarization sensitive and hence the modulated signal and pump signal must be polarization matched using a polarization controller, prior to their coupling. It can be seen from Fig. 3.31 that the lower sideband of the original signal corresponds to the upper sideband in the new signal and vice-versa. The resultant optical signal is then filtered, amplified and transmitted over the remaining half of the fiber link. Additionally, the effect of SPM, originally introduced in Section 2.1.1.3, is partially compensated by OPC [157]. Naturally, perfect compensation of the power-dependent SPM would have been possible only if the power variation

along the fiber length was perfectly symmetric with respect to the position of the phase conjugator [157]. However in reality, the optical power gradually reduces as the signal propagates through both the fiber segments in Fig. 3.30.

We now conclude our discussions on the family of techniques conceived for overcoming chromatic dispersion and move on to the next performance improvement technique, namely Digitized Radio Over Fiber (DROF). The digital optical link used in long-distance wired optical communication provides a better performance than the ROF link of Fig. 2.1. Hence, DROF aims for incorporating the advantages of a digital optical link in ROF communication.

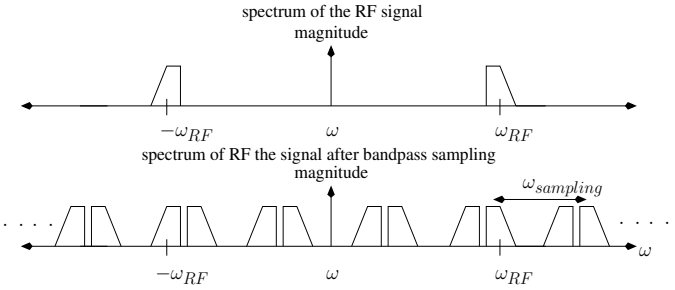

Figure 3.32: Bandpass sampling

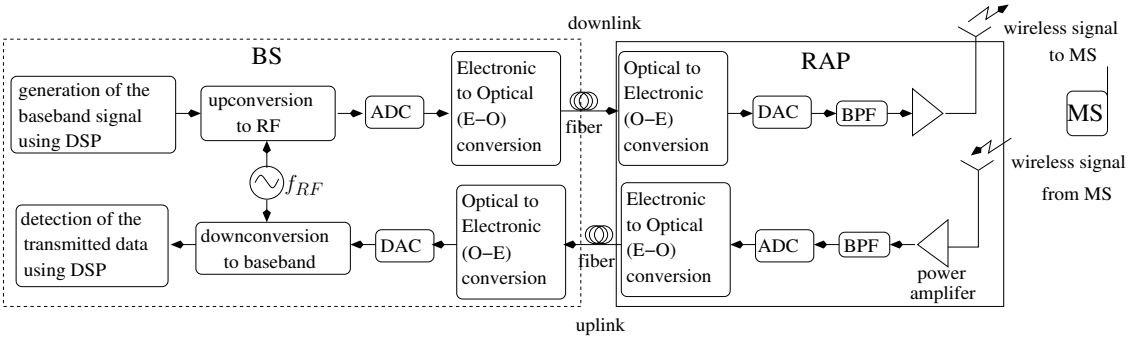

Figure 3.33: DROF link block diagram

3.1.12 Digitized radio over fiber architecture

All the ROF architectures discussed so far modulate the analog RF signal onto the optical carrier, as seen from Fig. 2.1, which, for the sake of contrast, we refer to as AROF. By contrast, in Digitized ROF (DROF), the RF signal is sampled, digitized and then is used for modulating the optical carrier. The main motivation behind the design of the DROF architecture is the desire to have a digital optical link and at the same time rely on centralised signal processing at the BS [46]. In the DROF architecture of Fig. 3.33, the signal processing required for generating the DL RF signal is carried out at the BS, where the RF signal is digitized before modulating the optical carrier [46]. Conventional sampling of the RF signal at a rate higher than twice the highest frequency present in the signal using the Nyquist Theorem is not practically feasible, because of the high values of the wireless carrier frequency. Hence, typically critical bandpass sampling is used [46], which is illustrated in Fig. 3.32, where the sampling frequency is chosen to satisfy the aliasing-free condition, so that the original analog RF signal can be

reconstructed by using a bandpass filter centered at $f_{RF} = \frac{\omega_{RF}}{2\pi}$ Hz and having a bandwidth of B_{RF} Hz. The valid bandpass sampling rates for a bandwidth of B are [46]:

$$\frac{2(f_{RF} + \frac{B_{RF}}{2})}{k} \leq f_s \leq \frac{2(f_{RF} - \frac{B_{RF}}{2})}{k-1} \; \forall \; 1 \leq k \leq \lfloor \frac{f_{RF} + \frac{B_{RF}}{2}}{B_{RF}} \rfloor, \tag{3.22}$$

where $\lfloor w \rfloor$ represents the integer part of w and k is an integer. Thus, when employing bandpass sampling, the sampling rate depends on the bandwidth of the signal, rather than, on the highest frequency present in the signal [46].

Fig. 3.33 illustrates the block diagram of a DROF architecture [46], where the DL BB signal is generated, up-converted and digitized using an Analog to Digital Converter (ADC) at the BS. The digitized signal is then employed in modulating the optical carrier. At the RAP, the photo-detected BB signal is fed to a Digital to Analog Converter (DAC) and the RF signal is reconstructed. The reconstructed RF signal is then amplified using a power amplifier and transmitted over the wireless channel. As shown in Fig. 3.33, the UL signal received at the RAP is amplified, bandpass filtered, digitized and employed for modulating the optical carrier. At the BS, the photo-detected signal is fed to a DAC, followed by down-conversion to a BB signal. The transmitted UL bits are then detected from the BB signal, by employing DSP techniques [46].

The advantage of employing optical BB modulation is that one can use inexpensive direct modulation [46] or an external modulator having a low-modulation bandwidth [160]. Furthermore, typically a performance improvement is achieved by employing a digital optical link. Employing a DROF architecture, that involves the transmission of optical signals carrying BB digital data, has a high degree of tolerance to the previously mentioned dispersion-induced power-penalty [2] and also ensures a higher degree of linearity of the optical-link. Hence, DROF provides a better performance than the conventional ROF architecture of Fig. 2.1 [46], [159]. However, the trade-off in this case is the need for using ADCs and DACs and hence DROF has a more complex and costly RAP than the conventional ROF link of Fig. 2.1. Furthermore, BB optical modulation is also employed in fiber-based wired optical communication and has been extensively dealt with in various tutorials [161] and books [31].

We now conclude our discussions on the performance improvement techniques designed for ROF communications by referring back to Fig 3.1 and Fig. 3.2. It becomes plausible from our discussions on the performance improvement techniques that while the designer has access to the plethora of techniques listed in Fig. 3.2 to choose from, there is also a cost to be paid, as seen from Fig 3.1. The higher the implementation al cost and complexity of the technique, the better the performance improvement is expected to be. Hence, we complete our discourse with a discussion of the various cost-reduction techniques designed for ROF communications, as listed in Fig. 3.2.

3.2 Cost reduction techniques

The various cost reduction techniques proposed for ROF communications, as seen from Fig. 3.2, include the family of techniques designed for integrating ROF communication with the existing Fiber To The Home (FTTH) optical networks, the family of techniques conceived for implementing wavelength reuse and the set of techniques proposed for reducing the number of lasers, which will be discussed in Sections 3.2.1, 3.2.2 and 3.2.3, respectively.

Table 3.4: ROF Cost Reduction Techniques (Part 1)

Technique	Year	Authors	Contribution
Integration with existing Fiber To The Home networks	1997	Blumenthal *et al.* [162]	Simultaneous optical modulation of a 2.5 Gbps BB signal and a 100 Mbps, 5.5 GHz RF signal on a single optical carrier was implemented using a MZM
	2001	Kamisaka *et al.* [163]	Simultaneous optical modulation of a 10 Gbps BB signal and a 155 Mbps, 60 GHz RF signal on a single optical carrier was done using an Electro-Absorption Modulator.
	2007	Jia *et al.* [47]	Simultaneous optical modulation of a 10 Gbps BB signal and a 2.5 Gbps, 20/30 GHz signal on a single optical carrier was implemented using a MZM and an interleaver. Frequency doubling generated a 40/60 GHz RF signal at the optical receiver.
	2007	Jia *et al.* [164]	Designed a testbed for simultaneous delivery of wired and wireless data using a single optical carrier in a 2-step optical BB and RF modulation.
	2007	Lin *et al.* [165]	Simultaneous optical modulation of a 1.25 Gbps BB signal and a 622 Mbps, 10 GHz RF signal on a single optical carrier was implemented using a nested-MZM. Frequency doubling ensured the generation of a 20 GHz RF signal at the optical receiver.
	2008	Llorente *et al.* [16]	Proposed the distribution of high-definition audio/video content by transmitting Ultra Wide Band (UWB) RF signals over FTTH networks. A BER below 10^{-9} was achieved when transmitting 1.25 Gbps UWB RF signals over 50 kms of fiber.

3.2.1 Integration with existing fiber-to-the-home optical networks

The penetration of the optical fiber to the end user is increasing at a rapid rate, because the telecommunication service providers are attempting to support increased wired data rates for their customers. These networks are referred to as *FTTH* networks. It should be noted here that wired signals in this report refer to the fiber signals for stationary devices like personal-computers, while wireless signals refers to the signals for mobile devices. The wired signal that is carried by the FTTH networks is of BB nature, while the ROF signal is of RF nature. Hence, transmitting the ROF signals over both the existing FTTH networks [16] and indoor optical networks [17] would result in significant cost advantages and in efficiently exploiting the bandwidth of the existing fibers. This kind of integration can be achieved in the following ways:

1. Employing separate optical carriers for optical BB and optical RF modulation [166];
2. Employing a single optical carrier for two-step optical BB and optical RF modulation;
3. Employing a single optical carrier for simultaneous optical BB and optical RF modulation.

Note that the terms optical BB modulation and optical RF modulation in this report refer to the modulation of electronic BB and electronic RF signals onto the optical carrier, respectively.

3.2.1.1 Employing separate optical carriers for optical baseband and optical RF modulation

Separate optical carriers can be employed at the BS for transmitting the BB wired signal and the ROF wireless signal. As shown in Fig. 3.34, lasers operating at optical frequencies of $f_{baseband} = \frac{\omega_{baseband}}{2\pi}$ Hz and $f_{ROF} = \frac{\omega_{ROF}}{2\pi}$ Hz are modulated by the BB wired signal and the RF wireless signal, respectively. These two signals are then multiplexed for generating a signal, whose spectrum is shown in Fig. 3.34.

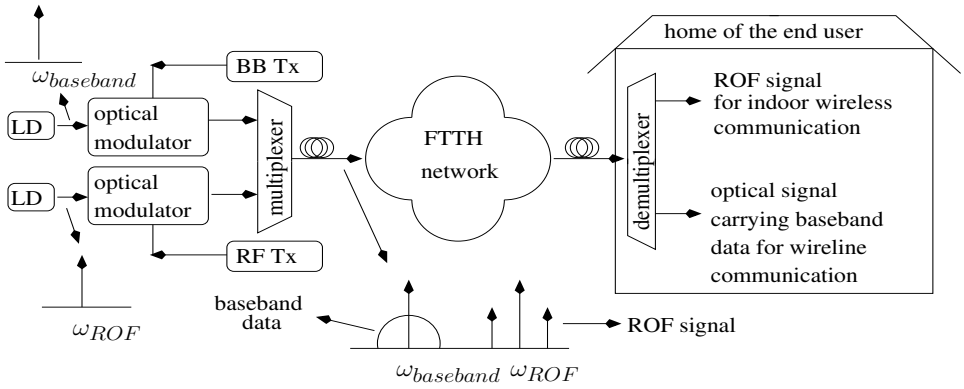

Figure 3.34: Using separate optical carriers for optical baseband and optical RF modulation

As shown in Fig. 3.34, the multiplexed signal is transported over the FTTH network to the home of the end user, where it is demultiplexed. The optical signal carrying the BB data directly supports the wired devices, while the ROF signal is fed to a RAP that supports indoor wireless communication [16]. In this case the BS would be several kilometers away from the customer premises. In the case of larger houses/buildings the demultiplexed ROF signal would enter an in-building optical network that supports several RAPs [49].

We now move on to the next member in the family of techniques for integrating ROF communication with the existing FTTH networks, which, unlike the above technique, relies on a single optical carrier.

3.2.1.2 Employing a single optical carrier for two-step optical baseband and RF modulation

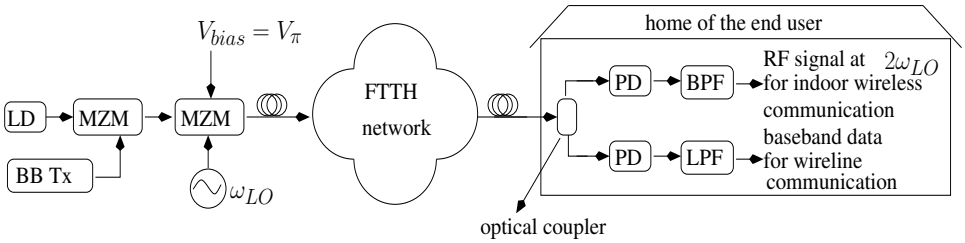

Figure 3.35: Employing a single optical carrier for two-step optical baseband and RF modulation

Instead of using separate optical carriers, the wired BB data and the wireless RF signal may be modulated onto the same optical carrier at the BS in two modulation steps and then transmitted to the RAP. Fig. 3.35 shows the block digram of a 2-step modulation for integrating ROF and FTTH transmission [164]. Observe in Fig. 3.35 that the output of the laser operating at an optical power of P_{in} is BB modulated by the bit stream $b(t)$ using an MZM having a switching voltage of V_π. Then, the BB modulated optical signal power P_{BB} is:

$$P_{BB} = P_{in}\left[1 - \cos(\frac{\pi b(t)}{V_\pi})\right], \tag{3.23}$$

where we have $b(t) = 0$ and $b(t) = V_\pi$ for bits '0' and '1', respectively. As shown in Fig. 3.35, the output of the BB modulation step is then OCS modulated using a RF tone $V_{LO}\cos(\omega_{LO}t)$ that drives a MITP biased MZM to generate a signal, whose optical power P_{total} is:

$$\begin{aligned} P_{total} &= P_{BB}\left[1-\cos(\frac{\pi V_{LO}\cos(\omega_{LO}t)}{V_\pi})\right] \\ &= P_{BB}\Bigg[1-J_0(\frac{\pi V_{LO}}{V_\pi}) \\ &\quad -2\sum_{n=1}^{\infty}(-1)^n J_{2n}(\frac{\pi V_{LO}}{V_\pi})\cos(2n\omega_{LO}t)\Bigg]. \end{aligned} \tag{3.24}$$

Then, as shown in Fig. 3.35, the signal is transmitted through the FTTH network and then fed to an optical coupler that splits the optical signal into two parts. The lower-branch is photo-detected using a low-bandwidth photo-detector for recovering the BB wired signal represented by $P_{BB}\left[1-J_0(\frac{\pi V_{LO}}{V_\pi})\right]$ in Equation (3.24), while upper-branch of the coupler is photo-detected using a high-bandwidth photo-detector to recover a RF signal represented by $2P_{BB}J_2(\frac{\pi V_{LO}}{V_\pi})\cos(2\omega_{LO}t)$ in Equation (3.24)[164].

We now continue our discourse on the family of techniques designed for integrating ROF communication with the existing FTTH networks by considering simultaneous optical baseband and optical RF modulation.

3.2.1.3 Simultaneous optical baseband and optical RF modulation

Instead of using the two-step modulation of Fig. 3.35, the wired BB data and the wireless RF signal could be simultaneously modulated onto the same optical carrier at the BS and then transmitted to the customer premises. This can be achieved using several techniques, including the use of the conventional external modulator (i.e. MZM and EAM) and of the sophisticated nested-external modulators.

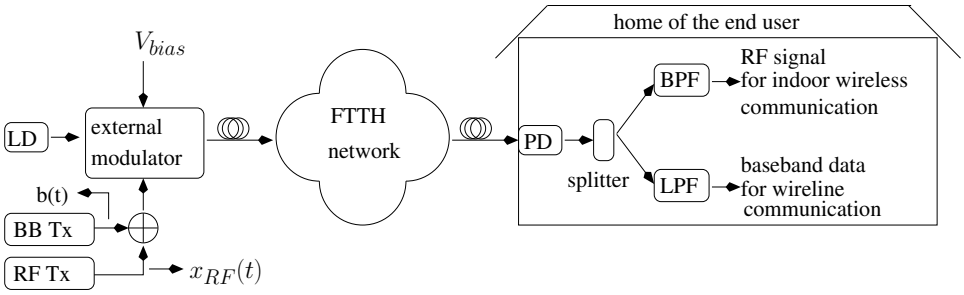

Figure 3.36: Simultaneous optical baseband and optical RF modulation using an external modulator

Simultaneous optical baseband and optical RF modulation relying on an external modulator Simultaneous modulation can be achieved using the MZM of Fig. 5.11 or the EAM of Fig. 2.10(a), where the architecture that achieves simultaneous optical baseband and RF modulation using an external modulator is shown in Fig. 3.36. Observe in Fig. 3.36 that the output of the laser is modulated by a MZM that is biased at $V_{bias} = -V_\pi/2$ and driven by a combination of the BB wired data $b(t)$ and the wireless RF signal $V(t)$. Subsequently, the modulated signal is transmitted from

the BS to the end user over the FTTH network, where it is photo-detected and filtered to separate the BB wired and RF wireless data. Using Equations (2.3b) or (2.6d), the photo-detected signal $I_{PD}(t) \propto P_{out}(t) = P_{in}[1 + \sin(\frac{\pi(b(t)+V(t))}{V_\pi})]$, which can be expanded using Taylor series [162] to:

$$\frac{P_{out}(t)}{P_{in}} = 1 + \sin(\frac{\pi b(t)}{V_\pi}) + \cos(\frac{\pi b(t)}{V_\pi})\frac{\pi V(t)}{V_\pi} - \frac{1}{2}\sin(\frac{\pi b(t)}{V_\pi})\frac{\pi^2 V^2(t)}{V_\pi^2} - \frac{1}{6}\cos(\frac{\pi b(t)}{V_\pi})\frac{\pi^3 V^3(t)}{V_\pi^3}..., \tag{3.25}$$

where,

$$b(t) = \begin{cases} V_b \text{ for bit '1'} \\ -V_b \text{ for bit '0'} \end{cases}$$

In Equation (3.25), the first two terms contain the desired BB signal, i.e. $P_{BB}(t) = 1 + \sin(\frac{\pi b(t)}{V_\pi})$ and the third term has the desired RF signal, $P_{RF}(t) = \cos(\frac{\pi b(t)}{V_\pi})\frac{\pi V(t)}{V_\pi}$, while the higher order terms produce intermodulation distortion both at the BB and RF frequencies. $\cos(\frac{\pi b(t)}{V_\pi})$ is the same for both values of $b(t)$, which implies that the desired RF signal in the third term of Equation (3.25) is not corrupted by the BB signal [162]. However, the BB transmission affects the power of the photo-detected RF signal. For the case of pure optical RF modulation, i.e. when $b(t) = 0$, the power in the desired third term of Equation (3.25) would be maximised, because we have $|\cos(\frac{\pi b(t)}{V_\pi})| = 1$, while for simultaneous optical modulation we have $|\cos(\frac{\pi b(t)}{V_\pi})| < 1$, because $b(t) \neq 0$. The performance of BB modulation is improved by using a larger difference between the optical power $P_{BB}(t)$ transmitted for bit '0' and bit '1'. This can be achieved by increasing the amplitude V_b of $b(t)$, which, however, reduces the value of $|\cos(\frac{\pi b(t)}{V_\pi})|$ and hence reduces $P_{RF}(t)$. Hence, the power in the detected RF signal is reduced when simultaneous optical BB and RF modulation is employed. For the case of pure optical BB modulation, i.e for $V(t) = 0$ in Equation (3.25), we would have chosen $V_b = V_\pi/2$ to ensure that the MZM is operating at its minimum and maximum $P_{BB}(t)$ for the bits '0' and '1', respectively. However, for the scenario that involves simultaneous BB and RF modulation, it is evident from Equation (3.25) that choosing $V_b = V_\pi/2$ would result in the desired third term $P_{RF}(t)$ going to zero, i.e. no RF transmission would occur. Thus, the BB optical modulation has to be carried out using non-optimum values of $P_{BB}(t)$ [162].

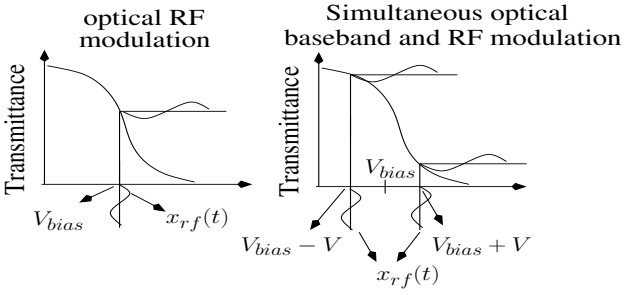

Figure 3.37: Optical modulation using the EAM

Additionally, the architecture of Fig. 3.36 can be implemented using the EAM of Fig. 2.10(a), where the condition of avoiding over modulation imposes an upper limit on the total drive voltage that can be applied to the EAM [163]. The BB signal $b(t)$ is combined with the RF signal $V(t)$ and

the combined signal is then added to the bias voltage V_{bias} to generate the drive voltage, which is applied to the EAM. In this scenario, the output intensity that would be photo-detected is [163]:

$$I_{PD}(t) \propto P(t) \propto T^2(V_{bias} + b(t) + V(t)), \tag{3.26}$$

where $T(v)$ is the transmittance of the EAM described in Section 2.1.1.2. Expanding Equation (3.26) using Taylor series we get:

$$\begin{aligned} I_{PD}(t) &\propto T^2(V_{bias} + b(t)) \\ &+ 2T(V_{bias} + b(t)) \left[\frac{d(T(v))}{dv}\right]_{v=V_{bias}+b(t)} V(t) + ... \end{aligned} \tag{3.27}$$

In Equation (3.27), the first term contains the desired BB signal, while the second term has the desired RF signal [163]. The higher order terms would produce intermodulation distortion at both the BB and RF frequencies. The BB signal is represented by $b(t) = V_b$ for bit '1' and $b(t) = -V_b$ for bit '0'. For the case of pure optical RF modulation, i.e. for $b(t) = 0$, the power in the desired second term would be maximised because the slope of the transmission curve, i.e. $\left[\frac{d(T(v))}{dv}\right]$, is maximised at $V = V_{bias}$, which is evident in Fig. 3.37. However, for simultaneous optical modulation, the slopes at $V = V_{bias} \pm V_b$ become lower than that at $V = V_{bias}$, as seen from Fig. 3.37 and hence the photo-detected RF signal power drops [163]. The performance of BB modulation is improved by using a larger difference in the optical power transmitted for bits '0' and '1', which can be arranged by increasing the amplitude V of $b(t)$. However, this reduces the slope values at $V = V_{bias} \pm V_b$. Thus, BB modulation has to be carried out using non-optimum values in the EAM transmission curve of Fig. 3.37.

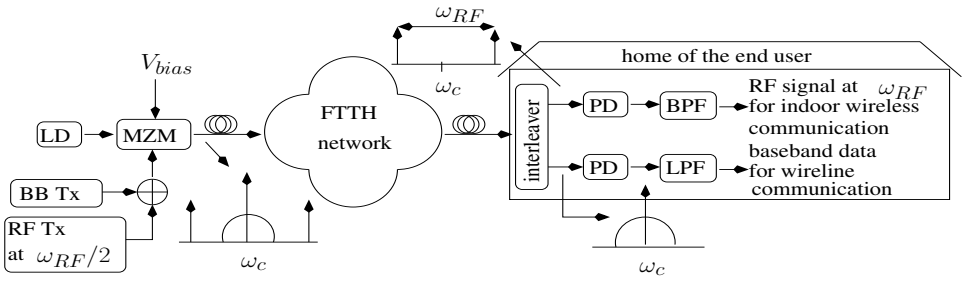

Figure 3.38: Simultaneous optical baseband and optical frequency-doubled RF modulation

In addition to the architecture of Fig. 3.36, the system shown in Fig. 3.38 also employs simultaneous optical BB and RF modulation with the additional advantage of being able to achieve frequency-doubling. Frequency-doubling helps generate high RF signals using lower electronic oscillator frequencies and optical modulators of lower electronic bandwidth. ROF transmission that implements frequency-doubling can be carried out along with simultaneous BB transmission, by using an interleaver [47]. In the architecture in Fig. 3.38, the output of the laser, operating at an optical frequency of $f_c = \frac{\omega_c}{2\pi}$ Hz, is modulated using a MZM that is driven by a combination of the wireless RF signal at $\omega_{RF}/2$ and the wired BB signal. As shown in Fig. 3.38 [47], the modulated BB data is present at the optical carrier ω_c, while the RF data is carried by the two first-order optical sidebands at $\omega_c \pm \omega_{RF}/2$. After transmission from the BS through the FTTH network, these optical sidebands are separated from the signal at the optical carrier frequency, by using an optical interleaver in the

end user's home. Subsequently, as shown in Fig. 3.38, the sidebands are photo-detected to generate a frequency-doubled wireless RF signal at ω_{RF}, while the signal at the optical carrier frequency is photo-detected to retrieve the BB wired signal [47], [167].

It may be concluded that the cost of carrying out simultaneous optical BB and optical RF modulation, as opposed to separate modulations, is that of striking a performance trade-off. Explicitly, the amplitudes of $b(t)$ and $V(t)$ in Fig. 3.36 have to be chosen in such a way that the required Quality of Service (QoS) can be achieved for both the BB and RF transmission [163]. A similar trade-off exists for the case of simultaneous modulation using a tri-band signal consisting of two RF signals at microwave and millimeter-wave frequencies along with a BB signal [69]. The stringency of this trade-off can be relaxed to some extent by using the more sophisticated nested-external modulator, as detailed in the next section.

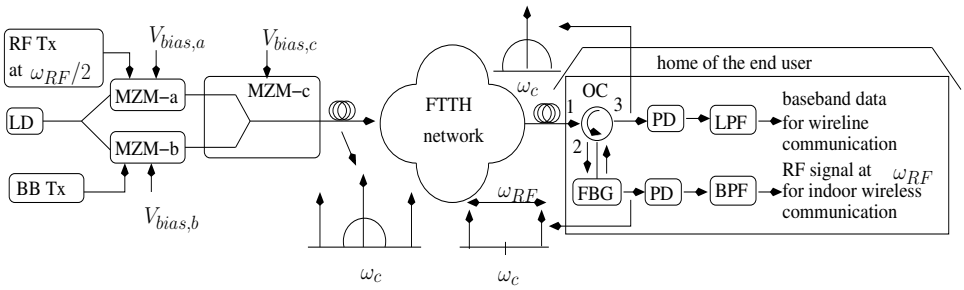

Figure 3.39: Simultaneous optical baseband and optical frequency-doubled RF modulation using nested MZM

Simultaneous modulation relying on a nested-external modulator Simultaneous optical BB and optical RF modulation may also be implemented using the architecture of Fig. 3.39. that uses a nested-MZM instead of the conventional MZM, where the output of the laser diode operating at $f_c = \frac{\omega_c}{2\pi}$ Hz is split into two branches, which then modulate a nested MZM consisting of three MZMs referred to as MZM-a, MZM-b and MZM-c in Fig. 3.39. Specifically, MZM-a of Fig. 3.39 is biased at MITP and it is driven by the RF signal at a frequency of $f_{RF}/2 = \frac{\omega_{RF}/2}{2\pi}$ Hz to achieve OCS modulation. On the other hand, OOK [161] optical BB modulation may be implemented using MZM-b, while MZM-c is biased at the MATP [165]. As seen in Fig. 3.39, the spectrum of the optical signal at the output of the nested MZM consists of the modulated BB data present at the optical carrier ω_c, while the RF data is carried by the two first-order optical sidebands at $\omega_c \pm \omega_{RF}/2$ [165]. After transmission from the BS to the customer premises through the FTTH network, the signal enters port 1 of the OC shown in Fig. 3.39 and exits from port 2, where the FBG filter of Fig. 2.18(a) reflects the signal at ω_c but lets the sidebands pass through. Subsequently, as shown in Fig. 3.39, the sidebands are photo-detected to generate a frequency-doubled wireless RF signal at $f_{RF} = \frac{\omega_{RF}}{2\pi}$ Hz, while the reflected optical signal enters port 2 and exits from port 3 of the OC in Fig. 3.39. This optical signal is then photodetected to retrieve the BB wired signal. The major advantage of this technique is that the two modulation schemes can be independently optimised [165]. However, for a fixed total optical power received at the photo-diode, increasing the modulation depth of one of the schemes increases its modulated optical power and hence improves this scheme's performance, while degrading the other scheme's performance [165].

We conclude our discussions on the family of techniques proposed for integrating ROF communi-

cation with existing FTTH networks by stating that they rely on infrastructure sharing to implement multiplexed optical communication. On the other hand, the techniques discussed in the next section, namely the family of techniques designed for wavelength reuse, relies on infrastructure sharing to implement duplexed optical communication.

Table 3.5: ROF Cost Reduction Techniques (Part 2)

Technique	Year	Authors	Contribution
Wavelength Re-use	1994	Wu *et al.* [168]	Introduced the concept of wavelength re-use by proposing the ORM arcitecture of Fig. 3.45.
	1998	Wu *et al.* [107]	
	1996	Welstand *et al.* [169]	The bias voltage was switched to obtain half-duplex operation when using a modulator-cum-photodetector, as shown in Fig. 3.49.
	1996	Westbrook *et al.* [170]	A single bias voltage was employed by the modulator-cum-photodetector, as shown in Fig. 3.50, at the cost of a DL versus UL performance trade-off.
	1997	Noel *et al.* [70]	
	1997	Wake *et al.* [171]	
	1999	Stohr *et al.* [71]	A pair of lasers were used at the BS along with a modulator-cum-photodetector at the RAP, as shown in Fig. 3.51, to implement wavelength re-use.
	2000	Kitayama *et al.* [32]	
	2001	Nirmalathas *et al.* [172]	Presented the OCRR techniques of Fig. 3.40 & Fig. 3.41.
	2003	Kuri *et al.*[173]	Employed the ORM architecture of Fig. 3.44, that relied on EAM-assisted intensity modulation in the DL as well as the UL.
	2005	Bakaul *et al.* [174]	Presented the OCRR technique of Fig. 3.43, which enables the implementation of OCRR in Wavelength-Interleaved Wavelength Division Multiplexing (WI-WDM) signals.
	2006	Kaszubowska *et al.* [175]	The OCRR technique of Fig. 3.41 was employed for remote delivery of the RF tone from the BS to the RAP.
	2006	Jia *et al.* [48]	The OCRR technique of Fig. 3.41 helped generate a frequency doubled RF signal.
	2006	Chen *et al.* [176]	The OCRR technique of Fig. 3.42 was employed in congugation with DL frequency doubling.
	2007	Yu *et al.* [177]	
	2007	Won *et al.* [178]	Implemented the ORM technique of Fig. 3.47 by using a gain saturated RSOA
	2008	Huang *et al.* [179]	The OCRR technique of Fig. 3.42 was employed in conjugation with DL frequency quadrupling.
	2008	Yu *et al.* [180]	Implemented ORM by employing optical phase modulation in the DL, while employing optical intensity modulation in the UL.
	2009	Ji *et al.* [181]	
	2013	Thomas *et al.* [2]	Implemented wavelength re-use by incorporating the performance improving Digitized ROF (DROF) technique in the UL of Fig. 3.45.

3.2.2 Wavelength re-use

Wavelength re-use is an optical duplexing technique, where UL communication is achieved by re-using the DL optical signal at the RAP. This leads to significant cost advantages, because the RAPs do not need to have their own optical sources, when wavelength re-use is employed. However, allocating a portion of the DL optical power to UL communication results in the degradation of the DL performance. The various ways of achieving wavelength re-use include Optical Carrier Recovery and Re-use (OCRR), Optical Re-Modulation (ORM) and employing a modulator-cum-photo-detector, which will be discussed in Sections 3.2.2.1, 3.2.2.2 and 3.2.2.3, respectively.

3.2.2.1 Optical carrier recovery and re-use

The techniques that involve the separation of the total or a fraction of the DL optical carrier power from the DL sidebands, for its reuse in UL communication, are referred to as Optical Carrier Recovery

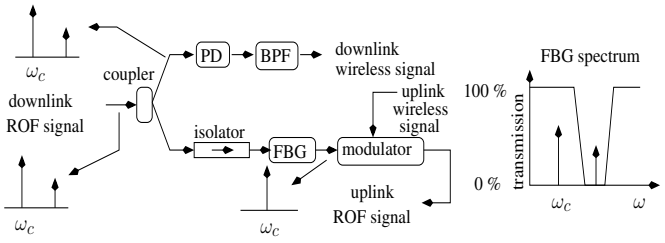

Figure 3.40: OCRR in the RAP employing an optical coupler and FBG

and Re-use (OCRR) techniques.

In the RAP of Fig. 3.40 [172], the DL OSSB signal power is split using an optical coupler, where the signal of the upper branch is photo-detected, while the lower branch-signal is fed to a FBG filter, whose transmission spectrum is also shown in Fig. 3.40. The FBG passes the optical carrier but reflects 100% of the sideband power. An isolator is incorporated at the input of the FBG filter to prevent the back propagation of the reflected sideband. The separated optical carrier that becomes available at the output of the FBG filter is then modulated by the UL RF signal and transmitted from the RAP to the BS over the fiber [172], hence achieving wavelength re-use.

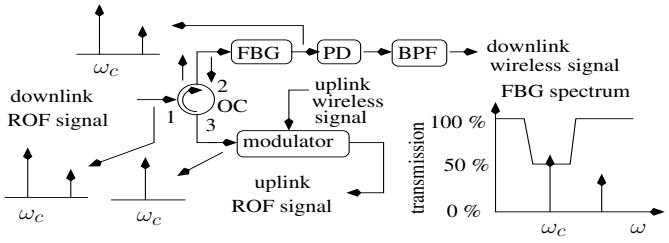

Figure 3.41: OCRR in the RAP using an OC and FBG

In the RAP of Fig. 3.41 [172], [175], the DL OSSB signal enters port 1 of the OC and exits from port 2, where a FBG filter, whose spectrum is also shown in Fig. 3.41, reflects 50% of the optical carrier's power. The remaining 50 % of the optical carrier's power along with 100% of the modulation sideband power propagates through the FBG filter and then it is photo-detected for generating the DL wireless signal. The reflected 50% of the optical carrier power enters the OC from port 2, exits from port 3 and then it is employed for optical UL modulation. For the case of an ODSB DL signal, the FBG filter of Fig. 3.41 can be designed for reflecting 100% of the optical carrier power, while the pair of sidebands propagate through the filter and are photo-detected for generating a frequency-doubled DL RF signal [48].

OCRR can also be achieved by employing an optical interleaver at the RAP[176]. As shown in the RAP of Fig. 3.42, the DL ODSB signal is fed to an interleaver that separates the optical carrier at ω_c Hz from the pair of first-order sidebands at $\omega_c \pm \omega_{RF}/2$, where $f_{RF}/2 = \frac{\omega_{RF}/2}{2\pi}$ is the frequency of the RF signal generated in the BS. The optical sidebands are then photo-detected to generate a frequency-doubled signal at f_{RF} Hz [176] [176], [177]. As shown in Fig. 3.42, the separated optical carrier of the lower branch can then be employed for wavelength re-use. If second-order optical sidebands at $\omega_c \pm \omega_{RF}$ are generated instead of the first-order ones, for example by using a MATP biased MZM at the BS, then, in the RAP, their separation from the optical carrier followed by the subsequent

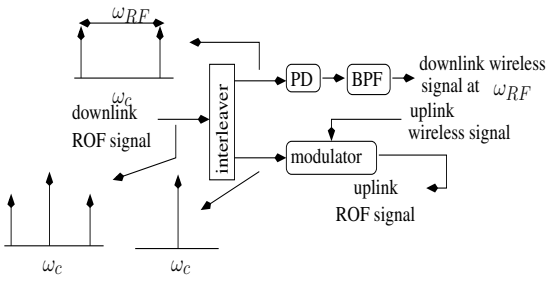

Figure 3.42: OCRR in the RAP using an interleaver

photo-detection yields a frequency-quadrapled signal [179].

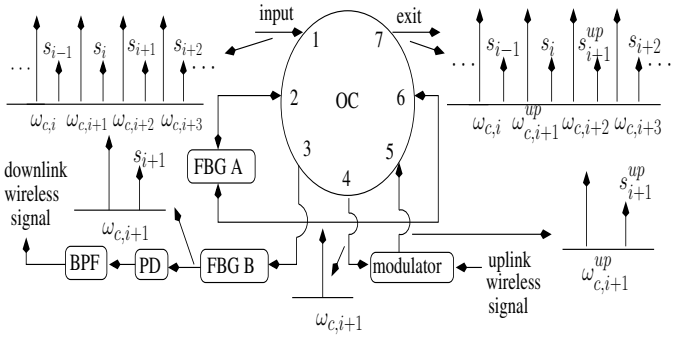

Figure 3.43: OCRR in the RAP of a ROF system employing WI-WDM signals

As mentioned previously in Section 3.1.1, a commonly employed WDM ROF signal is the WI-DWDM signal of Fig. 3.3. The architecture of Fig. 3.43 [174] may also be employed to implement wavelength re-use in the RAP of a ROF system employing WI-WDM signals, where again, the input DL WI-DWDM spectrum shown in Fig. 3.43 was discussed in Section 3.1.1. The WI-DWDM signal enters port 1 of the OC and exits from port 2. The channel that is to be dropped at the RAP is $\{\omega_{c,i+1}, s_{i+1}\}$. Hence, as shown in Fig. 3.43, the signal exiting port 2 is passed through the filter FBG A, that reflects both the optical carrier $\omega_{c,i+1}$ and the corresponding sideband s_{i+1}, which therefore may be referred to as a double-notch filter. The rest of the WDM signal is fed into port 6 and it finally leaves from port 7. Both the optical carrier $\omega_{c,i+1}$ and the sideband s_{i+1}, that were reflected by FBG A, enters port 2 and exits from port 3, where it encounters the second filter FBG B, as shown in Fig. 3.43. The FBG B filter is a notch-filter that reflects 50% of the optical carrier $\omega_{c,i+1}$. The remaining 50% of the optical carrier power and 100% of the sideband power is passed through and employed in DL photo-detection [174]. The reflected 50% of the optical carrier power re-enters port 3 and leaves from port 4, where is it employed in UL modulation. As shown in Fig. 3.43, the UL signal enters port 5 and exits via port 6, where it encounters FBG A, that has been designed to reflect both the optical carrier at $\omega_{c,i+1}$ and the corresponding sideband. Hence, the UL signal is reflected by FBG A, enters port 6 of the OC and exits via port 7. Thus, the optical signal exiting port 7 consists of the UL signal at $\omega_{c,i+1}$ and s_{i+1}, instead of the DL signal at that frequency [174]. It also contains the other carriers and sidebands of the input WI-DWDM signal.

The advantage of the design of Fig. 3.40 is its simplicity [172]. However, it wastes 50% of the modulated sideband power. This disadvantage is circumvented by the design of Fig. 3.41 [172], which

can also be extended to the SCM transmission regime of Fig. 2.22, regardless of the number of RF signals involved, since the FBG filter of Fig. 3.41 only has to reflect the optical carrier from the spectrum of Fig. 2.22. However, this design requires an OC, which is more complex and hence more expensive than an optical coupler. The design of Fig. 3.43 can be simultaneously used as an OADM and a wavelength re-use module in a bus- or ring-based ROF network. Again, the disadvantage of this design is its complexity. A common design challenge in the architectures of Figures 3.41 and 3.43 is the fact that the imperfect isolation of the OC ports and variations in the transmittance-reflectance characteristics of the temperature-sensitive FBG filters result in cross-talk between the DL and UL signals [174]. The design of Fig. 3.42 employs an optical interleaver, which is not as sensitive to temperature variations as a FBG filter [87]. However, in the design of Fig. 3.42, the weaker second-order optical sidebands at $\omega_c \pm \omega_{RF}$ have to be filtered out at the BS, otherwise they will be passed along with the separated optical carrier. This occurs because the transfer function of the interleaver consists of alternating passbands and stopbands.

Let us now continue our discussions on the the family of techniques invented for wavelength-reuse by considering the arrangements that implement ORM, which, unlike the above OCRR techniques, do not entail the separation of the optical carrier from its sidebands using high-selectivity optical filtering, but involve other constraints.

3.2.2.2 Optical re-modulation

In Optical Re-Modulation (ORM), the DL optical signal is remodulated by the UL data at the RAP, without relying on filtering for recovering the optical carrier. This can be achieved in a number of ways, as described below.

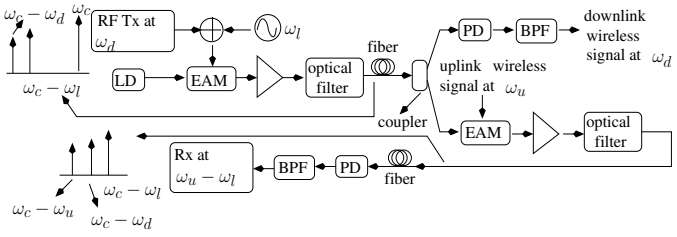

Figure 3.44: ORM using an Electro-Absorption Modulator

Fig. 3.44 [173] illustrates an architecture that employs the EAM of 2.10(a) to achieve ORM. In Fig. 3.44, the downlink signal at $f_d = \frac{\omega_d}{2\pi}$ Hz and a local oscillator tone at $f_l = \frac{\omega_l}{2\pi}$ Hz are combined with the aid of the SCM technique of Fig. 2.22 and the resultant signal is then used for modulating the DL optical carrier generated by the LD at $f_c = \frac{\omega_c}{2\pi}$ Hz. The ODSB modulated signal is then optically filtered for generating an OSSB signal, whose spectrum is also shown in Fig. 3.44 [173]. After transmission of this signal from the BS to the RAP over the fiber, as shown in Fig. 3.44, half of the signal power is photo-detected and bandpass filtered in the upper branch of the Fig. 3.44 for removing the local oscillator tone and then transmitted to the MS, On the other hand, the other half of the signal power in the lower branch is additionally remodulated using an EAM by the UL signal at $f_u = \frac{\omega_u}{2\pi}$ Hz. It is then amplified and optically filtered for ensuring that the UL optical signal consist of a tone at $(\omega_c - \omega_l)$, an UL sideband at $(\omega_c - \omega_u)$ and a residual DL sideband at $(\omega_c - \omega_d)$ [173]. The UL

optical signal is then transmitted from the RAP to the BS over the fiber, where it is photo-detected and bandpass filtered for removing the DL downlink signal. Finally, the down-converted uplink signal at $\omega_u - \omega_l$ is detected [173].

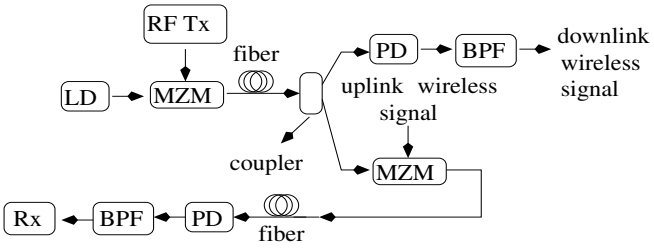

Figure 3.45: ORM with constraints on uplink/downlink frequency allocation

Another ORM architecture is shown in Fig. 3.45, where the output of a LD is modulated by the DL RF signal and it is then transmitted from the BS to the RAP. Then, a part of the DL signal power is separated using an optical coupler and additionally remodulated by the UL signal, using the MZM of the lower-branch in Fig. 3.45. The remodulated UL signal is transmitted from the RAP to the BS. Meanwhile, the signal in the upper-branch of Fig. 3.45 is photo-detected to generate the DL wireless signal. If the width of the UL and DL RF bands is less than an octave[1] and the frequency separation between the bands is more than the width of the bands, then the further modulated UL signal remains unaffected by the inter-modulation products between the DL and UL signals [107]. Thus, the UL signal can be filtered out from the signal that is photo-detected at the BS.

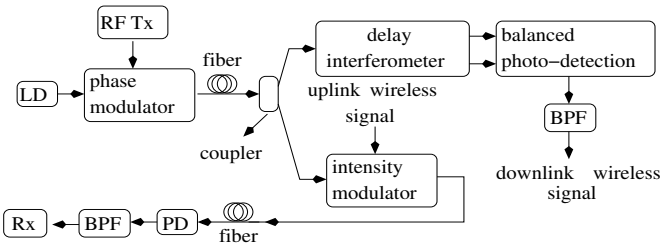

Figure 3.46: Optical Re-Modulation ORM using phase modulation and intensity modulation for downlink and uplink optical communication, respectively

Furthermore, it is possible to phase-modulate the optical carrier during its DL transmission and then intensity modulate the same optical carrier for its UL transmission as detailed below [180], [181], [1]. As shown in Fig. 3.46 [181], the output of the LD is phase-modulated by the RF signal and transmitted from the BS to the RAP over the fiber, where it was split into two branches by a coupler. The DL signal in the upper-branch of Fig. 3.46 is balanced photo-detected after performing a phase to intensity conversion using a delay interferometer such as the MZI of Fig. 2.19, as discussed in Section 2.1.2.2 [181]. An MZI assists in employing balanced photo-detection, as discussed in Section 3.1. It is worth mentioning that instead of performing phase-to-intensity conversion followed by direct balanced photo-detection, the coherent photo-detection of the phase-modulated signal may also be employed, as discussed Section 2.1.1.4. The lower branch of the coupler of Fig. 3.46 is intensity-modulated by the UL RF signal using an external modulator. Afterwards, the UL optical signal is transmitted from

[1] A frequency band from f_1 Hz to f_2 Hz is equal to an octave if $f_2 = 2f_1$

the RAP to the BS over the fiber, where it is photo-detected to generate the UL RF signal, which is subsequently bandpass filtered and fed to the RF receiver.

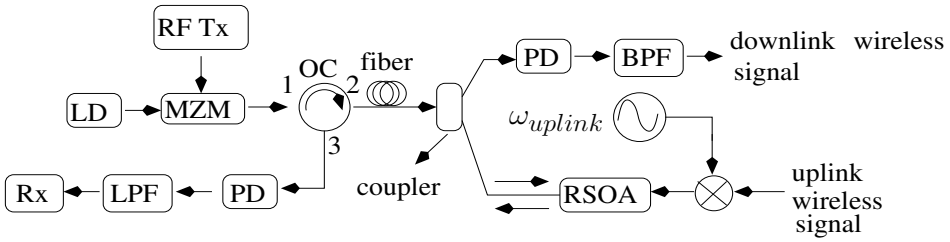

Figure 3.47: Optical Re-Modulation ORM using a RSOA

Additionally, the architecture of Fig. 3.47 can also be used, where the output of a laser source is modulated by the DL RF signal using a MZM. Subsequently, the DL optical signal enters port 1 and exits from port 2 of the OC. This signal is then transmitted from the BS to the RAP over the fiber, where the signal is split into two branches. The upper branch is photo-detected to generate the DL wireless signal [178], while the lower branch is fed to a gain-saturated Reflective Semiconductor Optical Amplifier (RSOA) in order to suppress the DL optical sidebands. As shown in Fig. 3.47, the optical carrier is simultaneously modulated by the UL BB data that is generated by down-converting the $f_{uplink} = \frac{\omega_{uplink}}{2\pi}$ Hz wireless signal from the MS, which is received at the RAP [178]. Hence, the UL transmission requires the oscillator operating at ω_{uplink} in the RAP. The UL optical signal exits the RSOA and then it is transmitted from the RAP to the BS through the optical fiber, where it enters port 2 and exits from port 3 of the OC. As shown in Fig. 3.47, the UL signal is then photo-detected and the resultant BB UL signal is filtered and detected [178].

Let us now briefly contrast the solutions in Figures 3.44 to 3.47. The design of Fig. 3.44 requires the UL signal to be amplified using Erbium Doped Fiber Amplifiers (EDFAs) which add ASE optical noise, as discussed in in Section 2.1.1.5. On the other hand, the design of Fig. 3.45 is simple, but it imposes certain conditions on the wireless frequency assignment. The design of Fig. 3.46 does not impose such restrictions, but requires either the phase-to-intensity conversion discussed in prior to the DL direct photo-detection or it has to employ the DL coherent photo-detection. Also, fiber dispersion converts the DL phase-modulation to intensity modulation, thereby corrupting the intensity modulation based UL transmission of Fig. 3.46. Moreover, any residual intensity-modulation of the DL transmission would degrade the UL transmission of the system in portrayed Fig. 3.46.

All the wavelength re-use techniques described so far, namely the OCRR and ORM techniques, employ a separate optical UL modulator and DL photo-detector in the RAP. However, in the next section we discuss wavelength re-use techniques that employ a single modulator-cum-photo-detector, thereby reducing the RAP complexity.

3.2.2.3 Employing a single device modulator-cum-photo-detector

The wavelength re-use techniques of Sections 3.2.2.1 and 3.2.2.2 need a photo-detector for detecting the DL optical signal and a separate modulator for transmitting the UL optical signal. However,

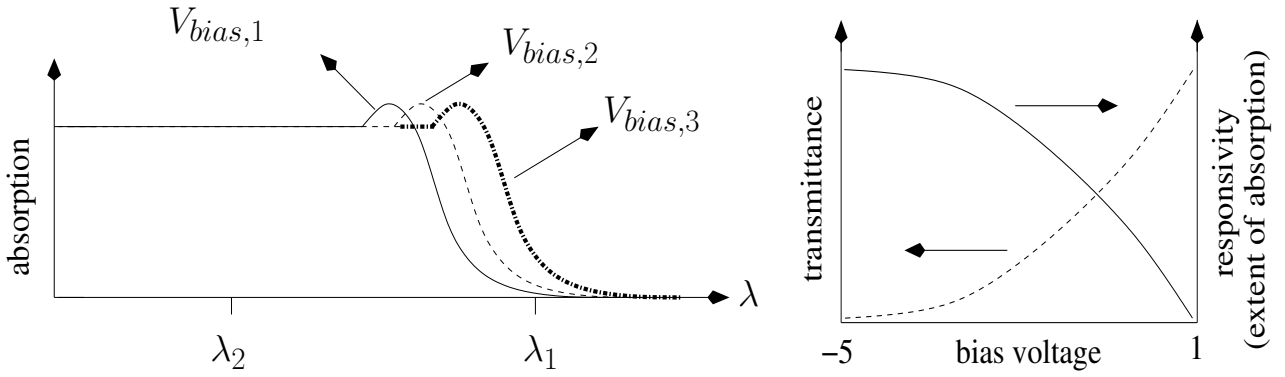

(a) EAM absorption at different optical wavelengths

(b) EAM absorption or transmission vs. bias voltage at λ_1

Figure 3.48: EAM absorption characteristics

it is possible to employ an EAM as a modulator-cum-photo-detector[1]. Both the operating optical wavelength and the bias-voltage has an influence on the transmission characteristics of the EAM. Fig. 3.77 illustrates the dependence of the EAM absorption on the operating wavelength [32]. As shown in Fig. 3.77, an optical input signal at a wavelength of λ_2 would be largely absorbed, i.e. it is largely photo-detected, regardless of the bias voltage, while an optical input signal at a wavelength of λ_1 would experience a bias-voltage-dependent absorption, i.e. a bias-voltage-dependent photo-detection, or transmittance level, as shown in Fig. 3.48(b) and discussed in Section 2.1.1.2. As shown in Fig. 3.48(b), a low level of transmittance corresponds to a high level of absorption, i.e a high level of photo-detection of the optical input signal by the EAM [70]. On the other hand, a high-level of transmittance would enable the modulation of the input optical signal by the electronic signal applied to the EAM. This property has been exploited for designing the following EAM-based optical transceivers.

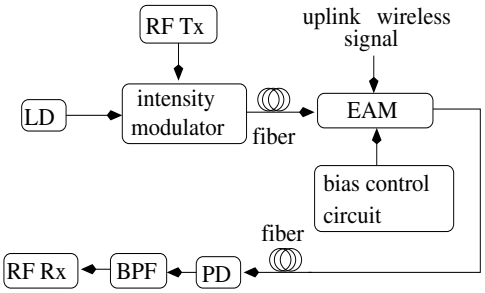

Figure 3.49: Half-duplex operation of EAM as modulator-cum-photo-detector

Single-wavelength half-duplex operation can be achieved using the EAM. When light at a wavelength λ_1 of Fig. 3.77 enters an EAM, achieving a high RF modulation efficiency requires the EAM to be biased at a point, where the slope of the transmission characteristics of Fig. 3.48(b) is maximum. This is true for moderate values of the reverse bias voltage, as seen from Fig. 3.48(b) [169]. On the other hand, it can also be seen from Fig. 3.48(b) that the optical input signal is largely absorbed, i.e. it is photo-detected, when a high reverse bias voltage is employed [70]. Thus, the EAM can be

[1]A single device that is capable of photo-detecting the DL optical signal as well as modulating it with the electronic UL signal.

operated both as a modulator and a photo-detector by appropriately switching the bias voltage applied to it [169], as shown in the architecture of Fig. 3.49, where the bias voltage applied to the EAM in the RAP is switched based on whether photo-detection of the DL optical signal from the BS or transmission of the UL optical signal to the BS is taking place. The major drawback of this technique is however that the bi-directional communication is half-duplex, because simultaneous photo-detection and modulation is not possible. Additionally, the need for employing bias control circuits is another complexity-related drawback.

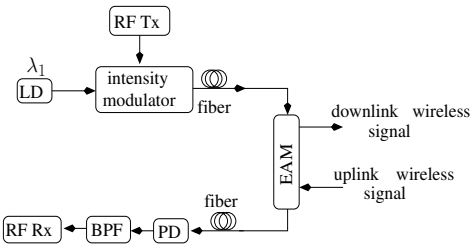

Figure 3.50: Full-duplex operation of EAM as modulator-cum-photo-detector

In contrast to Fig. 3.49 relying on a half-duplex operation, single-wavelength full-duplex operation can be used, as in the architecture of Fig. 3.50, where the operating wavelength is chosen to be λ_1 of Fig. 3.77 and the bias voltage is not switched. In the architecture of Fig. 3.50, the EAM bias voltage of Fig. 3.48(b) is adjusted to a specific value that would strike the desired compromise between the UL modulation efficiency and the DL photo-detection efficiency, along with the UL modulation non-linearity being at an acceptable level [170]. Hence, the EAM in the RAP is not operating in the ideal photo-detection region of Fig. 3.48(b) and it photo-detects the DL optical signal, while also modulating the UL wireless signal onto the optical carrier. It is possible to operate the EAM in a bias-free scenario, i.e. when a bias of zero volts is applied, but it can be seen from Fig. 3.48(b) that choosing a bias voltage of zero volts would result in the EAM becoming less efficient as a photo-detector than as a modulator. Hence different antenna gain values would have to be applied to the UL and DL signal at the mobile device to ensure a similar performance [171].

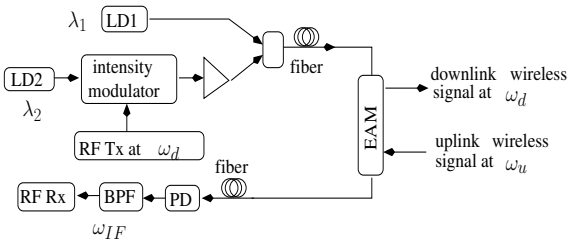

Figure 3.51: Full-duplex operation of EAM as modulator-cum-photo-detector

Finally in contrast to Fig. 3.49 and Fig. 3.50, dual-wavelength full-duplex operation may also be employed. The need to strike a compromise between the modulation efficiency and the photo-detection efficiency can be circumvented by adopting a dual-wavelength operation. In the architecture of Fig. 3.51 [71], the output of the laser LD2, operating at λ_2 of Fig. 3.77, is intensity modulated by a RF signal at $f_d = \frac{\omega_d}{2\pi}$ Hz. The modulated optical signal is then combined with the unmodulated output of the laser LD1 operating at λ_1 of Fig. 3.77. As shown in Fig. 3.51, this combined signal is

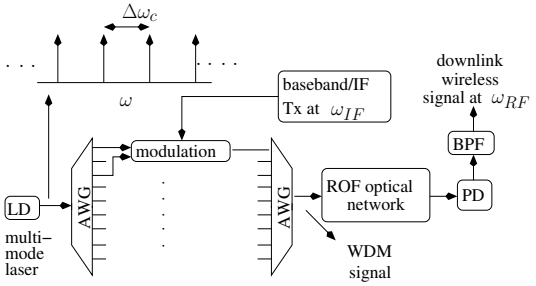

(a) WDM using a multimode optical source

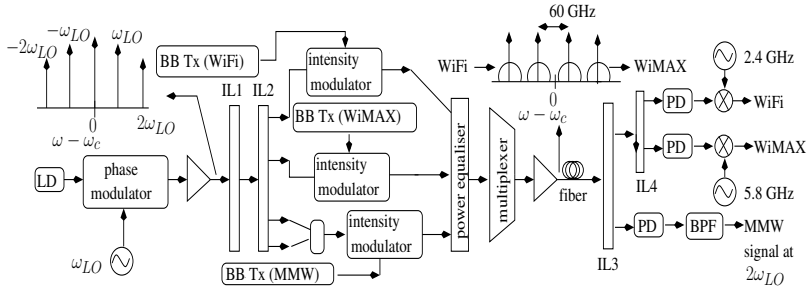

(b) Employing phase modulation harmonics to generate WDM signal

Figure 3.52: Techniques to reduce the number of lasers

transmitted from the BS to the RAP over the fiber, where the optical signal at λ_d is photo-detected by the EAM, while the optical signal at λ_1 is modulated by the EAM using the UL RF signal at $f_u = \frac{\omega_u}{2\pi}$ Hz [71]. The UL optical signal is transmitted from the RAP to the BS over the fiber and then it is photo-detected, filtered and detected.

Let us now consider the family of techniques proposed for reducing the number of lasers that are employed in the BS, unlike the above wavelength re-use techniques that aim to make the RAP laser-free.

Table 3.6: ROF Cost Reduction Techniques (Part 3)

Technique	Year	Authors	Contribution
Reducing the number of lasers	2005	Kuri *et al.* [182]	Employed the modes of a multi-mode super-continuum laser to support multiple users, as shown in Fig. 3.52(a).
	2006	Pakistani *et al.* [183]	A WDM ROF network relying on a multi-mode laser was shown to support over 10000 channels and a total data rate of 1.56 Tbps.
	2007	Olmos *et al.* [34]	A dynamic reconfigurable WDM ROF network relying on a multi-mode laser to support multiple channels was proposed.
	2009	Chowdhury *et al.* [49]	It employed the harmonics generated by optical modulation to support multi-band transmission of RF signals including WIFi, WiMax and a 60 GHz signal.
	2013	Thomas *et al.* [2]	It employed the harmonics generated by optical modulation to support multiple RAPs.

3.2.3 Reducing the number of lasers

While wavelength-reuse eliminates the need to have a laser source in the RAP, the BS still has to have several laser sources for supporting multiple RAPs by using the WDM signal of Fig. 2.24(a). The

need to have several laser sources in a network employing WDM can be totally or partially relaxed in the following ways:

3.2.3.1 Using a multi-mode optical source

A single-mode laser produces a tone at a single frequency, while a multi-mode laser produces tones at multiple optical frequencies [184]. As shown in Fig. 3.52(a)[182], the various $\Delta\omega_c$ spaced modes of a multi-mode laser are separated using a DEMUX. Then, pairs of modes having a separation of $N\Delta\omega_c$ are employed in optical modulation using a BB/IF signal at $f_{IF} = \frac{\omega_{IF}}{2\pi}$ Hz, where each pair of modes constitutes a channel and N is a positive integer. Subsequently, the modulated channels are multiplexed to generate the WDM signal of Fig. 3.52(a), which is transmitted through a ROF optical network to the RAP, where the heterodyne detection of the modes in each channel generates the DL RF signal at $\omega_{RF} = (N\Delta\omega_c + \omega_{IF})$. It has been shown in [182] that this technique can be used for generating upto 360 such channels, which can be used for supporting duplex communication with 180 RAPs. By additionally employing the SCM of Fig. 2.22 it is possible to support upto 10080 RF channels associated with a bandwidth of 250 MHz belonging to the unlicensed 60 GHz band [183]. The availability of a large number of channels can be exploited in the design of a dynamically reconfigurable WDM network carrying 60 GHz ROF signals [34].

3.2.3.2 Employing modulation harmonics

The harmonics that are imposed by the modulation of an RF tone on the laser's output can be beneficially harnessed as independent optical carriers [2] [49]. These modulation harmonics can support multi-band transmission to a single RAP. Fig. 3.52(b) illustrates an architecture in which the upper harmonics that are generated during phase modulation can be used for supporting the transmission of WiFi, WiMAX and 60 GHz signals to the RAP [49]. At the BS, the optical carrier is phase-modulated using a $f_{RF} = 30$ GHz $= \frac{\omega_{RF}}{2\pi}$ electronic tone at a phase modulation depth, which would result in first-order harmonic at $(\omega_c \pm \omega_{RF})$ and in significant second-order sidebands at $(\omega_c \pm 2\omega_{RF})$, in addition to the presence of the optical carrier at ω_c, as shown in Fig. 3.52(b) [49]. The optical carrier is removed by the first interleaver (IL1), while the second interleaver (IL2) separates the four sidebands, where there are two sidebands of the first-order and two of the second-order. The pair of second-order sidebands at $(\omega_c + 2\omega_{RF})$ and $(\omega_c - 2\omega_{RF})$ are considered as independent optical carriers and are modulated with the BB WiFi and BB WiMAX signals, respectively. The pair of $2f_{RF} = 60$ GHz spaced first-order sidebands at $(\omega_c + \omega_{RF})$ and $(\omega_c - \omega_{RF})$ are then combined and modulated with the BB data of the desired 60 GHz signal. The four sidebands are then combined to generate the spectrum seen in Fig. 3.52(b) and this multiplexed signal is transmitted from the BS to the RAP over the fiber. In the RAP, the first interleaver IL3 of Fig. 3.52(b) separates the first-order sidebands from the second-order sidebands [49]. The two first-order sidebands are heterodyne photo-detected to generate a 60 GHz millimeter-wave signal, while the second interleaver IL4 of Fig. 3.52(b) is used for separating the two second-order sidebands, followed by their individual photo-detection and upconversion to generate the 2.4 GHz WiFi and the 5.8 GHz WiMAX signals [49].

On the other hand, instead of supporting multiband transmission to a single RAP, as in Fig. 3.52(b), it is possible to employ the modulation harmonics as independent optical carriers that support

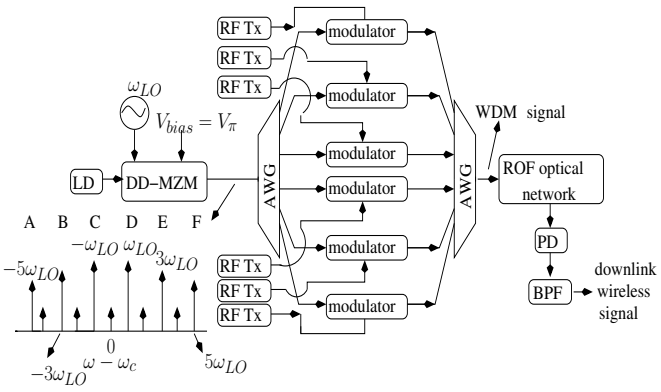

Figure 3.53: Exploiting Mach-Zehnder Modulator non-linearity to generate a WDM signal

multiple RAPs [29], [2], which could support DAS-based wireless MIMO communication [29]. As shown in Fig. 3.53, it is possible to generate multiple optical carriers by modulating the output of a LD, operating at an optical output of $f_c = \frac{\omega_c}{2\pi}$ Hz, using a sinusoidal modulating signal at $f_{LO} = \frac{\omega_{LO}}{2\pi}$ Hz and a high modulation depth [29],[2]. This is achieved using the OCS architecture in Section 2.1.2.1, which employs the dual-drive MZM of Fig. 2.8(b) that is biased at $V_{bias} = V_\pi$ and operating in the push-pull mode. As observed from the spectrum seen in Fig. 3.53, using a high modulation index results in the first harmonic at $(\omega_c \pm \omega_{LO})$, third harmonic at $(\omega_c \pm 3\omega_{LO})$ and fifth harmonic at $(\omega_c \pm 5\omega_{LO})$ having a significant magnitude. These can then be used as six independent optical carriers having an inter-carrier spacing of $2\omega_{LO}$ [29], [2], for supporting multiple RAPs, one of which is shown in Fig. 3.53.

Having discussed the performance improvement and cost reduction techniques, we move on to discussing the third focus area of this chapter, which is optical generation of high-RF signals.

3.3 Optical generation of high-RF signals

Classical generation of RF signals requires the upconversion of the baseband signals using electronic mixers. The electronics needed for generating baseband wireless signals has considerably matured over the past few decades. However, as discussed in Section 1.5.3, in the high-RF networks, the overall Bit Error Rate (BER) is severely limited by the quality of the broadband electronic mixers, especially in the case of millimeter-wave networks. The less expensive is the mixer, the more degrading is its effect on the BER. For reasons mentioned in the previous sections, such high-RF networks are expected to employ the ROF technique for the optical distribution of the RF signals. Hence, trying to generate these high-RF signals optically as well is a natural solution to the challenge of having to use high-RF mixers.However, this challenge is less pronounced in the Impulse Radio (IR) wireless technique, which does not employ upconversion using a RF tone but rather ensures that the baseband data is modulated onto the intensity, shape or position of pulses, where the spectrum of the pulses is usually in the 3.1 to 10.6 GHz range. However, in order to cover the entire spectral range spanning from 3.1 to 10.6 GHz, they employ pulses that must have a duration of around 200 ps [53], where the generation of such broadband signals in the electronic domain is challenging, as discussed in Section 1.5.3. Thus, as alluded to in Section 1.5.3, generating and distributing these IR signals optically is considered a

viable technique for future wireless networks. Optical generation and distribution of the RF signals is specially useful in the case of Wireless Personal Area Networks (WPANs), which either use the IR wireless technique or employ 60 GHz carriers, as discussed in Section 1.5.3. Optical techniques conceived for the generation of WPAN signals are highlighted in Sections 3.3.1 and 3.3.2.

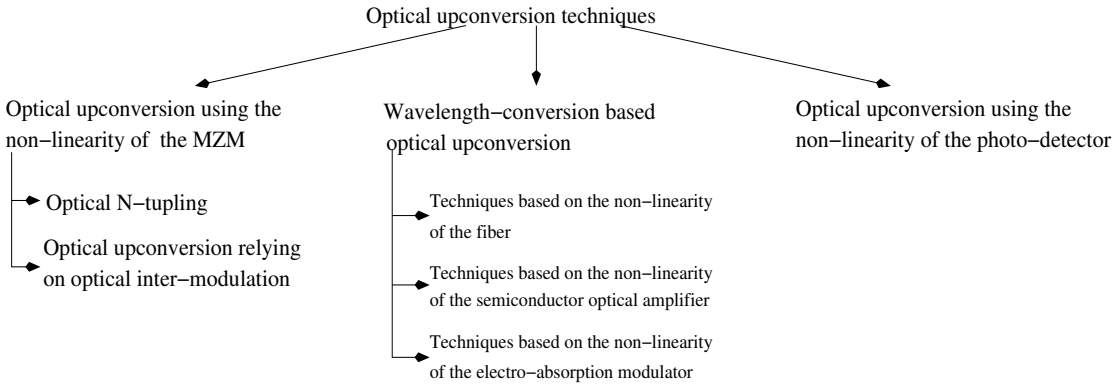

Figure 3.54: Optical upconversion techniques

3.3.1 Optical upconversion exploiting ROF link non-linearities

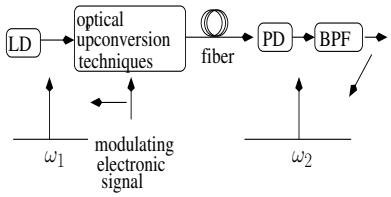

Figure 3.55: Optical Upconversion

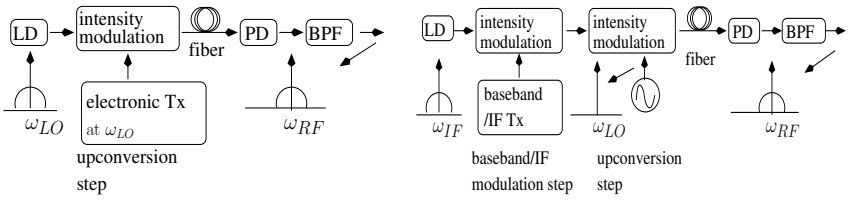

(a) One-Step optical upconversion (b) Two-Step optical upconversion

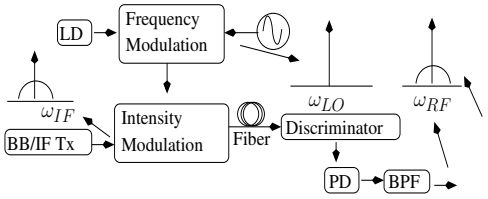

(c) Optical Frequency Multiplication

Figure 3.56: N-tupling architectures

The overall BER achieved by a ROF link that employs high RF frequencies is severely affected by the quality of the broadband mixers. These ROF links involve a stringent cost-performance trade-off

for the case of millimeter-wave mixers [56]. This can be overcome by employing optical upconversion techniques, which enable the generation of a photo-detected signal in the RAP at a frequency of $f_2 = \frac{\omega_2}{2\pi}$ Hz, that is higher than the frequency $f_1 = \frac{\omega_1}{2\pi}$ of the modulating electronic signal at the BS, as shown in Fig. 3.55, i.e. we have $f_2 > f_1$. As shown in Fig. 3.54, optical upconversion can be achieved by using the MZM's non-linearity [48], by employing wavelength conversion techniques [185] or by exploiting the photo-detector's non-linearity [186]. The wavelength conversion techniques rely on the inherent non-linearities present in various ROF link components, including the non-linearities in the fiber [185], the optical amplifier [187] or in the EAM [188]. The RF mixers operatng at a high frequency significantly degrade the performance of the wireless link. Hence, the major advantage of employing optical upconversion is the ability to avoid the employment of these high frequency RF mixers.

The family of MZM-assisted optical upconversion techniques of Fig. 3.54 allows us to vary the frequency of the transmitted wireless signal, without having to change the electronic Local Oscillator's (LO's) electronic frequency. Another advantage of MZM-assisted optical upconversion is the ability to generate a WDM signal by using a single external modulator, where each wavelength carries a high RF signal, thereby reducing the system's cost [158]. On the other hand, the family of wavelength conversion based optical upconversion techniques of Fig. 3.54 allows optical upconversion to be performed simultaneously with optical switching. For example, the routing of multiple channels at the same wavelength can be achieved by converting the signals to a different wavelength [189].

3.3.1.1 Optical upconversion using the non-linearity of the mach zehnder modulator

We commence our discussion of the optical upconversion techniques by considering the family of techniques that rely on the non-linearity of the MZM, as shown in Fig. 3.54. The non-linear nature of the MZM transmittance, as seen in Fig. 2.9(a), results in the generation of harmonics and intermodulation products, where the optical N-tupling technique to be detailed below employs the upper harmonics for achieving optical upconversion. On the other hand, optical intermodulation assisted upconversion exploits the intermodulation products for achieving optical upconversion.

Optical N-tupling We start our discussion of the family of techniques that rely on the non-linearity of the MZM for optical upconversion by considering the subclass of optical N-tupling techniques shown in Fig. 3.54. Specifically, the optical modulation techniques that employ an electronic signal at $f_{LO} = \frac{\omega_{LO}}{2\pi}$ Hz for generating a photo-detected signal at the N^{th} harmonic of f_{LO}, are referred to as N-tupling techniques. Optical N-tupling can be achieved using both intensity and angle modulation, where intensity modulation based optical N-tupling is implemented either using single-step or two-step N-tupling. Fig. 3.56(a) shows the architecture often employed for achieving **Single-step N-tupling**, where, in the BS, the output of the laser is employed in a single upconversion step achieved by using a MZM that is driven by a RF signal at f_{LO} Hz. Afterwards, the optical signal is transmitted through the optical fiber and photo-detected in the RAP, where the up-converted photo-detected signal at $f_{RF} = Nf_{LO}$ Hz can be retained using an electronic filter, as illustrated later in this section [54]. On the other hand, Fig. 3.56(b) shows the architecture that is employed to achieve **Two-step N-tupling**, where, in the BS, the output of the laser is employed in the the first step, which involved optical modulation using the $f_{IF} = \frac{\omega_{IF}}{2\pi}$ Hz baseband/Intermediate Frequency (IF) modulating signal.

This is followed by the upconversion step relying on a MZM driven by an electronic LO having a frequency of f_{LO} Hz. Then, the optical signal is transmitted through the optical fiber to the RAP and photo-detected. Subsequently, the up-converted photo-detected signal at f_{RF} Hz can be extracted by a filter[1], as detailed later in this section [190], where

$$f_{RF} = Nf_{LO} + f_{IF} \tag{3.28}$$

Note that in some cases the upconversion step of the above two techniques might be split into multiple steps. For example, frequency six-tupling might be implemented using frequency doubling followed by frequency quadrupling [54], as detailed later in this section.

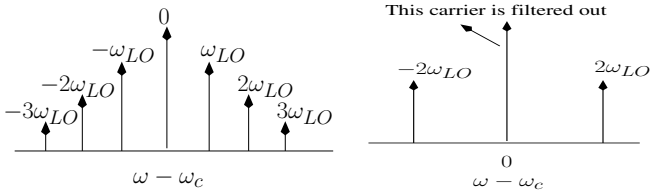

(a) Optical Frequency Modulation (b) Filtering of optical harmonics

Figure 3.57: N-tupling spectra

Another optical N-tupling technique that is robust to dispersion is Optical Frequency Multiplication (OFM) [191]. As shown in Fig. 3.56(c), instead of generating intensity-modulated harmonics, the output of the laser is frequency/phase modulated using the RF signal, which generates the spectrum of Fig. 3.57(a), followed by a conversion of these harmonics to intensity modulation using an optical frequency/phase discriminator, as discussed in Section 2.1.2.2.

In the N-tupling techniques optical filtering may be employed for removing the undesired optical harmonics in order to ensure that the photo-detected signal does not contain harmonics, which are stronger than the one required [192]. For example, if the required photo-detected signal has a frequency of $4f_{LO}$ Hz, then it can be generated by the beating of the sidebands located at $(\omega_c \pm 2\omega_{LO})$ in Fig. 3.57(b). However, a strong photo-detected signal is also generated at $2f_{LO}$ Hz by the beating of the optical carrier with each of the sidebands. Hence, the generation of this unwanted signal at $2f_{LO}$ Hz can be avoided by filtering out the optical carrier in the spectrum of Fig. 3.57(b) prior to photo-detection.

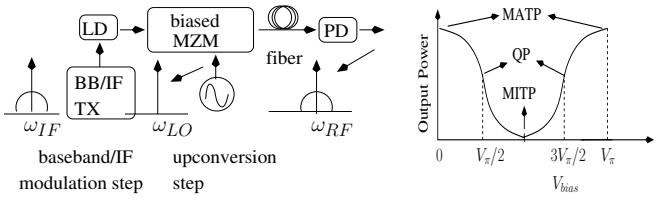

(a) MZM assisted Ntupling architecture (b) MZM bias points

Figure 3.58: MZM assisted Ntupling

Various MZM biasing techniques can be employed in optical N-tupling, where the point at which a MZM is biased within its non-linear transmittance curve of Fig. 3.58(b) decides the specific types of

[1] N is the selected harmonic number.

harmonics that are generated in the optical and photo-detected signal. Consider the BS of the two step N-tupling architecture of Fig. 3.58(a) and let $E_{BB}(t)$ be the output of the baseband/IF modulation step that is achieved using direct modulation. Then, the upconversion step is implemented using a biased MZM that is driven by the electronic local oscillator signal $V_{LO}(t) = V_{LO}\cos(\omega_{LO}t)$, as shown in Fig. 3.58(a). The MZM is usually of dual-drive type because of its ability to operate in the chirp-free push-pull mode. As shown in Fig. 3.58(b), the MZM can be biased at the QP, MATP or MITP, as described in the following discussion.

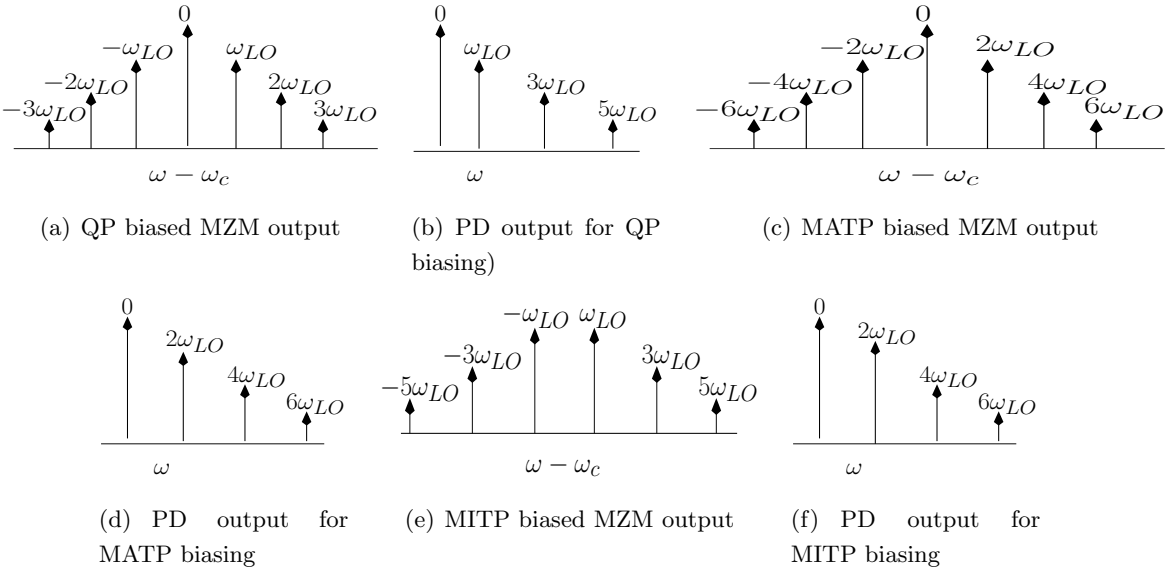

(a) QP biased MZM output

(b) PD output for QP biasing)

(c) MATP biased MZM output

(d) PD output for MATP biasing

(e) MITP biased MZM output

(f) PD output for MITP biasing

Figure 3.59: Optical and electronic spectrum when employing QP, MATP and MITP biasings

a) **Quadrature Point (QP) Biasing**: This technique requires the MZM of Fig. 3.58(a) to be biased at the QP, which corresponds to a bias voltage of $V_{bias} = (V_\pi/2 + m2V_\pi)$ or $V_{bias} = (-V_\pi/2 + m2V_\pi)$, where m is an integer. The difference between the two sets of bias points is only in the polarity of the harmonics in the photo-detected signal. If the MZM is of dual-drive type, as shown in Fig. 2.8(b), then it could be operated in the push-pull mode, as detailed in Section 2.1.1.2. Using Equations (2.6b) and (2.6d), the expressions for the optical field $E_{total}(t)$ at the output of the biased MZM in Fig. 3.58(a) and the photo-detected signal $I_{PD}(t)$ can be formulated as follows:

$$
\begin{aligned}
&E_{total}(t) \\
&= \cos(\pm\frac{\pi}{4} + \frac{\pi V_{LO}(t)}{2V_\pi})E_{BB}(t) \\
&= \frac{E_{BB}(t)}{\sqrt{2}}\left[cos(\frac{\pi V_{LO}\cos(\omega_{LO}t)}{2V_\pi}) \mp sin(\frac{\pi V_{LO}\cos(\omega_{LO}t)}{2V_\pi})\right] \\
&= \frac{E_{BB}(t)}{\sqrt{2}}\left[J_0(\frac{\pi V_{LO}}{2V_\pi}) + 2\sum_{n=1}^{\infty}(-1)^n J_{2n}(\frac{\pi V_{LO}}{2V_\pi})\cos(2n\omega_{LO}t)\right. \\
&\left.\pm\, 2\sum_{n=1}^{\infty}(-1)^n J_{2n-1}(\frac{\pi V_{LO}}{2V_\pi})\cos((2n-1)\omega_{LO}t)\right]
\end{aligned}
\tag{3.29}
$$

and

$$\begin{aligned} I_{PD}(t) &\propto |E_{total}(t)|^2 \\ &= \left[1 \mp \sin(\frac{\pi V_{LO}\cos(\omega_{LO}t)}{V_\pi})\right]\frac{|E_{BB}(t)|^2}{2} \\ &= \left[\frac{1}{2} \pm \sum_{n=1}^{\infty}(-1)^n J_{2n-1}(\frac{\pi V_{LO}}{V_\pi})\cos((2n-1)\omega_{LO}t)\right]|E_{BB}(t)|^2, \end{aligned} \tag{3.30}$$

where $J_n(x)$ is the Bessel function of order n. It can be seen from Equation (3.29) that the optical signal has both even harmonics, i.e. $N = 2n,$ where $n = 0, 1, ..$ and odd harmonics, i.e. $N = 2n - 1,$ where $n = 1, 2..$, as shown in Fig. 3.59(a). Fig. 3.59(a) illustrates the output optical spectrum of the QP biased MZM.

Additionally, it can be seen from Equation (3.30) that the photo-detected signal consists of a signal at the carrier and odd harmonic values associated with $N = 2k - 1,$ where $k = 1, 2, ...,$ as shown in Fig. 3.59(b). Note that Fig. 3.59(a) and Fig. 3.59(b) indicate only the harmonics generated by the upconversion step, i.e. assuming an unmodulated laser output of $E_{BB}(t) = \sqrt{2P_{in}}e^{j\omega_c t}$ in Equations (3.29) and (3.30), where $f_c = \frac{\omega_c}{2\pi}$ and P_{in} are the laser frequency and optical power, respectively. Any data employed in the prior baseband/IF modulation step would be located around the harmonics.

b) **Maximum Transmission Point (MATP) Biasing**: This technique requires the MZM of Fig. 3.58(a) to be biased at a voltage of $V_{bias} = (0 + m2V_\pi)$, where m is an integer. As seen from Fig. 3.58(b), this bias point corresponds to the maximum output optical power and hence it is referred to as the MATP [190]. Using Equations (2.6b) and (2.6d), the expressions for the optical field $E_{total}(t)$ at the output of the biased MZM in Fig. 3.58(a) and the photo-detected signal $I_{PD}(t)$ in the MATP biasing case can be represented as follows:

$$\begin{aligned} E_{total}(t) &= \cos(\frac{\pi V_{LO}\cos(\omega_{LO}t)}{2V_\pi})E_{BB}(t) \\ &= \frac{E_{BB}(t)}{\sqrt{2}}\left[J_0(\frac{\pi V_{LO}}{2V_\pi}) + 2\sum_{n=1}^{\infty}(-1)^n J_{2n}(\frac{\pi V_{LO}}{2V_\pi})\cos(2n\omega_{LO}t)\right] \end{aligned} \tag{3.31}$$

and

$$\begin{aligned} I_{PD}(t) \propto |E_{total}(t)|^2 &= \frac{|E_{BB}(t)|^2}{2}\left[1 + \cos(\frac{\pi V_{LO}\cos(\omega_{LO}t)}{V_\pi})\right] \\ &= \frac{|E_{BB}(t)|^2}{2}\left[1 + J_0(\frac{\pi V_{LO}}{V_\pi})\right. \\ &\quad \left. + 2\sum_{n=1}^{\infty}(-1)^n J_{2n}(\frac{\pi V_{LO}}{V_\pi})\cos(2n\omega_{LO}t)\right]. \end{aligned} \tag{3.32}$$

Observe from Equation (3.31) that the optical field has only even harmonics, i.e. optical harmonics of the order $2n,$ where $n = 0, 2, ...,$ as shown in Fig. 3.59(c). Additionally, it can be seen from Equation (3.32) that the photo-detected signal consists of even harmonics values, i.e. $N = 2k,$ where $k = 0, 1, 2, ...,$ as shown in Fig. 3.59(d). Note that Fig. 3.59(c) and Fig. 3.59(d) indicate only the harmonics generated by the upconversion step, i.e. assuming an unmodulated

laser output of $E_{BB}(t) = \sqrt{2P_{in}}e^{j\omega_c t}$ in Equations (3.31) and (3.32), while any data employed in the prior baseband/IF modulation step would be located around the harmonics.

c) **Minimum Transmission Point (MITP) Biasing**: This technique requires the MZM in Fig. 3.58(a) to be biased at a voltage of $V_{bias} = V_\pi + m2V_\pi$, where m is an integer. As seen from Fig. 3.58(b), this bias point corresponds to the minimum output optical power and hence it is referred to as the MITP [190]. Using Equations (2.6b) and (2.6d), the expressions for the optical field $E_{total}(t)$ at the output of the biased MZM in Fig. 3.58(a) and the photo-detected signal $I_{PD}(t)$ in the MITP biasing case are as follows:

$$\begin{aligned} &E_{total}(t) \\ &= \mp \sin(\frac{\pi V_{LO}\cos(\omega_{LO}t)}{2V_\pi})E_{BB}(t) \\ &= \pm\frac{E_{BB}(t)}{\sqrt{2}}\left[2\sum_{n=1}^{\infty}(-1)^n J_{2n-1}(\frac{\pi V_{LO}}{2V_\pi})\cos((2n-1)\omega_{LO}t)\right] \end{aligned} \tag{3.33}$$

and

$$\begin{aligned} &I_{PD}(t) \propto |E_{total}(t)|^2 \\ &= \frac{|E_{BB}(t)|^2}{2}\left[1-\cos(\frac{\pi V_{LO}\cos(\omega_{LO}t)}{V_\pi})\right] \\ &= \frac{|E_{BB}(t)|^2}{2}\Bigg[1 - J_0(\frac{\pi V_{LO}}{V_\pi}) \\ &- 2\sum_{n=1}^{\infty}(-1)^n J_{2n}(\frac{\pi V_{LO}}{V_\pi})\cos(2n\omega_{LO}t)\Bigg]. \end{aligned} \tag{3.34}$$

Observe from Equation (3.33) that the optical field has only odd harmonics, i.e optical harmonics of the order $(2n-1)$, where $n = 1, 2, ...$, as shown in Fig. 3.59(e). Additionally, it can be seen from Equation (3.34) that the photo-detected signal consists of even harmonics values, i.e. $N = 2n$, where $n = 0, 1, 2, ...$, as shown in Fig. 3.59(f). Note that Fig. 3.59(e) and Fig. 3.59(f) indicate only the harmonics generated by the upconversion step, i.e. assuming an unmodulated laser output of $E_{BB}(t) = \sqrt{2P_{in}}e^{j\omega_c t}$ in Equations (3.33) and (3.34), while any data employed in the prior baseband/RF modulation step would be located around the harmonics.

This technique is also referred to as OCS, because the optical carrier at ω_c is suppressed in the modulated signal, as shown in Fig. 3.59(e) [48]. The modulation voltage V_{LO} is much smaller than the switching voltage V_π of the MZM, hence in Equation (3.34), we have $\mathrm{J}_0(\frac{\pi V_{LO}}{V_\pi}) \approx 1$. Therefore, unlike in the MATP and QP biasing schemes of this section, the DC component in the photo-detected signal of MITP biasing, i.e. the term $[1 - J_0(\frac{\pi V_{LO}}{V_\pi})]$ in Equation (3.34), is highly suppressed. Hence, upon using Equations (2.36) and (2.37), it can be concluded that an advantage of a suppressed DC component is a low RIN and shot noise [129]. Furthermore, compared to the other N-tupling biasing techniques and the previously discussed OSSB and ODSB modulation, OCS has a better receiver sensitivity [158], [165].

Several values of N have been employed in the literature for N-tupling such as in doubling with $N = 2$, tripling with $N = 3$, quadrupling with $N = 4$, quintupling with $N = 5$, six-tupling with

$N = 6$ and 12-tupling with $N = 12$. These implementations rely on the previously discussed biasing techniques. In the following discussion, we present some of the commonly employed optical N-tupling implementations.

a) **Frequency doubling**: Frequency doubling refers to the scenario where the photo-detected signal has a carrier frequency that is twice that of the transmitted signal. Frequency doubling can be achieved in the following ways:

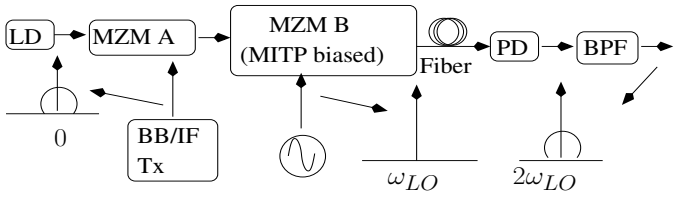

Figure 3.60: Frequency doubling using MITP biasing (or OOCS)

- Fig. 3.60 shows the block diagram of frequency doubling using MITP biasing, where the output of a laser in the BS is modulated using the $f_{IF} = \frac{\omega_{IF}}{2\pi}$ Hz baseband/IF electronic signal by the first MZM, namely MZM A [48]. When the the second MZM of Fig. 3.60, namely MZM B, is biased at the MITP and driven by an electronic tone at $f_{LO} = \frac{\omega_{LO}}{2\pi}$ Hz, the optical field consists of a suppressed carrier and odd harmonics, where the strongest ones are the two first-order harmonics on either side of the carrier, as shown in Fig. 3.59(e). During photo-detection in the RAP, these first order harmonics beat together to generate a signal, whose center frequency is $f_{RF} = (2f_{LO} + f_{IF})$ Hz, i.e. the center frequency is twice that of the modulating electronic tone [48]. This technique has been employed both in generating 40 GHz [48] and 60 GHz signals [88].

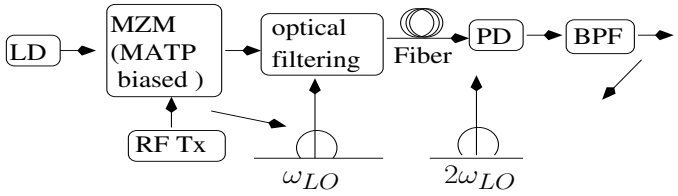

Figure 3.61: Frequency doubling using MATP biasing

- Fig. 3.61 shows the block diagram of frequency doubling using MATP biasing [179], where frequency doubling is carried out by feeding the output of a laser operating in the BS at $f_c = \frac{\omega_c}{2\pi}$ Hz to a MATP biased MZM that is driven by a RF signal at $f_{LO} = \frac{\omega_{LO}}{2\pi}$ Hz, in order to generate the spectrum of Fig. 3.59(c). Afterwards, the second-order optical harmonic at $(f_c - 2f_{LO})$ Hz will be eliminated by the optical filter in Fig. 3.61 to generate a dispersion tolerant OSSB signal having a single second order harmonic at $(f_c + 2f_{LO})$ Hz. Subsequently, photo-detection in the RAP generates a frequency-doubled electronic signal, because the single sideband at $(f_c + 2f_{LO})$ Hz beats with the optical carrier at f_c Hz.
- Fig. 3.62 shows the block diagram of frequency doubling using QP biasing, where frequency doubling can be achieved by feeding the output of a laser operating in the BS at $f_c = \frac{\omega_c}{2\pi}$

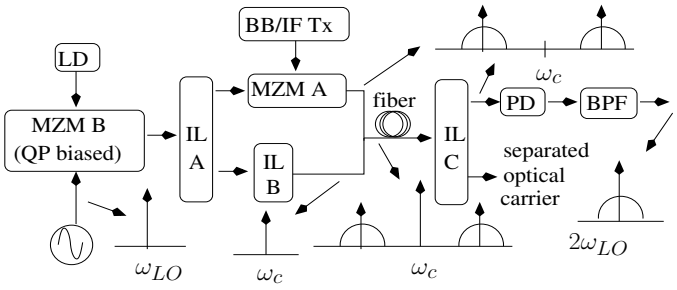

Figure 3.62: Frequency doubling using quadrature biasing

Hz to a quadrature point biased MZM, namely MZM A that is driven by a RF tone at $f_{LO} = \frac{\omega_{LO}}{2\pi}$ Hz [176], [54]. The output of MZM A, whose spectrum is shown in Fig. 3.59(a), is fed to the interleaver IL A of Fig. 3.62, which separates the odd optical harmonics from the even ones, where the most significant odd optical harmonics are the two first order harmonics at $(\omega_c \pm \omega_{LO})$ [176], which are modulated by the baseband/IF data using the second MZM, namely MZM B. The even optical harmonics primarily consist of the optical carrier and the second order harmonics. The pure optical carrier is separated using IL B. The optical carrier and the modulated first-order harmonics are then multiplexed together and transmitted over the fiber to the RAP. At the RAP, the optical carrier is separated out using IL C of Fig. 3.62, while the two first-order harmonics beat together during photo-detection in order to generate a frequency-doubled electronic signal [176]. The separated carrier of Fig. 3.62 can then be re-used for achieving uplink communication, which is known as wavelength-reuse.

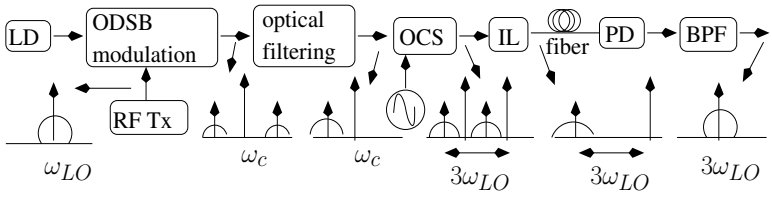

Figure 3.63: Frequency Tripling

b) **Frequency tripling**: Frequency tripling can be achieved by employing two MZMs in the up-conversion step, as shown in the BS of Fig. 3.63 [193], where the laser output at $f_c = \frac{\omega_c}{2\pi}$ Hz enters the first modulator, which is a MZM-based ODSB modulator that is driven by a RF signal at $f_{LO} = \frac{\omega_{LO}}{2\pi}$ Hz. The optical output of the ODSB modulator seen in Fig. 3.63 consists of the optical carrier and strong first-order harmonics. The first optical modulation is then followed by elimination of one of the first-order harmonics by the optical filter of Fig. 3.63. Afterwards, the filtered signal enters the second MZM, which implements OCS, i.e. it is biased at the MITP [193], and is driven by a RF tone at f_{LO} Hz, thereby generating a signal whose optical spectrum is shown in Fig. 3.63. As portrayed in Fig. 3.63, the interleaver (IL) selects the $3\omega_{LO}$ spaced harmonics, which are then transmitted over the fiber to the RAP. At the RAP, the $3\omega_{LO}$ Hz separated harmonics beat together during photo-detection to generate a frequency-tripled signal at $3f_{LO}$ Hz.

c) **Frequency quadrupling**: Frequency quadrupling can be implemented either using a MATP biased MZM or by using a nested-MZM, as discussed below:

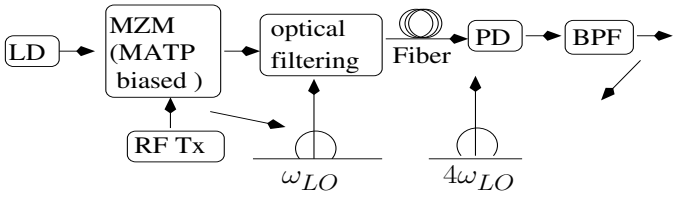

Figure 3.64: Frequency quadrupling by MATP biasing

- Fig. 3.64 shows the block diagram of frequency quadrupling using MATP biasing, where the output of the laser operating in the BS at $f_c = \frac{\omega_c}{2\pi}$ Hz is fed to an MATP-biased MZM whose output spectrum is shown in Fig. 3.59(c). Then, the optical carrier frequency in Fig. 3.59(c) is eliminated using a notch filter and then the remaining signal is transmitted over the fiber to the RAP. The subsequent photo-detection of the two $4\omega_{LO}$-spaced second-order harmonics seen at $\omega_c \pm 2\omega_{LO}$ in Fig. 3.59(c) produces a frequency-quadrupled signal, as shown in Fig. 3.64 [192]. This method has been employed for generating signals that are tunable from 32 to 50 GHz [192]. Instead of employing a notch filter at the BS, an interleaver may be employed at the RAP in a manner similar to that in Fig. 3.62 [194]. One of the outputs of the interleaver would consist of the second order harmonics, while the other output would be the separated carrier. The second-order harmonics are photo-detected for generating a frequency-quadrupled signal, while the separated carrier may be employed by the above-mentioned wavelength re-use technique [194][179], where again, wavelength re-use refers to the employment of the received downlink optical signal for uplink optical transmission.
- An alternative to applying an optical filter in Fig. 3.64 is to carefully set the depth of the optical modulation using the electronic LO, which is also referred to as the LO modulation index, to a value that suppresses the optical carrier [195], i.e. to ensure that $J_0(\frac{\pi V_{LO}}{2V_\pi}) = 0$ in Equation (3.31), which yields $V_{LO} = (2V_\pi/\pi) * 2.405$ [195]. However, at this LO modulation index, the strength of the optical harmonics in Equation (3.31), that are above the second-order harmonics, become significant [195].

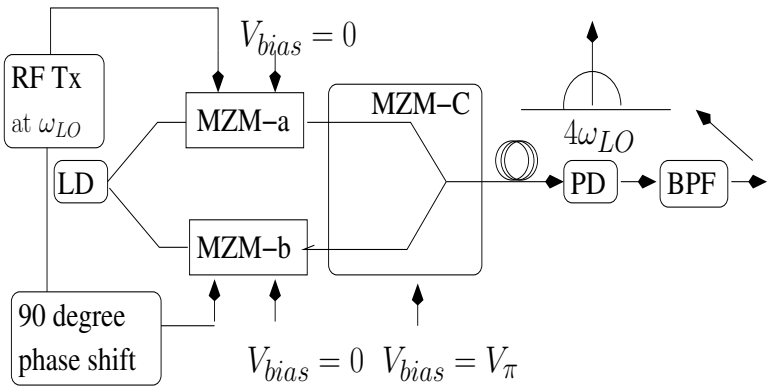

Figure 3.65: Frequency quadrupling by nested MZM

- Carrier suppression can also be achieved by feeding the output of a laser operating in the BS at $f_c = \frac{\omega_c}{2\pi}$ Hz to a nested MZM [196], [54], as shown in Fig. 3.65. In Fig. 3.65, the first two MZMs, namely MZM-a and MZM-b, are biased at $V_{bias} = 0$ and driven by the signals $V_{drive,a} = V_{RF} \sin \omega_{LO} t$ and $V_{drive,b} = V_{RF} \cos \omega_{LO} t$, respectively. Hence, using Equation (2.6b), the outputs of MZM-a and MZM-b are [196]:

$$E_{dual,a}(t) = \cos\left(\frac{\pi V_{LO} \sin \omega_{LO} t}{V_\pi}\right)\sqrt{2P_{in}}e^{j\omega_c t}$$
$$= [J_0(\frac{\pi V_{LO}}{V_\pi})$$
$$+ 2\sum_{k=1}^{\infty} J_{2k}(\frac{\pi V_{LO}}{V_\pi})\cos(2k\omega_{LO}t)]\sqrt{2P_{in}}e^{j\omega_c t} \quad (3.35)$$

and

$$E_{dual,b}(t) = \cos\left(\frac{\pi V_{LO} \cos \omega_{LO} t}{V_\pi}\right)\sqrt{2P_{in}}e^{j\omega_c t}$$
$$= [J_0(\frac{\pi V_{LO}}{V_\pi})$$
$$+ 2\sum_{k=1}^{\infty} (-1)^k J_{2k}(\frac{\pi V_{LO}}{V_\pi})\cos(2k\omega_{LO}t)]\sqrt{2P_{in}}e^{j\omega_c t}. \quad (3.36)$$

As shown in Fig. 3.65, the outputs of MZM-a and MZM-b are fed to the third MZM, namely MZM-c, which is biased at $V_{bias} = V_\pi$. Hence, resulting in:

$$E_{nested,c}(t) = \frac{E_{dual,a}(t) + e^{j\frac{\pi V_{bias}}{V_\pi}} E_{dual,b}(t)}{2} = \frac{E_{dual,a}(t) - E_{dual,b}(t)}{2} =$$
$$\frac{1}{2}\sum_{k=1}^{\infty} J_{4k-2}(\frac{\pi V_{RF}}{V_\pi})\cos((4k-2)\omega_{LO}t)\sqrt{2P_{in}}e^{j\omega_c t}.$$

Thus, $E_{nested,c}(t)$ has harmonics at $\omega_c \pm (4k-2)\omega_{LO}$, of which the ones at $(\omega_c \pm 2\omega_{LO})$ are the strongest. These harmonics beat during photo-detection in the RAP for generating a frequency-quadrupled signal at $4\omega_{LO}$.

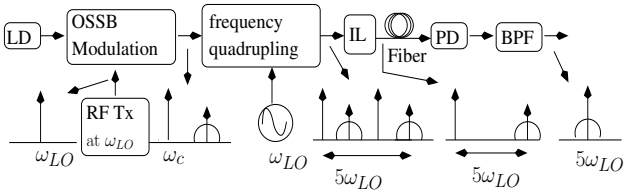

Figure 3.66: Frequency quintupling

d) **Frequency quintupling**: Fig. 3.66 shows the block diagram of frequency quintupling, which can be achieved by employing two stages. The output of a laser operating in the BS at $f_c = \frac{\omega_c}{2\pi}$ Hz enters the first modulation stage, which is driven by a RF signal at $f_{LO} = \frac{\omega_{LO}}{2\pi}$ Hz and it generates an OSSB signal, as shown in Fig. 3.66. The second stage is driven by a RF tone at f_{LO} Hz and it implements frequency quadrupling, which generates an optical signal whose spectrum

is shown in Fig. 3.66. The interleaver of Fig. 3.66 then separates the $5\omega_{LO}$-spaced sidebands, and these sidebands beat during the photo-detection in the RAP to generate a frequency-quintupled signal [54].

e) **Frequency six-tupling**: Frequency six-tupling refers to the technique where the PD's output signal has a carrier frequency that is six times that of the transmitted RF signal. Diverse architectures may be used for frequency six-tupling.

First, the previously discussed OFM architecture of Fig. 3.56(c) can be employed for achieving frequency six-tupling. The discriminator commonly used in OFM assisted N-tupling is an MZI [197]. The photo-detected signal of Fig. 3.56(c) includes the up-converted signals corresponding to all values of N, where frequency six-tupling can be achieved by filtering out the sideband at $N = 6$, resulting in $\omega_{RF} = 6\omega_{LO}$.

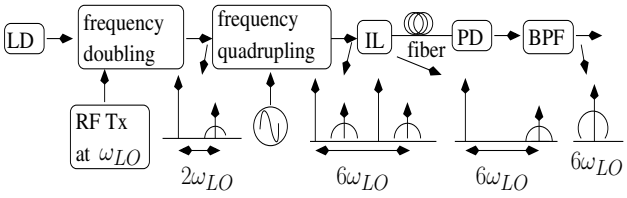

Figure 3.67: Frequency Six-tupling

Additionally, Fig. 3.67 shows another block diagram designed for achieving frequency six-tupling in two stages. The output of the laser in the BS is fed to the first stage, which implements frequency doubling by generating a frequency-doubled OSSB signal. The output of the first stage is then fed to the second stage, which implements frequency quadrupling, thereby generating an optical signal whose spectrum is shown in Fig. 3.67. The $6\omega_{LO}$-spaced sidebands are separated using an interleaver and are transmitted to the RAP over the optical fiber. At the RAP, these sidebands beat during photo-detection for generating a frequency six-tupled signal [54].

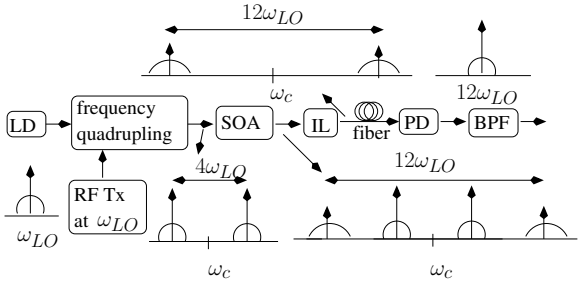

Figure 3.68: Frequency 12-tupling

f) **Frequency 12-tuping**: Fig. 3.68 shows a block diagram conceived for frequency 12-tupling, which can be achieved by feeding the output of a laser operating in the BS at $f_c = \frac{\omega_c}{2\pi}$ Hz to a frequency quadrupling stage. This generates $4\omega_{LO}$-spaced sidebands at $\omega_c \pm 2\omega_{LO}$, as shown in Fig. 3.68. Subsequently, the FWM in a SOA results in the generation of new optical frequencies at $(\omega_c \pm 6\omega_{LO})$ according to Equation (2.25). These $12\omega_{LO}$-spaced sidebands are then separated using the interleaver of Fig. 3.68. Then, during photo-detection in the RAP, the beating of these $12\omega_{LO}$-spaced sidebands generates a frequency 12-tupled signal [198].

The discussion presented so far in this section assumed having an ideal extinction ratio of $\gamma = 1$ in Equation (2.10b), because a non-ideal extinction-ratio results in imperfect attenuation of the suppressed harmonics in the optical field and hence reduces the power of the desired harmonics. For example, Equation (3.33) states that the optical field has only odd harmonics for case of MITP biasing. However, when we have $\gamma \approx 1$, the optical field also has imperfectly suppressed even harmonics.

The photo-detected signal power at a frequency of f_{RF} suffers from a Dispersion Induced Power Penalty (DIPP) due to the fiber's chromatic dispersion [190], where the extent of the power penalty depends on the modulation index of the modulation by the LO [190]. The distortion is minimized for the optimum values of the LO oscillator modulation index, for which the expression for DIPP can be simplified by neglecting non-dominant terms as follows [190]:

1. For QP biasing:

$$DIPP \approx \cos(\beta_2 f_{IF} f_{RF}) \cos(\beta_2 f_{LO} f_{RF}); \tag{3.37}$$

2. For MATP biasing

$$DIPP \approx \cos(\beta_2 f_{IF} f_{RF}) \ \ \forall \ N = 4 + 4k \tag{3.38a}$$
$$\approx \cos(\beta_2 f_{IF} f_{RF}) \cos(2\beta_2 f_{LO} f_{RF}) \ \forall \ N = 2 + 4k; \tag{3.38b}$$

3. For MITP biasing

$$DIPP \approx \cos(\beta_2 f_{IF} f_{RF}) \ \ \forall \ N = 2 + 4k \tag{3.39a}$$
$$\approx \cos(\beta_2 f_{IF} f_{RF}) \cos(2\beta_2 f_{LO} f_{RF}) \ \forall \ N = 4 + 4k; \tag{3.39b}$$

where we have $\beta_2 = (\pi D \lambda_c^2 L)/c$, D is the chromatic dispersion parameter, L is the length of the optical fiber, c is the speed of light in vacuum and λ_c is the optical carrier wavelength.

It is inferred from Equation (3.38) that when biasing at the MATP, it is better to employ photo-detected harmonics of the order $N = (4 + 4K)$ in order to minimize the DIPP. On the other hand, observe from Equation (3.39) that it is better to employ photo-detected harmonics of the order $N = (2 + 4K)$ [190], when biasing at MITP, in order to minimize the DIPP. In general, the extent of DIPP, when biasing is done at MATP or MITP is less than that for the case of QP biasing [199]. The values of f_{IF} and f_{RF} are decided by the specifications of the network for which the ROF link is the backhaul. Thus, observe from Equation (3.28) that there is an N versus f_{LO} trade-off, where a higher N results in the ability to employ a lower f_{LO} [190] and hence reducing the electrical bandwidth requirement of the MZM. On the other hand, when N increases, the strength of the LO signal that is required for generating a strong harmonic increases and the achievable strength of the up-converted photo-detected signal also decreases. Thus, for large values of N, a MZM that can handle high values of drive power is required. For example, a peak-to-peak amplitude larger than twice the switching voltage may be needed in the case of frequency quadrupling for achieving the desired performance [200]. One of the solutions proposed in [200] was to achieve frequency quadrupling by performing frequency doubling twice [200], [201], [202].

The N-tupling techniques employ optical harmonics instead of optical inter-modulation, where the difference between the two was detailed in Section 2.1.3.1. As discussed in Section 2.1.3.1, the undesired effect of optical inter-modulation occurs when a multi-channel, i.e. multi-frequency, modulating signal

is employed in optical modulation. Upon comparing the transmittance curves of Fig. 2.6(b) and Fig. 2.9(a), it can be stated that the more non-linear transfer function of the MZM results in the generation of stronger inter-modulation products, as compared to direct modulation. Single-step N-tupling in a multi-channel scenario involves the MZM assisted modulation using multiplexed RF signals and hence has strong optical inter-modulation products [90]. By contrast, the inter-modulation signals are weaker in 2-step N-tupling, because multiplexed IF signals can be employed in the more linear direct modulation during the first step, while the subsequent MZM assisted upconversion step uses a single-frequency LO tone. Additionally, one of the major advantages of such a two-step implementation of optical N-tupling can be observed in a WDM system, as shown in Fig. 3.69, which requires photo-detected signals to be generated at high RF carriers [203]. Direct modulation of the laser diodes cannot be readily achieved using RF signals at high frequencies, while the employement of an external modulator for each source is expensive. Hence, as shown in Fig. 3.69, the lasers are directly modulated with their respective baseband/IF data and then the multiplexed outputs are fed into a MZM modulator, that is driven by a local oscillator at f_{LO} Hz for simultaneous upconversion [158]. This ensures that each wavelength carries an up-converted optical signal. However, 2-step N-tupling results in an increased transmitter cost, since there are two modulation steps.

Furthermore, the two-step N-tupling may also be performed in the reverse order as shown in Fig. 3.62, where modulation using a LO (Upconversion step) followed by the modulation using the IF/baseband data is employed [176]. In this case the first modulation is RF and it may be beyond the direct modulation bandwidth of the laser to be used. Hence, such an ordering may require both steps to be based on external modulation.

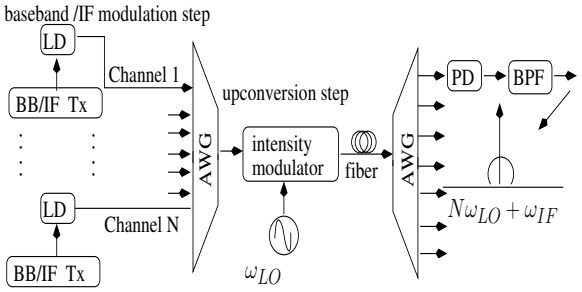

Figure 3.69: Optical upconversion of WDM signal

According to the discussions in Section 3.3.1.1, the photo-detected signal consists of either only odd or only even harmonics, when intensity modulation based N-tupling is employed. However, the OFM technique illustrated in Fig. 3.56(c) can employ any value of N [191], which provides a greater flexibility for the designer, including the ability to implement dynamic radio channel assignment [204],[191]. Explicitly, the designer can dynamically generate the wireless signal at any frequency, which is a multiple of f_{LO} Hz.

Having discussed the subclass of optical N-tupling techniques within the family of techniques in Fig. 3.54 that rely on the non-linearity of the MZM for optical upconversion, we now move on to discussing the next subclass within the same family of techniques. Optical N-tupling relied on optical harmonics for achieving optical upconversion. By contrast, the next subclass of techniques achieves optical upconversion by relying on optical inter-modulation, as shown in Fig. 3.54.

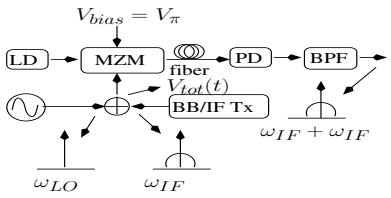

Figure 3.70: Optical upconversion using optical inter-modulationl

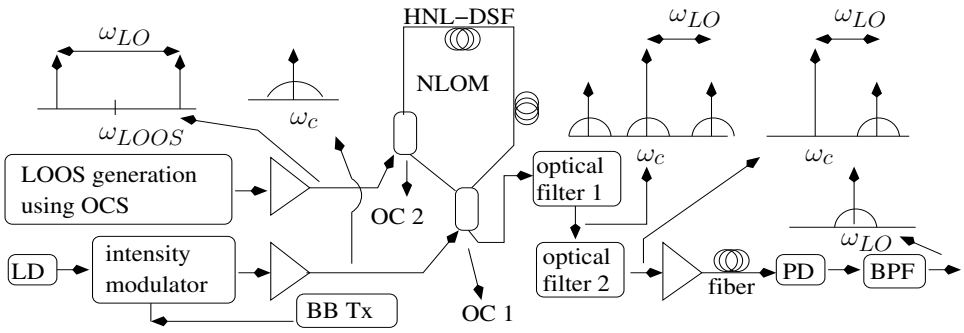

Figure 3.71: XPM assisted upconversion

Optical upconversion relying on optical inter-modulation It can be inferred from the transmittance curve of Fig. 2.9(a) that the highly non-linear transfer function of the MZM results in the generation of strong inter-modulation products, which can be exploited for achieving optical upconversion. The baseband/IF signal at $f_{IF} = \frac{\omega_{IF}}{2\pi}$ Hz is added to the local oscillator signal at $f_{LO} = \frac{\omega_{LO}}{2\pi}$ Hz, where the combined drive signal of $V_{tot}(t) = V_{IF}\cos(\omega_{IF}t) + V_{LO}\cos(\omega_{LO}t)$ is invoked for driving the MZM in the BS that is biased at MITP for achieving OCS intensity modulation, i.e. we have $V_{bias} = V_\pi + m2V_\pi$, where m is an integer. Using Equation (2.6d) and the Taylor series expansion of $\cos(x)$ [205], the intensity of the output is given by:

$$\begin{aligned} P(t) &= P_{in}[1 - \cos\left(\frac{\pi V_{tot}(t)}{V_\pi}\right)], \\ &= P_{in}\left[1 - \left(1 - \frac{1}{2}\left(\frac{\pi V_{tot}(t)}{V_\pi}\right)^2 + weaker\ terms\right)\right] \\ &\approx P_{in}\frac{\pi^2}{2V_\pi^2}[V_{IF}^2\cos^2\omega_{IF}t \\ &+ V_{LO}^2\cos^2\omega_{LO}t + 2V_{IF}V_{LO}\cos(\omega_{IF}t)\cdot\cos(\omega_{LO}t)] \end{aligned} \tag{3.40}$$

The third term in Equation (3.40) generates modulated RF signals at $\omega_{RF} = (\omega_{LO} \pm \omega_{IF})$. As mentioned previously, the photo-detected signal is proportional to the optical intensity. Hence, in the RAP, the up-converted signals at $\omega_{RF} = (\omega_{LO} \pm \omega_{IF})$ can be retained from the photo-detected signal by the BPF of Fig. 3.70 [206],[207]. Biasing at MATP also generates photo-detected signals at $\omega_{RF} = (\omega_{LO} \pm \omega_{IF})$, but the achievable optical SNR is higher if biasing is done at MITP than for MATP owing to the former's reduced RIN noise [129]. Hence the MZM performs the function of a mixer along with that of an optical modulator. This enables the ROF system to avoid the use of high RF mixers, which would have otherwise degraded the BER of wireless communication.

The optical upconversion techniques discussed so far exploited the non-linearity of the MZM situated at the transmitter. Let us now discuss the family of wavelength-conversion based optical upconversion techniques shown in Fig. 3.54, which rely on the non-linearity of other optical network components, such as the optical fiber, the SOA and the EAM.

3.3.1.2 Wavelength-conversion based optical upconversion

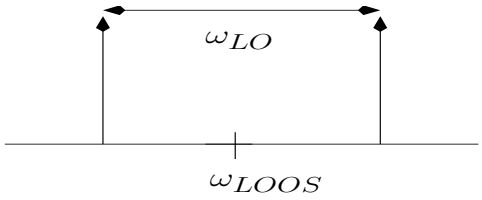

Figure 3.72: Local oscillator optical signal

Modulating the laser's $f_c = \frac{\omega_c}{2\pi}$ Hz output using a MZM biased at the MITP and driven by a RF tone at $f_{LO}/2$ Hz generates an optical signal that consists of odd harmonic frequencies with the first harmonics at $\omega_c \pm (\omega_{LO}/2)$ being dominant. This signal has the spectrum shown in Fig. 3.72 and is referred to as a f_{LO} Hz LO Optical Signal (LOOS) because its photo-detection generates a LO electronic signal at the difference frequency of $f_{LO} = \frac{\omega_{LO}}{2\pi}$ Hz. It must be noted that a f_{LO} Hz LOOS at f_{LOOS} Hz is located at an optical frequency of f_{LOOS} Hz and generates a f_{LO} Hz electronic tone on photo-detection.

Optical wavelength conversion refers to the process of copying the transmitted data from one wavelength at $f_c = \frac{\omega_c}{2\pi}$ Hz to another at $f_{LOOS} = \frac{\omega_{LOOS}}{2\pi}$ Hz. If the wavelength at ω_c carries the baseband/IF data signal, while the wavelength at ω_{LOOS} carries a LOOS prior to wavelength conversion, then the process of wavelength conversion also results in optical upconversion, i.e. the photo-detection of the output optical signal generates the up-converted data signal at f_{LO} Hz.

Wavelength conversion based non-linear techniques facilitate cost savings with the aid of wavelength re-use [208] and does not rely on the polarization-sensitive MZM. Additionally, the ability to move data from one wavelength to another facilitates optical switching [31], while using a f_{LOOS} Hz wavelength having different values of the f_{LO} Hz LOOS enables wireless frequency selection in WDM-ROF networks. Wavelength conversion techniques exploit the non-linearity of fibers [185], of the SOA [187] or EAM [188], as discussed in the following sections.

Techniques based on the non-linearity of the fiber As discussed in Section 2.1.1.3, the dependence of the fiber's refractive index on the optical power introduces a non-linear phenomenon referred to as XPM. Additionally, it was also mentioned in Section 2.1.1.3 that a second strong non-linear phenomenon known as FWM is present, when the dispersion parameter D is small. Most ROF optical systems operate at 1550 nm because of the low fiber attenuation at that wavelength, while zero dispersion occurs at 1300 nm [31]. A Highly Non-linear Dispersion-Shifted Fiber (HNL-DSF) is a special fiber that has a highly non-linear refractive-index, while the zero-dispersion wavelength is shifted from 1300 nm to 1550 nm. In the context of wavelength conversion techniques, the signals are propagated through a certain length of the HNL-DSF in order to exploit these non-linear phenomena.

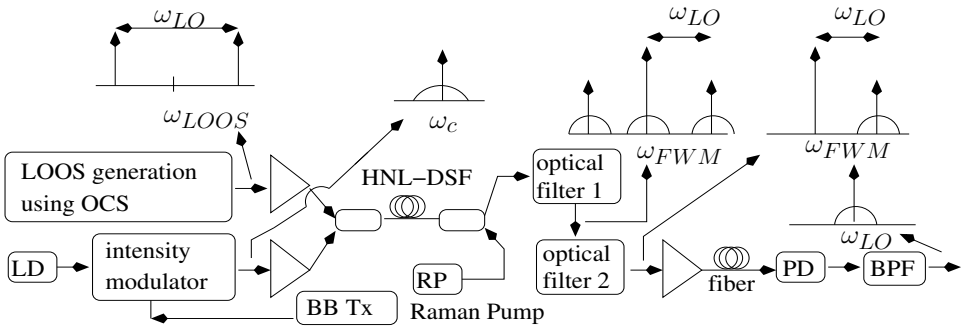

Figure 3.73: FWM assisted upconversion

Fig. 3.71 shows an XPM-assisted optical upconversion architecture, where, in the BS, the laser output at ω_c is modulated with the baseband data and then this signal is injected into a Non-linear Optical Loop Mirror (NOLM)[1] at OC 1 [185]. As shown in Fig. 3.71, a LOOS at ω_{LOOS} is injected into the loop at OC 2, where the LOOS modulates the phase of the two counter-propagating ω_c-frequency signals through XPM [185]. The two counter-propagating, phase modulated ω_c-frequency waves are then combined again at OC 1 after propagating through the entire loop. The intensity of the combined signal depends on the phase difference of the two waves. Thus, the NOLM induces XPM in the signal at ω_c using the signal at ω_{LOOS} and then performs phase-to-intensity conversion. Hence, the NOLM output consists of the LOOS at ω_{LOOS} and the XPM-assisted intensity-modulated signal at ω_c. The spectrum of the intensity modulated output of the NLOM at ω_c is similar to an ODSB signal, where Fig. 3.71 shows the ODSB spectrum after the elimination of the *LOOS* at ω_{LOOS} using optical filter 1 [185]. Afterwards, one of the sidebands of the ODSB signal is eliminated by optical filter 2 for generating an OSSB signal. The optical frequencies of $f_{LOOS} = \frac{\omega_{LOOS}}{2\pi}$ Hz and $f_c = \frac{\omega_c}{2\pi}$ Hz are not sufficiently close to each other for enabling the use of a single filter, instead of the two step filtering. The OSSB signal is then amplified, transmitted over the ROF link to the RAP and photo-detected for generating a RF signal at ω_{LO}. Although the architecture of Fig. 3.71 employs a single baseband-data modulated wavelength at ω_c, this concept can be extended to a WDM signal that is generated by combining the data-modulated outputs of several lasers. This WDM signal would then be combined with the LOOS at ω_{LOOS} in a NLOM and employed for optical upconversion [185].

Additionally, the FWM can be employed for achieving optical upconversion [209]. Fig. 3.73 shows the block diagram of an architecture that implements optical upconversion using FWM, where, in the BS, the laser output at ω_c is modulated by the baseband data. The modulated signal is then injected into the HNL-DSF of Fig. 3.73 along with a LOOS at ω_{LOOS}, as shown in Fig. 3.73. The FWM in the fiber generates new signals as per Equations (2.24) and (2.25), where the spectrum of the signal at the output of the HNL-DSF is shown in Fig. 3.74. The up-converted signal at ω_{FWM} is retained by eliminating the signals at ω_c and ω_{LOOS} through optical filtering. As shown in Fig. 3.73, optical filter 2 then converts the ODSB signal at ω_{FWM} to the OSSB signal, which is more chromatic dispersion tolerant. This signal is then transmitted over the fiber and photo-detected in the RAP for generating a RF signal at ω_{LO}. The strength of the FWM signal can be increased by employing

[1]A NOLM is an architecture where the input signal at ω_c is split into two waves by the coupler OC 1, as shown in Fig. 3.71. These two waves propagate in opposite directions (clockwise and counter-clockwise) in a fiber-loop made from HNL-DSF and hence acquire different phases due to fiber non-linearity.

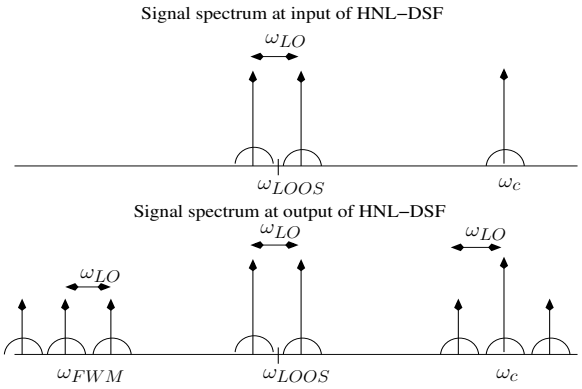

Figure 3.74: FWM assisted upconversion spectrum

the SRS described in Section 2.1.1.3 [209]. As shown in Fig. 3.73, the output of a laser, that is referred to as Raman Pump (RP), is counter-propagated, where the energy from the higher-frequency, higher-power pump signal is transferred to the lower-frequency, lower-power FWM with the aid of the SRS phenomenon discussed in Section 2.1.1.3 [209]. Although the architecture of Fig. 3.73 employs a single baseband-data modulated wavelength at ω_c, this concept can be extended to a WDM signal that is generated by combining the data modulated outputs of several lasers. This WDM signal would then be combined with the LOOS at ω_{LOOS} and employed for optical upconversion [209].

Techniques based on the non-linearity of the semiconductor optical amplifiers Semiconductor Optical Amplifiers (SOAs) exhibit non-linearities similar to those in optical fibers. Additionally, the SOAs also suffer from gain saturation. The SOAs can be utilised for optical upconversion by exploiting the XPM, FWM and Cross Gain Modulation (XGM) phenomena.

XPM occurs in a SOA in a manner similar to that in fibers, where an architecture similar to that in Fig. 3.71 can be used, except that the signals at ω_c and ω_{LOOS} are injected into a SOA-Mach Zehnder Interferometer (SOA-MZI) instead of the NOLM[187] of Fig. 3.71. Fig. 3.75 illustrates the architecture of an SOA-MZI, where the combining of the phase modulated signals in the SOA-MZI results in intensity modulation.

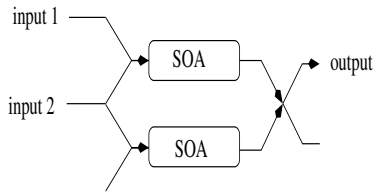

Figure 3.75: Semiconductor Optical Amplifier Mach Zehnder Interferometer

Furthermore, the phenomenon of FWM can also be exploited using SOAs, where a LOOS at ω_{LOOS} and an optical signal at ω_c carrying the baseband/IF signal are fed to a SOA. This architecture is similar to that of Fig. 3.73, except that the phenomenon of FWM in SOA is employed instead of the SRS-assisted FWM in HNL-DSF, where the process of FWM results in the generation of optical signals at new wavelengths, which result in up-converted RF signals after photo-detection in the RAP[210].

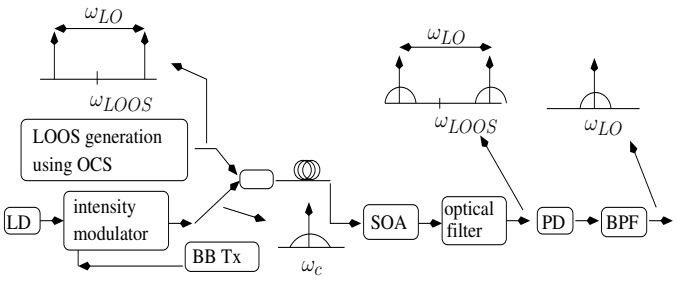

Figure 3.76: XGM assisted upconversion in a SOA

On the other hand, the optical gain of a SOA saturates as the total input power increases. As shown in Fig. 3.76, a high-power $P_c(t)$ dBm optical signal $E_c(t)$ at ω_c that carries a baseband/IF signal and a low-power $P_{LOOS}(t)$ dBm optical LOOS $E_{LOOS}(t)$ at ω_{LOOS} are combined and entered into the SOA. The gain $G_{amp}\{P_c(t) + P_{LOOS}(t)\}$ of the SOA varies as per the instantaneous power of the high-power optical signal at ω_c, i.e. the output $z(t)$ of the amplifier becomes:

$$\begin{aligned} z(t) &= G_{amp}\{P_c(t) + P_{LOOS}(t)\} \cdot [E_c(t) + E_{LOOS}(t)] \\ &= G_{amp}\{P_c(t)\}[E_c(t) + E_{LOOS}(t)] \text{ as } P_c(t) + P_{LOOS}(t) \approx P_c(t) \\ &= G_{amp}\{P_c(t)\} \cdot E_c(t) + G_{amp}\{P_c(t)\} \cdot E_{LOOS}(t). \end{aligned} \tag{3.41}$$

Thus, it can be seen from the second term of Equation (3.41) that the low-power LOOS is modulated in accordance with the intensity of the high-power signal. This effect is referred to as XGM [208]. As shown in Fig. 3.76, the signal at ω_c is eliminated from the output of the SOA by the optical filter, where the filtered optical spectrum of the XGM-modulated LOOS at ω_{LOOS} is shown in Fig. 3.76. After photodetection in the RAP, the modulated LOOS generates an up-converted RF signal at ω_{LO}, as shown in Fig. 3.76 [208].

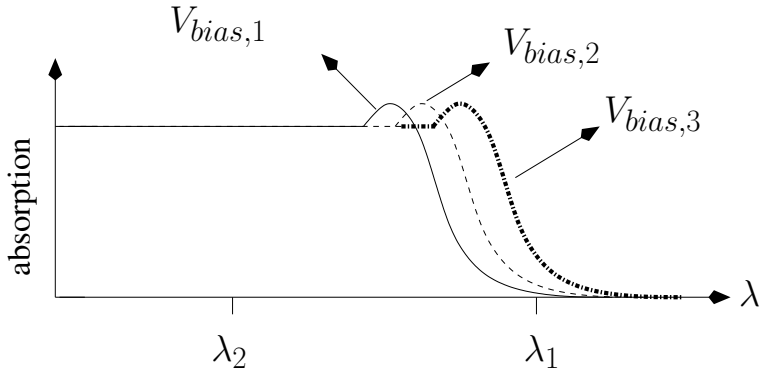

Figure 3.77: EAM absorption at different optical wavelengths

Techniques based on the non-linearity of the electro absorption modulator Fig. 3.77 shows the EAM's absorption/transmittance characteristics. While the wavelength λ_c, corresponding to frequency of $f_c = \frac{\omega_c}{2\pi}$ Hz, is largely absorbed, the wavelength λ_{LOOS}, corresponding to frequency of $f_{LOOS} = \frac{\omega_{LOOS}}{2\pi}$ Hz, is partially transmitted/absorbed. Fig. 3.78 shows the block diagram of an architecture that relies on the EAM's non-linearity for achieving optical upconversion, where, in the

BS, a high power optical signal at ω_c that carries IF/baseband data enters port 1 and exits from port 2 of the optical circulator, which is then injected into an EAM. A LOOS at ω_{LOOS} is also injected into the EAM. The absorption of the high power optical signal at ω_c results in the edge of the absorption spectrum[1] seen in Fig. 3.77 shifting to lower wavelengths due to the EAM's non-linearity. Hence, as the instantaneous power of the signal at ω_c increases, the extent of absorption of the signal at ω_{LOOS} drops and vice-versa [188], [211]. Thus, the signal at ω_{LOOS} is intensity modulated by the instantaneous power of the signal at ω_c, thereby resulting in the modulation of the LOOS at ω_{LOOS} by the IF/baseband data that was on the optical signal at ω_c. This phenomenon is referred to as Cross Absorption Modulation (XAM)[188]. As shown in Fig. 3.78, the modulated LOOS enters port 2 and exits via port 3 of the optical circulator. It is then transmitted to the RAP and photo-detected for generating an up-converted signal at ω_{LO} [188]. An isolator is used in the architecture of Fig. 3.78 for blocking the propagation of light into the LOOS generation module.

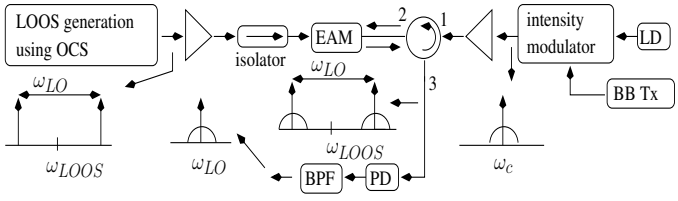

Figure 3.78: Optical upconversion using XAM in a SOA

Analysis of the wavelength conversion techniques The disadvantage of the techniques that exploit fiber non-linearity is the large length of the HNL-DSF that is needed. On the other hand, SOA amplifiers have a low modulation bandwidth and also suffer from a carrier-saturation effect [185]. The limited modulation bandwidth makes it difficult to employ a LOOS whose photo-detection would generate high RF signals, whilst the carrier saturation in a SOA limits the number of WDM channels that may be employed and hence it limits the capacity of the ROF network [185].

The advantage of FWM-based optical upconversion is that FWM does not depend on the bit-rate and on the wireless/optical modulation format [209]. Since XPM and XGM depend on the instantaneous optical power level, the efficiency of the wavelength converters based on these techniques depends both on the bit-rate and on the optical/wireless modulation formats employed, where only intensity modulated baseband/IF optical signals can be up-converted [185]. The main disadvantage of employing a XGM-based wavelength converter is the degradation of the extinction-ratio [3] due to the underlying bit-rate versus extinction-ratio trade-off. However, the conversion efficiency of the wavelength converters based on XPM/XGM is higher than those based on FWM [212].

Let us now discuss the final set of techniques conceived for optical upconversion, namely the family of techniques seen in Fig. 3.54 that rely on the non-linearity of the optical receiver. In other words, they rely on the non-linearity of the photo-detector.

[1] A plot representing the extent to which various frequencies are absorbed.

[3] Extinction-ratio is the ratio of the optical power transmitted for bit 1 to that transmitted for bit 0. It has an ideal value of ∞.

Table 3.7: Comparison of wavelength conversion techniques

phenomenon/hardware employed	challenges
fiber-based	large length of fiber needed
SOA-based	low modulation bandwidth, carrier saturation and polarization sensitivity
FWM	lower conversion efficiency than XPM/XGM
XPM/XGM	conversion efficiency depends on bit rate and modulation format

3.3.1.3 Optical upconversion using the non-linearity of the photodetector

The non-linear behaviour of the photo-detector can be exploited for achieving optical upconversion, where the mixing efficiency and hence the strength of the up-converted signal is not high [213]. The architectures that implement this kind of optical upconversion include modulating the bias voltage of the photo-detector as well as exploiting the non-linear nature of the photo-detector responsivity.

A photo-detector consists of a reverse biased diode that generates a current when illuminated with light, where the bias voltage is normally constant. Modulating the bias voltage of the photodetector can be used for optical upconversion[186], [213]. Fig. 3.79 shows the block diagram of optical upconversion relying on the modulation of the photo-detector's bias voltage, where the baseband/ IF modulated optical signal at ω_c and a LOOS at ω_{LOOS} are transmitted over two different fiber links from the BS to the RAP. The LOOS is generated at the BS and remotely transmitted to the RAP for photo-detection by PD 2 of Fig. 3.79 for generating a RF tone at ω_{LO}, which is then applied to the bias terminal of the photo-detector PD 1 employed for detecting the optical signal at ω_c. This would result in the photo-detected signal containing up-converted data at $\omega_{RF} = (\omega_{LO} \pm \omega_{IF})$ [214], where $f_{IF} = \frac{\omega_{IF}}{2\pi}$ is the frequency of the baseband/IF data. A single fiber link can also be employed instead of employing two fiber links, provided ω_c and ω_{LOOS} are not the same. Moreover, in such a scenario, optical filters would be needed at the BS to separate the signals at ω_c and ω_{LOOS}.

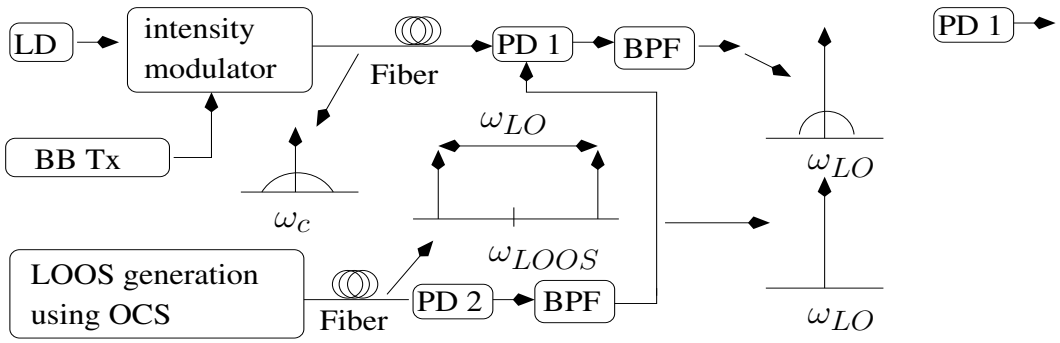

Figure 3.79: Optical upconversion by modulating PD bias

On the other hand, the photo-detector current is ideally linearly dependent on the incident optical power. However, the photo-detector's response becomes strongly non-linear, when the incident optical power is high and the reverse bias voltage is low [215],[213]. Fig. 3.80 shows the block digram of optical upconversion relying on the non-linear responsivity of the photo-detector, where, in the BS, the baseband/ IF modulated optical signal at ω_c and a LOOS at ω_{LOOS} are transmitted over the fiber and are then incident on a non-linear photo-detector in the RAP [213]. The photo-detected signal contains the up-converted data at $\omega_{RF} = (\omega_{LO} \pm \omega_{IF})$, where $f_{IF} = \frac{\omega_{IF}}{2\pi}$ is the frequency of the baseband/IF data [213]. The disadvantage of this technique is that reducing the reverse-bias voltage decreases the detection bandwidth of the photo-detector.

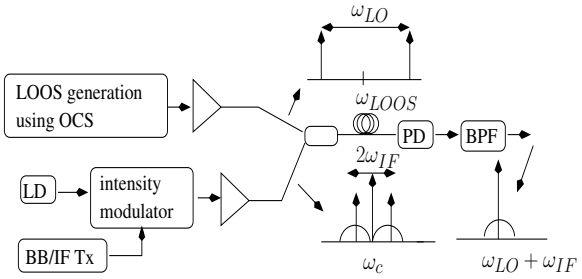

Figure 3.80: Optical upconversion using non-linear responsivity

In concluding this section, we emphasize that the techniques discussed in this section can be employed for generating high-RF MB-OFDM signals without relying on high-RF oscillators and mixers, whose employement would otherwise degrade the BER. In the next section we consider another WPAN communication technique, namely IR-UWB.

3.3.2 Optical generation of impulse radio ultra wide band signals

The challenges associated with the use of IR-UWB wireless signals in WPANs were discussed in Section 1.5.3.3, where the optical generation of these signals and their subsequent transmission using ROF links was advocated as a potential solution. A basic ROF link was discussed in Section 2.1.1, while this section discusses the various optical techniques used for the generation of IR-UWB signals.

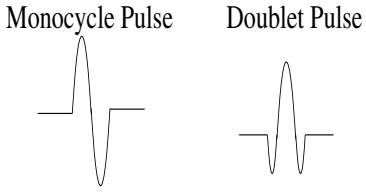

Figure 3.81: IR-UWB pulses

Fig. 3.81 shows the so-called Gaussian monocycle and Gaussian doublet pulses [52], which are the most commonly used pulses because of their attractive BER performance and their higher resilience to multi-path-induced wireless impairments [52]. As shown in Fig. 3.82, in OOK, bits '1' and '0' are transmitted using the presence and absence of a pulse in the bit-period, respectively, while PPM uses pulses with opposite polarity to transmit bits '1' and '0'. Finally, PSM uses two different pulse shapes,

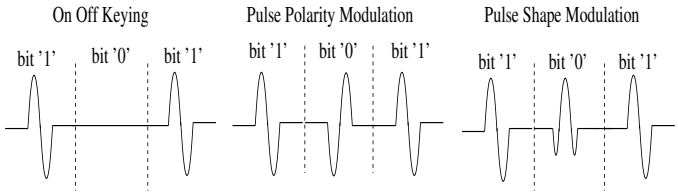

Figure 3.82: IR-UWB modulation schemes

such as the Gaussian monocycle and Gaussian doublet pulses, to transmit bits '1' and '0', as shown in Fig. 3.82.

3.3.2.1 Signal differentiation

The monocycle and doublet pulses of Fig. 3.81 discussed in Section 1.5.3.1 can be generated by differentiating the time-domain waveform of a Gaussian pulse optically/electronically in the following ways:

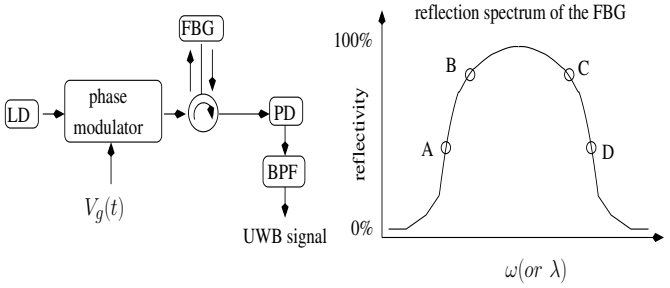

Figure 3.83: Differentiation of phase modulated signal using a FBG filter

Phase modulator and fiber bragg grating filter A FBG filter is constituted by a fiber section having a periodic perturbation of the effective refractive index along the length of the fiber core, which transmits some wavelengths and reflects others. Fig. 3.83 shows an architecture that optically generates the monocycle or doublet pulses of an IR-UWB signal [55], where the output of a phase modulator, that is fed by a laser and driven by a Gaussian pulse-train $V_g(t)$, enters a FBG optical filter that has the reflectivity profile of Fig. 3.83 and achieves phase to intensity conversion. Points {A, D } and {B, C} are located in the linear slope and quadrature slope regions of the reflectivity profile of Fig. 3.83, respectively. For optical carrier frequencies located at points A and B, the photo-detected signal is proportional to the first and second derivative of $V_g(t)$, respectively [55], which yields monocycle and doublet pulses, respectively [55]. Locating the optical carrier frequencies at points C and D generates inverted photo-detected doublet and monocycle pulses, respectively [55]. Thus, upon using two different optical frequencies we can generate a IR-UWB signal that utilises pulse polarity modulation (e.g. using points A and D) or pulse shape modulation (e.g. using points A and B) [55].

Phase modulator and optical fiber Another technique of generating IR-UWB signals for WPANs is to exploit the dispersive fiber's response, when employing phase modulated optical signals. Fig.

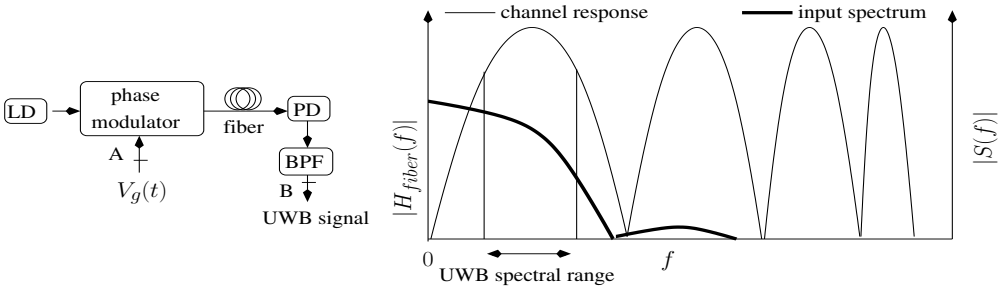

Figure 3.84: UWB generation using chromatic dispersion

3.84 shows an architecture implementing this technique. As shown in Fig. 3.84, the output of the laser operating at wavelength λ_c is phase modulated by a baseband binary signal $V_g(t)$ that employs Gaussian-like time domain pulses. This phase modulated signal then propagates to the RAP for photo-detection through a dispersive optical fiber of length L, where the frequency response between points A and B seen in Fig. 3.84 is dominated by the dispersive fiber as follows: $H_{fiber}(f) = \cos(\frac{\pi \cdot L \cdot D \cdot \lambda_c^2 \cdot f_{RF}^2}{c} + \frac{\pi}{2})$ [216], where D is the chromatic dispersion parameter, c is the speed of light in vacuum and f is the frequency of the modulating signal. As seen from Fig. 3.84, the frequency response has a bandpass nature with nulls at $f_{null,1} = 0$ Hz and $f_{null,2} = \sqrt{\frac{c}{LD\lambda_{OC}^2}}$ Hz, while it has an intermediate maximum at $f_{max} = \sqrt{\frac{c}{2LD\lambda_{OC}^2}}$ Hz, where this results in PM-IM conversion. By varying L, we can create a bandpass filter, which has a -10 dB bandwidth between 3 GHz and 10.9 GHz, which by definition represents the spectrum of a UWB signal [216]. For example, a baseband signal $V_g(t)$ consisting of a 13.5 Gbps stream of Gaussian-like time domain pulses, having a Full Width at Half Maximum (FWHM) of 63 ps, can be employed to generate doublet pulses having a FWHM of around 40 ps [216].

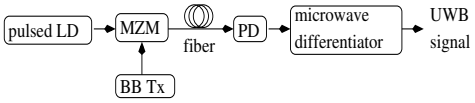

Figure 3.85: UWB generation using microwave differentiator

Microwave differentiator A pulsed laser source generates an optical pulse stream [31]. Fig. 3.85 shows an architecture in which the signal arriving from a Gaussian-pulsed laser is modulated with binary data and transmitted through the optical fiber to the RAP for photo-detection. After photo-detection the signal enters a microwave differentiator, where the differentiation of a Gaussian time domain pulse generates a monocycle pulse [217]. Finally, the differentiated signal is then transmitted by the antenna [217].

3.3.2.2 Signal delay line filtering

If $g(t)$ is a Gaussian time domain pulse, then a monocycle pulse $m(t)$ and a doublet pulse $d(t)$ can be generated by approximating the first and second order differentiation with the aid of the following

difference equations:

$$m(t) = g(t) + (-1 \times g(t-\tau)) \tag{3.42}$$

$$d(t) = g(t) + (-2 \times g(t-\tau)) + g(t-2\tau) \tag{3.43}$$

Equations (3.42) and (3.43) can be implemented in the several ways, two of which are detailed below.

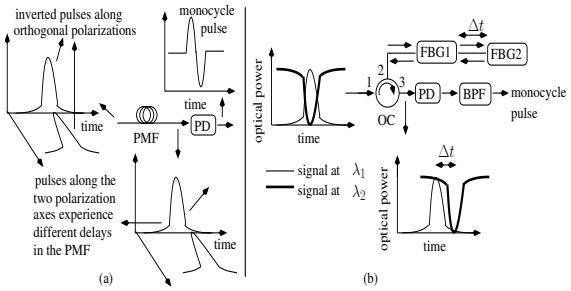

Figure 3.86: UWB generation employing a PMF to create optical delay

The phase shifts introduced by the optical phase modulator in an optical signal are different in the scenarios of the incoming signal being polarized along either of the two modulator axes. Usually, the input signal is polarized along one of the two modulator axes by using a Polarization Controller (PC). By contrast, in the architecture of Fig. 3.86 [218], the input signal is polarized at 45^o with respect to the principal axis, which results in orthogonally polarized components in the input signal along both the modulator axes. Then, a specifically chosen pulsed modulating voltage is applied to the phase modulator of Fig. 3.86, which would result in a phase difference of π between the optical pulses generated along the two modulator axes, which implies that the pulse along one of the axes is an inverted version of that along the other axis [218]. As shown in Fig. 3.86, the output of the phase modulator is adjusted by a second PC and its output is then fed to a Polarization Maintaining Fiber (PMF) in which the propagation delay of the two orthogonally polarized signals is different. Specifically, the fiber length is appropriately adjusted for ensuring that it would result in the inverted pulse being delayed by a particular amount with respect to the non-inverted pulse, for ensuring that the addition of the two pulse shapes through photo-detection results in a monocycle pulse, as shown in Fig. 3.86 [218].

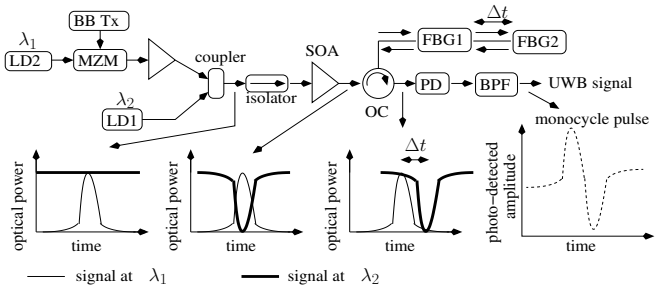

Figure 3.87: UWB generation employing an FBG to create optical delay

XGM in SOAs, which was discussed in Section 3.3.1.2, can be used for generating the negative coefficients of Equations (3.42) and (3.43). Fig. 3.87 shows an architecture in which the output of

laser LD1, that operates at wavelength λ_1 (i.e. frequency f_1), is intensity-modulated by a Gaussian time domain pulse stream, amplified and then combined with the unmodulated output of LD2, that operates at wavelength λ_2 (i.e. frequency f_2) [219]. The combined signal is injected into the SOA of Fig. 3.87, where the XGM results in λ_2 being modulated by the inverse of the data on λ_1, resulting in the signal of Fig. 3.87[219]. The two signals, with fields $E_1(t) = A_1(t)e^{jf_1t}$ and $E_2(t) = A_2(t)e^{jf_2t}$, then enter the OC from port 1 and exit from port 2 of the OC shown in Fig. 3.87, where the FBG filters FBG1 and FBG2 reflect the wavelengths λ_1 and λ_2, respectively. The propagation delay between the two filters introduces the time delay Δt between the reflected wavelengths, which then enter port 2 and exit from port 3 of the OC shown in Fig. 3.87, where photo-detection generates current: $I(t) = R|E_1(t) + E_2(t - \Delta t)|^2 = [A_1^2(t) + A_2^2(t - \Delta t)] + 2|A_1(t)||A_2(t - \Delta t)| \cos((f_1 - f_2)t + \delta\phi)$, with R being the photo-detector's responsivity. The high-frequency third term is filtered out, while the first two terms generate a monocycle pulse, because $A_2^2(t - \Delta t)$ is an inverted delayed version of $A_1^2(t)$ [219]. On the other hand, as seen in Equation (3.43), the generation of doublet pulses requires the formation of three Gaussian time domain pulses, two of which have the opposite polarity with respect to the third pulse. This can be achieved by slightly modifying the architecture of Fig. 3.87, i.e. by using three wavelengths instead of two. Two of these wavelengths are unmodulated and of low power, while the third high-power wavelength is modulated using Gaussian time domain pulses. Similar to Fig. 3.87, these three wavelengths then enter a SOA, where the associated XGM results in the two low-power wavelengths being modulated by an inverted Gaussian time domain pulse stream. Subsequently, three FBG filters are employed for adjusting the delays to that of Equation (3.43) in a manner similar to that in Fig. 3.87. Compared to the techniques that employ phase to intensity conversion, signal delay line based filtering has a higher flexibility, because it can implement various pulse shapes by performing appropriately delayed and scaled additions. However, it has a higher complexity and cost.

3.3.2.3 Signal frequency-to-time mapping

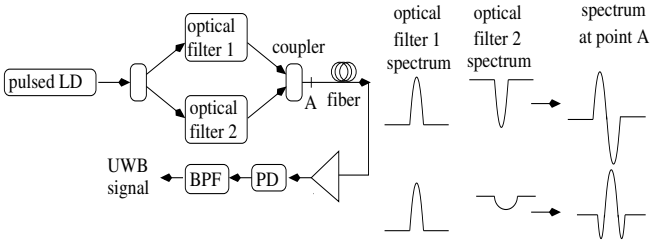

Figure 3.88: UWB generation employing signal frequency-to-time mapping

When an optical signal having particular spectral shape propagates through the fiber, then the fiber-induced dispersion results in the optical signal's time domain waveform acquiring a similar shape. This idea can be used for generating IR-UWB signals for WPANs, as shown in Fig. 3.88. In the architecture of Fig. 3.88, the output of a pulsed laser is fed to a fiber-optics based Frequency Transform Pulse Shaper (FTPS). A FTPS either uses free-space optics based [220] or fiber-optics based [221] optical filters for applying a particular frequency domain shaping function to the wide spectrum of a femto-second-scale pulse stream. The FTPS of Fig. 3.88 splits the input signal into two arms using a splitting ratio that depends on the insertion losses of the optical filters in the two arms [221], where

the spectrum of the two filters is specifically chosen to ensure that the spectrum of the combined signal acquires a shape that is similar to the desired time-domain pulse shape [221]. Subsequently, having been subjected to dispersive fiber propagation, the optical signal then attains a temporal shape that is a scaled version of the applied spectrum shape. This process is referred to as frequency-to-time mapping. As shown in the spectra of Fig. 3.88, a monocycle pulse can be generated by suitably choosing different center wavelengths for the two filters, while a doublet pulse can be generated by using optical filters with the same center wavelength but different spectral widths [221]. Moreover, the phase distortions introduced by the non-ideal antennas can also be overcome by carefully matching the signalling pulse shape to the transfer function of the antennas [222].

3.4 Chapter conclusions

In this chapter, we started our discourse in Section 3.1 by characterizing the main architectures that may be used for improving the ROF communications system's performance, which were categorized in Fig. 3.2. The wavelength-interleaved multiplexing technique discussed in Section 3.1.1 increases the optical spectral efficiency and hence the throughput of the ROF link, while the carrier suppression technique discussed in Section 3.1.2 improves the receiver sensitivity by increasing the depth of the optical modulation. On the other hand, the noise imposed by the optical link can be reduced by the techniques discussed in Sections 3.1.3 and 3.1.4, namely by low-biasing the optical modulator and by employing balanced photo-detection. These techniques have been illustrated in Fig. 3.10 and Fig. 3.11, respectively. The techniques of Optical Injection Locking and optical feed-forward linearization discussed in Sections 3.1.5 and 3.1.6, respectively, not only help in noise-reduction but also in increasing the linearity of the optical modulation. We then went on to discuss other techniques conceived for increasing the linearity of optical modulation, including the employment of linearized modulators, of optical filters as well as of electronic pre-distortion or post-compensation filters, which were portrayed in Fig. 3.16 to Fig. 3.22. We then discussed the multiple fiber transmission scheme of Fig. 3.23 designed for overcoming the non-linear effects of the optical fiber, followed by a discussion of the various schemes of Fig. 3.24 to Fig. 3.31 aimed at overcoming chromatic dispersion. These arrangements included the use of dispersion tolerant modulation schemes, fiber gratings, chirped optical signals, self-phase modulation and finally the use of optical phase conjugation. We then concluded our discussions by presenting the Digitized ROF architecture of Fig. 3.33, which aims for incorporating the benefits of digital optical communication in the conventional ROF link of Fig. 2.1, at the cost of a more complex RAP design.

Naturally, we have to strike a cost versus performance trade-off in the various ROF techniques. Since the performance enhancement techniques of Section 3.1 increase the cost of the ROF link, in Section 3.2 we additionally detail the main cost reduction techniques that may be used in the ROF link of Fig. 2.1. The integration of the ROF network with the FTTH network, as seen in Fig. 3.34 to Fig. 3.39, would reduce the installation costs. However, in such a scenario, the designer has to strike a trade-off between the performance of the baseband optical transmission of the FTTH network and the attainable performance of the ROF transmission. Cost reductions can also be achieved by making the RAP laser-free by re-using the DL optical signal for UL communication, as seen in the architectures of Fig. 3.40 to Fig. 3.51. However, the allocation of a portion of the DL optical power

for UL communication would degrade the DL performance. These wavelength re-use techniques rely on OCRR, ORM or on the use of a modulator-cum-photo-detector, which were discussed in Sections 3.2.2.1, 3.2.2.2 and 3.2.2.3, respectively. The OCRR techniques of Fig. 3.40 to Fig. 3.43 rely on the separation of the DL optical carrier from the DL modulation sidebands, which may require high-selectivity optical filtering. This requirement is relaxed in the ORM techniques of Fig. 3.44 to Fig. 3.47, which however imposes the restrictive conditions discussed in Section 3.2.2.2. The employment of a modulator-cum-photo-detector for implementing wavelength re-use ensures an additional cost reduction. When employing a modulator-cum-photo-detector, conceiving the half-duplex regime of Fig. 3.49 is straightforward. By contrast, the full-duplex communication of Fig. 3.50 or Fig. 3.51 either involves a DL versus UL performance trade-off or employs a pair of optical wavelengths, respectively. Finally, another technique of reducing the ROF system's cost in a multi-RAP and/or multi-user scenario is to decrease the number of lasers employed in the BS, which can be achieved by using multi-mode laser sources, as shown in Fig. 3.52(a) or by employing the modulation harmonics as shown in Fig. 3.52(b) and Fig. 3.53.

We then characterized the family of ROF links, that employ optical generation of the RF signals, as a solution to tackle the challenges in designing high data-rate WPANs based on the IEEE 802.15.3c and UWB standard. These standards use OFDM/MB-OFDM signals relying on high-RF carriers and IR-UWB signals based on narrow time domain pulses. A migration to higher RF carriers imposes the challenge of having to use small cells. Moreover, the UWB standard imposes strict limitations on the maximum tolerable wireless powers, which also results in the need to use small cells. Additionally, the employment of high-RF carriers requires the use of expensive broadband mixers in case of OFDM/MB-OFDM signals. Similarly, expensive electronic hardware is needed for the generation of the narrow pulses of IR-UWB systems.

Optical generation of RF signals at the BS enables the network designer to avoid the use of broadband mixers or expensive electronic hardware. We have shown in this chapter how to apply optical upconversion for WPANs using OFDM/MB-OFDM and also described the optical generation of the IR-UWB signals.

Having discussed the three design approaches of this chapter, we now present novel architectures that employ these approaches. While Chapter 4 presents novel architectures that employ cost reduction and optical RF-generation techniques, Chapter 5 presents a novel architecture employing the performance improving technique of digitized ROF.

Chapter 4

Novel low cost AROF architectures employing optical RF-generation

Various cost-reduction and performance improvement techniques were discussed in the previous chapter. In this chapter, we now employ these techniques to design three novel AROF architectures that have a low cost as well as a robust performance. Moreover, these architectures employ optical generation of RF signals through optical upconversion. It should be noted that we achieve cost reduction through complexity reduction. In other words, reducing the number of optical components required for supporting multiple users or services was the aim of our design. The novel architectures proposed in this chapter have a lower implementation cost, because they employ fewer or lower-complexity optical modulators or both. The difference in the cost between the proposed techniques and the classical approaches certainly becomes significant, when viewed in conjunction with the fact that having over 3 million small cells is forecast for 2016 [223]. Moreover, this number is expected to rapidly increase in the subsequent years. Any difference in their cost would become significant, when considering the large number of optical transmitters that would be needed.

Firstly, in Section 4.1, we propose and mathematically characterize a novel optical modulation technique for personal area networks, which uses a single optical modulator to modulate the intensity and phase of an optical carrier with two independent signals. This is achieved by the careful selection of the drive voltages applied to a dual-drive MZM. The detection of these two independent signals is also described in this section along with four possible applications of the proposed architecture. These applications allowed for simultaneous transmission of baseband and RF signals through the optical fiber. The viability of the proposed architecture was verified by our simulation-based study.

Optical Single Sideband (OSSB) signals are conventionally generated using a dual-drive Mach-Zehnder Modulator (MZM) or by using a single-drive MZM in conjunction with a Fiber Bragg Grating (FBG) filter. In Section 4.2, we propose and mathematically characterize a novel Radio Over Fiber (ROF) downlink in which an OSSB signal is generated using a single-drive, rather than dual-drive, MZM without any additional filter. Additionally, our proposed scheme can achieve optical upconversion of the electronic signal. Furthermore, in addition to cost advantages, the proposed scheme's BER performance is better than the classical OSSB signal generation scheme.

Finally, in Section 4.3, we propose and mathematically characterize a novel radio over fiber (ROF)

downlink, where the radio access point (RAP) benefits from the transmit diversity gain of space time block coding (STBC). Significantly, this transmit diversity is achieved using a single optical modulator in the base station (BS). In the proposed architecture, each RAP is fed with a single optical double side band (ODSB) signal, where each sideband transmits one of the two STBC encoded signals. This optical signal is generated in the BS by performing simultaneous optical upconversion of the baseband STBC signals using a single mach-zehnder modulator (MZM). The proposed optical backhaul is designed and simulated to impose negligible degradation to that imposed by the dominant wireless link, thereby enabling the designer to exploit the advantages offered by a wireless link having diversity gain.

We now discuss the first of the three proposed architectures in the next section.

4.1 Independent optical phase and intensity modulation using a single modulator for local area networks

The commonly employed ROF optical modulation schemes either modulate only the intensity, as in OOK, or only the phase of the optical carrier, as in Differential Phase Shift Keying (DPSK). Optical modulations, such as 16-level Quadrature Amplitude Modulation (QAM), modulate both the intensity and phase to transmit a single optical signal. However, they employ multiple optical modulators [224] and do not involve the transmission of two independent signals. However, the ROF architectures of [180], [181], [1] employed optical phase modulation and intensity modulation of the same carrier for the DL and UL transmission between the BS and RAP, respectively. This was achieved by employing two optical modulators, one in the BS for DL and one in the RAP for the UL. Finally, modulating only the optical carrier's intensity with multiple independent RF signals [90] or a combination of baseband and RF signals [162], [163], [165], whilst relying on Sub Carrier Multiplexing using a single optical modulator, has also been implemented.

However, none of the above systems facilitated the modulation of the optical carrier's intensity and phase with two independent signals, say $V_x(t)$ and $V_y(t)$, respectively, with the aid of a single optical modulator in the BS. We will demonstrate that this is achieved by our new architecture seen in Fig. 4.2. Fig. 4.1 shows four potential applications of the architecture of Fig. 4.2. Both $V_x(t)$ and $V_y(t)$ are digital BB signals in the applications of Fig. 4.1(a) and Fig. 4.1(b), with the difference being the fact that the up-converted version of $V_y(t)$ available at the receiver is down-converted to BB by the Optical Network Unit (ONU) in the application of Fig. 4.1(a), while the RAP of Fig. 4.1(b) employs the up-converted version of $V_y(t)$ for wireless transmission. On the other hand, $V_x(t)$ is a RF signal and $V_y(t)$ is a digital BB signal in the applications of Fig. 4.1(c) and Fig. 4.1(d). Again, the up-converted $V_y(t)$ is down-converted to BB by the ONU in the application of Fig. 4.1(c), while the RAP of Fig. 4.1(d) employs the up-converted $V_y(t)$ for wireless transmission. These applications will be discussed in greater detail in Section 4.1.2. It must be noted that $V_x(t)$ and/or $V_y(t)$ may themselves be multiplexed signals. Moreover, the ONUs and RAPs in the applications of Fig. 4.1 may be geographically distant points in the optical network. Thus, the novel contributions of our work are as follows:

1. Modulating two independent signals $V_x(t)$ and $V_y(t)$ onto the intensity and phase of the optical carrier, respectively, while employing a single optical modulator.

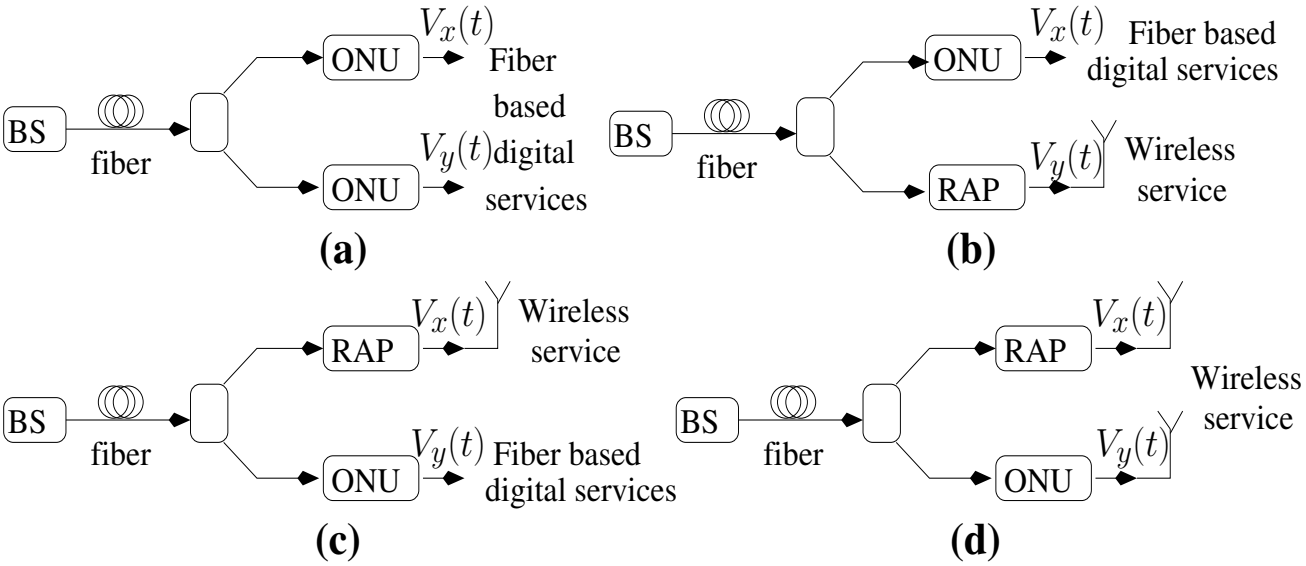

Figure 4.1: Applications of the proposed architecture

2. The proposed architecture allows the optical network to simultaneously support both BB and ROF transmission.

3. A mathematical characterization of the proposed system is presented.

In Section 4.1.1, we discuss the proposed system's architecture along with its mathematical characterization, while the results of a realistic simulation-based study are presented in Section 4.1.2.

4.1.1 Proposed system architecture and analysis

We present a theoretical analysis of the BS transmitter, modulation voltages and the receiver. of the applications shown in Fig. 4.1 in Sections 4.1.1.1, and , respectively.

4.1.1.1 Proposed transmitter

The LD in the BS of Fig. 4.2 operates at a frequency of f_c Hz, at an optical power of P_{in} and has an output optical field of [2], [84]:

$$E_{laser}(t) = \sqrt{2P_{in}}e^{j2\pi f_c t}. \tag{4.1}$$

The laser's output is modulated by the dual-drive MZM of Fig. 4.2. The two arms of the MZM are driven by the voltages $V_{drv1}(t)$ and $V_{drv2}(t)$, respectively. Using Equation (4.24), the output optical field of the MZM having an insertion loss of t_{attn} is formulated as:

$$\begin{aligned} E_{dual}(t) &= 0.5\sqrt{t_{attn}}[e^{j\frac{\pi V_{drv1}(t)}{V_\pi}} + e^{j\frac{\pi V_{drv2}(t)}{V_\pi}}]E_{laser}(t) \\ &= \sqrt{2P_{in}t_{attn}}cos(\frac{\pi(V_{drv1}(t) - V_{drv2}(t))}{2V_\pi})e^{j\frac{\pi(V_{drv1}(t)+V_{drv2}(t))}{2V_\pi}}e^{j2\pi f_c t}, \end{aligned} \tag{4.2}$$

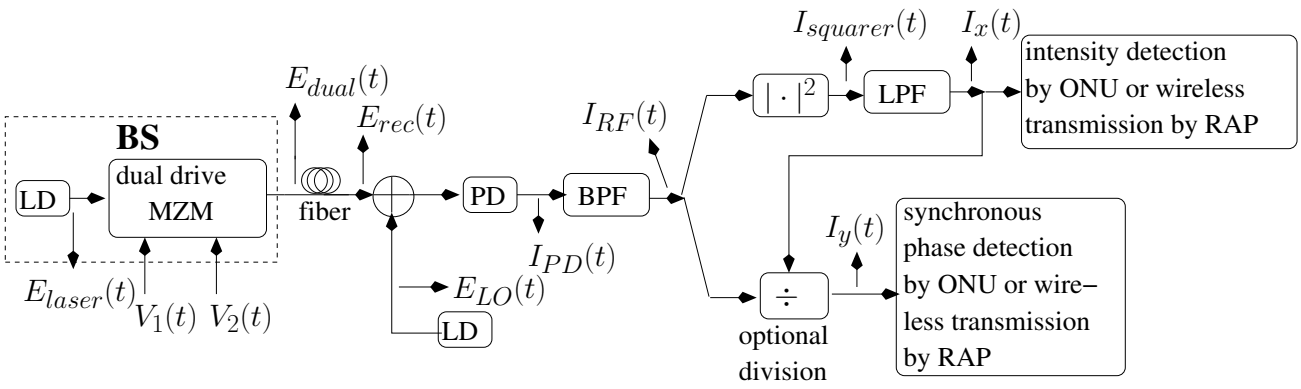

Figure 4.2: Proposed Architecture

where V_π is the modulator's switching voltage [84]. The optical intensity $P_{dual}(t) = |E_{dual}(t)|^2$ at the MZM's output is:

$$P_{dual}(t) = \sqrt{t_{attn}} P_{in}[1 + cos(\frac{\pi(V_{drv1}(t) - V_{drv2}(t))}{V_\pi})]. \tag{4.3}$$

Assuming $V_x(t)$ and $V_y(t)$ to be two independent signals, the drive voltages are chosen to meet the following conditions:

$$V_{drv1}(t) = V_y(t) + 0.5V_x(t); \tag{4.4a}$$

$$V_{drv2}(t) = V_y(t) - 0.5V_x(t). \tag{4.4b}$$

Substituting Equations (4.4a) and (4.4b) into Equations (4.2) and (4.3), we arrive at:

$$E_{dual}(t) = \sqrt{2P_{in}t_{attn}} cos(\frac{\pi V_x(t)}{2V_\pi}) e^{j[2\pi f_c t + \frac{\pi V_y(t)}{V_\pi}]} \tag{4.5a}$$

$$P_{dual}(t) = \sqrt{t_{attn}} P_{in}[1 + cos(\frac{\pi V_x(t)}{V_\pi})]. \tag{4.5b}$$

As evident from Equations (4.5), the optical carrier's intensity and phase were modulated with two independent signals $V_x(t)$ and $V_y(t)$, respectively, using a single optical modulator.

Having discussed the transmitter's architecture in Fig. 4.2, we move on to discussing the modulation voltages that were employed in our architecture in the next section.

4.1.1.2 Modulation voltages

As mentioned in Section 4.1, $V_x(t)$ may be a digital BB signal or a RF signal, while $V_y(t)$ is a digital BB signal[1]. If $V_x(t)$ is a digital BB signal, then we have:

$$V_x(t) = \begin{cases} V_{max} = 0 \text{ for bit } 1 \\ V_{min} \quad \text{for bit } 0. \end{cases} \tag{4.6}$$

[1] $V_y(t)$ could be RF but this is not necessary, because an up-converted version of $V_y(t)$ is heterodyne photo-detected at the receiver.

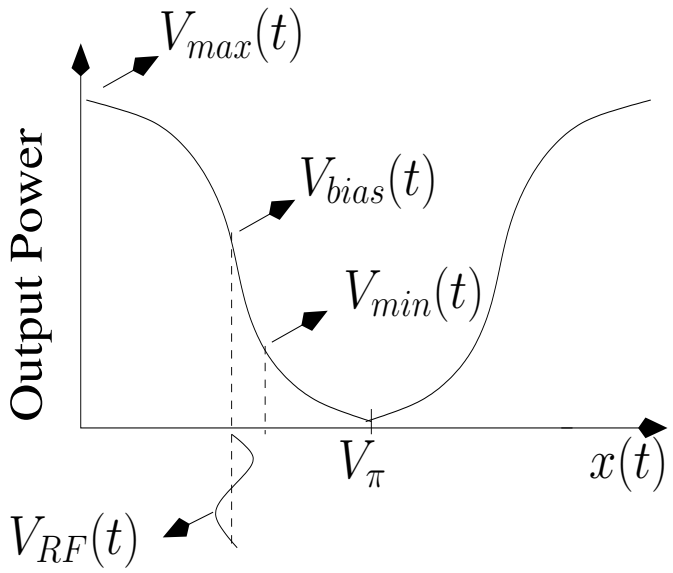

Figure 4.3: Transmittance of the MZM modulator

On the other hand, if $V_x(t)$ is a RF signal, then:

$$V_x(t) = V_{bias} + V(t), \tag{4.7}$$

where $V_{bias} = \frac{V_\pi}{2}$ is the bias voltage and $V(t)$ is the RF signal. Fig. 4.3 shows the transmittance curve of the MZM as per Equation (4.5b), with the voltages V_{max}, V_{min}, V_{bias} and $V(t)$ explicitly marked. We would have ideally wanted to transmit zero power for bit zero, i.e. $V_x(t) = V_{min} = V_\pi$, which however also corresponds to zero amplitude in Equation (4.5a), thereby leading to a loss of the phase information and hence that of the corresponding data. Thus, V_{min} is close to but not equal to V_π. Furthermore, V_{min} was set to a value that results in twenty five percent of the maximum power of Fig. 4.3. The digital BB signal $V_y(t)$ that modulates the optical phase is:

$$V_y(t) = \begin{cases} V_\pi/2 & \text{for bit 1} \\ -V_\pi/2 & \text{for bit 0.} \end{cases} \tag{4.8}$$

In the next section, we now discuss the receiver that was employed by the architecture in Fig. 4.2.

4.1.1.3 Proposed receiver

As shown in Fig. 4.2, the optical signal $E_{dual}(t)$ propagates through the optical fiber and it is received as $E_{rec}(t)$, which may be represented in terms of its amplitude $|E_{rec}(t)|$, phase $\phi_{rec}(t)$ and frequency f_c as follows:

$$E_{rec}(t) = |E_{rec}(t)|e^{j[2\pi f_c t + \phi_{rec}(t)]}. \tag{4.9}$$

Comparing $E_{rec}(t)$ of Equation (4.9) to $E_{dual}(t)$ of Equation (4.5a), it can be stated that the signal $V_x(t)$ is contained within $|E_{rec}(t)|$, while the signal $V_y(t)$ is contained within $\phi_{rec}(t)$. As shown in Fig. 4.2, a Local Oscillator (LO) laser signal having an optical field of $E_{LO}(t)$ is added to $E_{rec}(t)$, prior to heterodyne photo-detection, where we have:

$$E_{LO}(t) = \sqrt{2P_{LO}}e^{j[2\pi f_{LO} t + \phi_{LO}]}, \tag{4.10}$$

with P_{LO} and f_{LO} being the optical power and frequency of the local oscillator signal, while ϕ_{LO} is the phase of the LO laser signal, assuming that the BS's laser signal is the reference. Thus, the current generated by heterodyne photo-detection is:

$$\begin{aligned} I_{PD}(t) &= R|E_{LO}(t) + E_{rec}(t)|^2 \\ &= R|E_{LO}(t)|^2 + R|E_{rec}(t)|^2 \\ &\quad + 2R|E_{LO}(t)||E_{rec}(t)|\cos(\text{angular difference}). \end{aligned} \tag{4.11}$$

Now substituting Equations (4.9) and (4.10) into Equation (4.11), we arrived at:

$$\begin{aligned} I_{PD}(t) &= I_{dc} + R|E_{rec}(t)|^2 \\ &\quad + 2\sqrt{R}\sqrt{I_{dc}}|E_{rec}(t)|\cos(2\pi f_{diff} + \phi_{LO} - \phi_{rec}), \end{aligned} \tag{4.12}$$

where $I_{dc} = 2RP_{LO}$ and $f_{diff} = f_{LO} - f_c$. In Equation (4.12), it is the third term, i.e. the beat signal, which is the desired term, while the others are removed by the bandpass filter (BPF) in Fig. 4.2, whose output is:

$$I_{RF}(t) = 2\sqrt{R}\sqrt{I_{dc}}|E_{rec}(t)|\cos(2\pi f_{diff} + \phi_{LO} - \phi_{rec}). \tag{4.13}$$

The signal $I_{RF}(t)$ is used for reconstructing the transmitted signals $V_x(t)$ and $V_y(t)$, as detailed below in.

Detection of $V_x(t)$ The signal $I_{RF}(t)$ is fed to a squarer, whose output is as follows:

$$\begin{aligned} I_{squarer}(t) &= I_{RF}^2(t) = 2RI_{dc}|E_{rec}(t)|^2 \\ &\quad + 2RI_{dc}|E_{rec}(t)|^2\cos(2\pi(2f_{diff}) + 2\phi_{LO} - 2\phi_{rec}), \end{aligned} \tag{4.14}$$

which is then low-pass filtered for eliminating the high-frequency beat term at $2f_{diff}$ Hz in the expression of Equation (4.14). The output of the low-pass filter is:

$$I_x(t) = 2RI_{dc}|E_{rec}(t)|^2, \tag{4.15}$$

Thus, $I_x(t)$ is proportional to the intensity of $E_{rec}(t)$. As stated earlier, the signal $V_x(t)$ is contained in the intensity of $E_{rec}(t)$. Hence, $I_x(t)$ contains the signal $V_x(t)$, which was employed in optical intensity modulation at the transmitter.

If $V_x(t)$ is a digital BB signal, as in the applications seen in Fig. 4.1(a) and Fig. 4.1(b), then the bit values are detected by the ONU based on the amplitude of $I_x(t)$. On the other hand, if $V_x(t)$ is a RF signal at f_{RF}^x Hz, as in the applications seen in Fig. 4.1(c) and Fig. 4.1(d), then the RF signal can be transmitted directly over the wireless channel to the mobile device by the RAP. Note that f_{RF}^x should be less than $2f_{diff}$ Hz, so that the low pass filter applied to $I_{squarer}(t)$ can retain $I_x(t)$.

We now discuss the detection of $V_y(t)$ in the following paragraph.

Detection of $V_y(t)$ Now that we have $I_x(t)$, we can generate $I_y(t)$ through the following operation:

$$I_y(t) = \frac{I_{RF}(t)}{\sqrt{I_x(t)}} = \sqrt{2}\cos(2\pi f_{diff} + \phi_{LO} - \phi_{rec}). \tag{4.16}$$

Hence, $I_y(t)$ is a phase modulated signal having a carrier frequency of f_{diff} Hz and carrier phase of ϕ_{LO}. The phase of $I_y(t)$ contains the $\phi_{rec}(t)$, i.e the phase of the received optical field $E_{rec}(t)$, which carries $V_y(t)$. Thus, $I_y(t)$ is an up-converted, phase-modulated RF version of the BB signal $V_y(t)$. The division by $\sqrt{I_x(t)}$ in Equation (4.16) is optional and it was avoided in the simulations, because $I_x(t)$ and $\sqrt{I_x(t)}$ is always a real positive value and hence does not effect the phase of $I_{RF}(t)$.

The applications seen in Fig. 4.1(a) and Fig. 4.1(c) down-convert $I_y(t)$ through synchronous phase detection of $\phi_{rec}(t)$ in the ONU, where this is implemented in a manner similar to RF signals [225], [31]. On the other hand, in the applications seen in Fig. 4.1(b) and Fig. 4.1(d), the up-converted version of $V_y(t)$, i.e $I_y(t)$, is filtered and transmitted wirelessly by the RAP to the mobile device, where it is employed for synchronous phase detection.

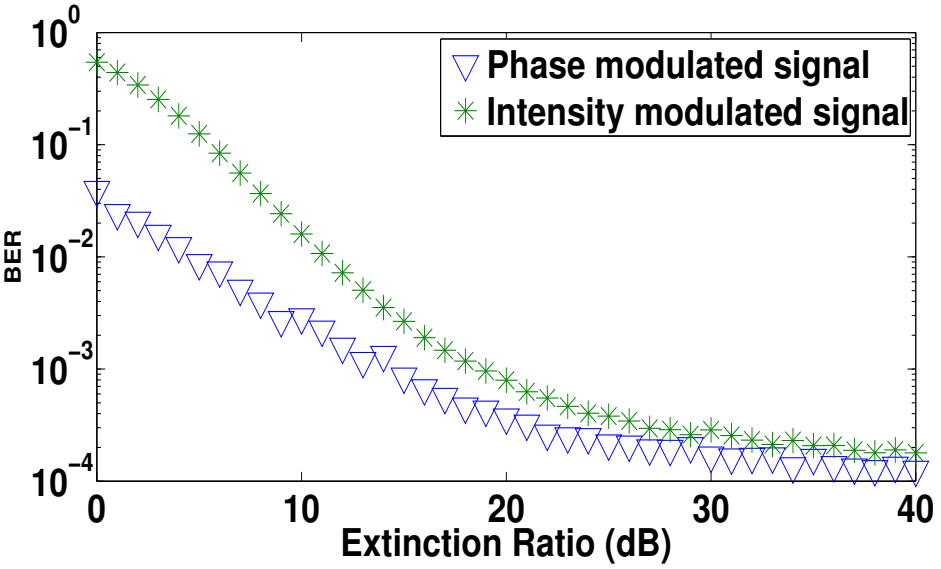

Figure 4.4: System performance for various extinction ratios in Type II application

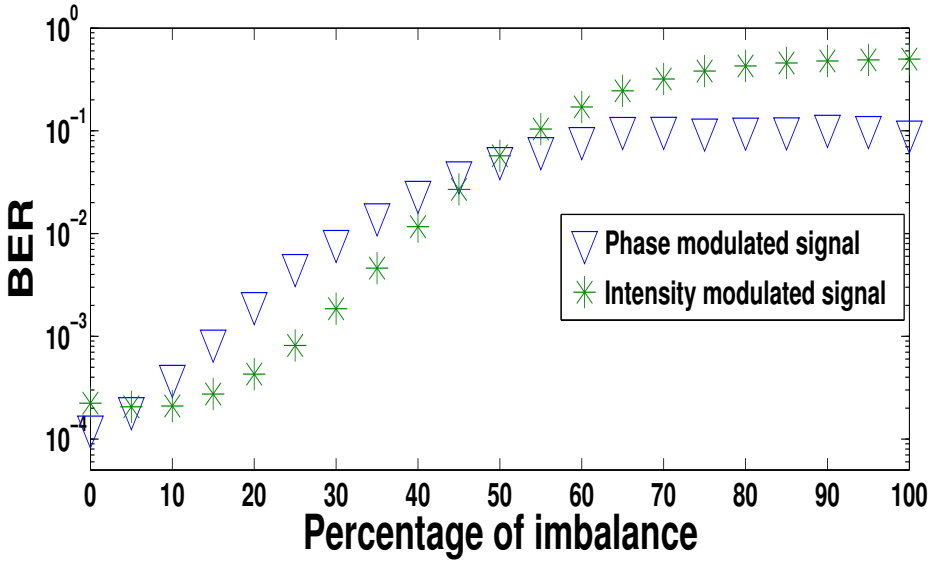

Figure 4.5: BER performance for the case of unbalanced feeding of the MZM in type II application

It should be noted that the theoretical analysis in this section did not include the effects of phase noise associated with coherent optical photodetection. A potential solution to this challenge is to ensure that both the optical carrier and the local oscillator signal are derived from the same laser source [226], in a manner similar to the architecture we proposed in Chapter 2. Alternatively, we have to ensure optical phase locking [31], which is an expensive proposition.

A discussion of a ROF link would not be complete without a proposal for the uplink. Hence, in the next section we discuss how uplink communication may be implemented in our proposed system.

4.1.1.4 Uplink communication in proposed architecture

The architecture of Fig. 4.2 may be used for UL communication with the LO laser in the RAP and the laser in the BS switching their roles. In other words, a portion of the LO signal power used in DL detection may be separated and then both its intensity as well as phase modulated with the UL signals, while in the BS, a portion of the laser signal power used in DL modulation may be separated and used as the LO signal for heterodyne UL photo-detection.

Having completed a theoretical study of the architecture in Fig. 4.2, we now move on to presenting in the next section the results of our simulation based study of this system.

4.1.2 Simulation Results

Table 4.1 shows the system parameters used in our system, where we included the effects of both the laser's Relative Intensity Noise (RIN) as well as the photo-detector's shot noise, thermal noise and dark current. Moreover, the simulations relied on SSFM [31] for simulating the optical fiber propagation in the presence of fiber dispersion, fiber non-linearity and fiber attenuation.

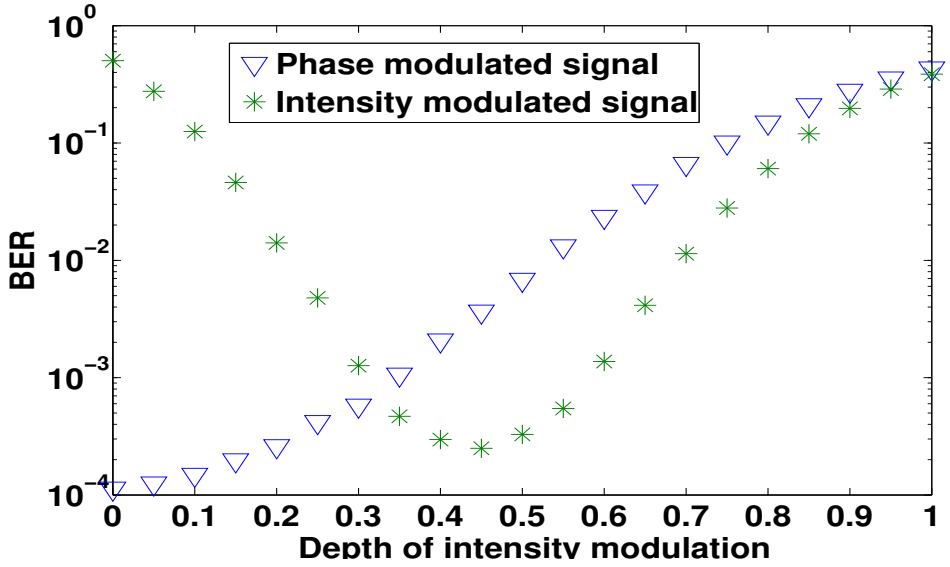

Figure 4.6: System performance for various depths of intensity modulation in type II application

In the application seen in Fig. 4.1(a) as well as in Fig. 4.1(b), both $V_x(t)$ and $V_y(t)$ are digital

Table 4.1: Parameter values of the ROF link

Parameter	Value	Parameter	Value
Bit rate of $V_x(t)$	1.024 Gbps	DD-MZM insertion loss t_{attn}	4 dB
Bit rate of $V_y(t)$	1.024 Gbps	DD-MZM extinction ratio ϵ	30 dB
optical frequency λ_c	1550 nm	fiber length	5 km
modulator switching voltage V_π	6 V	PD transimpedance	125 Ω
		Laser linewidth	1 MHz
fiber dispersion D	16 ps/km-nm	fiber Nonlinearity γ	1.2 /W/km
fiber attenuation α	0.2 dB/km	photo-receiver NF	6 dB
PD responsivity	0.8 A/W	f_{diff}	12.5 GHz
Laser RIN (dBc/Hz)	-155	f^x_{RF}	5 GHz

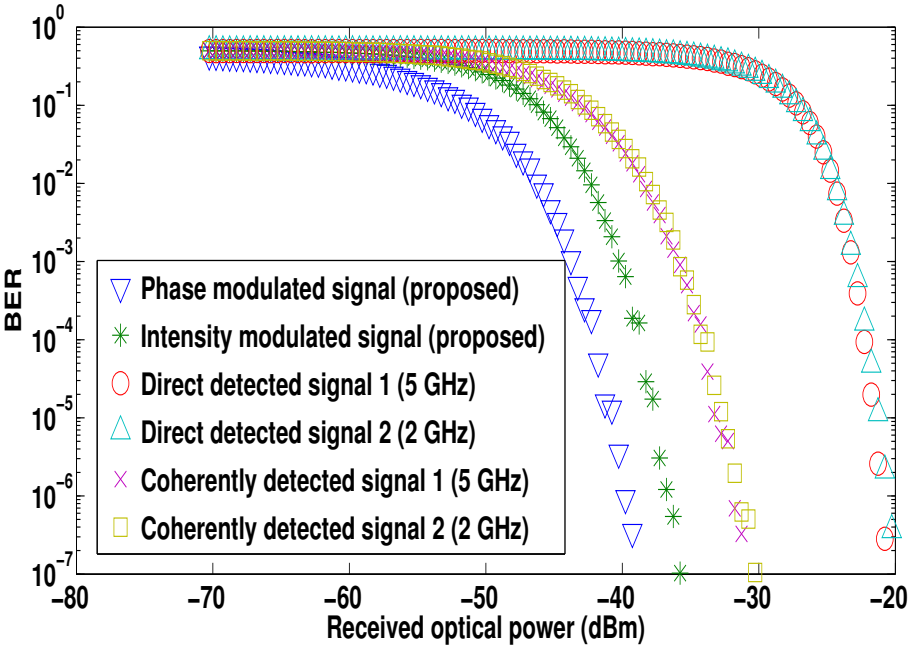

Figure 4.7: BER performance at various received optical powers for 30 dB extinction ratio and intensity modulation depth of 0.4 in type II application

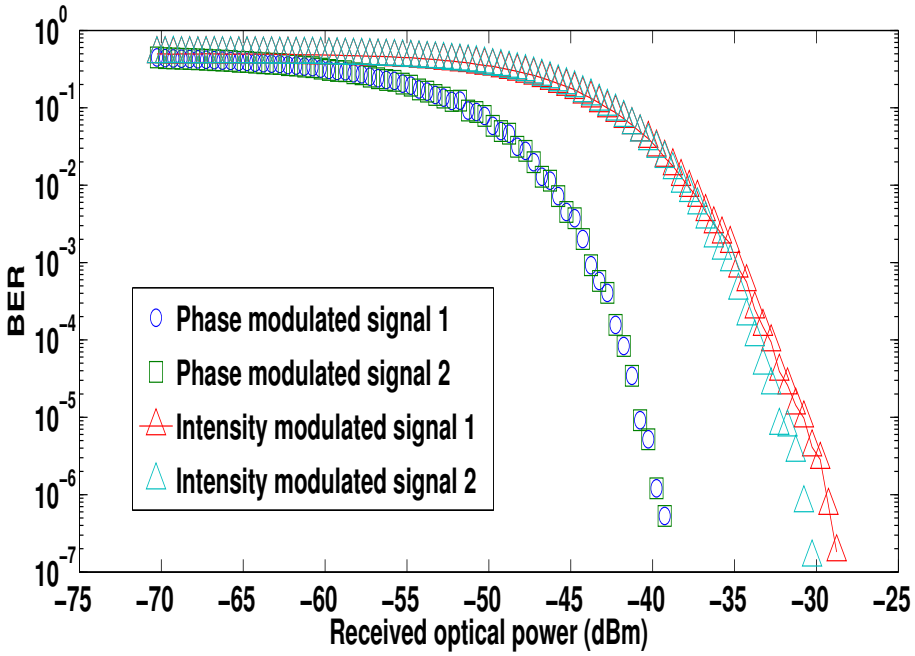

Figure 4.8: BER performance when using multiplexed signals for phase and intensity modulation in type II application

signals, as discussed in Section 4.1. Thus, they have the same optical link, with the difference being in the electronic signal processing after photo-detection. More specifically, as discussed in Section 4.1.1.3, in the application seen in Fig. 4.1(a), the synchronous phase detection of the $f_{diff} = 12.5\ GHz$ RF signal is carried out in the ONU, while, in the application seen in Fig. 4.1(b), it is done after the wireless transmission of the $f_{diff} = 12.5\ GHz$ RF signal from the RAP to the mobile device. Note that the aim of this section was to analyse the optical link of the proposed architecture, regardless of where the electronic phase detection is carried out. Hence, any wireless transmission was assumed to be ideal. Thus, the applications portrayed in Fig. 4.1(a) and Fig. 4.1(b) have a similar performance (i.e. optical performance) and are collectively termed here as the **Type I application**.

On the other hand, in the applications observed in Fig. 4.1(c) and Fig. 4.1(d), $V_x(t)$ is a RF signal at $f^x_{RF} = 5\ GHz$, while $V_y(t)$ is a digital BB signal. In the applications portrayed in Fig. 4.1(c) and Fig. 4.1(d) there is wireless transmission of the RF signal $V_x(t)$ at $f^x_{RF} = 5\ GHz$, while as discussed in Section 4.1.1.3, in the applications seen in Fig. 4.1(c) and Fig. 4.1(d), the synchronous phase detection of the up-converted version of $V_y(t)$ at $f_{diff} = 12.5\ GHz$ is carried out in the ONU and mobile device, respectively. For the same reasons as the Type I applications, the applications portrayed in Fig. 4.1(c) and Fig. 4.1(d) have a similar performance (i.e optical performance) and are collectively referred to as the **Type II application**.

We first discuss the performance results of the Type II application. Fig. 4.4 shows the effect of varying the extinction ratio of the MZM modulator, where in both scenarios the received optical power was set to the value that would give a BER of approximately 10^{-4} at an extinction ratio of 30 dB. It can be seen from Fig. 4.4 that the performance degradation is tolerable for an extinction ratio as low as 15 dB, thereby making this scheme viable for implementation using commercially available modulators. Implementation errors may result in an imbalance in the feeding of the two arms of

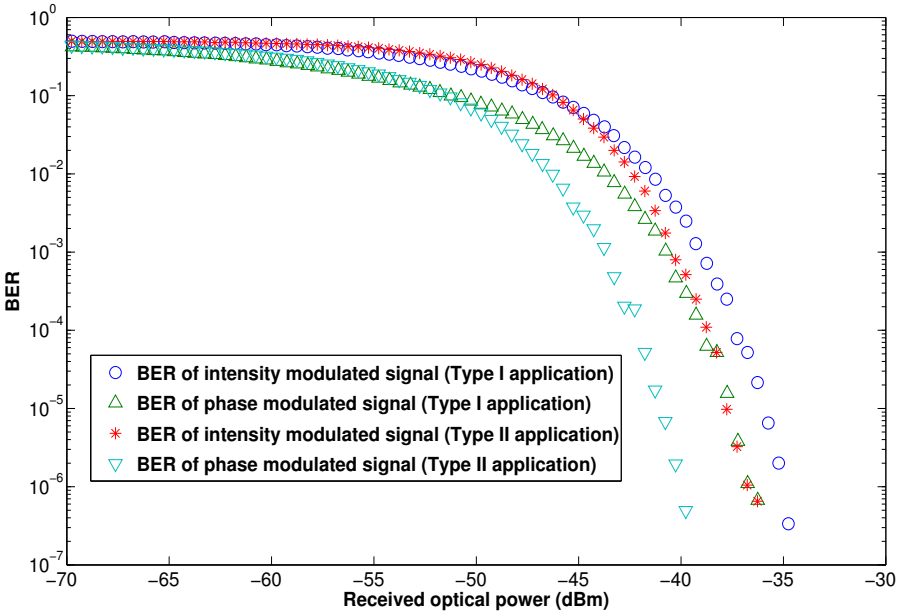

Figure 4.9: BER performance at various received optical powers

the MZM, where for an imbalance of k %, Equation (4.4b) would be reformulated as $V_{drv2}(t) = (1 + k/100) \times [V_y(t) - 0.5V_x(t)]$. The resultant phase-intensity coupling can be studied by setting $\gamma = 1$ and employing the reformulated Equation (4.4b) in Equations (4.5a) and (4.5b). Fig. 4.5 shows the effect of such an imbalance on the BER, where it can be seen that for a imbalance of upto 15% and 25%, the BER penalty is within an order of magnitude for phase and intensity modulation, respectively. The depth of intensity modulation is defined as $\frac{x_{RMS}}{V_\pi}$, where x_{RMS} is the RMS value of $V_x(t)$. Fig. 4.6 shows the effect of increasing the depth of intensity modulation, where the optical power employed in each of the two cases ensured a lowest attainable BER of 10^{-4}. As the depth of the intensity modulation increases, the proportion of the received power, that carries the intensity modulated signal increases, while that carrying the phase modulated signal decreases. This results in an increase in the BER of the phase modulated signal, as shown in Fig. 4.6. However, beyond a certain value of the depth of intensity modulation, the BER of the intensity modulated signal also increases, which is because of the non-linear nature of the modulation, as seen from the transmittance curve of Fig. 4.2. Fig. 4.7 shows the BER performance of the intensity and phase modulated links of the proposed architecture, where the optical link would ensure error-free performance ($BER < 10^{-9}$) for higher values of received optical power, in a scenario where the laser employs a typical transmit power of say 0-5 dBm. It can be seen from Fig. 4.7 that the proposed link outperforms two commonly employed transmission techniques operating at similar link parameters, each of which transmits a pair of independent RF signals at 5 GHz and 2 GHz. The first is a scenario in which two RF signals employ intensity modulation along with direct detection, while the second benchmark scheme employs intensity modulation and coherent detection. Note that the total data rate in all three scenarios is the same. Furthermore, Fig. 4.8 shows the performance when the signals $V_x(t)$ and $V_y(t)$ shown in Fig. 4.2 for modulating the intensity and phase, respectively, are themselves multiplexed signals. Since $V_y(t)$ is in the baseband, it now consists of two Time Division Multiplexed (TDM) signals, which would get

up-converted to f_{diff} Hz on photo-detection. On the other hand, the RF signal $V_x(t)$ now consists of two Frequency Division Multiplexed (FDM) RF signals at 5 GHz and 2 GHz. We can see that the system performs robustly in such a scenario as well. Note that similar results would be obtained if the baseband signal $V_x(t)$ is a Code Division Multiplexed (CDM) signal relying on orthogonal Walsh Hadamard codes [227].

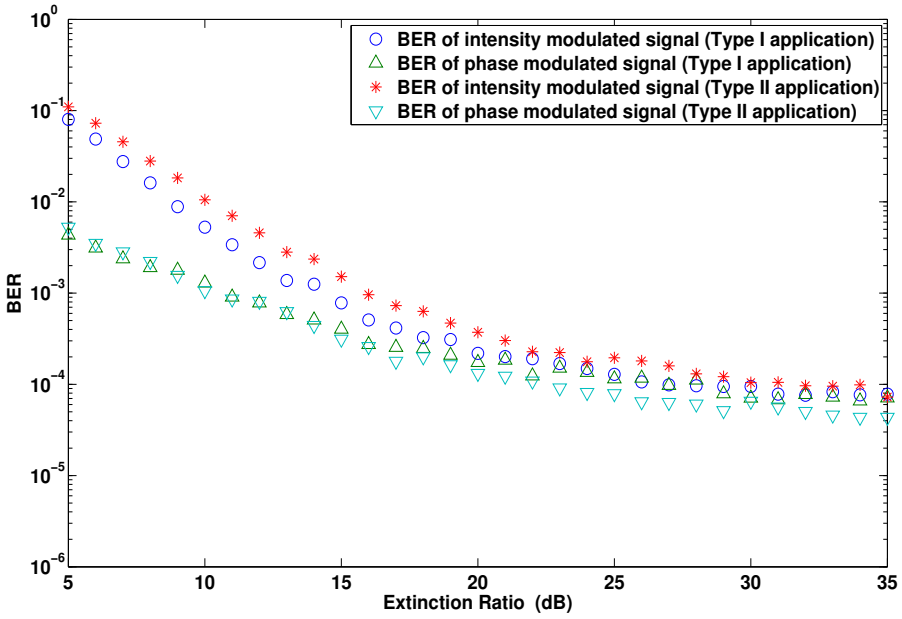

Figure 4.10: System performance at various extinction ratios

We now present the results of the type I application and compare it with the performance of the type II application. Fig. 4.9 shows the BER performance of the intensity and phase modulated links of Type I (and Type II) applications, where, as in the case of Type II application, the optical link ensures error-free performance, when the transmit laser employs a typical transmit power of say 0-5 dBm. Fig. 4.10 shows the effect of varying the extinction ratio of the MZM modulator of type I (and type II) application, where as in the previous case, the received optical power was set to the value that would give a BER of approximately 10^{-4} at an extinction ratio of 30 dB. Again, it can be seen from Fig. 4.10 that the performance degradation of the Type I application is tolerable for an extinction ratio as low as 15 dB, thereby making this scheme viable for implementation using commercially available modulators.

One of the disadvantages of employing ODSB optical modulation is that it is suffers from dispersion induced power attenuates. Hence, in the next section we propose an architecture that employs OSSB modulation, while relying on cost-saving and optical upconversion techniques.

4.2 Optical single sideband signal generation relying on a single-drive mach zehnder modulator for ROF communications

The 30 GHz and 60 GHz bands are viewed as potential frequency bands capable of supporting high data rates in next-generation wireless networks relying on a ROF backhaul [39]. A challenge in the commercial exploitation of these high frequencies is the degrading nature of electronic components, especially of electronic mixers, at these high frequencies. The optical generation of the Radio Frequency (RF) signals by employing optical upconversion is a potential solution to this challenge, which has been achieved in the proposed architecture by driving the Mach-Zehnder Modulator (MZM) using a sawtooth signal.

The most commonly employed Optical Double Side Band (ODSB) modulation suffers from fiber-dispersion-induced power attenuation, which becomes increasingly severe at higher RF carriers [4]. ODSB modulation may easily implemented using a direct modulation of the laser source [228]. Optical Single Side Band (OSSB) modulation scheme was then proposed for overcoming this challenge [229]. Whilst being tolerant to the fiber-dispersion-induced power attenuation, the OSSB modulation scheme requires the employment of a dual-drive modulator [5]. Alternatively, one can employ a single-drive modulator, but will have to employ an extra temperature-sensitive Fiber Bragg Grating (FBG) optical filter for eliminating one of the sidebands [4]. In this section, we propose a novel technique for generating an OSSB signal using a single-drive MZM without having to rely on an additional FBG filter, thereby providing substantial cost benefits.

Thus the novel features of the proposed scheme are as follows:

- Generation of a dispersion-tolerant OSSB signal using a single-drive, rather than a dual-drive, MZM with no subsequent optical filtering, thereby resulting in significant reduction of the system cost;
- Optical upconversion of the OSSB signal using a sawtooth signal for avoiding the performance degradation imposed by high-RF mixers;
- Our solution outperforms the classical OSSB technique for similar link parameters.

This section is organized as follows. The proposed system's architecture is discussed in Section 4.2.1, where a mathematical characterization of the system is also provided in order to confirm its feasibility. Subsequently, in Section 4.2.2, we present the results of a simulation-based study that relies on realistic parameter values of commercially available optical equipments.

4.2.1 Proposed system architecture and analysis

In this section, we discuss how an OSSB signal can be generated using a single-drive MZM, where Fig. 4.11 shows the architecture of the proposed system, including the transmitter and receiver. Firstly, we discuss the transmitter of the proposed architecture in Section 4.2.1.1, while the receiver of the proposed architecture is detailed subsequently in Section 4.2.1.2.

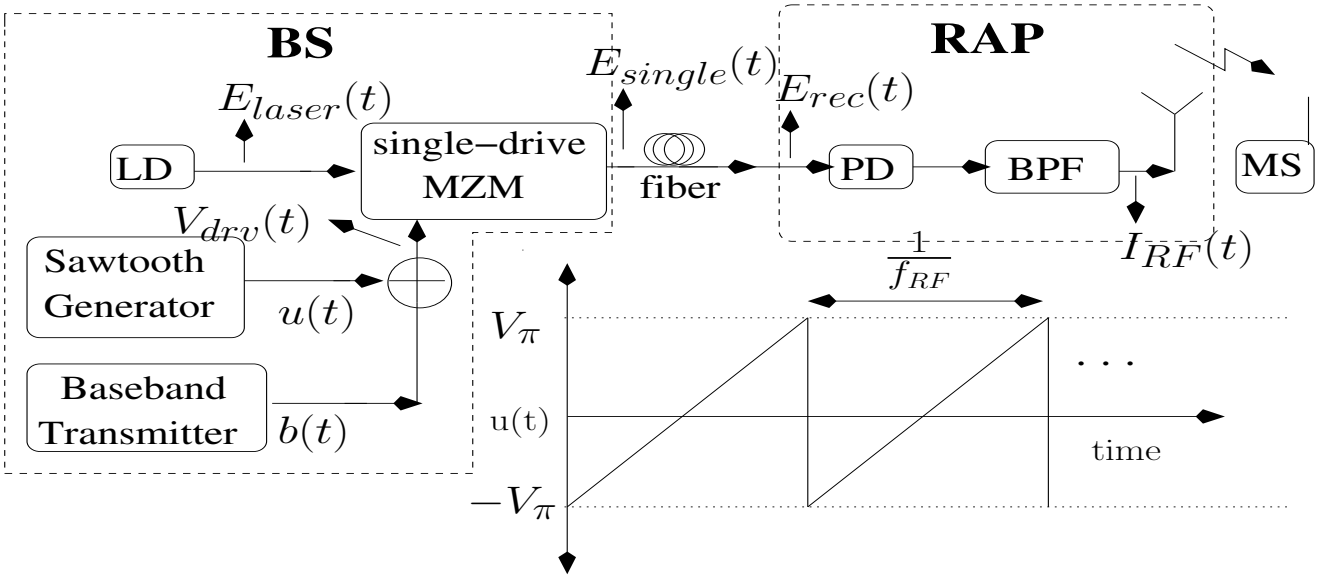

Figure 4.11: Proposed system architecture

4.2.1.1 Optical single side band modulation transmitter

The laser diode (LD) in the BS of Fig. 4.11 operates at an optical frequency of f_c Hz (wavelength λ_c) and at a power of P_{in} to generate an optical field of [4]:

$$E_{laser}(t) = \sqrt{2P_{in}}e^{j2\pi f_c t}, \tag{4.17}$$

where $E_{laser}(t)$ is fed to a single-drive MZM driven by $V_{drv}(t) = u(t) + b(t)$, with $b(t)$ being the baseband signal that is to be transmitted over the wireless link to the MS, while $u(t)$ is the sawtooth signal of Fig. 4.11, formulated as:

$$u(t) = modulo(2f_{RF}tV_\pi, 2V_\pi) - V_\pi, \tag{4.18}$$

where f_{RF} is the RF carrier frequency, while V_π is the switching voltage of the single-drive MZM. Note that $b(t) = +V$ for bit '1' and $b(t) = -V$ for bit '0'. As shown in Section 4.2.1.2, this results in phase modulated symbols of $e^{\pm j\frac{V}{V_\pi}}$ being received at the MS. Typically, phase modulation employs phases of $\frac{\pi}{2}$ and $-\frac{\pi}{2}$ for bits '1' and '0', respectively. The optical output field of the MZM having an insertion loss of t_{attn} is:

$$\begin{aligned} E_{single}(t) &= \frac{\sqrt{t_{attn}}}{2}[1 + e^{j\pi\frac{b(t)+u(t)}{V_\pi}}]E_{laser}(t) \\ &= \frac{\sqrt{t_{attn}}}{2}[1 - e^{j(\pi\frac{b(t)}{V_\pi}+2\pi f_{RF}t)}]E_{laser}(t). \end{aligned} \tag{4.19}$$

The spectrum of the OSSB signal $E_{single}(t)$ is shown in Fig. 4.12. In Fig. 4.12, the optical carrier signal at f_c Hz is represented by the first term in Equation (4.28), while the optical sideband at $f_c + f_{RF}$ Hz is represented by the second term in Equation (4.28). *Therefore, the system architecture of Fig. 4.11 is capable of generating an OSSB signal using a single-drive MZM.* The generation of an ODSB signal using a sawtooth waveform applied to a dual-drive MZM was presented in [7].

Generating a sawtooth signal using an Arbitrary Waveform Generator (AWG) would be an expensive proposition. However, the primary purpose of an AWG is to be able to generate arbitrary waveforms of many types, while our system needs only a sawtooth waveform generator. A more specific low-cost sawtooth signal generator can be readily constructed using only two op-amps, where the repetition frequency of the sawtooth waveform may be controlled using the resistance values employed [230] [231]. In the next section we discuss the receiver of the architecture in Fig. 4.11.

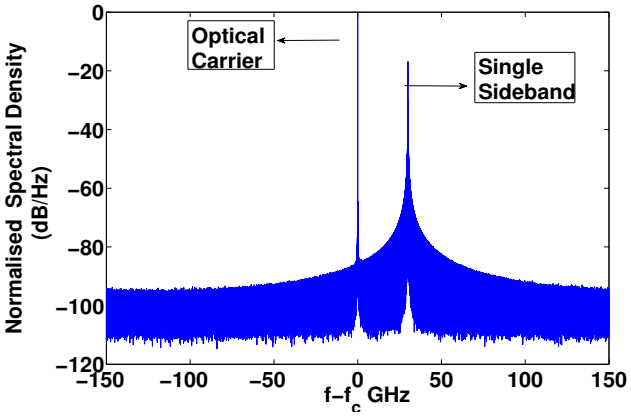

Figure 4.12: Spectrum of the transmitted optical signal

4.2.1.2 Optical single side band modulation Receiver

The optical signal $E_{single}(t)$ is transmitted through the optical fiber of length L to the RAP. A phase shift ϕ_{disp} is induced by fiber-dispersion in the sideband with respect to the carrier, while additionally the signal is attenuated by the fiber [4]. The output of the photo-detector (PD) is then filtered using a bandpass filter centered at f_{RF} Hz in order to separate the phase-modulated RF component of Equation (4.29). Thus, if R is the responsivity of the photo-diode and BPF is the bandpass filtering function, then using Equation (4.28), the photo-detected current is:

$$\begin{aligned} I_{RF}(t) &= BPF\{R|E_{rec}(t)|^2\} \\ &= BPF\{\ R\left|e^{\frac{\alpha}{2}L}\frac{\sqrt{t_{attn}}}{2}[1-e^{j(\pi\frac{b(t)}{V_\pi}+2\pi f_{RF}t+\phi_{disp})}]E_{laser}(t)\right|^2\ \} \\ &= -Re^{\alpha L}t_{attn}P_{in}\cos(2\pi f_{RF}t+\pi\frac{b(t)}{V_\pi}+\phi_{disp}), \end{aligned} \tag{4.20}$$

where α is the fiber attenuation parameter. *Thus, it can be seen from Equation (4.29) that the system architecture of Fig. 4.11 can achieve optical upconversion of the baseband signal $b(t)$ to the RF signal $I_{RF}(t)$ using the sawtooth signal $u(t)$.* The RF signal is then amplified and transmitted over the wireless link to the MS, where it is synchronously down-converted [232]. The RF signal is a *phase-modulated* up-converted version of the complex baseband signal $e^{j(\pi\frac{b(t)}{V_\pi}+\phi_{disp})}$. The fiber-dispersion rotates the symbols by a constant ϕ_{disp}. This can be considered as part of the wireless channel coefficient, when estimating the channel and performing phase rotation estimation. Hence, it is also readily estimated by the wireless channel estimation technique employed at the MS. In other words, if the wireless channel has a coefficient of h_{wl}, then the channel coefficient obtained from the estimation technique becomes $h_{wl}e^{j\phi_{disp}}$.

Just like other modulation scenarios, a practical implementation of the proposed architecture may employ a non-ideal MZM. A nth order Bessel function may be used for representing a non-ideal MZM's output [233]. Non-linear products like intermodulation and harmonics are generated by these imperfections [233]. However, we hasten to add that, just like the classical OSSB, these non-linear signals may be significantly suppressed by optical filtering or/and by electronic filtering before and/or after photo-detection, respectively.

Now that we have discussed the mathematical feasibility of the proposed architecture, we move on to presenting the results that were obtained using a simulation-based study employing realistic system parameters.

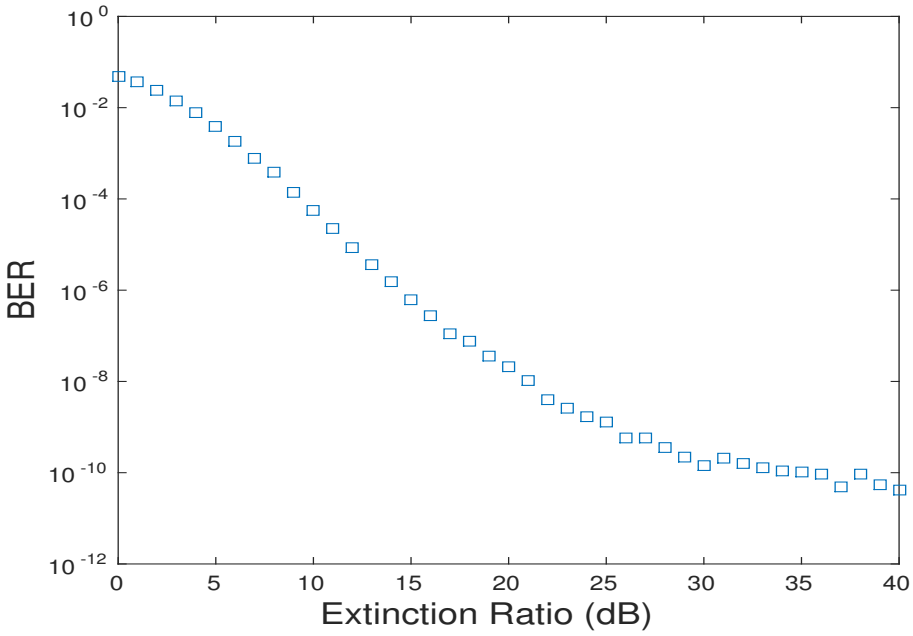

Figure 4.13: System performance for non-ideal MZM in transmitter

4.2.2 Simulation results and analysis

The theoretical discussions in Section 4.2.1 did not consider the effect of optical and electronic noise, neither was the impact of the non-ideal nature of the optical components considered. In our simulations, we consider a realistic laser diode (LD) which has a non-zero linewidth and adds both phase noise as well as Relative Intensity Noise (RIN). A non-ideal, realistic optical modulator having a finite extinction ratio as well as non-zero insertion loss is employed in these simulations. We have also analysed the effect of driving this optical modulator using a non-ideal sawtooth signal. **We have ensured that the optical power entering the MZM is not higher than 0 dBm. In fact, the highest optical power entering the MZM in our simulations was** -15 **dBm.** Additionally, this simulation-based study employs an optical fiber that imposes optical attenuation, dispersion as well as non-linearity on the propagating optical signal. Finally, we assume a photo-detector (PD) that imposes thermal noise, shot noise as well as dark current on the signal. Table I provides the simulation parameters employed in our study [31]. The optical fiber propagation was simulated using the Split

Table 4.2: Parameter values of the ROF link

Parameter	Value	Parameter	Value
Bit rate of $b(t)$	32 Mbps	MZM insertion loss t_{attn}	4 dB
Laser RIN (dBc/Hz)	-155	MZM extinction ratio ϵ	30 dB
optical wavelength λ_c	1550 nm	fiber length L	20 km
MZM switching voltage V_π	6 V	PD trans-impedance	125 Ω
		Laser linewidth	10 MHz
fiber dispersion D	16 ps/km-nm	fiber Non-linearity	1.2 /W/km
		Dark current	1 nA
fiber attenuation α	0.2 dB/km	photo-receiver NF	6 dB
PD responsivity R	0.8 A/W	f_{RF}	30 GHz

Step Fourier Method (SSFM) [31].

We now show that the technique works well with realistic MZMs, unlike the MZM having an ideal extinction ratio ϵ of infinity assumed in Equation (4.28). Commercial MZMs have

$$E_{single}(t) = \frac{\sqrt{t_{attn}}}{2}[1 + \gamma e^{j\frac{\pi V(t)}{V_\pi}}]E_{laser}(t). \tag{4.21}$$

with $\gamma = (\sqrt{\epsilon} - 1)/(\sqrt{\epsilon} + 1) < 1$. Upon reformulating Equation (4.29), we arrive at

$$I_{RF}(t) = -\gamma R e^{\alpha L} t_{attn} P_{in} \cos(2\pi f_{RF} t + \pi \frac{b(t)}{V_\pi} + \phi). \tag{4.22}$$

Thus, a non-ideal extinction ratio weakens the photo-detected RF signal and results in a BER degradation, which is quantified in Fig. 4.13 for various extinction ratios. As seen in Fig. 4.13, realistic MZMs having extinction ratios of about 20 dB impose a tolerable BER degradation of less than an order of magnitude compared to an ideal MZM with $\epsilon = \infty$ dB. An ideal MZM has an extinction ratio of ∞ dB. In the simulation of Fig. 4.13 , we operated the ROF link at an optical power that would yield a BER of approximately 10^{-9} for an ideal MZM, where this BER was due to the noise imposed by the ROF link. However, an additional BER degradation is imposed, if the MZM has a non-ideal extinction ratio, as seen from Fig. 4.13 . Hence, the BER floor in Fig. 4.13 indicates that the BER performance would approach its value for the case of an ideal MZM. Hence, we employ an extinction ratio of 30 dB in all our subsequent simulations.

The discussion in Section 4.2.1 assumed an ideal sawtooth signal capable of instantaneously switching from V_π to $-V_\pi$ volts. However, realistic realizations have a non-zero fall time. Fig. 4.14 shows a sawtooth signal with a non-zero fall time of T_{fall} seconds, where the repetition period of the sawtooth signal is T_{period} seconds. Fig. 4.15 shows the BER degradations for various non-zero fall times T_{fall} as a percentage of T_{period}, i.e. $\frac{T_{fall}}{T_{period}} \times 100$, where the laser was operated at a transmit power that would result in a BER of approximately 10^{-5} for a near-ideal sawtooth signal. It can be seen from Fig. 4.15 that a fall time of upto 10% of the repetition period of the sawtooth signal results in a tolerable BER degradation. Hence, in the following paragraphs we employ a fall time of 10% of the repetition period of the sawtooth signal.

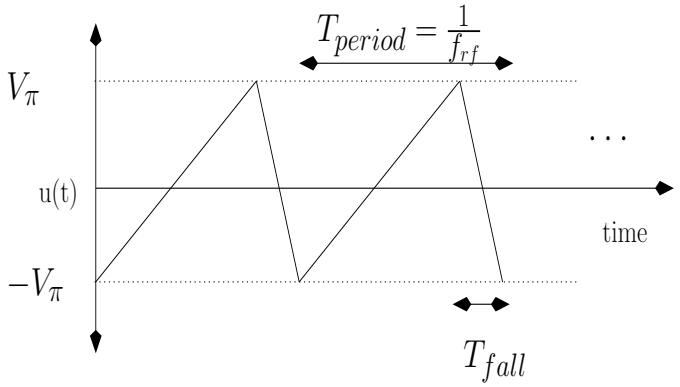

Figure 4.14: Non-ideal sawtooth signal with a non-zero fall time.

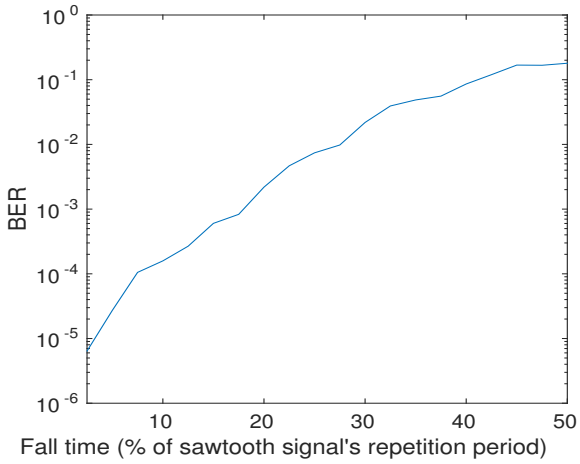

Figure 4.15: System performance for non-ideal sawtooth signal having a non-zero fall time.

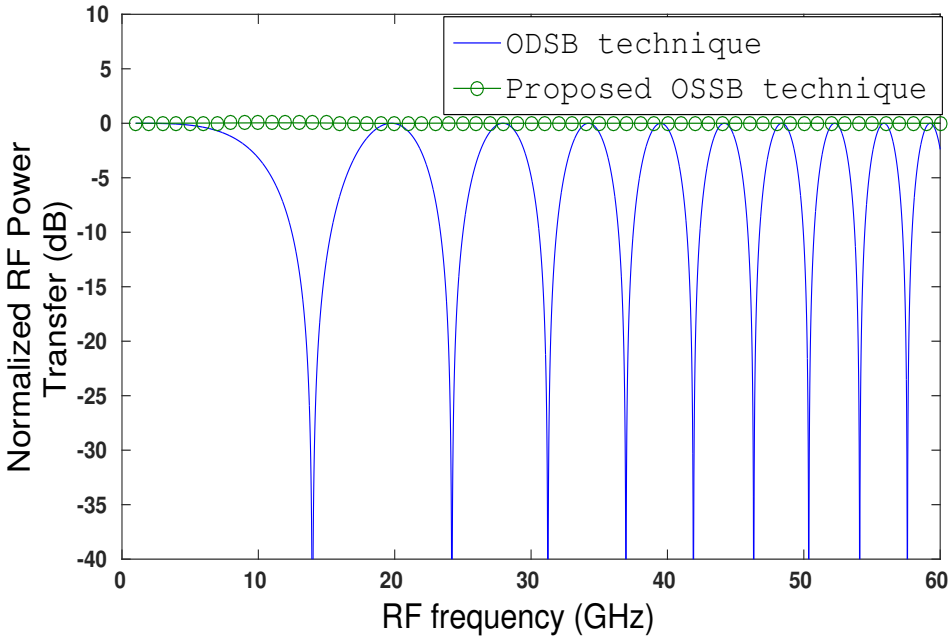

Figure 4.16: System performance for various RF carriers

The generation of the classical OSSB signal as well as of the chirp-free ODSB signal are discussed in [4]. Fiber dispersion results in the photo-detected power being attenuated for the case of the chirp-free ODSB signal according to [4]:

$$P_{RF} \propto \cos^2\left[\frac{\pi \cdot L \cdot D \cdot \lambda_c^2 \cdot f_{RF}^2}{c}\right], \tag{4.23}$$

where c is the speed of light in vacuum, which results in a BER degradation. Using the photo-detected power for the case of no fiber dispersion as our reference, the power penalty imposed by fiber dispersion on the photo-detected RF signal power is shown in Fig. 4.16. The photo-detected RF signal does not suffer from dispersion-induced power attenuation, when employing the classical OSSB modulation that relies on a dual-drive MZM [5]. It can be seen from Fig. 4.16 that our new OSSB modulation technique also provides the same advantage.

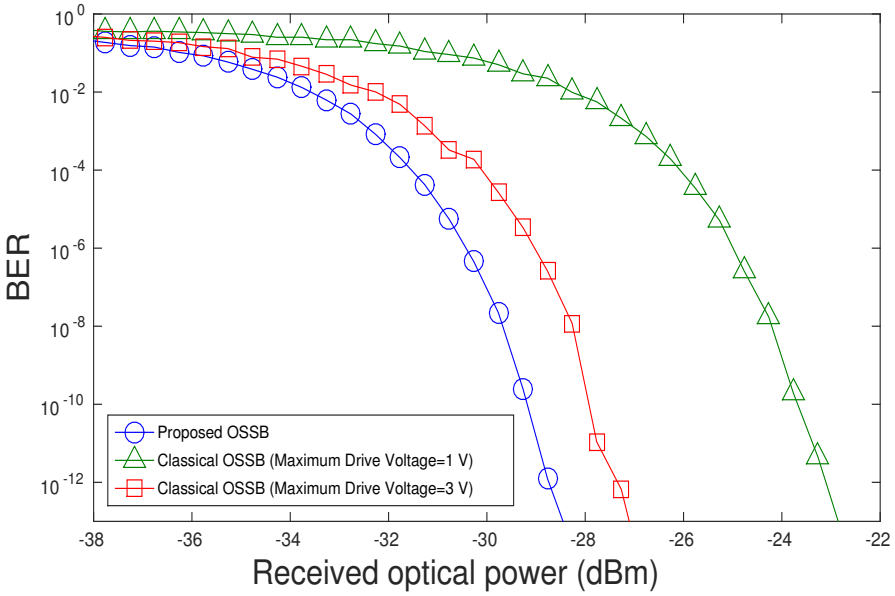

Figure 4.17: BER performance of the optical link

In the proposed architecture, the single sideband is generated by using the phase-shifter in the arm of a single-drive MZM for frequency shifting the optical sideband carrying a baseband electronic signal. Hence, as seen from Fig. 4.12, the proposed technique does not generate harmonics. On the other hand, Fig. 4.18 shows the optical spectrum of the classical OSSB signal, where we can observe the generation of harmonics because intensity-, rather than phase-modulation is employed. Fig. 4.19 shows the non-linear intensity transmittance of a dual-drive MZM, where the classical OSSB signal is generated by employing a bias voltage of $\frac{V_\pi}{2}$. The BER attained using the classical OSSB modulation depends on the maximum drive voltage employed. Explicitly, employing a higher drive voltage generates a stronger RF signal, but it also generates stronger harmonics. It can be seen from Fig. 4.19 that the drive voltage has an absolute maximum of $\frac{V_\pi}{2} = 3$ V. Drive voltages higher than $\frac{V_\pi}{2} = 3$ V would result in multiple values of the RF signal being transmitted using the same optical power, i.e. faithful one-to-one mapping between the RF voltage and optical power is lost. However, operating at a value close to the absolute maximum of 3 V generates strong non-linear

signals. The suppression of harmonics becomes important, when employing multiple RF signals, because the harmonics of one RF signal may corrupt another RF signal. Additionally, a higher drive voltage also results in stronger intermodulation products, when employing multiple RF signals, where the third order intermodulation products lie very close to the RF signals transmitted. Fig. 4.20 and Fig. 4.21 show the suppression of the optical and photodetected harmonics, respectively, with respect to the desired signal for various values of the maximum drive voltage. It can be seen from Fig. 4.20 and Fig. 4.21 that a differential maximum RF voltage of 1 V results in harmonics, which can be effectively suppressed by practical electronic filters. Nevertheless, in our simulations we consider both scenarios, i.e. scenarios having a maximum drive voltage of 1 V and 3 V.

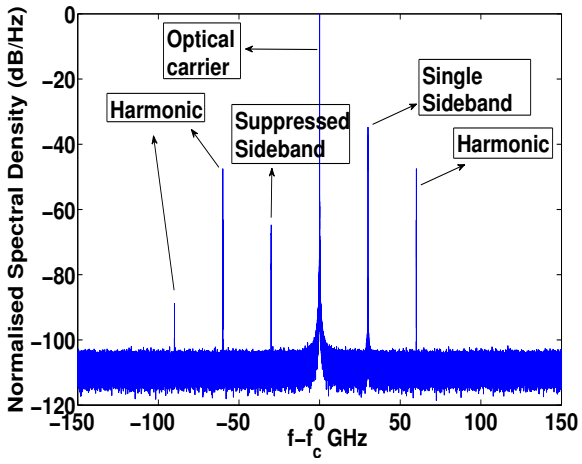

Figure 4.18: Optical spectrum of the classical OSSB signal.

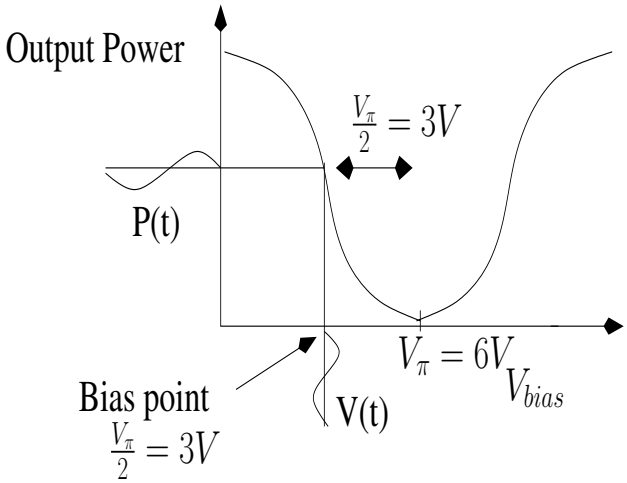

Figure 4.19: The transmittance of a dual-drive MZM.

Fig. 4.17 shows the BER performance of the optical link proposed in this section for the simulation parameters of Table 1. Fig. 4.17 shows the performance attained by the link in Fig. 4.11, when employing the classical dual-drive MZM based OSSB signal generation, instead of the proposed single-drive MZM. A maximum differential RF voltage of 1 V and 3 V was applied to the two arms of the dual-drive MZM. It can be seen from Fig. 4.17 that the performance of the proposed technique is better than that of the classical OSSB technique. Explicitly, the BER performance of the proposed scheme

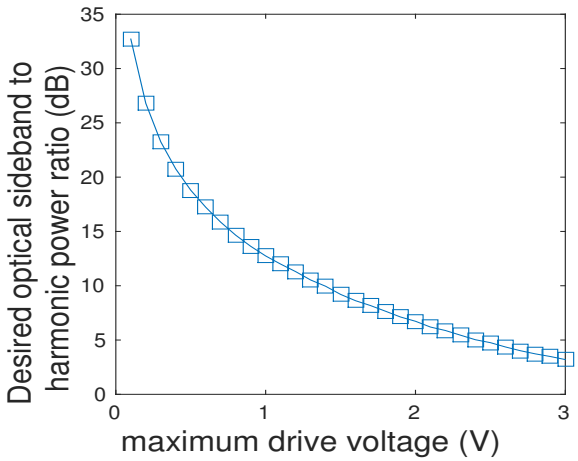

Figure 4.20: Desired sideband to harmonic power ratio for various values of the maximum drive voltage.

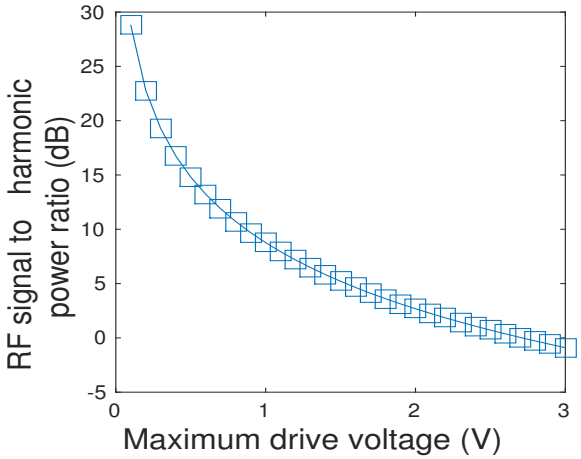

Figure 4.21: RF signal to harmonic power ratio for various values of the maximum drive voltage.

is better than the best-case performance achieved by the classical OSSB scheme using a maximum differential RF voltage of 3 V. *On the other hand, the cost of these performance improvements is the constraint of transmit optical modulation using a baseband electronic signal, which makes our proposed scheme suitable for only downlink transmission. Additionally, there is the constraint of having to employ phase modulation of RF signals, as seen in Equation (4.29).*

The classical approach of generating an OSSB signal relies on a dual-drive MZM [4]. A single drive MZM has only a single active arm with its associated driving circuitry, while the dual-drive MZM consists of two active arms along with the associated pair of electronic circuitry. Hence, the cost of a dual-drive MZM is higher than that of a single-drive MZM. The second classical approach of generating an OSSB using a single-drive MZM along with a FBG filter suffers from an increased cost due to the need for optical filtering [4]. Indeed, both the single- and dual- drive MZMs are commercially available. However, the difference in the cost of OSSB generation between relying on the proposed technique using only a single-drive MZM and on the classical methods, certainly becomes significant, when viewed in conjunction with the fact that over 3 million small cells are forecast for 2016 [223]. Moreover, this number is expected to rapidly increase in the subsequent years. Any

difference in the cost of generation would become significant, when considering the large number of optical transmitters that would be needed.

MIMO techniques are a powerful wireless communication technique for overcoming fading. However, the need to transmit multiple optical signals to the same RAP for MIMO downlink transmission of multiple RF signals would significantly increase the cost of the ROF link. In the next section, we present a novel architecture that is aimed at overcoming this challenge.

4.3 Single optical double side band radio-over-fiber signal supports space time block coding at each RAP

The optical-wireless backhaul technique of ROF makes a network employing small cells and high-RF carriers cost-effective. Each cell of a ROF-aided network is served by a RAP, while multiple RAPs are connected to a central BS via optical fiber [4, 5, 233]. Centralised signal processing at the BS simplifies the RAP and hence facilitates cost reduction [2, 6, 56].

4.3.1 Motivations for the proposed architecture

Some important challenges of large-scale employment of ROF-aided high-RF systems are as follows.

1. Electronic components, especially the mixers, exhibit a degraded performance at high frequencies [56]. Optical generation of the RF signal is a potential solution to this challenge [164]. For example, [234] is a recent paper that proposes a new method for optical generation of UWB RF signals.

2. Multiple input multiple output (MIMO) techniques like the classic STBC devised by Almouti in [235] can be employed in the wireless link of ROF systems to improve the downlink bit error rate (BER) performance [236], [227]. However, multiple optical modulators may be required at the central BS for supporting MIMO transmission from each RAP as in [236].

3. The most commonly employed ODSB modulation, unlike the optical single side band (OSSB) modulation, is severely affected by the chromatic dispersion-induced power attenuation at high RF carriers [43].

4.3.2 Advantages of the proposed architecture

The proposed architecture implements optical upconversion to avoid the use of electronic mixers [164]. Optical upconversion is implemented using a MZM driven by a sawtooth signal. Both sidebands of the classical ODSB carry the same signal[84]. In contrast to the classical ODSB, the optical signal generated in the proposed architecture is an ODSB signal in which the two sidebands transmit two different signals, namely the two STBC-encoded signals. Thus, a single dual-drive MZM supports 2×1 STBC Transmission from each RAP, thereby addressing the second challenge discussed in Section 4.3.1 In the RAP, the two sidebands are separately photo-detected, which gives it the performance advantages of an OSSB signal, thereby addressing the final challenge discussed in Section 4.3.1. Each RAP has a pair of antennas. The two photo-detected signals are transmitted to the mobile station

(MS) using different antennas, where the MS has a STBC receiver.

A theoretical study of the proposed architecture shown in Fig. 4.22 is provided in Section 4.3.3, while the results of our simulation-based study are presented in Section 4.3.4.

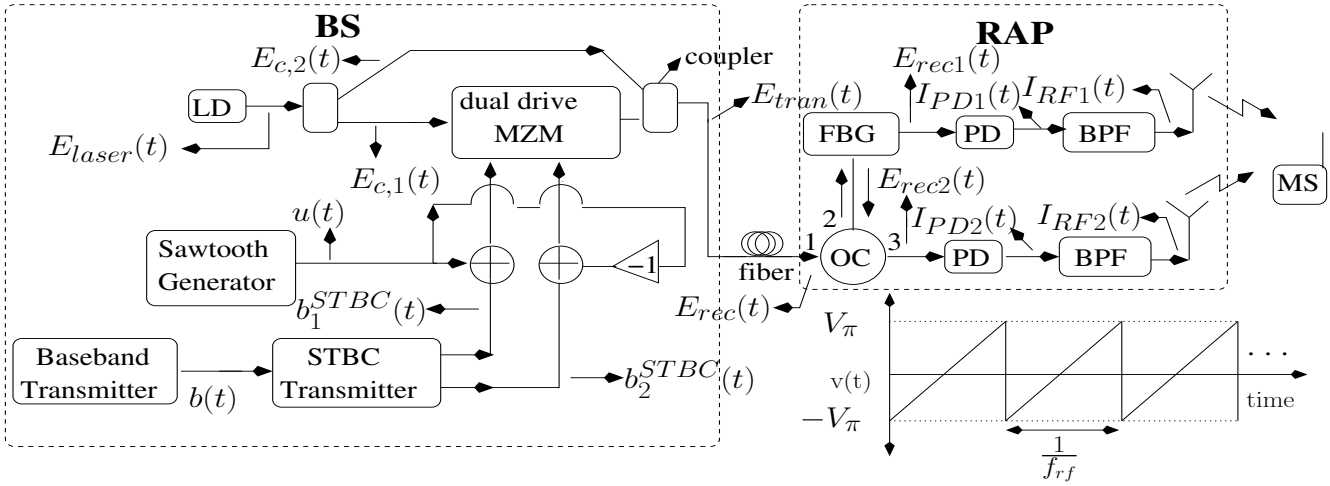

Figure 4.22: Proposed system architecture

4.3.3 Proposed downlink architecture and analysis

In the following sections we present a theoretical analysis of the architecture in Fig. 4.22, which includes transmitter in the BS and the receiver in the RAP.

4.3.3.1 Transmitter in the BS

The laser diode (LD) in the BS of Fig. 4.22 has an optical frequency of f_c Hz and a power of P_{LD}, while its optical output field is [2, 84]

$$E_{laser}(t) = \sqrt{2P_{LD}}e^{j2\pi f_c t}. \tag{4.24}$$

As shown in Fig. 4.22, the output of the laser is split by a 3 dB optical power splitter having an insertion loss of t_{sp} to yield

$$E_{c,1}(t) = E_{c,2}(t) = \sqrt{\frac{t_{sp}}{2}}E_{laser}(t). \tag{4.25}$$

The optical signal $E_{c,1}(t)$ is fed to a dual-drive MZM with its arms driven by signals $u(t) + b_1^{STBC}(t)$ and $-u(t) - b_2^{STBC}(t)$. If $b(t)$ is the baseband signal with bit-rate R_{bit} to be transmitted over the wireless link to the MS using RF phase modulation, then $b_1^{STBC}(t)$ and $b_2^{STBC}(t)$ are generated from $b(t)$ such that $e^{j(\pi\frac{b_1^{STBC}(t)}{V_\pi})}$ and $e^{j(\pi\frac{b_2^{STBC}(t)}{V_\pi})}$ are the STBC symbols transmitted to the MS [235]. If $b(t)$ consists of $2N$ symbols $\{x_k|1 < k < 2N\}$, then, for $1 < i < N$, the $(2i-1)^{th}$ and $(2i)^{th}$ symbols of the STBC signals are given by the first and second rows of the following matrix, respectively

$$[e^{j(\pi\frac{b_1^{STBC}}{V_\pi})}e^{j(\pi\frac{b_2^{STBC}}{V_\pi})}] = \begin{bmatrix} e^{j(\pi\frac{x_{2i-1}}{V_\pi})} & e^{j((\pi\frac{x_{2i}}{V_\pi}))} \\ -(e^{j(\pi\frac{x_{2i}}{V_\pi})})^* & (e^{j(\pi\frac{x_{2i-1}}{V_\pi})})^* \end{bmatrix}.$$

On the other hand, $u(t)$ is a sawtooth-shaped function given by

$$u(t) = modulo[2f_{RF}tV_\pi, 2V_\pi] - V_\pi \tag{4.26}$$

where f_{RF} is the RF carrier transmitted from the RAP to the MS, while V_π is the switching voltage of the dual-drive MZM. Fig. 4.22 shows the temporal plot of $u(t)$. If the MZM in the BS of Fig. 4.22 has an insertion loss of t_{attn} and it is driven by voltages $V_{drv1}(t$ and $V_{drv2}(t)$, then its output optical field is

$$\begin{aligned} E_{dual}(t) &= \frac{\sqrt{t_{attn}}}{2}[e^{j\frac{\pi V_{drv1}(t)}{V_\pi}} + e^{j\frac{\pi V_{drv2}(t)}{V_\pi}}]E_{c,1}(t) \\ &= \frac{\sqrt{t_{attn}}}{2}[e^{j\pi\frac{b_1^{STBC}(t)+u(t)}{V_\pi}} + e^{j\pi\frac{b_2^{STBC}(t)+u(t)}{V_\pi}}]E_{c,1}(t) \\ &= -\frac{\sqrt{t_{attn}}}{2}[e^{j(2\pi f_{RF}t+\pi\frac{b_1^{STBC}(t)}{V_\pi})} \\ &\qquad + e^{j(-2\pi f_{RF}t+\pi\frac{b_2^{STBC}(t)}{V_\pi})}]E_{c,1}(t). \end{aligned} \tag{4.27}$$

As shown in Fig. 4.22, the output of the MZM is combined with the second output $E_{c,2}(t)$ of the splitter to generate $E_{tran}(t)$. If the optical coupler's insertion loss is t_{sp}, then $E_{tran}(t)$ can be expressed from (4.25) and (4.27) as follows

$$\begin{aligned} E_{tran}(t) &= [-\frac{\sqrt{t_{attn}}}{2}e^{j(2\pi f_{RF}t+\pi\frac{b_1^{STBC}(t)}{V_\pi})} \\ &- \frac{\sqrt{t_{attn}}}{2}e^{j(-2\pi f_{RF}t+\pi\frac{b_2^{STBC}(t)}{V_\pi})} + 1]E_{laser}(t)\frac{t_{sp}}{2}. \end{aligned} \tag{4.28}$$

The spectrum of $E_{tran}(t)$ is shown in Fig. 4.23, where it can be seen that $E_{tran}(t)$ is an ODSB signal, in which the upper and lower sidebands carry $b_1^{STBC}(t)$ and $b_2^{STBC}(t)$, respectively.

We now discuss the receiver in the RAP of the architecture in Fig. 4.22.

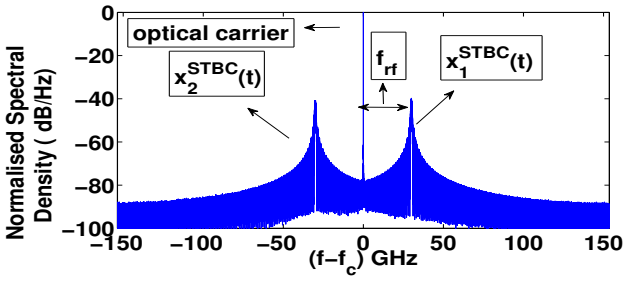

Figure 4.23: Spectrum of the generated signal

4.3.3.2 Receiver in the RAP

As shown in Fig. 4.22, the optical signal $E_{tran}(t)$ propagates through the optical fiber of length L and it is received as $E_{rec}(t)$ in the RAP. The fiber attenuates the signal and its dispersion imposes a phase shift ϕ_{disp} on the two sidebands with respect to the carrier [84]. Thus, from (4.28), the received

signal becomes

$$E_{rec}(t) = e^{\frac{\alpha}{2}L}[-\frac{\sqrt{t_{attn}}}{2}e^{j(2\pi f_{RF}t+\pi\frac{b_1^{STBC}(t)}{V_\pi}+\phi_{disp})} - \frac{\sqrt{t_{attn}}}{2}e^{j(-2\pi f_{RF}t+\pi\frac{b_2^{STBC}(t)}{V_\pi}-\phi_{disp})}+1]E_{laser}(t)\frac{t_{sp}}{2} \quad (4.29)$$

where α is the fiber's attenuation parameter. In the RAP of Fig. 4.22, the optical signal enters Port 1 of the optical circulator (OC) and exits from Port 2, where it encounters a fiber bragg grating (FBG) that reflects 50% of the carrier power in addition to the complete lower sideband. These filters are similar to those employed in [172]. The reflected signal then enters Port 2 of the OC and exits from Port 3. The signal passing through the FBG and the reflected signal exiting Port 3 have optical fields of $E_{rec1}(t)$ and $E_{rec2}(t)$, which can be expressed as

$$E_{rec1}(t) \quad (4.30)$$
$$= e^{\frac{\alpha}{2}L}[\frac{1}{\sqrt{2}} - \frac{\sqrt{t_{attn}}}{2}e^{j(2\pi f_{RF}t+\pi\frac{b_1^{STBC}(t)}{V_\pi}+\phi_{disp})}]E_{laser}(t)\frac{t_{sp}}{2},$$
$$E_{rec2}(t) \quad (4.31)$$
$$= e^{\frac{\alpha}{2}L}[\frac{1}{\sqrt{2}} - \frac{\sqrt{t_{attn}}}{2}e^{j(-2\pi f_{RF}t+\pi\frac{b_2^{STBC}(t)}{V_\pi}-\phi_{disp})}]E_{laser}(t)\frac{t_{sp}}{2}.$$

Subsequently, as seen in Fig. 4.22, $E_{rec1}(t)$and $E_{rec2}(t)$ are photo-detected using a photo-diode (PD) of responsivity R to generate currents, which can be expressed using (4.24), (4.25), (4.30) and (4.31) as

$$I_{PD1}(t) = R|E_{rec1}(t)|^2 = \frac{Re^{\alpha L}P_{LD}(t_{sp})^2}{2}[0.5 + \frac{t_{attn}}{4} - \sqrt{\frac{t_{attn}}{2}}\cos(2\pi f_{RF}t + \pi\frac{b_1^{STBC}(t)}{V_\pi} + \phi_{disp})] \quad (4.32)$$

$$I_{PD2}(t) = R|E_{rec2}(t)|^2 = \frac{Re^{\alpha L}P_{LD}(t_{sp})^2}{2}[0.5 + \frac{t_{attn}}{4} - \sqrt{\frac{t_{attn}}{2}}\cos(2\pi f_{RF}t + \pi\frac{b_2^{STBC}(t)}{V_\pi} - \phi_{disp})]. \quad (4.33)$$

The pair of photo-detected signals $I_{PD1}(t)$ and $I_{PD2}(t)$ are then filtered using bandpass filters centered at f_{RF} Hz, as shown in Fig. 4.22, in order to generate the RF signals

$$I_{RF1}(t) = K\cos(2\pi f_{RF}t + \pi\frac{b_1^{STBC}(t)}{V_\pi} + \phi_{disp}) \quad (4.34)$$

and

$$I_{RF2}(t) = K\cos(2\pi f_{RF}t + \pi\frac{b_2^{STBC}(t)}{V_\pi} - \phi_{disp}) \quad (4.35)$$

where K is the amplitude of the filtered signal. The above RF signals are amplified and transmitted over the wireless link to the MS of Fig. 4.22, where they are synchronously down-converted [227]. These RF signals are phase-modulated, up-converted versions of the STBC encoded complex baseband signals $e^{j(\pi\frac{b_1^{STBC}(t)}{V_\pi}+\phi_{disp})}$ and $e^{j(\pi\frac{b_2^{STBC}(t)}{V_\pi}-\phi_{disp})}$. Fiber-dispersion rotates all the symbols by a length-dependent constant phase of ϕ_{disp} radians, which may be considered as part of the complex-valued wireless channel and hence they are jointly estimated by the wireless channel estimation technique

used at the MS. In other words, if the wireless channel transmitting $I_{RF1}(t)$ and $I_{RF2}(t)$ has complex coefficients of h_1 and h_2, respectively, then the channel coefficients estimated at the MS and hence employed by the STBC receiver are $h_1 e^{j\phi}$ and $h_2 e^{-j\phi}$, respectively.

A practical implementation of the proposed architecture may employ a non-ideal MZM and a non-ideal sawtooth signal. A non-ideal MZM's output is given by the nth order Bessel function [233]. These imperfections generate non-linear products like intermodulation and harmonics [233]. However, we hasten to add that these non-linear signals may be significantly suppressed by the FBG filter in the receiver and by the electronic filter after photo-detection. If needed, an additional FBG filter may also be employed after port 3 of the OC in Fig. 1(a) for suppressing these signals before photo-detection by the lower photo-diode.

It is also worth mentioning at this point that the transmitter seen in Fig. 4.22 splits the optical signal and then combines it, which would result in a phase difference between the two signals in the two arms. However, it can be shown that this phase shift would only add to the existing dispersion-induced phase difference of ϕ_{disp} and it would not cause any additional power attenuation.

In the next section, we analyse the effect of employing a non-ideal transmitter and receiver as well as that of the fiber's dispersion and then characterize the overall system performance.

4.3.4 Simulation results of the proposed architecture

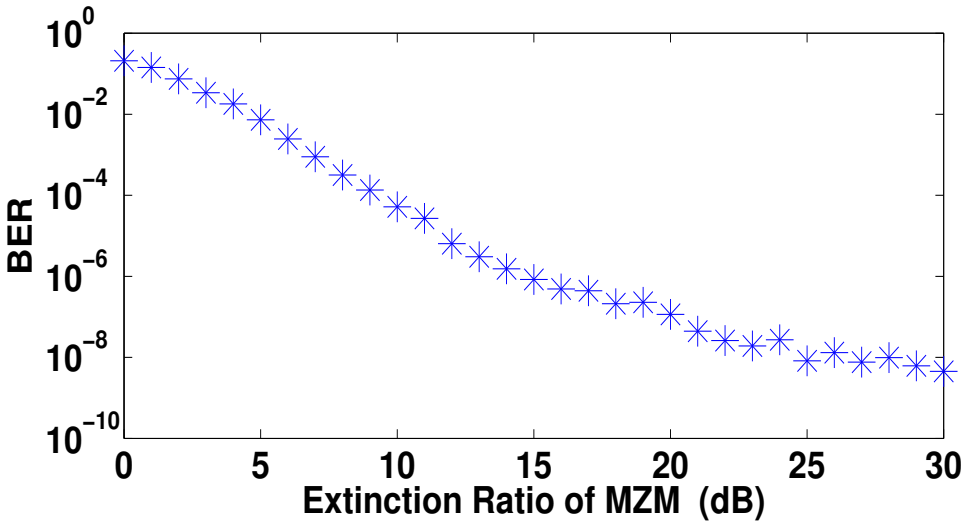

Figure 4.24: System performance when employing a non-ideal MZM in transmitter

Table 4.3 shows the system parameters employed in our simulations. The photo-detected current is given by (4.32) and (4.33) and the additional dark current I_{dark}. The relative intensity noise (RIN) power, shot noise power and thermal noise power imposed by the optical link are $\sigma^2_{RIN} = K_{RIN} I^2_{dc} \Delta f_{noise}$, $\sigma^2_{shot} = 2eI_{dc}\Delta f_{noise}$ and $\sigma^2_{thermal} = \frac{4k_bT}{R_L}\Delta f_{noise}$, respectively [31]. Here, I_{dc} is the average photo-detected current, Δf_{noise} is the optical receiver's bandwidth, k_b is the Boltzmann constant, T is the absolute temperature of 290 K, R_L is the load resistance, F_n is the optical receiver

amplifier's noise figure, while e is the charge of an electron. Optical propagation is given by

$$\frac{\partial A}{\partial z} = -\frac{\alpha}{2} - j\frac{\beta_2}{2}\frac{\partial^2 A}{\partial T^2} + j\gamma_{nl}\{|A|^2 A\} \tag{4.36}$$

where $A(z,T)$ is the envelope (or amplitude) of the modulated optical carrier after it has propagated through z km of SSMF, while $D = -\frac{2\pi c}{\lambda_c^2}\beta_2$, γ and α are the fiber's dispersion parameter, non-linearity parameter and attenuation parameter, respectively. Equation (4.36) was simulated using the split step Fourier method [31].

Table 4.3: Parameter values of the ROF link

Parameter	**Value**	**Parameter**	**Value**
R_{bit}	32 Mbps	t_{attn}	4 dB
t_{sp}	3 dB	ϵ	30 dB
λ_c	1550 nm	L	20 km
V_π	6 V	R_L	125 Ω
		Laser linewidth	10 MHz
D	16 ps/km-nm	γ	1.2 /W/km
		I_{dark}	1 nA
α	0.2 dB/km	F_n	6 dB
R	0.8 A/W	f_{RF}	30 GHz
K_{RIN} (dBc/Hz)	-155	Diversity employed	STBC

Equation (4.27) assumes an ideal MZM having an extinction ratio ϵ^2 of infinity in the transmitter. However, we have $E_{dual}(t) = \frac{\sqrt{t_{attn}}}{2}[e^{j\frac{\pi V_{drv1}(t)}{V_\pi}} + \gamma e^{j\frac{\pi V_{drv2}(t)}{V_\pi}}]E_{c,1}(t)$ for a practical MZM, where $\gamma = (\sqrt{\epsilon}-1)/(\sqrt{\epsilon}+1)$. Based on the discussions in Section 4.3.3, we arrive at

$$I_{RF1}(t) = K\cos(2\pi f_{RF}t + \pi\frac{b_1^{STBC}(t)}{V_\pi} + \phi_{disp}) \tag{4.37}$$

and

$$I_{RF2}(t) = K\gamma\cos(2\pi f_{RF}t + \pi\frac{b_2^{STBC}(t)}{V_\pi} - \phi_{disp}). \tag{4.38}$$

In other words, the two STBC signals that are transmitted from the RAP are not exactly of the same power, thereby resulting in a BER degradation. Fig. 4.24 shows the BER degradation for various extinction ratios. The simulation results shown in Fig. 4.24 relied on a transmit power that results in a BER of 10^{-8} for a near-ideal extinction ratio of 30 dB. It can be seen from Fig. 4.24 that the degradation is lower than an order of magnitude for commercially available MZMs having extinction ratios of about 20 dB.

The derivation of (4.34) and (4.35) assumed having an FBG filter in the receiver that perfectly reflected one of the sidebands, while transmitting the other. Let us now study the effect of employing a realistic, practical FBG filter that assumes an imperfect reflection of the sideband. Fig. 4.25 shows

[2]Extinction-ratio is defined as the ratio of the optical power transmitted for bit 1 to the power transmitted for bit 0 [31].

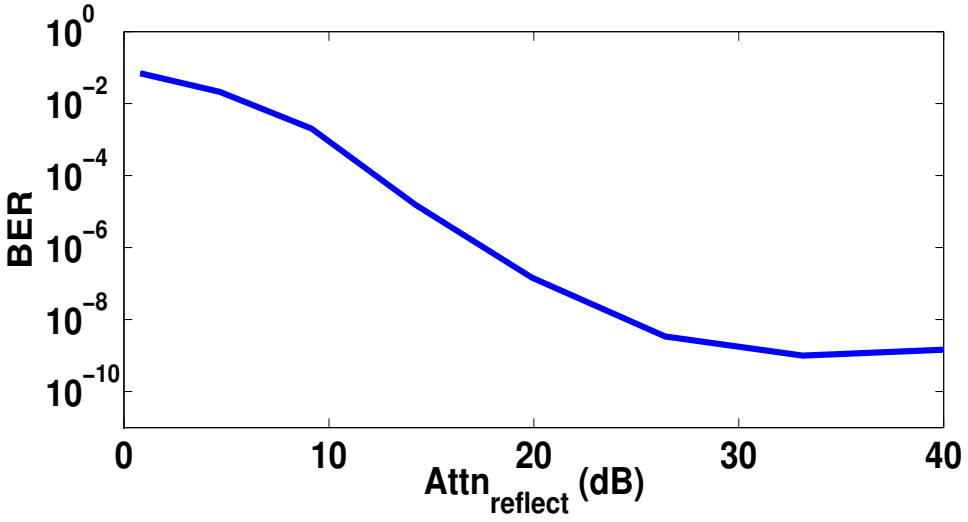

Figure 4.25: System performance for non-ideal optical filtering in receiver

the BER degradation for various attenuation levels $Attn_{reflect}$ of the reflected sideband w.r.t the transmitted sideband, where the ideal complete reflection of the reflected sideband corresponds to an attenuation of ∞ dB. The simulation results shown in Fig. 4.25 assume an ideal MZM in the transmitter in order to study the BER degradation imposed by the receiver alone. It can be seen from Fig. 4.25 that the BER degradation is lower than an order of magnitude for the typical attenuations of commercially available FBG filters.

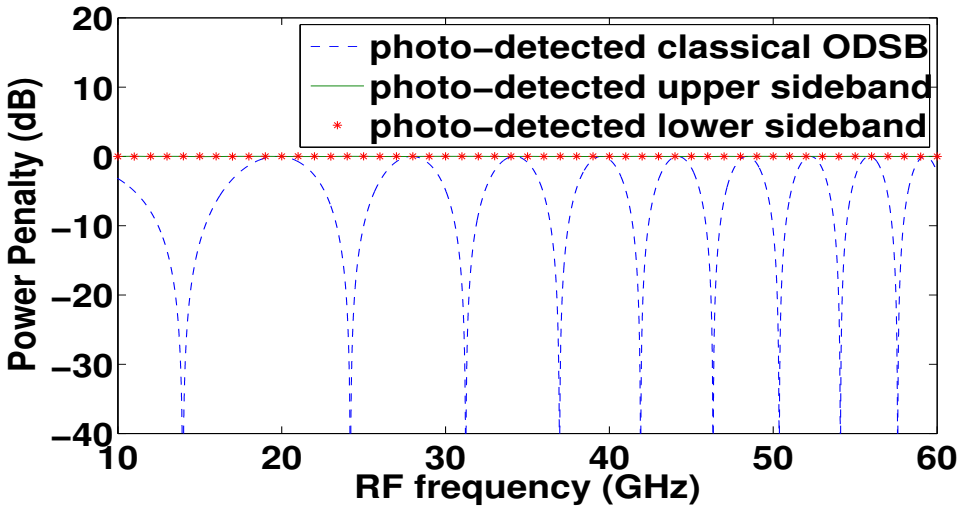

Figure 4.26: System performance for various RF carriers

The classical ODSB signal generated by employing a MZM biased at $V_\pi/2$ volts carries a single signal using both sidebands [84]. Naturally, fiber dispersion attenuates the photo-detected power of the classical chirp-free ODSB signal as per the following expression [83]

$$P_{RF} \propto \cos^2\left[\frac{\pi \cdot L \cdot D \cdot \lambda_c^2 \cdot f_{RF}^2}{c}\right] \tag{4.39}$$

where c is the speed of light in vacuum. This power attenuation results in a BER degradation. Fig.

4.26 shows the power penalty imposed on the photo-detected RF signal by fiber dispersion, where the reference is the photo-detected power for the case of no fiber dispersion. It can be seen from Fig. 4.26 that in the proposed scheme, the RF signals generated by the separate photo-detection of the upper and lower sidebands do not suffer from any dispersion-induced power attenuation. This is because their separate photo-detection gives the proposed scheme the advantage offered by OSSB modulation [43]. Fig. 4.27 shows the BER performance of the optical link proposed in this section for the simulation parameters of Table 4.3.

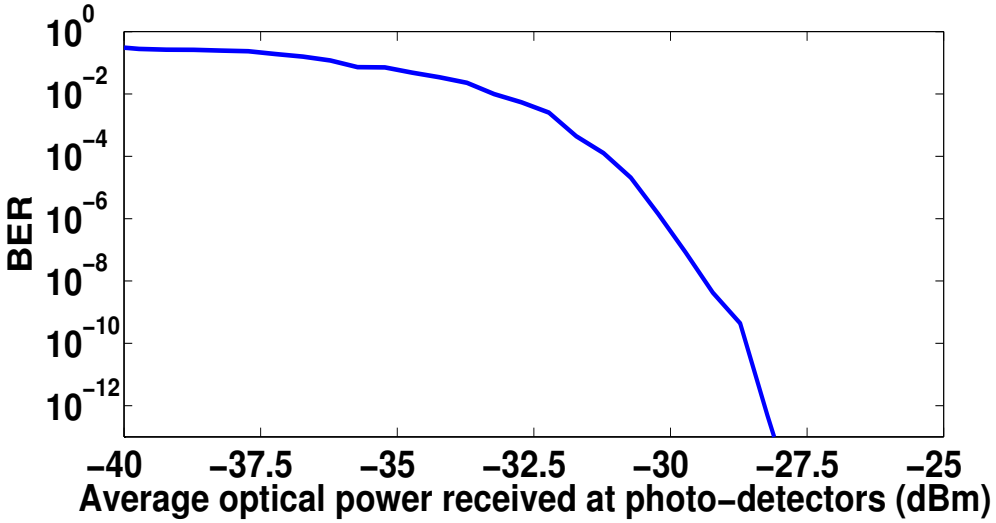

Figure 4.27: BER performance of the optical link

Having designed the optical link, we now study the performance of the overall ROF link including the wireless link. Fig. 4.28 shows the ideal error vector magnitude (EVM) performance of a wireless link employing STBC and no backhaul along with the EVM performance of the proposed ROF link for a laser transmit power of 0 dBm. It can be seen in Fig. 4.28 that the ROF backhaul imposes only negligible degradation, while enabling the designer to fully exploit the diversity gain of STBC [235]. Note that the term SNR of wireless channel in Fig. 4.28 refers to the SNR computed at the wireless receiver and it includes the noise added by the wireless link only.

4.4 Chapter conclusions

Three novel architectures that result in significant cost reductions as well as employ optical generation of RF signals were proposed in this chapter.

Firstly, in Section 4.1, an optical architecture was conceived for modulating two independent signals $x(t)$ and $y(t)$ onto the phase and intensity of the optical carrier, respectively, using a single optical modulator, which was then mathematically characterized. Four potential applications of this architecture were discussed and a simulation-based study was conducted for characterizing their performance.

Next, in Section 4.2, an OSSB modulation scheme was designed that relies on a single-drive, rather than dual-drive, MZM, while dispensing with the employment of an optical filter. Additionally, optical upconversion of the baseband signal to RF was facilitated by driving the single-drive MZM using a

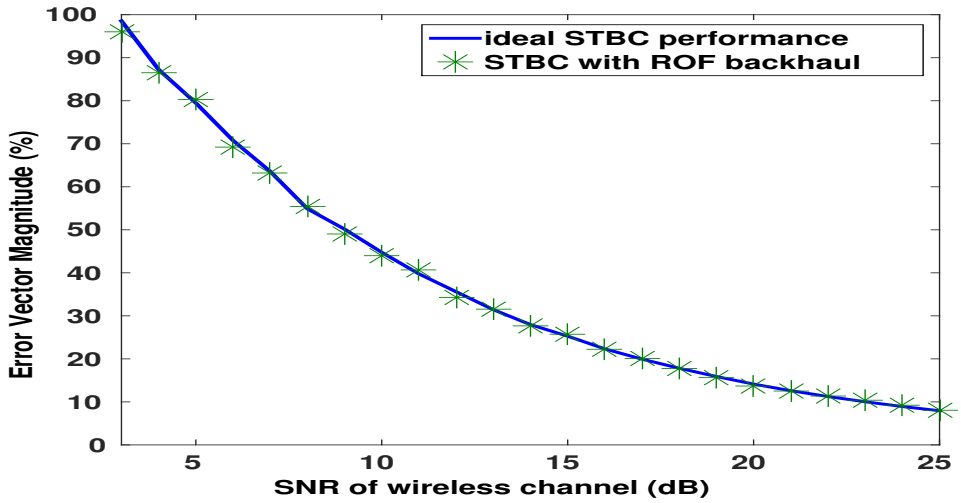

Figure 4.28: Performance of wireless link relying on a ROF backhaul

sawtooth signal. The proposed OSSB scheme was shown to outperform the conventional dual-drive MZM based OSSB technique.

Finally, in Section 4.3, a ROF backhaul was conceived for supporting 2×1-element downlink STBC. Each RAP was served by an ODSB signal, each of whose sidebands carried the RF signal for one of the two STBC antennas. The downlink signal was generated by a single MZM, where this MZM implemented optical upconversion. This backhaul imposed negligible degradation, while enabling the exploitation of the diversity gain of STBC.

Having proposed novel architectures that are aimed at cost reduction and optical generation of RF signals, we now turn our attention to the third design approach mentioned in Chapter 3, namely the employment of performance improving techniques. Explicitly, in Chapter 5 we focus on the performance improving technique of Digitized ROF.

Chapter 5

Digitized radio over fiber

Chapter 2 discussed the classical ROF link, which is also referred to as the AROF link, while Chapter 3 discussed a range of techniques that may be employed for achieving an improved link performance as well as techniques designed for achieving a reduced link cost. One of the performance improvement techniques discussed in Chapter 3 was the Digitized Radio Over Fiber (DROF) technique, which will be investigated in detail in this chapter.

One of the substantial advantages of the classical AROF link of Fig. 2.1 is the low complexity of its RAP, which makes the employment of a large number of such RAPs economically viable for the network service provider. As a price paid for its cost benefits, AROF also has some disadvantages, which are as follows:

1. *Fiber dispersion*: The Group Velocity Dispersion (GVD) discussed in Section 2.1.1.3 constitutes a major limitation of the AROF link. It was seen from the results of Section 2.1.5.7 that GVD limits the achievable fiber lengths and RF frequencies for the case of the most commonly employed ODSB modulation. A range of techniques designed for overcoming chromatic dispersion were discussed in Section 3.1.11. However, these techniques increase both the system's complexity and cost.

2. *Need to employ external modulation*: The ODSB signal discussed in Section 2.1.2.1 can be generated using both the direct and external modulation techniques of Section 2.1.1.2, while the OSSB and OCS signals discussed in Sections 2.1.2.1 and 2.1.2.1 cannot be generated using direct modulation. Moreover, the modulating RF signal's carrier frequency may be beyond the laser's direct modulation bandwidth of Fig. 2.7 [31]. Thus, the additional cost of external modulators increases the total system cost. Furthermore, as seen from Fig. 2.9(a) and Fig. 2.10(b), external modulators have a transmittance curve that is more non-linear than the P-I curve of direct modulation, which was shown in Fig. 2.6(b). Thus, employing external modulators results in the generation of the various higher harmonics and intermodulation products discussed in Section 2.1.3.1.

3. *The need for high electronic-bandwidth optical components*: In the case of AROF, the electronic bandwidth of the lasers/external-modulators and photo-detectors has to be higher than the electronic bandwidth of their counterparts in the more commonly employed digital optical link.

4. *Limited dynamic range*: The dynamic range of an AROF link is reduced linearly upon increasing the fiber length due to its attenuation [237].

The DROF architecture discussed in Section 3.1.12 can help overcome the above-mentioned challenges, where Section 5.1 provides a detailed study of the DROF technique. Subsequently, in Section 5.2, a duplex ROF ring architecture is proposed by taking into account the constraints imposed by the cost of fiber laying and that of the optical/electronic components, as well as the spectral efficiency and the duplex link performance. We show that relying on Analog ROF (AROF) and state-of-the-art DROF architectures for downlink and uplink transmission, respectively, results in a high-integrity duplex performance. A sophisticated amalgam of OCS, Code Division Multiplexing (CDM), Optical Frequency Multiplexing, Wavelength Reuse and Distributed Antennas is conceived.

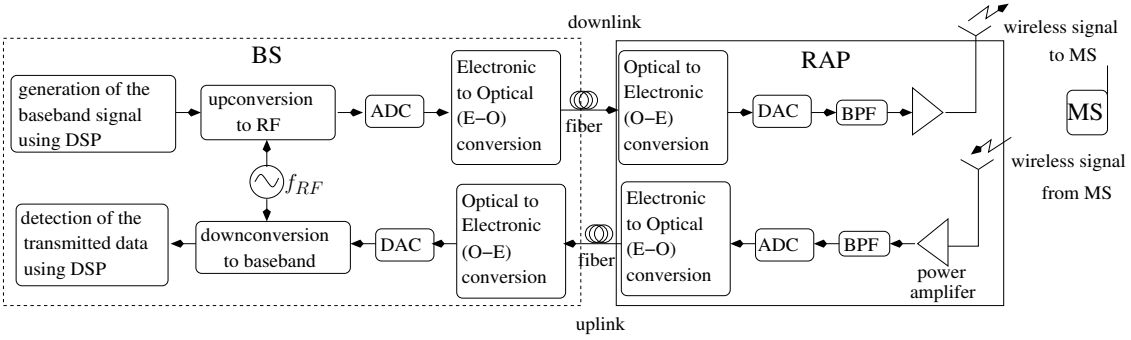

Figure 5.1: DROF link block diagram

5.1 Digitized radio over fiber

Fig. 5.1 shows the DROF architecture, where the basic principle employed is the digitization of the RF signals. In case of DL transmission, as shown in Fig. 5.1, the baseband signal is generated in the BS using the conventional baseband modulation techniques discussed in [225]. This is followed by its upconversion to RF using oscillators and mixers. In the case of the the classical AROF architecture of Fig. 2.1, this RF would have been directly transmitted using optical modulation. However, in the DROF architecture of Fig. 5.1, it is digitized using an ADC and following that it is conveyed optical modulation. The modulated optical signal is then transmitted to the RAP, where it is photo-detected followed by detection of the digitized bits. In the RAP of Fig. 5.1, the digitized signal is then fed to a Digital to Analog Converter (DAC) for reconstructing the RF signal, which is then filtered, amplified and wirelessly transmitted to the MS.

In the case of UL communication, as shown in Fig. 5.1, the RF signal received from the MS impinges at the antenna of the RAP. This RF signal is bandlimited using a bandpass filter and then fed to the ADC for digitization, followed by optical modulation conveying the digitized RF signal. As shown in Fig. 5.1, this is followed by the transmission of the optical signal to BS, where it is photo-detected for obtaining the digitized uplink signal. This signal is then fed to the DAC for reconstructing the uplink RF signal, which can then be down-converted and detected using the conventional detection techniques discussed in [225].

Thus, the DROF link relies on a digital optical link, i.e. a link in which digital/binary signalling is employed, while AROF employs a microwave/millimeter-wave optical link, i.e. a link in which RF signals are transmitted.

In this section, we discuss the basics of the DROF technique including its advantages and weaknesses in Sections 5.1.1 and 5.1.2, respectively. We then discuss the generation of the DROF signal in Section 5.1.3, while the transmission and the reception of the DROF signal are discussed in Section 5.1.4. The discussion of the DROF link would not be complete without a discussion of the noise processes and design trade-offs, which are presented in Sections 5.1.5 and 5.1.6, respectively. Finally, the results of a simulation-based study of the DROF link is presented in Section 5.1.8.

5.1.1 Advantages of the DROF architecture

DROF offers all the advantages of any ROF system, which were discussed earlier in Section 1.3. Additionally, the advantages of the DROF link seen in Fig. 5.1 over the classical AROF link of Fig. 1.8 are summarised as follows:

1. As stated above, in an AROF link, it was shown using the simulations of Section 2.1.5.7 that GVD limits the attainable fiber lengths and RF frequencies, in case of the most commonly employed ODSB modulation. However, the baseband nature of the modulating signal in DROF results in the chromatic dispersion being far less detrimental, thereby increasing the achievable fiber lengths and RF frequencies [117], as it becomes evident from the results that will be presented in Section 5.1.8.4. This is because the dispersion-induced power penalty in an AROF link, which is given by Equation (4.39), is absent in a DROF link, but the inevitable dispersion results in bit/pulse broadening.

2. The DROF system can be readily integrated with the backhaul constituted by the existing metro and wide area optical networks. This is because, unlike the AROF link, the DROF link employs digital optical communication, which is also the communication technique of the wide area optical networks [46].

3. Several digital signal processing techniques, which have been developed for the digital optical signals, including Optical Time Division Multiplexing (OTDM) [238], Optical Code Division Multiplexing (OCDM), optical pulse regeneration [239], [240], [241], [242], logical operations [125], [126], [243] etc, which may also be potentially exploited in a DROF link. It should be noted that optical signal processing has the advantage of imposing significantly lower latency than electronic signal processing.

4. The DROF link has a dynamic range that is almost entirely independent of the fiber length, provided that the received signal remains above the sensitivity of the link. However, beyond this erroneous transmissions occur [117].

5. As seen from Fig. 5.1, a DROF link, unlike the AROF link of Fig. 2.1, employs baseband electronic signals in optical modulation, which makes the low-cost direct modulation of the lasers a commonly employed modulation technique, as discussed in Section 2.1.1.2. This is because the bandwidth of the baseband signal would be well-within the electronic modulation

bandwidth of the laser, which was shown in Fig. 2.7. Thus, the option of avoiding external modulation results in the reduction of the DROF link's cost.

6. In contrast to the AROF link, the electronic bandwidth of the opto-electronic components, including the laser/external-modulator and the photo-detector does not have to be high, since the electronic signal that is being transmitted is in the baseband, which also reduces the DROF link's cost.

7. The digital optical communication techniques employed in a DROF link are more mature than the microwave/millimeter-wave optical techniques of an AROF link. This is because the existing long-haul optical communication links employ digital optical communication.

Having discussed the advantages of the DROF architecture, we now move on to discussing the weaknesses of the DROF architecture in the next section.

5.1.2 Disadvantages of the DROF architecture

Primarily, there are two disadvantages of employing the DROF architecture, which are as follows:

1. While the RAP of the DROF link seen in Fig. 5.1 has an ADC as well as a DAC, the RAP in the classical AROF link of Fig. 2.1 has no ADCs and DACs. Thus, the increased RAP complexity of DROF as compared to AROF is a distinct disadvantage.

2. The DROF link achieves a lower BER than AROF, but the digitization of the RF signal usually results in a bandwidth requirement that is higher than that of the RF signal [117]. Thus, the DROF technique results in a substantial transmission overhead, which is a disadvantage.

Now that we have introduced the wireless backhaul technique of DROF, next we discuss the generation, transmission and detection of the DROF signal in greater detail in Sections 5.1.3 and 5.1.4.

5.1.3 Generation of the DROF optical signal

It can be concluded from the discussions in Section 5.1 and from Fig. 5.1 that the generation of the optical signal to be transmitted over the DROF link is achieved in two steps, which are:

1. Digitization of the RF signal using bandpass sampling by the ADC of Fig. 5.1.

2. Electronic to Optical (E-O) conversion of Fig. 5.1.

The above steps are discussed in Section 5.1.3.1 and 5.1.3.2. This is followed by a discussion of the fiber-based transmission and detection of the DROF optical signal in Section 5.1.4.

5.1.3.1 Digitization of the RF signal

Fig. 5.2 shows the block diagram of the ADCs in Fig. 5.1. The digitization of the RF signal takes place in three steps:

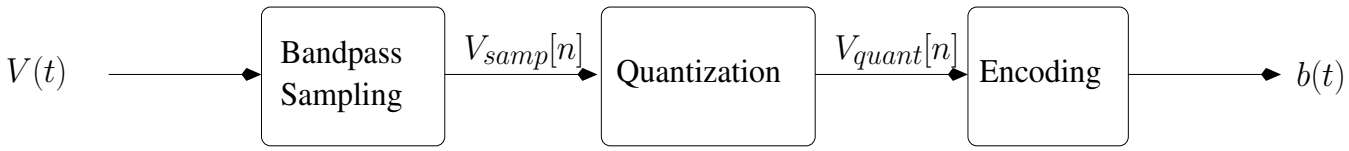

Figure 5.2: Block diagram of the ADC

1. Sampling of the RF signal;
2. Quantization of the sampled signal;
3. Encoding of the quantized values.

The above steps are discussed below in Sections (5.1.3.1) and (5.1.3.1).

Sampling of the RF signal: Nyquist's sampling theorem states that a signal has to be sampled at a rate, which is at least twice the highest frequency within its spectrum, in order to faithfully reconstruct the original signal from the sampled values [244]. Consider a RF signal $V(t)$ at f_{RF} Hz whose bandwidth is B, with f_u and f_l being the highest and lowest frequency components within the signal bandwidth, respectively. Then, the following is true:

$$B_{RF} = f_u - f_l; \tag{5.1a}$$

$$f_{RF} = \frac{f_u + f_l}{2}. \tag{5.1b}$$

As per Nyquist's sampling theorem, the above signal would have to be sampled at a rate of at least $2 \cdot f_u$ for ensuring faithful reconstruction of the RF signal from the sampled values. It can be seen from Equation (5.1b) that f_u has a RF value, thereby resulting in a high value of the minimum sampling rate stipulated by Nyquist's sampling theorem. Thus, employing classical sampling techniques in the ADCs of Fig. 5.1 is not feasible. Instead, the bandpass sampling technique of [245] is employed in these ADCs.

Consider the block diagram of Fig. 5.2, where the RF signal $V(t)$ is fed to the bandpass sampler to generate $V_{samp}[n]$, which is formulated as follows:

$$V_{samp}[n] = V(\frac{n}{f_{samp}}) \quad \text{n=0, 1 2 ...,} \tag{5.2}$$

where f_{samp} is the sampling rate. Fig. 5.3 shows the spectrum of the original signal $V(t)$, as well as that of the sampled signal $V_{samp}[n]$. When any analog signal is sampled, then the spectrum of the sampled signal is periodic with a period that equals the sampling rate f_{samp} [244]. As shown in Fig. 5.3, this periodic spectrum of $V_{samp}[n]$ consists of copies of the spectrum of $V(t)$, which have been shifted to the frequencies kf_{samp} for all integer values of k. Each of the copies of the spectrum of $V(t)$ within the spectrum of $V_{samp}[n]$ is referred to as a Nyquist zone and has been numbered from -9 to 9 in Fig. 5.3 [117].

Bandpass sampling relies on the principle that if the multiple copies of the original spectrum do not overlap, as is the case in the spectrum of Fig. 5.3, then the original signal $V(t)$ can be reconstructed

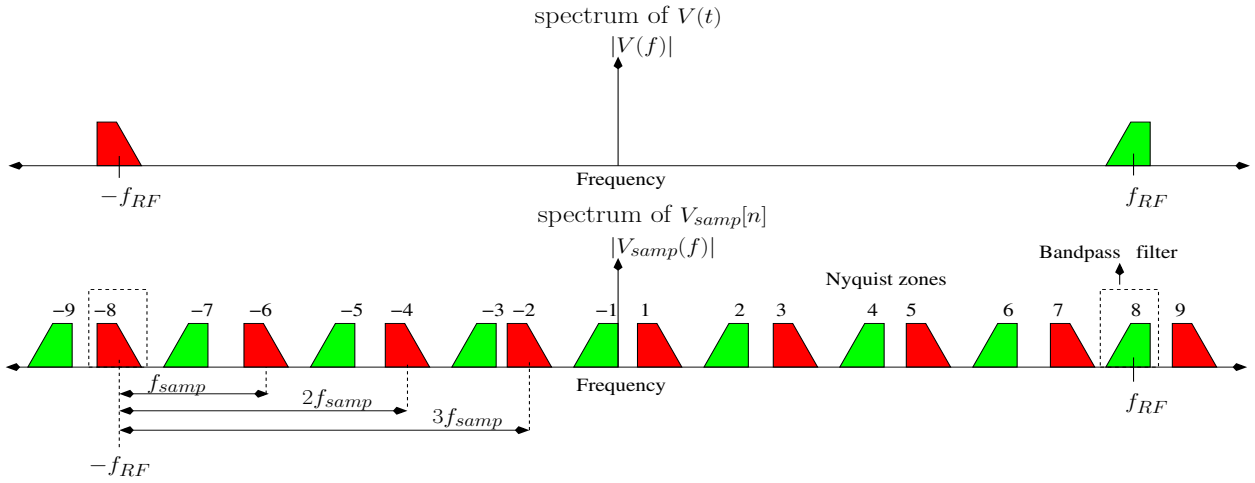

Figure 5.3: Electronic spectrum of $V(t)$ and $V_{samp}[n]$

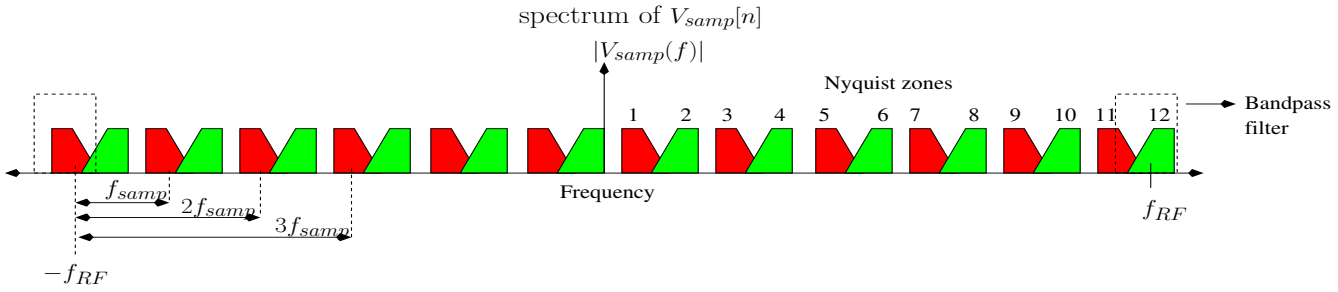

Figure 5.4: Electronic spectrum of $V_{samp}[n]$ showing aliasing

by applying a bandpass RF filter having a center frequency of f_{RF} Hz to $V_{samp}[n]$, as shown in Fig. 5.3. However, it is also evident from the spectrum of Fig. 5.3 that this is not possible for all values of f_{samp}. Fig. 5.4 shows the spectrum of $V_{samp}[n]$, when the sampling rate used results in an overlap between the different copies of the original spectrum, which is referred to as aliasing. As it becomes evident from Fig. 5.4, in such a scenario, the original signal $V(t)$ cannot be reconstructed using a bandpass filter.

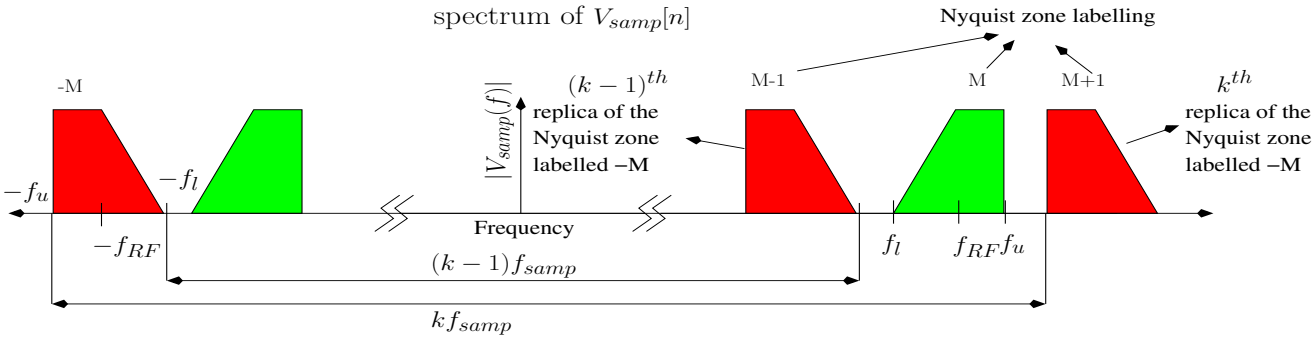

Figure 5.5: Derivation of the valid bandpass sampling rate

In the following paragraphs, we derive an expression for the range of sampling rates which will ensure a non-aliased spectrum, similar to that in Fig. 5.3, rather than the aliased spectrum of Fig. 5.4. We focus our attention on the required Nyquist zones, i.e. on the specific Nyquist zone that is retained by the bandpass filter for reconstructing $V(t)$ from $V_{samp}[n]$, as well as on the zones adjacent

to the required Nyquist zones. For example, in the spectrum of Fig. 5.3, the required Nyquist zones are the zones labelled ±8, while the adjacent ones are the zones labelled ±7 and ±9. We focus our attention only on the zones in the positive frequency domain, because the sampled signal is a real-valued signal whose spectrum has the property of conjugate symmetry. Thus, the spectrum in the negative frequency domain is the complex conjugate of the spectrum in the positive frequency domain, i.e. $V_{samp}(f) = [V_{samp}(-f)]^*$ [244]. Hence, if we can ensure that Nyquist zone 8 of Fig. 5.3 is not corrupted by aliasing, then the Nyquist zone labelled -8 in Fig. 5.3 would also remain uncorrupted by aliasing.

It can be seen from the spectrum of Fig. 5.3 that the Nyquist zones labelled -6, -4 and -2 are the first, second and third replica, respectively, of the spectrum within Nyquist zone -8. Similarly, the Nyquist zone labelled 7 and 9 are the seventh and eighth replica of the spectrum within the Nyquist zone labelled -8. Fig. 5.5 shows only the required zones and their adjacent zones assuming a more general scenario, where the required Nyquist zones are the ones labelled $\pm M$ and where the Nyquist zone labelled M is bounded on either side by the zones labelled $(M-1)$ and $(M+1)$, which are the $(K-1)^{th}$ and K^{th} replica of the spectrum in the Nyquist zone labelled $-M$.

It can be seen from Fig. 5.5 that to ensure that the Nyquist zone labelled $(M-1)$ does not overlap with the required Nyquist zone labelled M, we have to meet the following condition:

$$\begin{aligned} -f_l + (k-1)f_{samp} &\leq f_l \\ \implies \qquad f_{samp} &\leq \frac{2f_l}{(k-1)}. \end{aligned} \tag{5.3}$$

On the other hand, it can be seen from Fig. 5.5 that to ensure that the Nyquist zone labelled $(M+1)$ does not overlap with the required Nyquist zone labelled M, we have to meet the following condition:

$$\begin{aligned} -f_u + kf_{samp} &\geq f_u. \\ \implies \qquad f_{samp} &\geq \frac{2f_u}{k}. \end{aligned} \tag{5.4}$$

Combining the criterion of Equation (5.4) with the criterion seen in Equation (5.3), we get :

$$\begin{aligned} \frac{2f_u}{k} &\leq \frac{2f_l}{(k-1)} \\ \implies \frac{(k-1)f_u}{k} &\leq f_l \\ \implies f_u - \frac{f_u}{k} &\leq f_l \\ \implies f_u - f_l &\leq \frac{f_u}{k} \\ \implies B_{RF} &\leq \frac{f_u}{k} \\ \implies k &\leq \frac{f_u}{B_{RF}}, \end{aligned} \tag{5.5}$$

where, as mentioned earlier, B_{RF} is the bandwidth of the RF signal. Recall from the above discussions that the criteria seen in Equations (5.3), (5.4) and (5.5) were derived by ensuring that the $(k-1)^{st}$ and k^{th} replica of the spectrum of the original analog signal does not result in aliasing in the sampled signal's spectrum shown in Fig. 5.5. Thus, the variable k is constrained to be an integer, i.e we have .

$$k \in I. \tag{5.6}$$

Combining the criteria in Equations (5.3), (5.4), (5.5) and (5.6), we get the following single criterion for the valid bandpass sampling rates [245], [246]:

$$\frac{2f_u}{k} \leq f_{samp} \leq \frac{2f_l}{(k-1)} \quad \text{where} \quad k = 1, 2, 3...., \left\lfloor \frac{f_u}{B_{RF}} \right\rfloor, \tag{5.7}$$

where $\lfloor x \rfloor$ is the highest integer smaller than or equal to x. Again, the Nyquist criterion states that a signal should be sampled at least twice the highest frequency in it, in order to enable flawless recovery of the original signal. Thus, the Nyquist criterion represents a special case of bandpass sampling associated with $k = 1$ in Equation (5.7).

From Equation (5.1a) we have $f_l = f_u - B$. Substituting this into Equation (5.7) and then dividing the expression by B_{RF}, we can express it in the following normalised form [247]:

$$\begin{aligned} &\frac{2(f_u/B_{RF})}{k} \leq \frac{f_{samp}}{B_{RF}} \leq \frac{2((f_u/B_{RF})-1)}{(k-1)} \quad \text{where} \quad k = 1, 2, 3.... \left\lfloor \frac{f_u}{B_{RF}} \right\rfloor, \\ \implies &\frac{2f_u^{norm}}{k} \leq f_{samp}^{norm} \leq \frac{2(f_u^{norm}-1)}{(k-1)} \quad \text{where} \quad k = 1, 2, 3.... \lfloor f_u^{norm} \rfloor, \end{aligned} \tag{5.8}$$

where $f_u^{norm} = \frac{f_u}{B_{RF}}$ and $f_{samp}^{norm} = \frac{f_{samp}}{B_{RF}}$.

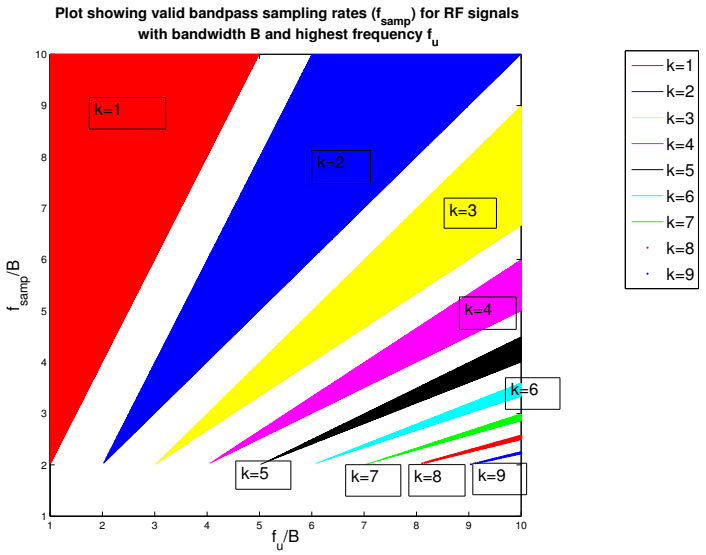

Figure 5.6: Derivation of the valid bandpass sampling rate

Fig. 5.6 shows the expression in Equation (5.7) in a lucid visual manner, where each point in the co-ordinate plane represents a particular combination of f_{samp}/B_{RF} and f_u/B_{RF}. In other words, it represents the specific scenario, in which a signal having a bandwidth of B_{RF} and highest frequency of f_u is sampled at a rate of f_{samp}. The combinations of f_{samp}/B_{RF} and the f_u/B_{RF}, which satisfy Equation (5.7) and hence do not result in aliasing are shown in colour, while the rest of the combinations are shown in white. All the combinations that satisfy Equation (5.7) using a particular value of k are shown using the same colour in Fig. 5.6.

Before delving into further discussions, we would like to mention the pair of salient challenges in implementing bandpass sampling, which are as follows:

1. While bandpass sampling reduces the actual sampling rate to be employed in the ADC, it does not alleviate the challenge of designing an ADC having a wide bandwidth. The ADC is still required to handle an input signal in the high RF domain.

2. The second challenge of implementing bandpass sampling is a magnification of the jitter noise. Lower is the order of Nyquist zone being employed, the higher is magnification of the jitter noise [248].

Having concluded our discussion of the bandpass sampling technique, we now discuss the subsequent processing of the sampled signal $V_{samp}[n]$ in the next section.

Quantization and encoding: The bandpass sampling of the RF signal $V(t)$ to obtain $V_{samp}[n]$ was discussed in Section 5.1.3.1. In this section we discuss the quantization of the sampled values and its subsequent encoding. Our final aim is to represent each sample of $V_{samp}[n]$ using n bits.

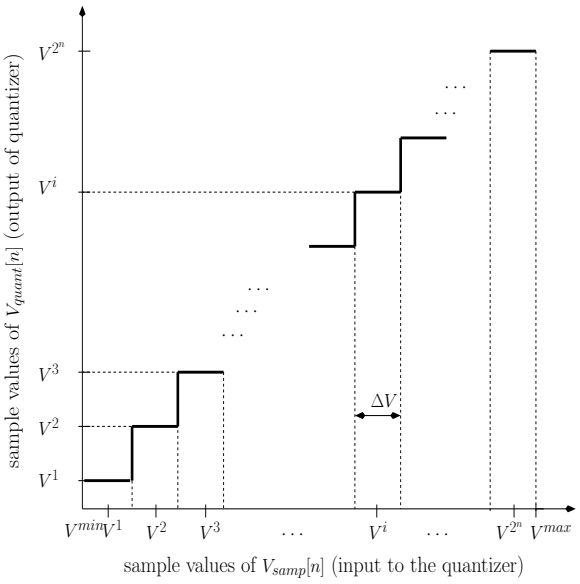

Figure 5.7: Quantization of the sampled signal

The signal $V_{samp}[n]$ satisfies the following relationship:

$$V^{min} \leq V_{samp}[n] \leq V^{max}, \tag{5.9}$$

where V^{min} and V^{max} are the minimum and maximum values of $V(t)$, respectively. Since the samples have to be represented using n bits, they can assume only 2^n values. Thus, the sample values in $V_{samp}[n]$ have to be rounded to the closest value from the set $\{V^i | i = 1, 2, 3..2^n\}$ of 2^n equi-spaced values between V^{min} and V^{max}. This is referred to as quantization [247]. If ΔV is the range of values of $V_{samp}[n]$ which are rounded to V^i, then the above discussion on how to generate the quantized signal $V_{quant}[n]$ is diagrammatically shown in Fig. 5.7. The following can be stated from Fig. 5.7 [247]:

$$V_{quant}[n] = V^i \text{ for } V^i - \frac{\Delta V}{2} \leq V_{samp}[n] \leq V^i + \frac{\Delta V}{2} \tag{5.10}$$

$$V^i - V^{i-1} = \Delta V = \frac{V^{max} - V^{min}}{2^n}. \tag{5.11}$$

Thus, each value of the quantized signal $V_{quant}[n]$ belongs to the set $\{V^i | i = 1, 2, 3..2^n\}$ of 2^n. Subsequently, the quantized signal $V_{quant}[n]$ is converted into a digital bit stream, with each value of $V_{quant}[n]$ being mapped to an n-bit binary code, where Table 5.1 shows this mapping. This technique is referred to as Pulse Code Modulation (PCM) [247].

Table 5.1: Mapping table for pulse code modulation

Sample Value	n-bit Binary code
V^1	$0000 \cdots 00$
V^2	$0000 \cdots 01$
V^3	$0000 \cdots 10$
$\cdots$	$\cdots$
$\cdots$	$\cdots$
V^{2^n}	$1111 \cdots 11$

The generated bit stream then modulates an optical carrier, as discussed in the next section.

5.1.3.2 Electronic to optical conversion

In the previous section, we discussed the generation of a bit stream through digitization of the RF signal by the ADCs of Fig. 5.1, while in this section we discuss the Electronic to optical (E-O) conversion of Fig. 5.1, i.e. the modulation of an optical carrier using this bit stream. Several optical modulation schemes may be employed for modulating the optical carrier with the bit-stream generated by digitizing the RF signal. However, we devote the discussion in this section to the most commonly employed optical intensity modulation scheme of optical OOK [161].

In this treatise, optical intensity modulation was first introduced in Section 2.1.2.1, where it was defined as modulating the intensity of the optical carrier with the aid of the modulating electronic signal. Note that the intensity of an optical signal is proportional to its optical power. More specifically, the optical intensity is the optical power per unit area, which is transmitted through an imaginary surface perpendicular to the direction of propagation. Thus, the terms optical intensity and power will be used interchangeably. In the optical intensity modulation scheme of OOK, an optical intensity (or power) of P_1 is transmitted for bit 1, while an optical intensity (or power) of $P_0 = 0$ is transmitted for bit 0. This may be achieved using direct modulation of the laser output, as discussed in Section 2.1.1.2, or by using external modulation of the laser output, as discussed in Section 2.1.1.2.

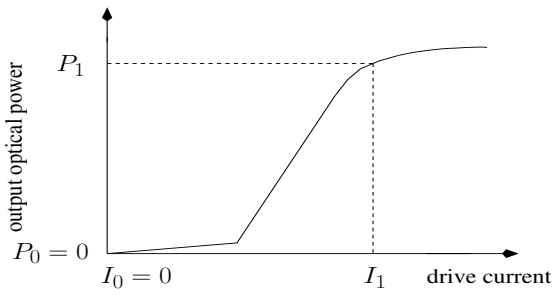

Figure 5.8: Power vs. drive current characteristic of a laser

Direct optical modulation using the bit stream: The power vs. drive current curve of a laser, discussed in Section 2.1.1.2, is shown again in Fig. 5.8 along with the modulation currents $I_0 = 0$ and I_1 that result in the optical power outputs of P_0 and P_1, respectively. Thus, OOK modulation is implemented using direct modulation by employing the following baseband drive current [31]:

$$I_{drive} \approx \begin{cases} I_0 & \text{for bit 0,} \\ I_1 & \text{for bit 1.} \end{cases} \tag{5.12}$$

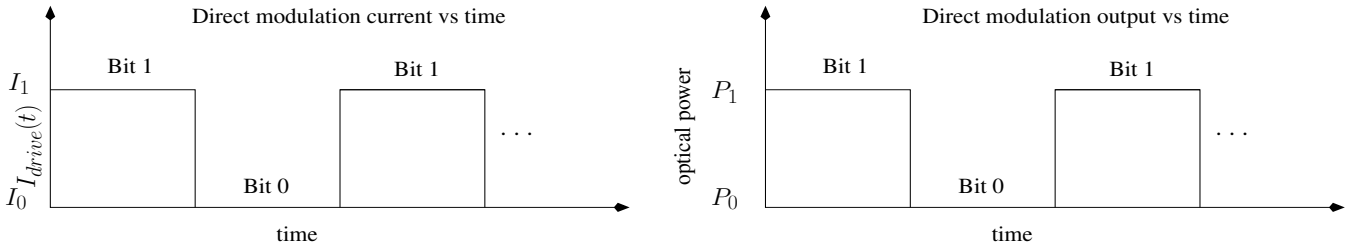

Figure 5.9: NRZ OOK optical modulation

The modulation current of Equation (5.12) would result in a Non Return to Zero (NRZ) OOK optical signal, whose intensity is shown in Fig. 5.9. On the other hand, the Return to Zero (RZ) pulsed OOK signal shown in Fig. 5.10 may be generated by employing the following pulsed modulating current:

$$I_{drive} \approx \begin{cases} I_0 & \text{for bit 0,} \\ I_1 \, e^{-\frac{\tau^2}{2T_{half}^2}} & \text{for bit 1,} \end{cases} \tag{5.13}$$

where τ is the time normalised with respect to the bit duration T_{bit}, i.e. τ varies from $-\frac{T_{bit}}{2}$ to $\frac{T_{bit}}{2}$ during each bit period. In Equation (5.13), T_{half} is the half-width of the electronic pulse, which is related to its FWHM through the following relationship [31]:

$$T_{FWHM} = 1.665 T_{half}. \tag{5.14}$$

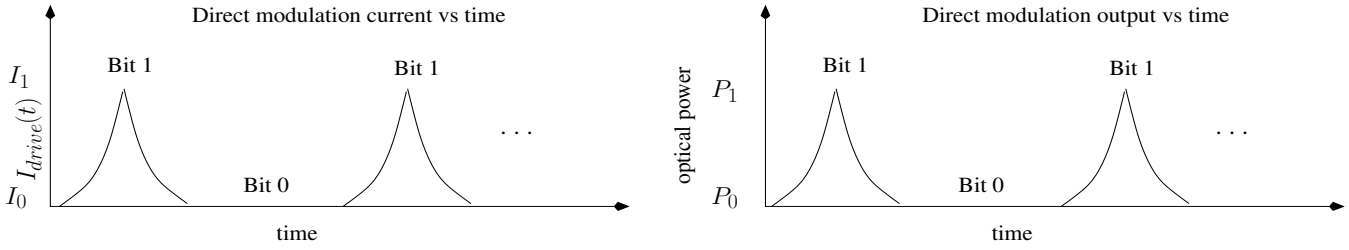

Figure 5.10: RZ OOK optical modulation

The RZ OOK optical signal of Fig. 5.10 may also be generated using a pulsed optical laser. A conventional continuous wave laser generates a sinusoidal signal whose amplitude, i.e. intensity, is constant. A pulsed optical laser generates a sinusoidal signal, whose intensity is a pulse stream. Thus, the pulsed signal of Fig. 5.10 may be generated by switching on and switching off this laser for the bits '1' and '0', respectively.

We now continue by discussing the modulation of an optical carrier with a bit stream using external modulators.

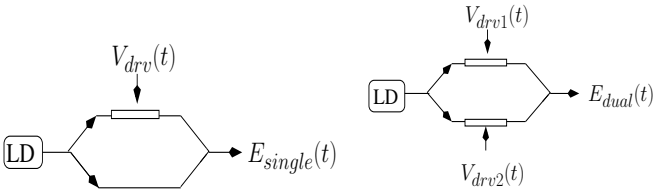

(a) Single Drive MZM (b) Dual Drive MZM

Figure 5.11: Single and Dual-drive MZM external modulators (LD- Laser Diode)

External optical modulation using the bit stream External modulation was introduced in Section 2.1.1.2, where it was mentioned that optical intensity modulation may be implemented using a MZM or an EAM. As introduced in Section 2.1.1.1, the output optical field of a laser operating at an optical frequency of $f_c = \frac{\omega_c}{2\pi}$ Hz and at an optical power of P_{in} is as follows:

$$E_{laser}(t) = \sqrt{2P_{in}} e^{j\omega_c t}. \tag{5.15}$$

As shown in Fig. 5.11(a), the output of the laser is fed to a MZM. As discussed in Section 2.1.1.2, the output optical field $E_{single}(t)$ and intensity $P_{single}(t)$ of the single-drive MZM of Fig. 5.11(a), which is driven by a voltage signal $V_{drv}(t)$, may be expressed as follows using Equation (5.15):

$$\begin{aligned} E_{single}(t) &= \frac{1}{2}[1 + e^{j\frac{\pi V_{drv}(t)}{V_\pi}}]E_{laser}(t) \\ &= \cos(\frac{\pi V_{drv}(t)}{2V_\pi}) e^{j\frac{\pi V_{drv}(t)}{2V_\pi}} E_{laser}(t), \end{aligned} \tag{5.16}$$

$$\begin{aligned} P_{single}(t) &= |E_{single}(t)|^2 \\ &= P_{in}[1 + \cos(\frac{\pi V_{drv}(t)}{V_\pi})], \end{aligned} \tag{5.17}$$

where, as discussed in Section 2.1.1.2, V_π is the switching voltage. It is desired that an optical power of $P_0 = 0$ be transmitted for bit '0' and that the power P_1 transmitted for bit '1' employs the maximum possible value. It is evident from Equation (5.17) that these requirements are met for the following baseband drive signal:

$$V_{drv}(t) \approx \begin{cases} V_0 = V_\pi & \text{for bit 0,} \\ V_1 = 0 & \text{for bit 1,} \end{cases} \tag{5.18}$$

where it can be seen from Equation (5.17) that employing these values of $V_{drv}(t)$ would result in the following values of the optical power for the transmitted OOK signal:

$$P_{single}(t) \approx \begin{cases} P_0 = 0 & \text{for bit 0,} \\ P_1 = 2P_{in} & \text{for bit 1.} \end{cases} \tag{5.19}$$

Fig. 5.12 shows the transmittance curve of a MZM that is driven by the electronic baseband digital signal $V_{drv}(t)$, along with the drive signal values $V_0 = V_\pi$ and $V_1 = 0$ that result in the optical power outputs of P_0 and P_1, respectively. Note that the input voltage applied to the MZM has a bias component according to the discussions in Section 2.1.1.2. This is because small-signal modulation around the bias point is employed, when $V_{drv}(t)$ is a RF modulating signal, as shown in Fig. 2.9(a). However, when $V_{drv}(t)$ is a baseband digital signal, large-signal modulation is employed, as shown in Fig. 5.12.

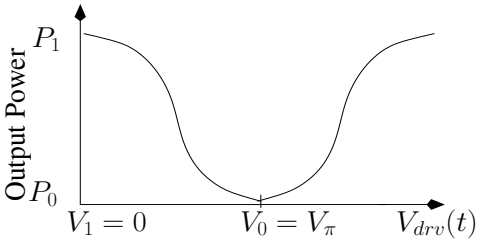

Figure 5.12: Optical intensity modulation by a MZM using a bit stream

The dual-drive MZM of Fig. 5.11(b) can also be used for generating an optical OOK signal, where the dual-drive MZM is fed by the laser, whose output optical field is given by Equation (5.15). Moreover, the voltage $V_{drv}(t)$ is differentially applied to the two arms of the MZM using the voltages $V_{drv1}(t)$ and $V_{drv2}(t)$, i.e.:

$$V_{drv}(t) = V_{drv1}(t) - V_{drv2}(t). \tag{5.20}$$

Based on the discussions in Section 2.1.1.2, the output optical field $P_{dual}(t)$ and optical intensity $P_{dual}(t)$ may be expressed as follows using Equation (5.20) and Equation (5.15):

$$\begin{aligned} E_{dual}(t) &= \frac{1}{2}[e^{j\frac{\pi V_{drv1}(t)}{V_\pi}} + e^{j\frac{\pi V_{drv2}(t)}{V_\pi}}]E_{laser}(t) \\ &= \cos(\frac{\pi(V_{drv1}(t) - V_{drv2}(t))}{2V_\pi})e^{j\frac{\pi(V_{drv1}(t)+V_{drv2}(t))}{2V_\pi}}E_{laser}(t), \\ &= \cos(\frac{\pi V_{drv}(t)}{2V_\pi})e^{j\frac{\pi(V_{drv1}(t)+V_{drv2}(t))}{2V_\pi}}E_{laser}(t), \\ P_{dual}(t) &= |E_{dual}(t)|^2 \\ &= P_{in}[1 + \cos(\frac{\pi V_{drv}(t)}{V_\pi})]. \end{aligned} \tag{5.21}$$

Comparing Equation (5.21) to Equation(5.17), it can be seen that the transmittance curve of the dual-drive MZM is similar to that of the single-drive MZM. Thus, the dual-drive MZM also employs the drive voltage of Equation (5.18), thereby yielding an output similar to that of Equation (5.19), i.e.:

$$P_{dual}(t) \approx \begin{cases} P_0 = 0 & \text{for bit 0,} \\ P_1 = 2P_{in} & \text{for bit 1.} \end{cases} \tag{5.22}$$

For the reasons discussed in Section 2.1.1.2, the voltages $V_{drv1}(t)$ and $V_{drv2}(t)$ are specifically chosen to ensure that the MZM operates in the push-pull mode, i.e. we have:

$$V_{drv1}(t) = -V_{drv2}(t) = \frac{V_{drv}(t)}{2}. \tag{5.23}$$

Hence, the drive voltage of Equation (5.18) would result in the NRZ OOK optical signal of Fig. 5.13, when using a single-drive or a dual-drive MZM. The pulsed RZ OOK signal shown in Fig. 5.10 may be generated by feeding the MZM with the output of a pulsed optical laser, instead of the output of a conventional continous wave laser, while still employing the drive voltage of Equation (5.18).

As discussed in Section 2.1.1.2, external modulation can also be achieved using an EAM, where Fig. 5.14 shows the transmittance curve of an MZM along with the reverse-biasing drive-voltages

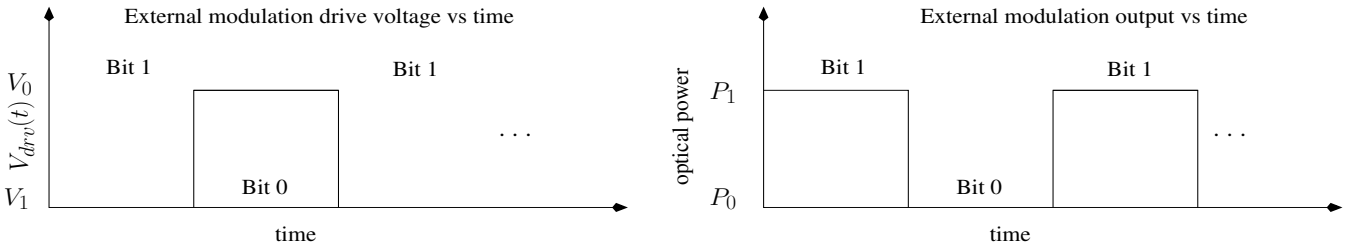

Figure 5.13: NRZ OOK optical modulation

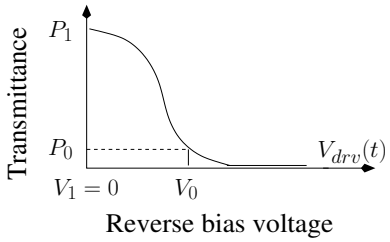

Figure 5.14: Optical intensity modulation by an EAM using a bit stream

V_0 and V_1, that result in the desired output optical power levels of P_0 and P_1 for bits '0' and '1', respectively.

The comparison of external modulation relying on a MZM to that relying on an EAM was carried out in Section 2.1.1.2 and it is true for the case of optical modulation using a bit stream. Furthermore, the comparative analysis of direct modulation and external modulation presented in Section 2.1.1.2 is also valid for the case of optical modulation using a bit stream, as in the DROF architecture. Thus, this analysis is not repeated in this section.

Having discussed the digitization of the RF signal in Section 5.1.3.1 and its subsequent conversion into an optical signal in Section 5.1.3.2, let us now discuss the fiber-based transmission as well as detection of the DROF optical signal in the next section.

5.1.4 Transmission and detection

The impairments imposed by the fiber channel in DROF is similar to that in AROF. As discussed in Section 2.1.1.3, optical signal propagation in a SMF is governed by a NLS equation [74] that is mathematically formulated as follows [74]:

$$\frac{\partial A}{\partial z} = -\frac{\alpha}{2} - j\frac{\beta_2}{2}\frac{\partial^2 A}{\partial T^2} + j\gamma_{nl}\{|A|^2 A\}. \tag{5.24}$$

Here $A(z,T)$ is the envelope (or amplitude) of the optical carrier after it has propagated through z km of SMF. Recall that the optical intensity (i.e. square of the optical carrier's amplitude) has been modulated using a MZM. Continuing, α is the fiber attenuation constant, β_2 is the second derivative of the fiber propagation constant, γ_{nl} is the parameter which accounts for fiber non-linearity, while T is the time measured in a frame of reference moving with the optical signal (as it propagates along

the fiber) at group velocity v_g, i.e. we have

$$T = t - \frac{z}{v_g}.$$

Here t denotes the real-time value and v_g is the propagation velocity of the optical carrier's envelope along the fiber.

Similarly, the detection of the DROF signal is carried out using the photo-detection techniques discussed in Section 2.1.1.4. It can be seen from the discussions in Section 2.1.1.4 that for the case of the most commonly employed direct photo-detection, the photo-current $I_{PD}(t)$ is directly proportional to $P_{single}(t)$ or $P_{dual}(t)$, when using single or dual-drive MZMs for OOK optical intensity modulation at the transmitter [31]. Thus, the bit values can be decided based on the amplitude of the photo-detected signals. The bit stream is then fed to the DAC, which reconstructs the quantized signal $V_{quant}[n]$. Assuming that the quantization error is negligible, we can state that the spectrum of $V_{quant}[n]$ is closely approximated by the spectrum of $V_{samp}[n]$ in Fig. 5.3. It can be seen from Fig. 5.3 that the RF signal $V_{drv}(t)$ can be reconstructed by applying a bandpass filter of bandwidth B_{RF} and having a center frequency of f_{RF} Hz to $V_{samp}[n]$, i.e. in our case to $V_{quant}[n]$. This reconstructed RF signal is then demodulated and detected at the BS, in case of UL communication. By contrast, it is transmitted over the wireless channel to the MS, in case of DL communication, as shown in Fig. 5.1.

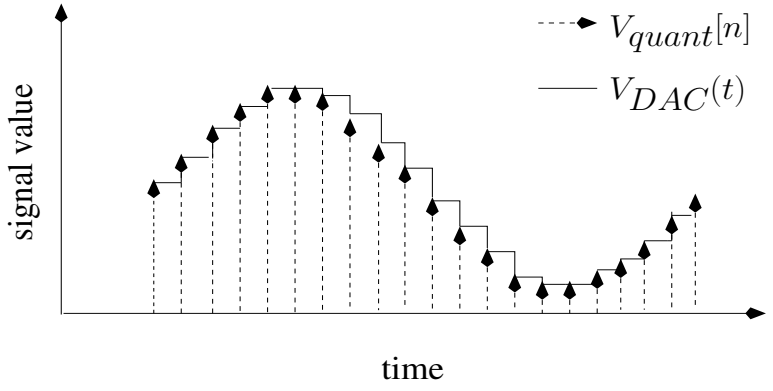

Figure 5.15: DAC output

The simplest DAC filter that can be employed is a zero-order hold filter. In such a DAC the quantized signal is recovered from the received bit stream and then each quantized value is held constant until the next quantized value becomes available at the start of the next clock cycle. The DAC clock frequency equals the bandpass sampling rate f_{samp} employed by the ADC in the transmitter. Thus, if the transmission of the bits in the DROF link was error-free, then the output of a zero-order hold DAC is as follows:

$$V_{DAC}(t) = V_{quant}[n] \text{ for } \frac{n}{f_{samp}} \leq t < \frac{(n+1)}{f_{samp}}, \tag{5.25}$$

where Fig. 5.15 shows the signals $V_{quant}[n]$ and $V_{DAC}(t)$.

The discussions so far assumed having an idealized noise-free DROF link. In the next section we will discuss the noise processes that are present in a DROF link.

5.1.5 Noise in a DROF link

The noise in a DROF link includes the noise processes discussed in Section 2.1.1.5 in addition to the following noise sources:

1. Aliased noise;
2. ADC jitter noise;
3. Quantization noise;
4. DAC jitter induced noise.

The above noise processes will be discussed in Sections 5.1.5.1, 5.1.5.2 and 5.1.5.3.

5.1.5.1 Aliased noise

If the power of the RF signal $V(t)$ having a bandwidth of B_{RF} is P_{RF} and if N_o is the power spectral density of the inband noise, then the SNR of $V(t)$ is:

$$SNR_{RF} = \frac{P_{RF}}{N_o B_{RF}}. \tag{5.26}$$

Let us assume that the RF signal $V(t)$ was also corrupted by out-of-band noise having a spectral density of N_{out}. The bandpass sampling rate f_{samp} of Equation (5.7) generates an alias-free output, provided that the signal being sampled is bandlimited to a bandwidth of B_{RF} around a carrier frequency of f_{RF} Hz. However, this is not true of the out-of-band noise, which would then become aliased into the desired bandwidth [245].

Assume that bandpass sampling is carried out by an ADC that can handle frequencies up to f_{max}^{DAC}, and that we divide the total spectral range spanning from $-f_{max}^{DAC}$ Hz to f_{max}^{DAC} Hz into spectral segments of width f_{samp} Hz, then the total number of segments becomes:

$$m = \frac{2f_{max}^{DAC}}{f_{samp}}. \tag{5.27}$$

Of these m segments one of the segments has the inband noise power spectral density of N_o, while the remaining $(m-1)$ has the out-of-band noise power spectral density of N_{out}. Since bandpass sampling results in the aliasing of the out-of-band noise into the desired band, the SNR of the bandpass sampled signal $V_{samp}[n]$ is [245]:

$$SNR_{samp} = \frac{P_{RF}}{(N_o + (m-1)N_{out})B_{RF}}. \tag{5.28}$$

The minimum value for f_{max}^{DAC} equals to the highest frequency f_u of $V(t)$. In such a scenario, the total number of segments m equals to the value of k, for which the sampling rate f_{samp} employed satisfies Equation (5.7). The SNR of the sampled signal in this scenario becomes [245]:

$$SNR_{samp} = \frac{P_{RF}}{(N_o + (k-1)N_{out})B}. \tag{5.29}$$

This increase in the noise is especially important for the case of the DROF UL of Fig. 5.1, because the UL signal at the RAP has significant out-of-band noise/interference, as compared to the DL signal at the BS. The SNR degradation due to the aliasing of the out-of-band noise can be minimized by reducing N_{out} by employing an anti-aliasing bandpass filter prior to bandpass sampling for removing the out-of-band noise/interference. It should be noted that adjacent RF channels would also be aliased into the desired bandwidth. Hence, these too have to be removed by using the anti-aliasing bandpass filter.

Having discussed the noise imposed by bandpass sampling through aliasing, let us now move on to discuss the noise imposed by bandpass sampling through sampling jitter.

5.1.5.2 ADC and DAC jitter-induced noise

The application of bandpass sampling for generating the DROF optical signal was discussed in Section 5.1.3.1. The sampling jitter is defined as the deviation of the actual sampling time instant from the ideal one due to implementational limitations of the ADC. Before delving into the mathematical characterization of the noise imposed by the ADC's sampling jitter, we state the following assumptions [249]:

1. The RF carrier frequency f_{RF} is significantly higher than the bandwidth B_{RF} of the RF signal, i.e. we have $f_{RF} \gg B_{RF}$. This assumption would allow us to approximate the modulated signal by a sinusoidal signal at f_{RF} Hz for jitter noise calculations, as argued in [249].

2. The sampling jitter is assumed to be a Gaussian process having zero mean [117]. In other words, the probability $P(\Delta t_{jit})$ of an error of Δt_{jit} seconds in the sampling time is formulated as follows:

$$P(\Delta t_{jit}) = \frac{1}{\sigma_{jit}^{ADC}\sqrt{2\pi}} e^{\frac{(\Delta t_{jit})^2}{2(\sigma_{jit}^{ADC})^2}}, \tag{5.30}$$

   where σ_{jit}^{ADC} is the standard deviation of the jitter in the ADC's sampling action [117].

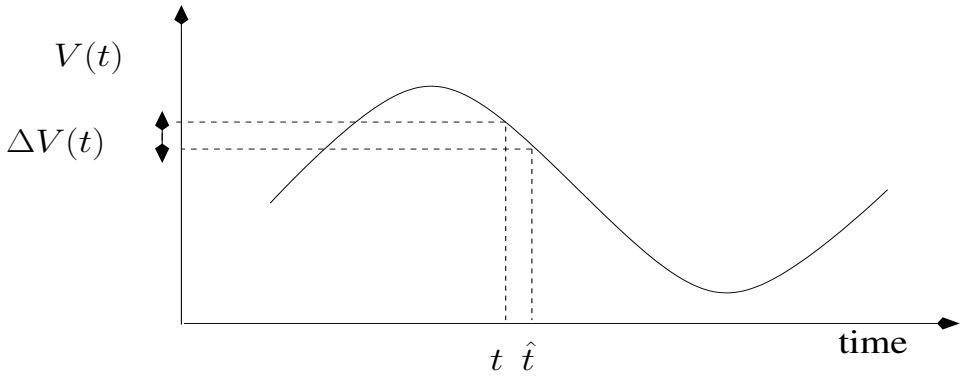

Figure 5.16: ADC sampling jitter

Fig. 5.16 shows the RF signal $V(t)$ that is approximated by a sinusoidal signal of frequency f_{RF} Hz. The signal $V(t)$ can ideally be assumed to be sampled at time instant t, resulting in a sampled

value of $V(t)$, but it is instead sampled at time instant $\hat{t}$, hence resulting in the sampled value of $V(\hat{t})$. Using the Taylor series expansion of a function, $V(\hat{t})$ is related to $V(t)$ through the following expression:

$$V(\hat{t}) = V(t) + \frac{d(V(t))}{dt}(t' - t) + \text{ weaker higher order terms.} \tag{5.31}$$

If $\hat{t}$ is sufficiently close to and tends to t, then we can neglect the weaker higher order terms. Hence, by exploiting the fact that the sampling jitter is given by $\Delta t_{jit} = (t' - t)$ and that $\Delta V(t) = V(\hat{t}) - V(t)$ in Equation (5.31) [249], we arrive at:

$$\Delta V(t) \approx \Delta t_{jit} \cdot \frac{d[V(t)]}{dt}. \tag{5.32}$$

If $E\{X\}$ is the expected value of a random variable X, then we have $E\{X \cdot Y\} = E\{X\} \cdot E\{Y\}$ for X and Y being independent random variables. Exploiting this relationship in Equation (5.32), where the signal value $V(t)$ and the error Δt_{jit} in the sampling time instant are independent, we arrive at:

$$E\{(\Delta V(t))^2\} = E\{(\Delta t_{jit})^2\} \cdot E\{\left(\frac{d(V(t))}{dt}\right)^2\}. \tag{5.33}$$

Now from the assumption that the RF signal can be approximated by a sinusoidal signal having a frequency of f_{RF} Hz and by exploiting the assumption that the sampling error is a Gaussian process, we have:

$$E\{(V(t))^2\} = \frac{V_{RF}^2}{2} \tag{5.34}$$

$$E\{\left(\frac{d(V(t))}{dt}\right)^2\} = V_{RF}^2 \cdot 2\pi^2 f_{RF}^2 \tag{5.35}$$

$$E\{(\Delta t_{jit})^2\} = (\sigma_{jit}^{ADC})^2, \tag{5.36}$$

where V_{RF} is the amplitude of the RF signal. Upon substituting Equations (5.35) and (5.36) into Equation (5.33), we arrive at [249]:

$$E\{(\Delta V(t))^2\} = V_{RF}^2 (\sigma_{jit}^{ADC})^2 2\pi^2 f_{RF}^2. \tag{5.37}$$

Thus, using Equations (5.34) and (5.37) the SNR due to the ADC jitter noise becomes as follows [249]:

$$\begin{aligned} SNR_{jitter}^{ADC}(dB) &= 10 \cdot log\left(\frac{E\{(V(t))^2\}}{E\{(\Delta V(t))^2\}}\right) \\ &= 10 \cdot log\left(\frac{1}{4\pi^2 (\sigma_{jit}^{ADC})^2 f_{RF}^2}\right) \\ &= -20 \cdot \log(2\pi \sigma_{jit}^{ADC} f_{RF}). \end{aligned} \tag{5.38}$$

Similar to the ADC, the DAC also suffers from clock jitters having an RMS value of σ_{jit}^{DAC} seconds, where the clock frequency equals the bandpass sampling rate f_{samp}. For the same assumptions as in the case of the ADC sampling jitter, it has been shown that the SNR due to the DAC clock jitter is [117], [249]:

$$SNR_{jitter}^{ADC} = (2\pi \sigma_{jit}^{DAC} f_{RF})^{-2} (sinc\left(\frac{f_{RF}}{f_{samp}}\right))^{-2}. \tag{5.39}$$

Having formulated the SNR degradation associated with the ADC sampling jitter and the DAC clock jitter, we next formulate the SNR degradation due to the signal quantization discussed in Section 5.1.3.1.

5.1.5.3 Quantization noise

The discussions on the detection of the DROF signal in Section 5.1.4 assumed that the spectrum of $V_{quant}[n]$ is similar to that of $V_{samp}[n]$. However, this assumption is only valid, if the quantization noise is low. Thus, the first step towards maintaining a low quantization noise is to formulate the SNR due to the quantization noise, which will be carried out in the following discussion.

We assume that the maximum value V^{max} and minimum value V^{min} of the RF signal $V(t)$ satisfy the following relationship [244]:

$$V^{max} = -V^{min}. \tag{5.40}$$

Substituting Equation (5.40) into Equation (5.11), we arrive at [244]:

$$\Delta V = \frac{2V^{max}}{2^{n_{bit}}}, \tag{5.41}$$

where n_{bit} is the resolution of the ADC, i.e. the number of bits used for representing each sample.

The quantization error $e_{quant}[n]$ is the difference between the actual signal sample and the quantized signal sample, i.e. we have: $e_{quant}[n] = V_{quant}[n] - V_{samp}[n]$. The following can be stated from Equation (5.10) and from Fig. 5.7:

$$\frac{-\Delta V}{2} \leq e_{quant}[n] \leq \frac{\Delta V}{2}. \tag{5.42}$$

We assume that the error signal $e_{quant}[n]$ has a zero mean as well as a uniform probability distribution in the interval $[\frac{-\Delta V}{2}, \frac{\Delta V}{2}]$, i.e. the probability $p_e(e)$ of $e_{quant}[n] = e$ is as follows:

$$p_e(e) = \frac{1}{\Delta V}. \tag{5.43}$$

Thus, using Equations (5.43) and (5.41), the mean squared value of the quantization error $e_{quant}[n]$ becomes [244]:

$$\begin{aligned} & E\{|e_{quant}[n]|^2\} \\ &= \int_{\frac{-\Delta V}{2}}^{\frac{\Delta V}{2}} e^2 p_e(e) de \\ &= \frac{1}{\Delta V}\left[\frac{e^3}{3}\right]_{\frac{-\Delta V}{2}}^{\frac{\Delta V}{2}} \\ &= \frac{(\Delta V)^2}{12} \\ &= \frac{(V^{max})^2}{3 * 2^{2n_{bit}}}. \end{aligned} \tag{5.44}$$

The SNR associated with the quantization noise, by definition, is the ratio of the signal power to the quantization noise power. In other words, using Equation (5.44) the SNR due to quantization may

be expressed as follows [244]:

$$\begin{aligned} SNR_{quant}(dB) &= 10 * \log\left(\frac{E\{|V(t)|^2\}}{E\{|e_{quant}[n]|^2\}}\right) \\ &= 10 * \log\left(3 * 2^{2n_{bit}} * \frac{E\{|V(t)|^2\}}{(V^{max})^2}\right) \\ &= 6.02n_{bit} + 4.77 - 10\log\left(\frac{(V^{max})^2}{E\{|V(t)|^2\}}\right) \\ &= 6.02n_{bit} + 4.77 - 10\log(PAPR), \end{aligned} \tag{5.45}$$

where PAPR is the peak to average power ratio of the signal being quantized. Thus, an increase in the ADC bit resolution by one bit increases the SNR_{quant} by approximately 6 dB [244].

After discussing the generation of the DROF optical signal in the design of Fig. 5.1, we then discussed the transmission of this signal and its detection in Section 5.1.4. Subsequently, we elaborated on the noise processes in a DROF link in Section 5.1.5. In the next section, we will now discuss the various design trade-offs encountered, while designing a DROF link.

5.1.6 Design trade-offs

This section discusses the various trade-offs in a DROF link, including the following:

1. Spectral usage versus sampling rate tolerance trade-off in Section 5.1.6.1;
2. Sampling rate versus sampling rate tolerance trade-off in Section 5.1.6.2;
3. Sampling rate versus anti-aliasing filter-order trade-off in Section 5.1.6.3;
4. DROF bitrate versus quantization noise trade-off in Section 5.1.6.4;
5. Sampling rate and sampling rate tolerance versus reconstruction filter-order trade-off in Section 5.1.6.5.

Recognizing these trade-offs is vital for designing a specific DROF link that is optimized for a particular scenario.

5.1.6.1 Spectral usage versus sampling rate tolerance

Fig. 5.17 shows the valid bandpass sampling regions of Fig. 5.6 for a particular value of k in Equation (5.7). A signal having the highest frequency of f_u and the bandwidth of B_{RF} is bandpass sampled at a selected bandpass sampling rate of f_{samp}. In Fig. 5.17, the upper boundary line of the valid region is decided by the upper limit of Equation (5.7), which is expressed as follows:

$$\begin{aligned} \frac{f_{samp}}{B_{RF}} &= \frac{2}{k-1}\frac{(f_u - B)}{B_{RF}} \\ \implies &\text{slope of upper boundary line} = \frac{2}{(k-1)}. \end{aligned} \tag{5.46}$$

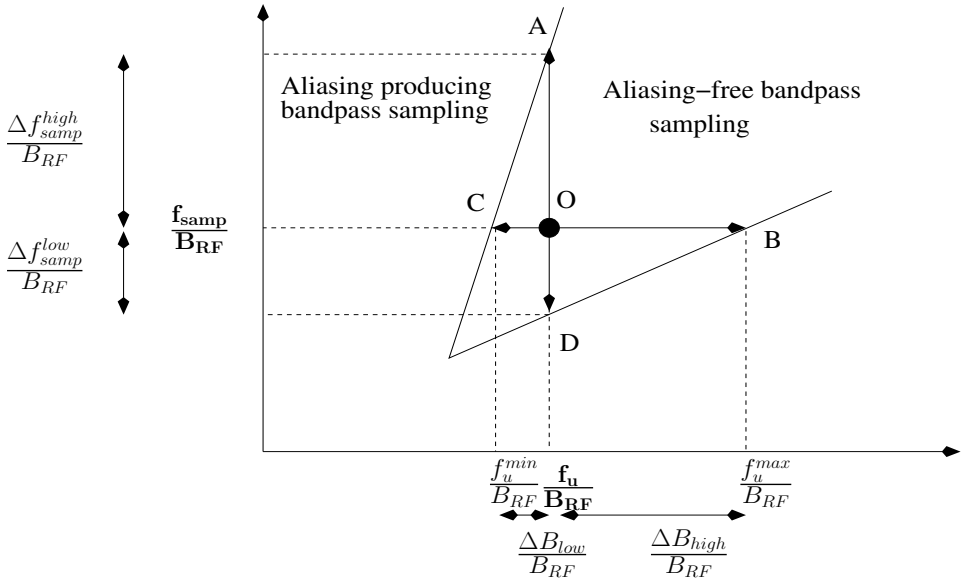

Figure 5.17: Sampling frequency tolerance

On the other hand, the lower boundary line of the valid region is decided by the lower limit of Equation (5.7), which is formulated as follows:

$$\frac{f_{samp}}{B_{RF}} = \frac{2}{k}\frac{f_u}{B_{RF}}$$
$$\Longrightarrow \text{slope of lower boundary line} = \frac{2}{k}. \tag{5.47}$$

For the bandpass sampling rate of f_{samp} invoked, the highest frequency f_u is permitted to become as low as f_u^{min}, whilst ensuring that no aliasing occurs. Similarly, for the specific bandpass sampling rate of f_{samp}, the highest frequency f_u may become as high as f_u^{max}, if we want to ensure that no aliasing occurs. Hence, we have to ensure that the lower guard band ΔB_{low} as well as the higher guard band ΔB_{high} meet the following conditions:

$$\Delta B_{low} = f_u - f_u^{min}; \tag{5.48}$$
$$\Delta B_{high} = f_u^{max} - f_u, \tag{5.49}$$
$$\tag{5.50}$$

as indicated in Fig. 5.17. It can also be seen from Fig. 5.17 that for the given signal, the bandpass sampling rate can increase from the selected value of f_{samp} by Δf_{samp}^{high} without imposing any aliasing. Alternatively, the bandpass sampling rate may be reduced from the selected value of f_{samp} by Δf_{samp}^{low} without imposing any aliasing.

The following can be stated about the triangle ODB in Fig. 5.17 using Equation (5.47):

$$\frac{OD}{OB} = \text{slope of lower boundary line}$$
$$\Longrightarrow \frac{\Delta f_{samp}^{low}}{\Delta B_{high}} = \frac{2}{k}$$
$$\Longrightarrow \Delta f_{samp}^{low} = \frac{2}{k}\Delta B_{high}. \tag{5.51}$$

Similarly, the following can be stated about the triangle OAC in Fig. 5.17 using Equation (5.46):

$$\begin{aligned} & \frac{OA}{OC} = \text{slope of lower boundary line} \\ \Longrightarrow & \frac{\Delta f_{samp}^{high}}{\Delta B_{low}} = \frac{2}{(k-1)} \\ \Longrightarrow & \Delta f_{samp}^{high} = \frac{2}{(k-1)} \Delta B_{low}. \end{aligned} \tag{5.52}$$

Thus, it can be seen from Equations (5.51) and (5.52) that increasing the guard bands ΔB_{low} and ΔB_{high} increases the affordable tolerances Δf_{samp}^{high} and Δf_{samp}^{low} in the bandpass sampling rates, respectively. However, an increase in the guard bands degrades the spectral efficiency, thereby resulting in a design trade-off.

5.1.6.2 Sampling rate versus sampling rate tolerance

The range of sampling rates that result in a non-aliased bandpass-sampled signal for a given value of k is shown in Equation (5.7), where the width of this range may be quantified as follows:

$$\Delta f_{samp} = \frac{2(f_u) - B_{RF})}{k-1} - \frac{2f_u}{k} = \frac{2B_{RF}}{k(k-1)}(\frac{f_u}{B_{RF}} - k). \tag{5.53}$$

The precision required in the selection of the sampling rate is inversely proportional to Δf_{samp}, i.e. for a larger acceptable range, the required precision becomes lower. Thus, we have [245],

$$\text{sampling rate precision} \propto \frac{1}{\Delta f_{samp}} \approx O(k^2). \tag{5.54}$$

Hence, employing lower values of k results in a lower precision being required for the sampling rate. This can also be seen from Fig. 5.6, where larger values of k have lower tolerable ranges [245]. However, the price that one pays for employing a lower value of k is the need to employ higher sampling rates, as seen from Equation (5.7). Thus, we encounter a sampling rate versus sampling rate tolerance trade-off [245]. In the next section, we discuss a design trade-off that affects the filtering requirements of bandpass sampling.

5.1.6.3 Sampling rate versus anti-aliasing filter-order

The extent of SNR degradation imposed by the aliasing of the out-of-band components into the signal bandwidth was quantified in Section 5.1.5.1, where it was stated that the extent of SNR degradation can be minimized by bandlimiting the signal using a bandpass filter centered at f_{RF} Hz and having a bandwidth of B_{RF}, prior to bandpass sampling . Using Equations (5.26) and (5.29), the extent of SNR degradation due to the out-of-band noise aliasing is formulated as follows:

$$\begin{aligned} SNR_{dgr} &= 10\log(\frac{SNR_{RF}}{SNR_{samp}}) \\ &= 10\log(1 + (k-1)\frac{N_{out}}{N_o}) \end{aligned} \tag{5.55}$$

If the noise inflicted upon the signal is white noise, then the following is true:

$$\frac{N_{out}}{N_o} = A_{atten}, \tag{5.56}$$

where A_{atten} is the out-of-band attenuation of the bandpass filter applied to the signal prior to bandpass sampling. Upon substituting Equation (5.56) in Equation (5.55), we arrive at:

$$SNR_{dgr} = 10\log(1 + \frac{(k-1)}{A_{atten}}). \tag{5.57}$$

Thus, when the out-of-band attenuation of the anti-aliasing bandpass filter is higher, then the SNR degradation is lower. It can be seen from Equation (5.57) that using lower bandpass sampling rates, i.e. higher values of k, will constraint us to employ anti-aliasing filters that have a high A_{atten}. In other words, sharp high-order filters will have to be employed.

5.1.6.4 DROF bitrate versus quantization noise

The term "DROF bitrate" is the bitrate of the digital signal generated by digitizing the RF signal using the ADCs of Fig. 5.1. When a bandpass sampling rate of f_{samp} satisfying Equation (5.7) and a resolution of n_{bit} bits/sample is used in the ADCs of the DROF link in Fig. 5.1, then it results in a DROF bitrate of [117]:

$$R_{DROF} = f_{samp} \cdot n_{bit}. \tag{5.58}$$

It is worth noting that the bit rate R_{RF} of the wireless RF signal resulting in the RF bandwidth of B_{RF} is different from R_{DROF}. Increasing the ADC's resolution increases the DROF bitrate R_{DROF} for a given wireless bit rate R_{RF}. We desire to employ the minimum possible R_{DROF}, i.e. minimum possible n_{bit}, for a given wireless signal having a bit rate of R_{RF}. However, employing a low n_{bit} also increases the quantization noise as per Equation (5.45), thereby resulting in a DROF bitrate versus quantization noise trade-off. Typically that value of resolution is employed, which would ensure that the overall noise in the DROF link is not dominated by the quantization noise [117]. Let us now discuss the final design trade-off in the next section.

5.1.6.5 Sampling rate and sampling rate tolerance versus reconstruction filter order

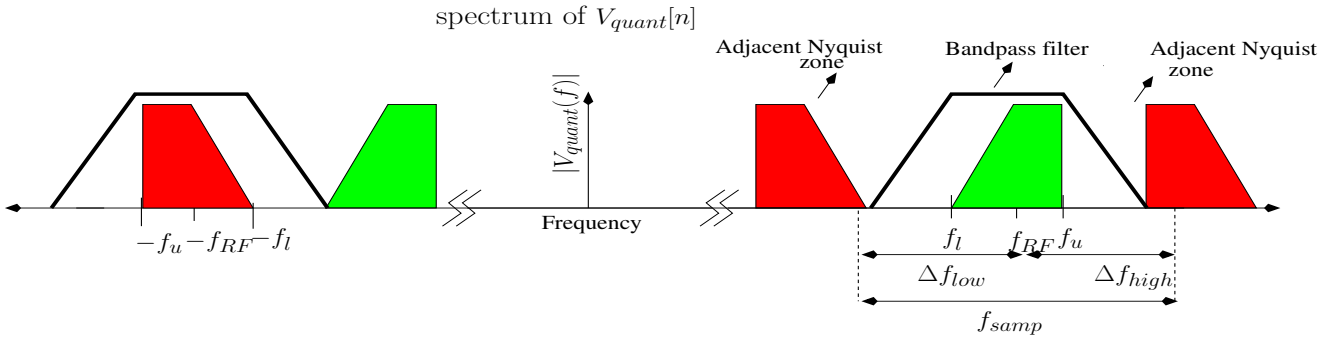

Figure 5.18: Sampling rate versus reconstruction filter order

The reconstruction of the RF signal $V(t)$ from the received copy of the quantized signal $V_{quant}[n]$ was discussed in Section 5.1.4. As shown in Fig. 5.18, this is achieved by applying a bandpass filter of bandwidth B_{RF} and having a center frequency of f_{RF} Hz to $V_{samp}[n]$, where B_{RF} and f_{RF} are the

bandwidth and center-frequency of the RF signal being transmitted by the DROF link. It can be seen from Fig. 5.18 and from the discussions of Section 5.1.3.1, that the separation between the desired Nyquist Zone and the adjacent Nyquist zones satisfies the following relationship:

$$\Delta f_{high} + \Delta f_{low} = f_{samp}. \tag{5.59}$$

The steepness of the roll-off required for the bandpass filter reconstructing the RF signal, can be reduced by ensuring a high value of both Δf_{high} as well as of Δf_{low}. This would however again increase the sampling rate required, as seen from Equation (5.59). Thus, it can be concluded from the discussions of this section that there exist a sampling rate versus reconstruction filter order trade-off.

Having discussed the various trade-offs in designing a DROF link, we next compare the various components of the DROF link seen in Fig. 5.1 to the components used in the AROF link of Fig. 2.1.

5.1.7 Comparison between AROF and DROF

The AROF and DROF techniques will be compared in terms of their transmitters, propagation properties and receivers in Sections 5.1.7.1, 5.1.7.2 and 5.1.7.3, respectively.

5.1.7.1 Comparison of the transmitters

As discussed in Section 5.1.3.2, the DROF link employs the more linear and robust family of digital optical modulations, while the AROF link relies on the modulation schemes of Section 2.1.2, such as the ODSB modulation discussed in Section 2.1.2.1. Three major optical impairments are imposed by a MZM in an AROF link, namely the:

1. Harmonics in the optical and photo-detected signal, as discussed in Section 2.1.3.1;
2. Intermodulation products in the optical and photo-detected signal, as detailed in Section 2.1.3.1;
3. Frequency chirping in the optical output of the modulator, as highlighted in Section 2.1.1.2.

When designing an AROF system, care should be taken that the undesired intermodulation products and harmonics do not corrupt the desired sidebands. Their distance from the desired sidebands on the frequency scale should ensure that they can be readily filtered out after photodetection. The second harmonic and third order intermodulation products are the most grave, since they lie closest to the required sidebands on the frequency scale. Fig. 2.23 shows the various significant harmonics and intermodulation products generated, when modulating an optical carrier using the twin sub-carrier multiplexed RF signals. In an application that employs WDM, it should be ensured that the harmonics and intermodulation products of a specific optical channel does not corrupt the co-propagating signals of the adjacent optical channels. WDM has been discussed in Section 2.1.3.2.

A positive chirp factor aggravates the already severe fiber-dispersion encountered in AROF systems. Thus, every effort must be made to employ a MZM modulator having a high extinction ratio. It becomes evident from the above discussions that the impairments imposed by the optical modulator becomes more severe in case of AROF (employing a RF modulating voltage) than in DROF (relying on a baseband digital modulating voltage). Let us now compare the AROF and DROF links from the point of view of signal propagation.

5.1.7.2 Comparison of the signal propagation

The undesired impact of fiber dispersion discussed in Section 2.1.1.3 increases, as the length of the optical fiber used increases. The effect of fiber dispersion in the digital optical link of DROF and in the microwave optical communication link of AROF is discussed as follows:

1. **The effect of fiber dispersion on the AROF link using ODSB modulation**: RF modulating signals are employed during optical modulation in AROF. The optical spectrum in this case consists of two sidebands, which are shifted to both sides of the optical carrier by a frequency offset that is equal to the RF carrier. Hence, the difference between the highest and lowest frequencies in the optical spectrum is substantial. This leads to a severe degradation due to fiber dispersion. At the receiver the process of photodetection involves a complex-valued addition of the intensities of the two sidebands. The intensities may add up constructively or destructively, depending on the specific value of the fiber dispersion induced phase difference between the two sidebands. Mathematically the power of the photodetected RF signal is given by [23]:

$$P_{RF} \propto \cos^2[\pi L c D (\frac{f_{RF}}{f_c})^2], \tag{5.60}$$

   where c is the speed of light, f_{RF} is the RF carrier frequency, f_c is the optical carrier frequency and L is total length of the optical fiber through which the signal propagates prior to photodetection.

2. **Effect of fiber dispersion on DROF**: Baseband modulating signals are employed during optical modulation in DROF. The impact of fiber dispersion during the transmission of a baseband modulating signal is significantly lower than in the case when RF modulating signals are being transmitted. This is because the baseband nature of the modulating signal ensures that the difference between the highest and lowest frequency component in the optical spectrum, that is centred around the optical carrier, is much lower than it was for the case of a RF modulating signal. Nevertheless, fiber dispersion becomes significant as the bandwidth of the baseband signal increases. An increase in the optical bandwidth may occur in the following scenarios [31]:

   (a) Increasing the bit rate of the baseband modulating signal;

   (b) Using a modulating signal that employs the Return-to-Zero (RZ) format with a low duty cycle;

   (c) Implementing baseband communication using narrow optical pulses emitted from a pulsed semiconductor laser. A pulsed semiconductor laser, unlike a continuous-wave laser, outputs optical pulses, i.e. the optical carrier frequency signal is emitted at regular intervals, rather than continuously. These emitted signals (pulses) can have an envelope of the desired width and shape, such as Gaussian, by suitably designing the laser. The pulses are emitted at a rate equal to the desired bit rate. Subsequently optical modulation is achieved by either amplifying or suppressing a pulse, depending on the specific binary baseband symbol being transmitted. Pulsed communication is inherently of RZ type.

Different optical power levels are used for signalling the various baseband symbols. However, as the level of fiber dispersion increases, the optical power from one symbol period may spread into the adjacent symbol periods due to temporal broadening. This can ultimately lead to an erroneous detection at the receiver. This specific manifestation of fiber dispersion is analogous to Inter Symbol Interference (ISI) in wireless signals. Fiber dispersion also increases as the length of the optical fiber increases and hence it sets a limit on the maximum affordable bit rates for a given fiber length. In other words, fiber dispersion sets a limit on the product of the bit rate and fiber length employed.

The effect of fiber non-linearity on baseband optical communication (as in DROF) and microwave optical communication (as in AROF) may be interpreted as follows:

1. **Effect of fiber non-linearity on DROF**: The rate of change in the instantaneous optical power (i.e. $dP(t)/dt$) is higher, when pulsed baseband communication is employed compared to the case of non-pulsed baseband communication. Thus, it may be concluded from the discussions in Section 2.1.1.3 that fiber non-linearity affects pulsed DROF to a significant extent.

2. **Effect of fiber non-linearity on AROF**: The rate of change in the instantaneous optical power is low, when analog modulating signals are used. Hence, the detrimental effect of fiber non-linearity is much lower in AROF than in pulsed DROF. It nevertheless sets a limit on the maximum optical power that can be coupled into the fiber [31].

Finally, we perform a comparative analysis of the detection techniques in AROF and DROF systems in the next section.

5.1.7.3 Comparison of the receivers

The impairments due to the photodiode discussed in Section 2.1.1.4 on ROF systems are as follows:

1. **Impairments in an AROF system**: The photodiode imposes noise on the photodetected signal. Moreover, the photodetector may become the limiting factor that decides the overall bandwidth of an AROF link, if the RF frequencies used are comparable to the bandwidth of the photodiode. Thus, AROF systems require the employment of expensive high-bandwidth photodiodes [46], especially when high RF frequencies are used.

2. **Impairments in a DROF system**: The photodiode imposes noise on the photodetected signal. However, the inherent noise immunity of a digital optical link is higher than that of an analog optical link. Furthermore, the baseband nature of the electronic signal transmitted permits the employment of a photodiode having a low 3 dB-bandwidth. Thus, an inexpensive photodiode of high noise figure and low bandwidth can be employed in a DROF system [46].

Having concluded our discussion of a basic DROF link, we present the results of our simulation-based study of a DROF link in the next section.

5.1.8 Performance analysis of DROF link

In this section we study the effect of various DROF link parameters on the performance of the DROF link of Fig. 5.1. The most common type of DROF link employs the low-complexity OOK intensity modulation discussed in Section 5.1.3.2 combined with direct photo-detection, as discussed in Section 2.1.1.4, which is also the scenario considered in this section.

Table 5.2: Simulation parameters of the DROF link

Parameter	**Value**	**Parameter**	**Value**
Bit rate RF signal	32 Mbps	MZM insertion loss t_{attn}	4 dB
Laser RIN	-155 dBc/Hz	MZM switching voltage V_π	5.5 V
optical wavelength λ_c	1550 nm	fiber length L	10 km
Laser linewidth	10 MHz	PD trans-impedance	125 Ω
fiber dispersion D	16 ps/km-nm	fiber Nonlinearity	1.2 /W/km
Filter roll-off factor	0.5	Dark current	1 nA
fiber attenuation α	0.2 dB/km	photo-receiver NF	6 dB
PD responsivity R	0.8 A/W	f_{rf}	5.6 GHz
Bandpass sampling rate	128 samples/s	ADC resolution	4 bits

5.1.8.1 Simulation parameters

The most commonly employed network topology is the star topology discussed in Section 2.1.3.3. In this section, we simulate a single point-to-point DROF downlink, where the star topology consists of multiple point-to-point links. In this section, we employ a BPSK RF signal at 5.6 GHz, which is generated using Root Raised Cosine (RRC) filters having a roll-off factor of 0.5. The RF signal has a bitrate of 32 Mbps.Unless stated otherwise, a bandpass sampling rate of 128×10^6 samples/second and a ADC resolution of 4 bits was employed. The impact of varying the ADC resolution will be discussed in Section 5.1.8.5. It is worth noting here that the RF signal employed in these simulations was a BOPSK signal. However, employing higher order QAM would require a higher resolution. The authors of [117] employed an ADC resolution of 8 bits for digitizing a 16-QAM signal. The Long term Evolution (LTE) Advanced RF signals may require an ADC resolution as high 12-13 bits, owing to the employment of high-order adaptive modulation schemes.

The commercially available laser of Section 2.1.1.1, which generates a 1550 nm optical carrier having a linewidth of 10 MHz and imposing a RIN noise of -155 dBc/Hz was employed in our optical transmitter [31]. The dual-drive MZM of Section 2.1.1.2 was used for performing the OOK optical modulation discussed in Section 5.1.3.2, where the MZM was assumed to have a switching voltage of $V_\pi = 5.5$ V [114]. Unless stated otherwise, ideal drive voltages and an ideal MZM having an extinction ratio of ∞ dB was assumed. Later we will also discuss the impact of employing non-ideal drive voltages and having a non-ideal extinction ratio in Sections 5.1.8.2 and 5.1.8.3, respectively. A 10 km long single-mode fiber of Section 2.1.1.3 having standard parameter values, i.e. $\alpha_{dB} = 0.2$ dB/km, $D = 16$ ps/km-nm and $\gamma_{nl} = 1.2$ /km/w was employed [31], where the optical propagation was simulated using the split-step technique of Section 2.1.4. Photodetection was performed using the photodiode presented in Section 2.1.1.4 having a responsivity of 0.8 A/W, a dark current of 1 nA and a wide detection bandwidth, i.e. a detection bandwidth that is significantly higher than 2.5 GHz,

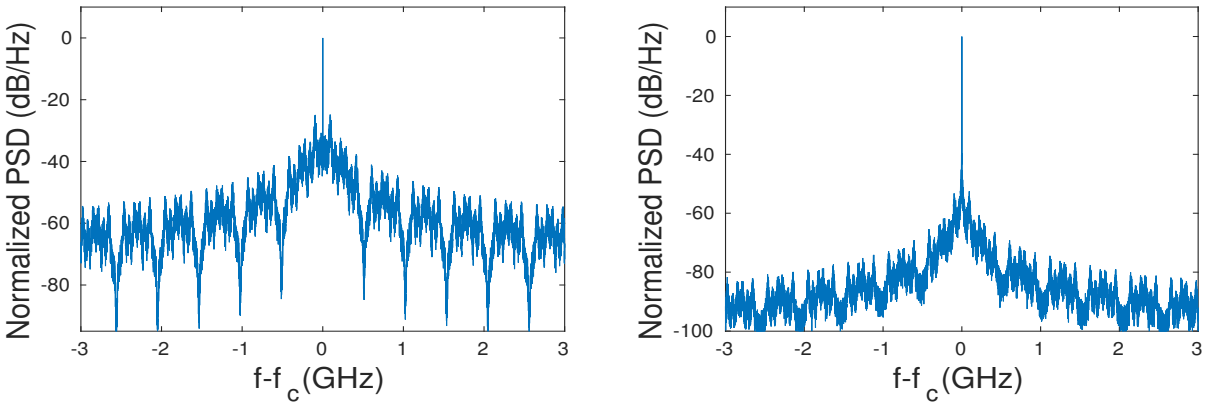

(a) $V_0 = V_\pi = 5.5$ V (b) $V_0 = 0.25 \times V_\pi = 1.375$ V

Figure 5.19: Spectra at various values of V_0

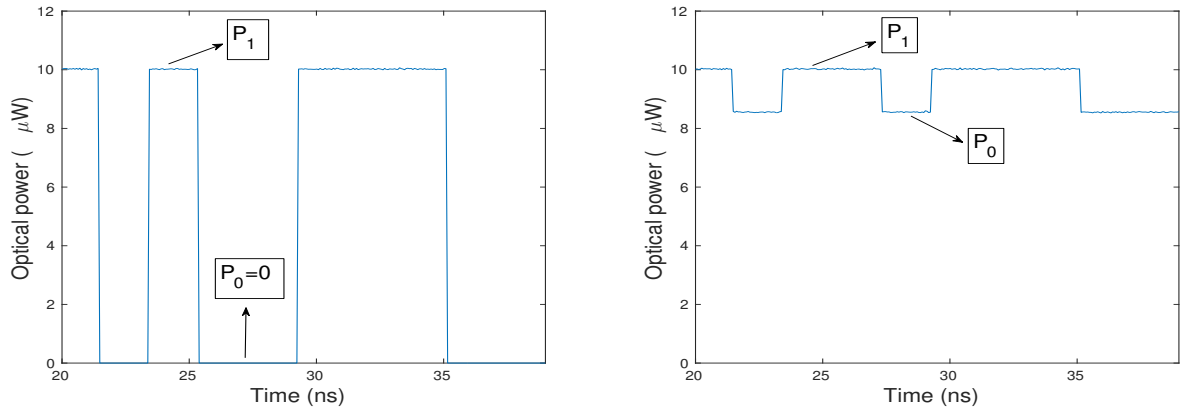

(a) $V_0 = V_\pi = 5.5$ V (b) $V_0 = 0.25 \times V_\pi = 1.375$ V

Figure 5.20: Time domain plots at various values of V_0

which is readily available [115] [116]. A low-cost optical receiver having a noise figure of 6 dB and a load resistance of 125 Ω was considered [117], where the noise processes encountered in the optical receiver were discussed in Section 2.1.1.5. Note that all the spectra presented in the following sections are normalized power spectral density plots, where the power values are normalized with respect to the peak power value. In other words, the peak power in a normalized power spectral density plot is 0 dB/Hz. A second point to note is that all the spectra are one-sided spectra. Just like an AROF link, a DROF link is also expected to maintain a BER of less than 10^{-9} over the optical link for ensuring that it does not further degrade the BER of the wireless link. The simulations in this section relied on an ideal wireless channel that imposes no noise in order to analyse the impact of the optical link. There are two BER metrics in a DROF link, namely the BER_{bb} of the baseband digitized bit stream, and the overall BER_{RF} of the RF signal transmitted through the DROF link. In the following sections, we study the effect of various parameters on both the BER metrics. Unless stated otherwise, the laser was operated at a power that would give a best-case BER of approximately 10^{-9}.

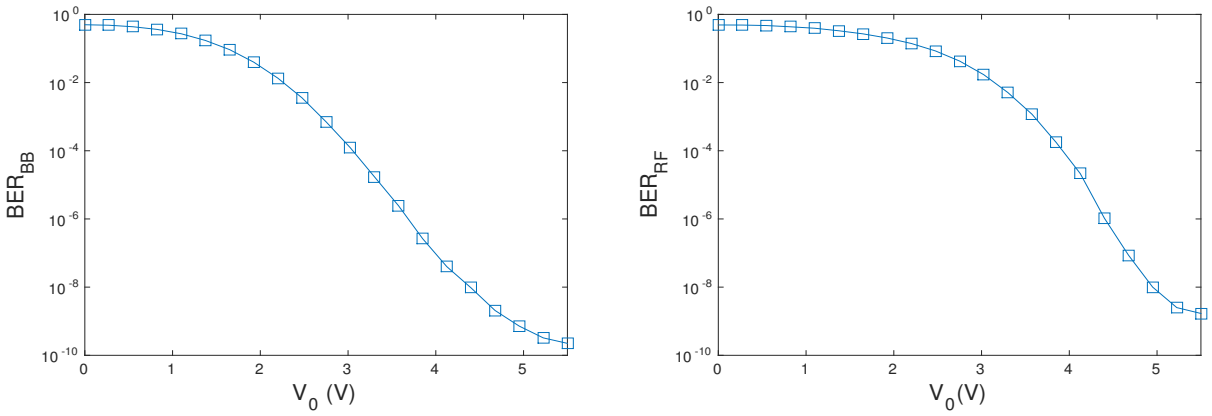

(a) BER of the digitized bit stream

(b) BER of RF signal

Figure 5.21: BER performance at various values of V_0

5.1.8.2 Effect of the optical modulation depth on the DROF performance

As discussed in Section 5.1.3.2, bit '1' is transmitted by employing a differential drive voltage of $V_{drv}(t) = V_1 = 0$ V, while bit '0' is transmitted using $V_{drv}(t) = V_0$. Hence, the maximum drive voltage is V_0, while the depth m_{DROF} of optical modulation is as follows:

$$m_{DROF} = \frac{V_0}{V_\pi} \times 100. \tag{5.61}$$

As discussed in Section 5.1.3.2, we have $V_0 = V_\pi$, which corresponds to $m_{DROF} = 100\%$ depth of the optical modulation. Fig. 5.19 shows the effect of using $V_0 < V_\pi$, i.e. using lower optical modulation depths, on the spectrum of the optical signal for the link parameters discussed in Section 5.1.8.1. Upon comparing the spectra in Fig. 5.19(a) and Fig. 5.19(b), it can be stated that employing a lower optical modulation depth, i.e. employing a lower V_0, results in the optical signal being weaker with respect to the optical carrier. Fig. 5.20 shows the time-domain plot of the optical intensity after modulation using the digitized bits, where the optical power employed for bits '1' and '0' are P_1 and P_0, respectively. It can be seen from comparing Fig. 5.20(a) to Fig. 5.20(b) that employing $V_0 < V_\pi$ results in $P_0 > 0$ being transmitted for bit '0', which is in contrast to the case of no optical power being transmitted for bit '0', i.e. $P_0 = 0$, when $V_0 = V_\pi$. This trend can also be observed from the transmittance plot of Fig. 5.12. A higher P_0 results in a lower noise margin and hence it increases the BER_{bb} of the digitized bit stream, which can also be observed from Fig. 5.21(a). An increased BER of the digitized bit stream results in a lower-integrity reconstruction of the RF signal in the DROF receiver and hence it results in a higher BER_{RF}. Thus, employing $V_0 < V_\pi$ results in a higher BER_{RF} as well. Explicitly, Fig. 5.21(b) shows BER_{RF} for various values of V_0. It can be seen from Fig. 5.21(a) and Fig. 5.21(b) that a 10% reduction of V_0 from its ideal value of V_π would result in less than an order of magnitude BER degradation. In the next section, we discuss the impact of employing a non-ideal extinction ratio.

5.1.8.3 Effect of the MZM extinction ratio on the DROF performance

An ideal dual-drive MZM has an extinction ratio of $\epsilon = \infty$ dB, while a non-ideal MZM has a lower extinction ratio. Let us consider the dual-drive MZM based optical modulation discussed in Section

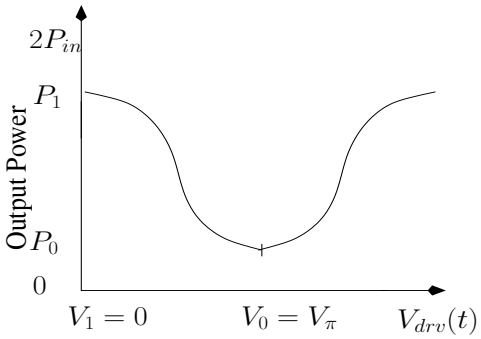

Figure 5.22: Optical intensity modulation by a MZM using a bit stream

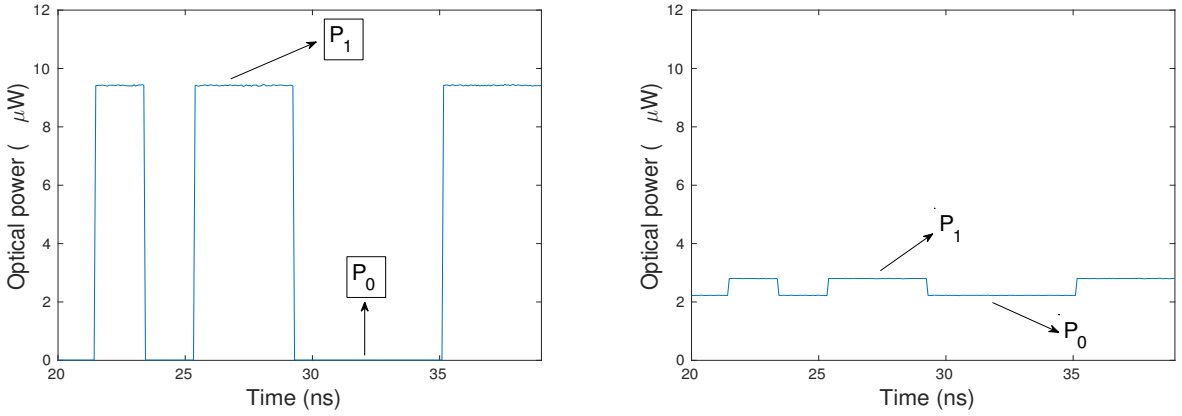

(a) Extinction ratio of 30 dB

(b) Extinction ratio of 1 dB

Figure 5.23: Time domain plots of the optical intensity after modulation

5.1.3.2. Employing a non-ideal dual-drive MZM would result in an optical power, which may be expressed as follows:

$$\begin{aligned} P_{dual}(t) &= |E_{dual}(t)|^2 \\ &= \left| \frac{1}{2}[e^{j\frac{\pi V_{drv1}(t)}{V_\pi}} + \gamma e^{j\frac{\pi V_{drv2}(t)}{V_\pi}}] E_{laser}(t) \right|^2 \\ &= P_{in}[1 + \gamma \cos(\frac{\pi V_{drv(t)}}{V_\pi})], \end{aligned} \tag{5.62}$$

where we have, $\gamma = (\sqrt{\epsilon}-1)/(\sqrt{\epsilon}+1)$. For the case of an ideal extinction ratio of $\epsilon = \infty$ dB, it can be seen that $\gamma = 1$. Substituting $\gamma = 1$ in Equation (5.62) gives us the power output of an ideal MZM, as shown in Equation (5.21). For a non-ideal MZM associated with $\epsilon < \infty$ dB we have $\gamma < 1$, which corresponds to a reduction of the peak output power and to an increased minimum output power in the MZM's transmittance characteristics, as shown in Fig. 5.22.

Hence, for the case of a non-ideal dual-drive MZM driven by a drive voltage as per Equation 5.18, the output powers for bits '1' and '0' are as follows:

$$P_{single}(t) \approx \begin{cases} P_0 = (1-\gamma)P_{in} & \text{for bit 0,} \\ P_1 = (1+\gamma)P_{in} & \text{for bit 1.} \end{cases} \tag{5.63}$$

Upon comparing Equation (5.63) to (5.19), we observe that employing a MZM associated with a non-ideal extinction ratio results in a reduction of the optical power transmitted for bit '1' and in an

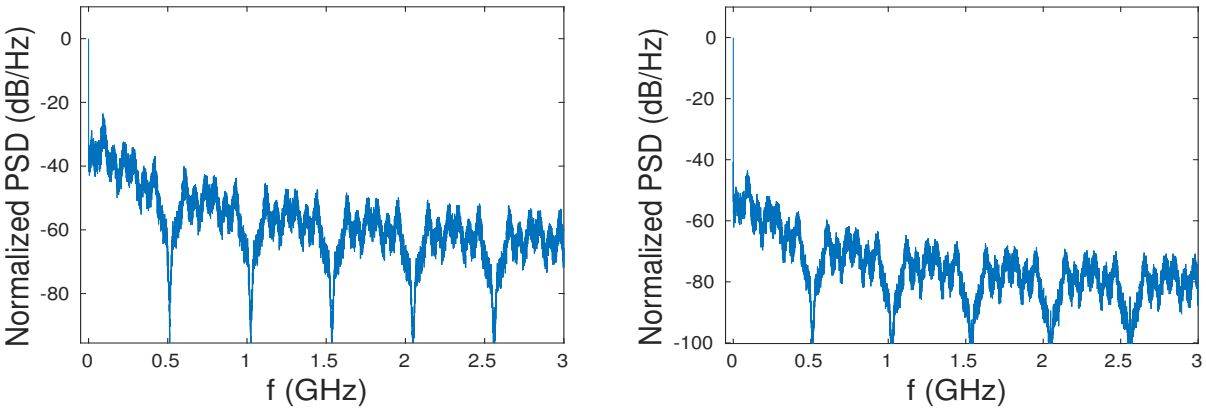

(a) Extinction ratio of 30 dB

(b) Extinction ratio of 1 dB

Figure 5.24: Effect of a non-ideal extinction ratio on the spectrum of the photodetected signal

increase of the optical power transmitted for bit '0', as seen from Fig. 5.23. Explicitly, Fig. 5.23(a) and Fig. 5.23(b) show the time domain plots of the optical intensity after modulation using the digitized bits for the scenarios of $\epsilon = 30$ dB and $\epsilon = 1$ dB, respectively. Fig. 5.24 shows the effect of a non-ideal extinction ratio on the spectrum of the photodetected signal. More specifically, the scenarios of $\epsilon = 30$ dB and $\epsilon = 1$ dB are shown in Fig. 5.24(a) and Fig. 5.24(b), respectively. The photodetector's noise was not considered in the results of Fig. 5.24 in order to avoid obfuscating the weakening of the signal's spectrum. It can be seen from Fig. 5.24 that a lower extinction ratio results in the optical signal being weaker with respect to the optical carrier, which would result in a higher BER. Fig. 5.25(a) shows the BER_{BB} for various values of the extinction ratio, where again, a lower extinction ratio results in a higher BER_{BB}. This is because a lower extinction ratio results in a reduced power difference between P_1 and P_0, which in turn reduces the noise margin and hence it increases the BER_{bb}. An increased BER of the digitized bit stream results in a lower-integrity reconstruction of the RF signal in the DROF receiver and hence it results in a higher BER_{RF}. Thus, a non-ideal extinction ratio results in a higher BER_{RF} as well, where Fig. 5.25(b) shows BER_{RF} for various values of the extinction ratio. It can be seen from Fig. 5.25 that employing commercially available MZMs having an extinction ratio of 20 dB would still give a robust performance. In the next section, we discuss the impact of varying the RF signal's carrier frequency.

5.1.8.4 Effect of varying the RF signal's carrier frequency

As discussed in Section 2.1.5.7, the classical AROF link employing ODSB modulation and direct photodetection imposes a dispersion-induced power penalty on the photodetected RF signal, which was shown in Fig. 2.40. Fig. 5.26(a) and Fig. 5.26(b) show the spectra of the received digitized signal for RF carriers at 1 GHz and 60 GHz, respectively, when employing the link parameters discussed in Section 5.1.8.1. It can be seen from Fig. 5.26 that the photodetected signal power is identical at both frequencies. Fig. 5.27 shows the normalized photodetected signal power of a DROF link for various RF carriers, where the normalization was carried out with respect to the power in a zero-dispersion scenario. It can be seen from Fig. 5.27 that the DROF link does not impose a dispersion-induced power penalty on the photodetected signal. Fig 5.28(a) and Fig 5.28(b) show the BER_{RF} and BER_{BB}

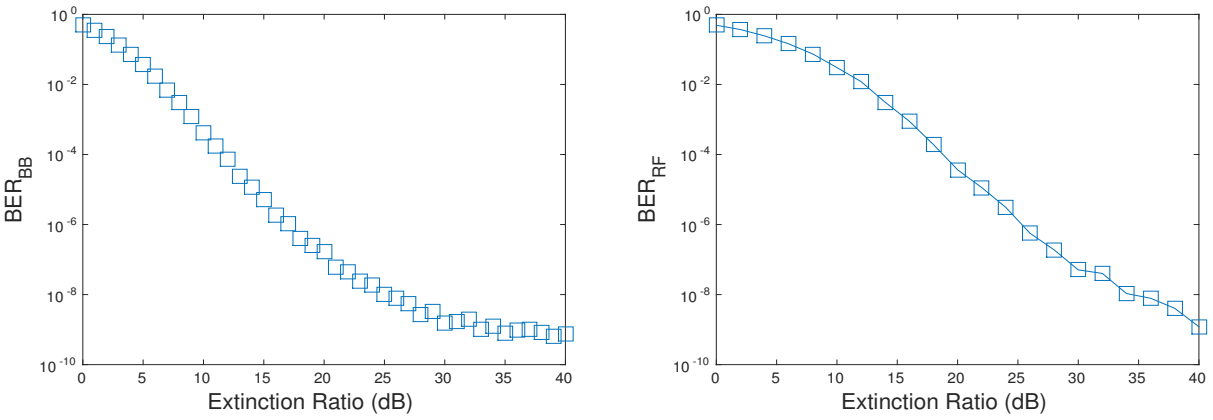

(a) BER of the digitized bit stream

(b) BER of RF signal

Figure 5.25: BER performance at various values of V_0

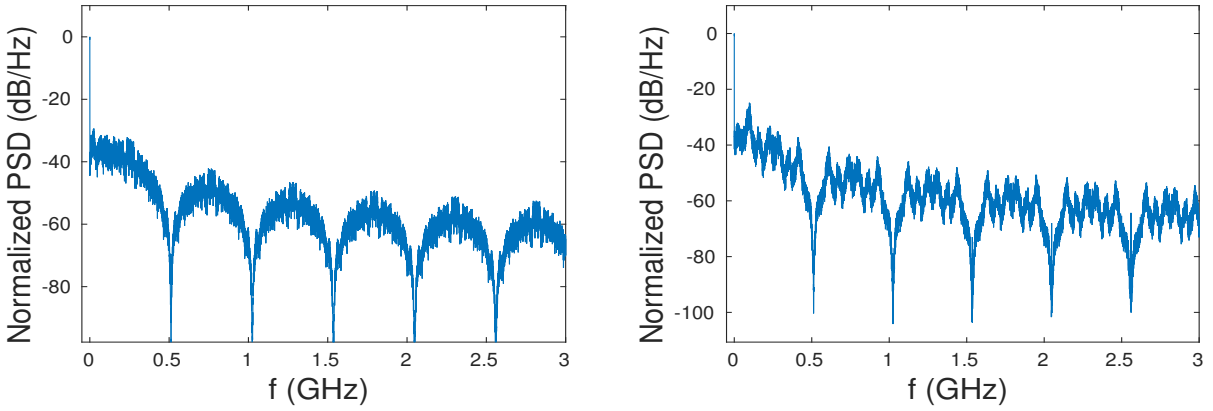

(a) 1 GHz RF signal

(b) 60 GHz RF signal

Figure 5.26: Spectra of the received digitized signal for different RF carriers

performance, respectively, for various RF carriers, where it can be seen that the performance does not degrade at higher frequencies as a benefit of having no dispersion-induced power penalty. Future wireless standards are expected to incorporate high RF signals, which cannot be readily transmitted over the classical AROF link relying on ODSB modulation. Fortunately, they can however be readily transmitted over a DROF link with no additional performance degradation.

5.1.8.5 Effect of varying the resolution of the ADC

As discussed in Section 5.1.3.1, the bandpass sampled signal is digitized by using a resolution of n_{bit} to represent each sample. As discussed in Section 5.1.5.3, naturally, this introduces quantization noise. Fig. 5.29 compares the transmit and receive filtered baseband signal for the scenarios of $n_{bit} = 1$ and $n_{bit} = 4$, where we observe that employing a higher value of n_{bit} reduces the quantization noise. It was proposed in [117] that the ADC resolution should be set to a value that would ensure that it does not become the limiting factor in the overall performance of the DROF link. Fig. 5.30(a) shows the BER_{RF} performance of the overall DROF link at various wireless SNRs, where it was ensured that we had $BER_{BB} < 10^{-9}$, while the ADC resolution was increased from $n_{bit} = 1$ to 6.

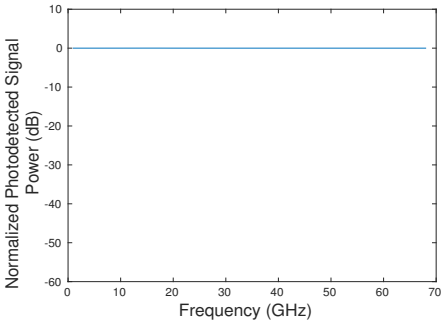

Figure 5.27: Normalized photodetected signal power for various RF carriers

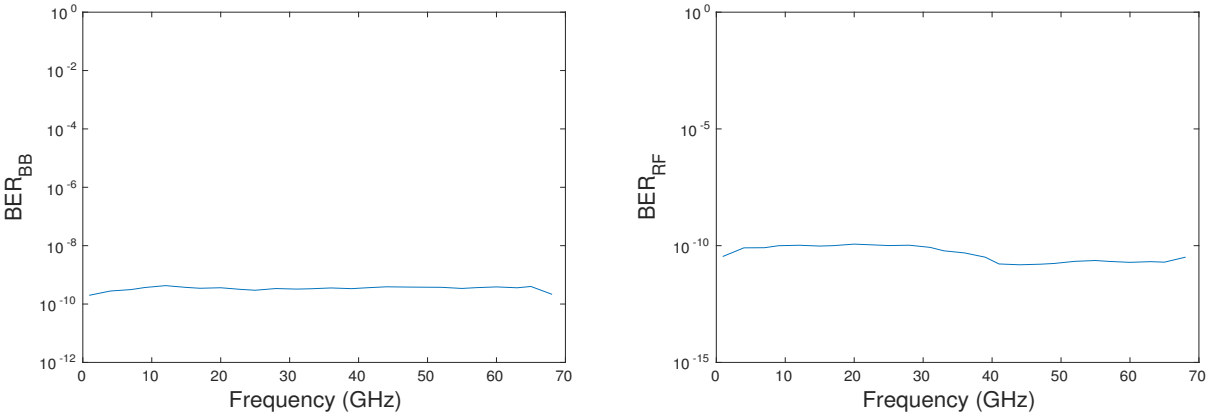

(a) BER of the digitized bit stream

(b) BER of RF signal

Figure 5.28: BER performance for various RF carriers

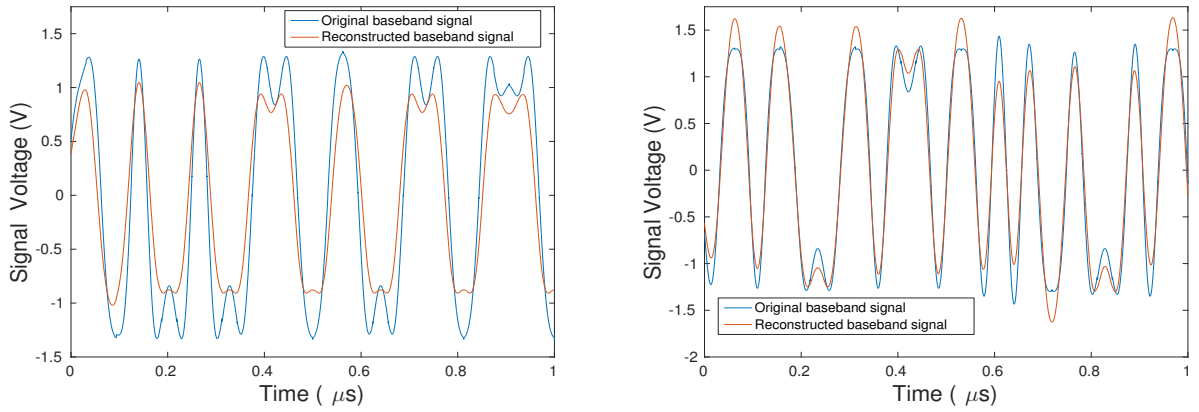

(a) $n_{bit} = 1$

(b) $n_{bit} = 4$

Figure 5.29: Transmit and receive filtered baseband signal for different ADC resolutions

It can be seen from Fig. 5.30(a) that for a BPSK signal, employing an ADC resolution of $n_{bit} = 4$ would suffice, because employing higher ADC resolutions would not provide any significant reduction of BER_{RF}, while requiring a higher operating power for the laser. This is because an increase of n_{bit} would increase the bit rate of the digitized bit stream and hence result in an increase of BER_{BB}. In order to constrain the BER_{BB} metric to a value less than 10^{-9}, the laser would have to be operated

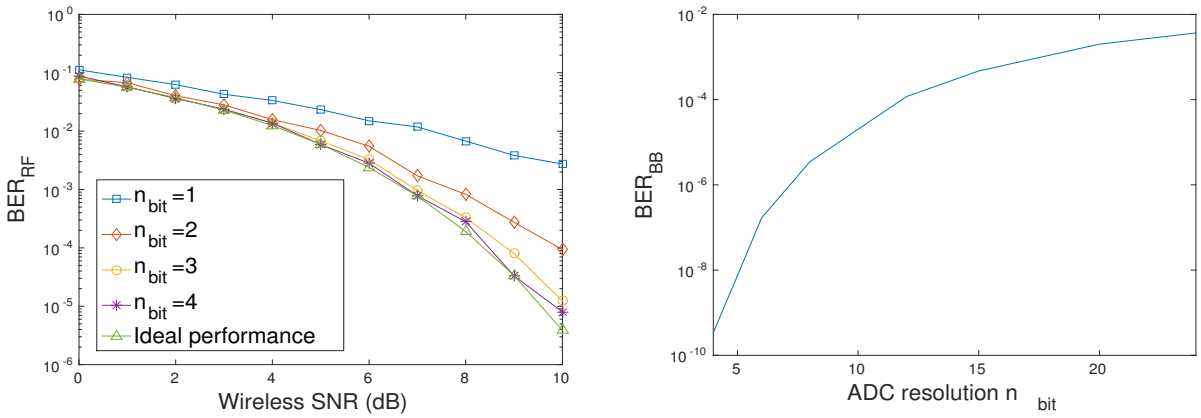

(a) $n_{bit} = 1$ (b) $n_{bit} = 4$

Figure 5.30: BER performance at different ADC resolutions

at a higher transmit power. Fig. 5.30(b) shows the increase in BER_{BB}, when the ADC resolution is increased to values above $n_{bit} = 4$, when considering a fixed transmit power. A similar trend is observed, when the bandpass sampling rate is increased, because that also increases the bitrate of the digitized bit stream, thereby requiring an increase in the operating power of the laser for ensuring $BER_{BB} < 10^{-9}$.

5.1.8.6 Effect of varying the received optical power

Fig. 5.31(a) shows the BER_{RF} performance for various received optical powers, when the link parameters are as discussed in Section 5.1.8.1. An MZM having an extinction ratio of 30 dB was employed. It can be seen from Fig. 5.31(a) that a lower received optical power results in a higher BER_{RF}. This is because a lower received optical power translates into a weaker photodetected optical signal. This in turn results in a lower signal-to-noise ratio of the photodetected signal, which results in a higher BER_{RF}. Fig. 5.31(b) shows the PSD of the photodetected baseband signal. The received optical power would change, if the laser's operating power is changed or if the length of the fiber is changed. Note that the attenuation imposed by the optical fiber on a propagating optical signal is 0.2 dB/km.

The classical ROF technique discussed in Chapter 2 is the low-cost AROF technique, while the DROF technique introduced in Chapter 3 and detailed in this chapter is an advanced performance improvement technique. In the next section, we propose an amalgamation of these two techniques in order to exploit the advantages of both techniques.

5.2 Hybrid analog/digitized radio over fiber architecture

A hybrid architecture that uses the state-of-the-art DROF architecture of Fig. 3.33 with the conventional ROF of Fig. 2.1 can be designed, where the conventional ROF is referred to as Analog ROF (AROF) in this section to distinguish it from DROF. In addition to the advantages of the DROF solution discussed in Section 3.1.12, there is also the advantage that multiple users may be optically code division multiplexed [2]. MSs' have different clock and carrier frequencies as well as different distances

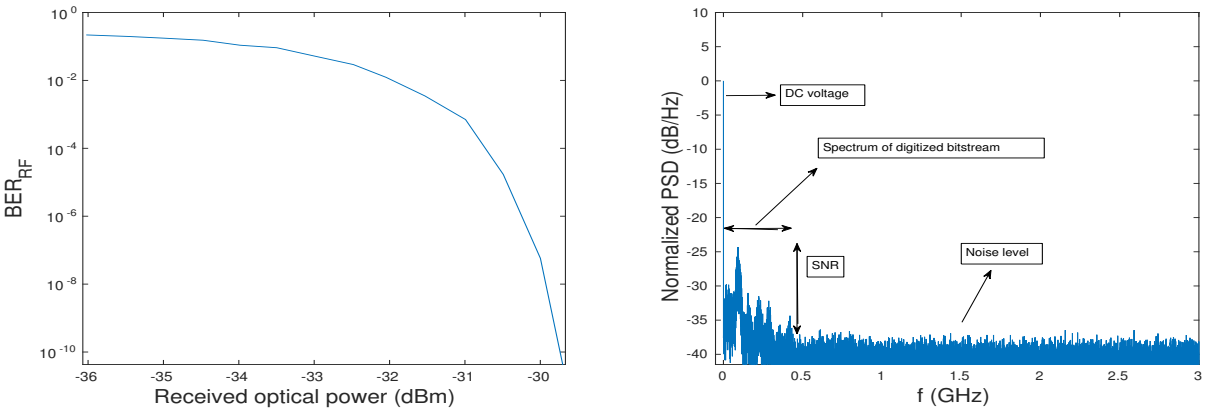

(a) BER performance at various received optical powers

(b) SNR of the photodetected signal

Figure 5.31: DROF link performance

from the RAP. Hence,, their UL signals arrive asynchronously at the RAPs. Additionally, imperfect power control as well as the inevitable multi-user interference result in the asynchronous wireless UL having a lower SNR than the synchronous DL [2]. Hence, a more robust, but more costly DROF link of Fig. 3.33 can be employed for the UL optical transmission, while the low-cost conventional AROF link of Fig. 2.1 can be employed for the DL [2]. As a further benefit, wavelength re-use relying on the ORM technique of Fig. 3.45 may be invoked because the UL BB signal of DROF may be transmitted by the same optical carrier used to transmit the DL RF signal of AROF. This also increases the optical spectral efficiency. The lower optical transmit power requirement of the DROF mode also supports the re-use of the DL optical carrier power. Moreover, the ring topology of the proposed architecture minimises the cost of fiber laying [2]. The technique of exploiting the modulation harmonics in an OCS signal, as discussed in Section 3.2.3.2, is also employed in the proposed architecture [2] for supporting multiple RAPs. As discussed in Section 1.3, wireless MIMO transmission, that relies on the use of DL transmit-antenna diversity and UL receive-antenna diversity, improves the wireless link performance of the proposed ROF system.

In ROF communication a Distributed Antenna System (DAS) is created, when multiple RAPs are connected to the same BS. These systems are designed utilising the optical multiplexing techniques that were discussed in Section 2.1.3. The previously discussed optical multiplexing techniques are employed in the proposed architecture, where WDM is employed to support multiple RAPs, while SCM is employed to support multiple wireless users. In the architecture proposed in this chapter, the technique of OCS was employed for generating the optical carriers of the WDM signal that support multiple RAPs, where each RAP is served by a unique optical carrier.

In Section 5.2.1, we present the proposed architecture, while in Section 5.2.2, we present the results of our simulation-based study of the proposed architecture.

5.2.1 Proposed radio over fiber network architecture

The proposed ring architecture is shown in Fig. 5.32. The proposed architecture consists of a single BS supporting 4 RAPs. The Optical carrier generator, BS transmitter, ROF ring, uplink transmitter in the RAP and the BS receiver that constitute the duplex link have been discussed in Sections 5.2.1.1,

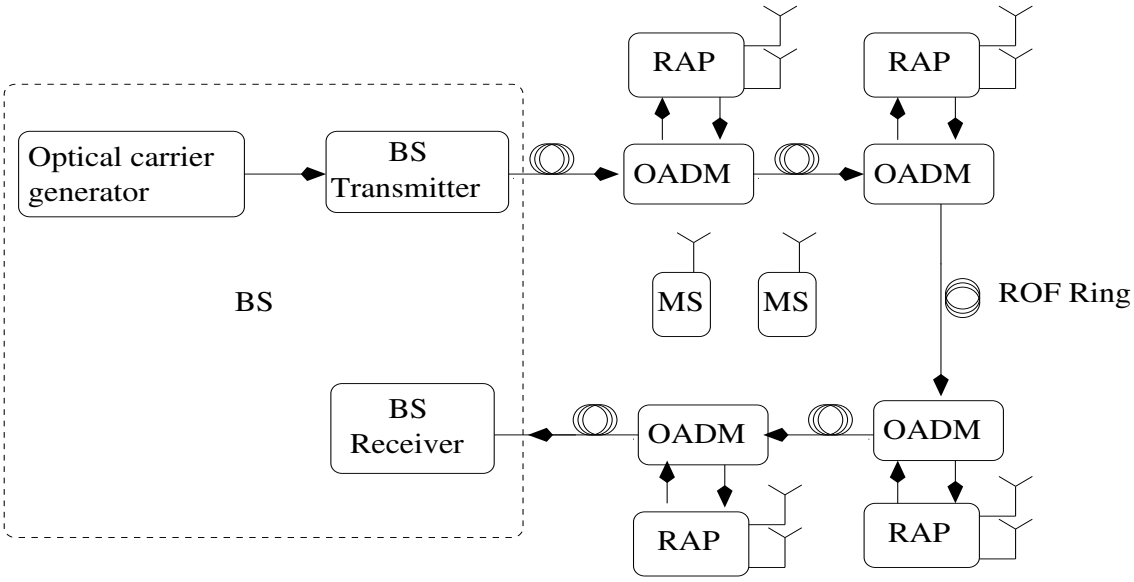

Figure 5.32: Block diagram of the proposed ROF architecture

5.2.1.2, 5.2.1.3, 5.2.1.4 and 5.2.1.5, respectively. Fig. 5.33 shows the components of the architecture in Fig. 5.32 in detail. The parameters used in the architecture are summarized in Table 5.3.

5.2.1.1 Optical carrier generator

The optical carriers are generated at the BS by exploiting the Dual Drive (DD) MZM non-linearity with the aid of OCS [250]. The output of the laser operating at the optical transmit of power P_{in} and frequency of f_c (wavelength λ_c) is:

$$E_{laser}(t) = (\sqrt{2P_{in}})e^{j2\pi f_c t}. \tag{5.64}$$

The output of the laser is fed to the Optical Carrier Generator (OCG) of Fig. 5.33. As discussed in Section 2.1.2.1, OCS is a commonly employed modulation format of the optical signal to a specific RAP. However, in the architecture of Fig. 5.33, the OCS technique is employed for exploiting the non-linearity of the optical modulator to generate multiple optical carriers from the output of a single laser. The drive voltages applied to the two arms of the DD-MZM are as follows:

$$V_{drv1}(t) = V_{dc1} + V_{RF}\sin(\omega_{RF}t + \phi_{RF1}), \tag{5.65a}$$

$$V_{drv2}(t) = V_{dc2} + V_{RF}\sin(\omega_{RF}t + \phi_{RF2}). \tag{5.65b}$$

Here $V_{bias} = V_{dc1} - V_{dc2} = V_\pi$, $\phi_{RF1} - \phi_{RF2} = \pi$. The Jacobi-Anger expansion for exponentials of trigonometric functions is as follows [251]:

$$e^{jz\cos\theta} = \sum_{n=-\infty}^{\infty} j^n J_n(z)e^{in\theta}, \tag{5.66a}$$

$$e^{jz\sin\theta} = \sum_{n=-\infty}^{\infty} J_n(z)e^{in\theta}. \tag{5.66b}$$

Using the expressions for the drive voltages from Equations (5.65a) and (5.65b) as well as the Jacobi-Anger expansion from Equation (5.66b) in Equation (2.6b), we get the the optical field at the output of the DD-MZM in the OCG to be as follows:

Table 5.3: Parameter values used in the ROF architecture

Parameter	Value	Parameter	Value
RF down-link f_{dwn1} & f_{dwn2}	2.47 GHz 5.8 GHz	PD receiver Noise Figure	6 dB
RF Modulation scheme	Binary Phase Shift Keying	PD receiver Trans-impedance	125 Ω
Fiber Dispersion	16 ps/km-nm	ADC Resolution	4 bits
λ_c	1550 nm	PD responsivity	0.8 A/W
RF downlink and uplink Bit rate	32 MBPS 16 MBPS	RF uplink f_{up1} & f_{up2}	2.416GHz 5.744GHz
RF channel width with guard band	60MHz (down-link) 30MHz (uplink)	Bandpass sampling rate f_{samp}	64×10^6 sample/s
RRC filter roll-off	0.5	f_{RF} used in OCG	12.5 GHz
downlink RF Diversity Scheme	Space Time Block Coding	length of fiber ring	25 km
uplink RF Diversity Scheme	Maximal Ratio Combining	DD-MZM t_{attn} & Extinction Ratio ϵ	4 dB 35 dB

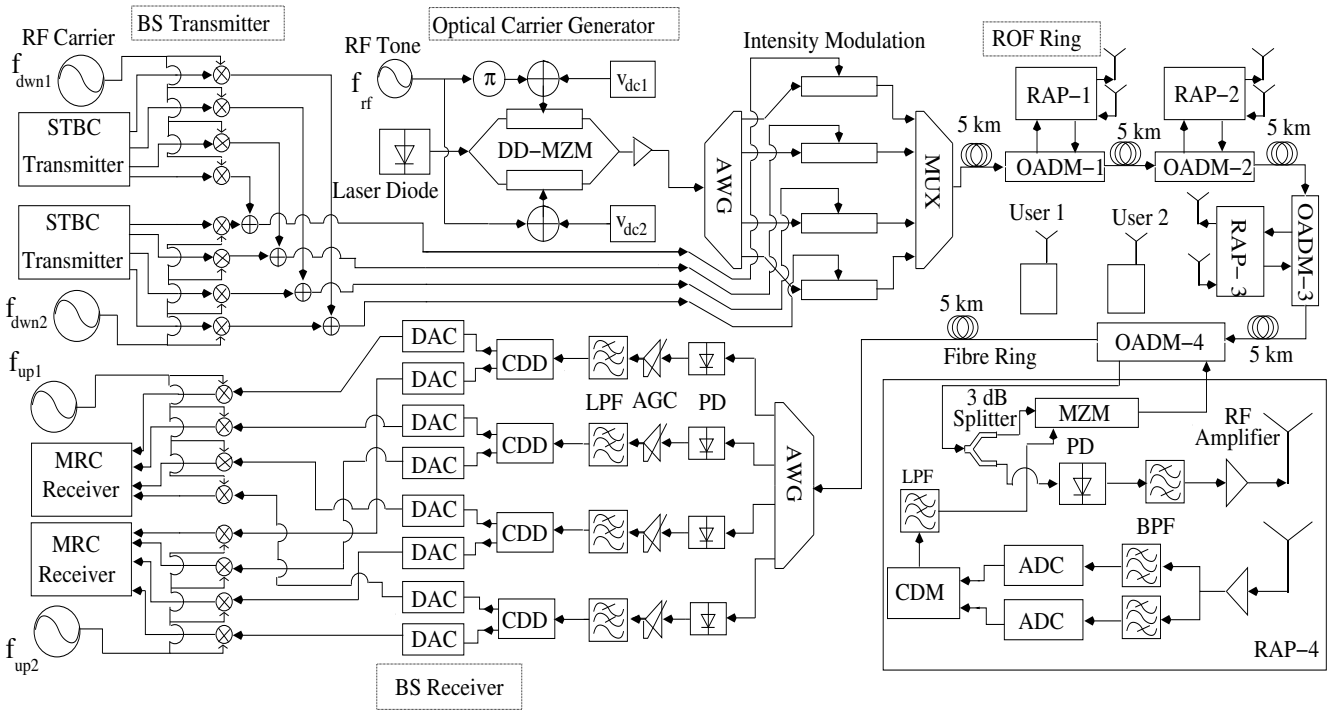

Figure 5.33: Proposed ROF architecture

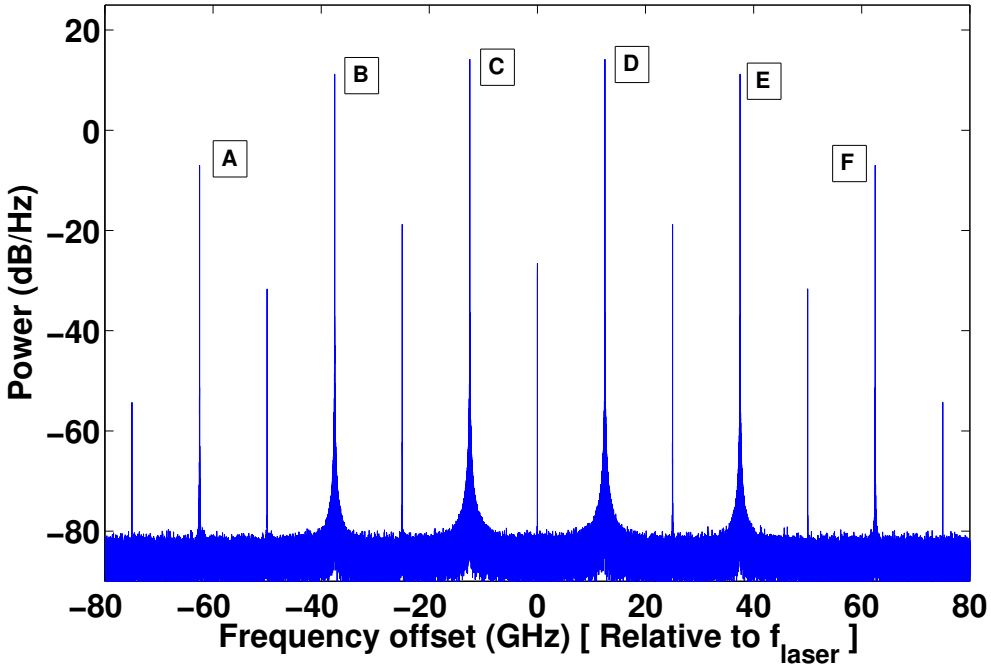

Figure 5.34: Optical spectrum of OCG output when the extinction ratio is 35 dB

$$E_{dual} = \frac{\sqrt{t_{attn}}E_{laser}(t)}{2}\left(\sum_{n=-\infty}^{\infty} jJ_n(2.82)(e^{jn\pi} - \gamma)e^{jn(2\pi f_{RF}t+\pi)}\right), \tag{5.67}$$

where t_{attn} is the insertion loss of the DD-MZM, $E_{laser}(t)$ is the laser output, while J_n is the Bessel function of first kind and order n. In the expression of Equation (5.67) a high value of $V_{RF} = 0.9V_\pi$ was chosen for generating strong harmonics and $V_{dc1} = V_\pi, V_{dc2} = 0, \phi_{RF1} = \pi, \phi_{RF2} = 0$. Fig. 5.34 shows the spectrum of the output signal of the OCG, where the output spectrum has six significant side bands (A-F) spaced at $2f_{RF}$ Hz that may be used as optical carriers in the proposed architecture through WDM.

In the next section, we discuss how each of the optical carrier generated by the OCG of Fig. 5.33 is modulated with the data for a particular RAP by the BS transmitter.

5.2.1.2 BS transmitter

The downlink RF signals transmitted to each RAP at frequencies $f_{dwn1} = 2.47\ GHz$ and $f_{dwn2} = 5.8\ GHz$ are multiplexed using SCM and used for intensity modulating the optical sidebands B to E of Fig. 5.34 at the output of OCG. Each of these sidebands now transmits a ODSB downlink optical signal to the 4 RAPs. The intensity $P_{RAPi}(t)$ of the downlink optical signal transmitted to RAP-i is:

$$P_{RAPi}(t) = 1 + k_{dwn}[V_{1,i}(t) + V_{2,i}(t)] + P_{harm}(t), \tag{5.68}$$

where $V_{1,i}(t)$, $V_{2,i}(t)$ are the downlink RF signals of users 1 and 2 sent to RAP-i. Still referring to Eq. (5.68), $P_{harm}(t)$ represents the weaker harmonics and k_{dwn} depends on the optical modulation index. Transmit diversity was achieved with the aid of STBC [33] following the generation of the Root

Raised Cosine (RRC) filtered BPSK signals. A single user per RF carrier was assumed. However, the concept may be extended to support multiple users per RF carrier by using wireless BPSK-CDMA signals.

After downlink optical modulation, the signals enter the ROF ring of Fig. 5.33, where the next section discusses downlink detection and uplink optical modulation in the RAPs.

5.2.1.3 ROF ring

The downlink ROF signals are transmitted through a SMF based ring. We use the 4 major sidebands in the OCG output for supporting 4 RAPs in the ring. Duplex optical transmission was used by each RAP at a single OCG output sideband via an OADM and Wavelength Reuse (WR). The block diagram of a RAP is shown in Fig. 5.33. The optical signal dropped at RAP-i is fed to a 3 dB splitter. One of the splitter outputs is photo-detected and amplified for recovering the downlink RF signal, while the other output is reused for uplink transmission and it is modulated by the uplink baseband DROF signal ($b_{RAPi}(t)$).

As discussed in Section 3.2.2, the reuse of the downlink optical carrier for uplink communication is referred to as WR. In the architecture of Fig. 5.33, the need for optical carrier recovery for WR is dispensed with. The same optical carrier supports both the uplink and downlink of a RAP. The need for optical carrier recovery is dispensed with by using AROF for the downlink and DROF for the UL. Thus, the downlink optical signal is a microwave-modulated optical signal, while the uplink optical signal is a baseband-modulated optical signal. This approach is similar to that in [160] and [252], where the authors employed the concept of multiplexing baseband wired data and RF wireless signal by reusing the downlink optical carrier for transmitting wired UL data.

In the architecture of Fig. 5.33, the baseband data modulates the reused downlink optical carrier and corrupts the two downlink sidebands, albeit fortunately this is not a problem, since the downlink signal has already been detected. Using Eq. (5.68), the intensity of the uplink optical signal transmitted from RAP-i, is:

$$\begin{aligned} P_{RAPi}^{reuse}(t) &= \tilde{P}_{RAPi}(t)[1 + k_{up} b_{RAPi}(t)] \\ &= 1 + k_{up} b_{RAPi}(t) + k_{dwn} V_{1,i}(t) + k_{dwn} V_{2,i}(t) \\ &+ k_{dwn} k_{up} V_{1,i}(t) b_{RAPi}(t) + k_{dwn} k_{up} V_{2,i}(t) b_{RAPi}(t) \\ &+ k_{up} b_{RAPi}(t) P_{harm}(t) + P_{harm}(t), \end{aligned} \tag{5.69}$$

where k_{up} depends on the depth of the uplink modulation. Since $\tilde{P}_{RAPi}(t)$ is an attenuated and dispersion contaminated version of $P_{RAPi}(t)$, they occupy the same frequency band. This permits the use of Eq. (5.68) in Eq. (5.69) for the above proof-of-concept mathematical analysis because our primary concern is the occupied frequency bands after uplink optical modulation. Only the second term in Eq. (5.69) is a baseband term and the rest may readily be filtered out using an inexpensive electronic filter after intensity detection using a PD. The users' wireless uplink signals were received at all RAPs and then combined by a MRC receive antenna diversity scheme [33] at the BS. The generation of $b_{RAPi}(t)$ as well as its employment in the modulation of the reused optical carrier is discussed in the next section.

5.2.1.4 Uplink transmission at the RAP

In the uplink optical transmitter at the RAP, using Nyquist sampling of the received BPSK RRC filtered RF signals at f_{up1} and f_{up2} Hz is not practically feasible. Hence, digitization of these signals was performed using the concept of bandpass sampling discussed in Section 5.1.3.1. The valid bandpass sampling rates for a bandwidth of B_{RF} are [3]:

$$\frac{2(f_u + \frac{B_{RF}}{2})}{k} \leq f_{samp} \leq \frac{2(f_u - \frac{B_{RF}}{2})}{k-1} \; \forall \; 1 \leq k \leq \lfloor \frac{f_u + \frac{B_{RF}}{2}}{B_{RF}} \rfloor, \tag{5.70}$$

where $\lfloor w \rfloor$ represents the integer part of w and $k \in I$. The use of BPSK modulation results in a low ADC/DAC resolution requirement. Nevertheless, the ADC resolution should guarantee that the link SNR is not dominated by the quantization noise [117]. Using the Equations in [117], a resolution of 4 bits/sample was found to satisfy this criterion, when using inexpensive ADCs having an RMS jitter of approximately 10ps. The pair of digitized RF signals were then code division multiplexed using orthogonal Walsh codes [33] to generate $b_{RAPi}(t)$ prior to optical modulation and transmission over the synchronous optical uplink.

Baseband optical modulation in the DROF uplink of the proposed architecture was implemented using a single-drive MZM, as discussed Section 5.1.3.2. The two level NRZ optical modulation can be implemented by operating the MZM at the maxima and minima of the transmittance characteristic to transmit the two electronic symbols [161], as discussed in Section 5.1.3.2. However, in the architecture of Fig. 5.33, the UL DROF signal was generated by code division multiplexing of the bit streams generated by digitizing RF signal received from two MSs. Thus, the DROF signal has three levels (symbols), namely [-1 0 1]. In this case, the third (i.e. middle) symbol may be transmitted by operating the single drive MZM of Fig. 2.8(a) at the half-power point of the transmission curve, i.e. using $V_{drv}(t) = \frac{V_{pi}}{2}$ in Equation (5.17). Thus, the transmitted optical power in this case would be:

$$P_{single}(t) \approx \begin{cases} P_{-1} = 0 & \text{for symbol -1,} \\ P_0 = P_{reuse} & \text{for symbol 0,} \\ P_1 = 2P_{reuse} & \text{for symbol 1,} \end{cases} \tag{5.71}$$

where P_{reuse} is the power of the optical carrier being reused for the uplink optical transmission.

It must be noted that in all the above cases the modulator is biased at the quadrature point $V_{bias} = V_\pi/2$ and driven to the required point on the transmittance curve [161]. Hence, the spectrum of the output signal will contain the optical carrier. Usually, the electronic NRZ signal is first filtered and then used to generate the drive voltages in order to minimize the bandwidth of the optical signal. Minimizing the difference between the highest and lowest frequency present in the optical spectrum minimizes the effect of fiber dispersion. Moreover, in systems that implement the SCM technique discussed in Section 2.1.3.1 or the DWDM technique discussed in Section 2.1.3.2, it becomes imperative to use filtered baseband electronic signals in order to prevent interference with the co-propagating signals.

The uplink optical signal is detected by the BS receive of Fig. 5.33, which is discussed in the next section.

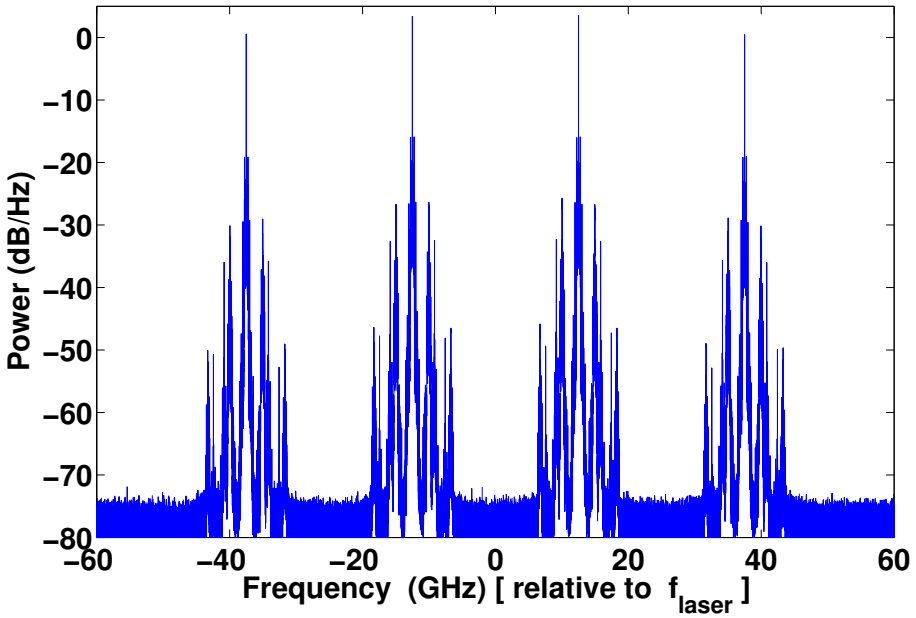

(a) Optical spectrum at the input of the BS receiver

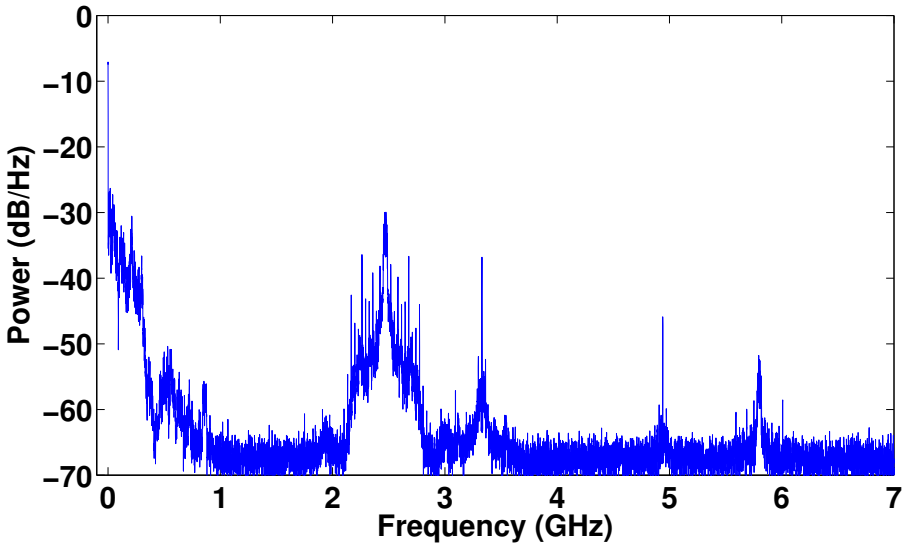

(b) Electronic spectrum after photodetection of the RAP uplink signal

Figure 5.35: Optical and electronic spectra after propagation along the ROF ring

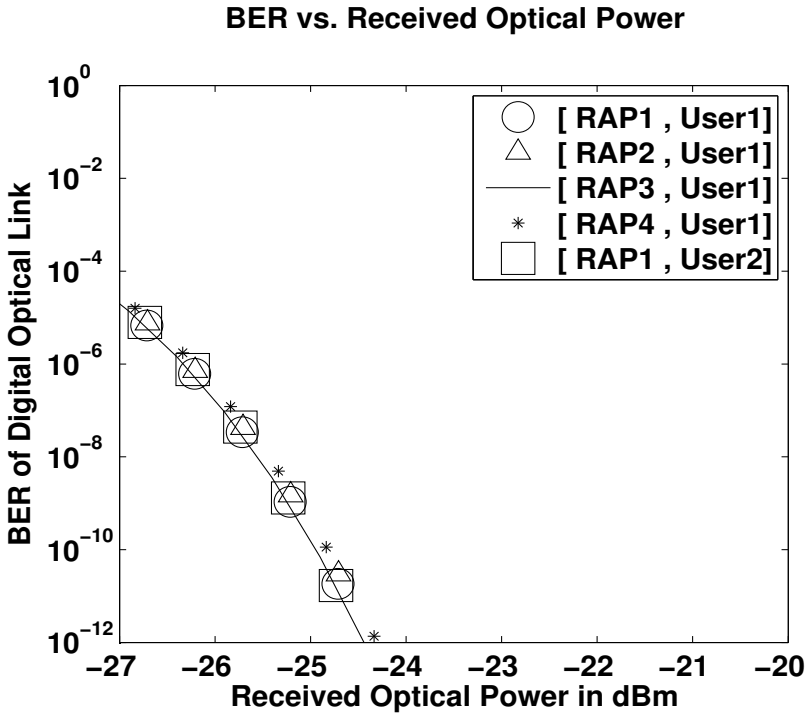

(a) BER performance of the DROF links

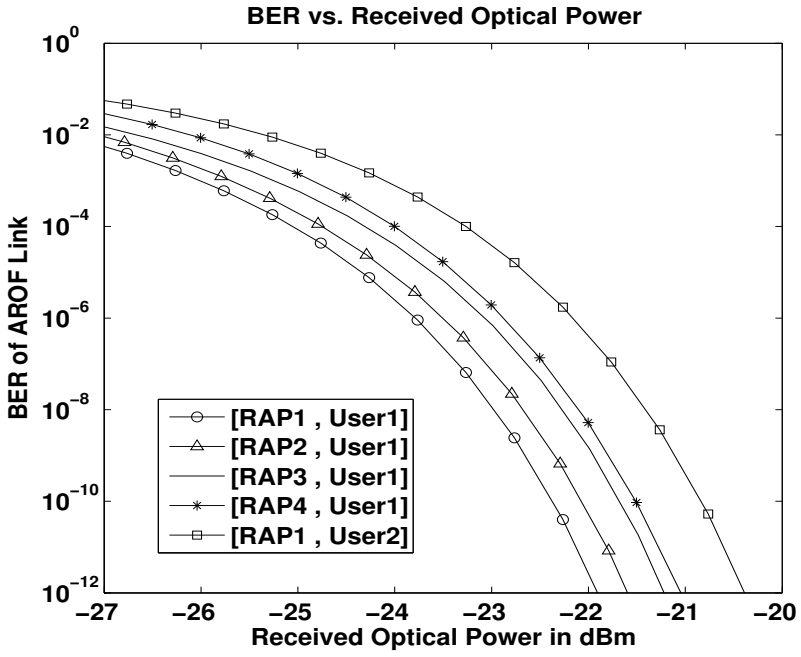

(b) BER performance of the AROF links

Figure 5.36: BER performance of the ROF links

5.2.1.5 BS receiver

The spectrum of the uplink ROF signal input to the BS receiver is shown in Fig. 5.35(a). The uplink signal is fed into a 1×4 AWG, each of whose outputs are photo-detected and the baseband signal is fed through a LPF, amplified using an automatic gain control amplifier, code division de-multiplexed (CDD) and used for recovering the four copies of the uplink RF signals which are then fed to a MRC block [33] .

Having concluded the theoretical discussion of the architecture in Fig. 5.33, in the next section, we present the results of our simulation-based performance analysis of the proposed architecture.

5.2.2 Performance of the proposed architecture

It can be observed from Fig. 5.36(a) and Fig. 5.36(b) that the sensitivity of the AROF link varies more significantly with the changes in the user's RF carrier as well as with the downlink fiber length as compared to the DROF link, which is due to the increased effects of chromatic dispersion and owing to the link's non-linearity. Moreover, the performance of the DROF link was found to be robust, despite reusing the downlink optical carrier and the MZM non-linearity. It is envisaged that the ROF technology will be extensively used in future RF systems, especially at mm-wave frequencies. Having a reduced AROF sensitivity, inflicted by the higher levels of chromatic dispersion, would further increase the level of signal corruption imposed by the optical link at higher RF carriers. This makes DROF more attractive for transporting the lower-integrity uplink signal, when relying on WR. Fig. 5.37(a) and Fig. 5.37(b) characterize the overall system performance, when both uplink and downlink diversity was exploited and 15 dBm of optical power entered the BS transmitter AWG. The wireless channel symbol energy was E_s and noise spectral density was N_o. Using STBC transmit-diversity in the downlink and MRC receive-diversity in the uplink helped combat the wireless channel's Rayleigh fading and hence improved the coverage quality. We emphasize here that despite the strong dependence of the AROF link's sensitivity on the RF carrier, the overall downlink system performance does not vary much between the users, since the lower-SNR wireless channel dominates the overall system performance. This however would not be the case for higher RF carriers.

The performance of both users us exoected to be very similar, which can also be seen in Fig. 5.37. However, it is worth mentioning that for a given transmit power, the received power and hence the received SNR for both users would be different, because both users would experience different channel fading and path loss.

Having completed our discussion of the proposed architecture, we offer our chapter conclusions in the next section.

5.3 Chapter conclusions

The DROF performance improvement technique of was detailed in this chapter, along with the simulation-based study of its parameters. The generation of the DROF signal, its transmission and detection were discussed in this chapter along with a detailed study of the noise processes involved and the various design trade-offs involved. Finally, a wireless campus network architecture was pro-

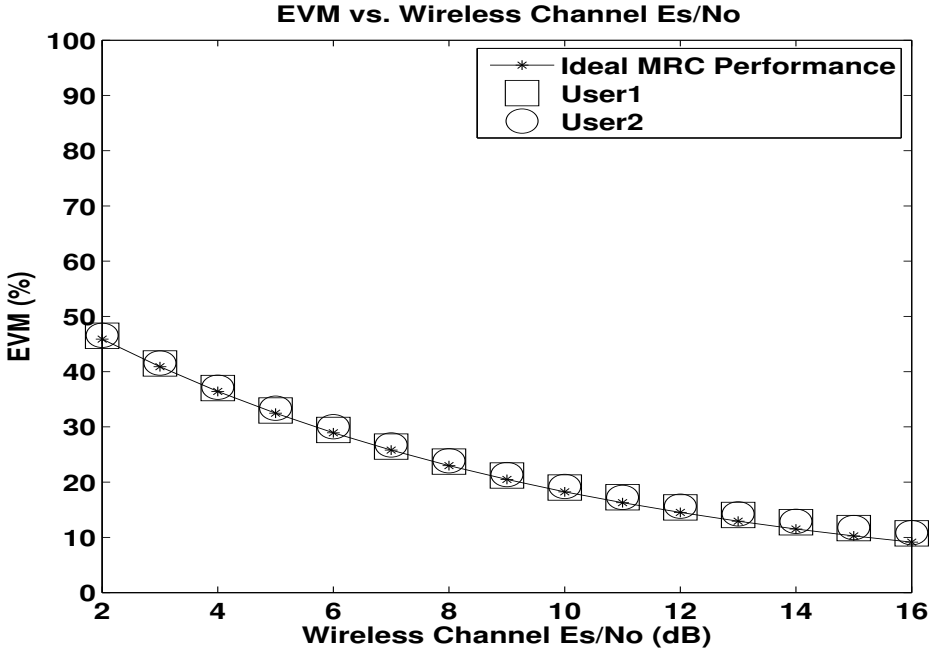

(a) Uplink performance using MRC and BPSK modulation

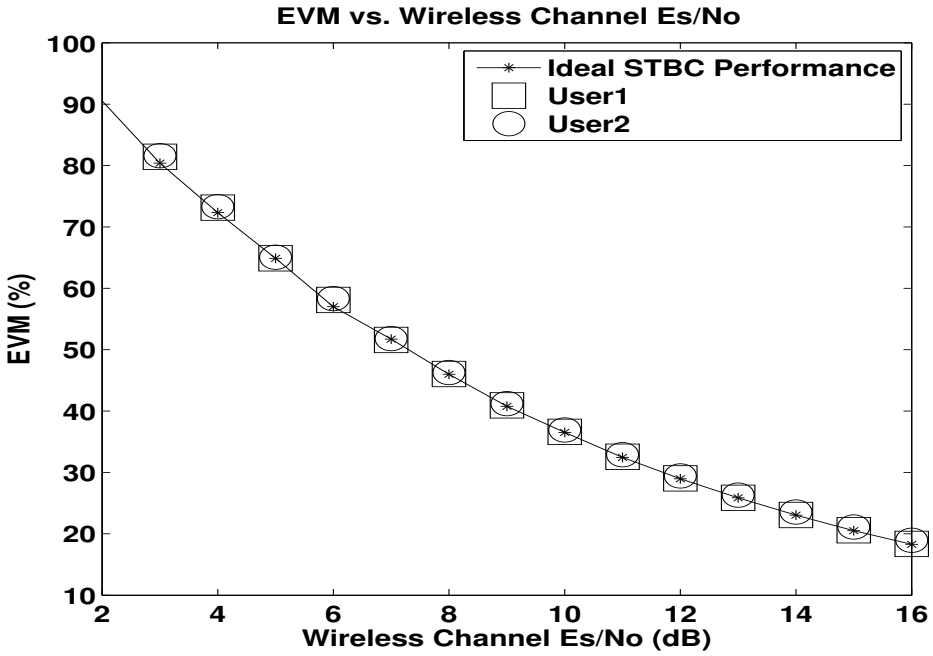

(b) Downlink performance using STBC and BPSK modulation

Figure 5.37: Overall system performance

posed that efficiently exploited the optical bandwidth and minimized the implementation cost, while maintaining a robust duplex performance. It relied on the AROF technique of Chapter 2 for the downlink, while having a lower transmit power requirement facilitated the employment of the WR aided DROF for the uplink. We dispensed with the need for optical carrier recovery for WR and conceived an architecture relying on a single laser source at the BS to support both the uplink and downlink of multiple RAPs. The ability of DROF to support multiple uplink users through CDM has also been shown. Thus, we have conceived a range of novel cost saving ROF techniques in Chapter 4, while diverse performance improvement techniques were discussed in Chapter 5. In the next chapter, we conclude by proposing an amalgam of both approaches by employing Plastic Optical Fiber (POF) based ROF links that employ the DROF technique.

Chapter 6

Conclusions and future work

In this chapter we conclude this thesis by providing a summary and design guidelines in Section 6.1. Subsequently, in Section 6.2, we discuss possible directions for future research both using multimode fibers like Plastic Optical Fiber (POF) as well as the conventional SMF. In this section, we also present our first results for one of the possible future directions, where we design a Digitized Radio Over Fiber (DROF) link that employs POF. The basics of POF based links are discussed in Section 6.2.1, while a novel ROF link that amalgamates the cost saving technique of employing POF and the performance improving technique of DROF is presented in Section 6.2.1.5. Fiber links that are at least a few hundreds of meters long are needed for in-building networks. However, the transmission of Radio Frequency (RF) signals through low-cost, easily installable POF is severely limited by their bandwidth-length product. DROF converts the RF signal into a baseband signal through bandpass sampling prior to its transmission, thereby reducing the fiber bandwidth required for the RF signal's transmission. In this study, we propose *for the first time* a POF-based DROF link relying on the Ethernet protocol and present our initial experimental results for a link that employs a 143 m long Step Index POF (SI-POF) and uncoded RF modulation. We transmit a 5 GHz RF signal through the POF. The same method can also be employed for higher RF carriers as well. The RF bit rate was approximately 30% of the protocol-dependent DROF bit rate.

6.1 Conclusions

In this section we present our chapter-by-chapter conclusions and design guidelines, The contributions of this thesis may be summarised as follows:

- **Chapter 1:** In Chapter 1, we introduced the ROF technique and discussed its advantages as well as compared it to other backhaul techniques. We then discussed three approaches that may be employed for designing advanced ROF links, namely the conception of performance improvement, cost reduction and optical RF-generation techniques. Then, we listed the major novel contributions of this thesis.
- **Chapter 2:** Subsequently, in Chapter 2, we discussed the classical ROF link, namely the AROF link. The block diagram for the classical AROF link was presented in Fig. 2.1 and a systematic discussion of the AROF transmitter, modulation techniques, fiber channel, ROF receiver as well

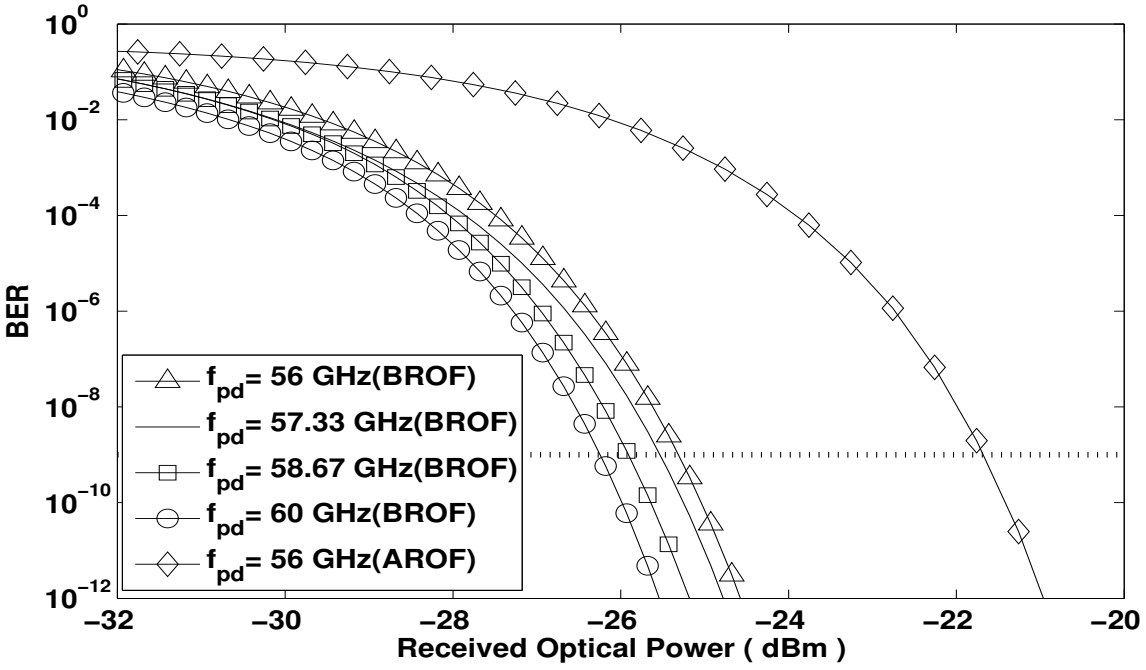

Figure 6.1: BER vs. received optical power of the proposed method and AROF

as noise processes was presented. Chapter 2 also discussed the optical components employed in the ROF link. Subsequently, the results of a simulation based study of the AROF link was presented. Finally, in Chapter 2, a novel technique was proposed for varying the carrier frequency of the signal, that is generated by heterodyne photo-detection of two optical signals.

The fiber channel imposes a chirp on a propagating optical pulse, where we used heterodyne photo-detection of two optical pulses for generating an electronic signal at a frequency that depends on the extent of overlap between the two pulses. Fig. 6.1 summarises the performance of this AROF architecture, which was also referred to as a Baseband-aided ROF (BROF) link. The results of Fig. 6.1 show the ability of the proposed architecture to generate electronic signals at four RF carrier frequencies using the same pair of optical signals. Fig. 6.1 also shows that the BER performance of the proposed scheme was better than that of a conventional AROF link relying on ODSB modulation.

- **Chapter 3:** Having discussed the classical AROF link, in Chapter 3, we presented three promising approaches that may be adopted for designing advanced ROF links, which are as follows:

  1. ROF links employing techniques aimed at improving its performance;
  2. ROF links employing techniques aimed at reducing the cost of employment;
  3. ROF links aimed at supporting high-RF signals.

  In Chapter 3, we provided a state-of-the-art study of these three approaches along with significant tutorial content. This review constituted the foundation of the novel designs proposed in the subsequent chapters. Fig. 6.2 summarises the various performance improvement and cost reduction techniques, while Fig. 6.3 portrays the family-tree of the various optical upconversion

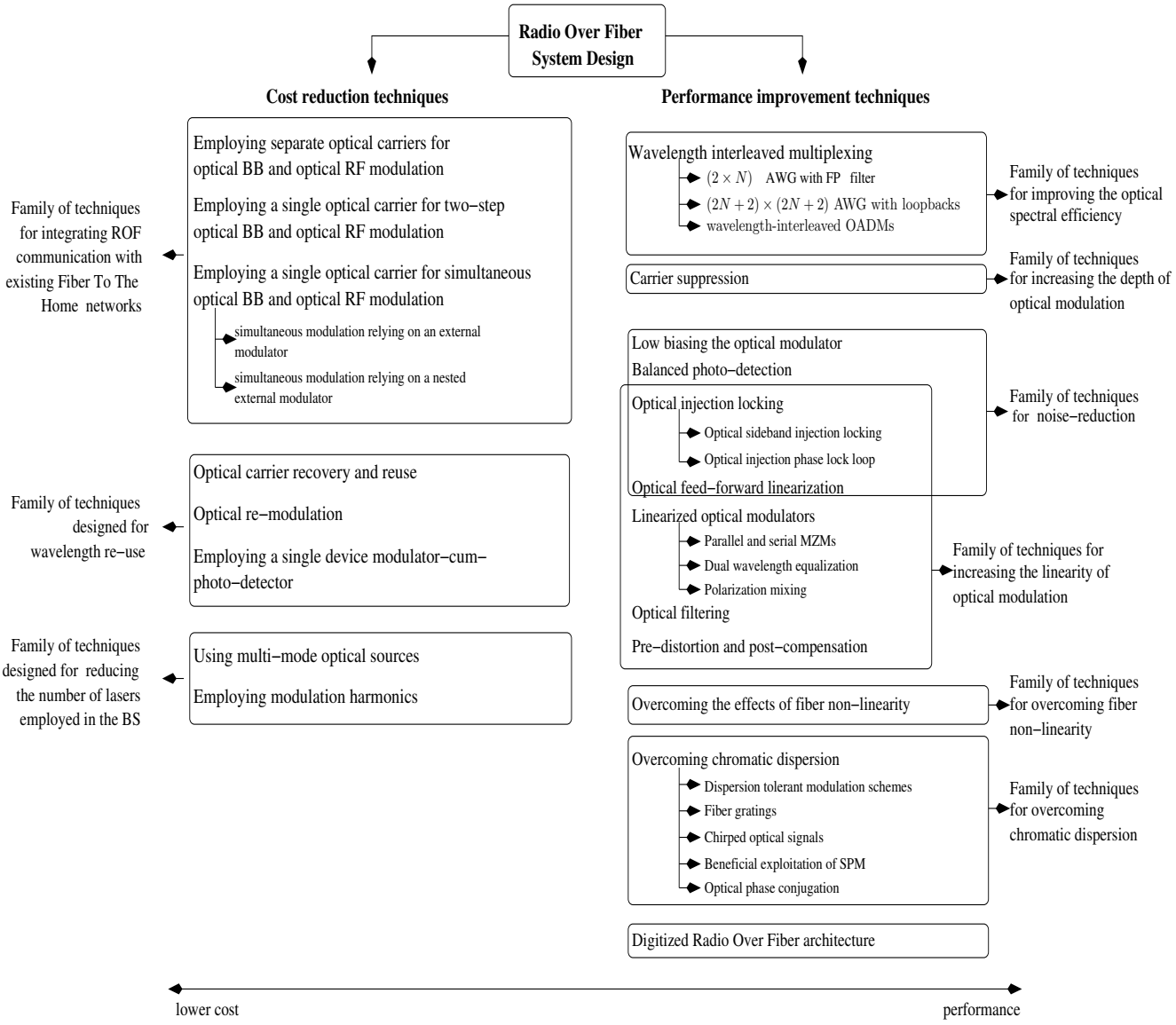

Figure 6.2: The various cost reduction and performance improvement techniques for ROF communications

techniques that may be employed for optical generation of the RF signal. The performance improvement techniques were aimed at ensuring that the optical backhaul satisfactorily supported the wireless front-end in meeting its BER, capacity and linearity requirements, as laid down by the standards. By contrast, the cost reduction techniques were aimed at ensuring that the ROF technique reduced the cost of setting up a network relying on small cells. Finally, the optical generation of RF signals enabled the generation of signals at high RF carriers, which could then be distributed through a ROF network. In other words, it facilitated pure optical signal processing for overcoming the bottlenecks imposed by electronic signal processing.

- **Chapter 4:** In Chapter 4, three novel architectures were proposed that incorporated the first two of the three approaches discussed in Chapter 3. The first of these architectures was aimed at reducing the number of optical modulators by transmitting two RF signals through simultaneous optical intensity and phase modulation using a single MZM. This was implemented through the

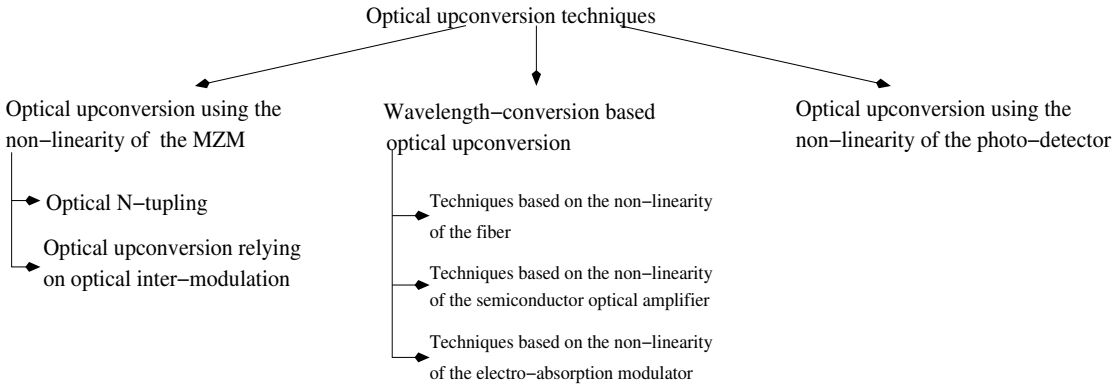

Figure 6.3: Optical upconversion techniques

careful selection of the drive voltages that are applied to a dual drive MZM, where Fig. 6.4 summarises the BER performance of this architecture for RF signals at 2 GHz and 5 GHz. Fig. 6.4 demonstrates that the proposed architecture outperforms the conventional technique relying on intensity modulation and direct/coherent photodetection.

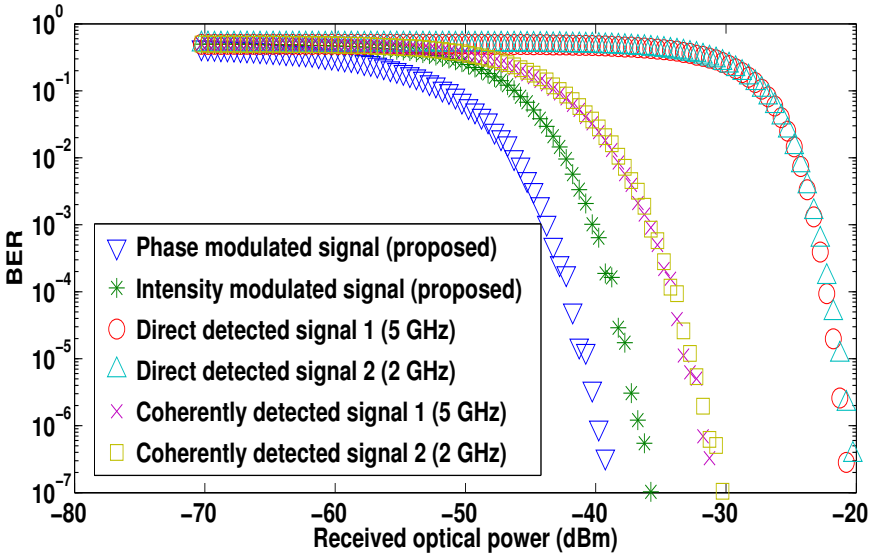

Figure 6.4: BER of system proposed in Section 4.1 at various received optical powers

The second one of these novel architecture was discussed in Chapter 4, which was designed for making the generation of OSSB signals more cost effective, where the typical approach requires a single-drive MZM in conjunction with a FBG filter or a dual-drive MZM. The second novel architecture discussed in Chapter 4 generated an OSSB signal using a single-drive, - rather than dual-drive - , MZM without any additional filtering. Our proposed scheme was capable of convenient optical upconversion of the electronic signal. Fig. 6.5 shows that the proposed scheme's BER performance is better than that of the classical OSSB signal generation scheme.

Having designed architectures that are aimed at making optical modulation techniques more cost-effective, the final one of our novel architectures conceived in Chapter 4 was aimed at making the wireless technique of MIMO cost-effective in the ROF context. In the proposed

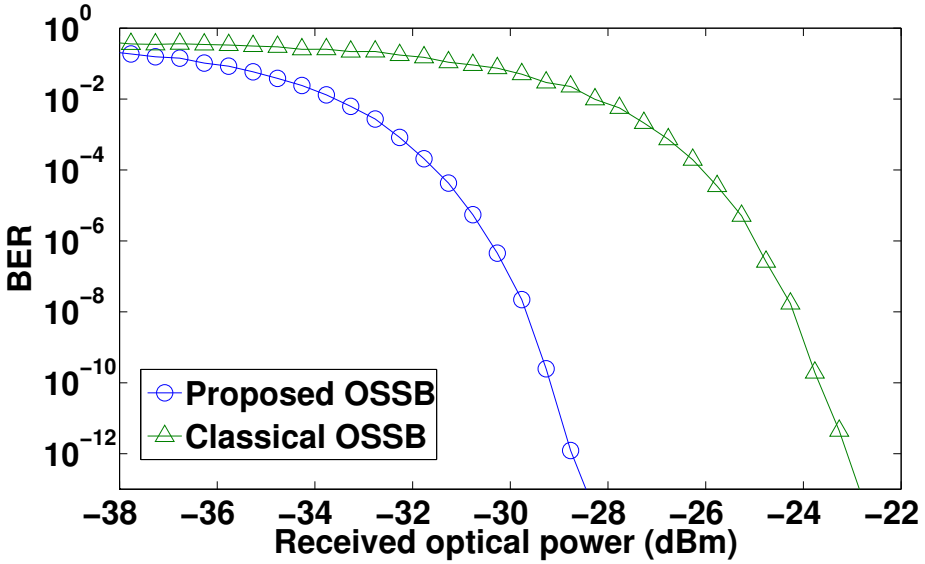

Figure 6.5: BER of system proposed in Section 4.2 at various received optical powers

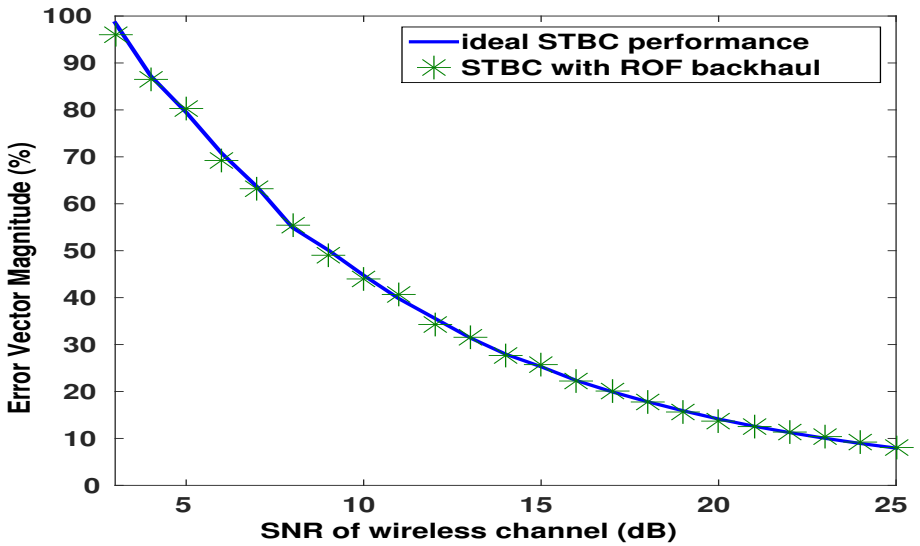

Figure 6.6: Performance of MIMO wireless link relying on the ROF backhaul proposed in Section 4.3

architecture, a single ODSB signal supported two antennas in each RAP, where each optical sideband transmitted one of the two STBC encoded signals. In the BS, this sophisticated signal was generated by a single-MZM through simultaneous optical upconversion of the baseband STBC signals. This was achieved by driving the dual-drive MZM using the following drive voltages:

$$V_{drv1} = u(t) + b_1^{STBC}(t); V_{drv2} = -u(t) - b_2^{STBC}(t), \tag{6.1}$$

where $u(t)$ is the sawtooth signal that facilitates optical upconversion, while $b_1^{STBC}(t)$ and $b_2^{STBC}(t)$ are the baseband STBC signals generated for the pair of antennas. Fig. 6.6 shows that the proposed ROF-aided wireless link suffers negligible performance degradation, when compared to the ideal STBC performance.

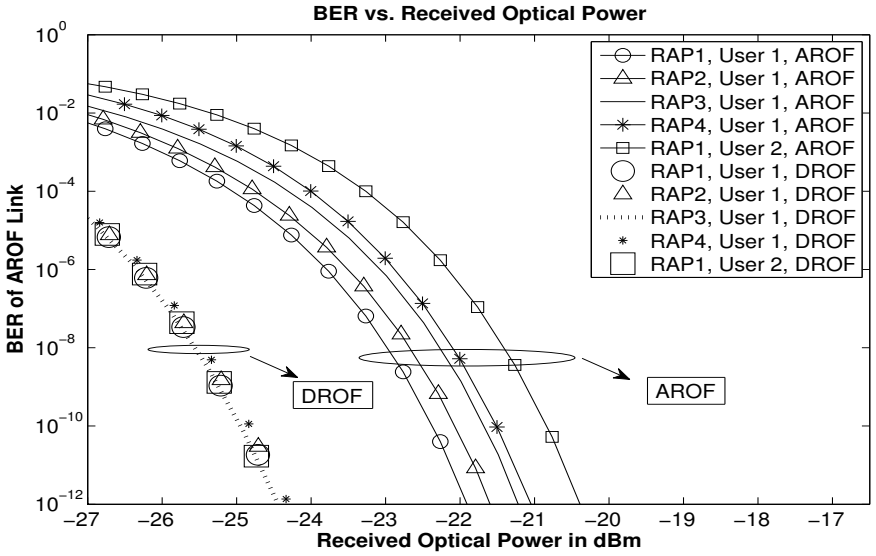

Figure 6.7: BER of the system proposed in Chapter 5 at various received optical powers

- **Chapter5**: Having discussed our novel architectures incorporating two of the tree approaches designed for advanced ROF links, in Chapter 5, we discussed the performance improvement technique of DROF. Subsequently, a duplex ROF ring architecture was proposed that considered the following design objectives: reducing the cost of fiber-laying and of the optical/electronic components, whilst maintaining high optical spectral efficiency as well as a robust duplex link performance. It was shown that relying on AROF and DROF techniques for the downlink and uplink transmission, respectively, attained a robust duplex performance. A sophisticated amalgam of Optical Carrier Suppression (OCS), Code Division Multiplexing (CDM), optical frequency multiplexing and Wavelength Reuse (WR) was conceived for supporting a DAS of four RAPs serving a pair of users. Fig. 6.7 summarises the performance of this architecture, where the performance improvements offered by DROF over the AROF scheme are indeed apparent. This is because the DROF employs the more linear and less dispersive digital optical link, while the AROF technique employs an analog optical link.

In the next section, we provide a set of design guidelines for ROF links.

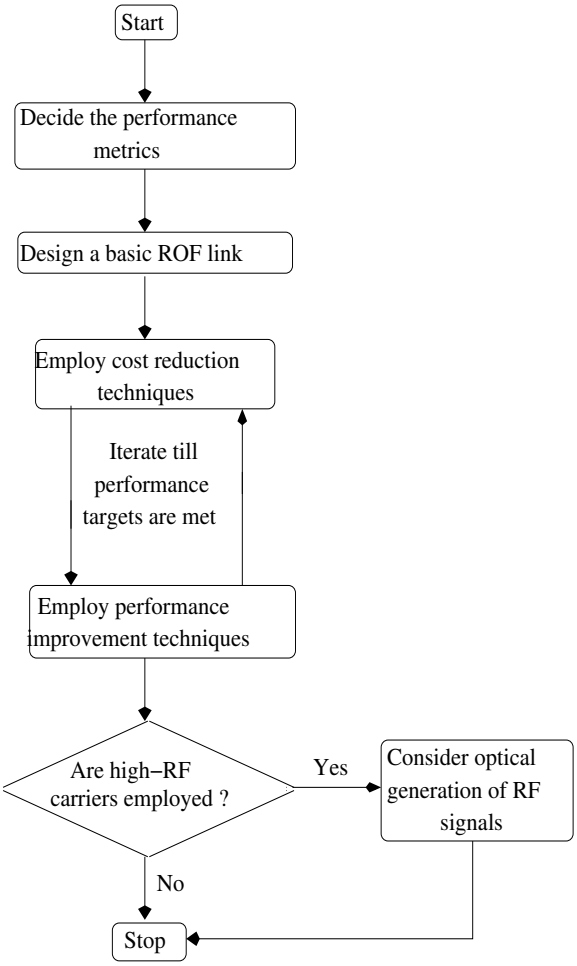

Figure 6.8: Flowchart detailing the design guidelines of ROF links

6.1.1 Design guidelines

Here we conclude by providing a set of design guidelines conceived for ROF links. Fig. 6.8 shows a flow-chart highlighting the various steps involved in designing a ROF link. These steps are detailed as follows:

- **Decide the choice of performance metrics:** In strict scientific terms, this would be referred to as the objective function of the system optimization. As shown in Fig. 6.8, we commence by deciding upon the performance metrics. The sensitivity of a ROF link is defined in terms of the received optical power, at which a BER of 10^{-9} is achieved [31]. On the other hand, the linearity of the ROF link, amongst others, may be expressed in terms of the suppression of the harmonics and intermodulation products in the photo-detected signal and also in terms of the BER degradation imposed by the fiber's non-linearity. Furthermore, the user-support capability of the ROF system may be defined as the number of RAPs or as the number of MSs that are supported by it. The first step in designing a ROF system is to set target values for the above performance metrics, based on the requirements of the wireless network, for which the ROF system forms the backhaul.

- **Design a basic ROF link:** Next, as shown in Fig. 6.8, we proceed by designing a basic ROF

link, based on the techniques listed in Fig. 2.2. The simplest ROF link is one that employs direct modulation of the optical carrier's intensity discussed in Section 2.1.1.2 for generating the ODSB signal detailed in Section 2.1.2.1. The ODSB signal is then detected by direct photo-detection, as highlighted in Section 2.1.1.4, with the associated multiplexing being implemented using the SCM technique of Section 2.1.3.1. However, the designer would be constrained to use external modulation, if the RF carrier is beyond the modulation bandwidth of the laser. For a high RF carrier, like a millimeter-wave carrier, the chromatic dispersion-induced power penalty would require the designer to employ the OSSB or OCS modulation schemes of Sections 2.1.2.1 and 2.1.2.1, respectively. In such a scenario, the designer may use an optical filter after the external modulator or alternatively employ a dual-drive MZM. However, if the sensitivity, i.e. BER requirements are too stringent for an intensity-modulated direct-detected link, then the designer may employ the optical angle modulation technique discussed in Section 2.1.2.2 along with the coherent photo-detection of Section 2.1.1.4. Coherent photo-detection requires an additional laser in the receiver, which may be avoided by using the optical discriminator of Section 2.1.2.2. This, however, would be at the expense of a performance degradation. Additionally, the designer may opt for the more complex WDM, instead of the SCM, if a large number of RAPs (or mobile users) have to be supported.

- **Employ cost reduction techniques:** As shown in Fig. 6.8, having designed a basic ROF link, the next priority of the designer should be to incorporate the most appropriate cost saving techniques of Fig. 3.2, while ensuring that the performance targets are still met. In urban areas, where a significant amount of fiber has already been laid for digital fiber-based services, the ROF network designer may rely on the family of ROF techniques conceived for integrating ROF communication with the existing FTTH networks, as discussed in Section 3.2.1. This must, however, ensure that the quality of service of the fiber-based digital services is not compromised. The designer may also employ the family of techniques designed for wavelength re-use, as discussed in Section 3.2.2. However, the allocation of a portion of the DL optical power for UL communication would degrade the DL performance and hence it must be ensured that the sensitivity targets are met. The wavelength re-use technique of OCRR may require high-selectivity optical filtering. This requirement is relaxed in the wavelength re-use technique of ORM, which however imposes the restrictive conditions of Section 3.2.2.2. When employing a modulator-cum-photodetector, conceiving the half-duplex regime of Fig. 3.49 is straightforward. By contrast, the full-duplex communication scenario of Fig. 3.50 or Fig. 3.51 either involves a DL versus UL performance trade-off or employs a pair of optical wavelengths, respectively. Finally, cost savings may also be achieved by reducing the number of lasers, as discussed in Section 3.2.3.

- **Employ performance improvement techniques:** When the basic ROF link does not meet one or more of the performance targets set by the wireless network, this may be alleviated by employing the performance improvement techniques listed in Fig. 3.2. The employment of a cost-saving technique might provide a significant economic advantage for the designer, but might also jeopardize the performance targets. In this scenario, the designer may combine cost-saving techniques with the most appropriate performance improvement techniques, provided that the total system's cost remains acceptable. If the target sensitivity of the ROF link is compromised, then the designer may invoke an appropriate technique for increasing the optical modulation depth, for noise-reduction or for overcoming chromatic dispersion, which were discussed in Sec-

tions 3.1.2 to 3.1.6 and in Section 3.1.11, respectively. Among these techniques, those employing carrier suppression, balanced photo-detection and dispersion-tolerant modulation schemes are easier to implement. On the other hand, if the target linearity of the ROF link is not met, then the designer may increase the linearity of optical modulation, as discussed in Sections 3.1.5 to 3.1.9 or aim for overcoming the fiber non-linearity, as discussed in Section 3.1.10. Employing linearized optical modulators reduces the strength of the required RF signal along with the suppression of the non-linear products, thereby degrading the link's sensitivity. Both Optical Injection Locking (OIL) and optical feed-forward linearization provides a beneficial noise-reduction in addition to improving the linearity of optical modulation. By contrast, the technique of electronic pre- and post-compensation is the simplest to implement. Finally, if the target number of users cannot be supported by the ROF link, then the designer may opt for improving the optical spectral efficiency, as discussed in Section 3.1.1. However, when it is not technically feasible to meet the performance targets, the analog optical link can be replaced by the more powerful Digitized Radio Over Fiber architecture of Fig. 3.2, which is detailed in Fig. 5.1. Alternatively, the sampled RF over fiber technique of Section 3.1.12 may be employed. As discussed in Chapter 5, the DROF architecture relies on the more robust digital optical link, but has a more complex RAP. Note that as shown in Fig. 6.8, we might have to iterate several times between employing various cost reduction and performance improvement techniques, before we succeed in satisfying the predefined performance targets of Step 1.

- **Employing optical generation of RF signals:** If very high data rates are needed, then high-RF carriers have to be employed for exploiting the entire free spectrum available at these frequencies, as discussed in Section 3.3. However, high-RF carriers require the employment of expensive broadband mixers in case of OFDM/MB-OFDM signals. Similarly, expensive electronic hardware is needed for the generation of the narrow pulses of IR-UWB systems. As shown in Fig. 6.8, the optical generation of RF signals at the BS may be invoked for avoiding the use of broadband mixers, as discussed in Section 3.3.1 or to circumvent the employment of expensive electronic hardware, as discussed in Section 3.3.2.

In the next section, we discuss a range of promising directions for future research.

6.2 Future work

A discussion of ROF would not be complete without exploring further avenues for future research. Hence, in this section we discuss several potential avenues of future research, which are are as follows.

6.2.1 POF-based links

In the literature, POF is also referred to as polymer optical fiber [253], where the core is typically made from Polymethyl methacrylate (PMMA) or Polystyrene, which have refractive indices of 1.49 and 1.59 respectively [253], while the fiber cladding is generally made from silicone resin [253]. The core diameter in a POF is several times higher than that of the extensively used glass (silica) based SMF. The large core diameter enables the fiber to support multiple transverse modes. Based on the refractive index profile, POFs may be classified into two categories as follows:

1. **Step Index Plastic Optical Fiber (SI-POF)**: In a SI-POF, there is an abrupt change in the fiber refractive index at the fiber core-cladding interface. These have a more restricted bandwidth due to the higher levels of modal dispersion [254]. Mathematically, this is formulated as follows:

$$n_r(r) = \begin{cases} n_1 & for\ 0 < r < a; \\ n_2 & for\ a < r < r_{total}, \end{cases} \tag{6.2}$$

where $n_r(r)$ is the refractive index at a distance r from the core axis at an optical angular frequency of ω, a is the core radius and r_{total} is the total radius of the fiber (i.e. including the cladding). The refractive indices of the core and cladding are equal to n_1 and n_2 respectively.

2. **Graded Index Plastic Optical Fiber (GI-POF)**: In a GI-POF, the fiber-core refractive index decreases smoothly from the core axis to the core-cladding interface. The refractive index of the fiber-core at the core-cladding interface is equal to the refractive index of the fiber-cladding. A lower level of fiber dispersion ensures a higher transmission bandwidth in a GI-POF than in a SI-POF [254]. Note that the transmission bandwidth is the maximum permissible bandwidth of the electronic signal that is modulated onto the optical carrier. In case of the most commonly used circularly-symmetric α_{GI}-profile GI-POF, the refractive index is formulated as follows [254]:

$$n_r(r) = \begin{cases} n_1[1 - 2\Delta_n(r/a)^{\alpha_{GI}}]^{1/2} & for\ 0 < r < a, \\ n_2 = n_1[1 - 2\Delta_n]^{1/2} & for\ a < r < r_{total} \end{cases} \tag{6.3}$$

The refractive indices of the core-axis and cladding are equal to n_1 and n_2, respectively, while Δ_n is the refractive index contrast between the core and cladding, and finally α_{GI} is the core index exponent. A step index optical fiber can be deemed to be a special case of a graded index optical fiber, in which the core index exponent, α_{GI} tends to infinity.

The discussion in this section is organized as follows. The advantages of using POF are presented in Section 6.2.1.1, while the challenges in the employement of POF-based networks are discussed in Section 6.2.1.2. This is followed by a discussion of the applications of POF based networks in Section 6.2.1.3. Finally, a discussion of light propagation in a POF is presented in Section 6.2.1.4.

6.2.1.1 Advantages of using plastic optical fibers

The major advantages of using POFs are as follows:

1. **Lower manufacturing cos**t: The use of plastic as the fiber material ensures that the manufacturing cost of a POF is lower than that of the glass-based optical fiber [255]. This makes them an extremely competitive option for in-house, intra-building and Personal Area Networks (PANs).

2. **Safety**: A glass-based optical fiber is typically operated in the 1300 nm and 1500 nm windows. However, for most POFs optimum performance is achieved in the visible-light spectrum, because of the lower fiber attenuation at these frequencies [254]. The POFs are typically used for transmitting light at wavelengths of 650 nm [256], 520 nm [257], 570 nm [254] and 850 nm [258]. In

the event of an optical leakage in a glass-based optical fiber system, the high-intensity laser light can burn the human retina and cause permanent blindness. However, in a POF-based system the leakage of light in the visible spectrum is far less hazardous [259], [260], [261].

3. **Higher flexibility and smaller bending radius**: The employment of plastic as the fiber material results in POFs being far more flexible [259] and having a smaller bending radius than glass-based optical fibers [262]. The fiber used in in-house and in intra-building networks experiences significant bending [261]. Hence, POFs are more suitable than glass-based optical fibers for these networks. It has been shown that adequate demodulator eye opening can be maintained, even when the fiber suffers a total bending equivalent to 10 turns around a cylinder of 10 mm radius [263].

4. **Ability to share the installation hardware of the electricity network**: POFs have a smaller diameter than the RJ45 copper cables, which are currently used for in-house networks. Moreover, POFs are more flexible than glass-based optical fibers. Hence, they can be installed using narrow shafts. The optical nature of the communication permits POFs to be installed within the same conduits that provide electricity. This is not possible with the copper cables, since the electromagnetic radiations from the electrical wiring may interfere with the transmitted signal [261].

5. **Ability to use inexpensive connectors** [262]: Clip-on connectors for a POF based communication system have been developed [264], which can be directly fixed on the external coating of the POF without using expensive tools. This is clearly not the case for the connectors of glass-based optical fiber networks. A short-reach PAN is expected to have a high density of connection points. Hence, employing POFs would significantly reduce the installation cost [265].

6. **Do-It-Yourself Installation**: The small core size in a single-mode glass-based optical fiber necessitates the employment of trained personnel and of high-precision equipment for installing the fiber [266]. However, a POF can be installed by untrained professionals on a 'plug and play' basis. This is due to its large core diameter and higher tolerable bending radius [266].

7. **Ability to provide triple-play services**: Extensive research has led to POFs having the capability of supporting 'triple-play services', which is vital for their successful deployment in modern PANs [261], where' triple-play service' refers to the simultaneous transmission of video, audio and data signals.

8. **Ability to support short-reach multi-Gigabit communication**: Multi-gigabit short-reach networks have been designed using GI-POFs [262], where Discrete Multi Tone (DMT) and OFDM based techniques have enabled Gigabit transmission in the networks that employ the low-bandwidth SI-POF [255].

9. **Ability to develop connectorless networks**: Connectorless SI-POF systems are in commercial use in the market, e.g. for in-house IP-TV distribution [255]. The ability to avoid using connectors reduces the attenuation, whilst simultaneously making installation easier.

10. **Ability to integrate with existing fiber networks**: POF based in-house networks can be integrated with the rapidly expanding FTTH service [267]. The optical signals received at the

customer premises through the FTTH network can then be distributed within the house through a POF-based network.

Having discussed the advantages of POF based networks, in the next section, we discuss the challenges in the employment of POF based networks.

6.2.1.2 Challenges in the employement of POF based networks

There are many open challenges in the employement of POFs, which are being systematically tackled, thanks to the sustained efforts of the research community and the industry. This technology has come a long way since it was first proposed, where the major challenges of employing POFs are as follows:

1. **Higher levels of fiber attenuation**: A POF suffers from higher levels of fiber attenuation than a glass-based optical fiber [254]. The attenuation of POFs has been significantly reduced through the development of fluorinated POFs. However, the employement of these fluorinated POFs has been limited by their high manufacturing cost [268].

2. **Higher levels of fiber dispersion**: The fiber attenuation in a POF is several orders of magnitude higher than that in the conventional Glass-based Optical Fiber (GOF). If N_{mode} is the total number of modes propagating in a POF then we have:

$$N_{mode} \propto a, \tag{6.4}$$

   where a is the core radius. Since the core radius of a POF is significantly higher than it is for a GOF, the number of modes propagating in a POF is much higher than that in a glass-based optical fiber [265]. This results in increased fiber dispersion [254],[269], which limits the bandwidth of the modulating signal that can be employed. Efforts have been made to overcome this impediment by sophisticated signal processing techniques, such as equalisation [256], [270], [271],[272] and pre-distortion/pre-emphasis [273], [274].

3. **Limitations imposed on the employment of WDM**: A WDM implementation in optical fibers is only possible if there is a sufficiently wide range of optical frequencies over which the fiber attenuation is low. The widest low-loss windows in SI-POFs and GI-POFs are centred around the optical wavelengths of 520 nm and 570 nm respectively [254]. However, these low-loss windows have a width of approximately 10 nm, which is much narrower than the 110 nm or 180 nm wide low-loss windows of glass optical fibers around the wavelengths of 1300 nm and 1500 nm respectively. Thus, a maximum of 10 and 8 optical channels can be multiplexed in SI-POFs and GI-POFs respectively [254].

4. **Higher cost of optical transceivers in the visible spectrum**: Again, the existing long-reach glass-based optical fiber networks typically operate at wavelengths in the 1300 nm and 1500 nm window. The larger market size of optical transceivers at these wavelengths result in their cost being lower than the cost of transceivers operating in the visible-light region of the electromagnetic spectrum (which is used in POF based communication) [261]. The number of commercial suppliers in this field is also low. However, this economic challenge can be overcome by the increasing proliferation of POF based short-reach networks.

5. **Lack of standards**: The lack of standards at a global level has been an impediment to the proliferation of POF based optical networks [275].

6. **Lack of awareness**: There is a lack of awareness on how to design efficient low-cost systems using the limited bandwidth provided by POFs. Incomplete certification programs from POF installers has also been an impediment to the on-field deployment of POF based optical networks [275].

7. **Infancy of research**: Research on POF based applications has not yet reached an advanced stage, especially when compared to its glass-based optical fiber counterpart. There is also significant scope for improvement in the manufacturing processes. The ability to manufacture perfluorinated POFs at a lower cost and the design of POFs that can withstand high temperatures reaching 125^0C are some examples of open questions at the manufacturing level.

In the next section, we present the various possible applications of POF based networks in order to establish the potential of POF based networks.

6.2.1.3 Applications of POF based networks

Despite its limitations, POF has found potential application in a number of scenarios. Some of these are discussed below:

1. **In-vehicle infotainment systems**: The range of multimedia services available inside automobiles is broadening rapidly. POFs provide an economically viable solution for developing in-vehicle infotainment systems [259]. Furthermore, high-speed wireless access in trains could be provided by employing a POF-based network [276]. The Digital Domestic Bus (D^2B) standard designed for supporting 5.6 Mbps intra-vehicle communication was released by Daimler-Benz in 1998. It employed a SI-POF of 1 mm core diameter. Subsequently, the Media-Oriented Systems Transport standard was released in 2001, which supported a data rate of 150 Mbps [277]. The 'byteflight' standard was released by BMW for supporting reliable communications at 10-50 Mbps [278]. Finally, the IEEE 1394b standard and the Intelligent Transportation System Data Bus standard were merged to create the IDB-1394 standard [278]. The IDB-1394 standard is capable of supporting in-house and intra-vehicle data rates of 250 Mbps using 20 to 30 m of SI-POF [279].

2. **ROF applications:** By integrating POF with the rapidly expanding FTTH networks, a POF based in-house ROF network may soon provide ubiquitous wireless broadband connectivity inside the homes [266]. In [264], a 60 GHz wireless link was designed, which employed POF for transporting the baseband signal. The ease of installation of these fibers will facilitate the proliferation of these short-reach, ROF-assisted wireless networks [280]. The ability to support multi-standard wireless transmissions using LTE, Wimax and UWB has also been demonstrated [267].

3. **In-home Gigabit communication**: Gigabit communication between various home appliances can be achieved using POFs [262]. The ability to achieve high-speed communications between the various electronic devices in a home is crucial for designing intelligent buildings.

4. **High-Definition (HD) video distribution**: Plastic optical fibers can be used for HD video distribution [281]. Such a POF network may be readily integrated with the FTTH backbone and employed for in-door CATV distribution [267]. It also has potential applications in telemedicine and distance learning [265].

5. **Design of optical telecommunication interconnects**: A 'plugless' transceiver can be designed using POF-based direct optical connections between the various active devices [282]. The design of intra-system connections in telecommunication systems using POFs has significant growth potential due to its ability to support high data rates over short distances [283] without using any special link-termination [282].

6. **Triple-play realisation**: The ability of POFs to support triple play services (IPTV, voice over IP and data transmission) was successfully demonstrated by the telecom operator Swisscom [284].

7. **Converged wired and wireless networks**: POFs have the ability to support converged broadband wired and wireless in-house networks [285]. Such a network can be integrated with a ROF over FTTH [16] long-reach network, which also aims for the simultaneous transmission of wired and wireless data.

8. **Consumer electronics**: Toshiba has released the TOSLINK standard designed for the Sony-Philips Digital InterFace (S/P DIF), which utilises POFs for high-quality digital audio transmission [279].

9. **In-Factory Communications**: POFs can be used to automize the control of machinery. The rugged hostile nature of shop-floors and industrial environments makes POF an ideal candidate for high-speed short-range communication. Industrial standards such as PROFIBUS, SERCOS and INTERBUS promote the use of POFs for factory communication. A POF based WDM architecture for factory communications was proposed in [286].

10. **Optical-wireless communication**: A POF-based optical-wireless communication architecture was proposed in [287] to support wireless devices within buildings and homes by exploiting the large wireless bandwidth available at optical frequencies. The use of POF for lighting purposes was demonstrated in [288]. Hence, a POF network has the future potential of simultaneously supporting both lighting and wireless data communication. Such an energy and cost-effective utilization of the home-infrastructure would assist in the development of smart homes.

In next section, we discuss the various aspects of light propagation through a POF.

6.2.1.4 Light propagation through a POF

Light propagation in a POF is of multimode nature. In addition to the ubiquitous optical attenuation and chromatic dispersion, which are similar to those of the SMF, the propagation of light in a POF is affected by the following factors:

1. Launch Misalignments;

2. Modal Dispersion;

3. Mode Coupling;

4. Differential Modal Attenuation.

This Section (6.2.1.4) firstly discusses the multimode nature of the propagation of light in a POF and then continues with detailing the effects of launch misalignments, modal dispersion, mode coupling and differential modal attenuation.

Let us begin by outlining a light propagation model conceived both for a Step Index and for a Graded Index POF.

Multimode propagation in step index POF: The ultimate governing equations of a dielectric wave guide are Maxwell's Equations. These reduce to specific wave equations for SI-POFs and GI-POFs. Here we focus our attention on the classical SI-POF, because this is a preliminary study in an open avenue for future ROF research. Let us assume that $\vec{E}_{POF}(\vec{r},\omega_c)$ and $\vec{H}_{POF}(\vec{r},\omega_c)$ represent the spatial distribution of the electric and magnetic fields of the modes, when the angular frequency of the optical carrier is ω_c. The refractive index of the optical fiber, n_r, is given by Equation (6.2) and the wave-number is $k_0 = \frac{2\pi}{\omega_c}$. If β is the propagation constant of the wave, $J_u(\cdot)$ is the Bessel function of order u and $K_u(\cdot)$ is the modified Bessel function of order u, then the propagation equation of the POF is as follows:

$$\left[\frac{J_u'(\kappa_{POF}a)}{\kappa_{POF}J_u(\kappa_{POF}a)} + \frac{K_u'(\gamma_{POF}a)}{\gamma_{POF}K_u(\gamma_{POF}a)}\right]\left[\frac{J_u'(\kappa_{POF}a)}{\kappa_{POF}J_u(\kappa_{POF}a)} + \frac{n_2^2}{n_1^2}\frac{K_u'(\gamma_{POF}a)}{\gamma_{POF}K_u(\gamma_{POF}a)}\right] = \left[\frac{u\beta k_0(n_1^2-n_2^2)}{an_1\kappa_{POF}^2\gamma_{POF}^2}\right]^2. \tag{6.5}$$

The mathematical expressions for κ_{POF} and γ_{POF} are as follows [74]:

$$\kappa_{POF} = (n_1^2k_0^2 - \beta^2)^{\frac{1}{2}} \tag{6.6a}$$

$$\gamma_{POF} = (\beta^2 - n_2^2k_0^2)^{\frac{1}{2}}. \tag{6.6b}$$

Equation (6.5) relying on the relationships in Equation (6.6a) and (6.6b) can be solved for deriving the various values of $\beta = \beta_{uv}$ for each combination of $u = 0, 1, 2, ...$ and $v = 0, 1, 2....$ Each combination of (u, v) is a supported mode of the fiber. In the literature u and v are referred to as the azimuthal and radial mode index. Not all modes (i.e not all combinations of $[u, v]$) are supported. Explicitly, only those modes are supported, which have a propagation constant β_{uv} that ensures that γ_{POF} is real-valued and hence can propagate through the fiber [74]. These are referred to as guided modes. Those modes which cannot propagate through the fiber are referred to as radiation modes. Using Equation (6.6b), the cuttoff criterion can be mathematically expressed as follows:

$$\beta_{uv}^2 \geq n_2^2k_0^2 \tag{6.7}$$

We know from Equation (6.5) that the propagation constant β depends on the refractive index of the core, cladding and the core radius. Hence, these parameters are the ultimate factors, which determine the specific modes that can propagate. A fiber is usually of single mode nature when the core radius

is only a few micrometers [74]. Henceforth, in this treatise the term *mode* will be used to refer to the guided modes unless otherwise stated.

The principal mode index, m, of a particular mode (u, v) is defined as follows [289], [290]:

$$m = 2v + u. \tag{6.8}$$

It was proposed in [289] that for step-index optical fibers the particular modes that have the same principal mode index m also have similar propagation constant β and they constitute a mode group. In a step-index fiber, the principal mode group index m of the excited mode depends only on the angle of incidence of the exciting ray (namely the ray entering the fiber), but not on the radial distance of the point of incidence from the fiber axis [291]. The angle of incidence of the exciting ray decides the angle of propagation θ with respect to the fiber axis. Hence, all the modes having the same principal mode index m, i.e. modes with the same mode group, propagate at the same θ. Additionally, as stated earlier, all modes within a mode group have a similar propagation constant β. The specific values of β and θ of the modes within the same mode group are related through the following mathematical relationship [291]:

$$\beta = \frac{2\pi\sqrt{n_1^2 - \sin^2(\theta_i)}}{\omega} = \frac{2\pi n_1}{\omega}\cos(\theta) \quad (for\ SI - POF). \tag{6.9}$$

The launch condition refers to the angle of incidence and the intensity of the light rays exciting the various modes within the fiber. It may hence be stated based on the above discussion that the launch condition decides which specific modes are excited and the particular strength of their excitation. In other words, the launch condition decides the exact nature of the fiber core's illumination by the optical transmitter and hence it significantly affects the bandwidth of the optical channel [292]. There are two important parameters of the launch condition that predetermine the achievable bandwidth of the optical fiber:

1. *Launching beam spot size*: This refers to the size of the spot formed by the launched beam on the fiber core. The spot size is directly proportional to the divergence of the launched optical signal. If $\theta_{i,highest}$ is the highest angle of incidence actually present in a particular launch condition, then $\theta_{i,highest}$ increases, as the spot size increases. A ray having a higher angle of incidence excites a higher order mode, i.e. it excites a mode having a higher principal mode index. However, the cutoff criterion of Equation (6.7) together with the relationship in Equation (6.9) results in the maximum cut-off angle of $\theta_{i,max} = \sin^{-1}(\sqrt{n_1^2 - n_2^2})$. The angle of incidence of the light ray has to be below $\theta_{i,max}$ for exciting a guided mode. The term $\sqrt{n_1^2 - n_2^2}$ is also referred to as the Numerical Aperture (NA) of the optical fiber. The launching conditions are classified into two categories based on the spot size:

   (a) Overfilled launch: In this case the spot size covers the entire core of the optical fiber. Hence, $\theta_{i,highest} \geqslant \theta_{i,max}$ thereby resulting in both higher-order and lower-order modes being excited. This is usually the case, when using an LED [73].

   (b) Underfilled launch or restricted mode launch: In this the spot size is much smaller than the core's cross-sectional area. Hence, we have $\theta_{i,highest} \ll \theta_{i,max}$, which results in the excitation of only the lower-order modes. This is usually the case, when using a semiconductor

laser [73]. Underfilled launch can also be achieved through a connector that restricts the launching numerical aperture [292]. Note that, in the underfilled launch condition, the specific modes that are excited can be varied by intentionally introducing launch misalignments between the transmitter and fiber core, where affect of this will be discussed later in this section.

2. *Launching beam intensity profile*: This refers to how the incident optical power (or intensity) varies across the launched beam spot. It decides the strength of each excited mode. If the optical power at a particular angle of incidence is higher, then the strength of the excited mode is higher. Launching conditions are classified into three categories based on the intensity profile.

   (a) Gaussian excitation: In this each radial distance corresponds to a particular launched optical power. The intensity is maximum along the fiber axis and decreases, as the radial distance from the fiber axis increases. Additionally, each radial distance corresponds to a particular angle of incidence, which in turn corresponds to a particular fiber propagation angle θ as per our previous discussion. Hence, the variation of the launched optical power as a function of the propagation angle θ is as follows [291]:

   $$P(\theta) = P_0 e^{-\frac{\theta-\theta_0}{\sqrt{2}\sigma}}, \tag{6.10}$$

   where P_0 is the maximum launched intensity and θ_0 is the angular misalignment of the transmitter with respect to the fiber's axis. For an optical transmitter with a Full Width at Half Maximum (FWHM) of θ_{FWHM} we have [31]:

   $$\sigma = \frac{\theta_{FWHM}}{2\sqrt{2\log_e(2)}}. \tag{6.11}$$

   Observe from Equation 6.10 that the optical intensity of the launched signal decreases at higher propagation angles. Hence, the strength of the excitation of the higher-order modes is low.

   (b) Uniform excitation: In this the optical intensity is constant throughout the launched beam spot. Hence, all the modes that are excited have an identical strength [293]. Perfectly uniform excitation cannot be achieved using any transmitter. Hence, a mode scrambler may be used at the transmitter to ensure that an equal power is launched into all the excited modes [294].

Thus, the launch conditions decide which particular modes are excited to what strength. Thus, any launch misalignments would significantly affect light propagation through the POF, where this is discussed in the next section.

Launch misalignments: The launch misalignments primarily affect two parameters:

1. Optical transmitter to fiber coupling efficiency: Launch misalignments result in the reduction of optical transmitter-to-fiber coupling efficiency. This effect is more pronounced in overfilled launch scenarios, since any movement of the large launch beam spot results in significant loss in the coupling efficiency [73]. This is also the case for misalignments between two sections of optical fibers.

2. Optical bandwidth: The bandwidth of the optical fiber is higher, when fewer modes are excited. This is because there is lower differential spread in the propagation delay of the different modes, which minimizes time dispersion. The effect of launch misalignments on the fiber's bandwidth is more pronounced in an underfilled launch than in an overfilled launch scenario [295]. As a benefit of its repeatability, the optical link's bandwidth obtained for the uniform overfilled launch condition constitutes the typical benchmark for the bandwidth of all other launch conditions. In an underfilled launch scenario only a small subset of the modes, which can be conveyed by the fiber is actually excited. When there are no misalignments, only the lower-order modes would have been excited. However, misalignments lead to the excitation of other subsets of the potentially excitable modes. Misalignments at the transmitter are of two typical types:

   (a) Angular misalignment: In this scenario the launched beam axis is not aligned with that of the optical fiber. When underfilled launching is encountered, the optical link bandwidths obtained for increasing angular misalignment obeys the following trend:

      i. Scenario A: When there is no angular misalignment, only the lower-order modes are excited. This results in the optical link bandwidth for the underfilled case being much higher than that of the overfilled scenario.

      ii. Scenario B: Any slight increase in the misalignment results in some lower-order modes and some higher-order modes. This imposes significant time dispersion, since there is a substantial difference in the propagation delay of the lower-order modes and the higher-order modes. Hence, the bandwidth of the underfilled launch drops below that of the overfilled launch [296].

      iii. Scenario C: When the angular displacement is further increased, only the higher-order modes are excited [296]. Hence, the bandwidth of the underfilled launch becomes again higher than that of the overfilled case, but lower than that in scenario A.

   It was suggested in [297] that it is better to deliberately operate in Scenario C, despite the bandwidth being lower than that in Scenario A. This is because of its higher reliance on connection errors. A system designed to operate in Scenario A might actually operate in Scenario B due to the associated connector tolerance and provide optical bandwidths, which are lower than that of the overfilled launch case.

   (b) Radial misalignment: In this case the launched beam spot is not centred around the fiber axis. When underfilled launching is carried out, the optical link bandwidths obtained upon increasing the radial misalignment follows the following trend:

      i. Scenario A: Similar to the angular misalignment, when there is no radial misalignment, only the lower order modes are excited. This results in the optical link bandwidth of the underfilled case being much higher than that of the overfilled scenario.

      ii. Scenario B: Any slight increase in the misalignment results in some lower-order modes and some higher-order modes. This again inflicts significant time dispersion, since there is a significant difference in the propagation delay of the lower-order modes and the higher-order modes. Hence, the bandwidth of the underfilled launch rapidly drops below that of the overfilled launch [298]. This typically occurs for misalignments in the range of 2 to 14 μm.

iii. Scenario C: When the angular displacement further increases, only the higher-order modes are excited [298]. This occurs for misalignments in the range of 14 to 20 μm. Hence, the bandwidth of the underfilled launch is again higher than that of the overfilled case, but lower than that in Scenario A.

It was suggested in [298] that it is better to consciously operate in Scenario C, despite the bandwidth being lower than that in Scenario A. This is because of its higher resilience to connection errors. Connector specifications allow an error of upto $6\mu m$. Thus, a system designed to operate in Scenario A might actually operate in Scenario B and provides optical bandwidths, which are less than that of the overfilled launch case.

The various modes that are excited by the optical transmitter propagate with different delays, hence resulting in modal dispersion, which will be discussed in the next section.

Modal dispersion: The transmitted signal is received via multiple modes. Each mode propagates through different path lengths via the plastic optical fiber. The mode groups which have a higher characteristic propagation angle (i.e. have a larger principal mode index) suffer from a larger number of total internal reflections within the fiber and hence propagates via a longer path. Therefore, the higher the mode-order, the longer the propagation time. Thus, the total number N_{mode} of potentially excitable modes, within the optical fiber is as follows [299]:

$$N_{mode} = \begin{cases} a^2 k_0^2 \frac{(NA)^2}{2} \left(\frac{\alpha_{GI}}{\alpha_{GI}+2} \right) & for\ GI-POF \\ a^2 k_0^2 \frac{(NA)^2}{2} & for\ SI-POF, \end{cases} \tag{6.12}$$

It can be observed from Equation (6.12) that the number of modes that can potentially propagate within the optical fiber (and hence the number of mode groups as well) increases, as the numerical aperture of the fiber or core index exponent α_{GI} of Equation (6.3) increases. It can be seen from Equation (6.12) that a step index optical fiber supports a larger number of fiber modes that a graded index POF. This results in modal dispersion being higher in SI-POF than in GI-POF. Increasing the numerical aperture increases the optical coupling efficiency, since more optical power is coupled from the optical transmitter into the fiber core, but at the same time it results in a lower bandwidth, because there are a higher number of potentially excitable modes.

One of the ways to reduce modal dispersion is to ensure that not all the modes from those which can propagate in the optical fiber are actually excited. This was discussed in earlier in this section, where it was stated that the modes being excited can be controlled by the careful choice of the launch conditions.

In the next section, we will discuss the exchange of power between the various modes of the fiber, as light propagates through the POF.

Mode coupling: The modes in a *perfect fiber* are orthogonal, i.e. there is no exchange of optical power between the modes during the course of propagation within the multimode fiber. However, the imperfections in the optical fiber result in the transfer of energy from one mode to another [73]. This phenomenon is referred to as mode coupling. The fiber imperfections that result in mode coupling are

a) connector misalignments, b) refractive index mismatch between fiber sections that are connected to each other, c) presence of impurities in the optical fiber, d) inconsistencies in the refractive index of an optical fiber, e) irregularities in the fiber geometry and f) bends in the optical fiber. Mode coupling usually results in the increase of the fiber bandwidth [73]. This is because it usually results in a reduction of the number of modes carrying a significant amount of power and hence reduces the multimode dispersion. However, the previously mentioned factors, that cause mode coupling, also result in a loss of the optical power. In the next section, we will discuss the final impairment that affects light propagation through the POF.

Differential modal attenuation: The attenuation suffered by an optical signal propagating through a fiber occurs due to : a) dissipative and scattering loss of the core and cladding materials, b) loss of optical power due to the finite with of the cladding and c) radiation loss suffered by modes, which are not fully trapped within the fiber [300]. In the above list, the third mechanism decides, whether a particular mode is a guided mode or not. The radiation loss associated with the specific modes that do not undergo total internal reflection is high and hence these modes are not guided through the fiber. The first and second loss mechanisms are also mode-dependent. Hence, the various guided modes experience varying degrees of attenuation. This phenomenon is referred to as differential mode attenuation or mode-dependent attenuation in the literature.

Having discussed the basics of POF based links, in the next section we will discuss a novel DROF link that employs POF [10].

6.2.1.5 Experimental demonstration of a plastic optical fiber based digitized radio over fiber downlink

The heterogeneous 5G networks will incorporate micro/pico-cells, where ROF constitutes an attractive optical backhaul technique for making these networks cost-effective [4, 5]. A low-complexity Radio Access Point (RAP) serves each cell of a ROF-based network, while multiple RAPs are served by a central Base Station (BS) that performs most of the uplink as well as downlink signal processing [4, 5]. The non-linearity and fiber-dispersion of the classical optical link between the BS and RAP limits both the attainable data rate as well as the employable fiber length [301, 229]. However, recently Digitized ROF (DROF) has been gaining popularity, because it is capable of overcoming these challenges [233, 302]. Additionally, there has been a growing interest in the employment of inexpensive Plastic Optical Fiber (POF) for indoor networks, where some major advantages include the ability to create a "do-it-yourself" network and a high-level of tolerance to bending [303]. The authors of [304] transmitted a 1.25 Gbits/s baseband signal over 10 meters (m) of Step-Index (SI) POF, while a UWB signal was transmitted over 50m of Graded Index (GI) POF by the authors of [305]. Again, typical in-building networks would need a few hundreds of meters of fiber. Although the typical bandwidth-length product of POFs severely limits the transmission of Radio Frequency (RF) signals through a POF, DROF techniques relax this constraint by converting the RF signal into a baseband signal with the aid of baseband sampling prior to the fiber-based transmission [302]. *Against this background, we propose for the first time a POF-based DROF link and present our first experimental results for a link that employs a 143 m long SI-POF and uncoded RF modulation at 5GHz.* We begin with a discussion of the proposed experimental architecture [10], while the results of

our experiments are presented subsequently in this section.

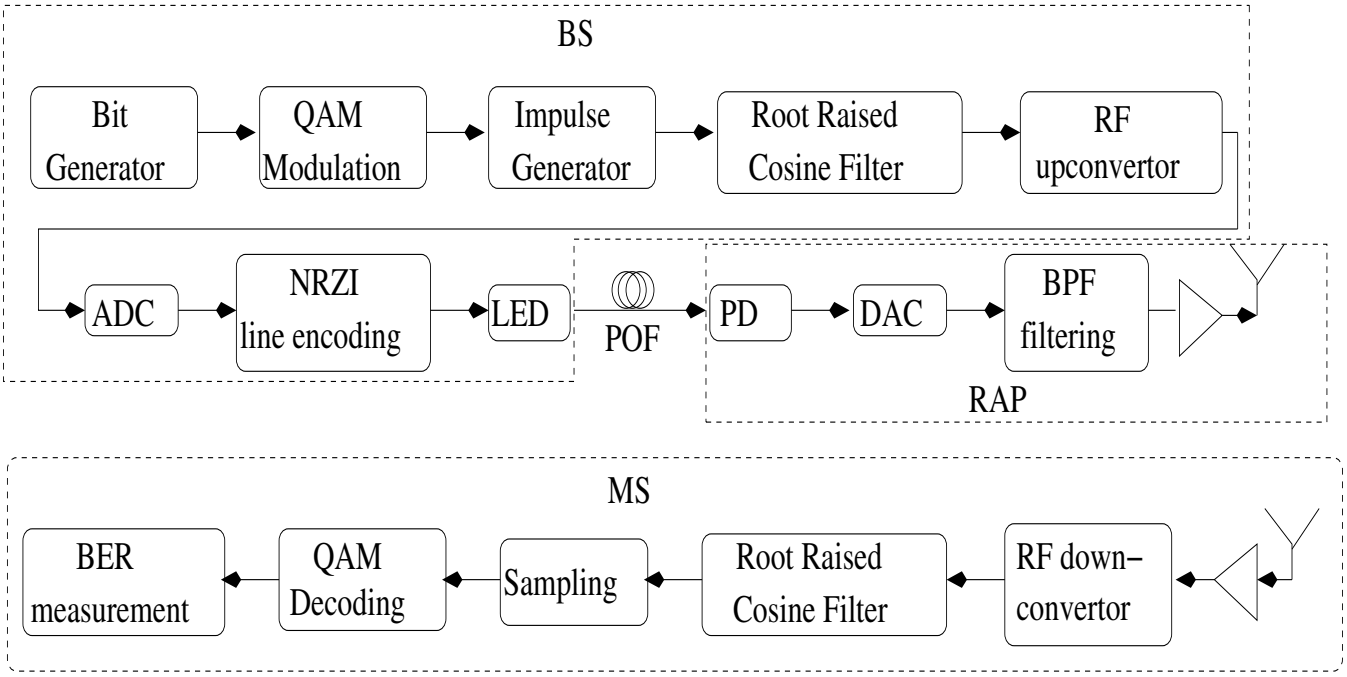

Figure 6.9: Proposed system architecture

Proposed experimental architecture: Fig. 6.9 shows the experimental set-up employed in our study, which included two computers for Matlab-based generation/detection of the RF signal and an optical link consisting of a Resonant-Cavity Light Emitting Diode (RCLED) based optical transmitter. Furthermore, a $d = 1mm$ core Polymethyl methacrylate (PMMA) SI-POF and a photodetector based optical receiver were used. In the following paragraphs, we describe the transmitter, then the fiber channel followed by the receiver.

Transmitter in the BS: We studied a downlink scenario using the transmitter of Fig. 6.9, where the transmitter generated a RF signal at $f_{RF} = 5GHz$ having a date rate of R_{bit} bits per second (bps), where employing M-QAM modulation resulted in a symbol rate of $R_s = \frac{R_{bit}}{\log_2 M}$. As shown in Fig. 6.9, a Root Raised Cosine (RRC) filter with a roll-off factor of $\alpha = 0.5$ was employed, resulting in a passband bandwidth of $B_{RF} = R_s(1 + \alpha)$. The RF signal was then digitized using an ADC having a resolution of n bits/sample and a bandpass sampling rate of f_{samp}. In order to prevent aliasing, the bandpass sampling rate f_{samp} should satisfy the following criterion [4]:

$$\frac{2(f_{RF} + \frac{B_{RF}}{2})}{k} \leq f_s \leq \frac{2(f_{RF} - \frac{B_{RF}}{2})}{k-1}, \ \forall \ 1 \leq k \leq \lfloor \frac{f_{RF} + \frac{B_{RF}}{2}}{B_{RF}} \rfloor, \tag{6.13}$$

where $\lfloor w \rfloor$ represents the integer part of w and k is an integer. Thus, when employing bandpass sampling, the sampling rate depends on the bandwidth of the signal, rather than on the highest frequency present in the signal [4].

As shown in Fig. 6.9, the digitized bits were then transmitted over the DROF link using the 100 Mbps Ethernet protocol, where a full-duplex Ethernet data rate of $R_{Ethernet} = 100$ Mbps or 1.25×10^7 bytes/second can be supported. We relied on the Ethernet protocol to ensure that our link was a

Table 6.1: RF bit rate R_{bit}(in Mbps) and BER for various scenarios

QAM	**n=1**	**n=2**	**n=3**	**n=4**	**n=5**	**n=6**
BPSK						
R_{bit}	31.30	15.61	10.43	7.82	6.26	5.22
BER	<1e-6	<1e-6	<1e-6	<1e-6	<1e-6	<1e-6
QPSK						
R_{bit}	62.60	31.22	20.86	15.64	12.52	10.44
BER	1.23e-2	8.89e-3	<1e-6	<1e-6	<1e-6	<1e-6
8-PSK						
R_{bit}	93.90	46.83	31.29	23.46	18.78	15.66
BER	1.29e-1	1.27e-1	1.06e-6	<1e-6	<1e-6	<1e-6
16-QAM						
R_{bit}	125.20	62.44	41.72	31.28	25.04	20.88
BER	1.82e-1	1.77e-1	8.39e-5	<1e-6	<1e-6	<1e-6
32-QAM						
R_{bit}	156.50	78.05	52.15	39.10	31.30	26.10
BER	2.49e-1	2.31e-1	4.50e-3	6.394e-6	<1e-6	<1e-6
64-QAM						
R_{bit}	187.80	93.66	62.58	46.92	37.56	**31.32**
BER	2.96e-1	2.85e-1	5.73e-2	4.72e-4	4.78e-6	**<1e-6**
128-QAM						
R_{bit}	219.10	109.27	73.01	54.74	43.82	36.54
BER	3.28e-1	3.16e-1	9.34e-2	9.40e-3	9.52e-5	1.25e-6

practical one, employable in the real world. The Ethernet frames were then employed for directly modulating the output of a RCLED operating at a visible light wavelength of $\lambda_c = 650nm$. As shown in Fig. 6.9, the optical modulation scheme employed was Non-Return-to-Zero Invert on ones (NRZI), where the optical power level does not change from that of the previous bit, when sending a bit '0', but inverts on the transmission of bit '1'.

The output of the RCLED was set to its maximum value of $P_{optical} = -2dBm$. Each Ethernet frame consisted of the original payload, which was 1460 bytes in our case, while the total size of the frame including the payload as well as the protocol overhead was 1538 bytes. Thus, the frame rate in our experiment was $\frac{1.25\times10^7}{1538} = 8124$ frames/sec. Accordingly, the payload data rate became $8124 \times 1460 = 11\ 861\ 040$ bytes/sec or $R_{payload} = 94.9$ Mbps. In other words, the values of f_{samp} and n should satisfy:

$$f_{samp}n = R_{payload}. \tag{6.14}$$

In the next section, we move on to discussing the POF channel.

POF channel: As shown in Fig. 6.9, our experiment employed a $d = 1mm$ core PMMA SI-POF having a core refractive index of $\eta_{core} = 1.49$ and a cladding refractive index of $\eta_{cladding} = 1.41$. The fiber diameter including the cladding was 2.2 mm, while the fiber attenuation was $\alpha = 0.19dB/m$. The maximum length of the fiber was experimentally evaluated by employing different fiber lengths,

Table 6.2: RF bit rate R_{bit}(in Mbps) and BER for various scenarios

QAM	**n=7**	**n=8**	**n=9**	**n=10**
BPSK				
R_{bit}	4.47	3.91	3.48	3.13
BER	<1e-6	<1e-6	<1e-6	<1e-6
QPSK				
R_{bit}	8.94	7.82	6.96	6.26
BER	<1e-6	<1e-6	<1e-6	<1e-6
8-PSK				
R_{bit}	13.41	11.73	10.44	9.39
BER	<1e-6	<1e-6	<1e-6	<1e-6
16-QAM				
R_{bit}	17.88	15.64	13.92	12.52
BER	<1e-6	<1e-6	<1e-6	<1e-6
32-QAM				
R_{bit}	22.35	19.55	17.40	15.65
BER	<1e-6	<1e-6	<1e-6	<1e-6
64-QAM				
R_{bit}	26.82	23.46	20.88	18.78
BER	<1e-6	<1e-6	<1e-6	<1e-6
128-QAM				
R_{bit}	31.29	27.37	24.36	21.91
BER	<1e-6	<1e-6	<1e-6	<1e-6

where it was found that our experimental setup supported a maximum length of $L = 143m$. Longer links resulted in failure of the Ethernet protocol aided transmission. It must be noted that optical propagation in a POF is of multi-mode type, where intermodal dispersion is a severe limiting factor. Having discussed both the optical transmitter and POF channel, in the next section, we discuss the optical receiver in the RAP

Receiver in the RAP: At the RAP, the photo-detected signal was filtered and then the transmitted digitized bits were detected, as shown in Fig. 6.9. These bits were then fed to an Digital-to-Analog (DAC) converter, which reconstructed a quantized version of the bandpass sampled RF signal. Filtering this bandpass sampled signal using a RF filter at f_{RF} Hz yielded the transmitted RF signal. This RF signal was then wirelessly transmitted to the MS. However, the goal of our study was to analyse the performance of the optical link. Hence, the output of the bandpass filter was then fed to the RF receiver of Fig. 6.9 that performed the downconversion, receive filtering, sampling and finally QAM detection.

Now that we have discussed all components of the proposed architecture, in the next section, we present the results of our experimental study.

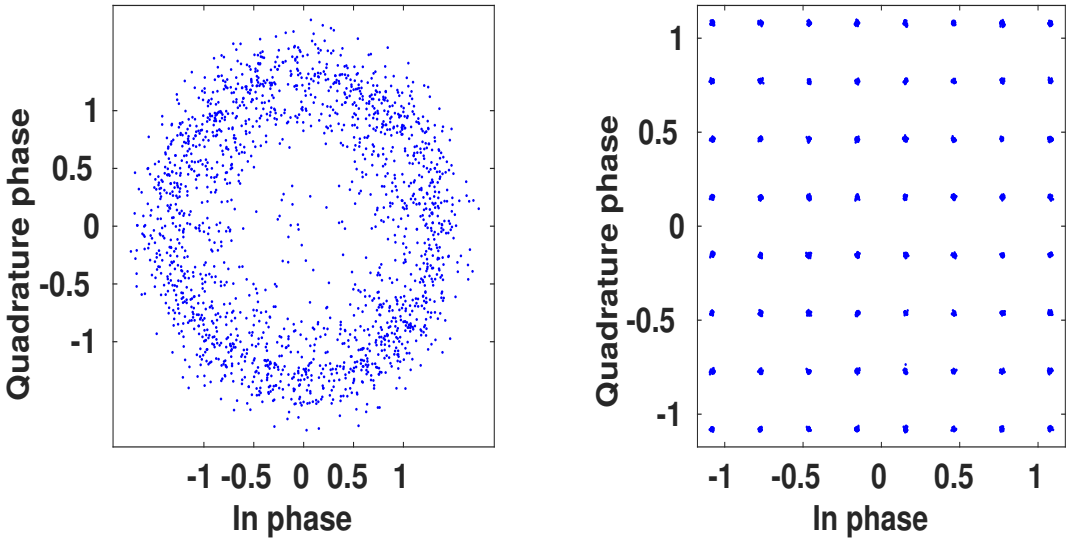

(a) ADC resolution n=1

(b) ADC resolution n=6

Figure 6.10: Experimentally received constellations using 64-QAM modulation

Experimental results and discussion: The maximum supported length of the fiber for the digital optical link described in the previous section was experimentally found to be 143 m, which depends on the minimum optical power needed for the successful operation of the Ethernet protocol in the receiver. The length of 143 m ensured error free transmission of the digitized bits using the Ethernet protocol. Thus, the BER of the DROF link would be decided by the impairments imposed by the wireless link, provided the quantization noise was not the dominant source of noise. Hence, we decided to ensure that the BER imposed by the quantization noise alone was less than 10^{-6}. To experimentally measure this BER, wireless transmission was not performed in the experimental setup of Fig. 6.9. Instead, the signal was demodulated and detected in the RAP itself. Note that we employed an uncoded RF signal in our experiments, dispensing with channel coding.

For a particular ADC resolution n, we can calculate f_{samp} using (6.14). Once we know f_{samp}, we can compute the maximum feasible B and hence R_s. Having computed R_s, we can then compute R_{bit} for each M-ary QAM scheme through $R_{bit} = R_s \log_2 M$. Finally, we experimentally transmit the RF signal at the calculated R_{bit} and calculate the BER. Table 6.1 and 6.2 shows the experimentally obtained BER imposed by the DROF link for different values of ADC resolution, when employing different M-ary QAM schemes.

Increasing the modulation order increases the minimum n needed for obtaining a quantization-induced BER of less than 10^{-6}. The final payload rate is fixed by the Ethernet protocol. Hence, the requirement of employing a higher n reduces the usable bandpass sampling rate f_{samp}, as per (6.14). A reduced bandpass sampling rate translates to a reduced employable RF bandwidth B and a lower RF symbol rate R_s. Thus, increasing the modulation order increases the number of bits per symbol $\log_2 M$, but reduces the employable R_s. Since, the bit rate $R_{bit} = R_s \log_2 M$, there is an optimum pair of modulation order and ADC resolution that maximises the bit rate under the constraint of the quantization-induced BER having to be less than 10^{-6}. As seen from Table 6.1, this combination was experimentally found to be a 64-QAM RF signal and $n = 6$, where the RF signal could have a

bit rate of upto 31.32 Mbps, when the Ethernet protocol imposed the constraint of the digitized bit rate having to be 100 Mbps. Fig. 6.11 summarises the main results that were obtained through the experimental study in a 3D plot. As seen once again from Fig. 6.11, employing 64-QAM and an ADC resolution of 6 bits maximized the DROF bit rate. Employing other combinations either resulted in a lower bit rate or resulted in a quantization-induced BER $> 10^{-6}$. Note that in Fig. 6.11, the throughput was set to zero for those combinations of modulations and ADC resolutions that resulted in a quantization-induced BER $> 10^{-6}$. Fig. 6.10 shows the experimentally received constellations for 64-QAM modulation, when employing an ADC resolution of n= 1 and n=6.

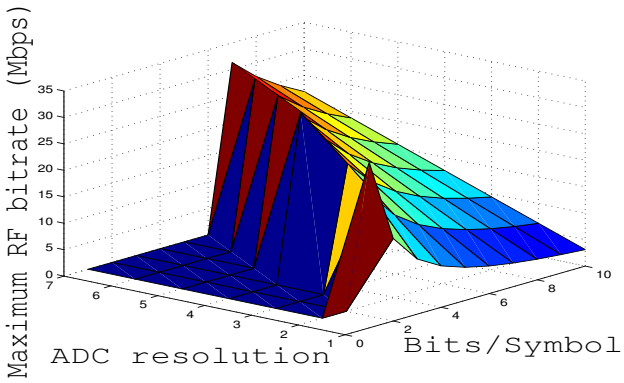

Figure 6.11: Throughput performance of POF link

Thus, we proposed for first time a POF-based DROF link, which was characterized by our initial experimental results for a link that employed a 143 m long SI-POF and an uncoded RF signal at $5GHz$. Employing the DROF technique reduced the optical bandwidth required for the POF by converting the RF signal to baseband through bandpass sampling prior to optical modulation. The DROF link was required to impose a BER of less than 10^{-6} for ensuring that the BER of the wireless channel would dominate. The highest RF bit rate-length product of $31.32 \times 10^6 \times 143$ *bps-m* was obtained for 64-QAM RF modulation and an ADC resolution of 6 bits. This RF bit rate is approximately 30% of the transmission rate of the DROF link's digitized bits. As this was the first study, the transmission of the digitized bits over the DROF link employed the classical 100 Mbps Ethernet standard. However, the procedure remains the same even when employing the 1 or 10 Gbps Ethernet standard or the architecture in [306] for the transmission of the digitized bits, where these would then support a higher RF bit rate,

In the next sections, we discuss other possible directions of future research.

6.2.2 Further research into ROF employing plastic optical fiber

The performance of a POF-based ROF link may be improved by employing innovative signal processing techniques [303]. Some possible approaches are as follows:

1. The DROF based POF link described in Section 6.2.1.5 employed the 100 Mbps Ethernet protocol for communication through the POF, which limited the bit rate of the RF signal that was employed. A similar link may be designed using the more recent 1 Gbps Ethernet protocol in

order to support a higher bit rate for the RF signal. This would be achieved at the cost of more sophisticated signal processing required for overcoming the bandwidth limitations of the fiber.

2. The DROF based POF link described in Section 6.2.1.5 may be extended to a multiuser scenario, where code division multiplexing is used for supporting the multiple users in a manner similar to our novel architecture proposed in [2]. In such an architecture, the RF signals of each user would be digitized and the resultant bit streams would be code division multiplexed, where each user is allocated a unique user-specific code in both directions. Such an architecture would be able to convert multiple RF signals into a single baseband signal. However, the errors that are imposed by multiuser interference would result in errors in the reconstructed RF signal. A simulation-based or experimental study would have to be performed in order to characterize the impact of multiuser interference imposed on the transmission of the digitized bits.

3. Sampled ROF links using POF: One of the motivations behind employing DROF in a POF based ROF link is to convert the RF signal to a baseband signal, which could then be transmitted through the bandwidth-limited POF [10]. However, one of the limitations of using DROF is the increase in the DROF bit rate with respect to the bit rate of the wireless signal, because each sample is encoded using n_{bit} bits. This fact, coupled with the low bandwidth of the POF severely limits the bit rates of the wireless signals that may be transmitted. Sampled ROF links rely on bandpass sampling the RF signal where the resultant baseband sampled signal is transmitted without any further encoding [159]. Sampled ROF transmission converts the RF signal to baseband, which would also enable the employment of POF. Sampled ROF transmission does not require a high POF bandwidth, as a benefit of dispensing with any further encoding process. The performance of such a link would be limited by the noise processes introduced by bandpass sampling [159].

4. The performance of DROF links may be improved by employing channel coding, which would result in a robust performance at a lower signal-to-noise ratio. Seminal work in this direction includes [307] and [308], where the authors of [307] employed Low Density Parity Check (LDPC) coding, while the authors of [308] employed Reed Solomon (RS) coding.

5. The frequency response of the POF is frequency selective [292],[309]. The lack of a flat-frequency response over a wide frequency range limits the bandwidth of the POF. However, the non-flat nature of the frequency response may be overcome by employing multi-carrier modulation techniques, such as Orthogonal Frequency Division Multiplexing (OFDM)[310],[311], where employing OFDM ensures a flat frequency response for each subcarrier.

6. **Coupling a microwave optical signal into a POF is challenge, which needs to be overocome for implementing AROF in POF based links. This is open research problem involving device development.**

Having discussed possible directions of future research employing POF, in the next section, we discuss a range of further avenues for future research in ROF employing glass-based optical fiber.

6.2.3 Further research into ROF employing glass-based optical fiber

Three major avenues for research in ROF links that employ glass-based optical fiber are as follows:

- **Integrating various millimeter-wave techniques with a ROF backhaul**: There are numerous open questions in integrating millimeter-wave techniques with a ROF backhaul. Experimental verification and fine-tuning of the system parameters is essential [312][313]. Employing phased array antennas and beam steering, when relying on a ROF backhaul is an example of an open area for future research [314].

- Experimental and simulation-based design of links employing RF signals compliant with wireless standards: The work in this treatise employed BPSK RF signals. However, wireless standards employ higher order QAM and also have control signalling. The hybrid AROF/DROF architecture proposed in Chapter 5 employed a CoMP-based MIMO signalling, where perfect wireless synchronization was assumed, because the aim of the study was the design of the RF link. However, synchronization in such an architecture significantly affects the performance [315]. Hence, a detailed study of ROF-based DASs incorporating the effects of synchronization has to be carried out.

- **Use of mode-division multiplexing in multimode optical fiber based ROF links**: Multimode fibers, including POF as well as glass-based multimode fibers, are in general more cost-effective than SMFs. However, they have a lower transmission capacity than a SMF. One of the approaches conceived for improving their capacity would be to employ the mode-division multiplexing, where each mode carries a different signal [316]. This approach has several challenges both in terms of the hardware needed as well as in terms of the signal processing involved. The presence of multiple modes also enables the employment of MIMO techniques through sophisticated signal processing [317].

- Optically powered RAPs: Designing optically powered RAPs is a possible direction for future research, where these RAPs would not need external electrical power supplies, such as batteries or public power lines [318].

We conclude by stating that there are numerous open areas for further research. Some of these areas include, although are not limited to, integrating various millimeter-wave techniques with a ROF backhaul [312][313], the use of mode-division multiplexing in multimode optical fibers for ROF [316], employing phased array antennas in a ROF link [314] and the use of plastic optical fiber for indoor personal area networks [303]. Multimode optical fibers, especially plastic optical fibers, are less expensive than single mode fibers. Having a large core size simplifies their connections and they can be used with low-cost LEDs and VCSELs. However, the multimode nature of their propagation inevitably limits their bandwidth and lengths. Significant research efforts have to be invested into overcoming this drawback with the aid of efficient signal processing.

Bibliography

[1] S. Ghafoor, V. A. Thomas, and L. Hanzo, "Duplex digitized transmission of 64-QAM signals over a single fiber using a single pulsed laser source," *IEEE Communications Letters*, vol. 16, pp. 1312–1315, August 2012.

[2] V. Thomas, S. Ghafoor, M. El-Hajjar, and L. Hanzo, "A full-duplex diversity-assisted hybrid analogue/digitized radio over fibre for optical/wireless integration," *IEEE Communications Letters*, vol. 17, pp. 1–4, February 2013.

[3] V. A. Thomas, S. Ghafoor, M. El-Hajjar, and L. Hanzo, "Baseband radio over fiber aided millimeter-wave distributed antenna for optical/wireless integration," *IEEE Communications Letters*, vol. 17, pp. 1012–1015, May 2013.

[4] V. Thomas, M. El-Hajjar, and L. Hanzo, "Performance improvement and cost reduction techniques for radio over fiber communications," *IEEE Communications Surveys & Tutorials*, vol. 17, pp. 627–670, May 2015.

[5] V. Thomas, M. El-Hajjar, and L. Hanzo, "Millimeter-wave radio over fiber optical upconversion techniques relying on link non-linearity," *IEEE Communications Surveys & Tutorials*, Early Access 2015.

[6] V. Thomas, M. El-Hajjar, and L. Hanzo, "Simultaneous optical phase and intensity modulation transmits independent signals in radio over fiber communication," *IEEE Communications Letters*, vol. 19, pp. 557–560, April 2015.

[7] V. Thomas, M. El-Hajjar, and L. Hanzo, "Single ODSB radio-over-fiber signal supports STBC at each RAP," *IEEE Communications Letters*, vol. 19, August 2015.

[8] V. Thomas, S. Ghafoor, M. El-Hajjar, and L. Hanzo, "Radio over fiber using radio access point for high data rate wireless personal area networks," *IEEE Microwave Magazine*, vol. 16, pp. 64–78, October 2015.

[9] V. Thomas, M. El-Hajjar, and L. Hanzo, "Optical single sideband signal generation relying on a single-drive MZM for radio over fiber communications," *Accepted for publication with minor changes by IET Communications.*

[10] V. Thomas, D. Liu, M. El-Hajjar, and L. Hanzo, "Experimental demonstration of plastic optical fibre-based digitised radio over fibre downlink," *Electronics Letters*, vol. 51, pp. 1679–1681, August 2015.

[11] V. Thomas, M. El-Hajjar, and L. Hanzo, "Error vector magnitude analysis of fading SIMO channels relying on MRC reception," *Accepted for publication with major revisions by IEEE Transactions on Communications.*

[12] V. Thomas, M. El-Hajjar, and L. Hanzo, "Error vector magnitude analysis of fading SIMO channels relying on selection combining," *To be submitted to IEEE Transactions on Vehicular Communications.*

[13] V. Thomas, M. El-Hajjar, and L. Hanzo, "Performance of Cognitive Go-back-N Hybrid ARQ Scheme," *Under preparation.*

[14] V. Thomas, M. El-Hajjar, and L. Hanzo, "Performance of Cognitive Selective Repeat Hybrid ARQ Scheme," *Under preparation.*

[15] J. O'Reilly and P. Lane, "Remote delivery of video services using mm-waves and optics," *IEEE/OSA Journal of Lightwave Technology*, vol. 12, pp. 369–375, February 1994.

[16] R. Llorente, T. Alves, M. Morant, M. Beltran, J. Perez, A. Cartaxo, and J. Marti, "Ultra-wideband radio signals distribution in FTTH networks," *IEEE Photonics Technology Letters*, vol. 20, pp. 945–947, June 2008.

[17] M. Huchard, M. Weiss, A. Pizzinat, S. Meyer, P. Guignard, and B. Charbonnier, "Ultra-broadband wireless home network based on 60-GHz WPAN cells interconnected via RoF," *IEEE/OSA Journal of Lightwave Technology*, vol. 26, pp. 2364–2372, August 2008.

[18] D. Tang, "Fiber-optic antenna remoting for multisector cellular cell sites," *IEEE International Conference on Communications*, vol. 1, pp. 76–81, June 1992.

[19] H. Harada, K. Sato, and M. Fujise, "A radio-on-fiber based millimeter-wave road-vehicle communication system by a code division multiplexing radio transmission scheme," *IEEE Transactions on Intelligent Transportation Systems*, vol. 2, pp. 165–179, December 2001.

[20] International Telecommunications Union, "World Telecommunication Development Report 2002: Reinventing Telecoms," March 2002.

[21] IEEE, "Ieee 802.11 standard," *IEEE Press.*

[22] D. M. Pozar, *Microwave and RF Design of Wireless Systems.* John Wiley and Sons, 2001.

[23] C. Lim, A. Nirmalathas, Y. Yang, D. Novak, and R .Waterhouse, "Radio-over-fiber systems," *Asia Communications and Photonics Conference and Exhibition (ACP)*, pp. 1 –10, November 2009.

[24] Y. Yang, C. Lim, and A. Nirmalathas, "Digitized RF-over-fiber technique as an efficient solution for wideband wireless OFDM delivery," *Optical Fiber Communication Conference (OFC)*, vol. 4, pp. 1–3, March 2012.

[25] A. Jung and B. Lee, "Centralized optical routing based on digitized radio-over-fiber technique for wireless backhauling," *OptoElectronics and Communications Conference (OECC)*, pp. 1–2, July 2013.

[26] J. Martinez, C. Tsekrekos, I. Tomkos, and B. Huiszoon, "Performance evaluation of a multi-layer reconfigurable optical-wireless network architecture employing digitized RoF," *Future Network Mobile Summit (FutureNetw)*, pp. 1–8, June 2011.

[27] O. Omomukuyo, M. Thakur, and J. Mitchell, "Simple 60-ghz mb-ofdm ultrawideband rof system based on remote heterodyning," *IEEE Photonics Technology Letters*, vol. 25, pp. 268–271, February 2013.

[28] X. Fernando, "Radio over fiber -an optical technique for wireless access," *IEEE Communications Society Presentation*, October 2009.

[29] S. Ghafoor and L. Hanzo, "Sub-carrier-multiplexed duplex 64-qam radio-over-fiber transmission for distributed antennas," *IEEE Communications Letters*, vol. 15, pp. 1368–1371, December 2011.

[30] W. Stephens, T. Joseph, and B. Chen, "Analog microwave fiber optic communications links," *IEEE MTT-S International Microwave Symposium Digest*, pp. 533–534, May 1984.

[31] G. P. Agrawal, "Fiber-Optic Communication Systems," *John Wiley and Sons, Third Edition, 2002.*

[32] K. Kitayama, A. Stohr, T. Kuri, R. Heinzelmann, D. Jager, and Y. Takahashi, "An approach to single optical component antenna base stations for broad-band millimeter-wave fiber-radio access systems," *IEEE Transactions on Microwave Theory and Techniques*, vol. 48, pp. 2588–2595, December 2000.

[33] L. Hanzo, L.L. Yang, E.L. Kuan,and K. Yen, "Single and Multicarrier DS-CDMA: Multi User Detection, Space-Time Spreading, Synchronization, Standards and Networking," *1st edition, John Wiley and Sons, 2003.*

[34] J.J. Vegas Olmos, T. Kuri and K. Kitayama, "Dynamic reconfigurable wdm 60-ghz millimeter-waveband radio-over-fiber access network: Architectural considerations and experiment," *IEEE/OSA Journal of Lightwave Technology*, vol. 25, pp. 3374–3380, November 2007.

[35] H. Al-Raweshidy and S. Komaki, "Radio over fiber technologies for mobile communication networks," *Artech House, First Edition, 2002.*

[36] T. Naveh, "Mobile backhaul: Fiber vs. microwave," *Ceragon White Paper*, vol. 1, pp. 1–11, October 2009.

[37] E. Dahlman, S. Parkvall, and J. Sköld, "4G: LTE/LTE-Advanced for mobile broadband," *Academic Press, 2011.*

[38] T. Kanesan, W. P. Ng, Z. Ghassemlooy, and C. Lu, "Experimental full duplex simultaneous transmission of lte over a dwdm directly modulated rof system," *IEEE/OSA Journal of Optical Communications and Networking*, vol. 6, pp. 8–17, January 2014.

[39] T. Rappaport, S. Sun, R. Mayzus, H. Zhao, Y. Azar, K. Wang, G. Wong, J. Schulz, M. Samimi, and F. Gutierrez, "Millimeter wave mobile communications for 5G cellular: it will work!," *IEEE Access*, vol. 1, pp. 335–349, May 2013.

[40] M. Attygalle, C. Lim, G. Pendock, A. Nirmalathas, and G. Edvell, "Transmission improvement in fiber wireless links using fiber bragg gratings," *IEEE Photonics Technology Letters*, vol. 17, pp. 190–192, January 2005.

[41] M. Farwell, W. Chang, and D. Huber, "Increased linear dynamic range by low biasing the mach-zehnder modulator," *IEEE Photonics Technology Letters*, vol. 5, pp. 779–782, July 1993.

[42] F. Yang, M. Marhic, and L. Kazovsky, "Nonlinear crosstalk and two countermeasures in SCM-WDM optical communication systems," *IEEE/OSA Journal of Lightwave Technology*, vol. 18, pp. 512–520, April 2000.

[43] G. Smith, D. Novak, and Z. Ahmed, "Technique for optical SSB generation to overcome dispersion penalties in fibre-radio systems," *Electronics Letters*, vol. 33, pp. 74–75, January 1997.

[44] M. Bakaul, A. Nirmalathas, C. Lim, D. Novak, and R. Waterhouse, "Simultaneous multiplexing and demultiplexing of wavelength-interleaved channels in DWDM millimeter-wave fiber-radio networks," *IEE/OSA Journal of Lightwave Technology*, vol. 24, pp. 3341–3352, September 2006.

[45] B. Masella, B. Hraimel, and X. Zhang, "Enhanced spurious-free dynamic range using mixed polarization in optical single sideband mach-zehnder modulator," *IEEE/OSA Journal of Lightwave Technology*, vol. 27, pp. 3034–3041, August 2009.

[46] A. Nirmalathas, P. Gamage, C. Lim, D. Novak, R. Waterhouse, and Y. Yang, "Digitized RF transmission over fiber," *IEEE Microwave Magazine*, vol. 10, pp. 75–81, June 2009.

[47] Z. Jia, J. Yu, A. Chowdhury, G. Ellinas, and G. K. Chang, "Simultaneous generation of independent wired and wireless services using a single modulator in millimeter-wave-band radio-over-fiber systems," *IEEE Photonics Technology Letters*, vol. 19, pp. 1691–1693, October 2007.

[48] Z. Jia, J. Yu, and G. K. Chang, "A full-duplex radio-over-fiber system based on optical carrier suppression and reuse," *IEEE Photonics Technology Letters*, vol. 18, pp. 1726–1728, August 2006.

[49] A. Chowdhury, H.-C. Chien, Y.-T. Hsueh, and G. K. Chang, "Advanced system technologies and field demonstration for in-building optical-wireless network with integrated broadband services," *IEEE/OSA Journal of Lightwave Technology*, vol. 27, pp. 1920–1927, June 2009.

[50] G. Aiello and G. Rogerson, "Ultra-wideband wireless systems," *Microwave Magazine, IEEE*, vol. 4, pp. 36–47, June 2003.

[51] T. Baykas, C.-S. Sum, Z. Lan, J. Wang, M. Rahman, H. Harada, and S. Kato, "IEEE 802.15.3c: the first IEEE wireless standard for data rates over 1 Gb/s," *IEEE Communications Magazine*, vol. 49, pp. 114–121, July 2011.

[52] J. Yao, "Photonics for ultrawideband communications," *IEEE Microwave Magazine*, vol. 10, pp. 82–95, June 2009.

[53] M. Jazayerifar, B. Cabon, and J. Salehi, "Transmission of multi-band OFDM and impulse radio ultra-wideband signals over single mode fiber," *IEEE/OSA Journal of Lightwave Technology*, vol. 26, pp. 2594–2603, August 2008.

[54] C.-T. Lin, J. Chen, P.-T. Shih, W.-J. Jiang, and S. Chi, "Ultra-high data-rate 60 GHz radio-over-fiber systems employing optical frequency multiplication and OFDM formats," *IEEE/OSA Journal of Lightwave Technology*, vol. 28, pp. 2296–2306, August 2010.

[55] F. Zeng and J. Yao, "Ultrawideband impulse radio signal generation using a high-speed electrooptic phase modulator and a fiber-bragg-grating-based frequency discriminator," *IEEE Photonics Technology Letters*, vol. 18, pp. 2062–2064, October 2006.

[56] G. H. Nguyen, B. Cabon, and Y. Le Guennec, "Generation of 60-GHz MB-OFDM signal-over-fiber by up-conversion using cascaded external modulators," *IEEE/OSA Journal of Lightwave Technology*, vol. 27, pp. 1496–1502, June 2009.

[57] C. Cox III, E. Ackerman, R. Helkey, and G. Betts, "Direct-detection analog optical links," *IEEE Transactions on Microwave Theory and Techniques*, vol. 45, pp. 1375–1383, August 1997.

[58] C. Carlsson, A. Larsson, and A. Alping, "RF transmission over multimode fibers using VCSELs-comparing standard and high-bandwidth multimode fibers," *IEEE/OSA Journal of Lightwave Technology*, vol. 22, pp. 1694 – 1700, July 2004.

[59] S. Ghafoor (Supervisor: L. Hanzo), *Radio Over Fibre Communication and Optical Baseband Signal Processing.* Transfer Report submitted in partial fulfilment of the requirements for the award of Doctor of Philosophy at the University of Southampton, June 2011.

[60] P. C. Becker, N. A. Olsson, Jay R. Simpson, "Erbium-Doped Fiber Amplifiers: Fundamentals and Technology," *Academic Press, 1999.*

[61] A. E. Siegman, "Lasers," *University Science Books*, 1986.

[62] H. Ghafouri-Shiraz, "Distributed Feedback Laser Diodes and Optical Tunable Filters," *John Wiley and Sons, New York, 2003.*

[63] J. Ma, J. Yu, C. Yu, X. Xin, J. Zeng, and L. Chen, "Fiber dispersion influence on transmission of the optical millimeter-waves generated using LN-MZM intensity modulation," *IEEE/OSA Journal of Lightwave Technology*, vol. 25, pp. 3244–3256, November 2007.

[64] R. Kalman, J. Fan, and L. Kazovsky, "Dynamic range of coherent analog fiber-optic links," *IEEE Journal ofLightwave Technology*, vol. 12, pp. 1263–1277, July 1994.

[65] G. Smith, D. Novak, and Z. Ahmed, "Overcoming chromatic-dispersion effects in fiber-wireless systems incorporating external modulators," *IEEE Transactions on Microwave Theory and Techniques*, vol. 45, pp. 1410 –1415, August 1997.

[66] F. Koyama and K. Iga, "Frequency chirping in external modulators," *IEEE/OSA Journal of Lightwave Technology*, vol. 6, pp. 87 –93, January 1988.

[67] H. Kim and A. Gnauck, "Chirp characteristics of dual-drive. mach-zehnder modulator with a finite dc extinction ratio," *IEEE Photonics Technology Letters*, vol. 14, pp. 298–300, March 2002.

[68] G. L. Li and P. K. Yu, "Optical intensity modulators for digital and analog applications," *IEEE/OSA Journal of Lightwave Technology*, vol. 21, pp. 2010–2030, September 2003.

[69] K. Ikeda, T. Kuri, and K. Kitayama, "Simultaneous three-band modulation and fiber-optic transmission of 2.5-Gb/s baseband, microwave, and 60-GHz-band signals on a single wavelength," *IEEE/OSA Journal of Lightwave Technology*, vol. 21, pp. 3194–3202, December 2003.

[70] L. Noel, D. Wake, D. Moodie, D. Marcenac, L. Westbrook, and D. Nesset, "Novel techniques for high-capacity 60-GHz fiber-radio transmission systems," *IEEE Transactions on Microwave Theory and Techniques*, vol. 45, pp. 1416–1423, August 1997.

[71] A. Stohr, K. Kitayama, and D. Jager, "Full-duplex fiber-optic RF subcarrier transmission using a dual-function modulator/photodetector," *IEEE Transactions on Microwave Theory and Techniques*, vol. 47, pp. 1338–1341, July 1999.

[72] I. Cox, C.H., E. Ackerman, G. Betts, and J. Prince, "Limits on the performance of RF-over-fiber links and their impact on device design," *IEEE Transactions on Microwave Theory and Techniques*, vol. 54, pp. 906–920, February 2006.

[73] H. J. R. Dutton, *Understanding optical communications.* IBM, 1998.

[74] G. P. Agrawal, "Nonlinear Fiber Optics," *Elsevier, Third Edition, January 2001.*

[75] L. Brillouin, *Wave Propagation And Group Velocity.* Academic Press Inc., 1960.

[76] R. Ramaswami and K. N. Savarajan, "Optical Networks: A practical Perspective," *Academic Press, 2nd Eidtion, 2002.*

[77] C. H. Lee, *Microwave Photonics.* CRC Press, 2007.

[78] E. Sackinger, "Broadband Circuits for Optical Fiber Communication," *John Wiley and Sons, First Edition, 2005.*

[79] J. O'Reilly, P. Lane, R. Heidemann, and R. Hofstetter, "Optical generation of very narrow linewidth millimetre wave signals," *Electronics Letters*, vol. 28, pp. 2309–2311, December 1992.

[80] D. K. C. MacDonald, *Noise and Fluctuations: An Introduction.* Wiley, 1962.

[81] W. R. Bennett, *Electrical Noise.* McGraw-Hill, 1960.

[82] F. N. H. Robinson, *Noise and Fluctuations in Electronic Devices and Circuits.* Oxford University Press, 1974.

[83] G. Smith and D. Novak, "Broad-band millimeter-wave (38 GHz) fiber-wireless transmission system using electrical and optical SSB modulation to overcome dispersion effects," *IEEE Photonics Technology Letters*, vol. 10, pp. 141 –143, January 1998.

[84] J. Corral, J. Marti, and J. Fuster, "General expressions for IM/DD dispersive analog optical links with external modulation or optical up-conversion in a Mach-Zehnder electrooptical modulator," *IEEE Transactions on Microwave Theory and Techniques*, vol. 49, pp. 1968–1976, October 2001.

[85] J. Park, W. Sorin, and K. Lau, "Elimination of the fibre chromatic dispersion penalty on 1550 nm millimetre-wave optical transmission," *Electronics Letters*, vol. 33, pp. 512–513, March 1997.

[86] R. Kashyap, "Fiber bragg gratings," *Academic Press, First Edition, 1999.*

[87] J. Yu, Z. Jia, L. Xu, L. Chen, T. Wang, and G. K. Chang, "DWDM optical millimeter-wave generation for radio-over-fiber using an optical phase modulator and an optical interleaver," *IEEE Photonics Technology Letters*, vol. 18, pp. 1418–1420, July 2006.

[88] M. Weiss, M. Huchard, A. Stohr, B. Charbonnier, S. Fedderwitz, and D. Jager, "60-GHz photonic millimeter-wave link for short to medium range wireless transmission up to 12.5 Gb/s," *IEEE/OSA Journal of Lightwave Technology*, vol. 26, pp. 2424–2429, August 2008.

[89] U. Gliese, S. Norskov and T. N. Nielsen, "Chromatic dispersion in fiber-optic microwave and millimeter-wave links," *IEEE Transactions on Microwave Theory and Techniques*, vol. 44, pp. 1716–1724, October 1996.

[90] R. Hui, B. Zhu, R. Huang, C. Allen, K. Demarest, and D. Richards, "Subcarrier multiplexing for high-speed optical transmission," *IEEE/OSA Journal of Lightwave Technology*, vol. 20, pp. 417–427, March 2002.

[91] V. Urick, F. Bucholtz, P. Devgan, J. McKinney, and K. Williams, "Phase modulation with interferometric detection as an alternative to intensity modulation with direct detection for analog-photonic links," *IEEE Transactions on Microwave Theory and Techniques*, vol. 55, pp. 1978–1985, September 2007.

[92] M. LaGasse and S. Thaniyavaru, "Bias-free high-dynamic-range phase-modulated fiber-optic link," *IEEE Photonics Technology Letters*, vol. 9, pp. 681–683, May 1997.

[93] H. Chi, X. Zou, and J. Yao, "Analytical models for phase-modulation-based microwave photonic systems with phase modulation to intensity modulation conversion using a dispersive device," *IEEE/OSA Journal of Lightwave Technology*, vol. 27, pp. 511–521, March 2009.

[94] J. Wyrwas and M. Wu, "Dynamic range of frequency modulated direct-detection analog fiber optic links," *IEEE/OSA Journal of Lightwave Technology*, vol. 27, pp. 5552–5562, December 2009.

[95] R. Olshansky, "Microwave subcarrier multiplexing: new approach to wideband lightwave systems," *IEEE Circuits and Devices Magazine*, vol. 4, pp. 8–14, November 1988.

[96] H. Toda, T. Yamashita, T. Kuri, and K. Kitayama, "Demultiplexing using an arrayed-waveguide grating for frequency-interleaved DWDM millimeter-wave radio-on-fiber systems," *IEEE/OSA Journal of Lightwave Technology*, vol. 21, pp. 1735–1741, August 2003.

[97] C. Oh and W. Gu, "Fiber induced distortion in a subcarrier multiplexed lightwave system," *IEEE Journal on Selected Areas in Communications*, vol. 8, pp. 1296–1303, September 1990.

[98] T. Darcie, "Subcarrier multiplexing for multiple-access lightwave networks," *IEEE/OSA Journal of Lightwave Technology*, vol. 5, pp. 1103 – 1110, August 1987.

[99] R. Olshansky, V. Lanzisera, and P. Hill, "Subcarrier multiplexed lightwave systems for broadband distribution," *IEEE/OSA Journal of Lightwave Technology*, vol. 7, pp. 1329–1342, September 1989.

[100] R. Gross and R. Olshansky, "Multichannel coherent FSK experiments using subcarrier multiplexing techniques," *IEEE/OSA Journal of Lightwave Technology*, vol. 8, pp. 406–415, March 1990.

[101] M. Phillips, T. Darcie, D. Marcuse, G. Bodeep, and N. Frigo, "Nonlinear distortion generated by dispersive transmission of chirped intensity-modulated signals," *IEEE Photonics Technology Letters*, vol. 3, pp. 481–483, May 1991.

[102] K. Iniewski, C. McCrosky and D. Minoli, "Network infrastructure and architecture: designing high-availability networks," *John Wiley and Sons, First Edition, 2008.*

[103] M. Smit and C. Van Dam, "PHASAR-based WDM-devices: principles, design and applications," *IEEE Journal of Selected Topics in Quantum Electronics*, vol. 2, no. 2, pp. 236–250, 1996.

[104] H. Uetsuka, "AWG Technologies for Dense WDM Applications," *IEEE Journal of Selected Topics in Quantum Electronics*, vol. 10, pp. 393–402, March/April 2004.

[105] C. Lim, A. Nirmalathas, D. Novak, and R. Waterhouse, "Capacity analysis for WDM fiber-radio backbones with star-tree and ring architecture incorporating wavelength interleaving," *IEEE/OSA Journal of Lightwave Technology*, vol. 21, pp. 3308–3315, December 2003.

[106] G. Castafion, G. Campuzano, and O. Tonguz, "High reliability and availability in radio over fiber networks," *Mobile networking for vehicular environments*, pp. 25–30, May 2007.

[107] J. S. Wu, J. Wu, and H. W. Tsao, "A radio-over-fiber network for microcellular system application," *IEEE Transactions on Vehicular Technology*, vol. 47, pp. 84–94, February 1998.

[108] D. Cutrer, J. Georges, T. Le, and K. Lau, "Dynamic range requirements for optical transmitters in fiber-fed microcellular networks," *IEEE Photonics Technology Letters*, vol. 7, pp. 564–566, May 1995.

[109] M. Shibutani, T. Kanai, W. Domom, W. Emura, and J. Namiki, "Optical fiber feeder for microcellular mobile communication systems (H-O15)," *IEEE Journal on Selected Areas in Communications*, vol. 11, pp. 1118–1126, September 1993.

[110] N. Pleros, K. Vyrsokinos, K. Tsagkaris, and N. Tselikas, "A 60 GHz radio-over-fiber network architecture for seamless communication with high mobility," *IEEE/OSA Journal of Lightwave Technology*, vol. 27, pp. 1957–1967, June 2009.

[111] G. K. Chang, A. Chowdhury, Z. Jia, H. C. Chien, M. F. Huang, J. Yu, and G. Ellinas, "Key technologies of WDM-PON for future converged optical broadband access networks [Invited]," *IEEE/OSA Journal of Optical Communications and Networking*, vol. 1, pp. C35–C50, September 2009.

[112] R. Ohmoto, H. Ohtsuka, and H. Ichikawa, "Fiber-optic microcell radio systems with a spectrum delivery scheme," *IEEE Journal on Selected Areas in Communications*, vol. 11, pp. 1108–1117, September 1993.

[113] R. Llorente, S. Walker, I. Monroy, M. Beltran, M. Morant, T. Quinlan, and J. Jensen, "Triple-play and 60-ghz radio-over-fiber techniques for next-generation optical access networks," *European Conference on Networks and Optical Communications (NOC)*, pp. 16–19, July 2011.

[114] "EO modulators from Thorlabs," *http://www.thorlabs.co.uk/*.

[115] H. T. Chen, P. Verheyen, P. De Heyn, G. Lepage, J. De Coster, P. Absil, G. Roelkens, and J. Van Campenhout, "High-responsivity low-voltage 28-Gbps Ge p-i-n photodetector with silicon contacts," *IEEE/ OSA Journal of Lightwave Technology*, vol. 33, pp. 820–824, February 2015.

[116] "50 GHz 1310 or 1550nm single high-speed photodetector from finisar," *https://www.finisar.com/optical-components/xpdv2320r*.

[117] P. A. Gamage, A. Nirmalathas, C. Lim, D. Novak and R. Waterhouse, "Design and Analysis of Digitized RF-Over-Fiber Links," *IEEE/OSA Journal of Lightwave Technology*, vol. 27, pp. 2052–2061, June 2009.

[118] "Defining optical modulation index," *Application note by M2optics, http://www.m2optics.com/*.

[119] E. Wooten, K. Kissa, A. Yi-Yan, E. Murphy, D. Lafaw, P. Hallemeier, D. Maack, D. Attanasio, D. Fritz, G. McBrien, and D. Bossi, "A review of lithium niobate modulators for fiber-optic communications systems," *IEEE Journal of Selected Topics in Quantum Electronics*, vol. 6, pp. 69–82, January 2000.

[120] H. Chi and J. Yao, "An Approach to Photonic Generation of High-Frequency Phase-Coded RF Pulses," *IEEE Photonics Technology Letters*, vol. 19, pp. 768–770, May 2007.

[121] M. Greenbaum, A. Kaufman, and A. Wallen, "Serrodyne frequency translation using stepped modulation waveforms," *IEEE Transactions on Aerospace and Electronic Systems*, vol. AES-10, pp. 537–538, July 1974.

[122] I. Tomita, H. Sanjoh, E. Yamada, and Y. Yoshikuni, "Novel method for generating multiple wavelengths by pulsed serrodyne modulation," *IEEE Photonics Technology Letters*, vol. 15, pp. 1204–1206, September 2003.

[123] J. Zhang, "Dual wavelength optical fiber hdtv distribution networks using self-synchronization technique and multistar topology," *IEEE Transactions on Consumer Electronics*, vol. 40, pp. 985–991, November 1994.

[124] K. P. Jackson, S. A. Newton, B. Moslehi, M. Tur, C. C. Cutler, J. W. Goodman and H. J. Shaw, "Optical fiber delay-line signal processing," *IEEE Transactions on Microwave Theory and Techniques*, vol. 33, pp. 193–210, March 1985.

[125] A. Bogris, P. Velanas and D. Syvridis, "Numerical investigation of a 160-Gb/s reconfigurable photonic logic gate based on cross-phase modulation in fibers," *IEEE Photonics Technology Letters*, vol. 19, pp. 402–404, March 2007.

[126] A. Bogoni, L. Poti, R. Proietti, G. Meloni, F. Ponzini and P. Ghelfi, "Regenerative and Reconfigurable All-Optical Logic Gates For Ultra-Fast Applications," *Electronics Letters*, vol. 41, pp. 435–436, March 2005.

[127] A. Wiberg, P. Prez-Milln, M. V. Andrs, P. A. Andrekson and P. O. Hedekvist, "Fiber-Optic 40-GHz mm-Wave Link With 2.5-Gb/s Data Transmission," *IEEE Photonics Technology Letters*, vol. 17, pp. 1938–1940, September 2005.

[128] C. Lim, A. Nirmalathas, D. Novak, R. Tucker, and R. Waterhouse, "Technique for increasing optical spectral efficiency in millimetre-wave wdm fibre-radio," *Electronics Letters*, vol. 37, pp. 1043–1045, August 2001.

[129] E. Ackerman, G. Betts, W. Burns, J. Campbell, I. Cox, C.H., N. Duan, J. Prince, M. Regan, and H. Roussell, "Signal-to-noise performance of two analog photonic links using different noise reduction techniques," *IEEE/MTT-S International Microwave Symposium*, pp. 51–54, June 2007.

[130] J. McKinney, M. Godinez, V. Urick, S. Thaniyavarn, W. Charczenko, and K. Williams, "Sub-10-dB noise figure in a multiple-GHz analog optical link," *IEEE Photonics Technology Letters*, vol. 19, pp. 465–467, April 2007.

[131] R.-P. Braun, G. Grosskopf, D. Rohde, and F. Schmidt, "Low-phase-noise millimeter-wave generation at 64 GHz and data transmission using optical sideband injection locking," *IEEE Photonics Technology Letters*, vol. 10, pp. 728–730, May 1998.

[132] L. Johansson and A. Seeds, "Generation and transmission of millimeter-wave data-modulated optical signals using an optical injection phase-lock loop," *IEEE/OSA Journal of Lightwave Technology*, vol. 21, pp. 511–520, February 2003.

[133] L. Chrostowski, X. Zhao, and C. Chang-Hasnain, "Microwave performance of optically injection-locked vcsels," *IEEE Transactions on Microwave Theory and Techniques*, vol. 54, pp. 788 – 796, February 2006.

[134] A. Ng'oma, D. Fortusini, D. Parekh, W. Yang, M. Sauer, S. Benjamin, W. Hofmann, M. Amann, and C. Chang-Hasnain, "Performance of a multi-Gb/s 60 GHz radio over fiber system employing a directly modulated optically injection-locked VCSEL," *IEEE/OSA Journal of Lightwave Technology*, vol. 28, pp. 2436–2444, August 2010.

[135] T. Ismail, C.-P. Liu, J. Mitchell, and A. Seeds, "High-dynamic-range wireless-over-fiber link using feedforward linearization," *IEEE/OSA Journal of Lightwave Technology*, vol. 25, pp. 3274–3282, November 2007.

[136] C. Lim, M. Attygalle, A. Nirmalathas, D. Novak, and R. Waterhouse, "Analysis of optical carrier-to-sideband ratio for improving transmission performance in fiber-radio links," *IEEE Transactions on Microwave Theory and Techniques*, vol. 54, pp. 2181–2187, May 2006.

[137] M. Attygalle, C. Lim, and A. Nirmalathas, "Extending optical transmission distance in fiber wireless links using passive filtering in conjunction with optimized modulation," *IEEE/OSA Journal of Lightwave Technology*, vol. 24, pp. 1703–1709, April 2006.

[138] A. Karim and J. Devenport, "Noise figure reduction in externally modulated analog fiber-optic links," *IEEE Photonics Technology Letters*, vol. 19, pp. 312–314, March 2007.

[139] R. Welstand, C. Sun, S. Pappert, Y. Liu, J. Chen, J. Zhu, A. Kellner, and P. Yu, "Enhanced linear dynamic range property of franz-keldysh effect waveguide modulator," *IEEE Photonics Technology Letters*, vol. 7, pp. 751–753, July 1995.

[140] C. Sun, S. Pappert, R. Welstand, J. Zhu, P. Yu, Y. Liu, and J. Chen, "High spurious free dynamic range fibre link using a semiconductor electroabsorption modulator," *Electronics Letters*, vol. 31, pp. 902–903, May 1995.

[141] J. Li, S. Fu, K. Xu, J. Q. Zhou, P. Shum, J. Wu, and J. Lin, "Photonic-assisted microwave frequency measurement with higher resolution and tunable range," *OSA Optics Letter*, vol. 34, pp. 743–745, March 2009.

[142] X. J. Meng, T. Chau, and M. Wu, "Improved intrinsic dynamic distortions in directly modulated semiconductor lasers by optical injection locking," *IEEE Transactions on Microwave Theory and Techniques*, vol. 47, pp. 1172–1176, July 1999.

[143] H. K. Sung, E. Lau, and M. Wu, "Optical single sideband modulation using strong optical injection-locked semiconductor lasers," *IEEE Photonics Technology Letters*, vol. 19, pp. 1005–1007, July 2007.

[144] L. Goldberg, H. Taylor, J. Weller, and D. Bloom, "Microwave signal generation with injection-locked laser diodes," *Electronics Letters*, vol. 19, pp. 491–493, June 1983.

[145] L. Johansson and A. Seeds, "36-GHz 140-Mb/s radio-over-fiber transmission using an optical injection phase-lock loop source," *IEEE Photonics Technology Letters*, vol. 13, pp. 893–895, August 2001.

[146] S. Korotky and R. De Ridder, "Dual parallel modulation schemes for low-distortion analog optical transmission," *IEEE Journal on Selected Areas in Communications*, vol. 8, pp. 1377–1381, September 1990.

[147] H. Skeie and R. V. Johnson, "Linearization of electro-optic modulators by a cascade coupling of phase-modulating electrodes," vol. 1583, pp. 153–164, December 1991.

[148] E. Ackerman, "Broad-band linearization of a mach-zehnder electrooptic modulator," *IEEE Transactions on Microwave Theory and Techniques*, vol. 47, pp. 2271–2279, December 1999.

[149] C. Lim, A. Nirmalathas, K.-L. Lee, D. Novak, and R. Waterhouse, "Intermodulation distortion improvement for fiber ndash;radio applications incorporating ossb+c modulation in an optical integrated-access environment," *IEEE/OSA Journal of Lightwave Technology*, vol. 25, pp. 1602–1612, June 2007.

[150] X. Fernando and A. Sesay, "Adaptive asymmetric linearization of radio over fiber links for wireless access," *IEEE Transactions on Vehicular Technology*, vol. 51, pp. 1576–1586, November 2002.

[151] L. Roselli, V. Borgioni, F. Zepparelli, F. Ambrosi, M. Comez, P. Faccin, and A. Casini, "Analog laser predistortion for multiservice radio-over-fiber systems," *IEEE/OSA Journal of Lightwave Technology*, vol. 21, pp. 1211–1223, May 2003.

[152] L. Johnson and H. Roussell, "Linearization of an interferometric modulator at microwave frequencies by polarization mixing," *IEEE Photonics Technology Letters*, vol. 2, pp. 810–811, November 1990.

[153] B. Haas and T. Murphy, "A simple, linearized, phase-modulated analog optical transmission system," *IEEE Photonics Technology Letters*, vol. 19, pp. 729–731, May 2007.

[154] Y. Chiu, B. Jalali, S. Garner, and W. Steier, "Broad-band electronic linearizer for externally modulated analog fiber-optic links," *IEEE Photonics Technology Letters*, vol. 11, pp. 48–50, January 1999.

[155] J. Marti, J. Fuster, and R. Laming, "Experimental reduction of chromatic dispersion effects in lightwave microwave/millimetre-wave transmissions using tapered linearly chirped fibre gratings," *Electronics Letters*, vol. 33, pp. 1170–1171, June 1997.

[156] F. Ramos, J. Marti, V. Polo, and J. Fuster, "On the use of fiber-induced self-phase modulation to reduce chromatic dispersion effects inmicrowave/millimeter-wave optical systems," *IEEE Photonics Technology Letters*, vol. 10, pp. 1473–1475, October 1998.

[157] H. Sotobayashi and K. Kitayama, "Cancellation of the signal fading for 60 GHz subcarrier multiplexed optical DSB signal transmission in nondispersion shifted fiber using midway optical phase conjugation," *IEEE/OSA Journal of Lightwave Technology*, vol. 17, pp. 2488–2497, December 1999.

[158] J. Yu, Z. Jia, L. Yi, Y. Su, G. K. Chang, and T. Wang, "Optical millimeter-wave generation or up-conversion using external modulators," *IEEE Photonics Technology Letters*, vol. 18, pp. 265–267, January 2006.

[159] Y. Yang, C. Lim, and A. Nirmalathas, "Investigation on transport schemes for efficient high-frequency broadband ofdm transmission in fibre-wireless links," *IEEE/OSA Journal of Lightwave Technology*, vol. 32, pp. 267–274, January 2014.

[160] L. Chen, Y. Shao, X. Lei, H. Wen, and S. Wen, "A novel radio-over-fiber system with wavelength reuse for upstream data connection," *IEEE Photonics Technology Letters*, vol. 19, pp. 387–389, March 2007.

[161] P. Winzer and R. Essiambre, "Advanced optical modulation formats," *Proceedings of the IEEE*, vol. 94, pp. 952–985, May 2006.

[162] D. Blumenthal, J. Laskar, R. Gaudino, S. Han, M. Shell, and M. Vaughn, "Fiber-optic links supporting baseband data and subcarrier-multiplexed control channels and the impact of MMIC photonic/microwave interfaces," *IEEE Transactions on Microwave Theory and Techniques*, vol. 45, pp. 1443–1452, August 1997.

[163] T. Kamisaka, T. Kuri, and K. Kitayama, "Simultaneous modulation and fiber-optic transmission of 10-Gb/s baseband and 60-GHz-band radio signals on a single wavelength," *IEEE Transactions on Microwave Theory and Techniques*, vol. 49, pp. 2013–2017, October 2001.

[164] Z. Jia, J. Yu, G. Ellinas, and G. K. Chang, "Key enabling technologies for optical x2013;wireless networks: Optical millimeter-wave generation, wavelength reuse, and architecture," *IEEE/OSA Journal of Lightwave Technology*, vol. 25, pp. 3452–3471, November 2007.

[165] C.-T. Lin, J. Chen, P.-C. Peng, C.-F. Peng, W.-R. Peng, B.-S. Chiou, and S. Chi, "Hybrid optical access network integrating fiber-to-the-home and radio-over-fiber systems," *IEEE Photonics Technology Letters*, vol. 19, pp. 610–612, April 2007.

[166] M. Bakaul, A. Nirmalathas, C. Lim, D. Novak, and R. Waterhouse, "Hybrid multiplexing of multiband optical access technologies towards an integrated DWDM network," *IEEE Photonics Technology Letters*, vol. 18, pp. 2311–2313, November 2006.

[167] C. Lim, A. Nirmalathas, D. Novak, R. Waterhouse, and G. Yoffe, "Millimeter-wave broadband fiber-wireless system incorporating baseband data transmission over fiber and remote lo delivery," *IEEE/OSA Journal of Lightwave Technology*, vol. 18, pp. 1355–1363, October 2000.

[168] J. Wu, J. S. Wu, and H. W. Tsao, "A fiber distribution system for microcellular radio," *IEEE Photonics Technology Letters*, vol. 6, pp. 1150–1152, September 1994.

[169] R. Welstand, S. Pappert, C. Sun, J. Zhu, Y. Liu, and P. Yu, "Dual-function electroabsorption waveguide modulator/detector for optoelectronic transceiver applications," *IEEE Photonics Technology Letters*, vol. 8, pp. 1540–1542, November 1996.

[170] L. Westbrook and D. Moodie, "Simultaneous bi-directional analogue fibre-optic transmission using an electroabsorption modulator," *Electronics Letters*, vol. 32, pp. 1806–1807, September 1996.

[171] D. Wake, D. Johansson, and D. Moodie, "Passive picocell: a new concept in wireless network infrastructure," *Electronics Letters*, vol. 33, pp. 404–406, February 1997.

[172] A. Nirmalathas, D. Novak, C. Lim, and R. Waterhouse, "Wavelength reuse in the WDM optical interface of a millimeter-wave fiber-wireless antenna base station," *IEEE Transactions on Microwave Theory and Techniques*, vol. 49, pp. 2006–2012, October 2001.

[173] T. Kuri, K. Kitayama, and Y. Takahashi, "A single light-source configuration for full-duplex 60-GHz-band radio-on-fiber system," *IEEE Transactions on Microwave Theory and Techniques*, vol. 51, pp. 431–439, February 2003.

[174] M. Bakaul, A. Nirmalathas, and C. Lim, "Multifunctional WDM optical interface for Millimeter-wave fiber-radio antenna base station," *IEEE/OSA Journal of Lightwave Technology*, vol. 23, pp. 1210–1218, March 2005.

[175] A. Kaszubowska, L. Hu, and L. Barry, "Remote downconversion with wavelength reuse for the radio/fiber uplink connection," *IEEE Photonics Technology Letters*, vol. 18, pp. 562–564, February 2006.

[176] L. Chen, H. Wen, and S. Wen, "A radio-over-fiber system with a novel scheme for millimeter-wave generation and wavelength reuse for up-link connection," *IEEE Photonics Technology Letters*, vol. 18, pp. 2056–2058, October 2006.

[177] J. Yu, Z. Jia, T. Wang, and G. Chang, "A novel radio-over-fiber configuration using optical phase modulator to generate an optical mm-wave and centralized lightwave for uplink connection," *IEEE Photonics Technology Letters*, vol. 19, pp. 140–142, February 2007.

[178] Y. Y. Won, H. C. Kwon, and S. K. Han, "1.25-Gb/s wavelength-division multiplexed single-wavelength colorless radio-on-fiber systems using reflective semiconductor optical amplifier," *IEEE/OSA Journal of Lightwave Technology*, vol. 25, pp. 3472–3478, November 2007.

[179] M. F. Huang, J. Yu, Z. Jia, and G. K. Chang, "Simultaneous generation of centralized lightwaves and double/single sideband optical millimeter-wave requiring only low-frequency local oscillator signals for radio-over-fiber systems," *IEEE/OSA Journal of Lightwave Technology*, vol. 26, pp. 2653–2662, August 2008.

[180] X. Yu, T. Gibbon, and I. Monroy, "Bidirectional radio-over-fiber system with phase-modulation downlink and RF oscillator-free uplink using a reflective SOA," *IEEE Photonics Technology Letters*, vol. 20, pp. 2180–2182, December 2008.

[181] H. C. Ji, H. Kim, and Y. C. Chung, "Full-duplex radio-over-fiber system using phase-modulated downlink and intensity-modulated uplink," *IEEE Photonics Technology Letters*, vol. 21, pp. 9–11, January 2009.

[182] T. Kuri, T. Nakasyotani, H. Toda, and K.-I. Kitayama, "Characterizations of supercontinuum light source for WDM millimeter-wave-band radio-on-fiber systems," *IEEE Photonics Technology Letters*, vol. 17, pp. 1274–1276, June 2005.

[183] T. Nakasyotani, H. Toda, T. Kuri, and K. Kitayama, "Wavelength-division-multiplexed millimeter-waveband radio-on-fiber system using a supercontinuum light source," *IEEE/OSA Journal of Lightwave Technology*, vol. 24, pp. 404–410, January 2006.

[184] P. Delfyett, S. Gee, M.-T. Choi, H. Izadpanah, W. Lee, S. Ozharar, F. Quinlan, and T. Yilmaz, "Optical frequency combs from semiconductor lasers and applications in ultrawideband signal processing and communications," *IEEE/OSA Journal of Lightwave Technology*, vol. 24, pp. 2701–2719, July 2006.

[185] Z. Jia, J. Yu, and G. K. Chang, "All-optical 16 times; 2.5 Gb/s WDM signal simultaneous upconversion based on XPM in an NOLM in ROF systems," *IEEE Photonics Technology Letters*, vol. 17, pp. 2724–2726, December 2005.

[186] C. S. Choi, H.-S. Kang, W.-Y. Choi, D.-H. Kim, and K.-S. Seo, "Photo-transistors based on InP HEMTs and their applications to millimeter-wave radio-on-fiber systems," *IEEE Transactions on Microwave Theory and Techniques*, vol. 53, pp. 256–263, January 2005.

[187] H. J. Song, J. S. Lee, and J.-I. Song, "Error-free simultaneous all-optical upconversion of WDM radio-over-fiber signals," *IEEE Photonics Technology Letters*, vol. 17, pp. 1731–1733, August 2005.

[188] C. S. Park, C. K. Oh, C. G. Lee, D.-H. Kim, and C.-S. Park, "A photonic up-converter for a WDM radio-over-fiber system using cross-absorption modulation in an EAM," *IEEE Photonics Technology Letters*, vol. 17, pp. 1950–1952, September 2005.

[189] S. J. B. Yoo, "Wavelength conversion technologies for wdm network applications," *IEEE/OSA Journal of Lightwave Technology*, vol. 14, pp. 955–966, June 1996.

[190] J. Fuster, J. Marti, J. Corral, V. Polo, and F. Ramos, "Generalized study of dispersion-induced power penalty mitigation techniques in millimeter-wave fiber-optic links," *IEEE/OSA Journal of Lightwave Technology*, vol. 18, pp. 933–940, July 2000.

[191] A. Koonen and L. Garcia, "Radio-over-MMF Techniques; part II: microwave to millimeter-wave systems," *IEEE/OSA Journal of Lightwave Technology*, vol. 26, pp. 2396–2408, August 2008.

[192] G. Qi, J. Yao, J. Seregelyi, S. Paquet, and C. Belisle, "Generation and distribution of a wide-band continuously tunable millimeter-wave signal with an optical external modulation technique," *IEEE Transactions on Microwave Theory and Techniques*, vol. 53, pp. 3090–3097, October 2005.

[193] Z. Jia, J. Yu, Y.-T. Hsueh, A. Chowdhury, H.-C. Chien, J. Buck, and G. K. Chang, "Multi-band signal generation and dispersion-tolerant transmission based on photonic frequency tripling technology for 60-GHz radio-over-fiber systems," *IEEE Photonics Technology Letters*, vol. 20, pp. 1470–1472, September 2008.

[194] J. Yu, Z. Jia, T. Wang, and G. K. Chang, "Centralized lightwave radio-over-fiber system with photonic frequency quadrupling for high-frequency millimeter-wave generation," *IEEE Photonics Technology Letters*, vol. 19, pp. 1499–1501, October 2007.

[195] J. O'Reilly and P. Lane, "Fibre-supported optical generation and delivery of 60 GHz signals ," *Electronics Letters*, vol. 30, pp. 1329–1330, August 1994.

[196] C.-T. Lin, P. T. Shih, J. Chen, W. Q. Xue, P. C. Peng, and S. Chi, "Optical millimeter-wave signal generation using frequency quadrupling technique and no optical filtering," *IEEE Photonics Technology Letters*, vol. 20, pp. 1027–1029, June 2008.

[197] M. Larrode, A. Koonen, J. Olmos, and A. Ng'Oma, "Bidirectional radio-over-fiber link employing optical frequency multiplication," *IEEE Photonics Technology Letters*, vol. 18, pp. 241–243, January 2006.

[198] P.-T. Shih, J. Chen, C.-T. Lin, W.-J. Jiang, H.-S. Huang, P.-C. Peng, and S. Chi, "Optical millimeter-wave signal generation via frequency 12-tupling," *IEEE/OSA Journal of Lightwave Technology*, vol. 28, pp. 71–78, January 2010.

[199] J. Fuster, J. Marti, and J. Corral, "Chromatic dispersion effects in electro-optical upconverted millimetre-wave fibre optic links," *Electronics Letters*, vol. 33, pp. 1969–1970, November 1997.

[200] J. Zhang, H. Chen, M. Chen, T. Wang, and S. Xie, "A photonic microwave frequency quadrupler using two cascaded intensity modulators with repetitious optical carrier suppression," *IEEE Photonics Technology Letters*, vol. 19, pp. 1057–1059, July 2007.

[201] Q. Chang, H. Fu, and Y. Su, "Simultaneous generation and transmission of downstream multi-band signals and upstream data in a bidirectional radio-over-fiber system," *IEEE Photonics Technology Letters*, vol. 20, pp. 181–183, February 2008.

[202] H. Chi and J. Yao, "Frequency quadrupling and upconversion in a radio over fiber link," *IEEE/OSA Journal of Lightwave Technology*, vol. 26, pp. 2706–2711, August 2008.

[203] K. Kojucharow, M. Sauer, H. Kaluzni, D. Sommer, F. Poegel, W. Nowak, A. Finger, and D. Ferling, "Simultaneous electrooptical upconversion, remote oscillator generation, and air transmission of multiple optical WDM channels for a 60-GHz high-capacity indoor system," *IEEE Transactions on Microwave Theory and Techniques*, vol. 47, pp. 2249–2256, December 1999.

[204] M. Larrode, A. Koonen, and J. Olmos, "Fiber-based broadband wireless access employing optical frequency multiplication," *IEEE Journal of Selected Topics in Quantum Electronics*, vol. 12, pp. 875–881, July 2006.

[205] M.Abramowitz and I. A. Stegun, "Abramowitz and stegun: handbook of mathematical functions," *National Bureau of Standards Applied Mathematics Series-55, Tenth Edition, 1972.*

[206] W. J. Jiang, C.-T. Lin, A. Ng"oma, P. T. Shih, J. Chen, M. Sauer, F. Annunziata, and S. Chi, "Simple 14-Gb/s Short-Range radio-over-fiber system employing a single-electrode MZM for 60-GHz wireless applications," *IEEE/OSA Journal of Lightwave Technology*, vol. 28, pp. 2238–2246, August 2010.

[207] Y. Le Guennec and R. Gary, "Optical frequency conversion for millimeter-wave ultra-wideband-over-fiber systems," *IEEE Photonics Technology Letters*, vol. 19, pp. 996–998, July 2007.

[208] J. H. Seo, C. S. Choi, Y. S. Kang, Y. D. Chung, J. Kim, and W. Y. Choi, "SOA-EAM frequency up/down-converters for 60-GHz bi-directional radio-on-fiber systems," *IEEE Transactions on Microwave Theory and Techniques*, vol. 54, pp. 959–966, February 2006.

[209] J. Yu, J. Gu, X. Liu, Z. Jia, and G. K. Chang, "Seamless integration of an 8 times;2.5 Gb/s WDM-PON and radio-over-fiber using all-optical up-conversion based on raman-assisted FWM," *IEEE Photonics Technology Letters*, vol. 17, pp. 1986–1988, September 2005.

[210] H. Kim, J. Song, H. Song, S. Lee, F. Breyer, B. Spinnler, and K. Petermann, "An all-optical frequency up-converter utilizing four-wave mixing in a semiconductor optical amplifier for sub-carrier multiplexed radio-over-fiber applications," *OSA Optics Express*, vol. 15, pp. 3384–3389, March 2007.

[211] J.M. Senior, "Optical fiber communications principles and practice," *Prentice Hall, Third Edition, 2009.*

[212] C. Joergensen, S. Danielsen, K. Stubkjaer, M. Schilling, K. Daub, P. Doussiere, F. Pommerau, P. Hansen, H. Poulsen, A. Kloch, M. Vaa, B. Mikkelsen, E. Lach, G. Laube, W. Idler, and K. Wunstel, "All-optical wavelength conversion at bit rates above 10 Gb/s using semiconductor optical amplifiers," *IEEE Journal of Selected Topics in Quantum Electronics*, vol. 3, pp. 1168–1180, October 1997.

[213] M. Tsuchiya and T. Hoshida, "Nonlinear photodetection scheme and its system applications to fiber-optic millimeter-wave wireless down-links," *IEEE Transactions on Microwave Theory and Techniques*, vol. 47, pp. 1342–1350, July 1999.

[214] H. Ogawa and Y. Kamiya, "Fiber-optic microwave transmission using harmonic laser mixing, optoelectronic mixing, and optically pumped mixing," *IEEE Transactions on Microwave Theory and Techniques*, vol. 39, pp. 2045–2051, December 1991.

[215] K. Williams, R. Esman, and M. Dagenais, "Nonlinearities in p-i-n microwave photodetectors," *IEEE/OSA Journal of Lightwave Technology*, vol. 14, pp. 84–96, January 1996.

[216] F. Zeng and J. Yao, "An approach to ultrawideband pulse generation and distribution over optical fiber," *IEEE Photonics Technology Letters*, vol. 18, pp. 823 –825, April 2006.

[217] W.-P. Lin and Y.-C. Chen, "Design of a new optical impulse radio system for ultra-wideband wireless communications," *IEEE Journal of Selected Topics in Quantum Electronics*, vol. 12, pp. 882–887, July 2006.

[218] H. Chen, M. Chen, T. Wang, M. Li, and S. Xie, "Methods for ultra-wideband pulse generation based on optical cross-polarization modulation," *IEEE/OSA Journal of Lightwave Technology*, vol. 26, pp. 2492–2499, August 2008.

[219] Q. Wang, F. Zeng, S. Blais, and J. Yao, "Optical ultrawideband monocycle pulse generation based on cross-gain modulation in a semiconductor optical amplifier," *Optics Letters*, vol. 31, pp. 3083–3085, November 2006.

[220] I. Lin, J. McKinney, and A. Weiner, "Photonic synthesis of broadband microwave arbitrary waveforms applicable to ultra-wideband communication," *IEEE Microwave and Wireless Components Letters*, vol. 15, pp. 226–228, April 2005.

[221] C. Wang, F. Zeng, and J. Yao, "All-fiber ultrawideband pulse generation based on spectral shaping and dispersion-induced frequency-to-time conversion," *IEEE Photonics Technology Letters*, vol. 19, pp. 137–139, February 2007.

[222] J. McKinney and A. Weiner, "Compensation of the effects of antenna dispersion on UWB waveforms via optical pulse-shaping techniques," *IEEE Transactions on Microwave Theory and Techniques*, vol. 54, pp. 1681–1686, June 2006.

[223] "Small cell forum," *http://www.smallcellforum.org/.*

[224] M. Seimetz, "Higher-order modulation for optical fiber transmission," *Springer, 2009.*

[225] L. Hanzo, S. X. Ng, T. Keller and W. Webb, "Quadrature amplitude modulation: from basics to adaptive trellis-coded, turbo-equalised and space-time coded OFDM, CDMA and MC-CDMA systems," *John Wiley and Sons, Second Edition, 2004.*

[226] T. Huynh, L. Nguyen, and L. Barry, "Delayed self-heterodyne phase noise measurements with coherent phase modulation detection," *IEEE Photonics Technology Letters*, vol. 24, pp. 249–251, February 2012.

[227] L. Hanzo, S. X. Ng, T. Keller, and W. Webb, "Quadrature amplitude modulation," *Wiley-IEEE Press, 2nd Edition, 2004.*

[228] Y. Zhang, J. Li, H. Chen, C. Yin, Y. Dai, F. Yin, and K. Xu, "Clip-and-filter-based crest factor reduction and digital predistortion for WLAN-over-fiber links," *IEEE Photonics Technology Letters*, vol. 26, pp. 2315–2318, December 2014.

[229] J. Beas, G. Castanon, I. Aldaya, A. Aragon-Zavala, and G. Campuzano, "Millimeter-wave frequency radio over fiber systems: A survey," *IEEE Communications Surveys Tutorials*, vol. 15, pp. 1593–1619, November 2013.

[230] S. Salivahanan and V. S. Kanchana Bhaaskaran, *Linear Integrated Circuits*. 1st ed. New Delhi, India.: Tata McGraw-Hill, 2008.

[231] U. A. Bakshi and A. P. Godse, *Linear IC Applications*. 1st ed. Pune, India.: Technical Publications, 2010.

[232] A. Goldsmith, *Wireless Communications*. 1st ed. NY, USA: Cambridge University Press, 2005.

[233] X. N. Fernando, *Radio over fiber for wireless communications: from fundamentals to advanced topics*. 1st ed. Chichester, U.K.: Wiley-IEEE, 2014.

[234] P. Cao, X. Hu, J. Wu, L. Zhang, X. Jiang, and Y. Su, "Photonic generation of 3-D UWB Signal using a dual-drive mach-zehnder modulator," *IEEE Photonics Technology Letters*, vol. 26, pp. 1434–1437, July 2014.

[235] S. Alamouti, "A simple transmit diversity technique for wireless communications," *IEEE Journal of Selected Areas in Communication*, vol. 16, pp. 1451–1458, October 1998.

[236] I. Amiri, S. Alavi, N. Fisal, A. Supa'at, and H. Ahmad, "All-optical generation of two IEEE 802.11n signals for 2 × 2 MIMO-RoF via MRR system," *IEEE Photonics Journal*, vol. 6, pp. 1–11, December 2014.

[237] P. M. Wala, "A new microcell architecture using digital optical transport," *Vehicular Technology Conference (VTC)*, pp. 585–588, May 1993.

[238] R. J. Essiambre, B. Mikkelsen and G. Raybon, "Intra-channel cross-phase modulation and four-wave mixing in high-speed TDM systems," *Electronics Letters*, vol. 35, pp. 1576–1577, September 1999.

[239] O. Leclerc, B. Lavigne, E. Balmefrezol, P. Brindel, L. Pierre, D. Rouvillain, and F. Seguineau, "Optical Regeneration at 40 Gb/s and beyond," *IEEE/OSA Journal of Lightwave Technology*, vol. 21, pp. 2779 – 2790, November 2003.

[240] L. Provost, C. Finot, P. Petropoulos and D. J. Richardson, "2R regeneration architectures based on multi-segmented fibres," *European Conference On Communication (ECOC)*, pp. 21–25, September 2008.

[241] M. Matsumoto, Y. Shimada and H. Sakaguchi, "Two-staged SPM-based all-optical 2R regeneration by bidirectional use of a highly nonlinear fiber," *IEEE Journal of Quantum Electronics*, vol. 45, pp. 51–58, January 2009.

[242] B-E Olsson and D. J. Blumenthal, "Pulse restoration by filtering of self-phase modulation broadened optical spectrum," *IEEE/OSA Journal of Lightwave Technology*, vol. 20, pp. 1113–1117, July 2002.

[243] J. H. Lee, T. Nagashima, T. Hasegawa, S. Ohara, N. Sugimoto and K. Kikuchi, "40 Gbit/s XOR and AND Gates using polarisation switching within 1 m-long bismuth oxide-based nonlinear fibre," *Electronics Letters*, vol. 41, pp. 1074–1075, March 2005.

[244] J. G. Proakis, "Digital communications," *McGraw-Hill International; 4th Edition*, August 2000.

[245] R. G. Vaughan, N. L. Scott and R. White, "The theory of bandpass sampling," *IEEE Transactions on Signal Processing*, vol. 39, pp. 1973–1984, September 1991.

[246] D. M. Akos, M. Stockmaster, J. B. Y. Tsui and J. Cashera, "Direct bandpass sampling of multiple distinct RF signals," *IEEE Transactions on Communications*, vol. 47, pp. 983–988, July 1999.

[247] J. G. Proakis and D. G. Manolakis, "Digital signal processing," *Pearson Education, Fourth Edition, 2007.*

[248] M. Patel, I. Darwazeh, and J. O'Reilly, "Bandpass sampling for software radio receivers, and the effect of oversampling on aperture jitter," vol. 4, pp. 1901–1905 vol.4, 2002.

[249] P. Smith, "Little known characteristics of phase noise," *Application Note, Analog Devices*, pp. 1–8, 2004.

[250] S. Ghafoor and L. Hanzo, "Reduced dispersion duplex DQPSK radio-over-fiber communications using single-laser-based multiple side-bands," *IEEE International Conference on Communications (ICC)*, pp. 1–5, June 2011.

[251] A. Cuyt, V. Peterson, B. Verdonk, H. Waadeland and W. B. Jones, *Handbook of continued fractions for special functions.* Springer, 2008.

[252] H. Chien, A. Chowdhury, Y. Hsueh, Z. Jia, S. Fan, J. Yu and G. Chang, "A novel 60-GHz millimeter-wave over fiber with independent 10-Gbps wired and wireless services on a single wavelength using PolMUX and wavelength-reuse techniques," *Conference on Optical Fiber Communication (OFC)*, pp. 1–3, March 2009.

[253] Andreas Weinert, *Plastic Optical Fibers Principles, Components, Installation.* Wiley, 2000.

[254] C. Koeppen, R. F. Shi, W. D. Chen and A. F. Garito, "Properties of plastic optical fibers," *Journal of Optical Society of America*, vol. 15, pp. 727–739, February 1998.

[255] S. C. J Lee, F. Breyer, S. Randel, R. Gaudino, G. Bosco, A. Bluschke, M. Matthews, P. Rietzsch, R. Steglich, H. van den Boom, and A. Koonen, "Discrete multitone modulation for maximizing transmission rate in step-index plastic optical fibers," *IEEE/OSA Journal of Lightwave Technology*, vol. 27, pp. 1503–1513, June 2009.

[256] C. M. Okonkwo, E. Tangdiongga, H. Yang, D. Visani, S. Loquai, R. Kruglov, B. Charbonnier, M. Ouzzif, I. Greiss, O. Ziemann, R. Gaudino and A. M. J. Koonen, "Recent results from the

eu pof-plus project: multi-gigabit transmission over 1 mm core diameter plastic optical fibers," *IEEE/OSA Journal of Lightwave Technology*, vol. 29, pp. 186–193, January 2011.

[257] A. M. J Koonen, J. Yang, J. M. S. Alfiad, X. Li and H. P. A. Van den Boom, "High-capacity data transport via large-core plastic optical fiber links using quadrature amplitude modulation," *Optical Fiber Communication and the National Fiber Optic Engineers Conference*, pp. 1–3, March 2007.

[258] Z. Bouhamri, Y. Le Guennec, J. M. Duchamp, G. Maury, A. Schimpf, V. Dobremez, L. Bidaux and B. Cabon, "Multistandard transmission over plastic optical fiber," *IEEE Transactions on Microwave Theory and Techniques*, vol. 58, pp. 3109–3116, November 2010.

[259] M.S. Ab-Rahman, H. Guna, M. H. Harun and K. Jumari, "A novel star topology POF-WDM system," *IEEE Symposium on Business, Engineering and Industrial Applications (ISBEIA)*, pp. 259–264, September 2011.

[260] R. Gaudino, "High speed optical transmission over plastic optical fibers," *European Conference on Optical Communication (ECOC)*, pp. 1–4, September 2009.

[261] J. Mateo, M. A. Losada and A. Lopez, "Application of the plastic optical fibre in domestic multimedia networks," *ICTON Mediterranean Winter Conference*, pp. 1–5, December 2009.

[262] D. Visani, C. Okonkwo, S. Loquai, H. Yang, Y. Shi, H. van den Boom, T. Ditewig, G. Tartarini, J. Lee, T. Koonen and E. Tangdiongga, "Beyond 1 Gbit/s transmission over 1 mm diameter plastic optical fiber employing DMT for in-home communication systems," *IEEE/OSA Journal of Lightwave Technology*, vol. 29, pp. 622–628, February 2011.

[263] J. B. Schlager, M. J. Hackert, P. Pepeljugoski and J. Gwinn, "Measurements for enhanced bandwidth performance over 62.5- mu;m multimode fiber in short-wavelength local area networks," *IEEE/OSA Journal of Lightwave Technology*, vol. 21, pp. 1276–1285, May 2003.

[264] C. Loyez, C. Lethien, N. Deparis, J. P. Vilcot, R. Kassi, N. Rolland, A. Goffin and P.A. Rolland, "An impulse system for 60-GHz wireless networks based on polymer optical fiber," *IEEE Photonics Technology Letters*, vol. 19, pp. 1964–1966, December 2007.

[265] Y. Koike, Y. and T. Ishigure, "High-bandwidth plastic optical fiber for fiber to the display," *IEEE/OSA Journal of Lightwave Technology*, vol. 24, pp. 4541–4553, December 2006.

[266] H. Lu, C. Chang, P. Peng, H. Su and H. Hu, "A radio-over-GI-POF transport system," *IEEE/OSA Journal of Lightwave Technology*, vol. 28, pp. 1917–1921, July 2010.

[267] C. Chang, H. Su, H. Lu, P. Peng, H. Hu, "Integrating fiber-to-the-home and POF in-door routing CATV transport system," *IEEE/OSA Journal of Lightwave Technology*, vol. 28, pp. 1864 –1869, June 2010.

[268] Jurgen C. Schlesinger, *Optical Fibers Research Advances*. Nova Publishers, 2007.

[269] H. Lu, C. Chang, P. Peng, H. Su and H. Hu, "A radio-over-GI-POF transport system," *IEEE/OSA Journal of Lightwave Technology*, vol. 28, pp. 1917–1921, July 2010.

[270] M. Atef, R. Swoboda, R. and H. Zimmermann, "1.25 Gbit/s over 50 m step-index plastic optical fiber using a fully integrated optical receiver with an tntegrated equalizer," *IEEE/OSA Journal of Lightwave Technology*, vol. 30, pp. 118–122, January 2012.

[271] S. Karabetsos, E. Pikasis, T. Nikas, A. Nassiopoulos and D. Syvridis, "DFT-spread DMT modulation for 1-Gb/s transmission rate over 100 m of 1-mm SI-POF," *IEEE Photonics Technology Letters*, vol. 24, pp. 836–838, May 2012.

[272] A. Antonino, D. Zeolla and R. Gaudino, "Experimental proof-of-concept of bidirectional gigabit transmission over single step-index plastic optical fiber," *IEEE Photonics Technology Letters*, vol. 22, pp. 923–925, June 2010.

[273] F. Breyer, S. C. J. Lee, S. Randel and N. Hani, "PAM-4 signalling for gigabit transmission over standard step-index plastic optical fibre using light emitting diodes," *European Conference on Optical Communication (ECOC)*, pp. 1–2, September 2008.

[274] S. C. Lee, F. Breyer, S. Randel, O. Ziemann, H. P .A van den Boom and A. M. J. Koonen, "Low-cost and robust 1-gigabit/s plastic optical fiber link based on light-emitting diode technology," *Optical Fiber Communication Conference (OFC)*, pp. 1–3, February 2008.

[275] P. Polishuk, "Plastic optical fibers branch out," *IEEE Communications Magazine*, vol. 44, pp. 140–148, September 2006.

[276] A. Shimura, Y. Sugawara, S. Haruyama, M. Nakagawa, H. Suzuki, A. Kondo, T. Ishigure and Y. Koike, "Train communication system using graded-index leaky plastic optical fiber," *IEEE International Conference on Industrial Technology (ICIT)*, pp. 78–83, December 2004.

[277] "Media oriented systems transport," *http://www.mostcooperation.com/.*

[278] O. Strobei, "Communication in transportation systems," *Information Science, 2010.*

[279] Yunzhi Dong and K. W. Martin, "Gigabit communications over plastic optical fiber," *IEEE Solid-State Circuits Magazine*, vol. 3, pp. 60–69, Winter Issue 2011.

[280] A. M. J. Koonen, M. G. Larrod, A. Ngoma, K. Wang, H. Yang, Y. Zheng, E. Tangdiongga, "Perspectives of radio over fiber technologies," *Optical Fiber Communication Conference (OFC)*, pp. 1–3, February 2008.

[281] Y. Shi, H. Yang, D. Visani, C. M. Okonkwo, H. P. A. van den Boom, H. Kragl, G. Tartarini, S. Randel, E. Tangdiongga and A. M. J. Koonen, "First demonstration of broadcasting high capacity data in large-core POF-based in-home networks," *European Conference on Optical Communication (ECOC)*, pp. 1–3, September 2010.

[282] T. Wipiejewski, T. Moriarty, V. Hung, P. Doyle, G. Duggan, D. Barrow, B. McGarvey, M. O'Gorman, T. Calvert, M. Maute, V. Gerhardt and J. D. Lambkin, "Gigabits in the home with plugless plastic optical fiber (POF) interconnects," *Electronics System-Integration Technology Conference (ESTC)*, pp. 1263–1266, September 2008.

[283] G. J. Grimes, L. L. Blyler Jr, C. J. Sherman, J. S. Nyquist and S. R. Peck, "Intrasystem interconnection in telecommunication platforms using plastic optical fiber," *IEEE Electronic Components & Technology Conference*, pp. 981–986, May 1998.

[284] H. Hirscher, "Triple play realization of swisscom with POF," *International Conference on Plastic Optical Fiber (ICPOF)*, September 2007.

[285] D. Visani, G. Tartarini, Y. Shi, H. Yang, C. M. Okonkwo, E. Tangdiongga and A. M. J. Koonen, "Towards converged broadband wired and wireless in-home optical networks," *International Conference on Optical Network Design and Modeling (ONDM)*, pp. 1–6, February 2011.

[286] M. Kamiya, H. Ikeda and S. Shinohara, "Wavelength-division-multiplexed analog transmission through plastic optical fiber for use in factory communications," *IEEE Transactions on Industrial Electronics*, vol. 49, pp. 507–510, April 2002.

[287] K. Wang, A. Nirmalathas, C. Lim and E. Skafidas, "Ultra-broadband indoor optical wireless communication system with multimode fiber," *OSA Optics Letters*, vol. 37, pp. 1514–1516, May 2012.

[288] J. Augustyniak, S. Binikiewicz, A. Luty and S. Patela, "The use of high brightness diodes and plastic optical fibers in high-tech lighting systems," *International Students and Young Scientists Workshop on Photonics and Microsystems*, pp. 7–11, July 2005.

[289] D. Gloge, "Optical power flow in multimode fibers," *Bell Systems Technology Journal*, vol. 51, pp. 1765–1783, October 1972.

[290] D. Gloge, "Impulse response of clad optical multimode fibres," *Bell Systems Technology Journal*, vol. 52, pp. 801–816, July 1973.

[291] M. Rousseau and L. Jeunhomme, "Numerical solution of the coupled-power equation in step-index optical fibers," *IEEE Transactions on Microwave Theory and Techniques*, vol. 25, pp. 577–585, July 1977.

[292] M. A. L. J. Mateo and J. Zubia, "Frequency response in step index plastic optical fibers obtained from the generalized power flow equation," *OSA Optics Express*, vol. 17, pp. 2850–2860, April 2009.

[293] G. Yabre, "Theoretical investigation on the dispersion of graded-index polymer optical fibers," *IEEE/OSA Journal of Lightwave Technology*, vol. 18, pp. 869–877, June 2000.

[294] J. Arrue, G. Aldabaldetreku, G. Durana, J. Zubia, I. Garces, and F. Jimenez, "Design of mode scramblers for step-index and graded-index plastic optical fibers," *IEEE/ OSA Journal of Lightwave Technology*, vol. 23, pp. 1253 – 1260, March 2005.

[295] D. Donlagic, "Opportunities to enhance multimode fiber links by application of overfilled launch," *IEEE/OSA Journal of Lightwave Technology*, vol. 23, pp. 3526–3540, November 2005.

[296] D. G. C. L. Raddatz, I. H. White and M. C. Nowell, "An experimental and theoretical study of the offset launch technique for the enhancement of the bandwidth of multimode fiber links," *IEEE/OSA Journal of Lightwave Technology*, vol. 16, pp. 324–331, March 1998.

[297] Z. Haas and M. Santoro, "An experimental and theoretical study of the offset launch technique for the enhancement of the bandwidth of multimode fiber links," *U.S. Patent*, no. 44318, 1993.

[298] D. G. C. L. Raddatz, I. H. White and M. C. Nowell, "Influence of restricted mode excitation on bandwidth of multimode fiber links," *IEEE Photonics Technology Letters*, vol. 10, pp. 534–536, April 1998.

[299] R. Olshansky, "Mode coupling effects in graded-index optical fibers," *OSA Journal of Applied Optics*, vol. 14, pp. 935–945, April 1975.

[300] D. Gloge, "Propagation effects in optical fibers," *IEEE Transactions on Microwave Theory and Techniques*, vol. 23, pp. 106–120, January 1975.

[301] S. Pinter and X. Fernando, "Concatenated fibre-wireless channel identification in a multiuser CDMA environment," *IET Communications*, vol. 1, pp. 937–944, September 2007.

[302] Y. Yang, C. Lim, and A. Nirmalathas, "Comparison of energy consumption of integrated optical-wireless access networks," *Optical Fiber Communication Conference (OFC)*, pp. 1–3, March 2011.

[303] A. Koonen and E. Tangdiongga, "Photonic home area networks," *IEEE/OSA Journal of Lightwave Technology*, vol. 32, pp. 591–604, February 2014.

[304] S. Lee, F. Breyer, D. Cardenas, S. Randel, and A. Koonen, "Real-time gigabit DMT transmission over plastic optical fibre," *Electronics Letters*, vol. 45, pp. 1342–1343, December 2009.

[305] H. Yang, Y. Shi, W. Wang, C. Okonkwo, H. van den Boom, A. Koonen, and E. Tangdiongga, "WiMedia-compliant UWB transmission over 1 mm core diameter plastic optical fibre," *Electronics Letters*, vol. 46, pp. 434–436, March 2010.

[306] R. Gandhi, A. Polley, and S. Ralph, "40 Gbps short reach links using plastic optical fiber," *19th Annual Meeting of the IEEE Lasers and Electro-Optics Society*, pp. 637–638, October 2006.

[307] I. Djordjevic, "LDPC-Coded OFDM transmission over graded-index plastic optical fiber links," *IEEE Photonics Technology Letters*, vol. 19, pp. 871–873, June 2007.

[308] A. Nespola, S. Straullu, P. Savio, D. Zeolla, S. Abrate, D. Cardenas, J. Ramirez, N. Campione, and R. Gaudino, "First demonstration of real-time LED-based Gigabit ethernet transmission on 50m of A4a.2 SI-POF with significant system margin," *Optical Communication (ECOC), 2010 36th European Conference and Exhibition on*, pp. 1–3, September 2010.

[309] K. Nehashi and Y. Koike, "Power flow equation analysis of graded-index polymer optical fibers," *SPIE OPTO: Integrated Optoelectronic Devices*, pp. 721318–721318, 2009.

[310] L. Peng, M. Helard, S. Haese, M. Liu, and J.-F. Helard, "Hybrid PN-ZP-DMT scheme for spectrum-efficient optical communications and its application to SI-POF," *IEEE/ OSA Journal of Lightwave Technology*, vol. 32, pp. 3149–3160, September 2014.

[311] C.-Y. Lin, C.-Y. Li, H.-H. Lu, C.-H. Chang, P.-C. Peng, C.-R. Lin, and J.-H. Chen, "A hybrid CATV/16-QAM-OFDM in-house network over SMF and GI-POF/VLC transport," *IEEE Photonics Technology Letters*, vol. 27, pp. 526–529, March 2015.

[312] H.-T. Huang, C.-T. Lin, Y.-T. Chiang, C.-C. Wei, and C.-H. Ho, "Simple 2x2 MIMO 60-GHz optical/wireless system with extending fiber transmission distance," *IEEE/OSA Journal of Lightwave Technology*, vol. 32, pp. 3660–3667, October 2014.

[313] S. Mikroulis, O. Omomukuyo, M. Thakur, and J. Mitchell, "Investigation of a SMF-MMF Link for a remote heterodyne 60-GHz OFDM RoF based gigabit wireless access topology," *IEEE/OSA Journal of Lightwave Technology*, vol. 32, pp. 3645–3653, October 2014.

[314] K. Lau, G. Lutes, and R. Tjoelker, "Ultra-stable RF-over-fiber transport in NASA antennas, phased arrays and radars," *IEEE/OSA Journal of Lightwave Technology*, vol. 32, pp. 3440–3451, October 2014.

[315] P. Marsch and G. P. Fettweis, "Coordinated Multi-Point in Mobile Communications," *Cambridge University Press, First Edition, 2011.*

[316] G. Gordon, M. Crisp, R. Penty, T. Wilkinson, and I. White, "Feasibility demonstration of a mode-division multiplexed MIMO-enabled radio-over-fiber distributed antenna system," *IEEE/OSA Journal of Lightwave Technology*, vol. 32, pp. 3521–3528, October 2014.

[317] S. Arik, J. Kahn, and K.-P. Ho, "MIMO signal processing for mode-division multiplexing: an overview of channel models and signal processing architectures," *IEEE Signal Processing Magazine*, vol. 31, pp. 25–34, March 2014.

[318] M. Matsuura and J. Sato, "Bidirectional radio-over-fiber systems using double-clad fibers for optically powered remote antenna units," *Photonics Journal, IEEE*, vol. 7, pp. 1–9, Feb 2015.